frontiers | Research Topics

Tooth enamel research: Enamel 10 and beyond

Edited by
Pamela Den Besten, Stefan Habelitz, Catherine Chaussain, Michael Lansdell Paine, Elia Beniash, Rodrigo S. Lacruz, Agnes Bloch-Zupan, Wendy J. Shaw, Henry Margolis and Meerim K. Nurbaeva

Published in
Frontiers in Physiology

ISSN 1664-8714
ISBN 978-2-8325-3607-0
DOI 10.3389/978-2-8325-3607-0

About Frontiers

Frontiers is more than just an open access publisher of scholarly articles: it is a pioneering approach to the world of academia, radically improving the way scholarly research is managed. The grand vision of Frontiers is a world where all people have an equal opportunity to seek, share and generate knowledge. Frontiers provides immediate and permanent online open access to all its publications, but this alone is not enough to realize our grand goals.

Frontiers journal series

The Frontiers journal series is a multi-tier and interdisciplinary set of open-access, online journals, promising a paradigm shift from the current review, selection and dissemination processes in academic publishing. All Frontiers journals are driven by researchers for researchers; therefore, they constitute a service to the scholarly community. At the same time, the *Frontiers journal series* operates on a revolutionary invention, the tiered publishing system, initially addressing specific communities of scholars, and gradually climbing up to broader public understanding, thus serving the interests of the lay society, too.

Dedication to quality

Each Frontiers article is a landmark of the highest quality, thanks to genuinely collaborative interactions between authors and review editors, who include some of the world's best academicians. Research must be certified by peers before entering a stream of knowledge that may eventually reach the public - and shape society; therefore, Frontiers only applies the most rigorous and unbiased reviews. Frontiers revolutionizes research publishing by freely delivering the most outstanding research, evaluated with no bias from both the academic and social point of view. By applying the most advanced information technologies, Frontiers is catapulting scholarly publishing into a new generation.

What are Frontiers Research Topics?

Frontiers Research Topics are very popular trademarks of the *Frontiers journals series*: they are collections of at least ten articles, all centered on a particular subject. With their unique mix of varied contributions from Original Research to Review Articles, Frontiers Research Topics unify the most influential researchers, the latest key findings and historical advances in a hot research area.

Find out more on how to host your own Frontiers Research Topic or contribute to one as an author by contacting the Frontiers editorial office: frontiersin.org/about/contact

Tooth enamel research: Enamel 10 and beyond

Topic editors

Pamela Den Besten — University of California, San Francisco, United States
Stefan Habelitz — University of California, San Francisco, United States
Catherine Chaussain — Université Paris Cité, France
Michael Lansdell Paine — University of Southern California, United States
Elia Beniash — University of Pittsburgh, United States
Rodrigo S. Lacruz — New York University, United States
Agnes Bloch-Zupan — Université de Strasbourg, France
Wendy J. Shaw — Pacific Northwest National Laboratory (DOE), United States
Henry Margolis — University of Pittsburgh, United States
Meerim K. Nurbaeva — Université Paris Cité, France

Citation

Besten, P. D., Habelitz, S., Chaussain, C., Paine, M. L., Beniash, E., Lacruz, R. S., Bloch-Zupan, A., Shaw, W. J., Margolis, H., Nurbaeva, M. K., eds. (2023). *Tooth enamel research: Enamel 10 and beyond*. Lausanne: Frontiers Media SA.
doi: 10.3389/978-2-8325-3607-0

Table of contents

frontiers | Frontiers in Physiology

TYPE Editorial
PUBLISHED 07 November 2023
DOI 10.3389/fphys.2023.1323504

OPEN ACCESS

EDITED AND REVIEWED BY
Thimios Mitsiadis,
University of Zurich, Switzerland

*CORRESPONDENCE
Pamela K. Den Besten,
pamela.denbesten@ucsf.edu

RECEIVED 17 October 2023
ACCEPTED 18 October 2023
PUBLISHED 07 November 2023

CITATION
Den Besten PK and Diekwisch TGH (2023), Editorial: Tooth enamel research: Enamel 10 and beyond.
Front. Physiol. 14:1323504.
doi: 10.3389/fphys.2023.1323504

Editorial: Tooth enamel research: Enamel 10 and beyond

Pamela K. Den Besten[1]* and Thomas G. H. Diekwisch[2]

[1]The Department of Orofacial Sciences at the University of California at San Francisco, San Francisco, CA, United States, [2]Eastman Institute for Oral Health, The University of Rochester, Rochester, NY, United States

KEYWORDS

enamel, amelogenesis, biomineralization, amelogene, ion transport

Editorial on the Research Topic
Tooth enamel research: Enamel 10 and beyond

Enamel 10—enamel in transition. Enamel 10 will forever be remembered as the Pandemic era enamel conference. Even though the number of COVID-19 infections was already declining by the time the meeting was finally held (May 8–11), some of the participants were still wearing masks, and social distancing, a term unheard of at any of the previous enamel meetings, was still encouraged. As part of pandemic era precautions, the meeting had to be postponed and no longer occurred at the Oglebay Research and Conference Center in Wheeling, West Virginia, but instead was held at the University of Pittsburgh, breaking with the long tradition of enamel meetings convened at locations remote from universities. And yet, the meeting still drew a remarkable number of more than 75 attendees fiercely committed to uphold the traditions of these legendary Enamel meetings giving testimony to the unbreakable spirit of conference participants and continued progress of enamel research even during a time of adversity. The papers in this Frontiers Research Topic, along with the abstracts of the presentations that can be viewed in the supplemental material, represent the state of the science of enamel research.

In the final discussion session of the meeting participants, there were reflections as to the beauty and complexity of the enamel structure, and the great work ahead to fully understand enamel structure and the biology of the cells and proteins that result in the synthesis of this unique tissue. The International Enamel symposiums, spanning from the first meeting in London in 1964 to the present, hold a history of research scientist who have made enormous contributions to the science of the field of enamel research. The proceedings of this Enamel 10 meeting includes a commemoration to one of the early heroes of enamel research, Dr. Alan G. Fincham, an early pioneer in amelogenin biochemistry and self-assembly research (Diekwisch).

In their discussions, the participants reflected on the complex systems that join together to form fully mineralized enamel, and the need for continued collaboration from scientists from different fields of research. Animal models hold great promise in understanding how individual genes, many of which were not known to have key roles in enamel formation. Characterization of these animal models requires collaboration or people sharing expertise, approaches and knowledge ranging from stem cells to structural biology. Along with *in vivo* models is the continued need to develop relevant *in vitro* models, to more directly assess cellular mechanisms. The group reflected on the translational implications of enamel research, including how enamel defects represent biomarkers for other systemic effect diseases; both environmental and genetic. The group encouraged future studies with broad

minded scientific approaches, including new opportunities in data science, and collaborations with scientists working in other organ systems.

The following is a list of categories of presentations, and the papers in each category. Further information on work that was presented at the Enamel 10 meeting can be viewed in the abstracts, that are included as a supplement to this Research Topic.

Enamel pathologies. Since the earliest years of anatomical studies, disease has been the teacher of developmental and structural insight. Two unique enamel pathologies have a critical role in health and wellbeing: molar hypoplasia and hereditary Amelogenesis imperfecta type enamel defects. Both of these conditions result in the need for extensive dental restorative treatment and frequently lead to tooth loss beginning in childhood. Molar hypoplasia, which is associated with trapped serum albumins in the tooth enamel of first permanent molars (Hubbard et al., 2021), likely due to early childhood or material events leading to hypomineralization, is highly associated with caries (Yardimci et al., 2021). In the present volume, Zhang et al. have used a machine learning approach to report on the protective association between dental fluorosis and molar hypomineralization (Zhang et al.).

Amelogenensis Imperfecta (AI) is a collection of genetic defects that result in poorly formed enamel. The Reference Centre for Rare Oral and Dental Diseases, has undertaken a re-classification of genetic data from 111 families and employed 567 genes based on their Next-generation sequencing (NGS) panel GenoDENT. This NGS study has emerged as a cost-effective approach to define the genetic basis of amelogenesis imperfecta (Rey et al., 2019; Bloch-Zupan et al.).

Amelogenin structural biology and histidines. Amelogenin structural biology has contributed greatly to our understanding of enamel development and protein/mineral interactions. While in the past, much attention has been paid to the elongated polyproline stretches at the C-terminus and the N-terminal alpha helix, this time around, the histidine-rich amelogenin stretches finally came to shine. Histidine is one of four amino acids uniquely elevated in amelogenins (Eastoe, 1963) and known for its buffering qualities and pH-dependent flexibility. In the present volume, investigators have studied the effect of histidine residues on adsorption interactions between amelogenin and apatites during mineralization (Tao et al.) and in self-assembly of the insoluble amelogenin self-assembly domain (Zhang et al.). Another study on the role of calcium on amelogenin self-assembly provided much insight into the role of calcium ions during amelogenin self-assembly (Zhang et al.; Zhang et al.).

Enamel rod formation. The unique perpendicular orientation of mammalian enamel rods is one of the hallmarks of vertebrate enamel structure (Figure 1). On a cellular level, the secretory pole of ameloblasts faces the growth end of elongating enamel rods. Relative ameloblast movement away from the secretory aspect of the elongating enamel rod facilitates the formation of the characteristic Herringbone pattern that contributes to enamel mechanical stability. Most recently, two molecules have been identified that may play a significant role in the formation of enamel prisms: i) ADAM10 and ii) the ameloblastin amphipathic helix. ADAM10 is a Disintegrin And Metalloproteinase (ADAM) family member and sheddase that cleaves anchored cell surface proteins (Shahid et al.). ADAM10 may also promote cell movement through its interactions with tetraspannins, lending credibility to a potential role in prism formation and decoupling between ameloblasts and growing prism surfaces. The discovery of ADAM10 function in prism elongation coincided with another key discovery related to enamel prism growth, the role of the Ameloblastin amphipathic helix in the regulation of several cell polarization genes, including Vangl1, Vangl2, Prickl1, ROCK1, ROCK2 and Par3 (Su et al., 2022). As a result, the amphipathic ameloblastin matrix may play a role in facilitating cell membrane interactions and ameloblast cell polarization as the onset of enamel prism formation (Su et al., 2022).

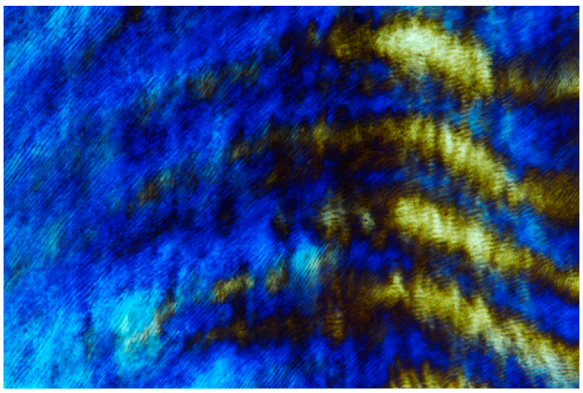

FIGURE 1
Polarization microscopic image of human enamel prisms.

Ion transport. One of the most intriguing questions in enamel research has been the question how massive amounts of calcium, phosphate and other ions are transported from the blood vessels into the mineralizing enamel layer. Pioneering studies by Lacruz and coworkers (Lacruz et al., 2017) have established the role of calcium stores (SOCE) and Ca^{2+} release activating Ca^{2+} (CRAC) channels in the control of these channels and processes by stromal interaction molecules 1 & 2 (STIM1 and 2), and the plasma membrane pore subunit of the CRAC channel ORAL1 (Lacruz et al., 2017; Said et al.). Studies in this volume (Said et al.) have demonstrated that loss of STIM1 results in a hypomineralized enamel phenotype and misregulation of several calcium transport-associated genes. Not only calcium and phosphate, but also other ions such as sodium and potassium contribute to the mineral phase of tooth enamel. New reports at the Enamel 10 symposium suggest that potassium transport is regulated by Kir4.2 in maturation ameloblasts and sodium uptake is regulated by the Na^{+}/Ca^{2+} exchanger Nckx4 (Ngu et al.). *In vitro* evidence suggests that K+ and Na2x uptake may be regulated through WDR72-mediated pH dependent endocytosis and membrane trafficking, another line of evidence for the importance of pH in amelogenesis (Ngu et al.).

Non-SCPP proteins in the enamel organ. Previous enamel meetings prominently featured temporo-spatial proteomics studies (Pandya et al., 2017) or the spatial distribution and function of non-amelogenin SCPP proteins (Diekwisch, 2011). In

contrast, the current proceedings highlighted several of the proteins in the enamel matrix previously not linked to amelogenins or SCPP proteins, including STIM1 (Said et al.) and Keratin 75 (Deshmukh et al.). These and another study related to Keratin 14 (Lu et al., 2011) pay homage to the role of keratins as epithelial structural proteins in the enamel organ as an epithelial tissue. Together, these five paragraphs feature some of the trends and highlights of Enamel X. We apologize in advance to those authors who have contributed excellent papers but whom we have not mentioned in this overview due to limitations of space.

The future: Enamel in Paris. The next enamel meeting, Enamel XI, will be organized by Drs. Sylvie Babajko and Catherine Chaussain in Paris in 2026, once more gathering enamel scientists from all over the world. It is anticipated that the current trends in enamel research will continue, especially in the areas of environmentally caused enamel defects, ion transport and enamel prism growth. Matching trends in other disciplines, such as single cell-based studies, will shed light on the contribution of individual enamel organ cells toward amelogenesis; and tissue engineering approaches will have become further advanced in terms of biological and synthetic enamel engineering. Regardless of the individual area of research, chances are that young and old enamel researchers will stroll on the shores of the river Seine and walk along the Tuileries to discuss questions about enamel research. Enamel research will have made much progress due to the multitude of models and resources available through the EnamelBase consortium (https://www.facebase.org/resources/enamelbase/), and results from studies involving all of these intriguing new model systems will be shared in the city of eternal Gothic architecture somewhere between Sainte Chapelle and Notre Dame (reconstruction anticipated in April 2024).

Author contributions

PD: Conceptualization, Writing–original draft, Writing–review and editing. TD: Conceptualization, Writing–original draft, Writing–review and editing.

Funding

The author(s) declare financial support was received for the research, authorship, and/or publication of this article. Generous support by NIDCR grant #R01DEO27972 to PD, and UG3/UH3-DE028869 to TD are gratefully acknowledged.

Conflict of interest

The authors declare that the research was conducted in the absence of any commercial or financial relationships that could be construed as a potential conflict of interest.

The author(s) declared that they were an editorial board member of Frontiers, at the time of submission. This had no impact on the peer review process and the final decision.

Publisher's note

References

Diekwisch, T. (2011). Evolution and ameloblastin. *Eur. J. Oral Sci.* 119, 293–297. doi:10.1111/j.1600-0722.2011.00931.x

Eastoe, J. (1963). The amino acid composition of proteins from the oral tissues—II: the matrix proteins in dentine and enamel from developing human deciduous teeth. *Archives Oral Biol.* 8, 633–652. doi:10.1016/0003-9969(63)90078-5

Hubbard, M. J., Mangum, J. E., Perez, V. A., and Williams, R. (2021). A breakthrough in understanding the pathogenesis of molar hypomineralisation: the mineralisation-poisoning model. *Front. Physiology* 12, 2316. doi:10.3389/fphys.2021.802833

Lacruz, R. S., Habelitz, S., Wright, J. T., and Paine, M. L. (2017). Dental enamel formation and implications for oral health and disease. *Physiol. Rev.* 97, 939–993. doi:10.1152/physrev.00030.2016

Lu, X., Ito, Y., Kulkarni, A., Gibson, C., Luan, X., and Diekwisch, T. G. (2011). Ameloblastin-rich enamel matrix favors short and randomly oriented apatite crystals. *Eur. J. oral Sci.* 119, 254–260. doi:10.1111/j.1600-0722.2011.00905.x

Pandya, M., Liu, H., Dangaria, S. J., Zhu, W., Li, L. L., Pan, S., et al. (2017). Integrative temporo-spatial, mineralogic, spectroscopic, and proteomic analysis of postnatal enamel development in teeth with limited growth. *Front. Physiology* 8, 793. doi:10.3389/fphys.2017.00793

Rey, T., Tarabeux, J., Gerard, B., Delbarre, M., Le Béchec, A., Stoetzel, C., et al. (2019). Protocol GenoDENT: implementation of a new NGS panel for molecular diagnosis of genetic disorders with orodental involvement. *Odontogenesis Methods Protoc.* 2019, 407–452. doi:10.1007/978-1-4939-9012-2_36

Su, J., Bapat, R. A., Visakan, G., and Moradian-Oldak, J. (2022). Coemergence of the amphipathic helix on ameloblastin with mammalian prismatic enamel. *Mol. Biol. Evol.* 39, msac205. doi:10.1093/molbev/msac205

Yardimci, H., Aslan Çin, N. N., and Özçelik, A. Ö. (2021). Is there an impact of social factors and food on early childhood caries? A cross-sectional study. *Sage Open* 11, 2158244021997413. doi:10.1177/2158244021997413

frontiers | Frontiers in Physiology

TYPE Original Research
PUBLISHED 24 October 2022
DOI 10.3389/fphys.2022.993674

OPEN ACCESS

EDITED BY
Michael Lansdell Paine,
University of Southern California,
United States

REVIEWED BY
Adriana Bona Matos,
University of São Paulo, Brazil
Asmaa Aly Yassen,
Cairo University, Egypt

*CORRESPONDENCE
P. E. Lancaster,
p.e.lancaster@leeds.ac.uk

SPECIALTY SECTION
This article was submitted to Craniofacial Biology and Dental Research,
a section of the journal Frontiers in Physiology

RECEIVED 13 July 2022
ACCEPTED 20 September 2022
PUBLISHED 24 October 2022

CITATION
Lancaster PE, Carmichael FA, Clerehugh V and Brettle DS (2022), Emissivity evaluation of human enamel and dentin.
Front. Physiol. 13:993674.
doi: 10.3389/fphys.2022.993674

Emissivity evaluation of human enamel and dentin

P. E. Lancaster[1]*, F. A. Carmichael[2], V. Clerehugh[1] and D. S. Brettle[3]

[1]Department of Restorative Dentistry, School of Dentistry, University of Leeds, Leeds, United Kingdom, [2]Department of Dental and Maxillofacial Radiology, Leeds Dental School, Leeds, United Kingdom, [3]Department of Medical Physics and Engineering, St. James's University Hospital, Leeds, United Kingdom

Background: Human enamel and dentin temperatures have been assessed with non-contact infrared imaging devices for safety and diagnostic capacity and require an emissivity parameter to enable absolute temperature measurements. Emissivity is a ratio of thermal energy emitted from an object of interest, compared to a perfect emitter at a given temperature and wavelength, being dependent on tissue composition, structure, and surface texture. Evaluating the emissivity of human enamel and dentin is varied in the literature and warrants review. The primary aim of this study was to evaluate the emissivity of the external and internal surface of human enamel and dentin, free from acquired or developmental defects, against a known reference point. The secondary aim was to assess the emissivity value of natural caries in enamel and dentin.

Method: Fourteen whole human molar teeth were paired within a thermally stable chamber at 30°C. Two additional teeth (one sound and one with natural occlusal caries–ICDAS caries score 4 and radiographic score RB4) were sliced and prepared as 1-mm-thick slices and placed on a hot plate at 30°C within the chamber. A 3M Scotch Super 33 + Black Vinyl Electrical Tape was used for the known emissivity reference-point of 0.96. All samples were allowed to reach thermal equilibrium, and a FLIR SC305 infrared camera recorded the warming sequence. Emissivity values were calculated using the Tape reference point and thermal camera software.

Results: The external enamel surface mean emissivity value was 0.96 (SD 0.01, 95% CI 0.96–0.97), whereas the internal enamel surface value was 0.97 (SD 0.01, 95% CI 0.96–0.98). The internal crown-dentin mean emissivity value was 0.94 (SD 0.02, 95% CI 0.92–0.95), whereas the internal root-dentin value was 0.93 (SD 0.02, 95% CI 0.91–0.94) and the surface root-dentin had a value of 0.84 (SD 0.04, 95% CI 0.77–0.91). The mean emissivity value of the internal enamel surface with caries was 0.82 (SD 0.05, 95% CI 0.38–1.25), and the value of the internal crown-dentin with caries was 0.73 (SD 0.08, 95% CI 0.54–0.92).

Conclusion: The emissivity values of sound enamel, both internal and external, were similar and higher than those of all sound dentin types in this study. Sound dentin emissivity values diminished from the crown to the root and root surface. The lowest emissivity values were recorded in caries lesions of both tissues. This methodology can improve emissivity acquisition for comparison of absolute

temperatures between studies which evaluate thermal safety concerns during dental procedures and may offer a caries diagnostic aid.

KEYWORDS

emissivity, thermal imaging, enamel, dentin, caries

1 Introduction

1.1 Infrared imaging

Infrared imaging devices (such as thermal cameras) collect emitted infrared radiation and process this to provide a quantitative temperature measurement. The use of such an infrared imaging device, that collects, rather than projects, infrared radiation to provide an absolute temperature, is based on the theory that any tissue with a temperature above absolute zero emits infrared radiation. Absolute zero (0 K or −273.15°C) is where molecular motion is predicted to cease, resulting in no emittance of infrared radiation (Gaussorgues, 1994).

With technological developments, these devices are now more affordable and accessible, and, to provide accurate temperatures, certain parameters are required, which include the emittance-value or emissivity ($\mathcal{E}$) of the object of interest.

1.2 Use of infrared imaging in dentistry

The use of non-contact infrared imaging devices to report temperature *via* thermography has benefits, which include data-collection from inaccessible areas, provision of areas of interest rather than a point of contact and avoidance of loss-of-contact during data-recording, and reduced cross-infection risk which, in turn, has a cost-benefit, compared to contact devices such as thermometers, thermocouples, and thermistors. The latter aspect of cross-infection is particularly beneficial for medical application.

With increased interest in the use of infrared imaging devices to assess the temperature of mineralized tooth tissue, it is relevant to assess the emissivity of each sample to report a valid temperature. Many *in vitro* studies have been carried out with thermal imaging devices to assess potential damage to both the soft and mineralized tooth tissue from temperature changes, e.g., during laser application (Launay, et al., 1987; Pogrel, et al., 1988; Anić, et al., 1993; Arima & Matsumoto, 1993; Neev, et al., 1993; Arrastia, et al., 1994; Anić and Matsumoto, 1995; Arrastia, et al., 1995; Machida, et al., 1995; Wilder-Smith, et al., 1995; Anić, et al., 1996a; Anić, et al., 1996b; Meyer & Foth, 1996; Neev, et al., 1996; Whitters & Strang, 2000; Yu, et al., 2000; Yamazaki, et al., 2001; Kishen, et al., 2003; Ishizaki, et al., 2004; Madura, et al., 2004; Wang, et al., 2005; Ana, et al., 2007; Da Costa Ribeiro, et al., 2007; Stock, et al., 2011; Da Silva Barbosa, et al., 2013; Uzunov, et al., 2014; Forjaz, et al., 2022), light-curing-composite (Al-Qudah, et al., 2005; Bouillaguet, et al., 2005; Aksakalli, et al., 2014; Jo, et al., 2019; Mouhat, et al., 2021), endodontic treatment (McCullagh, et al., 1997; McCullagh, et al., 2000; Behnia & McDonald, 2001; Lipski and Zapałowicz, 2002; Lipski & Woźniak, 2003; Lipski, 2004; Lipski, 2005a; Lipski, 2005b; Lipski, 2006; Hsieh, et al., 2007; Ulusoy, et al., 2015; Diegritz et al., 2020; Podolak, et al., 2020), pin-placement (Biagioni, et al., 1996), post-removal (Budd, et al., 2005; Lipski et al., 2010a), cavity preparation and restoration (Carson, et al., 1979; Lipski et al., 2020), caries assessment (Liu, et al., 2021; Roointan, et al., 2021), and bleaching (Gontijo, et al., 2008; Kabbach, et al., 2008).

A smaller number of *in vivo* studies have also assessed the temperature of tooth tissue and oral soft tissue, e.g., investigation of infection (Crandell & Hill, 1966; Pedreira, et al., 2016; Aboushady, et al., 2021), vitality (Hartley, et al., 1967; Pogrel, et al., 1989; Kells, et al., 2000b; Mendes, et al., 2020), composite curing (Hussey, et al., 1995), and tooth temperature after laser application (Arrastia, et al., 1994). A small infra-camera has been developed and used clinically to assess root caries *in vivo* (Yang et al., 2020), progressing the application of infrared imaging in clinical dentistry. However, recognition of the emissivity value of mineralized tooth tissue and the method of calculation is very varied within the dental literature, with values ranging from 0.65 to 1.0 (Table 1). Some studies report the method of emissivity assessment, some reference other studies for the transferred value, some have previously reported a value in a study, and others may not report a methodology due to space available in the article or due to prior unpublished work ascertaining the emissivity value. Diegritz, et al., 2020, stated '*it is of vital importance to determine the emissivity of the object of interest as it will affect the radiation emitted and, therefore, also affect the temperature measurement*'. Without the emissivity value, the temperature reported may be of limited value, as seen from the range of temperatures in Figure 1.

1.3 Emissivity

When the thermal stability of an object is achieved, there is a balance between the radiation entering and emitted from an object. To maintain this thermal equilibrium, when the energy is absorbed, energy must also be released, which is the emitted radiation ($\mathcal{E}$). This amount is dependent on the temperature, wavelength, material composition, and surface texture, as well as the viewing angle (Gaussorgues, 1994; Vollmer & Möllmann,

TABLE 1 Emissivity values sourced in literature to July 2022 for mineralized human tooth tissue.

Emissivity (ε)	Author	Year	Tissue (E, D, R)	*In vivo* (VV) *In vitro* (VT)	Sample S or W	Calculation method
1.0	Jo, et al.	2019	D	VT	W	Default setting of the program
0.98	Mouhat, et al.	2021	D	VT	W	Previous study by same group 2017 with no method given
0.98	Kaneko, et al.	1999	E demineralized	VT	W	Assumed
0.98	Preoteasa, et al.	2010	E	VV	W	Referenced Voicu et al., 2009
0.97	Soori, et al.	2020	E	VT	W	Thermocouple comparison 40°C–60°C
0.97	Meyer & Foth	1996	E & D	VT	S	Assumed
0.96	Soori, et al.	2020	E	VT	W	Thermocouple comparison 20°C–40°C
0.96	Lancaster, et al.	2017	E & D	VT	S	.
0.92	Liu, et al.	2021	E	VT	W	Comparison with the original reference image to ambient temperature
0.92	Soori, et al.	2020	D	VT	W	Thermocouple comparison 40°C–60°C
0.92	Dabrowski, et al.	2000	E	VT	W	Reflection method
0.92	Lee, et al.	2016a	R	VT	W	.
0.92	Lin, et al.	2010a	D	VT	S	Manufacturer's guide
0.91	Forjaz, et al.	2022	R	VT	W	Considering emissivity to be equal to 0.91
0.91	Soori, et al.	2020	E	VT	W	Thermocouple comparison 20°C–40°C
0.91	Mendes, et al.	2020	E	VV	W	Resultant from the vestibular surface of the assessed teeth
0.91	Podolak, et al.	2020	R	VT	W	Referenced Kells et al. (2000a)
0.91	Arslan, et al.	2018	R	VT	W	Calibrated to the specific root
0.91	Lee, et al.	2016b	E	VT	S	.
0.91	Lipski, et al.	2020	Roof of pulp chamber	VT	W	Referenced Kells et al. (2000a)
0.91	Lipski	2005a	R	VT	W	Referenced Kells et al. (2000a)
	Lipski, et al.	2010a				
	Lipski, et al.	2010b				
0.91	Lipski	2005b	R	VT	W	.
0.91	Lipski	2006	R	VT	W	Camera calibration
0.91	Ana, et al.	2007	E & D	VT	S	.
0.91	Da Costa Ribeiro, et al.	2007	R	VT	W	Referenced McCullagh et al. (2000)
0.91	Da Silva Barbosa, et al.	2013	E Deciduous	VT	S	Referenced Ana et al. (2007)
0.91	Kabbach, et al.	2008	RD	VT	W	.
0.91	Lin, et al.	2010a	E	VT	S	Manufacturer's guide
0.91	Kilic, et al.	2013	R	VT	W	Referenced Lipski et al. (2010a) & Kells et al. (2000a)
0.91	Ulusoy, et al.	2015	R	VT	W	.
0.9	Diegritz, et al.	2020	R	VT	W	Thermal comparison with thermocouple
0.84	Paredes, et al.	2018	E	VT	W	Reference tape
0.8	Neev, et al.	1993	D	VT	S	Black paint assumed-emissivity 1
0.65	Kells, et al.	2000a and b	E	VT/VV	W	Spot-measurement from within the hot oven and software
0.65	Kells, et al.	2000a and b	E	VT/VV	W	Spot-measurement from within the hot oven and software

E, enamel; D, dentin; R, root; RD, root-dentin; VV, *in vivo*; VT, *in vitro*; S, sectioned flat surface of a slice; W, whole tooth.

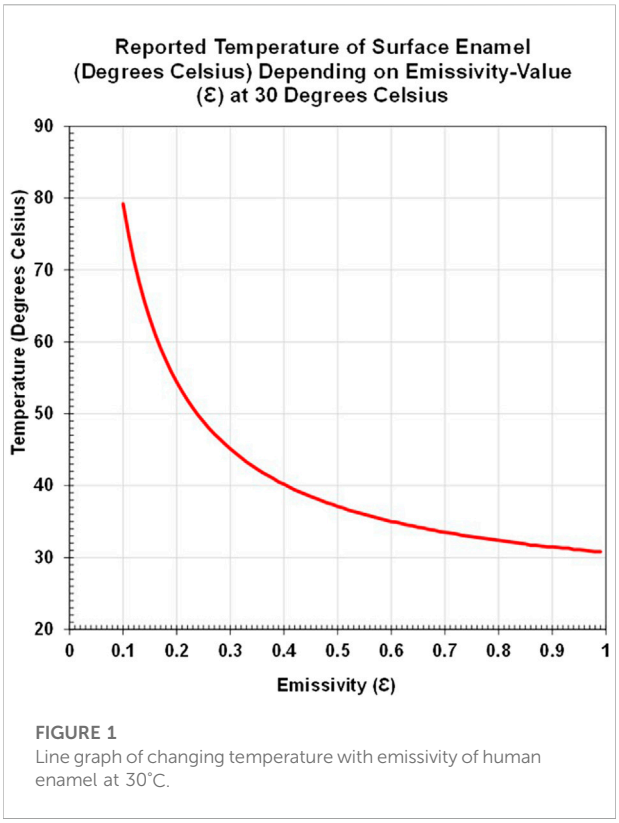

FIGURE 1
Line graph of changing temperature with emissivity of human enamel at 30°C.

2010), although the visible color of the object is not influential (Hardy, 1934).

The maximum potential value for the emitted radiation is 1 and is described for an idealistic blackbody, which theoretically absorbs all incident radiation and can subsequently emit all of it. Commercially available blackbodies have reported emittance values of 0.98 or 0.99 rather than 1, which is the highest empirical value achievable (Vollmer & Möllmann, 2010). The emissivity value, which is unitless and can range from 0 to 1, is the ratio of the emitted radiation from the surface-of-interest, compared to that emitted by a blackbody at the same wavelength and temperature.

Emissivity calculation methods may involve a blackbody, but this is expensive and often unavailable. Temperature measurement has also been described (Webb, 1991) but requires bespoke software to compute the value and an environment with known stable temperatures to assess the samples, whereas a known reference allows emissivity calculation using the thermal camera's software and is accessible to all with such a camera. Stability of the thermal environment is still an important consideration. An affordable and accessible reference, which may be a black paint or black tape with reported emissivity, e.g., 3M Scotch Super 33 + Black Vinyl Electrical Tape (≈$12 for 20 m) has a recorded value of 0.96 (British Standards, 2008; FLIR ThermaCAM™ Researcher Professional, 2010).

Emissivity may vary due to composition, tissue structure, surface contour (as seen with occlusal fissures and the natural curve of a whole tooth crown, compared to the flat internal surface of a tooth slice), and the tissue temperature and wavelength-collection of different thermal devices. Transfer of emissivity values, as seen in multiple articles (Lipski, 2005a; Da Costa Ribeiro, et al., 2007; Lipski, et al., 2010a; Lipski, et al., 2010b; Preoteasa, et al., 2010; Da Silva Barbosa, et al., 2013; Kilic, et al., 2013; Lipski et al., 2020; Podolak, et al., 2020), requires care, and a standardized approach to assess the emissivity of tooth tissue would be beneficial. As seen in Figure 1, a difference in emissivity can lead to large temperature differences. In a stable environment of ≈30°C, the surface enamel may be reported to have a temperature of 79.2°C, with an emissivity value of 0.1, whereas a temperature of 30.8°C is reported with an emissivity value of 0.99, a difference of 48.4°C. If used for assessing temperature differences with new equipment or comparing with threshold values for safety, this can lead to misleading outcomes if incorrectly applied.

Two studies were sourced in a literature search of Medline, Web of Science, and Scopus databases up to July 2022, which focused solely on emissivity values of human mineralized tooth tissue (Dabrowski, et al., 2000; Soori, et al., 2020). The recent study by Soori, et al. (2020) reported experimental estimation of human enamel and dentin emissivity to be 0.96 ± 0.01 and 0.92 ± 0.01, respectively, between 20 and 40°C, 0.97 ± 0.01, and 0.93 ± 0.01, respectively, between 40 and 60°C, which lies within previously reported values from thermal studies (Table 1) and reports the variances are due to compositional and structural differences in the tissues, as well as surface quality. Thermocouples were used internally on the teeth, which could not be applied clinically. Dabrowski, et al. (2000) reported an enamel emissivity of 0.92 and also recognized the kind of material that affects this parameter. To assist the clinical evaluation of emissivity, a non-invasive method is desirable.

1.4 Composition, structure, and surface texture of human teeth–health and caries

The composition, structure, and surface texture of the human tooth can be variable, and this will be reviewed considering the implications for the range of emissivity values for human enamel, both external surface-enamel and internal enamel visible when a tooth is sliced, internal crown and root-dentin, as well as external surface root-dentin. The impact of dental caries on the composition, structure, and surface texture is also considered as emissivity may offer an additional diagnostic tool for detecting demineralized tissue.

The human tooth has a clinical crown visible in the oral cavity and a root, invisible in the oral cavity, which attaches to the alveolar bone of the jaw *via* a soft tissue, the periodontal ligament. There are three mineralized tissues that compose a tooth: enamel,

dentin, and cementum, and one soft tissue internally encased in the mineralized tooth tissue: the pulp.

Developmentally, enamel has an epithelial origin, whereas dentin, cementum, and the alveolar bone are mesenchymal in origin. Despite different origins and final structure, which relates to tissue function, the underlying mineral of the tooth enamel, dentin, and cementum is quite similar, being calcium hydroxyapatite ($Ca_{10}(PO_4)_6(OH)_2$).

1.4.1 Enamel

During tooth development, ameloblasts produce enamel (amelogenesis) after dentin formation (dentinogenesis), commencing from odontoblasts within the central pulp-tissue. The enamel forms the external surface of the tooth exposed in the oral cavity and has a varying thickness depending on age, sex, genetics, developmental anomalies, location, and physiological and pathological wear.

The enamel is a very hard and organized tissue primarily composed of inorganic calcium hydroxyapatite ($Ca_{10}(PO_4)_6(OH)_2$) (96% by weight when mature— Goldberg, et al., 2011) and soft organic tissue, such as the non-collagenous structural proteins, amelogenin, ameloblastin, and enamelin, as well as proteinases, kallikrein-related peptidase-4 (KLK4) and matrix metalloproteinases-20 (MMP20) (Simmer, et al., 2012; Bartlett, 2013; Smith, et al., 2017). As the enamel matures, mineral content increases with the loss of protein and water, most likely resulting in a non-homogenous mineral distribution (Cuy, et al., 2002; He, et al., 2010; Zheng, et al., 2013), although Glas (1962) reported little mineral change across the enamel. This non-homogenous distribution can lead to different properties of the tissue in different places.

The structure of the enamel and dentin is quite different and can explain their different properties.

The initial layer of enamel interdigitates with dentin and has no rods. Rods are produced later with thousands of crystallites which vary in size, increasing with maturity (≈5 μm cross-section diameter—Meckel, et al., 1965), up to 40,000 crystallites per bundle, varying in thickness from 30 nm × 30 nm (Robinson, et al., 2003) and width 26 nm × 68 nm (Kerebel, et al., 1979), producing smooth surfaces extending the full width of enamel to the surface (Daculsi & Kerebel, 1978; Daculsi, et al., 1984). Between the rods are an organic rod-sheath and an interrod area of differently orientated crystals. Human rod cross-sections are key-hole-shaped, with a circular head and elongated tail. Adjacent enamel crystals have been reported to be misoriented with a range of 0–30° and a mean of 2–8° (Stifler et al., 2021), and this relates with the reported hardness of this unique tissue, which is the hardest tissue in man. This change in orientation produces Hunter–Schreger bands which are observed to be horizontal at the side of a cusp, as the rods may be viewed in cross-section or longitudinal. At the occlusal surface, a final aprismatic enamel layer (30–70 μm) overlies the radial enamel, which has rods parallel to each other and perpendicularly orientated to the surface (Speirs, 1971; Whittaker, 1982; Maas & Dumont, 1999; Popowics, et al., 2004; Cui & Ge, 2007; Risnes & Li, 2018), unlike the body of enamel. The post-secretory maturing ameloblasts secrete proteases which degrade the matrix, reducing the extracellular content from 20 to 0.4–0.6%, and with crystal growth, the peptides are removed (Goldberg, et al., 2014).

As seen, there is a difference between the cross-section internal structure of enamel compared with the outer aprismatic layer, followed by the outer radial prismatic layer and finally the inner enamel with Hunter–Schreger bands, compared to the sound intact outer surface enamel, which may be totally aprismatic (40%–47%) (Risnes & Li, 2018), with areas of the ends of radial prisms visible, or, subject to greater enamel loss, may show areas of Hunter–Schreger bands from the inner enamel (Whittaker, 1982). With sufficient enamel loss, the inner layer may be seen in the transverse section clinically. The prism-free enamel is less rough than that with prisms, especially when etched. The surface enamel on unerupted teeth shows primarily small crystals (5 nm), which are loosely packed, with a few larger plate-like crystals (1.0μm—50 nm). Following the eruption, such crystals were not observed, and aprismatic enamel had crystals of 40 nm or more (Palamara et al., 1980). The surface enamel may be fissured occlusally or curved over the cusps and buccal and lingual surface, whereas the inner surface will be flat following slicing.

Enamel is deposited rhythmically by each ameloblast producing individual prisms, and collectively the striae of Retzius demonstrate the overall enamel deposition and growth, which results in the presence of enamel surface ridges—the perikymata. This is the interface with the oral cavity and will be examined clinically and thermographically for the external surface of the enamel. All of these enamel types are in a different orientation internally compared to externally, with or without wear, and this may affect the emissivity value of the tissue due to surface texture.

1.4.2 Dentin

Beneath the enamel lies the dentin, which forms the bulk of the tooth's mineralized tissue, both in the crown and the root, which is less mineralized than enamel at 70% by weight (Goldberg, et al., 2011). Physiological deposition of dentin continues throughout the vital life of the tooth from odontoblasts at the outer edge of the pulp, which moves toward the center of the tooth, secreting the collagenous predentin matrix 15–20 μm thick and commencing mineralization of intra- and extra-fibrillar crystals in a ratio of 25–30% and 70–75%, respectively (Kinney, et al., 2001; Kinney, et al., 2003; Balooch, et al., 2008), which is dissimilar to enamel but similar to bone (Bonar, et al., 1985; Pidaparti, et al., 1996). Development of matrix vesicles from odontoblasts is reported early in dentin-formation, which is similar to bone and may contribute to mineralization of dentin (Goldberg, et al., 2011).

There are multiple types of dentin, each with structural and compositional differences. Mantle dentin is the first formed coronally, without tubules as the odontoblast process develops later. In the root, a Tomes granular layer with interglobular spaces, with or without the hyaline Hopewell–Smith layer, is deposited, and tubules are rare in any peripheral dentin (Goldberg, et al., 2011). Primary dentin (circumpulpal dentin) is composed of three dentin types: intertubular dentin may account for up to 90% with 30% mineral and Type I collagen as the main protein, intratubular dentin and peritubular dentin in the human may account for 10%–20%, with 95% mineral with no collagen, and the latter two are often considered one tissue. This is variable depending on the location. The crystals of intertubular dentin form from two plates and may be 2–5 nm thick and 60 nm long, whereas peritubular dentin crystals of 25 nm appear isodiametric, and, when viewed with higher resolution dimensions are 36 nm × 25 nm × 9.75 nm (Goldberg, et al., 2011). Once erupted and contacting the opposing dentition, physiological deposition of secondary dentin continues at a slower rate than that of primary dentin.

Tertiary dentin may be produced in response to a pathological stimulus, e.g., caries, which offers additional protection of the pulp from the original odontoblast (reactionary dentin) or from odontoblast-like cells differentiated from pulpal stem cells following the death of the original odontoblast. This dentin differs from physiological and reactionary dentin as the odontoblast-like cells do not have an odontoblast process around which a tubule forms (Smith, et al., 1995). The odontoblast process may extend up to 1 mm into the dentin, resulting in cellularity, unlike enamel (Pashley, 1996). The tubule diameter varies across the dentin-thickness, being larger at the pulp-face (2.5–3.5 μm) than at the periphery of the amelodentinal junction (0.6–1.5 μm) (Fearnhead, 1957; Linde and Goldberg, 1993; Pashley, 1996; Montoya, et al., 2015).

1.4.3 Root

The root of the tooth is not normally visible intra-orally when held in a healthy periodontium, and the outer surface is covered with a thin layer of the mineralized tissue cementum. There are several types of cementum—acellular, cellular, mixed, and acellular afibrillar—composed of small mineralized plates similar to bone (Yamamoto et al., 2010; Nanci, 2012).

1.5 Properties

These compositional and structural differences between enamel and dentin can impact their properties, e.g., conductivity, diffusivity, and emissivity.

Thermal conductivity of the enamel is reported to range between 0.65 and 0.93 W m·K (Lisanti and Zander, 1950; Phillips et al., 1956; Craig and Peyton, 1961; Braden, 1964; Lin, et al., 2010b; Lancaster, et al., 2017), indicating enamel is an insulator offering thermal protection to the underlying dentin and pulp. Consideration was given to the orientation of enamel rods (parallel to or perpendicular to) in one study (Soyenkoff and Okun, 1958), but it did not impact the outcome, as both orientations produced a value of 0.65 W m·K. A later study did report a higher value (0.93 W m·K) when analyzing parallel rods. However, neither study had large sample sizes (2 v 7 respectively), and each used different temperatures, i.e., 26–29°C v 50°C, to record thermal conductivity with different devices, e.g., thermistor v thermocouple.

The thermal conductivity of dentin is reported to range between 0.108 and 0.959 W m·K (Lisanti & Zander, 1950; Phillips, et al., 1956; Soyenkoff & Okun, 1958; Craig & Peyton, 1961; Braden, 1964; Brown et al., 1970; Fanibunda and de Sa, 1975; Minesaki et al., 1983; Fukase et al., 1992; Panas et al., 2003; Little, et al., 2005; De Magalhaes et al., 2008; Lin et al., 2010b; Lancaster, et al., 2017), which is a 10-fold change rather than a 1.5-fold change for enamel. Dentin structure may have greater variability than enamel, especially when reviewing crown- and root-dentin and young and mature dentin. Tubule orientation was viewed in parallel and perpendicular, giving similar results with a range of 0.4–0.6 W m·K.

Human enamel thermal diffusivity ranges from 0.23 to 0.47 × 10^{-6} m^2/s, approaching twice the value of human dentin at 0.18–0.26 × 10^{-6} m^2/s (Lisanti & Zander, 1950; Phillips et al., 1956; Soyenkoff & Okun, 1958; Craig & Peyton, 1961; Braden, 1964; Brown et al., 1970; Fanibunda and de Sa, 1975; Minesaki et al., 1983; Fukase et al., 1992; Panas et al., 2003; Little, et al., 2005; De Magalhaes et al., 2008; Lin, et al., 2010b; Lancaster, et al., 2017).

1.6 Caries

During the life of a human tooth, there is likely to be a physiological and pathological impact on the tissue from abrasion and/or attrition, which may smooth the surface or expose the underlying structure clinically; demineralization and remineralization due to erosion or caries with an ionic exchange, e.g., calcium, phosphate, magnesium, and fluoride can result in a changeable composition (Fejerskov, 1997).

Immature teeth may be susceptible to caries due to increased porosity, incomplete mineralization, and plaque accumulation (Carvalho, 2014). Caries initially has a subsurface effect with an intact surface layer of 20–50 μm, which may have surface roughness and pore volume of 1% (Darling, 1958) and an increasing porosity below the body of the lesion (5%–25%), with increased loss of mineral, e.g., magnesium, which may arrest or progress, leading to breakdown of the surface and underlying tooth structure. The crystal size is affected, reducing to 10–30 nm in the body of the lesion, and also

TABLE 2 ICDAS II Merged Caries Codes adapted from Pitts et al. (2013).

ICDAS II Caries code	Merged codes	Description
0+/−	0−no caries evident	Sound tooth—no or questionable changes in enamel translucency viewed clean and after prolonged air-drying of 5 s
1+/−	A+/−initial stage decay	Initial stage of caries—first visible change in the enamel observed as a caries opacity or discoloration of pits after drying with air, not consistent with sound enamel. No surface breakdown or dentin shadowing.
2+/−		Change in enamel visible on moist enamel, extending beyond pits
3+/−	B+/−moderate decay	White or brown spot lesion with localized enamel destruction, without visible dentin
4+/−		Underlying dentin shadow with or without localized enamel destruction
5+/−	C+/−extensive decay	Clear cavity, less than half of the dental surface, in enamel showing dentin
6+/−		Extensive cavity, more than half the tooth surface, which is deep and wide, extending into the dentin

alters the structure and composition of the enamel, which may also affect the emissivity value.

Dentin may also be affected if caries progresses, leading to bacterial invasion and a zone of destruction and degradation of the organic matrix with loss of extrafibrillar mineral initially (Frank, 1990; Pugach, et al., 2009).

Coronal caries can be visually and radiographically characterized for research using the International Caries Detection and Assessment System (ICDAS) and ICDASII, with scores for enamel and dentin ascertained by assessing the surface changes of a tooth, which has been related to the histological extent of the lesion (Pitts et al., 2013). This improves the consistency of reporting caries compared to a basic indication of the presence or absence of decay. For the unrestored tooth, caries can be visually scored from 0 to 6, ± for activity status, as well as by merged variations to simplify the classification process–Tables 2, 3.

The impact of natural caries on human enamel is reported to reduce the thermal conductivity for both enamel (0.22 W m·K) and dentin (0.24 W m·K) (Lancaster, et al., 2017), and this may also affect the emissivity value.

1.7 Aims

The primary aim of this study is to evaluate the emissivity of the external and internal surface of human enamel and dentin from a known reference of 3M Scotch Super 33 + Black Vinyl Electrical Tape. The secondary aim is to assess the emissivity of natural caries in internal enamel and dentin.

The hypothesis for this study is that emissivity will be the same for all enamel and dentin types, whether sound or carious.

2 Materials and methods

Ethical approval was gained from Leeds Dental Institute Research Tissue-Bank for all teeth. Two teeth, one sound and one with a natural carious lesion, were radiographed (70kV/7mA/0.16s) with a Focus 50420 radiographic unit (Instrumentarium Dental TUUSULA, Finland) sliced bucco-lingually at 1-mm intervals with an Accutom-5 (Struers, Copenhagen, Denmark) and polished with an 800-grit abrasive sheet, while being cleansed with distilled water as necessary. The slices were immersed in distilled water and stored flat in boxes, which were refrigerated until needed.

Fourteen whole human molar teeth were held as pairs within a purpose-built unit, numbered 1 to 7, for ease of placement and removal from a fixed, rigid aluminum frame attached to an aluminum cube at a focal distance of 8 cm from the thermal camera. The frame had two supports to hold the paired units of teeth with the Tape attached, which were secured with wing-nuts (Figures 2A,B). The pairs of teeth were embedded within a simulated alveolar bone of Aluwax (www.Aluwaxdental.com) and secured with Green Stick Compound (www.kerrdental.com).

A thermal camera (FLIR SC305 with x4 lens, 100 µm spatial resolution) was attached to the aluminum cube with macro- and micro-thermal-regulation (previously described by Lancaster, et al., 2017), with a focal distance of 8 cm to the object of interest. Parameters of reflected apparent temperature (assessed with a thermal image of crumpled aluminum foil) were 27.2°C with a humidity of 50% (Prime Capsule Data Logger—www.perfect-prime.com) at a stable cube temperature of 22°C for the slices and 34.6°C with a humidity of 29% at a stable cube temperature of 30°C for whole teeth.

A Bibby Hotplate Techne DB-2TC (www.bibby-scientific.com) with an aluminum block was secured within the cube and provided a stable heat source of 30°C. A hand carrier with a copper baseplate (0.5 mm × 50 mm × 50 mm) and attached thermal tape (6 W m·K; www.thegamebooth.co.uk) transported the paper-dried tooth slices for heating on the heated aluminum block (Figure 3). The 3M Scotch Super 33 + Black Vinyl Electrical Tape was used for the known emissivity reference-point of 0.96 (ε = 0.96). The sliced samples were heated within the cube for 20 min, when thermal equilibrium was achieved, and emissivity was calculated against the reference Tape using the thermal camera software (ThermaCAM Researcher Professional 2.10).

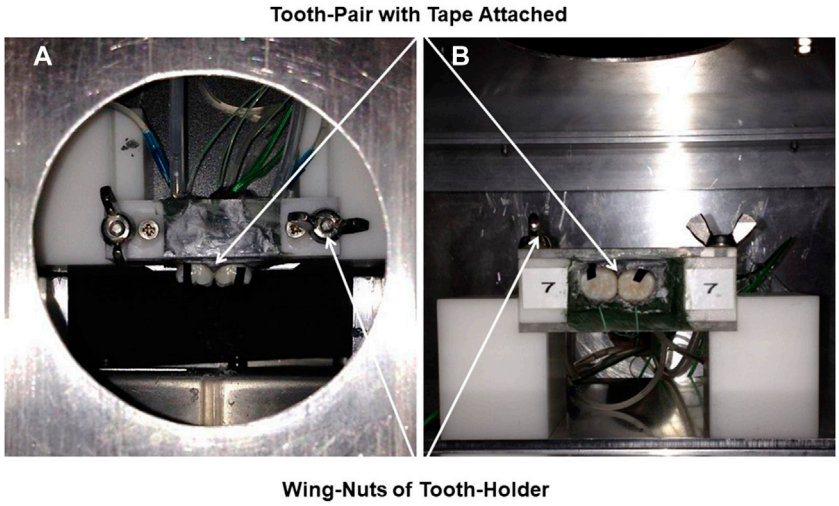

FIGURE 2
(A): Vertical and **(B)**: horizontal close-up of the tooth-pair unit secured by wing-nuts to the rigid-stand in the aluminium cube. 3M Scotch Super 33+ Black Vinyl Electrical Tape attached to tooth-surface for emissivity-reference-point of 0.96.

A stable thermal environment of 30°C was provided within the cube for the whole teeth, and, when in thermal equilibrium, the enamel-surface emissivity was assessed from the thermographs against the reference Tape attached to each tooth.

Data were processed and analyzed with ThermaCAM Researcher Professional 2.10 Software, which was also embedded in a Macro-enabled Microsoft Excel File (Microsoft®), and 95% confidence interval and Intraclass correlation coefficient were calculated in IBM SPSS Statistics Version 23.

3 Results

3.1 Descriptive data of teeth

The fourteen whole molar teeth evaluated for the emissivity of surface enamel comprised three upper-third molars, four lower-third molars, one lower-second molar, five upper-first molars, and one lower-first molar. Nine were donated by females and five by males. The mean age of donors was 16 years 11 months (range 10–28 years). Twelve donors were of white ethnic origin, and two were unknown.

A lower-third molar from a female donor, aged 18 years, of unknown ethnic origin, and an upper-third molar, also from a female donor, aged 28 years, also of unknown ethnic origin, provided five slices from each tooth. The caries lesion of the whole upper third molar tooth was classified as ICDAS II caries score 4 and radiographic score RB4.

3.2 Thermal equilibrium

Thermal equilibrium was achieved for each sample prior to emissivity assessment. As seen in Figure 4, the tooth slice warmed from the base temperature (lowest value of 28.2°C for the root surface) to 31.8°C for all tissues and materials bar one in approximately 360 s (6 min) and remained stable (±0.3°C) for the rest of the 20-min sequence, at the end of which the emissivity value was calculated. The lowest value found was for the root surface of dentin (green line), which stabilized between 31.5°C and 31.1°C.

3.3 Enamel and dentin emissivity

Table 4 and Table 5 show the results for the emissivity value by sample location (external or internal) and sub-sample slice with and without caries and descriptive statistics for emissivity values of sound external enamel, internal enamel, dentin, root-face dentin, and caries-affected internal enamel and dentin, respectively.

Comparison of enamel emissivity produced similar outcomes for the external enamel ($\bar{x}$ = 0.96, SD 0.01) and internal enamel ($\bar{x}$ = 0.97, SD 0.01), both falling within the 95% confidence interval. Repeat sequences of two slices gave an Intraclass Correlation Coefficient of 0.86 for the internal enamel.

Comparison of internal caries enamel emissivity ($\bar{x}$ = 0.82, SD 0.05) indicated a potential difference in emissivity, falling below the 95% confidence interval of 0.96–0.98 for sound internal enamel.

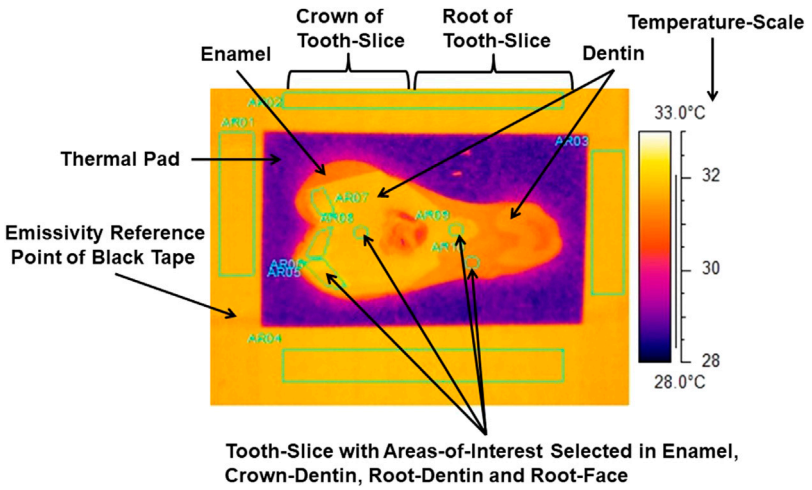

FIGURE 3
Thermograph with areas-of-interest selected in internal enamel, crown-dentin, root-dentin and root-face of a slice of tooth. Emissivity-reference-point provided by 3M Scotch Super 33+ Black Vinyl Electrical Tape.

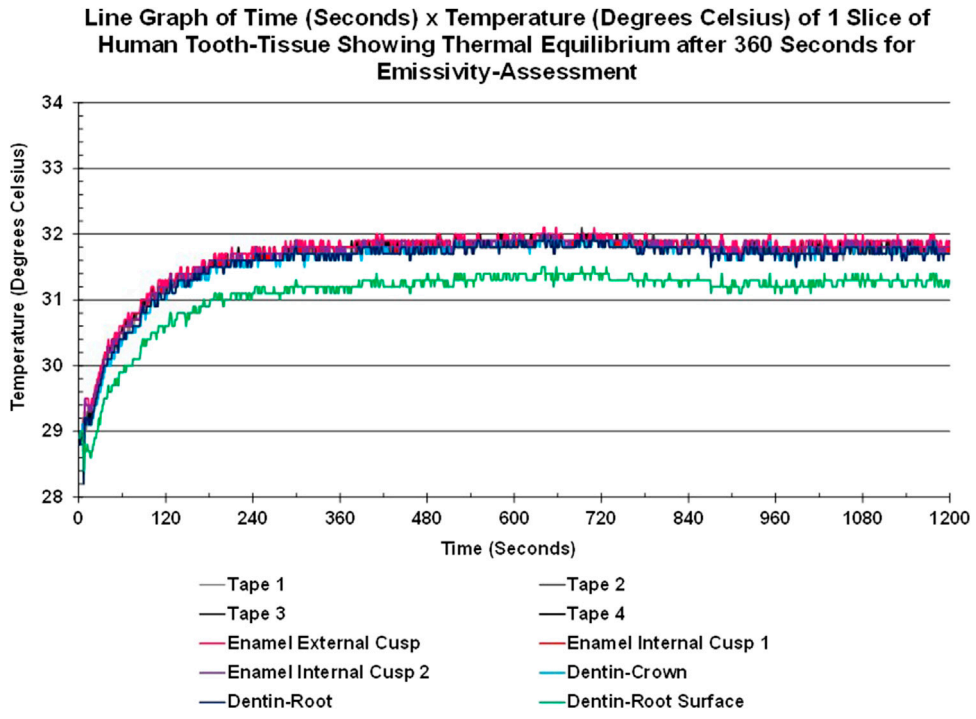

FIGURE 4
Line graph showing the Time-Temperature Curves of areas-of-interest of enamel, crown-dentin, root-dentin, root-surface-dentin of a slice of human tooth-tissue and tape areas-of-interest achieving thermal equilibrium within the cube after approximately 6 min and remaining stable over the next 14 min.

Comparison of the internal crown ($\bar{x}$ = 0.94, SD 0.02) and root dentin ($\bar{x}$ = 0.93, SD 0.02) emissivity produced similar outcomes, both falling within the 95% confidence interval. Repeat sequences of two slices gave an ICC of 0.86 for internal root dentin.

Comparison of the external root-face dentin ($\bar{x}$ = 0.84, SD 0.04) with the internal crown and root dentin indicates potential differences in emissivity, with the root-face falling below the confidence interval of both internal crown and root dentin.

Comparison of internal carious crown dentin ($\bar{x}$ = 0.73, SD 0.08) indicated potential difference with the respective sound tissue, falling below the 95% confidence interval of 0.92–0.95 and having the lowest of all emissivity values.

Based on the above-mentioned findings, the study hypothesis was rejected.

4 Discussion

The British Standards and Manufacturer's Infrared Thermography Handbook (British Standards, 2008; FLIR ThermaCAM™ Researcher Professional, 2010) provide a simple and recognized method of calculating emissivity by using a reference point of known emissivity, e.g., 3M Scotch Super 33 + Black Vinyl Electrical Tape.

Multiple samples (14) were used in this study to assess the emissivity value of the external surface of the enamel of whole teeth compared to one sample from Kells, et al. (2000a), despite their study considering multiple teeth: one sample by Lin, et al. (2010a) and three samples by Soori, et al. (2020). A total of 10 slices were used from two teeth to assess the emissivity of internal enamel and dentin from healthy and caries-affected teeth, and caution is needed when reviewing the outcomes from the slices as their independence will not be as great as that of 10 individual teeth. To the author's knowledge, assessment of internal sound and carious mineralized tissue has not previously been reported from empirical data as undertaken in this study, although an assumed emissivity of 0.98 was used by Kaneko, et al. (1999) when assessing the feasibility of caries-detection using thermal data. The overall mean emissivity values of healthy enamel were found to be similar, at 0.97 for the internal flat surface and 0.96 for the external curved surface, and had the greatest mean emissivity value of any of the mineralized tooth-tissue assessed. This is similar to previous reports ranging from 0.96 to 0.98 and higher than others with a range of 0.65–0.9 (Table 1). Sound crown dentin tended to have a higher mean emissivity value (0.94) than root dentin (0.93), but not enamel, and the root face had the lowest mean emissivity value (0.84) of all sound mineralized tooth tissue. Both caries-affected enamel (0.82) and dentin (0.73) had lower emissivity values than their sound equivalents.

This can be attributed to different tissue compositions and structures, with enamel having a higher mineral content (95%) than dentin (60%) and dentin being composed of mineralized tubules rather than prisms and inter-prismatic crystals, as seen in enamel. Enamel will have natural surface irregularities seen as perikymata as well as internal irregularities from the prisms and inter-prismatic crystals. These surface textures appear to emit infrared radiation in a similar way, despite one being an internal surface and one an external surface. Assessment of an area of tissue may also account for this as a local change may be compensated for within the area calculation, compared to a spot-measurement as undertaken by Kells, et al. (2000a). The duration for which the teeth used in this study had been in the oral environment after eruption was unknown, and, thus, the degree of maturity of enamel was also unknown, which may affect the mineral content, as enamel increases in mineral composition following eruption.

The root-face returns the lowest value of all healthy mineralized tooth-tissue assessed and not only has a greater curvature than the flat surface of the cut crown-dentin and root-dentin but may also contain remnants of the cementum which has a reduced mineral content at 50% compared to the rest of dentin. There may be soft-tissue traces from the periodontal ligament as well, which influences the activity of the radiant energy.

The crown-dentin and root-dentin values are slightly higher than the published values of 0.8, produced from comparison with a black paint assumed to have an emissivity of 1 (Neev, et al., 1993). This is very improbable, as a perfect blackbody is empirically unlikely. The temperature of the assessment was also unknown. All tissue samples are non-homogenous and will vary in mineral composition and structure, all of which can affect the emissivity values and may account for some of the variations and demonstrates the need to assess each tooth.

Once dental caries demineralizes the tooth tissue, the mineral content changes and emissivity assessment may offer a diagnostic option early in the disease process. The lesion assessed in this study was advanced. However, attempts to assess caries due to thermal changes have been challenging, and the assessment of the emissivity may be sufficient to demonstrate early changes in tissue composition. The caries tissues all produced lower emissivity values than healthy tissues in thermal equilibrium. Occlusal caries assessment may present challenges from increased curvature of the cusps and the fissures which trap the radiation, and further studies are needed to explore emissivity further as a diagnostic aid.

4.1 Acceptance of methodology

The Tape method of assessing emissivity was simple and cheap and would be recommended for providing actual emissivity values for tooth tissue in any *in vitro* study,

TABLE 3 ICDAS Radiographic Scores adapted from Pitts et al. (2013).

ICDAS Radiographic score	Codes	Description
0	No radiolucency	
RA: initial stages	RA 1	Radiolucency outer half enamel
	RA 2	Radiolucency inner half of enamel ± enamel dentin junction
	RA 3	Radiolucency limited to outer third of dentin
RB: Moderate stages	RB 4	Radiolucency reaching middle third dentin
RC: Extensive stages	RC 5	Radiolucency reaching inner third dentin and clinically cavitated
	RC 6	Radiolucency into pulp and clinically cavitated

TABLE 4 Emissivity value by sample location (external or internal) and sub-sample slice with and without caries.

Whole samples (n = 14)	External enamel	Sub-sample slices (n = 2)	Internal enamel	Dentin			Internal enamel caries	Internal dentin caries
				Crown	Root	Root-face		
1	0.955	15a	0.973	0.950	0.921			
2	0.965	15b	0.971	0.917	0.926			
3	0.970	15c	0.957	0.943	0.940	0.838		
4	0.970	15d	0.991	0.960	0.943	0.902		
5	0.959	15e	0.951			0.827		
6	0.966	16a	-			0.796		
7	0.961	16b	0.960	0.897	0.907			0.714
8	0.967	16c	0.978	0.930	0.910		0.781	0.658
9	0.963	16d	0.976	0.931	0.926		0.849	0.809
10	0.959	16e	0.992	0.960	0.960			
11	0.958							
12	0.954							
13	0.940							
14	0.948							

TABLE 5 Descriptive statistics for emissivity values of sound external enamel, internal enamel, dentin, root-face dentin, and caries-affected internal enamel and dentin.

Tissue	n =	Mean	Std. deviation	Std. error mean	95% Confidence interval
External enamel	14	0.96	0.01	0.002	0.96–0.97
Internal enamel	2 (nine slices)	0.97	0.01	0.005	0.96–0.98
Internal dentin					
Crown	2 (eight slices)	0.94	0.02	0.008	0.92–0.95
Root	2 (eight slices)	0.93	0.02	0.006	0.91–0.94
Root face	2 (four slices)	0.84	0.04	0.022	0.77–0.91
Internal enamel caries	1 (two slices)	0.82	0.05	0.034	0.38–1.25
Internal dentin caries	1 (three slices)	0.73	0.08	0.044	0.54–0.92

allowing consistency of methodology between research groups to report absolute temperatures. The emissivity of this Tape has been validated by the British Standards, and no independent evaluation of emissivity was carried out. In this study, the Tape was placed on the whole tooth sample and by the side of the slices. This may be criticized as the Tape was not physically on

the slices. However, the slices were 1 mm thick and reached thermal equilibrium within 6 min. It is acknowledged that two teeth have been prepared to produce 10 slices for the assessment of internal emissivity of enamel and dentin and one tooth for the assessment of caries, which reduces the independence of outcomes described.

There were no measurements of the mineral density of any tissue, and, as such, the stage of demineralization is unknown for enamel and dentin and can be explored in a further study, having established the principle.

5 Conclusion

The method of calculation was cheap, simple and practical and can improve emissivity acquisition for comparison of absolute temperatures between studies evaluating thermal safety concerns for dental procedures and may offer a diagnostic aid in detecting demineralization and caries of tooth tissue.

Enamel had a high emissivity, which was similar whether from the internal flat surface of sliced enamel or the external curved enamel surface of a whole tooth and was reduced in caries-affected enamel.

Dentin also had a high emissivity (but not as high as enamel), which varied with location, with crown dentin being the highest compared to root dentin, and the root face had the lowest emissivity value but was still a good emitter of infrared radiation. Dentin emissivity was similarly reduced when affected by caries.

Data availability statement

The raw data supporting the conclusion of this article will be made available by the authors, without undue reservation.

Author contributions

PL and DB designed; undertook data collection, analysis and interpretation of data; wrote the first draft; provided contribution to revision and final approval of the manuscript; and are accountable for the work presented. FC and VC were involved with the design concept, revision, and approval of the manuscript.

Acknowledgments

Thanks are extended to Jing Kang for statistical support; Mick Devlin, Clinical Skills Facilities Engineer/Manager, for all the engineering skills in developing the bespoke equipment; and to the Medical Physics Department, Leeds Teaching Hospital Trust for accommodating this research.

Conflict of interest

The authors declare that the research was conducted in the absence of any commercial or financial relationships that could be construed as a potential conflict of interest.

Publisher's note

All claims expressed in this article are solely those of the authors and do not necessarily represent those of their affiliated organizations, or those of the publisher, the editors and the reviewers. Any product that may be evaluated in this article, or claim that may be made by its manufacturer, is not guaranteed or endorsed by the publisher.

References

Aboushady, M. A., Talaat, W., Hamdoon, Z., Elshazly, T. M., Ragy, N., Bourauel, C., et al. (2021). Thermography as a non-ionizing quantitative tool for diagnosing periapical inflammatory lesions. *BMC Oral Health* 21 (1), 260–267. doi:10.1186/s12903-021-01618-9

Aksakalli, S., Demir, A., Selek, M., and Tasdemir, S. (2014). Temperature increase during orthodontic bonding with different curing units using an infrared camera. *Acta Odontol. Scand.* 72 (1), 36–41. doi:10.3109/00016357.2013.794954

Al-Qudah, A. A., Mitchell, C. A., Biagioni, P. A., and Hussey, D. L. (2005). Thermographic investigation of contemporary resin-containing dental materials. *J. Dent.* 33 (7), 593–602. doi:10.1016/j.jdent.2005.01.010

Ana, P. A., Blay, A., Miyakawa, W., and Zezell, D. M. (2007). Thermal analysis of teeth irradiated with Er, Cr: YSGG at low fluences. *Laser Phys. Lett.* 4 (11), 827–834. doi:10.1002/lapl.200710060

Anić, I., Dzubur, A., Vidović, D., and Tudja, M. (1993). Temperature and surface changes of dentine and cementum induced by CO2 laser exposure *Int. Endod. J.* 26 (5), 284–293. doi:10.1111/j.1365-2591.1993.tb00573.x

Anić, I., and Matsumoto, K. (1995). Dentinal heat transmission induced by a laser-softened gutta-percha obturation technique. *J. Endod.* 21 (9), 470–474. doi:10.1016/s0099-2399(06)81531-1

Anić, I., Pavelić, B., Perić, B., and Matsumoto, K. (1996a). *In vitro* pulp chamber temperature rises associated with the argon laser polymerization of composite resin *Lasers Surg. Med.* 19 (4), 438–444. doi:10.1002/(SICI)1096-9101(1996)19:4<438::AID-LSM9>3.0.CO;2-T

Anić, I., Tachibana, H., Masumoto, K., and Qi, P. (1996b). Permeability, morphologic and temperature changes of canal dentine walls induced by Nd: YAG, CO2 and argon lasers *Int. Endod. J.* 29 (1), 13–22. doi:10.1111/j.1365-2591.1996.tb01354.x

Arima, M., and Matsumoto, K. (1993). Effects of ArF: Excimer laser irradiation on human enamel and dentin. *Lasers Surg. Med.* 13 (1), 97–105. doi:10.1002/lsm.1900130116

Arrastia, A. M. A., Machida, T., Smith, P. W., and Matsumoto, K. (1994). Comparative study of the thermal effects of four semiconductor lasers on the enamel and pulp chamber of a human tooth. *Lasers Surg. Med.* 15 (4), 382–389. doi:10.1002/lsm.1900150408

Arrastia, A. M. A., Wilder-Smith, P., and Berns, M. W. (1995). Thermal effects of CO2 laser on the pulpal chamber and enamel of human primary teeth: An *in vitro* investigation. *Lasers Surg. Med.* 16 (4), 343–350. doi:10.1002/lsm.1900160405

Arslan, D., and Kuştarcı, A. (2018). The effect of the KTP laser on smear layer and temperature change: An *in vitro* study. *Lasers Med. Sci.* 33 (1), 149–157. doi:10.1007/s10103-017-2374-8

Balooch, M., Habelitz, S., Kinney, J. H., Marshall, S. J., and Marshall, G. W. (2008). Mechanical properties of mineralized collagen fibrils as influenced by demineralization. *J. Struct. Biol.* 162 (3), 404–410. doi:10.1016/j.jsb.2008.02.010

Bartlett, J. D. (2013). Dental enamel development: Proteinases and their enamel matrix substrates. *Int. Sch. Res. Notices*, 2013, 684607. doi:10.1155/2013/684607

Behnia, A., and McDonald, N. J. (2001). *In vitro* infrared thermographic assessment of root surface temperatures generated by the thermafil plus System. *J. Endod.* 27 (3), 203–205. doi:10.1097/00004770-200103000-00016

Biagioni, P. A., Hussey, D., Mitchell, C. A., Russell, D. M., and Lamey, P. J. (1996). Thermographic assessment of dentine pin placement *J. Dent.* 24 (6), 443–447. doi:10.1016/s0300-5712(96)80481-7

Bonar, L. C., Lees, S., and Mook, H. A. (1985). Neutron diffraction studies of collagen in fully mineralized bone. *J. Mol. Biol.* 181 (2), 265–270. doi:10.1016/0022-2836(85)90090-7

Bouillaguet, S., Caillot, G., Forchelet, J., Cattani-Lorente, M., Wataha, J. C., and Krejci, I. (2005). Thermal risks from led- and high-intensity QTH-curing units during polymerization of dental resins. *J. Biomed. Mat. Res. B Appl. Biomater.* 72 (2), 260–267. doi:10.1002/jbm.b.30143

Braden, M. (1964). Heat conduction in normal human teeth. *Arch. Oral Biol.* 9 (4), 479–486. doi:10.1016/0003-9969(64)90033-0

British Standard (2008). *Conditioning monitoring and diagnostics of machines – thermography Part 1 general procedures BS ISO18434-1*. 1st Ed. London, United Kingdom: BSI.

Brown, W. S., Dewey, W. A., and Jacobs, H. R. (1970). Thermal properties of teeth. *J. Dent. Res.* 49 (4), 752–755. doi:10.1177/00220345700490040701

Budd, J. C., Gekelman, D., and White, J. M. (2005). Temperature rise of the post and on the root surface during ultrasonic post removal. *Int. Endod. J.* 38 (10), 705–711. doi:10.1111/j.1365-2591.2005.01002.x

Carson, J., Rider, T., and Nash, D. (1979). A thermographic study of heat distribution during ultra-speed cavity preparation. *J. Dent. Res.* 58 (7), 1681–1684. doi:10.1177/00220345790580070401

Carvalho, J. C. (2014). Caries process on occlusal surfaces: Evolving evidence and understanding. *Caries Res.* 48 (4), 339–346. doi:10.1159/000356307

Craig, R. G., and Peyton, F. A. (1961). Thermal conductivity of tooth structure, dental cements and amalgam. *J. Dent. Res.* 40 (3), 411–418. doi:10.1177/00220345610400030501

Crandell, C. E., and Hill, R. P. (1966). Thermography in dentistry: A pilot study. *Oral Surg. Oral Med. Oral Pathol.* 21 (3), 316–320. doi:10.1016/0030-4220(66)90064-8

Cui, F. Z., and Ge, J. (2007). New observations of the hierarchical structure of human enamel, from nanoscale to microscale. *J. Tissue Eng. Regen. Med.* 1 (3), 185–191. doi:10.1002/term.21

Cuy, J. L., Mann, A. B., Livi, K. J., Teaford, M. F., and Weihs, T. P. (2002). Nanoindentation mapping of the mechanical properties of human molar tooth enamel. *Arch. Oral Biol.* 47 (4), 281–291. doi:10.1016/s0003-9969(02)00006-7

Da Costa Ribeiro, A., Nogueira, G. E. C., Antoniazzi, J. H., Moritz, A., and Zezell, D. M. (2007). Effects of diode laser (810nm) irradiation on root canal walls: Thermographic and morphological studies. *J. Endod.* 33 (3), 252–255. doi:10.1016/j.joen.2006.09.002

Da Silva Barbosa, P., da Ana, P. A., Poiate, I. A. V. P., Zezell, D. M., and de Sant'Anna, G. R. (2013). Dental enamel irradiated with A low-intensity infrared laser and photoabsorbing cream: A study of microhardness, surface and pulp temperature. *Photomed. Laser Surg.* 31 (9), 439–446. doi:10.1089/pho.2013.3485

Dabrowski, M., Dulski, R., Żmuda, S., and Zaborowski, P. (2000). "Emission properties of dental materials and hard dental tissues", in Seminar 64 Proceedings of Quantitative Infrared Thermography 5, Reims. doi:10.21611/qirt.2000.003

Daculsi, G., and Kerebel, B. (1978). High-resolution electron microscope study of human enamel crystallites: Size, shape, and growth. *J. Ultrastruct. Res.* 65 (2), 163–172. doi:10.1016/s0022-5320(78)90053-9

Daculsi, G., Menanteau, J., Kerebel, L. M., and Mitre, D. (1984). Length and shape of enamel crystals. *Calcif. Tissue Int.* 36 (1), 550–555. doi:10.1007/BF02405364

Darling, A. I. (1958). Studies of the early lesion of enamel caries. Its nature, mode of spread and points of entry. *Br. Dent. J.* 105, 119–133.

De Magalhaes, M. F., Ferreira, R. A. N., Grossi, P. A., and de Andrade, R. M. (2008). Measurement of thermophysical properties of human dentin: Effect of open porosity. *J. Dent.* 36 (8), 588–594. doi:10.1016/j.jdent.2008.04.006

Diegritz, C., Gerlitzki, O., Fotiadou, C., and Folwaczny, M. (2020). Temperature changes on the root surface during application of warm vertical compaction using three different obturation units. *Odontology* 108 (3), 358–365. doi:10.1007/s10266-019-00472-0

Fanibunda, K. B., and de Sa, A. (1975). Thermal conductivity of normal and abnormal human dentine *Arch. Oral Biol.* 20 (7), 457–459. doi:10.1016/0003-9969(75)90233-2

Fearnhead, R. W. (1957). Histological evidence for the innervation of human dentine *J. Anat.* 91 (2), 267–277.

Fejerskov, O. (1997). Concepts of dental caries and their consequences for understanding the disease. *Community Dent. Oral Epidemiol.* 25 (1), 5–12. doi:10.1111/j.1600-0528.1997.tb00894.x

FLIR ThermaCAM™ Researcher Professional (2010). *Help guide*. FLIR® Systems. Publ.No.T559009 Rev.a470-English (En).

Forjaz, C. R. H., Zezell, D. M., and Ana, P. A. (2022). Temperature generation and transmission in root dentin during Nd:YAG laser irradiation for preventive purposes. *IFMBE Proc.* 83, 1141–1146.

Frank, R. M. 1990. Structural events in the caries process in enamel, cementum, and dentin. *J. Dent. Res.* 69(2 Suppl), pp. 559–566. doi:10.1177/00220345900690S112

Fukase, Y., Saitoh, M., Kaketani, M., Ohashi, M., and Nishiyama, M. (1992). Thermal coefficients of paste-paste type pulp capping cements. *Dent. Mat. J.* 11 (2), 189–196. doi:10.4012/dmj.11.189

Gaussorgues, G. (1994). Infrared thermography translated, by S. Chomet (original French title: La thermographie infrarouge). *Microw. Technol. Ser.* 5 8–60. English Language Ed.

Glas, J. E. (1962). Studies on the ultrastructure of dental enamel—II: The orientation of the apatite crystallites as deduced from X-ray diffraction. *Arch. Oral Biol.* 7 (1), 91–104. doi:10.1016/0003-9969(62)90052-3

Goldberg, M., Kellermann, O., Dimitrova-Nakov, S., Harichane, Y., and Baudry, A. (2014). Comparative studies between mice molars and incisors are required to draw an overview of enamel structural complexity. *Front. Physiol.* 5, 359. doi:10.3389/fphys.2014.00359

Goldberg, M., Kulkarni, A. B., Young, M., and Boskey, A. (2011). Dentin: Structure, composition and mineralization *Front. Biosci.* 3, 711–735. doi:10.2741/e281

Gontijo, I. T., Navarro, R. S., Ciamponi, A. L., Miyakawa, W., and Zezell, D. M. (2008). Color and surface temperature variation during bleaching in human devitalized primary teeth: An *in vitro* study. *J. Dent. Child.* 75 (3), 229–234.

Hardy, J. D. (1934). The radiation of heat from the human body: III. The human skin as a black-body radiator. *J. Clin. Invest.* 13 (4), 615–620. doi:10.1172/JCI100609

Hartley, J. L., Stanfill, D. F., and Plakun, B. D. (1967). Thermography of the human dentition. SAM-TR-67-57. [Technical Report] SAM-TR. USAF School of Aerospace Medicine, 1–40.

He, B., Huang, S., Jing, J., and Hao, Y. (2010). Measurement of hydroxyapatite density and Knoop hardness in sound human enamel and a correlational analysis between them. *Arch. Oral Biol.* 55 (2), 134–141. doi:10.1016/j.archoralbio.2009.12.005

Hsieh, Y. D., Gau, C. H., Kung Wu, S. F., Shen, E. C., Hsu, P. W., and Fu, E. (2007). Dynamic recording of irrigating fluid distribution in root canals using thermal image analysis. *Int. Endod. J.* 40 (1), 11–17. doi:10.1111/j.1365-2591.2006.01168.x

Hussey, D. L., Biagioni, P. A., and Lamey, P. J. (1995). Thermographic measurement of temperature change during resin composite polymerization *in vivo*. *J. Dent.* 23 (5), 267–271. doi:10.1016/0300-5712(95)91149-h

Ishizaki, N. T., Matsumoto, K., Kimura, Y., Wang, X., Kinoshita, J. I., Okano, S., et al. (2004). Thermographical and morphological studies of Er, Cr: YSGG laser irradiation on root canal walls. *Photomed. Laser Surg.* 22 (4), 291–297. doi:10.1089/pho.2004.22.291

Jo, S. A., Lee, C. H., Kim, M. J., Ferracane, J., and Lee, I. B. (2019). Effect of pulse-width-modulated LED light on the temperature change of composite in tooth cavities. *Dent. Mat.* 35 (4), 554–563. doi:10.1016/j.dental.2019.01.009

Kabbach, W., Zezell, D. M., Pereira, T. M., Albero, F. G., Clavijo, V. R. G., and de Andrade, M. F. (2008). A thermal investigation of dental bleaching *in vitro*. *Photomed. Laser Surg.* 26 (5), 489–493. doi:10.1089/pho.2007.2221

Kaneko, K., Matsuyama, K., and Nakashima, S. (1999). "Quantification of early carious enamel lesions by using an infrared camera *in-vitro*. Stookey GK," in Proceedings of the 4th Annual Indiana Conference, Indianapolis, United States, May 19–22, 1999, 83–100.

Kells, B. E., Kennedy, J. G., Biagioni, P. A., and Lamey, P. J. (2000a). Computerized infrared thermographic imaging and pulpal blood flow: Part 1. A protocol for thermal imaging of human teeth. *Int. Endod. J.* 33 (5), 442–447. doi:10.1046/j.1365-2591.2000.00257.x

Kells, B. E., Kennedy, J. G., Biagioni, P. A., and Lamey, P. J. (2000b). Computerized infrared thermographic imaging and pulpal blood flow: Part 2. Rewarming of healthy human teeth following a controlled cold stimulus. *Int. Endod. J.* 33 (5), 448–462. doi:10.1046/j.1365-2591.2000.00236.x

Kerebel, B., Daculsi, G., and Kerebel, L. M. (1979). Ultrastructural studies of enamel crystallites. *J. Dent. Res.* 58 (B), 844–851. doi:10.1177/00220345790580023701

Kilic, K., Er, O., Kilinc, H. I., Aslan, T., Bendes, E., Sekerci, A. E., et al. (2013). Infrared thermographic comparison of temperature increases on the root surface during dowel space preparations using circular versus oval fiber dowel systems. *J. Prosthodont.* 22 (3), 203–207. doi:10.1111/j.1532-849X.2012.00919.x

Kinney, J. H., Marshall, S. J., and Marshall, G. W. (2003). The mechanical properties of human dentin: A critical review and Re-evaluation of the dental literature. *Crit. Rev. Oral Biol. Med.* 14 (1), 13–29. doi:10.1177/154411130301400103

Kinney, J. H., Pople, J. A., Marshall, G. W., and Marshall, S. J. (2001). Collagen orientation and crystallite size in human dentin: A small angle X-ray scattering study. *Calcif. Tissue Int.* 69 (1), 31–37. doi:10.1007/s00223-001-0006-5

Kishen, A., Murukeshan, V. M., Krishnakumar, V., Lim, C. S., and Asundi, A. (2003). Digital speckle pattern interferometric (DSPI) and thermo-graphic investigations on the thermal responds in human teeth. *Opt. Lasers Eng.* 39 (4), 489–500. doi:10.1016/s0143-8166(02)00031-3

Lancaster, P., Brettle, D., Carmichael, F., and Clerehugh, V. (2017). *In-vitro* thermal maps to characterize human dental enamel and dentin. *Front. Physiol.* 8, 461. doi:10.3389/fphys.2017.00461

Launay, Y., Mordon, S., Cornil, A., Brunetaud, J. M., and Moschetto, Y. (1987). Thermal effects of lasers on dental tissues. *Lasers Surg. Med.* 7 (6), 473–477. doi:10.1002/lsm.1900070606

Lee, R. C., Darling, C. L., and Fried, D. (2016a). Assessment of remineralized dentin lesions with thermal and near-infrared reflectance imaging. *Lasers in Dentistry XXII* 9692, 39–43. SPIE. doi:10.1117/12.2218661

R. C. Lee, M. Staninec, O. Le, and D. Fried (2016b). "Infrared Methods for Assessment of the Activity of Natural Enamel Caries Lesions," in IEEE Journal of Selected Topics in Quantum Electronics, May–June, 2016 22 (3), 102–110. doi:10.1109/JSTQE.2016.2542481

Lin, M., Liu, Q. D., Kim, T., Xu, F., Bai, B. F., and Lu, T. J. (2010b). A new method for characterization of thermal properties of human enamel and dentine: Influence of microstructure. *Infrared Phys. Technol.* 53 (6), 457–463. doi:10.1016/j.infrared.2010.09.004

Lin, M., Liu, Q. D., Xu, F., Bai, B. F., and Lu, T. J. (2010a). "*In vitro* investigation of heat transfer in human tooth," in *4th international conference on experimental mechanics*. Editor C. Quan.

Linde, A., and Goldberg, M. (1993). Dentinogenesis. *Crit. Rev. Oral Biol. Med.* 4 (5), 679–728. doi:10.1177/10454411930040050301

Lipski, M. (2006). *In vitro* infrared thermographic assessment of root surface temperatures generated by high-temperature thermoplasticized injectable gutta-percha obturation technique. *J. Endod.* 32 (5), 438–441. doi:10.1016/j.joen.2005.10.047

Lipski, M. (2005a). Root surface temperature rises during root canal obturation, *in vitro*, by the continuous wave of condensation technique using System B heatsource. *Oral Surg. Oral Med. Oral Pathol. Oral Radiol. Endod.* 99 (4), 505–510. doi:10.1016/j.tripleo.2004.07.014

Lipski, M. (2004). Root surface temperature rises *in vitro* during root canal obturation with thermoplasticized gutta-percha on a carrier or by injection. *J. Endod.* 30 (6), 441–443. doi:10.1097/00004770-200406000-00016

Lipski, M., Dębicki, M., and Droździk, A. (2010a). Effect of different water flows on root surface temperature during ultrasonic removal of posts. *Oral Surg. Oral Med. Oral Pathol. Oral Radiol. Endod.* 110 (3), 395–400. doi:10.1016/j.tripleo.2010.04.022

Lipski, M., Mrozek, J., and Droździk, A. (2010b). Influence of water cooling on root surface temperature generated during post space preparation. *J. Endod.* 36 (4), 713–716. doi:10.1016/j.joen.2010.01.005

Lipski, M. (2005b). Root surface temperature rises *in vitro* during root canal obturation using hybrid and microseal techniques. *J. Endod.* 31 (4), 297–300. doi:10.1097/01.don.0000140575.67887.e7

Lipski, M., and Woźniak, K. (2003). *In vitro* infrared thermographic assessment of root surface temperature rises during thermafil retreatment using System B. *J. Endod.* 29 (6), 413–415. doi:10.1097/00004770-200306000-00008

Lipski, M., Woźniak, K., Szyszka-Sommerfeld, L., Borawski, M., Droździk, A., and Nowicka, A. (2020). *In vitro* infrared thermographic assessment of temperature change in the pulp chamber during provisionalization: Effect of remaining dentin thickness. *J. Healthc. Eng.* 2020, 8838329. doi:10.1155/2020/8838329

Lipski, M., and Zapałowicz, Z. (2002). "*In vitro* infrared thermographic assessment of root surface temperatures generated by thermoplasticized gutta-percha root canal obturation using System B heat source," in Proceedings of the Heat Exchange and Renewable Energy Sources. International Symposium, 139–144.

Lisanti, V. F., and Zander, H. A. (1950). Thermal conductivity of dentin. *J. Dent. Res.* 29 (4), 493–497. doi:10.1177/00220345500290041201

Little, P. A., Wood, D. J., Bubb, N. L., Maskill, S. A., Mair, L. H., and Youngson, C. C. (2005). Thermal conductivity through various restorative lining materials. *J. Dent.* 33 (7), 585–591. doi:10.1016/j.jdent.2004.12.005

Liu, H., Chang, N.-Y., Gao, W., and Fried, D. (2021). Infrared imaging confirms the role of the transparent surface zone in arresting dental caries. *Proc. SPIE. Int. Soc. Opt. Eng.* 11627, 116270O. doi:10.1117/12.2584907

Maas, M. C., and Dumont, E. R. (1999). Built to last: The structure, function, and evolution of primate dental enamel. *Evol. Anthropol.* 8 (4), 133–152. doi:10.1002/(sici)1520-6505(1999)8:4<133::aid-evan4>3.0.co;2-f

Machida, T., Wilder-Smith, P., Arrastia, A. M., Liaw, L. H. L., and Berns, M. W. (1995). Root canal preparation using the second harmonic ktp: YAG laser: A thermographic and scanning electron microscopic study. *J. Endod.* 21 (2), 88–91. doi:10.1016/S0099-2399(06)81102-7

Madura, H., Dąbrowski, M., Dulski, R., Żmuda, S., and Zaborowski, P. (2004). Thermographic method for evaluation of thermal influence of Nd: YAG laser on a tooth root during sterilization process. *Infrared Phys. Technol.* 46 (1-2), 167–171. doi:10.1016/j.infrared.2004.03.021

McCullagh, J. J. P., Biagioni, P. A., Lamey, P. J., and Hussey, D. L. (1997). Thermographic assessment of root canal obturation using thermomechanical compaction. *Int. Endod. J.* 30 (3), 191–195. doi:10.1046/j.1365-2591.1997.00072.x

McCullagh, J. J. P., Setchell, D. J., Gulabivala, K., Hussey, D. L., Biagioni, P., Lamey, P. J., et al. (2000). A comparison of thermocouple and infrared thermographic analysis of temperature rise on the root surface during the continuous wave of condensation technique. *Int. Endod. J.* 33 (4), 326–332. doi:10.1046/j.1365-2591.2000.00302.x

Meckel, A. H., Griebstein, W. J., and Neal, R. J. (1965). Structure of mature human dental enamel as observed by electron microscopy. *Arch. Oral Biol.* 10 (5), 775–783. doi:10.1016/0003-9969(65)90131-7

Mendes, S., Mendes, J., Moreira, A., Clemente, M. P., and Vasconcelos, M. (2020). Thermographic assessment of vital and non-vital anterior teeth: A comparative study. *Infrared Phys. Technol.* 106, 103232. doi:10.1016/j.infrared.2020.103232

Meyer, D. H., and Foth, H. J. (1996). Thermal stress in dentin and enamel under CO₂ laser irradiation. *Proc. SPIE Int. Soc. Opt. Photonics* 2623, 117–129. doi:10.1117/12.230323

Minesaki, Y., Muroya, M., Higashi, R., Shinohara, N., Jimi, T., Fujii, K., et al. (1983). A method for determining of thermal diffusivity of human teeth. *Dent. Mat. J.* 2 (2), 204–209. doi:10.4012/dmj.2.204

Montoya, C., Arango-Santander, S., Peláez-Vargas, A., Arola, D., Ossa, E. A., and Pelaez-VargAs, A. (2015). Effect of aging on the microstructure, hardness and chemical composition of dentin. *Arch. Oral Biol.* 60 (12), 1811–1820. doi:10.1016/j.archoralbio.2015.10.002

Mouhat, M., Stangvaltaite-Mouhat, L., Mercer, J., Nilsen, B. W., and Örtengren, U. (2021). Light-curing units used in dentistry: Effect of their characteristics on temperature development in teeth. *Dent. Mater. J.* 40 (5), 1177–1188. doi:10.4012/dmj.2020-305

Nanci, A. (2012). *Ten cate's oral histology development, structure, and function*. 8th Ed. Amsterdam, Netherlands: Elsevier.

Neev, J., Pham, K., Lee, J. P., and White, J. M. (1996). Dentin ablation with three infrared lasers. *Lasers Surg. Med.* 18 (2), 121–128. doi:10.1002/(SICI)1096-9101(1996)18:2<121::AID-LSM1>3.0.CO;2-U

Neev, J., Stabholtz, A., Liaw, L. H. L., Torabinejad, M., Fujishige, J. T., Ho, P. D., et al. (1993). Scanning electron microscopy and thermal characteristics of dentin ablated by A short-pulse xecl excimer laser. *Lasers Surg. Med.* 13 (3), 353–362. doi:10.1002/lsm.1900130312

Palamara, J., Phakey, P. P., Rachinger, W. A., and Orams, H. J. (1980). Electron microscopy of surface enamel of human unerupted and erupted teeth. *Arch. Oral Biol.* 25 (11-12), 715–725. doi:10.1016/0003-9969(80)90125-9

Panas, A. J., Żmuda, S., Terpiłowski, J., and Preiskorn, M. (2003). Investigation of the thermal diffusivity of human tooth hard tissue. *Int. J. Thermophys.* 24 (3), 837–848. doi:10.1023/a:1024004803596

Paredes, A., Forner, L., Llena, C., Priego, J. I., Salvador, R., and Cibrian, R. M. (2018). Thermographic analysis of tooth vascularization using thermal stimulation. *Eur. Endod. J.* 3 (2), 73. doi:10.14744/eej.2018.69885

Pashley, D. H. (1996). Dynamics of the pulpo-dentin complex. *Crit. Rev. Oral Biol. Med.* 7 (2), 104–133. doi:10.1177/10454411960070020101

Pedreira, A. A., Wanderley, F. G., Sa, M. F., Viena, C. S., Perez, A., Hoshi, R., et al. (2016). Thermographic and clinical evaluation of 808-nm laser photobiomodulation effects after third molar extraction. *Minerva Stomatol.* 65 (4), 213–222.

Phillips, R. W., Johnson, R. J., and Phillips, L. J. (1956). An improved method for measuring the coefficient of thermal conductivity of dental cement. *J. Am. Dent. Assoc.* 53 (5), 577–583. doi:10.14219/jada.archive.1956.0217

Pidaparti, R. M. V., Chandran, A., Takano, Y., and Turner, C. H. (1996). Bone mineral lies mainly outside collagen fibrils: Predictions of a composite model for osteonal bone *J. Biomech.* 29 (7), 909–916. doi:10.1016/0021-9290(95)00147-6

Pitts, N. B., and Ekstrand, K. R. ICDAS Foundation (2013). International caries detection and assessment System (ICDAS) and its international caries classification and management System (ICCMS)–methods for staging of the caries process and enabling dentists to manage caries. *Community Dent. Oral Epidemiol.* 41 (1), e41–e52. doi:10.1111/cdoe.12025

Podolak, Bł., Nowicka, A., Woźniak, K., Szyszka-Sommerfeld, L., Dura, Wł., Borawski, M., et al. (2020). Root surface temperature increases during root canal filling *in vitro* with Nd:YAG laser-softened gutta-percha. *J. Healthc. Eng.*, 2020, 8828272. doi:10.1155/2020/8828272

Pogrel, M. A., Yen, C. K., and Taylor, R. C. (1988). A thermographic evaluation of the temperatures achieved by a carbon dioxide laser on soft tissues and teeth. *Thermology* 3, 50–52.

Pogrel, M. A., Yen, C. K., and Taylor, R. C. (1989). Studies in tooth crown temperature gradients with the use of infrared thermography. *Oral Surg. Oral Med. Oral Pathol.* 67 (5), 583–587. doi:10.1016/0030-4220(89)90277-6

Popowics, T. E., Rensberger, J. M., and Herring, S. W. (2004). Enamel microstructure and microstrain in the fracture of human and pig molar cusps. *Arch. Oral Biol.* 49 (8), 595–605. doi:10.1016/j.archoralbio.2004.01.016

Preoteasa, E., Iosif, L., Amza, O., Preoteasa, C. T., and Dumitrascu, C. (2010). Thermography, an imagistic method in investigation of the oral mucosa status in complete denture wearers. *J. Optoelectron. Adv. Mater.* 12 (11), 2333–2340.

Pugach, M. K., Strother, J., Darling, C. L., Fried, D., Gansky, S. A., Marshall, S. J., et al. (2009). Dentin caries zones: Mineral, structure and properties. *J. Dent. Res.* 88 (1), 71–76. doi:10.1177/0022034508327552

Risnes, S., and Li, C. (2018). Aspects of the final phase of enamel formation as evidenced by observations of superficial enamel of human third molars using scanning electron microscopy. *Arch. Oral Biol.* 86, 72–79. doi:10.1016/j.archoralbio.2017.11.008

Robinson, C., Shore, R. C., Wood, S. R., Brookes, S. J., Smith, D. A. M., Wright, J. T., et al. (2003). Subunit structures in hydroxyapatite crystal development in enamel: Implications for amelogenesis imperfecta. *Connect. Tissue Res.* 44 (1), 65–71. doi:10.1080/03008200390152115

Roointan, S., Tavakolian, P., Sivagurunathan, K. S., Mandelis, A., and Abrams, S. H. (2021). Detection and monitoring of early dental caries and erosion using three-dimensional enhanced truncated-correlation photothermal coherence tomography imaging. *J. Biomed. Opt.* 26 (4), 046004. doi:10.1117/1.JBO.26.4.046004

Simmer, J. P., Richardson, A. S., Hu, Y. Y., Smith, C. E., and Ching-Chun Hu, J. (2012). A post-classical theory of enamel biomineralization. . . and why we need one. and why we need one. *Int. J. Oral Sci.* 4 (3), 129–134. doi:10.1038/ijos.2012.59

Smith, A. J., Cassidy, N., Perry, H., Bègue-Kirn, C., Ruch, J. V., and Lesot, H. (1995). Reactionary dentinogenesis. *Int. J. Dev. Biol.* 39 (1), 273–280.

Smith, C. E., Poulter, J. A., Antanaviciute, A., Kirkham, J., Brookes, S. J., Inglehearn, C. F., et al. (2017). Amelogenesis imperfecta; genes, proteins, and pathways. *Front. Physiol.* 8, 435. doi:10.3389/fphys.2017.00435

Soori, A., Kowsary, F., and Kasraei, S. (2020). Experimental estimation of the emissivity of human enamel and dentin. *Infrared Phys. Technol.* 106, 103234. doi:10.1016/j.infrared.2020.103234

Soyenkoff, B. C., and Okun, J. H. (1958). Thermal conductivity measurements of dental tissues with the aid of thermistors. *J. Am. Dent. Assoc.* 57 (1), 23–30. doi:10.14219/jada.archive.1958.0234

Speirs, R. L. (1971). The nature of surface enamel in human teeth. *Calcif. Tissue Res.* 8 (1), 1–16. doi:10.1007/BF02010118

Stifler, C. A., Jakes, J. E., North, J. D., Green, D. R., Weaver, J. C., and Gilbert, P. U. (2021). Crystal misorientation correlates with hardness in tooth enamels. *Acta Biomater.* 120, 124–134. doi:10.1016/j.actbio.2020.07.037

Stock, K., Graser, R., Udart, M., Kienle, A., and Hibst, R. (2011). Diode laser for endodontic treatment: Investigations of light distribution and disinfection efficiency. *Proc. SPIE-International Soc. Opt. Photonics* 7884, 788402. doi:10.1117/12.875109

Ulusoy, Ö. I., Yılmazoğlu, M. Z., and Görgül, G. (2015). Effect of several thermoplastic canal filling techniques on surface temperature rise on roots with simulated internal resorption cavities: An infrared thermographic analysis. *Int. Endod. J.* 48 (2), 171–176. doi:10.1111/iej.12297

Uzunov, T., Grozdanova, R., Popova, E., and Uzunov, T. (2014). Thermal changes in the hard dental tissue at diode laser root canal treatment. *Acta Medica Bulg.* 41 (2), 31–35. doi:10.1515/amb-2014-0018

Vollmer, M., and Möllmann, K.-P. (2010). *Infrared thermal imaging - fundamentals, research and applications*. Germany: WILEY-VCH Verlag GmbH & Co.

Voicu, M., Mihai, A., Rujinsky, A. D., Mateiasi, G., Dumitrascu, C., Popovici, V., et al. (2013). Nondestructive Examinations *Printech* 325, 311–315.

Wang, X., Sun, Y., Kimura, Y., Kinoshita, J. I., Ishizaki, N. T., and Matsumoto, K. (2005). Effects of diode laser irradiation on smear layer removal from root canal walls and apical leakage after obturation. *Photomed. Laser Surg.* 23 (6), 575–581. doi:10.1089/pho.2005.23.575

Webb, P. W. (1991). Thermal imaging of electronic devices with low surface emissivity. *IEE Proc. F. Radar. Signal. Process. UK.* 138 (3), 390–400. doi:10.1049/ip-g-2.1991.0065

Whittaker, D. K. (1982). Structural variations in the surface zone of human tooth enamel observed by scanning electron microscopy. *Arch. Oral Biol.* 27 (5), 383–392. doi:10.1016/0003-9969(82)90147-9

Whitters, C. J., and Strang, R. (2000). Preliminary investigation of a novel carbon dioxide laser for applications in dentistry. *Lasers Surg. Med.* 26 (3), 262–269. doi:10.1002/(sici)1096-9101(2000)26:3<262::aid-lsm3>3.0.co;2-7

Wilder-Smith, P. B. B., Arrastia-Jitosho, A. M. A., Grill, G., Liaw, L. H. L., and Berns, M. W. (1995). Thermal and microstructural effects of nanosecond pulsed Nd: YAG laser irradiation on tooth root surface. *Proc. SPIE Int. Soc. Opt. Photonics* 2394, 170–179. doi:10.1117/12.207438

Yamamoto, T., Li, M., Liu, Z., Guo, Y., Hasegawa, T., Masuki, H., et al. (2010). Histological review of the human cellular cementum with special reference to an alternating lamellar pattern. *Odontology* 98 (2), 102–109. doi:10.1007/s10266-010-0134-3

Yamazaki, R., Goya, C., Yu, D. G., Kimura, Y., and Matsumoto, K. (2001). Effects of erbium, chromium: YSGG laser irradiation on root canal walls: A scanning electron microscopic and thermographic study. *J. Endod.* 27 (1), 9–12. doi:10.1097/00004770-200101000-00003

Yang, V., Zhu, Y., Curtis, D., Le, O., Chang, N. Y. N., Fried, W. A., et al. (2020). Thermal imaging of root caries *in vivo*. *J. Dent. Res.* 99 (13), 1502–1508. doi:10.1177/0022034520951157

Yu, D. G., Kimura, Y., Tomita, Y., Nakamura, Y., Watanabe, H., and Matsumoto, K. (2000). Study on removal effects of filling materials and broken files from root canals using pulsed Nd: Yag laser. *J. Clin. Laser Med. Surg.* 18 (1), 23–28. doi:10.1089/clm.2000.18.23

Zheng, Q., Xu, H., Song, F., Zhang, L., Zhou, X., Shao, Y., et al. (2013). Spatial distribution of the human enamel fracture toughness with aging *J. Mech. Behav. Biomed. Mat.* 26, 148–154. doi:10.1016/j.jmbbm.2013.04.025

frontiers | Frontiers in Physiology

TYPE Mini Review
PUBLISHED 25 November 2022
DOI 10.3389/fphys.2022.1032383

OPEN ACCESS

EDITED BY
Rodrigo S. Lacruz,
New York University, United States

REVIEWED BY
Sylvie Babajko,
Centre de Recherche des Cordeliers (CRC) (INSERM), France
Claire Bardet,
Université de Paris, France
Thomas G. H. Diekwisch,
University of Rochester Medical Center, United States

*CORRESPONDENCE
John D. Bartlett,
Bartlett.196@osu.edu

†PRESENT ADDRESS
Atsushi Ikeda,
Okayama University Hospital, Okayama, Japan

SPECIALTY SECTION
This article was submitted to Craniofacial Biology and Dental Research, a section of the journal Frontiers in Physiology

RECEIVED 30 August 2022
ACCEPTED 14 November 2022
PUBLISHED 25 November 2022

CITATION
Shahid S, Ikeda A, Layana MC and Bartlett JD (2022), ADAM10: Possible functions in enamel development. *Front. Physiol.* 13:1032383. doi: 10.3389/fphys.2022.1032383

ADAM10: Possible functions in enamel development

Shifa Shahid, Atsushi Ikeda†, Michelle C. Layana and John D. Bartlett*

Division of Biosciences, College of Dentistry, The Ohio State University, Columbus, OH, United States

ADAM10 is A Disintegrin And Metalloproteinase (ADAM) family member that is membrane bound with its catalytic domain present on the cell surface. It is a sheddase that cleaves anchored cell surface proteins to shed them from the cell surface. ADAM10 can cleave at least a hundred different proteins and is expressed in most tissues of the body. ADAM10 is best characterized for its role in Notch signaling. Interestingly, ADAM10 is transported to specific sites on the cell surface by six different tetraspanins. Although the mechanism is not clear, tetraspanins can regulate ADAM10 substrate specificity, which likely contributes to the diversity of ADAM10 substrates. In developing mouse teeth, ADAM10 is expressed in the stem cell niche and subsequently in pre-ameloblasts and then secretory stage ameloblasts. However, once ameloblasts begin transitioning into the maturation stage, ADAM10 expression abruptly ceases. This is exactly when ameloblasts stop their movement that extends enamel crystallites and when the enamel layer reaches its full thickness. ADAM10 may play an important role in enamel development. ADAM10 can cleave cadherins and other cell-cell junctions at specific sites where the tetraspanins have transported it and this may promote cell movement. ADAM10 can also cleave the transmembrane proteins COL17A1 and RELT. When either *COL17A1* or *RELT* are mutated, malformed enamel may occur in humans and mice. So, ADAM10 may also regulate these proteins that are necessary for proper enamel development. This mini review will highlight ADAM10 function, how that function is regulated by tetraspanins, and how ADAM10 may promote enamel formation.

KEYWORDS

ameloblasts, cell migration, enamel defects, cell surface proteins, sheddase, COL17A1, RELT

Overview of enamel development

In the continuously erupting mouse incisor, enamel development starts with the stem cell niche in the apical loop that is furthest away from the incisor eruption point (Figure 1). Stem cells migrate out of the loop, develop into pre-ameloblasts and begin their journey moving distally to where the incisor erupts. The pre-ameloblasts form a single layer aligned along a basement membrane and as they move distally in the direction of eruption, they pass through defined developmental stages. First, the pre-dentin matrix begins to form and as development progresses, the pre-ameloblasts extend finger-like

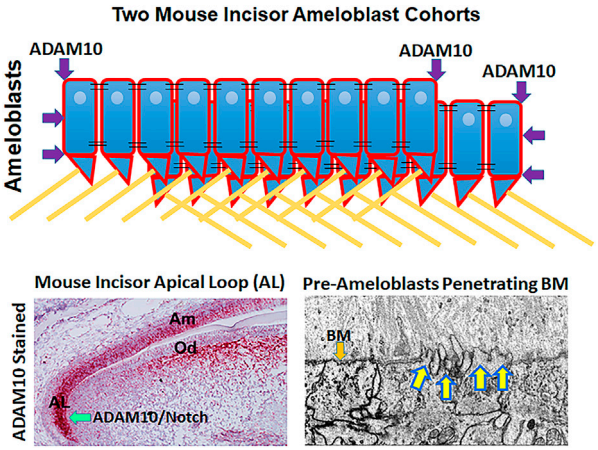

FIGURE 1
Possible mechanisms by which ADAM10 may facilitate enamel development. (Top) Schematic showing how ADAM10 may cleave the ends of ameloblast cohorts so that they can slide by one another during the secretory stage of enamel development. The cell-cell connections would also be removed between the sliding cells (not shown). Black parallel lines, tight junctions; right triangles, Tomes' processes; yellow lines, enamel rods (interrods not shown). (Bottom Left) Mouse incisor section stained red by *in situ* hybridization for ADAM10 (Ikeda et al., 2019). *Adam10* expression begins in the apical loop and continues until the ameloblasts reach the transition stage of enamel development. Adam10 may facilitate Notch signaling to maintain the stem cell niche within the apical loop (Felszeghy et al., 2010). (Bottom Right) Focused Ion Beam Scanning Electron Microscopy (FIB-SEM) demonstrating that pre-ameloblasts extent finger-like projections to penetrate the basement membrane (BM) that separates the pre-ameloblastss from the predentin organic matrix (Bartlett et al., 2021). Since ADAM10 is expressed during this time, it is possible that it assists in penetrating the basement membrane.

protrusions that penetrate the basement membrane and move in between the pre-dentin collagen fibrils.

At approximately this point, the pre-ameloblasts become secretory stage ameloblasts because they initiate the secretion of amelogenin. Eventually the entire basement membrane is removed and after this, the pre-dentin begins to mineralize starting near the ameloblast layer. Once the dentin near the ameloblasts is mineralized, ameloblasts start the growth of enamel ribbons that appear to initiate on the mineralized collagen fibers within the dentin. These ribbons extend and are intimately associated with the ameloblast cell membrane. The initial enamel ribbons are the beginning of the developing interrod enamel. The ameloblasts move back to allow the ribbons to grow in length. As this occurs, space is created to allow the ameloblasts to form Tomes' processes that then initiate rod enamel ribbon formation. The rod and interrod enamel ribbons are within a few degrees of being at right angles to one another (Bartlett et al., 2021).

Secretory stage ameloblasts will eventually define the full thickness of the developing enamel layer. It is during this stage that amorphous ribbons convert into crystallites and when large amounts of enamel proteins are secreted into the enamel matrix. These proteins include amelogenin, ameloblastin, enamelin, and matrix metalloproteinase-20 (MMP20, enamelysin). It is during the secretory stage that cohorts of ameloblasts slide by one another to begin forming the decussating (crisscrossing) enamel rod pattern characteristic of mouse incisor enamel. How these cohorts of ameloblast stay attached to each other while detaching from adjacent cohorts remains a mystery.

Another mystery is in understanding why deletion or mutations in Plectin (*PLEC*), Laminin 332 (*LAMA3*, *LAMB3*, and *LAMC2*), COL17A1, and α6ß4 (*ITGA6* and *ITGB4*) cause enamel malformations. These proteins combine to form an attachment complex in skin. It was postulated (Simmer et al., 2021) that these proteins also serve to attach enamel ribbons at the ameloblast membrane by forming a complex that may bind enamel matrix proteins necessary for ribbon growth, such as binding to enamelin and/or ameloblastin. This could allow the ameloblasts to lengthen the ribbons as they move back to facilitate crystallite growth. In support of this postulate, full-length, uncleaved enamelin is only found abutting the ameloblast membrane and if enamelin is deleted from the mouse genome, no enamel, and virtually no mineral forms, near the dentin (Hu et al., 2014). And, previous studies have demonstrated that laminin 332 is necessary for ameloblast attachment to the underlying secretory stage enamel (Sahlberg et al., 1998; Ryan et al., 1999).

As the secretory stage nears its end, the enamel is protein-rich and has a soft cheese-like consistency. However, this dramatically changes as the secretory stage ameloblasts transition into maturation stage ameloblasts. The tall columnar secretory stage ameloblasts become reduced in height and start secreting kallikrein-related peptidase 4 (KLK4), which cleaves the enamel matrix proteins to

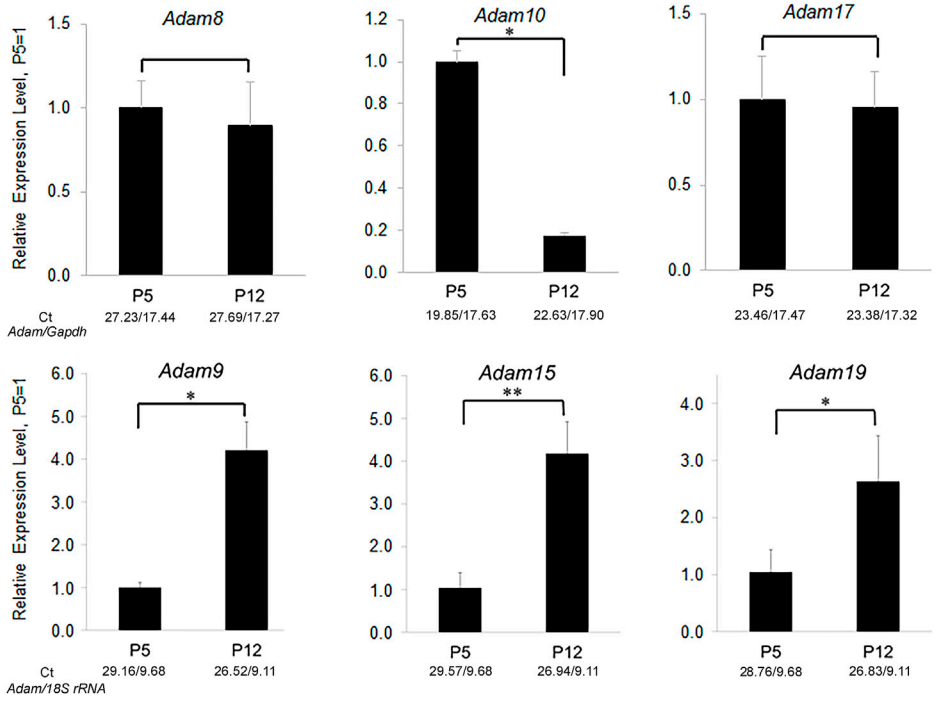

FIGURE 2
Relative expression levels of ADAM family members in murine first molar enamel organs from P5 (secretory stage) and P12 (maturation stage) mice. qPCR demonstrated that *Adam8, 9, 10, 15, 17,* and *19* were expressed in mouse enamel organs (Ikeda et al., 2019). However, only *Adam10* was expressed predominantly in the secretory stage when ameloblast movement occurs. Three biological replicates were analyzed for each of three experiments (*, $p < 0.05$; **, $p < 0.01$; Ct, cycle threshold).

facilitate their export out of the enamel matrix. It is during the maturation stage of enamel development that the enamel crystallites grow in width and thickness to form a virtually protein free enamel layer that is the hardest most mineralized substance in the body. After this stage the ameloblasts become reduced in size and cover the hardened enamel as tooth eruption occurs (Bartlett, 2013).

Introduction to ADAMs

ADAMs are a family of metalloproteinases characterized by having A Disintegrin And Metalloproteinase domain. They also contain a cysteine rich domain followed by a transmembrane region and a cytoplasmic tail. Therefore, the ADAMs are transmembrane proteins with their catalytic domains located outside the cell near the cell surface where they cleave the extracellular domains of membrane bound proteins. This process is termed ectodomain shedding (Reiss and Saftig, 2009).

ADAMs have an N-terminal pro-domain that covers an otherwise active catalytic domain. Its removal by proteolysis results in ADAM catalytic activation. ADAMs cleave type I and Type II transmembrane and glycosylphosphatidylinositol (GPI)-anchored proteins near the plasma membrane (Wetzel et al., 2017). ADAMs have been implicated in numerus physiological roles including, cell signaling, development, wound healing, inflammation, and migration. Twenty two ADAMs have been identified in humans. However only twelve are capable of becoming catalytically active and the other ten have non-functional catalytic domains and are therefore not as well studied (Harrison et al., 2021). Previously we performed an active ADAM screen of the mouse enamel organ and discovered that ADAM10 was the only ADAM expressed predominantly in early, but not late enamel development (Figure 2).

Here we will review the functional characteristics of ADAM10, show what is known about ADAM10 in enamel development, and present evidence about ADAM10's possible mechanistic function during enamel formation.

ADAM10 overview

ADAM10 starts as an inactive zymogen and is activated in the trans-Golgi network by two pro-protein convertases that cleave the ADAM pro-domain (Vincent, 2016). Additionally,

ADAM10 is glycosylated in four places in its extracellular domain and these glycosylations ensure proper trafficking and stability (Vincent, 2016). A select group of six different tetraspanins can each traffic ADAM10 from the endoplasmic reticulum, through the Golgi and to the cell surface. Depending on the tetraspanin involved, ADAM10 will localize to different subcellular locations. Therefore, tetraspanins can direct ADAM10 to the substrates it may cleave and ADAM10 is known to have over 100 substrates (Harrison et al., 2021). However, its proteolytic activity can be inhibited by both tissue inhibitor of metalloproteinase-1 and -3 (Timp1 and Timp3) (Giebeler and Zigrino, 2016). Since *Adam10*-ablated mice die at embryonic day 9.5, ADAM10 is essential for embryonic development (Weber et al., 2011).

Human ADAM10 haploinsuficiency causes the rare hyperpigmentation skin disease named reticulate acropigmentation of Kitamura (Kono and Akiyama, 2019). To date no other defects including enamel defects are reported in these patients, likely indicating that for all other organs ADAM10 haploinsuficiency is adequate for proper development.

ADAM10 and the Notch pathway

The best characterized function of ADAM10 is in Notch signaling. ADAM10 cleaves/sheds Notch proteins, which subsequently allows the remaining truncated membrane tethered Notch fragment to undergo intramembrane proteolysis by a ɣ-secretase. This allows translocation of the Notch intracellular domain into the nucleus where it can function as a transcriptional regulator (Matthews et al., 2017). ADAM10 deficient mice have similar defects as Notch knockout mice, such as CNS, somite and cardiovascular defects, which suggests a major role for ADAM10 in Notch signaling (Hartmann et al., 2002). Notch pathway loss-of-function phenotypes are also observed when ADAM10 is deleted from epithelial tissues (Weber et al., 2011).

Ameloblasts are the cells responsible for enamel formation and Notch proteins may maintain their stem cell niche in the apical loop of the continuously erupting mouse incisor (Felszeghy et al., 2010). However, Notch 1, 2, and 3 are not expressed by both pre-ameloblasts and ameloblasts (Mitsiadis et al., 1995), which are the cells that initiate and facilitate enamel formation.

ADAM10 and cell migration

Cancer cell migration and physiological migration, such as T-cell migration through endothelial cell layers are well documented to be facilitated by ADAM10 (Reiss and Saftig, 2009). The vast majority of ADAM10 literature points to ADAM10 shedding substrates from the cell surface on the same cells where both ADAM10 and the substrates reside. These substrates include cell-cell binding proteins such as E-, N- and VE-cadherins (Dempsey, 2017) and tight junction proteins such as F11R and JAM3 (Wetzel et al., 2017). However, evidence exists that ADAM10, either directly or indirectly, cleaves substrates that are not specifically present on a cell surface. For example, Type IV collagen is a major component of basement membranes and ADAM10 was demonstrated to cleave Type IV collagen *in vitro* (Millichip et al., 1998). ADAM10 also facilitates the migration of bone marrow derived mast cells (BMMC) through collagen IV-coated transwells when compared to *Adam10* ablated BMMCs (Faber et al., 2014). At least two other studies have demonstrated, by use of transwell assays with matrigel coated filters, that active ADAM10 facilitates cell migration/invasion through these coated filters (Ikeda et al., 2019; Sun et al., 2019).

Additionally, ADAM10 overexpression *in vivo* in a mouse emphysema model was responsible for the destruction of lung parenchyma with associated basement membrane proteolysis. Note that Type IV collagen is the most abundant non-fibril forming collagen in lung tissue and is present in both alveolar and capillary basement membranes. ADAM10 was overexpressed by use of an adenovirus gene transfer vector coding for human ADAM10 that was introduced intratracheally into mice. Assessment of their lungs after 2 months, demonstrated enlarged airspaces, as would occur with emphysema. The authors cautioned that ADAM10 could have acted by directly destroying the lung tissue or may have acted indirectly by causing inflammation and/or apoptosis (Saitoh et al., 2009).

ADAM10 and tetraspanins (Tspans)

Tetraspanins are a superfamily of 33 membrane proteins (Tspan1–Tspan33) in mammals, which transport and regulate partner proteins containing transmembrane domains. In addition to transporting proteins from the ER through the Golgi and to the cell surface, Tspans also bind with partner proteins that influence Tspan intracellular trafficking, clustering, lateral mobility and compartmentalization (Matthews et al., 2018). Once at the cell surface, Tspans form small assemblies of approximately ten members of a single type per cluster (Harrison et al., 2021).

A subset of Tspans are the TspanC8s, which contain eight cysteine residues in their extracellular domains. Six different TspanC8s (Tspan 5, 10, 14, 15, 17, and 33) transport and regulate ADAM10 at the cell surface. Additionally, TspanC8s will localize ADAM10 to specific subcellular domains and astonishingly, can influence ADAM10 substrate specificity. This was first observed when it was discovered that Tspan15/ADAM10 is associated with N-cadherin shedding (Harrison

et al., 2021). It also fits with the observation that ADAM10 substrate preferences have little correlation with the protein sequence of their substrates (Matthews et al., 2017). It is unclear precisely how TspanC8s modulate ADAM10 substrate specificity. Mechanisms may include subcellular localization, direct interaction with substrates and/or modulation of ADAM10 conformation (Harrison et al., 2021). Therefore, ADAM10 likely has six different sets of substrate specificities depending on the TspanC8 it associates with and this likely contributes to its diverse substrate repertoire of over 100 substrates. Interestingly, it was previously suggested that since ADAM10 can be delivered by tetraspanins to specific cell surface locations, that this may be a way for ADAM10 to specifically separate cell-cell connections between cohorts of ameloblasts that move in opposite directions. Therefore, the tetraspanins may allow ADAM10 to cleave cell-cell connections between adjacent cohorts but leave the cohorts intact (Ikeda et al., 2019).

ADAM10 substrates pertinent to enamel formation

Since ADAM10 expression initiates in the apical loop of the mouse incisor (Figure 1) and its expression continues throughout the secretory stage of enamel development, ADAM10 may participate in growth of the enamel crystallites until they lengthen to form the full thickness of the developing enamel. Below are proteins that are shed by ADAM10 and that are expressed by ameloblasts. When mutated, these proteins can cause enamel malformation.

Type XVII collagen

Collagen XVII (COL17A1) is a homotrimer of three alpha1-XVII chains. It is a type II transmembrane protein that is a member of the superfamily of transmembrane collagens. Originally it was discovered in epithelial cell hemidesmosomes where it plays an important role in hemidesmosome stability and epithelial attachment (McGrath et al., 1995). Although functionally not well characterized, it is also present in other tissues in a hemidesmosome-independent manner, such as in the brain, kidney, placenta (Tuusa et al., 2021) and enamel organ.

COL17A1 deletion or mutations can cause non-Herlitz junctional epidermolysis bullosa (JEB), which manifests when the epidermis separates from the dermis (Tuusa et al., 2021). Patients with *COL17A1*-mediated JEB typically also have enamel malformations characterized by enamel hypoplasia and pitting of the enamel surface (Asaka et al., 2009). Of interest is that COL17A1 is expressed during the secretory stage of enamel development (Simmer et al., 2021) when ADAM10 is also expressed. Both ADAM9 and ADAM10 were demonstrated to shed COL17A1 from the cell surface of keratinocytes (Franzke et al., 2009). However, in contrast to ADAM10, little to no ADAM9 is expressed in mouse molar enamel organs that are predominantly in the secretory stage of enamel development (Figure 2). Therefore, COL17A1 could be an ADAM10 substrate of interest during the early stages of enamel formation.

A possible mechanism of how ADAM10 may function to promote enamel development could involve its shedding of COL17A1 from ameloblasts. Perhaps, as previously proposed (Simmer et al., 2021), COL17A1 is a component of the apparatus that attaches the forming ribbons to the retreating ameloblasts as the ribbons grow in length. If ribbon growth requires the disengagement and then reattachment of the ribbons to the apical end of ameloblasts, then it may be possible that ADAM10 functions to promote the detachment process by cleaving COL17A1, which could dislodge the ameloblasts from the lengthening ribbons and subsequently allow the ameloblasts to reattach at a site distal to the previous attachment site. However, this postulated mechanism will need to be experimentally validated.

Type IV collagen

Currently it is unknown how the basement membrane between pre-ameloblasts and the pre-dentin matrix is removed. Ameloblasts have finger-like projections that protrude through the basement membrane as they initiate its removal. So, the possibility exists that a membrane bound proteinase would help the projections to penetrate the basement membrane. ADAM10 is expressed in the mouse incisor apical loop well before the basement membrane is degraded and its expression persists well after the basement membrane is removed. Perhaps, ADAM10 could pair with a different tetraspanin to degrade the basement membrane Type IV collagen and switch to another tetraspanin once the membrane is removed. However, this supposition needs to be demonstrated.

RELT

RELT is a member of the tumor necrosis factor receptor superfamily (TNFRSF). The TNFRSF members are transmembrane proteins that regulate biological processes such as cell death, inflammation plus cell differentiation and development. RELT is highly expressed in lymphoid tissues, hence it was named Receptor Expressed in Lymphoid Tissues. An interesting aspect of RELT is its designation as an orphan receptor because to date, no ligand has been identified that binds to RELT. However, *RELT* mutations cause autosomal recessive amelogenesis imperfecta where the dental enamel is of normal or near normal volume in unerupted teeth, but is hypomineralized, which causes the enamel to abrade from erupted teeth. This

phenotype is typically indicative of a maturation stage defect. However in mice, *Relt* is only expressed on pre-ameloblasts and secretory stage ameloblasts, but not on maturation stage ameloblasts (Kim et al., 2019). Moreover, the human enamel prism pattern that is established during the secretory stage of enamel development, was abnormal in a patient with a *RELT* mutation (Nikolopoulos et al., 2020). Previously our group demonstrated that ADAM10, but not ADAM17 can cleave the RELT extracellular domain (Ikeda et al., 2019). Therefore, ADAM10 may be an important modulator of RELT function that is necessary for proper enamel formation.

Nectin1 and Nectin4

Nectins are a Ca^{2+}-independent sub-family of immunoglobulin-like cell-cell adhesion molecules. All four nectins (NECTINS 1, 2, 3, and 4) are expressed within the mouse enamel organ by postnatal day 0 (Yoshida et al., 2010). Both NECTINS 1 and 4 are ADAM10 substrates (Kim et al., 2010; Buchanan et al., 2017).

Although *NECTIN1* mutations are not yet documented to cause enamel malformation in humans, deletion of *Nectin1* in mice causes their incisors to become hypomineralized. The maturation stage of development was shortened in these mice because during this stage the ameloblasts separated from the stratum intermedium and formed blister-like structures (Barron et al., 2008). Since ADAM10 is not expressed during the maturation stage of enamel development, it is unlikely that ADAM10 modulates NECTIN1 function during this stage.

Biallelic mutations in the human *NECTIN4* gene cause ectodermal dysplasia-syndactyly syndrome 1 (EDSS1). Two reports of EDSS1 had patients with associated enamel hypoplasia (Raza et al., 2015; Rotunno et al., 2021). Perhaps ADAM10 modulates NECTIN4 expression at the cell surface. However, ADAM17 also sheds NECTIN4 (Buchanan et al., 2017). Although it is unknown if ADAM17 is expressed on ameloblasts, it is expressed during the secretory stage in mouse molar enamel organs (Figure 2). Therefore, it remains possible that ADAM17 can substitute for the loss of ADAM10 in regulating NECTIN4 expression.

Conclusion

ADAM10 has the possibility of performing several functions during enamel development. These possibilities include: ADAM10 may maintain the stem cell niche through Notch signaling so that the stem cells can properly develop into mature enamel organ cells. In support of this, a recent study showed that ADAM10-mediated Notch signaling is necessary for proper enamel formation (Mitsiadis et al., 2022). Once the stem cells become pre-ameloblasts, it is not known how the pre-ameloblasts begin to penetrate the basement membrane that separates them form the pre-dentin matrix. Although ADAM10 is expressed prior to and after basement membrane removal, the possibility exists that it could participate in its removal when paired with a tetraspanin that may promote its ability to cleave basement membrane proteins. Once murine incisor pre-ameloblasts become secretory stage ameloblasts, two types of ADAM10 function could promote the completion of the secretory stage of enamel development. First, ADAM10 could be directed to specific cell sites by tetraspanins such that it could separate the cohorts of ameloblasts that slide by one another to create the characteristic decussating enamel prism pattern (Figure 1). Therefore, this location-specific shedding of cell-cell contacts would separate the cells into cohorts, but would not separate the cells within a cohort. Second, ADAM10 can cleave the cell surface proteins COL17A1 and RELT that are present on ameloblasts during the secretory stage of enamel development. Both of these proteins are essential for proper enamel formation as their mutation was shown to cause enamel defects. Therefore, ADAM10 may be an important regulator of their function. Much remains to be characterized about the role of ADAM10 during enamel development to determine which, if any of these potential mechanisms of ADAM10 function are valid.

Author contributions

SS and AI prepared the figures and reviewed the manuscript. ML reviewed and contributed to the manuscript. JB wrote the initial draft of the manuscript. All authors contributed to the work and have approved the final manuscript.

Funding

This research was supported by the National Institute of Dental and Craniofacial Research of the National Institutes of Health under award number R01DE028297 (JB).

Acknowledgments

We thank James P. Simmer for helpful discussions about the manuscript.

Conflict of interest

The authors declare that the research was conducted in the absence of any commercial or financial relationships that could be construed as a potential conflict of interest.

Publisher's note

References

Asaka, T., Akiyama, M., Domon, T., Nishie, W., Natsuga, K., Fujita, Y., et al. (2009). Type XVII collagen is a key player in tooth enamel formation. *Am. J. Pathol.* 174 (1), 91–100. doi:10.2353/ajpath.2009.080573

Barron, M. J., Brookes, S. J., Draper, C. E., Garrod, D., Kirkham, J., Shore, R. C., et al. (2008). The cell adhesion molecule nectin-1 is critical for normal enamel formation in mice. *Hum. Mol. Genet.* 17 (22), 3509–3520. doi:10.1093/hmg/ddn243

Bartlett, J. D. (2013). Dental enamel development: Proteinases and their enamel matrix substrates. *ISRN Dent.* 2013, 684607. doi:10.1155/2013/684607

Bartlett, J. D., Smith, C. E., Hu, Y., Ikeda, A., Strauss, M., Liang, T., et al. (2021). MMP20-generated amelogenin cleavage products prevent formation of fan-shaped enamel malformations. *Sci. Rep.* 11 (1), 10570. doi:10.1038/s41598-021-90005-z

Buchanan, P. C., Boylan, K. L. M., Walcheck, B., Heinze, R., Geller, M. A., Argenta, P. A., et al. (2017). Ectodomain shedding of the cell adhesion molecule Nectin-4 in ovarian cancer is mediated by ADAM10 and ADAM17. *J. Biol. Chem.* 292 (15), 6339–6351. doi:10.1074/jbc.M116.746859

Dempsey, P. J. (2017). Role of ADAM10 in intestinal crypt homeostasis and tumorigenesis. *Biochim. Biophys. Acta. Mol. Cell Res.* 1864 (11), 2228–2239. doi:10.1016/j.bbamcr.2017.07.011

Franzke, C. W., Bruckner-Tuderman, L., and Blobel, C. P. (2009). Shedding of collagen XVII/BP180 in skin depends on both ADAM10 and ADAM9. *J. Biol. Chem.* 284 (35), 23386–23396. doi:10.1074/jbc.M109.034090

Faber, T. W., Pullen, N. A., Fernando, J. F., Kolawole, E. M., McLeod, J. J., Taruselli, M., et al. (2014). ADAM10 is required for SCF-induced mast cell migration. *Cell. Immunol.* 290 (1), 80–88. doi:10.1016/j.cellimm.2014.05.005

Felszeghy, S., Suomalainen, M., and Thesleff, I. (2010). Notch signalling is required for the survival of epithelial stem cells in the continuously growing mouse incisor. *Differentiation.* 80 (4-5), 241–248. doi:10.1016/j.diff.2010.06.004

Giebeler, N., and Zigrino, P. (2016). A disintegrin and metalloprotease (ADAM): Historical overview of their functions. *Toxins (Basel)* 8 (4), 122. doi:10.3390/toxins8040122

Harrison, N., Koo, C. Z., and Tomlinson, M. G. (2021). Regulation of ADAM10 by the TspanC8 family of tetraspanins and their therapeutic potential. *Int. J. Mol. Sci.* 22 (13), 6707. doi:10.3390/ijms22136707

Hartmann, D., de Strooper, B., Serneels, L., Craessaerts, K., Herreman, A., Annaert, W., et al. (2002). The disintegrin/metalloprotease ADAM 10 is essential for Notch signalling but not for alpha-secretase activity in fibroblasts. *Hum. Mol. Genet.* 11 (21), 2615–2624. doi:10.1093/hmg/11.21.2615

Hu, J. C., Hu, Y., Lu, Y., Smith, C. E., Lertlam, R., Wright, J. T., et al. (2014). Enamelin is critical for ameloblast integrity and enamel ultrastructure formation. *PLoS One* 9 (3), e89303. doi:10.1371/journal.pone.0089303

Ikeda, A., Shahid, S., Blumberg, B. R., Suzuki, M., and Bartlett, J. D. (2019). ADAM10 is expressed by ameloblasts, cleaves the RELT TNF receptor extracellular domain and facilitates enamel development. *Sci. Rep.* 9 (1), 14086. doi:10.1038/s41598-019-50277-y

Kim, J., Lilliehook, C., Dudak, A., Prox, J., Saftig, P., Federoff, H. J., et al. (2010). Activity-dependent alpha-cleavage of nectin-1 is mediated by a disintegrin and metalloprotease 10 (ADAM10). *J. Biol. Chem.* 285 (30), 22919–22926. doi:10.1074/jbc.M110.126649

Kim, J. W., Zhang, H., Seymen, F., Koruyucu, M., Hu, Y., Kang, J., et al. (2019). Mutations in RELT cause autosomal recessive amelogenesis imperfecta. *Clin. Genet.* 95 (3), 375–383. doi:10.1111/cge.13487

Kono, M., and Akiyama, M. (2019). Dyschromatosis symmetrica hereditaria and reticulate acropigmentation of Kitamura: An update. *J. Dermatol. Sci.* 93 (2), 75–81. doi:10.1016/j.jdermsci.2019.01.004

Matthews, A. L., Koo, C. Z., Szyroka, J., Harrison, N., Kanhere, A., and Tomlinson, M. G. (2018). Regulation of leukocytes by TspanC8 tetraspanins and the "molecular scissor" ADAM10. *Front. Immunol.* 9, 1451. doi:10.3389/fimmu.2018.01451

Matthews, A. L., Szyroka, J., Collier, R., Noy, P. J., and Tomlinson, M. G. (2017). Scissor sisters: Regulation of ADAM10 by the TspanC8 tetraspanins. *Biochem. Soc. Trans.* 45 (3), 719–730. doi:10.1042/BST20160290

McGrath, J. A., Gatalica, B., Christiano, A. M., Li, K., Owaribe, K., McMillan, J. R., et al. (1995). Mutations in the 180-kD bullous pemphigoid antigen (BPAG2), a hemidesmosomal transmembrane collagen (COL17A1), in generalized atrophic benign epidermolysis bullosa. *Nat. Genet.* 11 (1), 83–86. doi:10.1038/ng0995-83

Millichip, M. I., Dallas, D. J., Wu, E., Dale, S., and McKie, N. (1998). The metallo-disintegrin ADAM10 (MADM) from bovine kidney has type IV collagenase activity *in vitro*. *Biochem. Biophys. Res. Commun.* 245 (2), 594–598. doi:10.1006/bbrc.1998.8485

Mitsiadis, T. A., Jimenez-Rojo, L., Balic, A., Weber, S., Saftig, P., and Pagella, P. (2022). Adam10-dependent Notch signaling establishes dental epithelial cell boundaries required for enamel formation. *iScience* 25 (10), 105154. doi:10.1016/j.isci.2022.105154

Mitsiadis, T. A., Lardelli, M., Lendahl, U., and Thesleff, I. (1995). Expression of Notch 1, 2 and 3 is regulated by epithelial-mesenchymal interactions and retinoic acid in the developing mouse tooth and associated with determination of ameloblast cell fate. *J. Cell Biol.* 130 (2), 407–418. doi:10.1083/jcb.130.2.407

Nikolopoulos, G., Smith, C. E. L., Brookes, S. J., El-Asrag, M. E., Brown, C. J., Patel, A., et al. (2020). New missense variants in RELT causing hypomineralised amelogenesis imperfecta. *Clin. Genet.* 97 (5), 688–695. doi:10.1111/cge.13721

Raza, S. I., Nasser Dar, R., Shah, A. A., and Ahmad, W. (2015). A novel homozygous nonsense mutation in the PVRL4 gene and expansion of clinical spectrum of EDSS1. *Ann. Hum. Genet.* 79 (2), 92–98. doi:10.1111/ahg.12094

Reiss, K., and Saftig, P. (2009). The "a disintegrin and metalloprotease" (ADAM) family of sheddases: Physiological and cellular functions. *Semin. Cell Dev. Biol.* 20 (2), 126–137. doi:10.1016/j.semcdb.2008.11.002

Rotunno, R., Diociaiuti, A., Dentici, M. L., Rinelli, M., Callea, M., Retrosi, C., et al. (2021). Ectodermal dysplasia-syndactyly syndrome with toe-only minimal syndactyly due to a novel mutation in NECTIN4: A case report and literature review. *Genes (Basel)* 12 (5), 748. doi:10.3390/genes12050748

Ryan, M. C., Lee, K., Miyashita, Y., and Carter, W. G. (1999). Targeted disruption of the LAMA3 gene in mice reveals abnormalities in survival and late stage differentiation of epithelial cells. *J. Cell Biol.* 145 (6), 1309–1323. doi:10.1083/jcb.145.6.1309

Sahlberg, C., Hormia, M., Airenne, T., and Thesleff, I. (1998). Laminin gamma2 expression is developmentally regulated during murine tooth morphogenesis and is intense in ameloblasts. *J. Dent. Res.* 77 (8), 1589–1596. doi:10.1177/00220345980770080601

Saitoh, H., Leopold, P. L., Harvey, B. G., O'Connor, T. P., Worgall, S., Hackett, N. R., et al. (2009). Emphysema mediated by lung overexpression of ADAM10. *Clin. Transl. Sci.* 2 (1), 50–56. doi:10.1111/j.1752-8062.2008.00085.x

Simmer, J. P., Hu, J. C., Hu, Y., Zhang, S., Liang, T., Wang, S. K., et al. (2021). A genetic model for the secretory stage of dental enamel formation. *J. Struct. Biol.* 213 (4), 107805. doi:10.1016/j.jsb.2021.107805

Sun, S. Q., Ren, L. J., Liu, J., Wang, P., and Shan, S. M. (2019). Sevoflurane inhibits migration and invasion of colorectal cancer cells by regulating microRNA-34a/ADAM10 axis. *Neoplasma* 66 (6), 887–895. doi:10.4149/neo_2018_181213N962

Tuusa, J., Kokkonen, N., and Tasanen, K. (2021). BP180/Collagen XVII: A molecular view. *Int. J. Mol. Sci.* 22 (22), 12233. doi:10.3390/ijms222212233

Vincent, B. (2016). Regulation of the α-secretase ADAM10 at transcriptional, translational and post-translational levels. *Brain Res. Bull.* 126 (2), 154–169. doi:10.1016/j.brainresbull.2016.03.020

Weber, S., Niessen, M. T., Prox, J., Lullmann-Rauch, R., Schmitz, A., Schwanbeck, R., et al. (2011). The disintegrin/metalloproteinase Adam10 is essential for epidermal integrity and Notch-mediated signaling. *Development* 138 (3), 495–505. doi:10.1242/dev.055210

Wetzel, S., Seipold, L., and Saftig, P. (2017). The metalloproteinase ADAM10: A useful therapeutic target? *Biochim. Biophys. Acta. Mol. Cell Res.* 1864 (11), 2071–2081. doi:10.1016/j.bbamcr.2017.06.005

Yoshida, T., Miyoshi, J., Takai, Y., and Thesleff, I. (2010). Cooperation of nectin-1 and nectin-3 is required for normal ameloblast function and crown shape development in mouse teeth. *Dev. Dyn.* 239 (10), 2558–2569. doi:10.1002/dvdy.22395

frontiers | Frontiers in Physiology

TYPE Original Research
PUBLISHED 29 November 2022
DOI 10.3389/fphys.2022.1062042

OPEN ACCESS

EDITED BY
Pamela Den Besten,
University of California, San Francisco, United States

REVIEWED BY
Catherine Chaussain,
Université Paris Cité, France
Sylvie Babajko,
INSERM U1138 Centre de Recherche des Cordeliers (CRC), France

*CORRESPONDENCE
Hidemitsu Harada,
hideha@iwate-med.ac.jp
Keishi Otsu,
kotsu@iwate-med.ac.jp

SPECIALTY SECTION
This article was submitted to Craniofacial Biology and Dental Research, a section of the journal Frontiers in Physiology

RECEIVED 05 October 2022
ACCEPTED 15 November 2022
PUBLISHED 29 November 2022

CITATION
Arai H, Inaba A, Ikezaki S, Kumakami-Sakano M, Azumane M, Ohshima H, Morikawa K, Harada H and Otsu K (2022), Energy metabolic shift contributes to the phenotype modulation of maturation stage ameloblasts.
Front. Physiol. 13:1062042.
doi: 10.3389/fphys.2022.1062042

Energy metabolic shift contributes to the phenotype modulation of maturation stage ameloblasts

Haruno Arai[1,2], Akira Inaba[1,2], Shojiro Ikezaki[1], Mika Kumakami-Sakano[1], Marii Azumane[1,3], Hayato Ohshima[4], Kazumasa Morikawa[2], Hidemitsu Harada[1]* and Keishi Otsu[1]*

[1]Division of Developmental Biology and Regenerative Medicine, Department of Anatomy, Iwate Medical University, Yahaba, Japan, [2]Division of Pediatric and Special Care Dentistry, Department of Oral Health Science, School of Dentistry, Iwate Medical University, Morioka, Japan, [3]Division of Oral and Maxillofacial Surgery, Department of Reconstructive Oral and Maxillofacial Surgery, Iwate Medical University, Morioka, Japan, [4]Division of Anatomy and Cell Biology of the Hard Tissue, Department of Tissue Regeneration and Reconstruction, Niigata University Graduate School of Medical and Dental Sciences, Niigata, Japan

Maturation stage ameloblasts (M-ABs) are responsible for terminal enamel mineralization in teeth and undergo characteristic cyclic changes in both morphology and function between ruffle-ended ameloblasts (RA) and smooth-ended ameloblasts (SA). Energy metabolism has recently emerged as a potential regulator of cell differentiation and fate decisions; however, its implication in M-ABs remains unclear. To elucidate the relationship between M-ABs and energy metabolism, we examined the expression pattern of energy metabolic enzymes in M-ABs of mouse incisors. Further, using the HAT7 cell line with M-AB characteristics, we designed experiments to induce an energy metabolic shift by changes in oxygen concentration. We revealed that RA preferentially utilizes oxidative phosphorylation, whereas SA depends on glycolysis-dominant energy metabolism in mouse incisors. In HAT7 cells, hypoxia induced an energy metabolic shift toward a more glycolytic-dominant state, and the energy metabolic shift reduced alkaline phosphatase (ALP) activity and calcium transport and deposition with a change in calcium-related gene expression, implying a phenotype shift from RA to SA. Taken together, these results indicate that the energy metabolic state is an important determinant of the RA/SA phenotype in M-ABs. This study sheds light on the biological significance of energy metabolism in governing M-ABs, providing a novel molecular basis for understanding enamel mineralization and elucidating the pathogenesis of enamel hypomineralization.

KEYWORDS

tooth, enamel, ameloblast, energy metabolism, OxPhos, glycolysis, hypoxia, mineralization

Introduction

Enamel is the most highly mineralized tissue in the vertebrate body and is composed of substituted hydroxyapatite, primarily calcium and inorganic phosphate. Ameloblasts, which are responsible for enamel formation, are oral epithelial cells of ectodermal origin. The proliferating inner enamel epithelium (IEEs) differentiates into secretory stage ameloblasts (S-AMs), and they differentiate into maturation stage ameloblasts (M-ABs) through transition stage ameloblasts (T-ABs) (Figures 1A–E). S-AMs secrete enamel matrix proteins, which form the base of enamel and contribute to the initial calcification, while M-ABs modulate enamel mineralization by transporting minerals, controlling pH, and modulating protein degradation and absorption (Nanci, 2008; Bartlett, 2013).

During the maturation stage, ameloblasts change their morphology in a unique series of modulations (cyclical changes) between a ruffle-ended (RA) appearance and a smooth-ended (SA) appearance in coordinated groups, appearing as bands of similar morphology (Warshawsky and Smith, 1974; Reith and Boyde, 1981). RA cells are characterized by distinct distal striated or ruffled borders (Reith and Boyde, 1979). In contrast, SA cells exhibit a complete absence of the distal ruffled border (Sasaki et al., 1987). RA has a greater capacity to transport ions into and away from the enamel matrix and to absorb the enamel matrix protein debris. SA with incomplete junctional complexes may engage in the paracellular movement of fluids and ions, which may contribute to the neutralization of pH in the enamel matrix (Lacruz, 2017). SA appear at ~8.5 h intervals in rat incisors, and

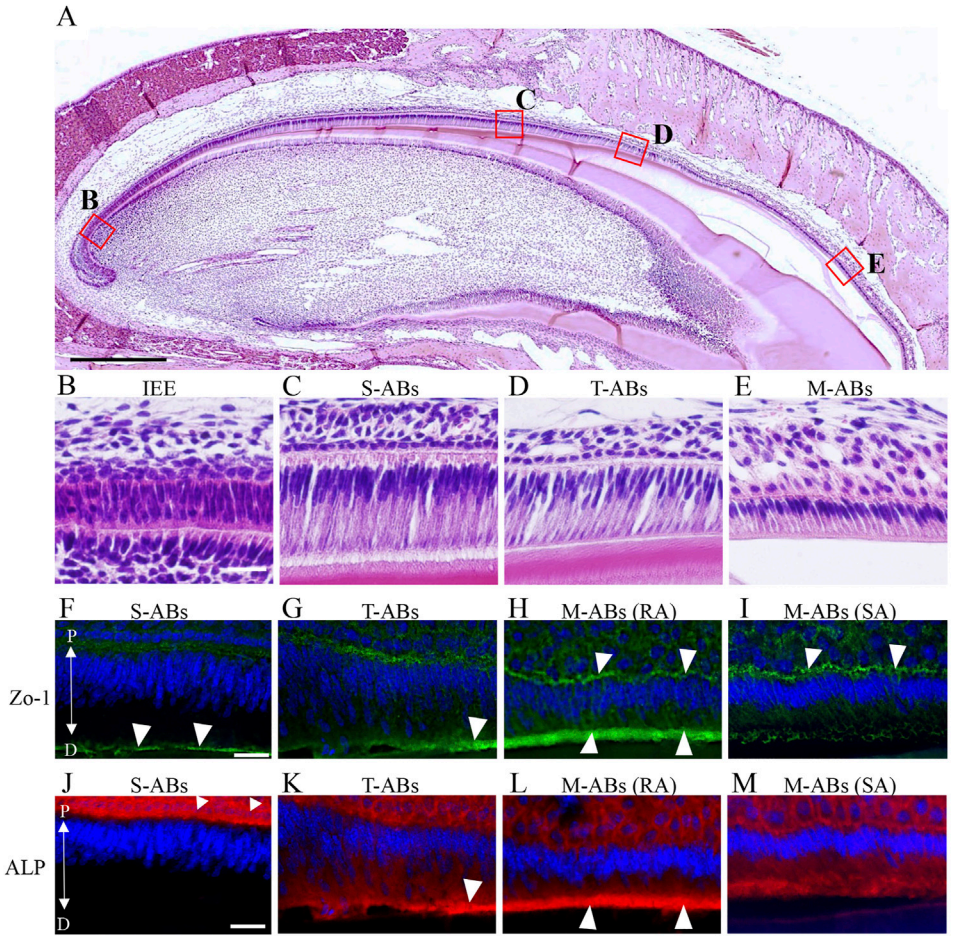

FIGURE 1
Differential expression of Zo-1 and ALP during amelogenesis in the maxillary incisor. **(A)** Low magnification image of H&E-stained sections of mouse maxillary incisors. The boxed areas in **(A)** are magnified in **(B–E)**. **(B)** Inner enamel epithelium cells. **(C)** Secretory stage ameloblasts. **(D)** Transition stage ameloblasts **(E)** Maturation stage ameloblasts. **(F–I)** Zo-1 immunostaining of mouse maxillary incisor ameloblasts. **(J–M)** ALP staining of mouse maxillary incisor ameloblasts. The nucleus is stained with DAPI (blue). S-ABs, secretory stage ameloblasts; T-ABs, transition stage ameloblasts; M-ABs, maturation stage ameloblasts; RA, ruffle-ended ameloblasts; SA, smooth-ended ameloblasts; P, proximal; D, distal. Scale bars: 500 μm **(A)**; 20 μm **(B–M)**.

these ameloblasts change into RA cells after 2 h, reforming their characteristic features at the distal border (Smith et al., 1987). Thus, cyclic RA-SA modulation is crucial for normal enamel mineralization. However, the regulatory mechanisms and determinants that distinguish RA from SA are not yet understood.

A close relationship between energy metabolism, cellular differentiation, and fate decisions has emerged in recent years. Early embryos are dependent on oxidative phosphorylation (OXPHOS). As developmental stages progress, they utilize the glycolytic system to synthesize ATP, which peaks after implantation and slowly declines as oxidative metabolism is reinitiated by vascularization (Folmes et al., 2012). Human ES and iPS cells differ in their energy metabolism state between the naïve type, which is close to the internal cell mass before implantation, and the primed type, which resembles pluripotency in the epiblast after implantation (Tsogtbaatar et al., 2020). Recently, we reported that, in ameloblasts, slowly dividing dental epithelial stem cells are glycolytic-dominated, while rapidly dividing transient amplifying (TA) cells are OXPHOS-dominated in their energy metabolism (Otsu et al., 2021), indicating the implication of energy metabolism in the cell fate decision of ameloblasts. Based on this, we hypothesized that energy metabolism is involved in RA-SA modulation in M-ABs.

In this study, we explored the change of energy metabolic characteristics in M-ABs immunohistochemically. To elucidate the effect of an energy metabolic shift on M-ABs, we utilized the change of oxygen concentration. We found that RA and SA have distinct characteristics of energy metabolism and that metabolic shift is a potential regulator of RA-SA modulation of M-ABs. Our study proposes a novel perspective on enamel research and attempts to elucidate the pathogenesis of enamel hypomineralization.

Materials and methods

Animals and preparation of tissues

All animal experiments complied with the guidelines of the Ministry of Education, Culture, Sports, Science and Technology, the Ministry of Environment, and the Science Council of Japan, and were carried out in accordance with the Act on Welfare and Management of Animals. The experimental protocol was approved by the Institutional Animal Care and Use Committee (approval no. 01-007). For hematoxylin and eosin (H&E) staining and immunostaining, ddY male mice (Japan SLC) mouse jaws were fixed in 4% paraformaldehyde (PFA) and decalcified using Osteosoft (#101728, Merck, Darmstadt, Germany) and paraffin-embedded thin tissue sections (thickness, 6-7 μm) were used. Kawamoto's film method was used to detect the activity of alkaline phosphatase (ALP) in mouse incisors (Kawamoto, 2003). Briefly, the jaws were taken from ddYmice, snap-frozen directly, soaked in hexane with dry ice, and embedded in an embedding medium. The samples were sectioned at 10 μm thickness using a cryostat. Sections were moved to a container filled with the appropriate amount of 100% ethanol, fixed with 4% paraformaldehyde (PFA) for 5 min, and washed. The specimens were stained with the ImmPACT Vector Red Alkaline Phosphatase Substrate kit (#SK-5105, Vector, Burlingame, CA, United States) according to the manufacturer's protocol. For analysis of cytochrome oxidase (CO) activity in ameloblasts using transmission electron microscopy, the animals (30-day-old Wistar rats) were anesthetized and perfused through the ascending aorta with physiological saline, followed by 2.5% glutaraldehyde in 0.1 M phosphate buffer (pH 7.4) at 4°C for 10 min. The removed maxillae were immersed in the same fixative at 4°C for 2 h before decalcification in 5% ethylenediaminetetraacetic acid (EDTA) at 4°C for 3 weeks, then sagittally sectioned (90-μm sections) using a vibratome (Brunswick, St. Louis, MO, United States). At least three animals were studied for each experiment.

Cell culture

The ameloblast cell line HAT7 was established from rat incisors and cultured as previously described (Kawano et al., 2002). The cells were maintained in Dulbecco's modified Eagle's medium (DMEM/F12) (#11330-032; Life Technologies, Inc., Grand Island, NY, United States) supplemented with 10% fetal bovine serum (#12483-020, Thermo Scientific, Waltham, MA, United States) and 1% penicillin-streptomycin (#15140; Thermo Fisher Scientific). To induce hypoxia, the cells were cultured in hypoxic chambers (MCO-5M, PHCbi, Tokyo, Japan) with 5% O_2, 5% CO_2, and 90% N_2. Nitrogen gas was supplied to the chambers to induce a controlled reduced percentage of oxygen. For normoxia, the cells were cultured in incubators at 5% CO_2 and 21% O_2. Apoptotic cells were determined by Annexin V staining (#A13199, Thermo Fisher Scientific) according to the manufacturer's instructions. As a positive control of apoptosis induction, the cells were treated with mitomycin C (#M4287, Sigma-Aldrich, St Louis, MO, United States, 50 μM) for 6 h.

Alizarin red staining

For alizarin red staining for calcium deposition, HAT7 cells were cultured in 24-well plastic plates coated with collagen type I (#638-00781, Nitta Gelatin Co., Osaka, Japan) at confluence in calcification induction medium; DMEM/F12 supplemented with 10% FBS, dexamethasone (10 nM), $CaCl_2$ (final concentration 2.1 mM) for 7 days under normoxia (21% O_2) or hypoxia (5% O_2), or for 5 days with UK-5099 (#S5317,

Selleckchem, Randnor, PA, United States). The culture supernatant in the wells was removed, and the cells were washed with PBS, fixed with 4% PFA, and then washed three times with distilled water. Next, a 1.0% Alizarin Red S (#A5533, Sigma-Aldrich) stain was added, and the mixture was allowed to stand at room temperature for 30 min. The cells were then washed three times with PBS. The collagen gels with the cells were placed on the prepared slide and then dried at 37°C for 1 h. After drying, the gels were observed.

Alkaline phosphatase staining

HAT7 cells were cultured in 24-well plastic plates at confluence and cultured under normoxia or hypoxia for 48 h, or with UK-5099 for 48 h. The culture supernatant was removed, and the cells were washed with PBS and then fixed in wells with 4% PFA for 10 min at room temperature (RT). Thereafter, the fixative solution was removed, and the cells were washed three times with PBS. Subsequently, the substrate (ImmPACT Vector Red Alkaline Phosphatase Substrate) was added and reacted at 37°C for 30 min. Finally, after washing three times with PBS, the staining was observed.

In vitro calcium transport assay

HAT7 cells were grown on permeable polyester Transwell culture inserts with a 0.4-μm pore size (#353095 Corning Inc., Corning, NY, USA) at confluence. The medium in both the upper and lower chambers was then changed to an induction medium, and the cells were cultured under normoxia or hypoxia. After 24 h, the medium in the lower chamber was replaced with Ca^{2+}-free DMEM (#21068028, Thermo Fisher Scientific, Waltham, MA, United States), and the cells were continuously cultured. At various time intervals (6, 12, 24, and 48 h after medium change), 50 μl aliquots of media from the lower chamber were collected into 1.5 ml Eppendorf tubes. The amount of Ca^{2+} in the media was evaluated with an Amplite™ Fluorimetric Calcium Quantitation Kit (#36360, AAT Bioquest, CA, United States) by measuring the fluorescence intensity using a multi-mode microplate reader (SpectraMax M2, Molecular Devices, CA, United States) with excitation at 540 nm and emission at 590 nm, according to the manufacturer's protocol. Increases in the amount of Ca^{2+} transferred through the cell layer from the upper chamber to the lower chamber indicate increased Ca^{2+} transport across the cells. After reaching confluence, the HAT7 cells on Transwell filters were fixed in 4% PFA, and the filters were removed from the plastic inserts and cut into strips. Some strips were processed for paraffin cross-sections, dewaxed, and stained with H&E. To obtain an en-face view, other strips were transferred to 24-well plates, rinsed in PBS containing Triton X-100 (0.01% v/v), immunoreacted with primary antibodies, followed by incubation with secondary fluorescent antibodies, and then observed.

ATP measurement in culture cells

HAT7 cells were cultured in 24-well plastic plates at confluence and then maintained under normoxia or hypoxia for 48 h. The cells were harvested using the extraction solution provided in the Intracellular ATP assay kit (#IC2-100, Toyo Ink Group, Tokyo, Japan). Luciferin substrate and luciferase enzyme were added, and bioluminescence was assessed using a multi-mode microplate reader according to the manufacturer's instructions. Cellular ATP levels were evaluated and expressed as the ratio of hypoxic to normoxic conditions.

Staining of mitochondria with probes

HAT7 cells were cultured in 96-well plastic plates at confluence and then maintained under normoxia or hypoxia for 48 h. Mito Tracker Orange CMXRos (500 nM, #M7510, Thermo Fisher Scientific) or JC-1 (2 μmol/l, #MT09, Dojindo, Kumamoto, Japan) was added to the cells and incubated for 60 min at 37°C. The cells were washed 2 × with culture media, and fluorescence images were obtained using a fluorescence microscope (BX51, IX71, Olympus, Tokyo, Japan). JC-1 green/red fluorescence ratios were calculated and analyzed statistically.

Lactate assay

HAT7 cells were cultured in 24-well plastic plates at confluence and then maintained under normoxia or hypoxia for 48 h. The supernatant was collected, and the released lactate level in the medium was measured using a Lactate Assay Kit-WST (#L256, Dojindo) following the manufacturer's instructions.

Immunohistochemistry and immunofluorescence

Immunohistochemical (IHC) and immunofluorescent (IF) staining were performed as previously described (Otsu et al., 2011). After blocking, the samples were incubated with the following antibodies (1:100): PDH (MA5-14805, Thermo Fisher Scientific), Zo-1 (sc-33725, Santa Cruz, Dallas, TX, USA) and LDH (ab52488, Abcam). DAPI (300 nM; D1306), Hoechst 33,342 (#R37605), Alexa Fluor 488 (1:500), and Alexa Fluor 546 (1:500) secondary antibodies were purchased from Thermo Fisher Scientific. Images were obtained using a

10.3389/fphys.2022.1062042

TABLE 1 List of PCR primer used in this study.

mRNA	Orientation	Sequence (5'-> 3')
Gapdh	Forward	GGCACAGTCAAGGCTGAGAATG
	Reverse	ATGGTGGTGAAGACGCCAGTA
ZO-1	Forward	CGGAAATGTGTAAATCACCTGGAA
	Reverse	CATGCGTCCTGAACACATCAAAC
Wdr72	Forward	GAACTCGGCAAACTTCCAAGATACA
	Reverse	GGAGCACACCTTCGCTATCCA
Klk-4	Forward	TTTTGCCAACGACCTCATGCTC
	Reverse	AACCAGAAACTAGGCAGGTATCCC
Stim1	Forward	CTCCAGGGCTCCATTCAGACA
	Reverse	ACAGCTTTGGCATCTACTCATCCTC
Orai1	Forward	TCAAAGCCTCCAGCCGAAC
	Reverse	GATGAGTAACCCTGGCGGGTAGT
Cnmm4	Forward	AGATGGCGGCTTTCAACGA
	Reverse	GCATGCCGCACCTACAGAGA
Slc24a4	Forward	TAGCTTGGCACATCCCATGAAC
	Reverse	TTGCCCAGAAAACAGGAGGAAC
Odam	Forward	CGATTGCTCCACTGCTTCCA
	Reverse	ACGCCAAGGTACCATCTCATCTTC
Cldn1	Forward	AAGGCTTTCGGTTGTGAGTCAG
	Reverse	AGGCAGAAGGATGTTTGTGTGG
Cldn2	Forward	ATTCGAGTCATCGCCCATCAG
	Reverse	CCAGGCAGAAGTTCACCAATCA
Cldn4	Forward	ACGAGACCGTCAAGGCCAAG
	Reverse	GTCCAGGACACAGGCACCATAA
Cldn8	Forward	TTATGCACACTGCTTCAATTGTTCC
	Reverse	GAAATCGCAGCTTAAACCAACAGTC
Cldn12	Forward	ATGTGAGATGGCGCAGCAAG
	Reverse	ACAGGGCGTATGTACACGCAGA
Cldn19	Forward	GGCAGGTGCAATGCAAACTCTA
	Reverse	CTGAGCACCATGGCCACAA
Glut1	Forward	ATAGTCACAGCACGTCCATTC
	Reverse	TGTAGAACTCCTCAATTACCTTCTG
Hk2	Forward	GAACAGCCTAGACCAGAGCATCC
	Reverse	ACGGCAACCACATCCAGGTC
PDK1	Forward	TCAACTACATGTACTCAACTGCAC
	Reverse	ACTCCGTTGACAGAGCCTTAATA
PDK2	Forward	CCATGAAGCAGTTTCTAGACTTCG
	Reverse	CAGACTCTGGACATACCAGCTC
PDK3	Forward	TGTGAACAGTATTACCTGGTAGCTC
	Reverse	CTGTTGCTCTCATCGAGTTCTTG
LDHA	Forward	GTGCACTAAGCGGTCCCAAA
	Reverse	GCAAGCTCATCAGCCAAGTC

fluorescence microscope (BX51, IX71; Olympus) or laser-scanning confocal microscope (C1si, Nikon). Image analyses were performed using ImageJ or software provided by the microscope. Fluorescence intensity was quantitated in at least five randomly chosen fields of view using the same threshold. Appropriate positive and negative controls were used for each experiment.

RT-PCR

Total RNA was extracted using the RNeasy Mini Kit (#74104, Qiagen, Hilden, Germany). Reverse transcription of total RNA was performed using the PrimeScript RT reagent kit (#RR037A, Takara Bio, Otsu, Japan). Quantitative analysis of gene expression was performed by qRT-PCR using the TB Green Fast qPCR Mix (#RR430A, Takara Bio, Otsu, Japan) and oligonucleotide primers specific for the target sequences (Table 1) on a Thermal Cycler Dice (Takara Bio, Otsu, Japan) according to the manufacturer's protocol. The specificity of the PCR was confirmed by the appearance of a single band of PCR product in 2% agarose gel stained with ethidium bromide. The target gene expression levels were normalized to the corresponding levels of GAPDH mRNA. Gene expression levels were calculated relative to the values in control cultures using the comparative Ct ($2^{-\Delta\Delta CT}$) method. The experiments were performed in triplicates.

Transmission electron microscopy

Analysis of cytochrome oxidase activity in ameloblasts using transmission electron microscopy has been described previously (Ohshima et al., 1998). The sections (90-μm) were incubated for the demonstration of CO activity according to Seligman et al. (Seligman et al., 1968): preincubation in 0.1 M phosphate buffer (pH 7.4) with 1 mg/ml catalase for 10 min at 37°C, and incubation immediately in a medium consisting of 0.1 M phosphate buffer (pH 7.4) containing 1 mg/ml 3,38-diaminobenzidine (DAB) tetrahydrochloride, 0.1 mg/ml catalase, 1 mg/ml cytochrome c (horse heart, type III, Sigma Chemical Co., St Louis, MO), 85 mg/ml sucrose at 37°C for 1 h. After washing in the cold phosphate buffer, the incubated sections were post-fixed in 1% osmium tetroxide containing 1.5% potassium ferrocyanide for 1 h, and then dehydrated through a graded series of ethanol, and embedded in Epon 812. Ultrathin sections (70 nm) were prepared using a Reichert Ultracut-N ultramicrotome (Reichert-Nissei, Tokyo, Japan) with a diamond knife. Samples were examined under a Hitachi H-7000 transmission electron microscope (Hitachi Co. Ltd., Tokyo, Japan) without staining.

Statistical analyses

All data are reported as the mean ± SD. Differences were considered statistically significant if $p < 0.05$ by Student's *t*-test. * denotes $p < 0.05$.

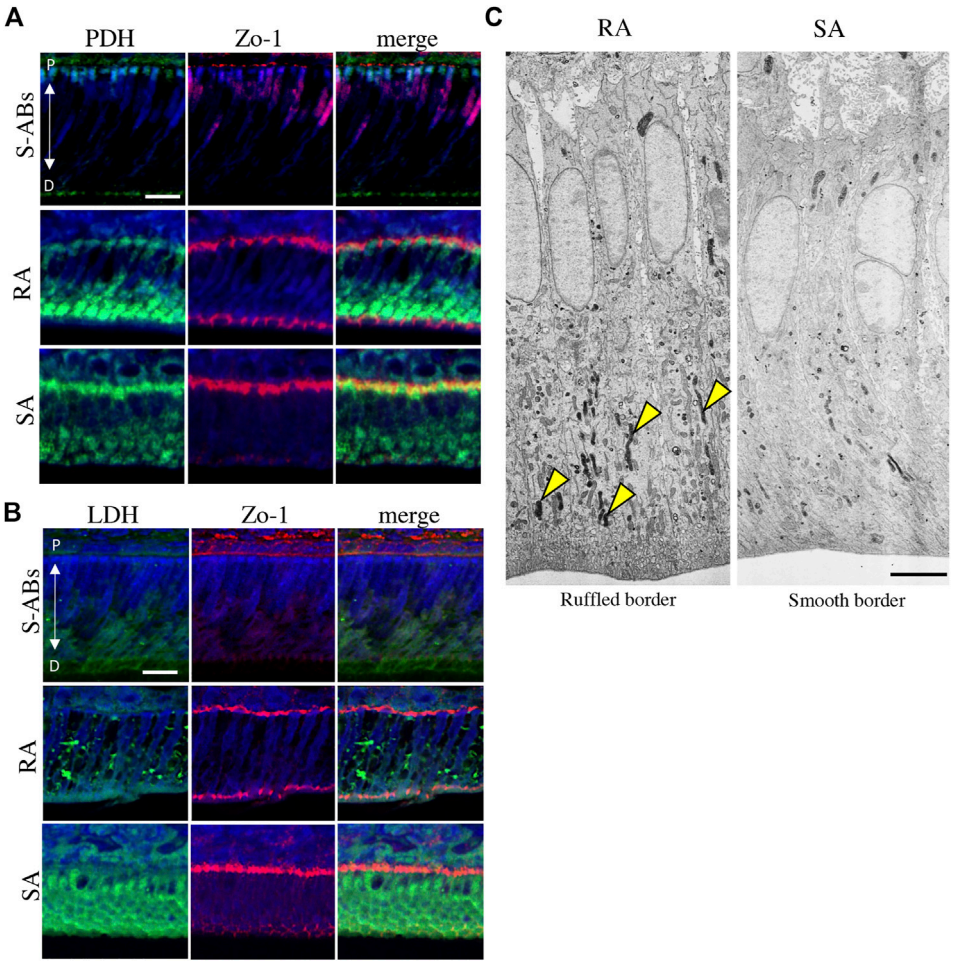

FIGURE 2
Energy metabolic state during ameloblasts differentiation *in vivo*. Double immunostaining for Zo-1 and PDH **(A)** and LDH **(B)** in P10 mouse maxillary incisors. Nuclei were stained with DAPI (blue). **(C)** Electron microscopic images of cytochrome oxidase (CO) activity in rat ruffle-ended (left) and smooth-ended (right) ameloblasts. Arrowheads indicate CO-positive mitochondria. Scale bars:20 μm **(A,B)** and 5 μm **(C)**.

Results

Identification of differential developmental stage of ameloblasts

First, we investigated differences in the distribution of tight junction proteins and ALP activity in each differentiation stage of ameloblasts from S-ABs to early M-ABs in mouse incisors. Immunofluorescence showed that a punctiform expression of Zo-1 was observed at the distal end of S-ABs (Figure 1F, arrowheads). The expression in T-ABs gradually became stronger toward the incisal end (Figure 1G, arrowhead). Distinct expression of Zo-1 was observed at both the distal and proximal ends of the RA (Figure 1H, arrowheads) but only at the proximal end of the SA (Figure 1I, arrowheads). ALP staining revealed that S-ABs did not show any ALP activity, whereas the strong activity was observed in the stratum intermedium (Figure 1J arrowheads). The activity gradually increased at the distal end of T-ABs (Figure 1K, arrowhead). Strong ALP activity was observed at the distal end of the RA (Figure 1L, arrowheads), but it was weak in the SA (Figure 1M).

Energy metabolic shift occurs during ameloblasts differentiation *in vivo*

We further examined the difference in the energy metabolic state between S-ABs and early M-ABs. The expression of pyruvate dehydrogenase (PDH), which aerobically catalyzes the conversion of pyruvate to acetyl-CoA for use in mitochondrial metabolism (Harris et al., 2002), gradually increased from S-ABs to RA, and a distinct expression was

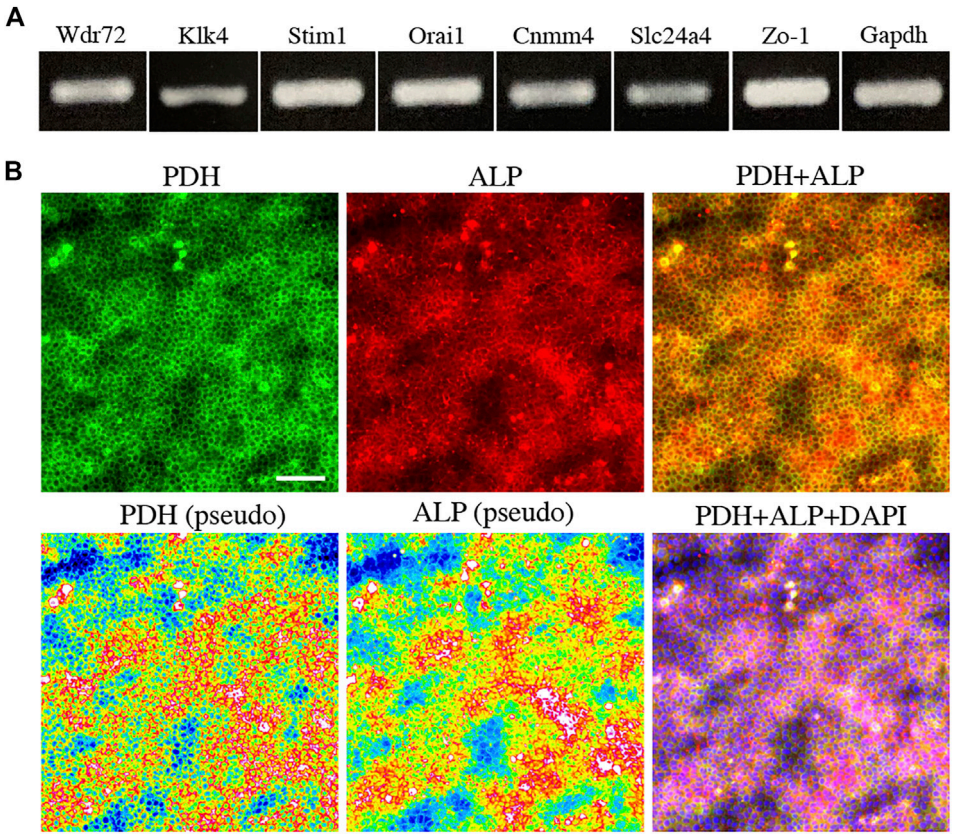

FIGURE 3
The expression of marker for maturation stage ameloblasts and energy metabolism in HAT7 cells. **(A)** The expression of maturation stage ameloblasts marker in HAT7 cells, as determined by RT-PCR. **(B)** Double staining of PDH and ALP in HAT7 cells. The bottom left and bottom middle images are the pseudo-color images of PDH and ALP, respectively. The nucleus is stained with DAPI (blue). Scale bars: 50 μm.

observed at the distal end of RA. In contrast, expression in SA was weaker than that in RA (Figure 2A). The expression of LDH, which catalyzes the conversion of pyruvate to lactate during glycolysis (Doherty and Cleveland, 2013), was weak in S-ABs. The expression of LDH in RA cells exhibited a punctate pattern in the cytoplasm, whereas it became stronger throughout the cytoplasm in SA cells (Figure 2B).

The well-developed mitochondrial apparatus has been implicated as an important indicator of substantial energy-generating potential, permitting, for example, active ion transport function (Garant and Nalbandian, 1968; Hubbard, 2000). To compare the functional activity of mitochondria in RA and SA *in vivo*, the activity of CO, a membrane-bound mitochondrial enzyme involved in OXPHOS, was analyzed using transmission electron microscopy (TEM). A large population of mitochondria in the distal cytoplasm was positive for CO (Figure 2C, arrowheads), whereas mitochondria in the distal cytoplasm displayed diversity in the proportion of CO activity in SA, suggesting that the activity of mitochondria in RA was higher than that in SA. Together, these results indicate that during differentiation, ameloblasts change their energy metabolic status and suggest that RA preferentially utilizes OXPHOS in mitochondria with high oxygen consumption, whereas SA undergoes a metabolic switch toward glycolysis-dominant energy metabolism.

Energy metabolic shift by oxygen in HAT7 cells

To further elucidate the relationship between M-ABs and energy metabolic states, we performed *in vitro* experiments using the ameloblast cell line HAT7, which has been shown to possess some of characteristics of M-ABs (Bori et al., 2016). First, we validated the expression of the M-AB marker in HAT7 cells. PCR analysis revealed that HAT7 cells expressed Wdr72, Klk4, Stim1, Orai1, Cnmm4, Slc24a4, and Zo-1 (Figure 3A). Furthermore, HAT7 cells expressed PDH, and the expression pattern was consistent with that of ALP activity (Figure 3B), consistent with *in vivo* results (Figures 1L,M, 2A).

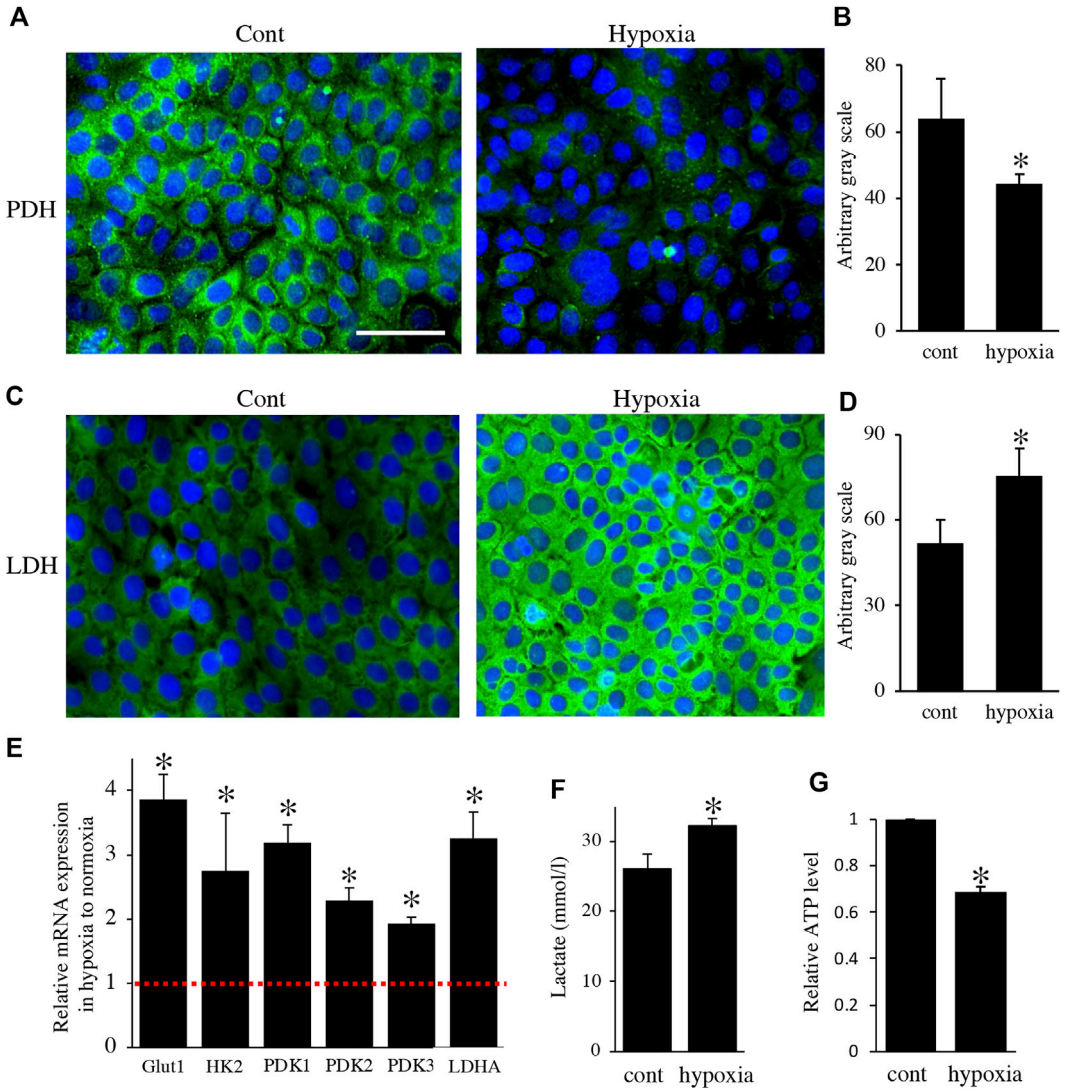

FIGURE 4
Environmental hypoxia induced energy metabolic shift to glycolysis in HAT7 cells. Immunostaining for PDH **(A)** and LDH **(C)** in HAT7 cells cultured under normoxia (left) and hypoxia (right) for 48 h. Nuclei were stained with DAPI (blue). Quantification of PDH **(B)** and LDH **(D)** fluorescence; $n = 3$ each. **(E)** Relative expression of the target genes in HAT7 cells under hypoxia for 48 h under normoxia; $n = 3$. **(F)** Lactate secretion into the culture medium of HAT7 cells incubated for 48 h under normoxia or hypoxia; $n = 3$. **(G)** Intracellular ATP production in HAT7 cells incubated for 48 h under normoxia or hypoxia ($n = 3$). Data are presented as the mean ± SD. *$p < 0.05$ (unpaired two-tailed Student's *t*-test).

Next, to analyze the effect of energy metabolic shift on HAT7 cells, we designed experiments to induce an energy metabolic shift by hypoxia. Immunofluorescence revealed that hypoxic culture (5% O_2 48 h) decreased PDH expression (Figures 4A,B) and increased LDH expression (Figures 4C,D) possibly without induction of apoptosis (Supplementary Figure S1). qPCR analysis also showed that hypoxia increased the gene expression of glycolytic markers, such as Glut1, Hexokinase 2 (HK2), PDK1, PDK2, PDK3, and LDHA (Figure 4E), and lactate production (Figure 4F), and decreased intracellular ATP production (Figure 4G). We further analyzed the effect of hypoxia on the mitochondrial membrane potential and morphology. JC-1 dye accumulates preferentially in polarized mitochondria, existing as green fluorescent monomers at low membrane potentials and as red fluorescent aggregates at high membrane potentials. Under hypoxia, the red/green fluorescence ratio decreased (Figures 5A–C), indicating depolarization of the mitochondrial membrane potential. Mitochondrial morphology was evaluated using MitoTracker™ Orange CMTMRos. Under normoxia, large mitochondria exhibited a spherical or oval morphology (Figures 5D–F), whereas, under hypoxia, mitochondria exhibited a tubular morphology (Figures 5G–I).

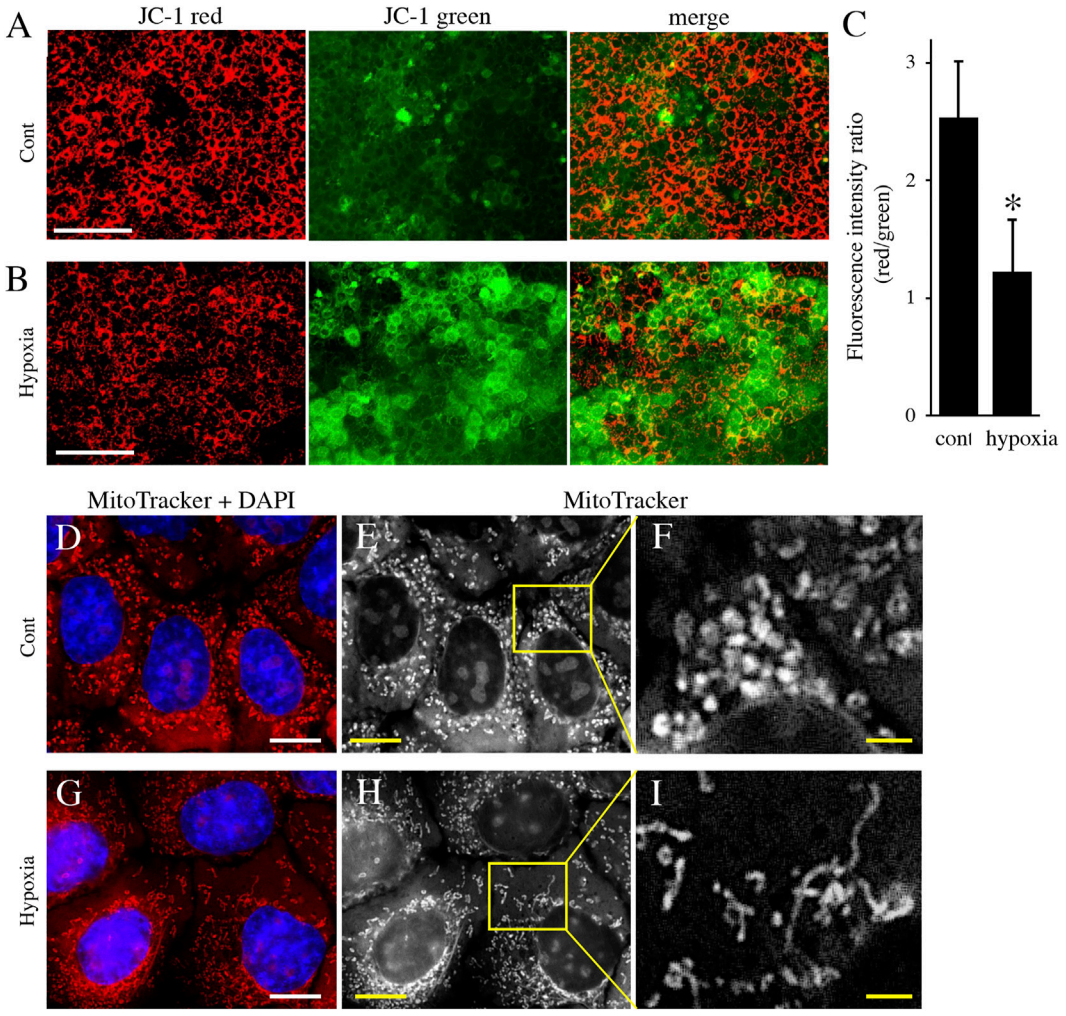

FIGURE 5
The effect of environmental hypoxia on mitochondrial membrane potential and morphology in HAT7 cells. **(A,B)** HAT7 cells cultured in hypoxia display a decrease in mitochondrial membrane potential is evident by the lack of red JC-1 aggregate (red) accumulation and higher staining for JC-1 green monomers. **(C)** Quantification of red/green JC-1 staining indicative of membrane potential. $n = 3$. MitoTracker Orange CMXRos staining of HAT7 cells cultured in normoxia **(D–F)** and hypoxia **(G–I)** for 48 h. The boxed area in **(E,H)** are magnified in **(F,J)**, respectively. The nucleus is stained with DAPI (blue). Data are represented as their mean ± SD. $*p < 0.05$ (unpaired two-tailed Student's *t*-test). Scale bars, 100 μm **(A,B)**; 10 μm **(D,E,G,H)**; 2 μm **(F–I)**.

These results indicate that HAT7 cells undergo an energy metabolic shift that is dependent on oxygen concentration, accompanied by changes in mitochondrial function and morphology.

Effect of energy metabolic shift on maturation stage ameloblasts function

We examined the effect of the oxygen-mediated energy metabolic shift on HAT7 cells. During enamel mineralization, calcium is transported from the blood vessels in the papillary layer to the enamel matrix across M-ABs. Therefore, we developed an *in vitro* experimental model to analyze calcium transport across M-ABs in HAT7 cells. The cells were cultured on Transwell culture inserts, reached confluence, and then cultured under normoxia or hypoxia for 24 h. Subsequently, the culture medium in the lower chamber was replaced with Ca^{2+} free medium. The amount of Ca^{2+}in the medium of the lower chamber under normoxia or hypoxia was measured using a fluorescent Ca^{2+} probe at each time point (Figure 6A). HE staining of the transverse section after reaching confluence showed that the cells mostly formed a single or 2-cell layer (Figure 6B). We confirmed that the cell layer significantly hindered Ca^{2+} transfer from the upper chamber to the lower chamber compared to the control Transwell surface covered with

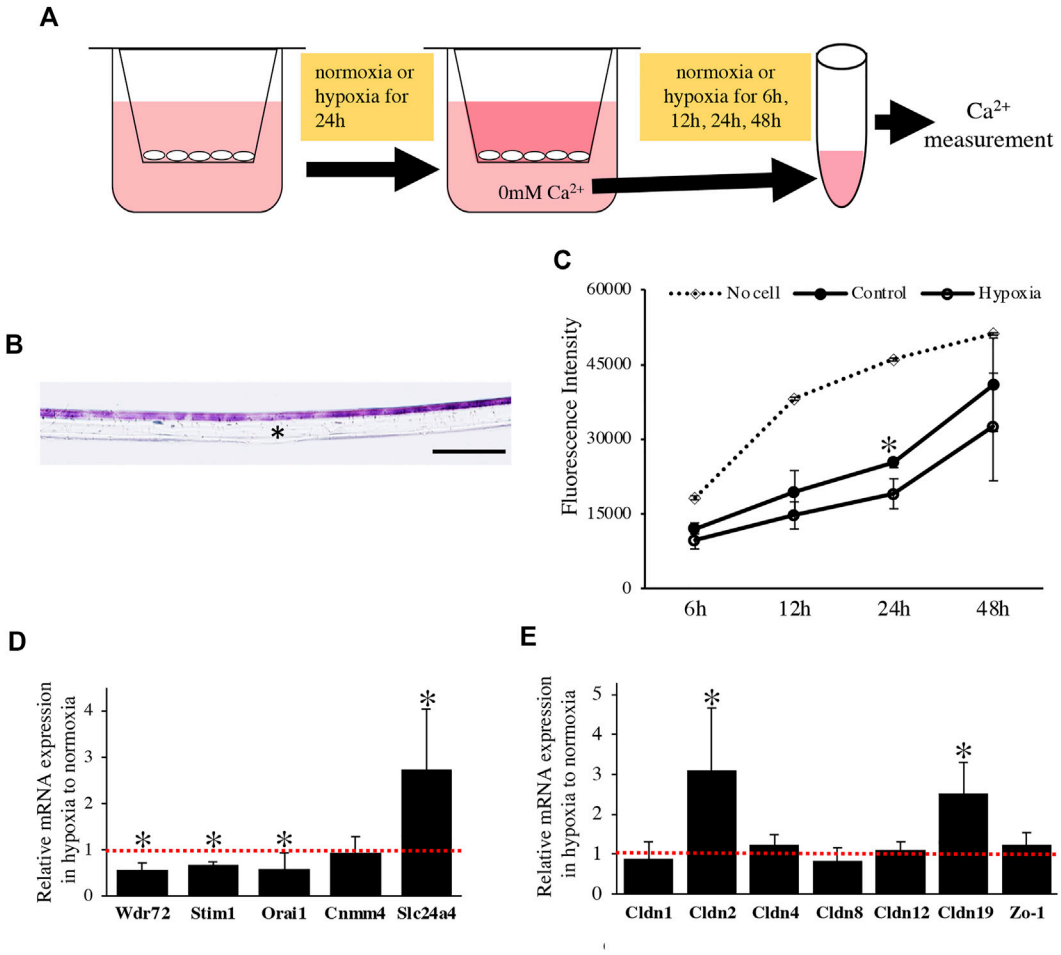

FIGURE 6
The effect of oxygen-mediated energy metabolic shift on Ca^{2+} transport of HAT7 cells. **(A)** The experimental procedure for *in vitro* calcium transport assay. For more detailed information, see the materials and methods section. **(B)** HE staining of HAT7 cells cultured on Transwell filter in cross-section. **(C)** Changes over time in the amount of calcium in the lower chamber. Calcium was transferred from the upper chamber to the lower chamber through HAT7 cells cultured in normoxia or hypoxia. $n = 3$. **(D,E)** Relative expression of target genes in HAT7 cells under hypoxia for 48 h to normoxia; $n = 3$. Data are represented as their mean ± SD. $^*p < 0.05$ (unpaired two-tailed Student's *t*-test). Scale bars, 100 μm **(B)**.

no cells under normoxia (Figure 6C). Furthermore, hypoxia significantly reduced Ca^{2+} transport (Figure 6C).

We performed a qPCR assay to determine the effect of the oxygen-mediated energy metabolic shift on gene expression related to transcellular and paracellular Ca^{2+} transport. Hypoxia significantly decreased the expression of mRNA related to transcellular Ca^{2+} transport, such as Wdr72, Stim1, and Orai1, and increased Slc24a4 (Figure 6D). Claudin (Cldn) determines the barrier function of tight junctions and creates paracellular pores (channels) for Ca^{2+} between neighboring cells (Günzel and Yu, 2013). In HAT7 cells, hypoxia increased the mRNA expression of Cldn2 and Cldn19, but not that of Cldn1, 4, 8, 12, or Zo-1 (Figure 6E).

Finally, we examined the effects of energy metabolic shifts on ALP activity and Ca^{2+} deposition. ALP staining revealed that ALP activity was reduced by hypoxia (Figures 7A,B). Alizarin red staining also showed that hypoxia inhibited Ca^{2+} deposition (Figures 7C,D and Supplementary Figure S2A). Furthermore, UK-5099, an inhibitor of the mitochondrial pyruvate transporter (MPT) that induces energy metabolic shift from OXPHOS to glycolysis (Zhong et al., 2015), significantly decreased ALP activity and PDH expression (Figures 8A–C) possibly without induction of apoptosis (Figure 8D). UK-5099 also inhibited Ca^{2+} deposition (Figures 8E,F and Supplementary Figure S2B).

Discussion

In this study, we have shown that, *in vivo*, RA cells are in an OXPHOS-dominant energy metabolic state, whereas SA cells are

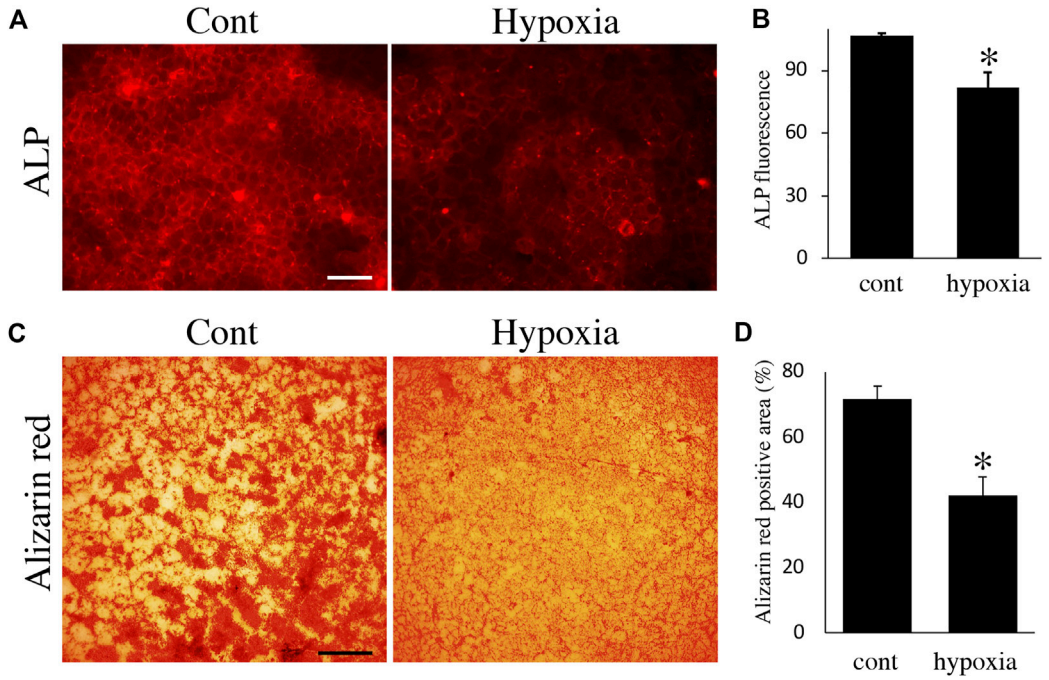

FIGURE 7
The effect of oxygen-mediated energy metabolic shift on mineralization. **(A)** ALP staining of HAT7 cells cultured in normoxia (left) and hypoxia (right) for 48 h. **(B)** Quantification of ALP fluorescence; $n = 3$. **(C)** Alizarin red staining of HAT7 cells cultured in normoxia (left) and hypoxia (right) for 7 days. **(D)** Image analysis of the mineral coverage (Alizarin red positive) in the culture dish; $n = 3$. Data are represented as their mean ± SD. $*p < 0.05$ (unpaired two-tailed Student's *t*-test). Scale bars, 50 μm **(A)**; 500 μm **(C)**.

in a glycolysis-dominant energy metabolic state. *In vitro* experiment revealed that an energy metabolic shift from OXPHOS to glycolysis decreased the mineralization function by suppressing ALP activity and Ca^{2+} transport, implying the induction of phenotypic changes from RA to SA. Together, we have identified differences in the energy metabolic properties of RA and SA in M-ABs and highlighted the importance of the energy metabolic state for M-AB regulation (Figure 9).

A metabolic switch is activated during ameloblast differentiation

We identified the differentiation stages of ameloblasts based on the expression of Zo-1 (Inai et al., 2008) and ALP (Okumura et al., 2010) and examined the expression of metabolic markers in each cell. From S-ABs to RA, the expression of OXPHOS markers increased, whereas that of glycolytic markers decreased. In contrast, from RA to SA in early M-ABs, OXPHOS markers and mitochondrial activity decreased, and glycolytic markers increased. This indicated that a gradual metabolic shift to an OXPHOS-dominant energy metabolism state occurs from S-ABs to RA, and conversely, a shift to a glycolysis-dominant energy metabolism state occurs from RA to SA. In line with this, previous studies have shown that in the transition stage, the expression of many genes involved in ion transport, proteolysis, and pH homeostasis, which required sufficient ATP production, was upregulated (Hu et al., 2012; Lacruz et al., 2012; Wang et al., 2014; Yin et al., 2014). Ultrastructural and cytochemical studies have suggested that in comparison with RA, SA is metabolically inactive and renews exhausted cytoplasmic organelles (Takano and Ozawa, 1980). We also showed that sodium-dependent active glucose transporter 2 (SGLT2), which is expressed in highly metabolically active cells, is expressed in RA but not in SA (Ida-Yonemochi et al., 2020). These results strongly indicated that ameloblasts could shift their metabolic state to meet the cell energy demand for their respective cellular functions, allowing us to identify the differentiation stage of ameloblasts in terms of energy metabolic status.

Environmental oxygen induces energy metabolic shifts

To analyze the effect of energy metabolic shift on HAT7 cells, we performed experiments to induce an energy metabolic shift by hypoxia. For most cell types, hypoxia has been found to decrease the levels of respiratory enzymes and oxygen consumption rate

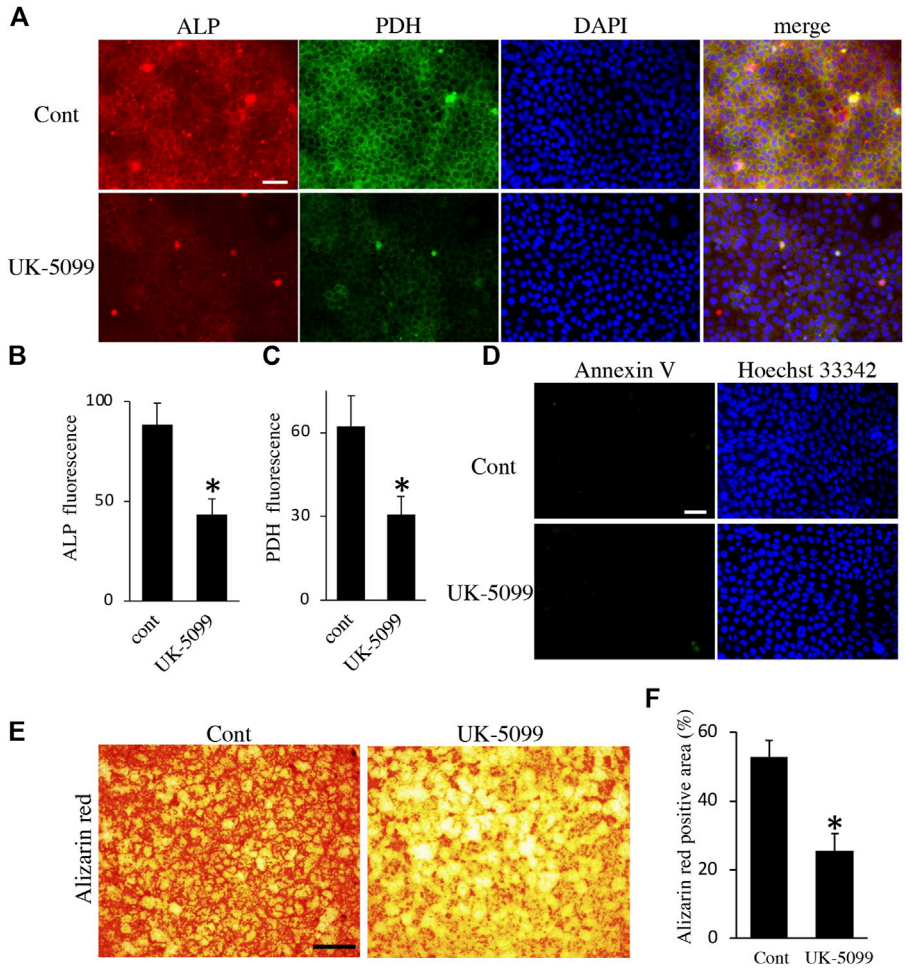

FIGURE 8
The effect of UK-5099 on mineralization. **(A)** Double staining of ALP and PDH in HAT7 cells treated with DMSO (upper: control) and 10 μM UK-5099 (lower) for 48 h. The nucleus is stained with DAPI (blue). Quantification of ALP **(B)** and PDH **(C)** fluorescence; $n = 3$ each. **(D)** Annexin V staining of HAT7 cells cultured with DMSO (upper: control) and 10 μM UK-5099 (lower) for 48 h. The nucleus is stained with Hoechst 33,342 (blue). **(E)** Alizarin red staining of HAT7 cells cultured with DMSO (left: control) and 10 μM UK-5099 (right) for 5 days. **(F)** Image analysis of the mineral coverage (Alizarin red positive) in the culture dish; $n = 3$. Data are represented as their mean ± SD. *$p < 0.05$ (unpaired two-tailed Student's *t*-test). Scale bars, 50 μm **(A,D)**; 500 μm **(E)**.

but increase the production of glycolytic enzymes and lactate, which eventually forces the cells to rely on glycolysis (Kierans and Taylor, 2021). Indeed, in HAT7 cells, hypoxia increases lactate production and the expression of Glut1 (Ebert et al., 1995; Ida-Yonemochi et al., 2020), HK2 (Iyer et al., 1998), PDH (Golias et al., 2016), PDK1-3 (Kim et al., 2006; Lu et al., 2008; Takubo et al., 2013), and LDHA (Yang et al., 2014). Hypoxia alters mitochondrial morphology and function (Galloway et al., 2012). Under hypoxia, the activity of the mitochondrial electron transport chain decreases, and energy needs to shift from OXPHOX to glycolysis (Ježek et al., 2010). We demonstrated that in HAT7 cells, hypoxia changed mitochondrial morphology and reduced ATP production and JC-1 red/green ratio, indicating mitochondrial depolarization and loss-of-function. These results indicated that hypoxia induced an energy metabolic shift in HAT7 cells from OXPHOS-dominant to a more glycolysis-dominant state, implying a phenotypic change from RA to SA.

Energy metabolic shift affects M-ABs mineralization function

M-ABs are responsible for enamel mineralization through an increase in calcium influx across the ameloblast layer into the enamel matrix. Here, we have shown that an energy metabolic shift alters the enamel mineralization function of M-ABs. We developed a novel *in vitro* experimental model and demonstrated

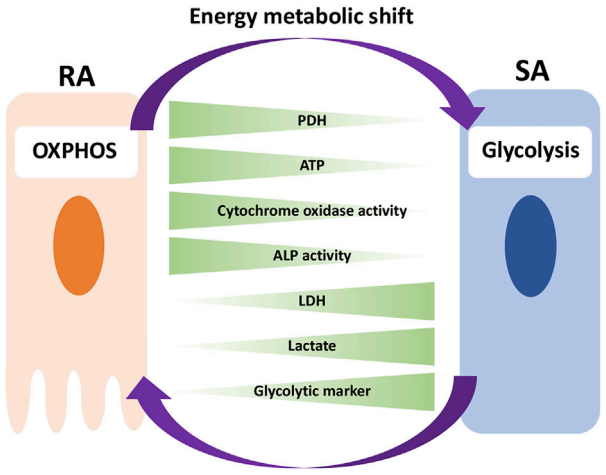

FIGURE 9
Model for the implication of energy metabolism in RA-SA modulation. RA cells are in an OXPHOS-dominant energy metabolic state, whereas SA cells are in a glycolysis-dominant energy metabolic state. An energy metabolic shift from OXPHOS to glycolysis decreases the mineralization function of M-ABs, implying a phenotypic change from RA to SA.

that hypoxia-induced energy metabolic shift to a glycolysis-dominant state reduced Ca^{2+} transport across M-ABs, Ca^{2+} deposition and ALP activity. Further, we demonstrated that UK-5099, that induces energy metabolic shift from OXPHOS to glycolysis, inhibited Ca^{2+} deposition and ALP activity. These findings indicate the critical involvement of energy metabolism in enamel mineralization. Consistent with our findings, Kim et al. demonstrated that hypoxia inhibited normal enamel mineralization in a tooth germ transplantation model (Kim et al., 2021).

Involvement of energy metabolic shift in trans- and intracellular Ca^{2+} transport in M-ABs

Recent reports suggest that Ca^{2+} transport follows a proximal to distal route across the ameloblast cell layer to form mature enamel crystals. The principal mode of Ca^{2+} transport appears to be the transcellular route (Paine et al., 2008; Lacruz et al., 2013), while the contribution of the paracellular passage of Ca^{2+} during the RA to SA cycles has been indicated (Smith, 1979; Nanci, 2008). In the present study, we showed that oxygen-mediated energy metabolic shifts affected the expression of genes involved in both trans- and paracellular Ca^{2+} transport. We showed that hypoxia decreased the expression of Orai1 and Stim1. When Stim1 senses a decrease in Ca^{2+} in the endoplasmic reticulum, it forms clusters in the proximal region of the ER and plasma membrane and activates Orai1, which triggers store-operated Ca^{2+} entry (SOCE) (Prakriya and Lewis, 2015). In M-ABs, SOCE *via* the Orai1-Stim1 complex has been suggested to be the main calcium influx pathway (Nurbaeva et al., 2017), and patients with loss-of-function or null mutations in the STIM1 and ORAI1 genes present with a hypocalcified form of amelogenesis imperfecta (Mccarl et al., 2009; Picard et al., 2009; Fuchs et al., 2012). Thus, an energy metabolic shift may have a significant effect on transcellular calcium transport *via* the Orai1-Stim1 complex in M-ABs. In addition, Orai1 and Stim1 were reported to be predominantly expressed in RA compared to SA (Nurbaeva et al., 2015; Nurbaeva et al., 2017), indicating that Ca^{2+} uptake may predominantly occur in RA, which requires more oxygen for energy production than SA. Therefore, hypoxia may have a greater effect on RA function than on SA.

Furthermore, hypoxia reduced WDR72 expression. Mutation of the WDR72 gene results in hypomaturation defects of the enamel, which are thought to be caused by the abnormal removal of enamel matrix proteins and subsequent enamel mineralization (Katsura et al., 2014; Wang et al., 2015). Mutations in WDR72 have also been shown to decrease the number and size of blood vessels in the capillary layer and alter the subcellular localization of SLC24a4 (sodium/potassium/calcium exchanger 4; NCKX4), which is critical for transcellular Ca^{2+} transport in M-ABs (Wang et al., 2015). Interestingly, our data showed that hypoxia increased SLC24a4 mRNA expression. We speculated that this may have occurred to compensate for the mislocalization of Slc24a4 caused by the decrease in WDR72.

Paracellular access of ions and small molecules to form enamel depends on the composition of TJs, including members of the zonula occludens, occludin, and claudin families (Denker and Sabath, 2011). A combination of different claudins either allows intercellular passage of ions or is tightly closed and restricts passage (Günzel and Yu, 2013). We demonstrated that hypoxia decreased Ca^{2+} transport across HAT7 cells with an increase in CLND2 and 19 mRNA expression. This result suggests that CLDN2 and 19 may contribute to inhibit paracellular Ca^{2+} transport in M-ABs. CLDN2 has been identified as a cation pore-forming protein (Günzel and Yu, 2013). In the renal proximal tubule, TJs containing CLDN 2 have been shown to be leaky and have low transepithelial resistance (Denker and Sabath, 2011). Recently, a missense mutation in Cldn2 associated with obstructive azoospermia in a four-generation spanning family has been identified (Seker et al., 2019). Cldn2 KO mice have also shown higher urinary fractional excretion of Ca^{2+} in renal proximal tubules (Muto et al., 2010). However, the function of CLDN2 in the ameloblasts remains unclear. Cldn19 has been shown to be located in tight junctions of ameloblasts in mice and rats, where it plays a role in regulating extracellular pH, which is critical for the processing and secretion of extracellular matrix proteins (Bardet et al.,

2017; Yamaguti et al., 2017). Mutations in CLDN19 are associated with amelogenesis imperfecta, a genetic disorder characterized by tooth enamel defects (Bardet et al., 2017; Yamaguti et al., 2017). These reports indicate that CLDN19 plays a critical role in amelogenesis. However, the detailed involvement of paracellular Ca^{2+} transport in M-ABs is unknown. Thus, further investigation of the role of each CLDN isoform in paracellular Ca^{2+} transport in M-ABs is required.

Although we used HAT7 cells to clarify the implication of an energy metabolic shift in M-ABs, we must note the limitation of the model. HAT7 cells are established from rat ameloblasts and express M-ABs markers, but alone cannot be a sufficient model for M-ABs. Besides Ca^{2+} transport and mineralization, additional mechanisms have to be identified, such as morphological change and protein degradation and absorption, as well as their coordinating mechanism. Thus, more complex cell culture models and analysis methods need to be developed in the future for better modeling of M-ABs. In addition, the oxygen concentration of M-ABs *in vivo* is different from *in vitro* conditions. Therefore, direct measurements of oxygen concentration *in vivo* and animal experiments under hypoxic conditions will help to identify the correlation between oxygen concentration and energy metabolism in M-ABs, and elucidate the regulatory mechanisms underlying RA-SA modulation.

Contribution and importance of this research in clinical dental medicine

In this study, we uncovered the energy metabolic characteristics of ameloblasts and demonstrated the involvement of energy metabolic shifts in the phenotype modulation of M-ABs. This discovery not only has a significant impact on our understanding of the regulatory mechanism underlying normal amelogenesis but also raises the possibility that failure of this mechanism can cause enamel malformation in human patients. To date, a variety of causal genes for inherited enamel malformations have been identified. These genes are involved in diverse functions, such as the secretion of enamel matrix proteins and their proteolytic processing enzymes, vesicle transport, pH sensing, calcium homeostasis, and cell adhesion (Smith et al., 2017). However, the involvement of energy metabolism in enamel malformation has not been demonstrated. Intriguingly, it was recently suggested that more common enamel defects, such as molar incisor hypomineralization (MIH), defined as a qualitative, demarcated, enamel defect of hypomineralization affecting at least one first permanent molar, while permanent incisors are often affected (Weerheijm et al., 2001), were caused by perinatal hypoxia (Garot et al., 2022). Therefore, further studies to clarify whether the abnormality of energy metabolic regulation causes enamel defects by interacting with intracellular signal networks and environmental factors in humans will aid in the development of novel treatment and prevention strategies for enamel malformations.

Data availability statement

Datasets are available on request: The raw data supporting the conclusions of this article will be made available by the authors, without undue reservation.

Ethics statement

The animal study was reviewed and approved by the Institutional Animal Care and Use Committee in Iwate medical University (approval no. 01-007).

Author contributions

HA contributed to conception and design, data acquisition, analysis, and interpretation, drafted and critically revised the manuscript; AI, SI, MK-S, MA, and HO contributed to data acquisition, analysis, and interpretation, drafted and critically revised the manuscript; KM contributed to conception and design, drafted and critically revised the manuscript; HH contributed to conception and design, data acquisition and interpretation, and critically revised the manuscript; KO contributed to conception and design, data acquisition, analysis, and interpretation, and drafted and critically revised the manuscript.

Funding

This work was financially supported by JSPS KAKENHI (Grant Numbers 21K09832 and 18K09526 to KO, 18H02984 to HH) and a KEIRYOKAI Research grant (Collaborative project 2017-2019) (to KO).

Acknowledgments

We thank T. Fukasawa, T. Sugawara, M. Takahashi (Center for *In Vivo* Science, Iwate Medical University), and Aya Kikuchi (Division of Developmental Biology and Regenerative Medicine, Department of Anatomy, Iwate Medical University) for providing technical assistance and Yukiko Onuma (Division of Developmental Biology and Regenerative Medicine, Department of Anatomy, Iwate Medical University) for their secretarial support.

Conflict of interest

The authors declare that the research was conducted in the absence of any commercial or financial relationships that could be construed as a potential conflict of interest.

Publisher's note

All claims expressed in this article are solely those of the authors and do not necessarily represent those of their affiliated organizations, or those of the publisher, the editors and the reviewers. Any product that may be evaluated in this article, or claim that may be made by its manufacturer, is not guaranteed or endorsed by the publisher.

Supplementary material

The Supplementary Material for this article can be found online at: https://www.frontiersin.org/articles/10.3389/fphys.2022.1062042/full#supplementary-material

SUPPLEMENTARY FIGURE S1

Annexin V staining of HAT7 cells cultured in hypoxia. **(A)** Double staining of Hoechst 33342 (left) and Annexin V (middle) in HAT7 cells cultured on plastic plates under normoxia (upper: control) and hypoxia (lower) for 48 h. **(B)** Double staining of Hoechst 33342 (left) and Annexin V (middle) in HAT7 cells treated with 50 μM mitomycin C for 6 h. Scale bars, 50 μm.

SUPPLEMENTARY FIGURE S2

DAPI staining of HAT7 cells cultured on plastic plates coated with collagen type I for alizarin red staining. **(A)** DAPI staining of HAT7 cells cultured under normoxia (left) and hypoxia (right) for 7 days. **(B)** DAPI staining of HAT7 cells cultured with DMSO (left: control) and UK-5099 (right) for 5 days. Scale bars, 200 μm.

References

Bardet, C., Ribes, S., Wu, Y., Diallo, M. T., Salmon, B., Breiderhoff, T., et al. (2017). Claudin loss-of-function disrupts tight junctions and impairs amelogenesis. *Front. Physiol.* 8, 326. doi:10.3389/fphys.2017.00326

Bartlett, J. D. (2013). Dental enamel development: Proteinases and their enamel matrix substrates. *ISRN Dent.* 2013, 684607. doi:10.1155/2013/684607

Bori, E., Guo, J., Rácz, R., Burghardt, B., Földes, A., Kerémi, B., et al. (2016). Evidence for bicarbonate secretion by ameloblasts in a novel cellular model. *J. Dent. Res.* 95, 588–596. doi:10.1177/0022034515625939

Denker, B. M., and Sabath, E. (2011). The biology of epithelial cell tight junctions in the kidney. *J. Am. Soc. Nephrol.* 22, 622–625. doi:10.1681/ASN.2010090922

Doherty, J. R., and Cleveland, J. L. (2013). Targeting lactate metabolism for cancer therapeutics. *J. Clin. Invest.* 123, 3685–3692. doi:10.1172/JCI69741

Ebert, B. L., Firth, J. D., and Ratcliffe, P. J. (1995). Hypoxia and mitochondrial inhibitors regulate expression of glucose transporter-1 via distinct cis-acting sequences. *J. Biol. Chem.* 270, 29083–29089. doi:10.1074/jbc.270.49.29083

Folmes, C. D., Dzeja, P. P., Nelson, T. J., and Terzic, A. (2012). Metabolic plasticity in stem cell homeostasis and differentiation. *Cell Stem Cell* 11, 596–606. doi:10.1016/j.stem.2012.10.002

Fuchs, S., Rensing-Ehl, A., Speckmann, C., Bengsch, B., Schmitt-Graeff, A., Bondzio, I., et al. (2012). Antiviral and regulatory T cell immunity in a patient with stromal interaction molecule 1 deficiency. *J. Immunol.* 188, 1523–1533. doi:10.4049/jimmunol.1102507

Galloway, C. A., Lee, H., and Yoon, Y. (2012). Mitochondrial morphology-emerging role in bioenergetics. *Free Radic. Biol. Med.* 53, 2218–2228. doi:10.1016/j.freeradbiomed.2012.09.035

Garant, P. R., and Nalbandian, J. (1968). Observations on the ultrastructure of ameloblasts with special reference to the Golgi complex and related components. *J. Ultrastruct. Res.* 23, 427–443. doi:10.1016/s0022-5320(68)80108-x

Garot, E., Rouas, P., Somani, C., Taylor, G. D., Wong, F., and Lygidakis, N. A. (2022). An update of the aetiological factors involved in molar incisor hypomineralisation (MIH): A systematic review and meta-analysis. *Eur. Arch. Paediatr. Dent.* 23, 23–38. doi:10.1007/s40368-021-00646-x

Golias, T., Papandreou, I., Sun, R., Kumar, B., Brown, N. V., Swanson, B. J., et al. (2016). Hypoxic repression of pyruvate dehydrogenase activity is necessary for metabolic reprogramming and growth of model tumours. *Sci. Rep.* 6, 31146. doi:10.1038/srep31146

Günzel, D., and Yu, A. S. (2013). Claudins and the modulation of tight junction permeability. *Physiol. Rev.* 93, 525–569. doi:10.1152/physrev.00019.2012

Harris, R. A., Bowker-Kinley, M. M., Huang, B., and Wu, P. (2002). Regulation of the activity of the pyruvate dehydrogenase complex. *Adv. Enzyme Regul.* 42, 249–259. doi:10.1016/S0065-2571(01)00061-9

Hu, P., Lacruz, R. S., Smith, C. E., Smith, S. M., Kurtz, I., and Paine, M. L. (2012). Expression of the sodium/calcium/potassium exchanger, NCKX4, in ameloblasts. *Cells Tissues Organs* 196, 501–509. doi:10.1159/000337493

Hubbard, M. J. (2000). Calcium transport across the dental enamel epithelium. *Crit. Rev. Oral Biol. Med.* 11, 437–466. doi:10.1177/10454411000110040401

Ida-Yonemochi, H., Otsu, K., Harada, H., and Ohshima, H. (2020). Functional expression of sodium-dependent glucose transporter in amelogenesis. *J. Dent. Res.* 99, 977–986. doi:10.1177/0022034520916130

Inai, T., Sengoku, A., Hirose, E., Iida, H., and Shibata, Y. (2008). Differential expression of the tight junction proteins, claudin-1, claudin-4, occludin, ZO-1, and PAR3, in the ameloblasts of rat upper incisors. *Anat. Rec.* 291, 577–585. doi:10.1002/ar.20683

Iyer, N. V., Kotch, L. E., Agani, F., Leung, S. W., Laughner, E., Wenger, R. H., et al. (1998). Cellular and developmental control of O2 homeostasis by hypoxia-inducible factor 1 alpha. *Genes Dev.* 12, 149–162. doi:10.1101/gad.12.2.149

Ježek, P., Plecitá-Hlavatá, L., Smolková, K., and Rossignol, R. (2010). Distinctions and similarities of cell bioenergetics and the role of mitochondria in hypoxia, cancer, and embryonic development. *Int. J. Biochem. Cell Biol.* 42, 604–622. doi:10.1016/j.biocel.2009.11.008

Katsura, K. A., Horst, J. A., Chandra, D., Le, T. Q., Nakano, Y., Zhang, Y., et al. (2014). WDR72 models of structure and function: A stage-specific regulator of enamel mineralization. *Matrix Biol.* 38, 48–58. doi:10.1016/j.matbio.2014.06.005

Kawamoto, T. (2003). Use of a new adhesive film for the preparation of multi-purpose fresh-frozen sections from hard tissues, whole-animals, insects and plants. *Arch. Histol. Cytol.* 66, 123–143. doi:10.1679/aohc.66.123

Kawano, S., Morotomi, T., Toyono, T., Nakamura, N., Uchida, T., Ohishi, M., et al. (2002). Establishment of dental epithelial cell line (HAT-7) and the cell differentiation dependent on Notch signaling pathway. *Connect. Tissue Res.* 43, 409–412. doi:10.1080/03008200290000637

Kierans, S. J., and Taylor, C. T. (2021). Regulation of glycolysis by the hypoxia-inducible factor (HIF): Implications for cellular physiology. *J. Physiol.* 599, 23–37. doi:10.1113/JP280572

Kim, E. J., Lee, J. E., Yoon, S., Lee, D. J., Mai, H. N., Ida-Yonemochi, H., et al. (2021). Hypoxia-responsive oxygen nanobubbles for tissues-targeted delivery in developing tooth germs. *Front. Cell Dev. Biol.* 9, 626224. doi:10.3389/fcell.2021.626224

Kim, J. W., Tchernyshyov, I., Semenza, G. L., and Dang, C. V. (2006). HIF-1-mediated expression of pyruvate dehydrogenase kinase: A metabolic switch required for cellular adaptation to hypoxia. *Cell Metab.* 3, 177–185. doi:10.1016/j.cmet.2006.02.002

Lacruz, R. S. (2017). Enamel: Molecular identity of its transepithelial ion transport system. *Cell Calcium* 65, 1–7. doi:10.1016/j.ceca.2017.03.006

Lacruz, R. S., Smith, C. E., Bringas, J. R., P., Chen, Y..B., Smith, S. M., Snead, M. L., et al. (2012). Identification of novel candidate genes involved in mineralization of dental enamel by genome-wide transcript profiling. *J. Cell. Physiol.* 227, 2264–2275. doi:10.1002/jcp.22965

Lacruz, R. S., Smith, C. E., Kurtz, I., Hubbard, M. J., and Paine, M. L. (2013). New paradigms on the transport functions of maturation-stage ameloblasts. *J. Dent. Res.* 92, 122–129. doi:10.1177/0022034512470954

Lu, C. W., Lin, S. C., Chen, K. F., Lai, Y. Y., and Tsai, S. J. (2008). Induction of pyruvate dehydrogenase kinase-3 by hypoxia-inducible factor-1 promotes

metabolic switch and drug resistance. *J. Biol. Chem.* 283, 28106–28114. doi:10.1074/jbc.M803508200

Mccarl, C. A., Picard, C., Khalil, S., Kawasaki, T., Röther, J., Papolos, A., et al. (2009). ORAI1 deficiency and lack of store-operated Ca2+ entry cause immunodeficiency, myopathy, and ectodermal dysplasia. *J. Allergy Clin. Immunol.* 124, 1311–1318. e7. doi:10.1016/j.jaci.2009.10.007

Muto, S., Hata, M., Taniguchi, J., Tsuruoka, S., Moriwaki, K., Saitou, M., et al. (2010). Claudin-2–deficient mice are defective in the leaky and cation-selective paracellular permeability properties of renal proximal tubules. *Proc. Natl. Acad. Sci. U. S. A.* 107, 8011–8016. doi:10.1073/pnas.0912901107

Nanci, A. (2008). *Ten cate's oral histology*. edn 7. Elsevier.

Nurbaeva, M. K., Eckstein, M., Concepcion, A. R., Smith, C. E., Srikanth, S., Paine, M. L., et al. (2015). Dental enamel cells express functional SOCE channels. *Sci. Rep.* 5, 15803. doi:10.1038/srep15803

Nurbaeva, M. K., Eckstein, M., Feske, S., and Lacruz, R. S. (2017). Ca^{2+} transport and signalling in enamel cells. *J. Physiol.* 595, 3015–3039. doi:10.1113/JP272775

Ohshima, H., Maeda, T., and Takano, Y. (1998). Cytochrome oxidase activity in the enamel organ during amelogenesis in rat incisors. *Anat. Rec.* 252, 519–531. doi:10.1002/(SICI)1097-0185(199812)252:4<519:AID-AR3>3.0.CO;2-I

Okumura, R., Shibukawa, Y., Muramatsu, T., Hashimoto, S., Nakagawa, K.-I., Tazaki, M., et al. (2010). Sodium-calcium exchangers in rat ameloblasts. *J. Pharmacol. Sci.* 112, 223–230. doi:10.1254/jphs.09267fp

Otsu, K., Ida-Yonemochi, H., Ikezaki, S., Ema, M., Hitomi, J., Ohshima, H., et al. (2021). Oxygen regulates epithelial stem cell proliferation via RhoA-actomyosin-YAP/TAZ signal in mouse incisor. *Development* 148, dev194787. doi:10.1242/dev.194787

Otsu, K., Kishigami, R., Fujiwara, N., Ishizeki, K., and Harada, H. (2011). Functional role of Rho-kinase in ameloblast differentiation. *J. Cell. Physiol.* 226, 2527–2534. doi:10.1002/jcp.22597

Paine, M. L., Snead, M. L., Wang, H. J., Abuladze, N., Pushkin, A., Liu, W., et al. (2008). Role of NBCe1 and AE2 in secretory ameloblasts. *J. Dent. Res.* 87, 391–395. doi:10.1177/154405910808700415

Picard, C., Mccarl, C. A., Papolos, A., Khalil, S., Lüthy, K., Hivroz, C., et al. (2009). STIM1 mutation associated with a syndrome of immunodeficiency and autoimmunity. *N. Engl. J. Med.* 360, 1971–1980. doi:10.1056/NEJMoa0900082

Prakriya, M., and Lewis, R. S. (2015). Store-operated calcium channels. *Physiol. Rev.* 95, 1383–1436. doi:10.1152/physrev.00020.2014

Reith, E. J., and Boyde, A. (1979). A correlated scanning and transmission electron microscopic study of maturation ameloblasts in developing molar teeth of rats. *Cell Tissue Res.* 197, 421–431. doi:10.1007/BF00233567

Reith, E. J., and Boyde, A. (1981). The arrangement of ameloblasts on the surface of maturing enamel of the rat incisor tooth. *J. Anat.* 133, 381–388.

Sasaki, T., Debari, K., and Garant, P. R. (1987). Ameloblast modulation and changes in the Ca, P, and S content of developing enamel matrix as revealed by SEM-EDX. *J. Dent. Res.* 66, 778–783. doi:10.1177/00220345870660031501

Seker, M., Fernandez-Rodriguez, C., Martinez-Cruz, L. A., and Müller, D. (2019). Mouse models of human claudin-associated disorders: Benefits and limitations. *Int. J. Mol. Sci.* 20, E5504. doi:10.3390/ijms20215504

Seligman, A. M., Karnovsky, M. J., Wasserkrug, H. L., and Hanker, J. S. (1968). Nondroplet ultrastructural demonstration of cytochrome oxidase activity with a polymerizing osmiophilic reagent, diaminobenzidine (DAB). *J. Cell Biol.* 38, 1–14. doi:10.1083/jcb.38.1.1

Smith, C. E. (1979). Ameloblasts: Secretory and resorptive functions. *J. Dent. Res.* 58, 695–707. doi:10.1177/00220345790580022101l

Smith, C. E. L., Poulter, J. A., Antanaviciute, A., Kirkham, J., Brookes, S. J., Inglehearn, C. F., et al. (2017). Amelogenesis imperfecta; genes, proteins, and pathways. *Front. Physiol.* 8, 435. doi:10.3389/fphys.2017.00435

Smith, C. E., Mckee, M. D., and Nanci, A. (1987). Cyclic induction and rapid movement of sequential waves of new smooth-ended ameloblast modulation bands in rat incisors as visualized by polychrome fluorescent labeling and GBHA-staining of maturing enamel. *Adv. Dent. Res.* 1, 162–175. doi:10.1177/08959374870010020401

Takano, Y., and Ozawa, H. (1980). Ultrastructural and cytochemical observations on the alternating morphologic changes of the ameloblasts at the stage of enamel maturation. *Arch. Histol. Jpn.* 43, 385–399. doi:10.1679/aohc1950.43.385

Takubo, K., Nagamatsu, G., Kobayashi, C. I., Nakamura-Ishizu, A., Kobayashi, H., Ikeda, E., et al. (2013). Regulation of glycolysis by Pdk functions as a metabolic checkpoint for cell cycle quiescence in hematopoietic stem cells. *Cell Stem Cell* 12, 49–61. doi:10.1016/j.stem.2012.10.011

Tsogtbaatar, E., Landin, C., Minter-Dykhouse, K., and Folmes, C. D. L. (2020). Energy metabolism regulates stem cell pluripotency. *Front. Cell Dev. Biol.* 8, 87. doi:10.3389/fcell.2020.00087

Wang, S., Choi, M., Richardson, A. S., Reid, B. M., Seymen, F., Yildirim, M., et al. (2014). STIM1 and SLC24A4 are critical for enamel maturation. *J. Dent. Res.* 93, 94S–100S. doi:10.1177/0022034514527971

Wang, S. K., Hu, Y., Yang, J., Smith, C. E., Nunez, S. M., Richardson, A. S., et al. (2015). Critical roles for WDR72 in calcium transport and matrix protein removal during enamel maturation. *Mol. Genet. Genomic Med.* 3, 302–319. doi:10.1002/mgg3.143

Warshawsky, H., and Smith, C. E. (1974). Morphological classification of rat incisor ameloblasts. *Anat. Rec.* 179, 423–446. doi:10.1002/ar.1091790403

Weerheijm, K. L., Jälevik, B., and Alaluusua, S. (2001). Molar-incisor hypomineralisation. *Caries Res.* 35, 390–391. doi:10.1159/000047479

Yamaguti, P. M., Neves, F. A., Hotton, D., Bardet, C., de La Dure-Molla, M., Castro, L. C., et al. (2017). Amelogenesis imperfecta in familial hypomagnesaemia and hypercalciuria with nephrocalcinosis caused by CLDN19 gene mutations. *J. Med. Genet.* 54, 26–37. doi:10.1136/jmedgenet-2016-103956

Yang, C., Jiang, L., Zhang, H., Shimoda, L. A., Deberardinis, R. J., and Semenza, G. L. (2014). Analysis of hypoxia-induced metabolic reprogramming. *Methods Enzymol.* 542, 425–455. doi:10.1016/B978-0-12-416618-9.00022-4

Yin, K., Hacia, J. G., Zhong, Z., and Paine, M. L. (2014). Genome-wide analysis of miRNA and mRNA transcriptomes during amelogenesis. *BMC Genomics* 15, 998. doi:10.1186/1471-2164-15-998

Zhong, Y., Li, X., Yu, D., Li, X., Li, Y., Long, Y., et al. (2015). Application of mitochondrial pyruvate carrier blocker UK5099 creates metabolic reprogram and greater stem-like properties in LnCap prostate cancer cells *in vitro*. *Oncotarget* 6, 37758–37769. doi:10.18632/oncotarget.5386

frontiers | Frontiers in Physiology

TYPE Original Research
PUBLISHED 29 November 2022
DOI 10.3389/fphys.2022.1034662

OPEN ACCESS

EDITED BY
Zhi Chen,
Wuhan University, China

REVIEWED BY
Cecile Feuillie,
Centre National de la Recherche Scientifique (CNRS), France
Zhuo Chen,
Zhejiang University, China

*CORRESPONDENCE
Wendy J. Shaw,
wendy.shaw@pnnl.gov

SPECIALTY SECTION
This article was submitted to Craniofacial Biology and Dental Research,
a section of the journal Frontiers in Physiology

RECEIVED 01 September 2022
ACCEPTED 14 November 2022
PUBLISHED 29 November 2022

CITATION
Tao J, Hanson E, Dohnalkova AC, Buchko GW, Jin B, Shaw WJ and Tarasevich BJ (2022), Changes in the C-terminal, N-terminal, and histidine regions of amelogenin reveal the role of oligomer quaternary structure on adsorption and hydroxyapatite mineralization.
Front. Physiol. 13:1034662.
doi: 10.3389/fphys.2022.1034662

Changes in the C-terminal, N-terminal, and histidine regions of amelogenin reveal the role of oligomer quaternary structure on adsorption and hydroxyapatite mineralization

Jinhui Tao[1], Emma Hanson[1], Alice C. Dohnalkova[1], Garry W. Buchko[1,2], Biao Jin[1], Wendy J. Shaw[1]* and Barbara J. Tarasevich[1]

[1]Pacific Northwest National Laboratory, Richland, WA, United States, [2]School of Molecular Biosciences, Washington State University, Pullman, WA, United States

Adsorption interactions between amelogenin and calcium phosphate minerals are believed to be important to amelogenin's function in enamel formation, however, the role of specific amino acid residues and domains within the protein in controlling adsorption is not well known. We synthesized "mechanistic probes" by systematically removing charged regions of amelogenin in order to elucidate their roles. The probes included amelogenin without the charged residues in the N-terminus (SEKR), without two, three, or eight histidines (H) in the central protein region (H2, H3, H8), or without the C-terminal residues (Delta). *In-situ* atomic force microscopy (AFM) adsorption studies onto hydroxyapatite (HAP) single crystals confirmed that the C-terminus was the dominant domain in promoting adsorption. We propose that subtle changes in protein-protein interactions for proteins with histidines and N-terminal residues removed resulted in changes in the oligomer quaternary size and structure that also affected protein adsorption. HAP mineralization studies revealed that the oligomer-HAP binding energy and protein layer thickness were factors in controlling the amorphous calcium phosphate (ACP) to HAP induction time. Our studies with mechanistic probes reveal the importance of the oligomer quaternary structure in controlling amelogenin adsorption and HAP mineralization.

KEYWORDS

amelogenin, oligomer, atomic force microscopy, hydroxyapatite, amorphous calcium phosphate

Introduction

The biomineralization of hard tissue structures including mollusk shells, vertebrate teeth, and vertebrate bones involves a complex interplay between proteins, mineral ions, and mineral precipitates (Lowenstam and Weiner, 1989). Proteins and polysaccharides are excreted into extracellular spaces that mineralize over time. The extracellular biomacromolecules are believed to guide the mineralization process by promoting nucleation, affecting growth, and controlling phase transformations of metastable precursors to the final minerals (Simmer and Fincham, 1995; Mann, 2001). In some cases, growth involves particle mediated processes where proteins promote the aggregation and phase transformation of precursor particles into the final mineral shape and phase (Jin et al., 2018). The protein matrices either remain in place as part of the hard tissue structure, such as collagen matrices in bone or tooth dentin (George and Veis, 2008), or become almost completely removed by enzymes, such as in tooth enamel (Bartlett, 2013).

Amelogenin is a protein that is critical to the formation of HAP in tooth enamel (Fincham et al., 1999). The absence of amelogenin in knock-out mice results in greatly reduced HAP thickness and HAP that is lacking in mesoscale order (Hu et al., 2016). Ameloblasts secrete amelogenin as well as other proteins into the extracellular matrix during the secretory phase of enamel development (Fincham and Simmer, 1997). It was suggested by diffraction studies that ACP is initially formed within the matrix (Beniash et al., 2009) and ACP particles assemble into long thin structures that are parallel to each other and separated by protein matrix (Simmer et al., 2012). ACP transforms to HAP in the later secretory stages (Beniash et al., 2009) and then HAP crystals further widen and thicken during the maturation phase (Simmer et al., 2012; Bartlett, 2013). The adsorption of amelogenin onto calcium phosphate is believed to be critical in affecting each step *in vivo*, promoting the alignment of ACP particles into ribbons, inhibiting the transformation of ACP to HAP until protein is removed by the protease MMP20 (Beniash et al., 2009; Shin et al., 2020; Bartlett et al., 2021), and inhibiting the lateral growth of HAP crystals until protein is removed by the enzyme KLK4 (Simmer et al., 2012; Bartlett, 2013). Numerous *in vitro* studies have shown the importance of amelogenin adsorption onto calcium phosphates in affecting the ACP to HAP transformation and crystal growth (Kwak et al., 2009; Kwak et al., 2016; Tao et al., 2019).

Although the adsorption of amelogenin onto calcium phosphates appears to be critical to its function in enamel formation, there are questions as to what primary amino acid sequences or domains in amelogenin control adsorption. Amelogenin is less charged than other biomineralization proteins and self-assembles into oligomers that in turn assemble into larger nanospheres (Fang et al., 2011). The quaternary structure of the oligomers, defined as the spatial arrangement of monomers and the size of the oligomers, has been found to be very unique, consisting of pairs of dimers that assemble to form a ring (Fang et al., 2011). Although there was a distribution of ring diameters, the most prominent ring consisted of six pairs of dimers to form a dodecamer. It has been suggested that the C-terminal domain (residues A167—D180) (Moradian-Oldak et al., 2002) and the N-terminal domain (residues M1–M42) (Aoba et al., 1989; Lu J. X. et al., 2013) may have roles in the adsorption of amelogenin since all of the 13 charged residues in the protein's primary sequence are located in these regions. These regions have been found to be located on the outside of amelogenin assemblies (Moradian-Oldak et al., 2001) and may interact directly with mineral surfaces. In addition to the highly charged residues, phage display techniques have suggested that the weakly basic histidines found in the central region of amelogenin may also be important for binding onto calcium phosphate (Gungormus et al., 2008; Gungormus et al., 2012). There is also evidence that the N-terminus and histidine residues have roles in promoting protein-protein interactions involved in oligomer and nanosphere self-assembly (Paine and Snead, 1997; Moradian-Oldak et al., 2000; Bromley et al., 2011).

In this study, we set out to test the role of polar/charged N-terminal, C-terminal, and histidine amino acid residues of amelogenin in modulating adsorption interactions with HAP and the ACP to HAP transformation during mineralization by selectively removing the residues from amelogenin. This approach is complimentary to examining the role of specific amino acid residues by studying smaller peptides containing those residues. The resulting "mechanistic probes" consisted of amelogenin with four amino acids removed in the N-terminus (SEKR), two to eight histidine residues removed in the central region (H2, H3, H8), and the C-terminus removed (Delta). We studied the adsorption of the wild-type protein, rpM179, and the mechanistic probes onto HAP single crystals using *in situ* AFM and the kinetics of mineralization of HAP in the presence of the variants. Our studies confirm that the C-terminus is the most important domain involved in amelogenin adsorption, consistent with other studies (Moradian-Oldak et al., 2002). We also conclude that the removal of residues in the N-terminus and histidines in the central region can change the quaternary structure of the adsorbate oligomers that in turn affect their adsorption interactions.

Materials and methods

Amelogenin preparation and purification

Synthetic genes for the five mechanistic probe variants, SEKR, H2, H3, H8, and Delta, were prepared commercially (DNA2.0, Menlo Park, CA) by making the appropriate

FIGURE 1
Primary amino acid sequences for rpM179 and the mechanistic probes SEKR, H2, H3, H8, and Delta. The amino acids that are removed from rpM179 to form the mechanistic probes are indicated by dashes. SEKR is formed by the removal of S16, E18, K24, and R31 in the N-terminus, H2 by the removal of H91 and H92, H3 by the removal of H67, H68, and H69, H8 by the removal of H58, H62, H67, H68, H69, H91, H92, and H99, and Delta by the removal of A167WPATDKTKREEVD180 in the C-terminus. Amino acids with side chains that are acidic, strongly basic, and weakly basic (histidines) are colored red, yellow, and purple, respectively. The serine at S16 that undergoes post translational phosphorylation is colored green. Note that the methionine at M1 is removed during the recombinant synthesis process.

variations to the original *E. coli* optimized rpM179 DNA sequence and inserting into the expression vector pJexpress414. These plasmids were used to transform BL21 (DE3) competent cells (Novagen, Madison, WI) *via* a heat-shock method. Starting with frozen 12% glycerol stocks prepared from a single colony, uniformly ^{15}N-labelled rpM179 and the five protein variants were expressed using a minimal media based autoinduction protocol (Studier, 2005). Because the expressed protein contained no affinity tag, it was purified following a previously described protocol starting by lysing the frozen cell pellet at 70°C in 40 ml of 2% acetic acid over 30 min (Buchko et al., 2013). The entire solution was then dialyzed twice in 5 L of 2% acetic acid (3.5 kDa MW cutoff), centrifuged, and the supernatant applied onto an Xbridge Preparative C18 (5 µm, 10 mm × 250 mm) reverse phase column (Water, Milford, MA). After application of a gradient of 70% aqueous CH_3CN in 0.05% TFA, the major fractions containing amelogenin were pooled, frozen at −80°C, lyophilized, and stored at 4°C until ready to use. The primary amino acid sequence for the non-native amelogenin variants were verified by the collection of an ^{1}H-^{15}N HSQC spectrum in 2% acetic acid and comparison to the assigned ^{1}H-^{15}N HSQC spectrum for full length rpM179 (Buchko et al., 2008a). The spectra were essentially identical except for positions at, or 1–2 residues from, the site of the amino deletions (Buchko et al., 2013). Intact protein mass spectra for each of the constructs (unlabeled protein) further confirmed the primary amino acid sequence of the expressed protein as the major m/z peak for each of the protein constructs corresponded to its expected molecular weight. Figure 1 shows the complete sequences of each protein.

Protein solution preparation

Solutions of rpM179 and the variants were prepared by dissolving 5–10 mg/ml of protein in water. After one to three days of dissolution, the solutions were filtered with 0.2 µm pore membranes, the concentrations of the protein solutions were determined using UV-vis spectroscopy (Nanoprobe), and the stock protein solutions were diluted into 25 mM Tris-HCl buffer adjusted to pH 8.0. These solutions were used for the dynamic light scattering (DLS) and AFM studies. The pH 8.0 solution condition was used in order to be higher than the isoelectric point of the proteins to avoid extensive protein agglomeration. The highest isoelectric point is for Delta at 7.23 as shown in Supplementary Table S1. Also, amelogenin nanospheres have narrow size distributions at this pH (Moradian-Oldak et al., 1998). This pH is in within the range of pH values up to pH 8.5 found within enamel tissue (Lyman and Waddell, 1977; Lacruz et al., 2010). The net charge and hydrophobicity

of the proteins were calculated using the protein calculator at http://protcalc.sourceforge.net/ and ProtParam tool at http://web.expasy.org/protparam/ (Supplementary Figure S8 and Supplementary Table S1).

Dynamic light scattering

DLS measurements of the protein solutions were performed using a Brookhaven Instruments 90 Plus equipped with a 657 nm wavelength, 35 mW laser. Time dependent fluctuations in the scattered intensity were measured using a Bl-APD digital correlator. Protein solutions were analyzed using a 90° scattering angle at 25.0 °C. Data were collected as co-added runs of 2 min collected for a total of 6–12 min. The autocorrelation functions were deconvoluted to obtain size distributions using the non-negatively constrained least squares fit (multiple pass NNLS). The nanosphere size was obtained as the most prominent peak in the volume-weighted distribution and was averaged over at least 3 runs. The standard deviation of the mean nanosphere size averaged 12.2% over all measurements.

Atomic force microscopy imaging

Details of the use of AFM to study amelogenin adsorption onto the (100) face of micron-sized single crystals of HAP were described in our previous publications (Tao et al., 2015; Tao et al., 2019) and in the Supplementary Information. The adsorption kinetics of proteins in 25 mM Tris buffer, pH 8.0, ambient temperature solutions at concentrations of 15.6 μg/ml and 125 μg/ml were studied. Adsorption amounts were obtained from the coverage of adsorbates determined from the adsorbate areas calculated by the Particle and Pore Analysis module included in the SPIP 5.1.4 software. The adsorption kinetics of rpM179 and H8 were also studied at 7.8, 31.3, 62.5, 180 and 250 μg/ml (ppm) protein concentration in order to have enough data points to perform Hill analyses of the equilibrium adsorption coverages as a function of protein concentration, as described in detail previously (Tao et al., 2015; Tao et al., 2019) and in the Supplementary Information. The equilibrium coverages are the coverages obtained from the kinetic curves at maximum adsorption. Equilibrium coverage data of rpM179 from a previous publication (Tao et al., 2019) was included with the newer rpM179 data obtained in this study for the Hill analyses. The equilibrium adsorption coverages for each concentration of wild-type and variant protein were averaged from at least three experiments resulting in standard deviations of 10% or less. Height distributions of the adsorbates from protein solutions at 15.6 μg/ml were determined using the Particle & Pore Analysis module included in the SPIP 5.1.4 software for over 100 adsorbates and the mean of the distribution was determined.

Transmission electron microscopy studies of protein oligomer structure

The size and structure of oligomers of rpM179, H3, and H8 were studied by placing drops of pH 8, 25 mM Tris•HCl, 62.5 μg/ml or 125 μg/ml protein onto formvar-carbon coated nickel TEM grids placed over an ice bath. The grids were cleaned by plasma exposure immediately before use. After 30–60 s of adsorption time, the grids were blotted, rinsed by placing the grids on top of water droplets, and blotted. NanoW negative stain (5 μl, 2% organotungsten compound, Nanoprobes, Inc.) was dropped onto the grids for 10 s and then blotted and the grids were dried. TEM imaging was performed using a Tecnai T-12 TEM (FEI) with a LaB_6 filament operating at 120 kV with images obtained in focus or underfocus. Images were collected digitally using an Ultrascan 1000 CCD. Size distributions of oligomer diameters were obtained by the measurement of 100–300 oligomers.

Mineralization studies

The mineralization of calcium phosphate was studied in the presence of rpM179 and the variants. Stock solutions of protein were dissolved in water as described above and were diluted into water to give final concentrations of 200 μg/ml protein. Aliquots of 50 mM $CaCl_2$ and 30 mM KH_2PO_4 stock solutions in water were sequentially added to give final concentrations of 2.5 mM $CaCl_2$ and 1.5 mM KH_2PO_4. The pH was increased to a final pH of 7.8 by slowly adding KOH. The sample vial was placed into a jacketed beaker at 22°C and the growth kinetics were monitored by changes in pH over a 6 h time period using a Microelectronics combination electrode and Orion pH meter, a method commonly used to monitor HAP formation (Kwak et al., 2009). Induction times for ACP to HAP transformation were obtained from the pH change curves. Reported mean induction times were obtained over three to six experimental repetitions.

Transmission electron microscopy studies of mineral structure

Samples for TEM analysis of mineral were prepared by dropping mineralization suspensions after 0.5 and 24 h onto formvar-carbon coated copper grids. TEM imaging was performed using a Tecnai T-12 TEM (FEI) with a LaB_6 filament operating at 120 kV. Images were collected digitally using an Ultrascan 1000 CCD.

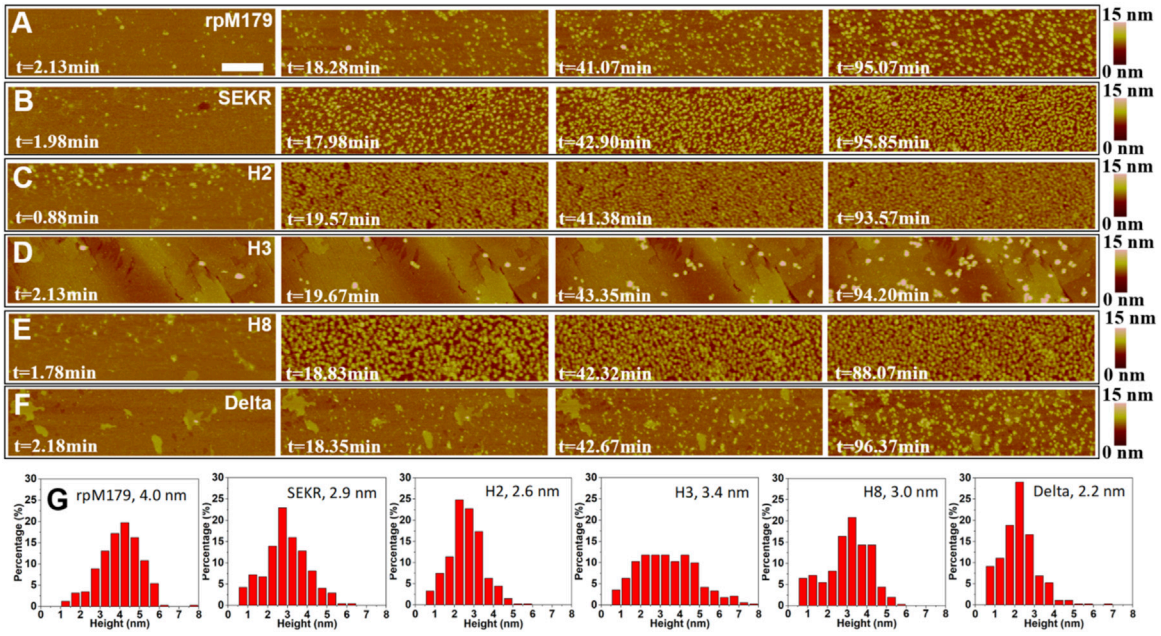

FIGURE 2
(A–F) *In situ* AFM images of adsorbates from 15.6 μg/ml protein, 25 mM Tris●HCl, pH 8 solutions at various time periods and showing at most one monolayer of adsorbates. The zero point of time is defined as the time when protein solutions are injected into the AFM liquid cell. The scale bar is 200 nm. All the micrographs are the same size. **(G)** Height distributions of the adsorbates with the mean height shown in the label. The second and third images in **(A)** were taken from Tao et al., 2019.

Statistical Analysis

T-tests at 0.05 significance level were used to determine the statistical significance of AFM determined height differences, TEM determined diameter differences, and induction time differences between the variants and rpM179.

Results

Adsorption of mechanistic probes onto the HAP (100) surface

The adsorption of mechanistic probes and wild-type rpM179 onto single crystal HAP (100) surfaces was studied by *in situ* AFM. Figures 2A–F and Supplementary Videos S1–S6 show AFM images of the adsorbates from solutions at various time points and a protein concentration of 15.6 μg/ml relative to the bare HAP substrates shown in Supplementary Figure S2. Individual adsorbates could be resolved at this low concentration at early time points and height distributions were obtained as shown in Figure 2G. The mechanistic probe adsorbates were 2–3 nm in height, statistically smaller than the rpM179 adsorbates at 4–5 nm. The protein adsorbates were smaller than the larger nanospheres that were detected in solution by DLS (Supplementary Figure S1). We call these adsorbates "oligomers" and define them as smaller subunits of the larger nanospheres (Fang et al., 2011). We propose that the oligomers adsorb onto the surface by the disassembly of the nanospheres present in solution as we have shown previously (Tarasevich et al., 2009; Tao et al., 2015) and/or the oligomers are present in solution although not detected by DLS and preferentially adsorb onto the surface.

The images in Figures 2A–F show that at low coverage, the adsorbates consisted of isolated oligomers or small clusters of oligomers, and at high coverage, the adsorbates formed dense monolayers of oligomers. The adsorbates for H3 and Delta appeared to consist of wider assemblies of oligomers, suggesting different interactions with the HAP surface compared to rpM179. The protein coverage was determined from the AFM-measured area of the oligomer, adjusted for tip diameter, relative to the entire area. Figure 3A shows the kinetics of adsorption coverage as a function of time at 15.6 μg/ml and indicated that the protein coverage increased with time until an equilibrium coverage was reached. H3 and Delta resulted in the lowest equilibrium protein coverages at 15.6 μg/ml, and SEKR, H2, and H8 had the highest coverages.

Adsorption studies at higher protein concentrations at 125 μg/ml (Supplementary Figures S3, S4, and Supplementary Videos S7–S12) showed that adsorption at first resulted in an almost complete monolayer of oligomers followed by the adsorption of a second layer of oligomers. Figure 3B shows the equilibrium

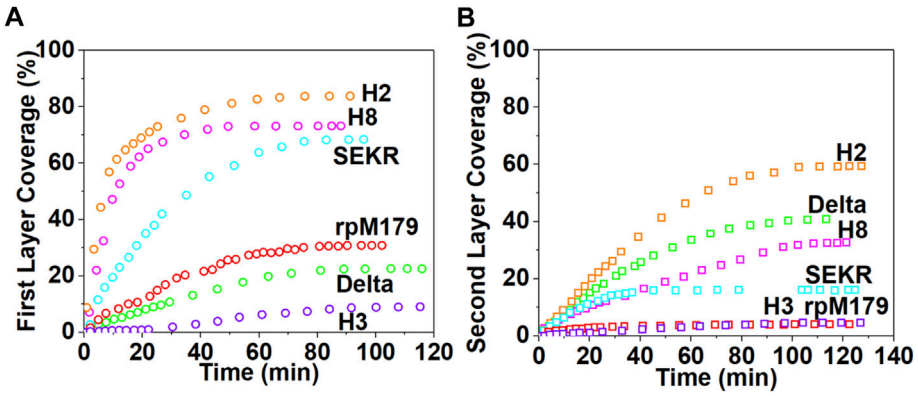

FIGURE 3
The kinetics of protein adsorption determined from the areal coverage of oligomer adsorbates obtained from AFM data for **(A)** the first layer of adsorption from solutions at 15.6 μg/ml and **(B)** the second layer of adsorption from solutions at 125 μg/ml. The data for rpM179 is from Tao et al., 2019.

TABLE 1 Hill coefficients (n) and binding energies (ΔG) for oligomer-HAP and oligomer-oligomer interactions on the HAP surface obtained from the first layer adsorption data and the second layer adsorption data, respectively. The adsorption data for rpM179 was new data combined with data from previous publications (Tao et al., 2015; Tao et al., 2019).

Interaction	n	ΔG (k_BT)
rpM179-HAP (100)	3.34 ± 0.40	−17.2 ± 2.9
H8-HAP (100)	0.51 ± 0.06	−19.6 ± 3.3
rpM179-rpM179	0.42 ± 0.01	−7.8 ± 0.4
H8-H8	2.11 ± 0.06	−15.1 ± 0.6

adsorption coverage of the second layer as a function of time at 125 μg/ml. There was a small amount of second layer adsorption for rpM179 and H3 and a larger amount of second layer adsorption for SEKR, H2, H8, and Delta. Supplementary Figure S4 shows the distribution of second layer oligomers at various time points for rpM179 and H8. The second layer adsorbates of rpM179 were smaller in size than the first layer adsorbates and the second layer adsorbates of H8 changed in size over time as smaller initial adsorbates aggregated to form larger adsorbates.

Adsorption was studied at a wider range of protein concentrations for rpM179 and H8 (Supplementary Videos S5, S11, S13–S15). The equilibrium adsorption amounts at various concentrations were analyzed using the Hill equation that included a cooperative effect on binding quantified by the Hill coefficient, n, where protein binding to the surface is enhanced by existing protein adsorbates when n is greater than 1 (see Supplementary Information text). Hill plots are shown in Supplementary Figure S5A for an analysis of the first layer of adsorption to obtain oligomer-HAP binding energies and in Supplementary Figure S5B for an analysis of the second layer adsorption to obtain oligomer-oligomer binding energies. Table 1 shows the resulting Hill coefficients, n, oligomer-HAP, and oligomer-oligomer binding energies. The data show that the oligomer-HAP binding energy and oligomer-oligomer binding energy were higher for H8 compared to rpM179.

Oligomer quaternary structure by transmission electron microscopy

Further information on the oligomer size and structure was obtained by TEM examination of oligomers adsorbed onto grids. TEM imaging can have higher resolution than AFM imaging and can provide more detail on the oligomer structure. Also, size measurements give oligomer diameters, complimentary information to the oligomer heights obtained by AFM. Figure 4A shows white, unstained oligomeric adsorbates of rpM179 distributed onto the darker, stained grid surface. In some cases, structures consisting of a white ring surrounding a darker center could be resolved (Figure 4B), similar to the ring-like structures previously observed by cryo-EM (Fang et al., 2011). The rings are believed to be formed by the interaction of two monomers to form dimers joined by the C-terminus and the assembly of pairs of dimers into the ring-like structure. Individual dimers were resolved in one of the TEM images in Figure 4B. Ring-like structures were also observed for H3 (Figure 4C) and H8 (Figure 4D). The hole in the ring was not always observed. The ability to see the change in electron density in the center of the ring seemed to be promoted by optimizing the focus conditions and staining. Also, the ability to see the rings would depend on having the orientation of the ring parallel to the surface.

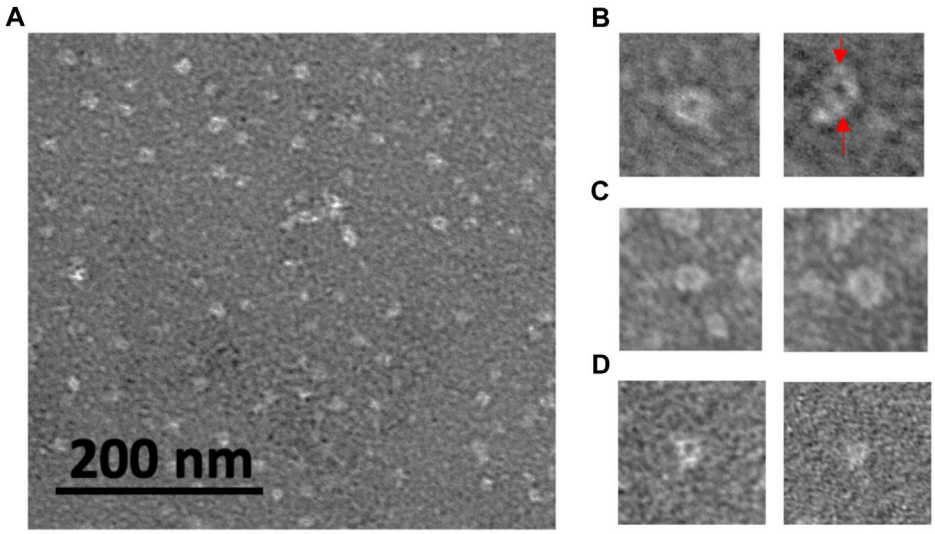

FIGURE 4
TEM images of protein oligomers adsorbed onto grids for **(A)** rpM179; select images of oligomer rings for **(B)** rpM179 (arrows point to individual dimers), **(C)** H3, and **(D)** H8. The widths of the frames in **(B–D)** are 50 nm.

The sizes distributions of the oligomers were determined as shown in Supplementary Figure S6 and the mean diameters of the oligomers were 12.7, 8.9, and 8.6 nm for the rpM179, H3, and H8 proteins, respectively. T-tests showed that the H3 and H8 diameters were significantly smaller than the rpM179 diameter.

Hydroxyapatite mineralization

The mineralization of HAP with no protein and in the presence of the various proteins at 200 μg/ml was studied by monitoring changes in pH of the mineralization solutions as shown in Figure 5A. There was an initial stage of a slow decrease in pH (P1), followed by a region of a faster decrease in pH (P2), and a third stage of no change in pH (P3). Calcium phosphate nanoparticles were formed at 0.5 h in the P1 region for rpM179 as shown in Figure 5C and the particles were found to be amorphous ACP (Figure 5D). By the P3 region, the calcium phosphate was found to consist of ribbon-like, moderately crystalline HAP imbedded in a low contrast matrix as shown in the image in Figure 5E and diffraction patterns in Figure 5F for rpM179 at 24 h. The other proteins resulted in similar mineral structures at 24 h as shown in Supplementary Figure S7. P2, therefore, was found to correspond to the phase transformation of ACP into HAP and the duration of P1 is the induction time for the ACP to HAP transformation (Ding et al., 2014). Figure 5B shows the mean induction times for the ACP to HAP transformation for the control (CTRL) in the absence of protein, rpM179, and the mechanistic probes. The induction times for the proteins were significantly longer than for the control solution suggesting that the proteins inhibited the ACP to HAP phase transformation. H2, H3, and Delta had significantly shorter induction times compared to the wild-type rpM179.

Discussion

Adsorbed oligomer quaternary structure

Amino acid residues thought to be important for the function of amelogenin including the charged C-terminus, histidine residues at various locations, and polar/charged residues in the N-terminus were systematically removed from the protein (Figure 1). Adsorption studies by AFM showed that all of the proteins adsorbed as oligomeric structures. Previous cryo-EM studies found that rpM179 monomers at pH 8 were around 1.8 nm in diameter and aggregated to form dimers and then oligomer rings with the C-terminal domains located on the outside of the oligomers (Fang et al., 2011). The most prominent oligomer in that study was a dodecamer composed of a ring of six dimers. Our TEM studies confirmed that the rpM179 oligomers were shaped like rings.

In contrast to rpM179, the previous cryo-EM studies showed that rpM166 (Delta in our studies) went from monomers to nanospheres with no intermediate oligomeric structure (Fang et al., 2011). Our studies showed that Delta adsorbed as 2.2 nm height oligomers. The Fang et al. study suggests that the Delta adsorbates would not be as highly structured as the rpM179 oligomers. That study indicated that the C-terminal domain is important in forming the highly structured oligomer

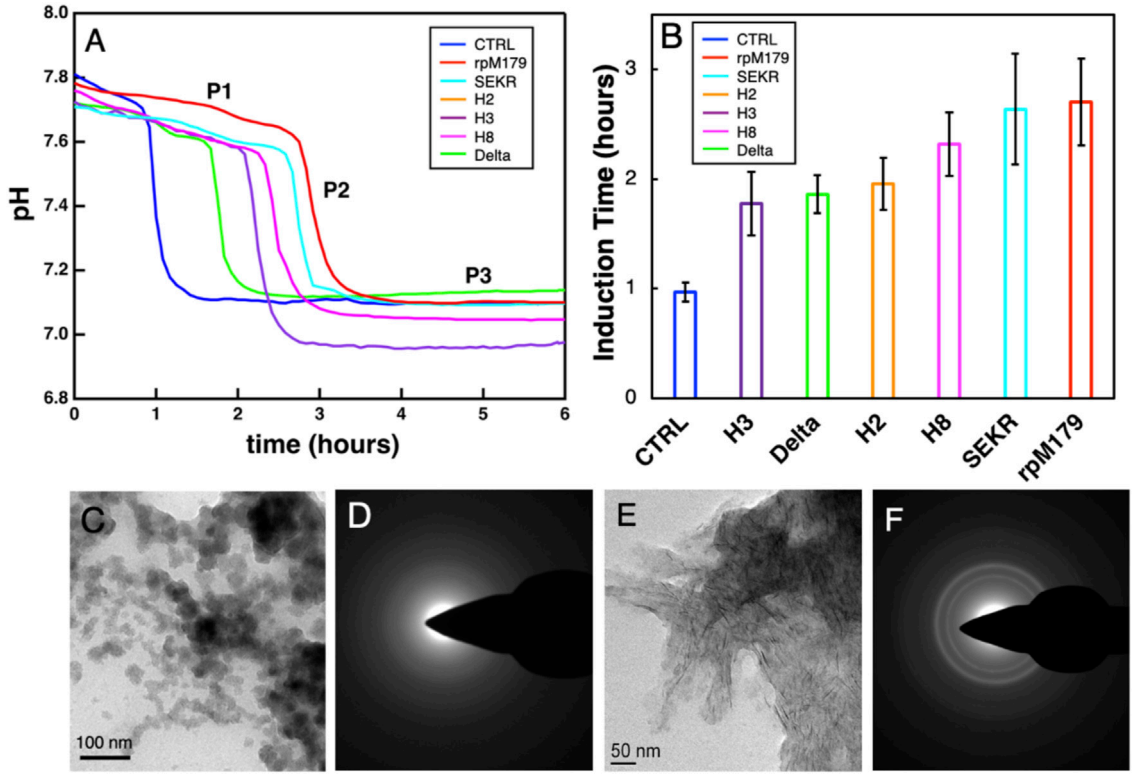

FIGURE 5
(A) Typical curves for the kinetics of mineralization of calcium phosphate in the absence of protein (CTRL) or the presence of 200 μg/ml wild-type and mechanistic probe proteins at 22°C. The rpM179 curve (red) is labeled to show the different stages of mineralization: P1, the formation of ACP; P2, the ACP to HAP transition region; and P3, the growth and ripening of HAP. **(B)** Mean induction times (duration of P1) for the ACP to HAP phase transformation listed from the shortest induction time to the longest induction time. **(C)** TEM image showing ACP nanoparticles formed during P1 (0.5 h) for rpM179. **(D)** TEM electron diffraction pattern for the image in **(C)**. **(E)** TEM image showing HAP ribbons formed at 24 h for rpM179. **(F)** TEM electron diffraction pattern for the image in **(C)**.

ring. Recent solid state NMR (ssNMR) studies have shown that the C-terminal domains overlap in an antiparallel conformation to form the dimer (Arachchige et al., 2018). We hypothesized that rpM179 and the variants SEKR, H2, H3, and H8 would form ring-like oligomers because they all contain the C-terminus. The oligomers with C-termini we have studied by TEM (rpM179, H3, and H8) all formed ring-like oligomers, consistent with this hypothesis.

H2, H3, H8, and SEKR all adsorbed as oligomers that were primarily around 2.6–3.0 nm in height, smaller than the rpM179 oligomers. TEM studies confirmed that the oligomer diameters for H3 and H8 were smaller than the rpM179 diameters. The smaller sizes suggest that the quaternary structure of the oligomers has changed with fewer dimers involved in the formation of the ring-like structures found for H3 and H8 compared to rpM179. These variants, therefore, would be smaller than the 12-mer found for rpM179. This indicates that the histidines deleted from H2, H3, and H8, and the S16, E18, K24, and R31 residues deleted from SEKR have a role in promoting the aggregation of protein dimers into oligomeric intermediates. Previously, the N-terminus has been suggested to be important in the self-assembly of amelogenin monomers to form oligomers. For example, DLS studies showed that amelogenin with the N-terminus from 1 to 42 removed resulted in a significant population of amelogenin monomers within the solution (Moradian-Oldak et al., 2000). A yeast two-hybrid assay revealed that a peptide consisting of the N-terminus interacts strongly with amelogenin (Paine and Snead, 1997) and solution NMR studies showed that amelogenin monomers interact first at the N-terminus upon addition of salt (Buchko et al., 2008b). Histidines are believed to promote the aggregation of oligomers to form nanospheres as the pH is increased from 5 to 7.4 because of the reduction in histidine charge (Bromley et al., 2011). Protein-protein interactions can also be promoted by π–π stacking between aromatic rings of histidines (Heyda et al., 2010; Tao et al., 2015). Removal of the SEKR or H residues, therefore, resulted in smaller oligomers because of a reduction in protein-protein interactions.

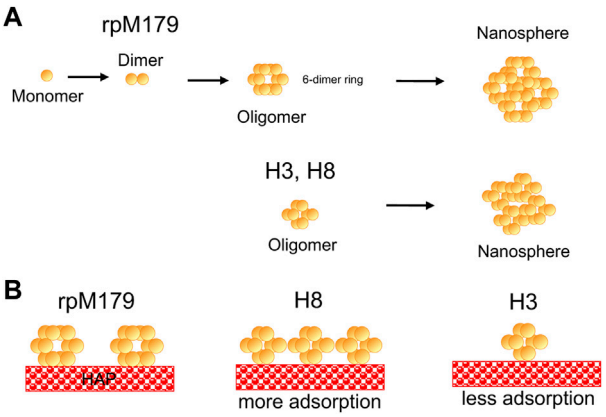

FIGURE 6
Schematic drawings of **(A)** the hierarchical quaternary structure of rpM179 from monomer to dimer to six-dimer oligomer ring to nanosphere as suggested by the literature (Bromley et al., 2011; Fang et al., 2011) and from oligomer ring to nanosphere for H3 and H8 as suggested by the adsorption and DLS results of this study. Smaller oligomers are shown for H3 and H8 as indicated by the AFM and TEM results. **(B)** Differences in adsorption onto HAP resulting in higher adsorption amounts for H8, and lower adsorption amounts for H3 compared to rpM179. The oligomer rings are oriented perpendicular to the surface for clarity in the schematic and because that orientation would promote interactions with the C-terminus. The orientation of rings onto the HAP surface is not known at the present time, however.

Adsorption amounts

The AFM studies showed that there were significant differences in the adsorption amounts for the mechanistic probes and rpM179 onto the HAP (100) face at 15.6 μg/ml. The mechanistic probe protein lacking the C-terminus, Delta, had low amounts of adsorption while all of the other proteins that had a C-terminus, except for H3, had higher protein amounts. This result confirms the importance of the C-terminus in amelogenin binding to HAP resulting in interactions between the C-terminal dimers located on the outside of the oligomers (Fang et al., 2011) and the surface (Moradian-Oldak et al., 2002).

We were surprised to see significant increases in the adsorption amounts for SERK compared to rpM179 because of the removal of charged residues that have the potential for adsorption interactions. Also, it was remarkable to see that H3 had significantly lower amounts of adsorption compared to H2 and H8. The schematic in Figure 6 summarizes the trends in oligomer adsorption for H3, H8, and rpM179. To understand these results, we considered the effect of the protein charge since Supplementary Table S1 showed that there were differences in the calculated overall charge of the protein monomers at pH 8. A plot of adsorption coverage at 15.6 μg/mL as a function of the protein monomer charge at pH 8 in Supplementary Figure S9 showed a relatively weak correlation between the monomer charge and adsorption amount. Although there was a trend that Delta had a lower charge and lower adsorption amount compared to rpM179 while SEKR had the highest protein charge and a high adsorption amount, there were four proteins at moderate charge that had a wide range of adsorption amounts, ranging from 8% for H3 to 85% for H2. The charge of the protein monomer, therefore, may not be a very good predictor of the adsorption of the protein oligomer.

As discussed above, we observed that the removal of H and residues in the N-terminus, sequences that are known to be important in protein-protein interactions, led to changes in these interactions that resulted in smaller adsorbed oligomers compared to rpM179. We hypothesize that these changes in protein-protein interactions led to changes in the structure of the oligomer that in turn affected the adsorption interactions with HAP. For example, changes in the oligomer structure may have led to changes in the exposure of the C-terminus on the oligomer surface, modulating adsorption interactions with the HAP surface to either promote (H2, H8, SEKR) or inhibit (H3) adsorption interactions with HAP relative to rpM179. The change in oligomer quaternary structure might alter the surface charge of the oligomers, modifying their electrostatic interactions with the surface. Further studies of the structure of the oligomers adsorbed onto HAP using high resolution techniques will be necessary to develop a molecular level understanding of how the adsorption behavior is altered for the mechanistic probes compared to the wild-type protein.

Amorphous calcium phosphate to hydroxyapatite phase transition

The mineralization of HAP involves the formation of ACP nanoparticles, their aggregation into larger structures, followed by their transformation to the thermodynamically stable phase, HAP (Tao et al., 2008; Habraken et al., 2013). Our mineralization studies showed that this transformation was inhibited by the protein adsorbates. It is well known that adsorbates can inhibit the ACP to HAP transformation (Posner et al., 1977), and adsorbed amelogenin has been observed to inhibit this phase transformation both *in vivo* (Beniash et al., 2009; Shin et al., 2020) and *in vitro* (Kwak et al., 2016; Tao et al., 2019). The induction time for the ACP to HAP transformation was significantly lower for Delta (rpM179 minus the C-terminus) compared to the wild-type protein. *In vivo* studies have shown that wild-type amelogenin is cleaved by MMP20 to form amelogenin without the C-terminus during the secretory stage of enamel formation. There is a gradient of wild-type protein during the secretory stage from high amounts in the freshly formed outer enamel to low amounts in the older, inner enamel (Uchida et al., 1991).

Also, *in vivo* studies found that the older, inner enamel transforms to HAP before the outer, newer enamel (Beniash et al., 2009). Our *in vitro* results would predict that amelogenin regions within enamel that have more C-termini removed, the inner enamel region, would convert to HAP sooner and this is consistent with the *in vivo* results.

Although the mechanisms of the phase transformation from ACP to HAP have not been studied in detail in the presence of amelogenin, there are a number of previous studies of the transformation without protein. Several studies have shown that HAP nucleates onto the surface or within ACP particles and then the HAP nuclei grow (Tao et al., 2008; Xie et al., 2014; Lotsari et al., 2018). The ACP to HAP transformation, therefore, may be slowed by two mechanisms: 1) protein adsorption onto ACP that inhibits the interfacial nucleation of HAP and 2) protein adsorption onto HAP nuclei that inhibits the growth of HAP. Our AFM studies of protein adsorption onto HAP can provide direct insights into the inhibition of the phase transformation by the second mechanism. The adsorption of protein onto ACP, however, has not been studied previously or in this study because of the instability of ACP. Although the bulk structural unit of ACP has been found to be similar to that of HAP (Habraken et al., 2013), and trends in adsorption onto ACP and HAP might be similar, there is no data to confirm this at the present time.

Our previous study of single amino acid variants showed that an increase in the oligomer-HAP binding energy resulted in a longer ACP to HAP induction time (Tao et al., 2019). The variations in induction time between the mechanistic probe proteins, therefore, might relate to the binding energy of the proteins—the higher the binding energy, the greater the induction time. For mineralization studies at 200 μg/ml protein concentration, the AFM adsorption studies suggest that all of the proteins would have reached saturation adsorption and would form a complete oligomer monolayer in the first layer. The proteins with a lower binding energy, however, would have a higher degree of protein exchange with the solution at equilibrium, more easily allowing the incorporation of ions and promoting the nucleation of HAP onto ACP and the growth of the newly formed HAP nuclei. Proteins with a higher binding energy, on the other hand, would have a lower degree of protein exchange with the solution and would inhibit the flux of ions necessary for the ACP to HAP transformation as well as growth of HAP nuclei.

Since we hypothesize that the induction times might be correlated with the oligomer-HAP binding energies and we have limited binding energy data in this study, we plotted the experimentally determined oligomer-HAP binding energies for H8, rpM179, and single amino acid variant proteins from our previous study (Tao et al., 2019) versus the equilibrium adsorption amounts at 15.6 μg/ml. Supplementary Figure S10 shows that there is a linear relationship between the oligomer-HAP binding energies that we have data for and the adsorption coverages at 15.6 μg/ml, suggesting that we can use the resulting equation of fit to estimate binding energies for the proteins in this study knowing their adsorption coverages at 15.6 μg/ml. Next, we plotted the induction times versus the estimated binding energies for proteins in this study to see if there is a relationship between the induction time and the oligomer-HAP binding energies (Figure 7A). This plot shows that the induction time for the ACP to HAP transformation increases with binding energy up to a point, but then decreases at higher binding energies above 18.5 kT. For example, H2 and H8 have shorter induction times than rpM179 even though they have higher estimated binding energies. This suggests that binding energy alone does not control the induction time and that other factors may be involved.

There were variations in the mean height of the oligomeric adsorbates for all of the proteins as shown in Figure 2G. At the protein concentration used for the mineralization experiments, 200 μg/ml, a complete monolayer of protein would be adsorbed in the first layer. Assuming that the thickness of the adsorbed protein layer can be approximated by the mean height of the oligomers adsorbed from Figure 2G, we plotted the induction times as a function of the first protein layer thickness as shown in Figure 7B. There was a general trend in increasing induction time with increasing protein layer thickness for most of the proteins. Even though H2 and H8 had higher binding energies than rpM179, they had lower protein thicknesses and shorter induction times. The protein thickness, therefore, may have a role in affecting the ACP to HAP phase transformation in combination with the binding energy. Since the transformation of ACP involves the nucleation of HAP and the growth of HAP from ions in the interfacial area, the adsorbates may block access of ions to the growing HAP nucleus. A thicker protein layer may be more effective in blocking ions compared to a thinner protein layer.

Further multivariate experimentation and analysis will be necessary to determine the relative importance of the oligomer binding energy and oligomer thickness to affect the ACP to HAP induction time. In addition, other factors may have roles in controlling the induction time. For example, the structure and orientation of the adsorbed oligomers may have an effect on controlling the diffusion of ions to the ACP surface. SEKR had a moderate protein thickness and a longer induction time than expected compared to the linear fit shown in Figure 7B. Previous solid state NMR (ssNMR) studies have shown that the N-terminus of rpM179 has a β-sheet structure when adsorbed onto the surface (Lu J.-X. et al., 2013; Arachchige et al., 2018). The removal of S16, E18, K24, and R31 may affect the secondary structure of amelogenin in the N-terminus resulting in a different oligomer structure and orientation on the surface that might prevent the diffusion of

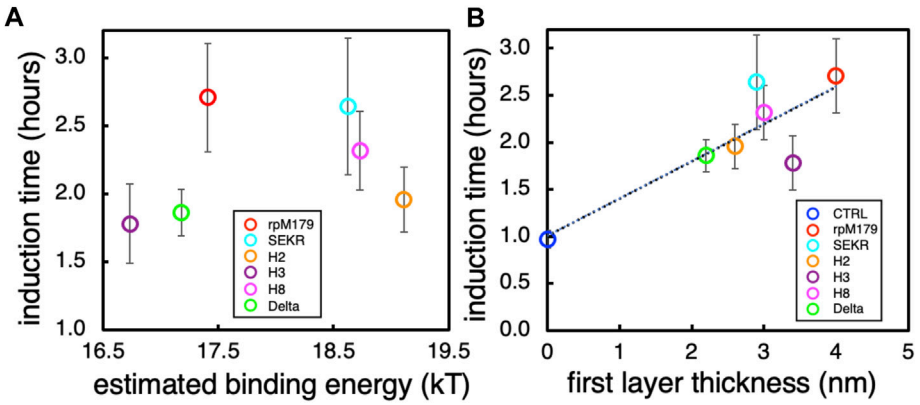

FIGURE 7
(A) The induction time for the ACP to HAP transformation as a function of the estimated binding energies obtained from Supplementary Figure S10. **(B)** The induction time as a function of the estimated thickness of the first layer of adsorbates obtained from the mean heights of the oligomers from Figure 2G.

ions to the surface of ACP or the growing HAP nucleus even though the adsorbed layer is thinner. Studies of the secondary structure of the SEKR protein in the N-terminal region as well as the structure and orientation of the oligomer would be necessary to explain how the ACP to HAP transformation is inhibited by SEKR.

Conclusion

Amelogenin is critical to the formation of enamel in teeth. The adsorption of amelogenin onto mineral surfaces has been found to be important in affecting the growth of calcium phosphates and the transformation of ACP to HAP both *in vivo* and *in vitro*. Our *in vitro* studies confirm that the C-terminus is the dominant domain promoting adsorption onto HAP surfaces and that histidines in the central region and SEKR residues in the N-terminus are primarily involved in controlling protein-protein interactions. The loss of the histidine and SEKR residues resulted in subtle changes in protein-protein interactions that affected the oligomer adsorbate sizes. We hypothesize that changes in these interactions also changed the oligomer quaternary structure to either promote (H2, H8, SEKR) or inhibit (H3) adsorption interactions relative to rpM179. Our studies confirmed the importance of amelogenin adsorption in affecting the ACP to HAP transformation and revealed new information on the mechanisms of this control. Mineralization studies found that the induction time for the ACP to HAP phase transformation was affected not only by the oligomer-HAP binding energy but also by the thickness of the adsorbed protein layer. The combination of mechanistic probes, *in situ* AFM monitoring, and mineralization kinetics studies have led to new insights into how the oligomer structure affects adsorption and calcium phosphate mineralization behavior. These studies reveal the importance of the amelogenin oligomer mesostructure on enamel mineralization *in vivo*.

Data availability statement

The raw data supporting the conclusions of this article will be made available by the authors, without undue reservation.

Author contributions

BT conceived the idea, performed DLS studies, TEM sample preparation, and wrote the paper. AD performed TEM experiments. JT performed the AFM experiments and contributed to paper writing. BJ helped perform TEM experiments. EH performed the mineralization experiments. GB prepared proteins and assisted with writing WS conceived the idea and helped to write the paper.

Funding

This work was funded by the National Institutes of Health. Support for this work was provided by NIH–National Institute of Dental and Craniofacial Research Grant SR01DE015347-14. The research was performed at PNNL, a facility operated by Battelle for the US Department of Energy. A portion of the research was performed using the Environmental Molecular Sciences Laboratory, a national scientific user facility sponsored by

the Department of Energy's Office of Biological and Environmental Research and located at PNNL.

Acknowledgments

We thank Mowei Zhou (PNNL) for collecting and analyzing mass spectral data for our amelogenin constructs.

Conflict of interest

The authors declare that the research was conducted in the absence of any commercial or financial relationships that could be construed as a potential conflict of interest.

Publisher's note

Supplementary material

The Supplementary Material for this article can be found online at: https://www.frontiersin.org/articles/10.3389/fphys.2022.1034662/full#supplementary-material

References

Aoba, T., Moreno, E. C., Kresak, M., and Tanabe, T. (1989). Possible roles of partial sequences at N- and C-termini of amelogenin in protein-enamel mineral interaction. *J. Dent. Res.* 68, 1331–1336. doi:10.1177/00220345890680090901

Arachchige, R. J., Burton, S. D., Lu, J. X., Ginovska, B., Harding, L. K., Tao, J. H., et al. (2018). Solid-state NMR identification of intermolecular interactions in amelogenin bound to hydroxyapatite. *Biophys. J.* 115, 1666–1672. doi:10.1016/j.bpj.2018.08.027

Bartlett, J. D. (2013). Dental enamel development: Proteinases and their enamel matrix substrates. *ISRN Dent.* 2013, 684607–684624. doi:10.1155/2013/684607

Bartlett, J. D., Smith, C. E., Hu, Y., Ikeda, A., Strauss, M., Liang, T., et al. (2021). MMP20-generated amelogenin cleavage products prevent formation of fan-shaped enamel malformations. *Sci. Rep.* 11, 10570. doi:10.1038/s41598-021-90005-z

Beniash, E., Metzler, R. A., Lam, R. S. K., and Gilbert, P. U. P. A. (2009). Transient amorphous calcium phosphate in forming enamel. *J. Struct. Biol.* 166, 133–143. doi:10.1016/J.Jsb.2009.02.001

Bromley, K. M., Kiss, A. S., Lokappa, S. B., Lakshminarayanan, R., Fan, D., Ndao, M., et al. (2011). Dissecting amelogenin protein nanospheres: Characterization of metastable oligomers. *J. Biol. Chem.* 40, 34643–34653. doi:10.1074/jbc.M111.250928

Buchko, G. W., Bekhazi, J., Cort, J. R., Valentine, N. B., Snead, M. L., and Shaw, W. J. (2008a). 1H, 13C, and 15N resonance assignments of murine amelogenin, an enamel biomineralization protein. *Biomol. NMR Assign.* 2, 89–91. doi:10.1007/S12104-008-9092-X

Buchko, G. W., Lin, G. Y., Tarasevich, B. J., and Shaw, W. J. (2013). A solution NMR investigation into the impaired self-assembly properties of two murine amelogenins containing the point mutations T21 -> I or P41 -> T. *Arch. Biochem. Biophys.* 537, 217–224. doi:10.1016/j.abb.2013.07.015

Buchko, G. W., Tarasevich, B. J., Bekhazi, J., Snead, M. L., and Shaw, W. J. (2008b). A solution NMR investigation into the early events of amelogenin nanosphere self-assembly initiated with sodium chloride or calcium chloride. *Biochemistry* 47, 13215–13222. doi:10.1021/Bi8018288

Ding, H. C., Pan, H. H., Xu, X. R., and Tang, R. K. (2014). Toward a detailed understanding of magnesium ions on hydroxyapatite crystallization inhibition. *Cryst. Growth Des.* 14, 763–769. doi:10.1021/cg401619s

Fang, P. A., Conway, J. F., Margolis, H. C., Simmer, J. P., and Beniash, E. (2011). Hierarchical self-assembly of amelogenin and the regulation of biomineralization at the nanoscale. *Proc. Natl. Acad. Sci. U. S. A.* 108, 14097–14102. doi:10.1073/pnas.1106228108

Fincham, A. G., Moradian-Oldak, J., and Simmer, J. P. (1999). The structural biology of the developing dental enamel matrix. *J. Struct. Biol.* 126, 270–299. doi:10.1006/jsbi.1999.4130

Fincham, A. G., and Simmer, J. P. (1997). Amelogenin proteins of developing dental enamel. *Ciba Found. Symp.* 205, 118–130. doi:10.1002/9780470515303.ch9

George, A., and Veis, A. (2008). Phosphorylated proteins and control over apatite nucleation, crystal growth, and inhibition. *Chem. Rev.* 108, 4670–4693. doi:10.1021/cr0782729

Gungormus, M., Fong, H., Kim, I. W., Evans, J. S., Tamerler, C., and Sarikaya, M. (2008). Regulation of *in vitro* calcium phosphate mineralization by combinatorially selected hydroxyapatite-binding peptides. *Biomacromolecules* 9, 966–973. doi:10.1021/bm701037x

Gungormus, M., Oren, E. E., Horst, J. A., Fong, H., Hnilova, M., Somerman, M. J., et al. (2012). Cementomimetics-constructing a cementum-like biomineralized microlayer via amelogenin-derived peptides. *Int. J. Oral Sci.* 4, 69–77. doi:10.1038/ijos.2012.40

Habraken, W. J. E. M., Tao, J. H., Brylka, L. J., Friedrich, H., Bertinetti, L., Schenk, A. S., et al. (2013). Ion-association complexes unite classical and non-classical theories for the biomimetic nucleation of calcium phosphate. *Nat. Commun.* 4, 1507–1512. doi:10.1038/ncomms2490

Heyda, J., Mason, P. E., and Jungwirth, P. (2010). Attractive interactions between side chains of histidine-histidine and histidine-arginine-based cationic dipeptides in water. *J. Phys. Chem. B* 114, 8744–8749. doi:10.1021/jp101031v

Hu, Y. Y., Smith, C. E., Cai, Z. H., Donnelly, L. A. J., Yang, J., Hu, J. C. C., et al. (2016). Enamel ribbons, surface nodules, and octacalcium phosphate in C57BL/6 Amelx(-/-) mice and Amelx(+/-) lyonization. *Mol. Genet. Genomic Med.* 4, 641–661. doi:10.1002/mgg3.252

Jin, W. J., Jiang, S. Q., Pan, H. H., and Tang, R. K. (2018). Amorphous phase mediated crystallization: Fundamentals of biomineralization. *Crystals* 8, 48–24. doi:10.3390/cryst8010048

Kwak, S. Y., Wiedemann-Bidlack, F. B., Beniash, E., Yamakoshi, Y., Simmer, J. P., Litman, A., et al. (2009). Role of 20-kDa amelogenin (P148) phosphorylation in calcium phosphate formation *in vitro*. *J. Biol. Chem.* 284, 18972–18979. doi:10.1074/Jbc.M109.020370

Kwak, S. Y., Yamakoshi, Y., Simmer, J. P., and Margolis, H. C. (2016). MMP20 proteolysis of native amelogenin regulates mineralization *in vitro*. *J. Dent. Res.* 95, 1511–1517. doi:10.1177/0022034516662814

Lacruz, R. S., Nanci, A., Kurtz, I., Wright, J. T., and Paine, M. L. (2010). Regulation of pH during amelogenesis. *Calcif. Tissue Int.* 86, 91–103. doi:10.1007/s00223-009-9326-7

Lotsari, A., Rajasekharan, A. K., Halvarsson, M., and Andersson, M. (2018). Transformation of amorphous calcium phosphate to bone-like apatite. *Nat. Commun.* 9, 4170–4181. doi:10.1038/s41467-018-06570-x

Lowenstam, H. A., and Weiner, S. (1989). *On Biomineralization*. New York: Oxford University Press.

Lu, J.-X., Xu, Y. S., Buchko, G. W., and Shaw, W. J. (2013a). Mineral association changes the secondary structure and dynamics of murine amelogenin. *J. Dent. Res.* 92, 1000–1004. doi:10.1177/0022034513504929

Lu, J. X., Xu, Y. S., and Shaw, W. J. (2013b). Phosphorylation and ionic strength alter the LRAP-HAP interface in the N-terminus. *Biochemistry* 52, 2196–2205. doi:10.1021/bi400071a

Lyman, G. E., and Waddell, W. J. (1977). pH gradients in the developing teeth of young mice from autoradiography of [14C]DMO. *Am. J. Physiol.* 232, F364–F367. doi:10.1152/ajprenal.1977.232.4.F364

Mann, S. (2001). *Biomineralization: Principles and Concepts in Bioinorganic Materials*. Oxford University Press.

Moradian-Oldak, J., Bouropoulos, N., Wang, L. L., and Gharakhanian, N. (2002). Analysis of self-assembly and apatite binding properties of amelogenin proteins lacking the hydrophilic C-terminal. *Matrix Biol.* 21, 197–205. doi:10.1016/s0945-053x(01)00190-1

Moradian-Oldak, J., Jimenez, I., Maltby, D., and Fincham, A. G. (2001). Controlled proteolysis of amelogenins reveals exposure of both carboxy- and amino-terminal regions. *Biopolymers* 58, 606–616. doi:10.1002/1097-0282(200106)58:7<606::AID-BIP1034>3.0.CO;2-8

Moradian-Oldak, J., Leung, W., and Fincham, A. G. (1998). Temperature and pH-dependent supramolecular self-assembly of amelogenin molecules: A dynamic light-scattering analysis. *J. Struct. Biol.* 122, 320–327. doi:10.1006/jsbi.1998.4008

Moradian-Oldak, J., Paine, M. L., Lei, Y. P., Fincham, A. G., and Snead, M. L. (2000). Self-assembly properties of recombinant engineered amelogenin proteins analyzed by dynamic light scattering and atomic force microscopy. *J. Struct. Biol.* 131, 27–37. doi:10.1006/jsbi.2000.4237

Paine, M. L., and Snead, M. L. (1997). Protein interactions during assembly of the enamel organic extracellular matrix. *J. Bone Min. Res.* 12, 221–227. doi:10.1359/jbmr.1997.12.2.221

Posner, A. S., Betts, F., and Blumental, N. C. (1977). Role of ATP and Mg in the stabilization of biological and synthetic amorphous calcium phosphates. *Calcif. Tissue Res.* 22, 208–212. doi:10.1007/BF02064066

Shin, N. Y., Yamazaki, H., Beniash, E., Yang, X., Margolis, S. S., Pugach, M. K., et al. (2020). Amelogenin phosphorylation regulates tooth enamel formation by stabilizing a transient amorphous mineral precursor. *J. Biol. Chem.* 295, 1943–1959. doi:10.1074/jbc.RA119.010506

Simmer, J. P., and Fincham, A. G. (1995). Molecular mechanisms of dental enamel formation. *Crit. Rev. Oral Biol. Med.* 6, 84–108. doi:10.1177/10454411950060020701

Simmer, J. P., Richardson, A. S., Hu, Y. Y., Smith, C. E., and Hu, J. C. C. (2012). A post-classical theory of enamel biomineralization... and why we need one. *Int. J. Oral Sci.* 4, 129–134. doi:10.1038/Ijos.2012.59

Studier, F. W. (2005). Protein production by auto-induction in high density shaking cultures. *Protein Expr. Purif.* 41, 207–234. doi:10.1016/j.pep.2005.01.016

Tao, J., Buchko, G. W., Shaw, W. J., De Yoreo, J. J., and Tarasevich, B. J. (2015). Sequence-defined energetic shifts control the disassembly kinetics and microstructure of amelogenin adsorbed onto hydroxyapatite (100). *Langmuir* 31, 10451–10460. doi:10.1021/acs.langmuir.5b02549

Tao, J., Pan, H. H., Wang, J. R., Wu, J., Wang, B., Xu, X. R., et al. (2008). Evolution of amorphous calcium phosphate to hydroxyapatite probed by gold nanoparticles. *J. Phys. Chem. C* 112, 14929–14933. doi:10.1021/jp804371u

Tao, J., Shin, Y., Jayasinha, R., Buchko, G. W., Burton, S. D., Dohnalkova, A. C., et al. (2019). The energetic basis for hydroxyapatite mineralization by amelogenin variants provides insights into the origin of amelogenesis imperfecta. *Proc. Natl. Acad. Sci. U. S. A.* 116, 13867–13872. doi:10.1073/pnas.1815654116

Tarasevich, B. J., Lea, S., Bernt, W., Engelhard, M., and Shaw, W. J. (2009). Adsorption of amelogenin onto self-assembled and fluoroapatite surfaces. *J. Phys. Chem. B* 113, 1833–1842. doi:10.1021/Jp804548x

Uchida, T., Tanabe, T., Fukae, M., Shimizu, M., Yamada, M., Miake, K., et al. (1991). Immunochemical and immunohistochemical studies, using antisera against porcine 25 kDa amelogenin, 89 kDa enamelin and the 13-17 kDa nonamelogenins, on immature enamel of the pig and rat. *Histochemistry* 96, 129–138. doi:10.1007/BF00315983

Xie, B., Halter, T. J., Borah, B. M., and Nancollas, G. H. (2014). Tracking amorphous precursor formation and transformation during induction stages of nucleation. *Cryst. Growth Des.* 14, 1659–1665. doi:10.1021/cg401777x

frontiers | Frontiers in Physiology

TYPE Brief Research Report
PUBLISHED 01 December 2022
DOI 10.3389/fphys.2022.1069519

OPEN ACCESS

EDITED BY
Pamela Den Besten,
University of California, San Francisco, United States

REVIEWED BY
Gabor Varga,
Semmelweis University, Hungary
Yan Zhang,
University of California, San Francisco, United States

*CORRESPONDENCE
Janet Moradian-Oldak,
joldak@usc.edu

SPECIALTY SECTION
This article was submitted to Craniofacial Biology and Dental Research, a section of the journal Frontiers in Physiology

RECEIVED 14 October 2022
ACCEPTED 21 November 2022
PUBLISHED 01 December 2022

CITATION
Visakan G, Bapat RA, Su J and Moradian-Oldak J (2022), Modeling ameloblast-matrix interactions using 3D cell culture.
Front. Physiol. 13:1069519.
doi: 10.3389/fphys.2022.1069519

Modeling ameloblast-matrix interactions using 3D cell culture

Gayathri Visakan, Rucha Arun Bapat, Jingtan Su and Janet Moradian-Oldak*

Center for Craniofacial Molecular Biology, Herman Ostrow School of Dentistry, University of Southern California, Los Angeles, CA, United States

The distinct morphology adopted by ameloblasts during amelogenesis is highly stage specific and involved intimately with the development of a hierarchical enamel microstructure. The molecular mechanisms that govern the development of an elongated and polarized secretory ameloblast morphology and the potential roles played by the enamel matrix proteins in this process are not fully understood. Thus far, the *in vitro* models that have been developed to mimic these early cell-matrix interactions have either been unable to demonstrate direct morphological change or have failed to adapt across ameloblast cell lines. Here, we use a recently established 3D cell culture model to examine the interactions between HAT-7 cells and the major enamel matrix proteins, amelogenin and ameloblastin. We demonstrate that HAT-7 cells selectively respond to functional EMPs in culture by forming clusters of tall cells. Aspect ratio measurements from three-dimensional reconstructions reveal that cell elongation is 5-times greater in the presence of EMPs when compared with controls. Using confocal laser scanning microscopy, we observe that these clusters are polarized with asymmetrical distributions of Par-3 and claudin-1 proteins. The behavior of HAT-7 cells in 3D culture with EMPs is comparable with that of ALC and LS-8 cells. The fact that the 3D model presented here is tunable with respect to gel substrate composition and ameloblast cell type highlights the overall usefulness of this model in studying ameloblast cell morphology *in vitro*.

KEYWORDS

ameloblasts, ameloblastin, amelogenin, polarization, cell morphology, Geltrex®, 3D cell culture

Introduction

Enamel's unique mechanical strength stems from the hierarchical arrangement of hydroxyapatite crystals into prisms with interprismatic mineral (Boyde, 1997; Chai et al., 2009). Although mature enamel is acellular, the generation of a prismatic enamel microstructure has been linked to features of ameloblast morphology during the early stages of amelogenesis - like the Tomes' processes. During enamel development, ameloblasts undergo a complicated set of movements with each one contributing to unique structural features in mature enamel's final microstructure. Ameloblasts move away from the developing enamel matrix, and adjacent sheets of ameloblasts move relative

to one another resulting in a decussating pattern of enamel rods in higher mammals (Boyde, 1964; Boyde, 1997). However, the mechanisms underlying the formation of this unique, highly specialized ameloblast morphology are not fully understood.

The roles of enamel matrix proteins in amelogenesis - either individually or corporately are constantly evolving (Hatakeyama et al., 2009; Moradian-Oldak, 2012; Mazumder et al., 2016; Lacruz et al., 2017; Bapat et al., 2020; Moradian-Oldak and George, 2021). Genetically engineered mouse models have shown that, in addition to affecting enamel mineralization, components of the extracellular milieu like matrix proteins (ameloblastin and enamelin) and proteinases (MMP20) may influence ameloblast cell behavior (Fukumoto et al., 2005; Guan and Bartlett, 2013; Hu et al., 2014; Shin et al., 2018). The truncation of ameloblastin (removal of exons 5 and 6) results in the loss of secretory ameloblast elongation and polarization with a resultant de-differentiation into an inner enamel epithelium-like stage (Fukumoto et al., 2004). MMP20 overexpression disrupts the coordinated ameloblast movements, resulting in an abnormal migration of the ameloblasts into the papillary layers with a concomitant loss of ameloblast cell polarity (Shin et al., 2018). Additionally, MMP20 has been shown to regulate ameloblast movement through Wnt- and beta-catenin-mediated pathways by catalyzing the cleavage of ameloblast cell surface cadherins (Bartlett et al., 2011; Guan et al., 2016).

Reliable *in vitro* 3D cell culture models have proven invaluable for examining the interactions between ameloblasts and the enamel extracellular matrix (He et al., 2010; Földes et al., 2021). *In vitro* and cell culture systems provide for precise control over experimental conditions and the ability to isolate and examine the role of individual components in the matrix. When primary human enamel epithelial cells are co-cultured with dental pulp cells in a 3D Matrigel, they form spheroidal structures, increasing both their size and the expression levels of integrins (Li et al., 2006; He et al., 2010). Since ameloblasts are lost after amelogenesis, several ameloblast cell lines have been developed that are immortalized, either spontaneously (Nakata et al., 2003) or by viral transfection (Chen et al., 1992). These ameloblast cell lines exhibit characteristic and distinct phenotypes in culture and can represent different ameloblast stages (Sarkar et al., 2014). Using bioreactor-based 3D embedded cultures of HAT-7 cells, it was shown that HAT-7 cells display immunoreactivity to amelogenin and actin when co-cultured with dental pulp cells and in the presence of enamel matrix proteins (Pandya et al., 2021). The differentiation of cells into an ameloblast-like state in 3D culture is often demonstrated with differential gene expression patterns (Jiang et al., 2018). Given the pivotal roles played by ameloblast morphology in patterning the overall microstructure of enamel, ameloblast cell responses need to be methodically characterized, particularly the morphological changes occurring in response to the extracellular matrix composition.

We recently established a 3D cell culture model that is adaptable across gel substrates and allows for the quantification of changes in cell morphology and polarization in response to the matrix composition (Visakan et al., 2022a; Visakan et al., 2022b). Here, our optimized 3D model will be used to culture HAT-7 cells, which are often the cell line of choice for examining functional cell polarization (Bori et al., 2016). Using a systematic protocol for assessing changes in cell morphology by means of cell aspect ratio measurements and polarization by confocal microscopy, we observed that the addition of recombinant amelogenin (AMEL) and ameloblastin (AMBN) to the gel resulted in the formation of elongated and polarized HAT-7 cell clusters. These changes in HAT-7 cells are comparable to those of ALC and LS-8 cells, which have been previously studied (Visakan et al., 2022a). Since the composition of the 3D gel matrix is tunable, this model also allowed us to tailor the cell microenvironment using a combination of proteins or their proteolytic cleavage fragments as shown here with the recombinant AMBN 17 kDa. The proteolytic processing of ameloblastin by MMP-20 results in the production of three N-terminal cleavage fragments that weigh 17, 15 and 13 kDa (Iwata et al., 2007; Chun et al., 2010). Among these N-terminal cleavage fragments, the 17 kDa fragment predominates and exhibits potential regenerative properties when used on artificial periodontal defects (Fukae et al., 2006). We also examined the effect of ameloblastin lacking a potential cell binding domain (Su et al., 2020) on HAT-7 cells, suggesting that this system can be expanded to model disorders of enamel development.

Methods

Recombinant protein expression and purification

Recombinant amelogenin and ameloblastin (AMEL, AMBN, AMBNΔ5) were expressed and purified based on published protocols and as described in the Supplementary Material (Su et al., 2019a; Bapat et al., 2020).

Recombinant 17 kDa ameloblastin cleavage fragment expression, purification and characterization

To purify the 17 kDa fragment of ameloblastin, the full-length Ambn pET32a plasmid was first purified using the Monarch Miniprep kit (New England Biolabs). The 17 kDa fragment within the plasmid was selectively amplified using forward (atatatggatccgtgccggcatttcctcaac) and reverse primers (ttttttctcgagtcaacgggcgatctggaac). The PCR product and new pET32a plasmids (EMD Millipore) were digested using

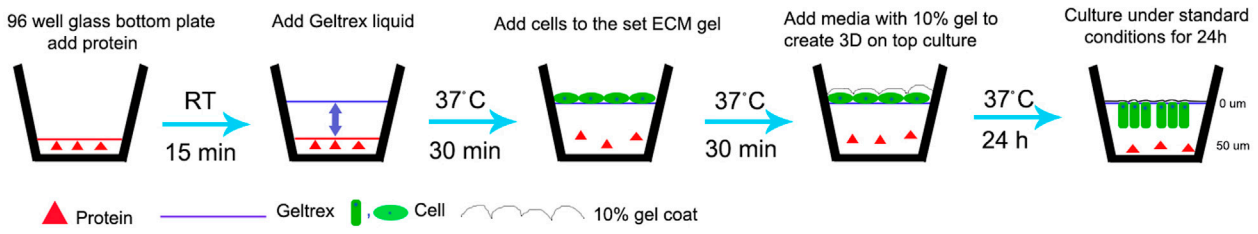

FIGURE 1
Schematic representation of modified 3D-on-top culture method (side view). Red triangle represents proteins-test (AMEL, AMBN, AMBN 17kDa, AMBN Δ5) and control (BSA, heat denatured AMBN). Green oval and rectangle represent HAT-7 cells. Solid line- GFR Geltrex after polymerization and scalloped line denotes 10% gel overlaid on cells. 0 and 50um markings are used to indicate the Z position on the surface (0 um) and within the gel (50 um) after 24 h resulting in elongation of the cells as shown in Figures 2D,E and Figure 4.

BamHI and XhoI enzymes (New England Biolabs). Then, they were purified using a QIAgen gel extraction kit and ligated. The ligated plasmid was transferred into Dh5α competent *E. coli* using the heat shock technique. Bacterial colonies were screened for successful transformation using ampicillin agar plates. The 17 kDa Ambn plasmid from selected colonies was amplified, purified, and sequenced. 17kDa Ambn was expressed in BL21 *E. coli*, and the protein was purified using the previously published protocol for full-length Ambn and characterized as described in the Supplementary Material.

HAT-7 characterization in 2D cell culture

HAT-7 cells were obtained as a gift from Prof. Hidemitsu Harada (Tokyo). HAT-7 cells were cultured following standard protocols (Kawano et al., 2002). Briefly, cells were cultured in 13 mm culture dishes (Corning) with low glucose Dulbecco's Modified Eagle Medium (DMEM) (Gibco, Thermo) supplemented with 10% FBS (Thermo) and 1% penicillin/streptomycin (Thermo). This supplemented DMEM is referred to as cell culture media. Cultures were maintained under 5% CO_2 at 37 ˚C until they achieved 80% or greater confluence. HAT-7 cells were characterized using immunofluorescence staining for amelogenin and ameloblastin proteins.

3D cell culture and aspect ratio measurement

A previously developed, optimized 3D-on-top type culture technique for the culture of ameloblast cell lines was used (Lee et al., 2007; Visakan et al., 2022a; Visakan et al., 2022b). Briefly, pre-chilled glass-bottomed 96-well plates (Mattek) were coated with 20 ug/ml test (AMBN, AMEL, AMBN Δ5, AMBN 17 kDa) and control (heat denatured AMBN, BSA and PBS) proteins. Ice-cold, growth-factor-reduced Geltrex (GFR Geltrex; Thermo) was overlaid on coated plates and incubated at 37 ˚C for 30 min. HAT-7 cells were detached from the culture dishes at 80% or greater confluence and were centrifuged at 200 x g for 5 min to obtain a soft pellet. The cells were resuspended in cell culture media and inoculated atop set GFR Geltrex gels to create a 3D-on-top-type culture (Figure 1). These 3D gels were incubated at 37 ˚C in a standard cell culture incubator for 24–72 h. At the end of the experiment, the cells were fixed with 25% glutaraldehyde for 15 min at room temperature. Cells in the 3D gel were labeled with 1:1000 DiD and 1:1000 DAPI and were visualized using Keyence BZX810 with objective PlanApo λ NA 0.75. Sequential Z stacks were recorded with a pitch of 0.4 µm. Z stacks were reconstructed using the Keyence Image Viewer (software version 1.1.1.8), and the 3D measure-tool was used to record the cell width along the XY plane and cell height along the *Z* axis. These values were tabulated, and the aspect ratio was calculated using the following formula: $Aspect\ ratio = \frac{Cell\ height\ (Z)}{Cell\ width\ (XY)}$. Repeated measurements of the aspect ratio were recorded to analyze for statistical significance, and the experiments were repeated three times.

Immunofluorescence labelling

All steps were carried out in the dark at room temperature. Immunofluorescence labeling of whole cultures was carried out without the extraction of cells from the 3D gel (Lee et al., 2007). Cells in 3D that were fixed with glutaraldehyde were permeabilized with 0.1% Triton-X-100 for 5 min at room temperature. Then, the cells were incubated with 10% serum from the species of secondary antibody for 30 min at room temperature and were labelled with primary antibodies against Par-3, Actin and claudin-1. Fluorescently conjugated secondary antibodies (Jackson Immuno) were used for immunodetection for 1 h at room temperature. For

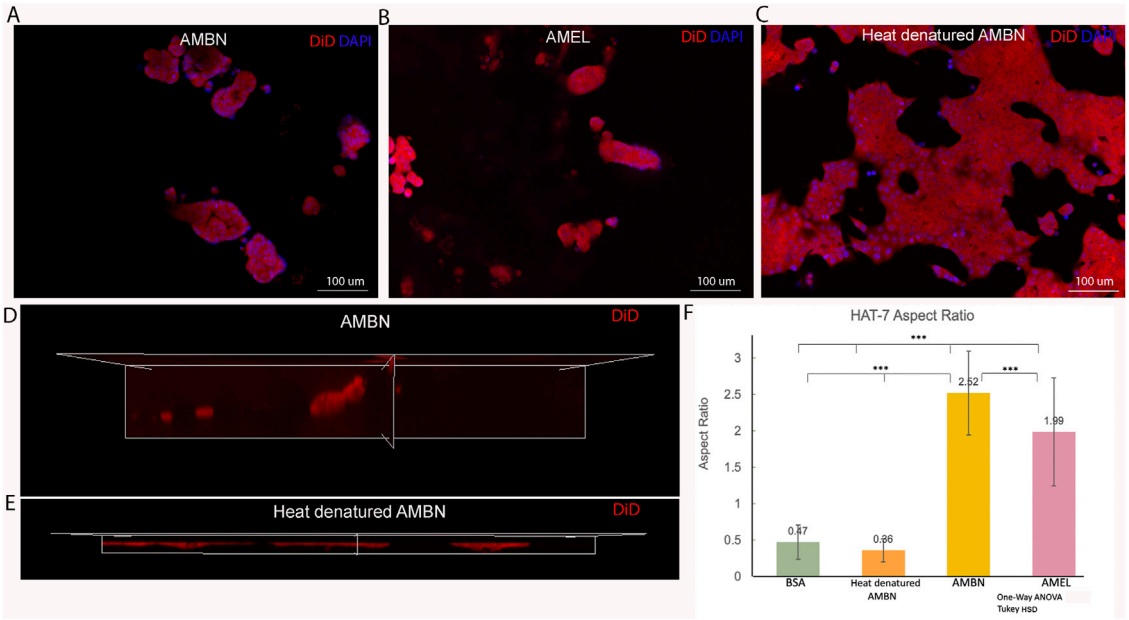

FIGURE 2
HAT-7 cells in modified 3D-on-top culture using growth-factor reduced Geltrex; 24h. **(A–C)**. 2D surface images (top view, XY plane) of HAT-7 cells in the presence of AMBN, AMEL and heat denatured AMBN (negative control) respectively. Cell membrane labeled with DiD (red) and nucleus with DAPI (blue). HAT-7 cells organize into distinct cell clusters in **(A)** and **(B)** unlike in the control **(C)** where the cells are spread along the XY plane. **(D, E)**. 3D reconstruction and axial view (side view, XZ plane) of representative samples from AMBN and heat denatured AMBN groups respectively. Cell outline as visualized by DiD reveals elongated, tall cells in **(D)** unlike the planar, flat cells with **(E)**. **(F)** Aspect ratio measurements of HAT-7 cells from test and control groups. HAT-7 cells are statistically significantly elongated in the presence of AMEL and AMBN. *$p < 0.05$; **$p < 0.01$; ***$p < 0.001$.

characterization of HAT-7 cells, anti-amelogenin and anti-ameloblastin antibodies were used. A 2D monolayer of cells was fixed using 4% paraformaldehyde, was permeabilized using 0.1% Triton-X-100, and was labeled following standard protocols for immunofluorescence. Antibody dilutions for both 3D and 2D are provided in Supplementary Table S1. All images were created with confocal microscopy as described, except the image in Figure 2 and Supplementary Figure S2 which was made using an inverted fluorescence microscope (Keyence BZX810, Keyence, United States).

Confocal imaging

Confocal imaging was carried out using the Lecia Stellaris 5 confocal microscope with an oil immersion objective HCX PL APO CS 63 x (NA 1.4). Sequential Z stacks were recorded with an optical pitch of 0.5 µm. Alexa Fluor 488 was detected at 502–552 nm (excitation at 488 nm), DiD was detected at 645–695 nm (excitation at 633 nm), and Alexa Fluor 647 was detected at 650–695 nm (excitation at 647 nm). Z stacks were 3D reconstructed and viewed using the LAS-X version 1.8.1.13759.

Statistical analysis

Data from aspect ratio measurements was analyzed with Microsoft Excel (version 16.66.1) using One-way ANOVA, independent Student's *t*-test and Tukey HSD. *p* values less than 0.05 were considered as statistically significant. All experiments were performed in triplicates. For all experiments 90 cells in total were examined.

Results

3D culture to analyze morphology and aspect ratios in HAT-7 cells in response to AMEL and AMBN

Confluent 2D monolayers of HAT-7 cells were characterized by immunofluorescence staining for amelogenin and ameloblastin. We observed the expression of both proteins intracellularly using confocal microscopy, confirming the ameloblast characteristics of the HAT-7 cells (Supplementary Figure S1). HAT-7 cells that were cultured in the presence of enamel matrix proteins in 3D culture displayed characteristic differences in their morphology when compared with controls at

the end of 24 h (Figure 2). HAT-7 cells organized into clusters in the presence of AMBN and AMEL as visualized with cell membrane labeling using DiD (Figures 2A,B). This morphology adopted by the HAT-7 cells contrasts strikingly with the controls (gel alone, BSA and heat denatured ameloblastin) where cells-maintained cell-cell contacts and were spread along the XY plane (Figure 2C). 3D reconstruction from sequential Z stacks revealed that the HAT-7 clusters in the presence of AMEL and AMBN were composed of tall cells that preferentially elongated along the *Z* axis (Figure 2D). Meanwhile, in the controls, the cells appeared planar without any significant height (Figure 2E). To quantify the cell elongation that occurs in the presence of enamel matrix proteins (EMPs), the aspect ratio of the individual cells was recorded. Repeated measurements of the cell aspect ratio revealed that, after 24 h of 3D culture, HAT-7 cells elongated 5.42 times greater with EMPs when compared to the controls (i.e., in the presence of BSA and heat denatured AMBN). This increase in the aspect ratio was statistically significantly different between all groups ($n = 90$; $p < 0.001$) with the greatest cell elongation achieved in the presence of AMBN ($n = 90$; $p < 0.001$) (Figure 2F). This pattern of cell behavior was consistent at the end of 72 h of culture (Supplementary Figure S2).

Morphology and aspect ratios in HAT-7 cells in response to 17 kDa AMBN and AMBN Δ5

Recent work has identified the presence of a highly conserved amphipathic helix (AH) forming, cell binding motif within the exon 5 region of AMBN (Su et al., 2019b; Su et al., 2020). To verify the function of the N-terminal domain identified within exon 5 of *Ambn,* the 3D culture model was used to examine the effect of 17 kDa AMBN (a proteolytic fragment contains the AH domain) and AMBN Δ5 (a mutant lacks the AH domain) on HAT-7 morphology. The theoretical molecular mass of AMBN 17 kDa was calculated using ProtParam and was found to be 17,990.53 Da. SDS-PAGE gels revealed that the protein migrated at an apparent molecular weight higher than the expected theoretical value (Supplementary Figure S3A). Mass spectra (ESI) of the band around 20 kDa in SDS-PAGE showed that the molecular mass of the protein was 17,991 Da, close to the theoretical value of 17,990.53 Da, suggesting that the purified protein was the AMBN 17 kDa fragment (Supplementary Figure S3B). The difference in the theoretical and experimental mass of the protein was 0.47 Da, suggesting that the protein identified in the peak was intact. The amino acid sequence of the 17 kDa cleavage fragment is shown in Supplementary Figure S3C. When cultured with the recombinant AMBN 17 kDa cleavage fragment, HAT-7 cells responded similarly to full-length ameloblastin. At comparable molar concentrations of both proteins (0.48 μM), the 17 kDa fragment was sufficient to recapitulate the cell clustering and elongation achieved with full-length AMBN (Figures 3A,B). Measurements of the aspect ratio confirmed this, where no statistically significant difference was observed between the 17 kDa fragment and the full-length AMBN ($p > 0.05$) (Figure 3C). The 3D model was then used to observe how the removal of highly conserved key domains from AMBN affected HAT-7 morphology. Culturing HAT-7 cells with AMBN Δ5 lacking the exon 5 encoded region resulted in a complete reversal of the cells' behavior in 3D. HAT-7 cells failed to cluster and, instead, appeared distinct like in the negative controls (Figures 3D,E). Aspect ratio measurements confirmed the lack of cell elongation in the AMBN Δ5 mutant when compared with the wild-type AMBN ($p < 0.001$) (Figure 3F).

Asymmetric distribution of Par-3 and claudin-1 upon HAT-7 polarization with AMBN

3D clusters of HAT-7 cells that were elongated in the presence of AMBN were labeled with anti-actin, anti-Par-3, and anti-claudin-1 antibodies (Figure 4). They were then examined under a confocal laser scanning microscope with the 3D reconstruction of sequential Z stacks. Actin labeling (grey pseudo color) confirmed the cell elongation (Supplementary Figure S4A,B) observed earlier with DiD (Figure 2). Actin labeling patterns within individual cells in HAT-7 clusters (formed in the presence of AMBN) were uniform and symmetrical with signals being detected throughout the entire outline of the cells (Figure 4B). Cell polarity protein Par-3 (red) localization, however, was polarized with signals being restricted to the cell membrane basal to nucleus (Figure 4C). Additionally, colocalization of actin and Par-3 was restricted to one pole of the cell (white arrows in Figure 4D). XY plane images acquired at two different Z depths from the surface of the cells revealed that, at higher Z depths, only actin signals were detectable, which confirms the polarized distribution of Par-3 (Supplementary Figures S5A–F). Like Par-3, tight junction protein claudin-1 (green) was also asymmetrical in its distribution compared to that of cell membrane label DiD (grey pseudo color) with its localization being restricted basal to nucleus (Figures 4E–H). The planar cells in the control did not display any polarization in the distribution of Par-3 (Supplementary Figure S6). The HAT-7 clusters formed in the presence of 17 kDa AMBN were also polarized with the Par-3 localization patterns being comparable with that of the full-length AMBN (Figures 4I–L).

Discussion

It has been proposed that ameloblast morphology is directly or indirectly related to the development of an overall prismatic

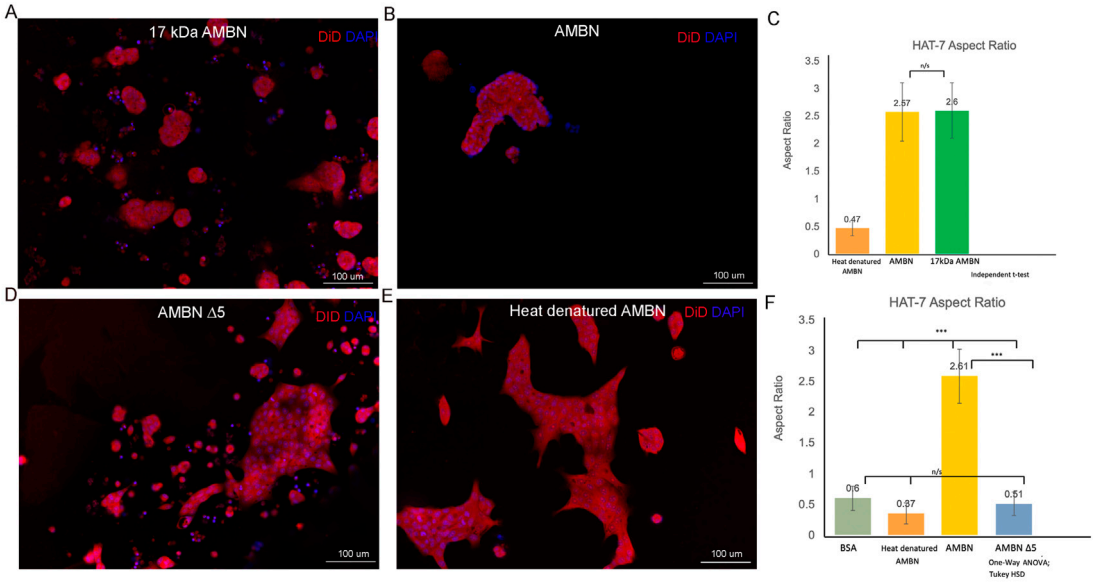

FIGURE 3
HAT-7 cells cultured with AMBN 17 kDa fragment and AMBN Δ5 mutant. **(A,B)**. XY surface images of HAT-7 cells cultured in the presence of AMBN 17 kDa fragment and wild-type full-length AMBN respectively. HAT-7 cells organized into distinct clusters of cells in both groups as visualized using DiD (red) and DAPI (blue). **(C)**. Aspect ratio measurements of HAT-7 cells cultured with 17 kDa fragment, positive and negative controls revealing statistically comparable HAT-7 cell elongation in AMBN 17 kDa cleavage fragment and positive control (full-length AMBN); $p > 0.05$. **(D,E)**. XY surface images of HAT-7 cells cultured with mutant AMBN Δ5, and heat denatured AMBN respectively. **(F)**. Aspect ratio measurements of HAT-7 cells in the presence of AMBN Δ5. Removal of exon 5 encoded sequence resulted in HAT-7 cells remaining planar with aspect ratio values statistically significantly lower than wild-type AMBN $p < 0.001$. AMBN Δ5 aspect ratios are comparable with those of negative controls $p > 0.05$. $*p < 0.05$; $**p < 0.01$; $***p < 0.001$.

enamel architecture (Boyde, 1964, Boyde, 1997; Nanci, 2017). Ameloblast elongation and polarization were severely impacted in genetically engineered mouse models lacking functional ameloblastin or enamelin (Fukumoto et al., 2004; Hu et al., 2014), resulting in a lack of true enamel. The severe dysmorphology in genetically engineered animal models makes it challenging to observe and examine the molecular mechanisms that govern the formation of this highly specialized ameloblast morphology, thereby necessitating the need for *in vitro* models.

Here, we demonstrate that the changes in cell morphology and polarization upon addition of enamel matrix proteins can be modeled using a recently-established, *in-vitro* 3D cell culture (Visakan et al., 2022a). This model enabled such differential cell responses to be readily visualized and quantified in a systematic manner in three different ameloblast-like cell lines (i.e., ALC, LS-8 and HAT-7). Using immunofluorescent staining and aspect ratio measurements, we observed that HAT-7 cells exhibited a preferential elongation along the *Z* axis, resulting in the formation of clusters of tall cells when cultured in the presence of AMBN or AMEL. Formation of these tall cells in the presence of the 17 kDa AMBN suggests a potential *in vivo* significance of this response, considering that the 17 kDa cleavage fragment persists in the prism sheaths of the developing enamel matrix (Uchida et al., 1991).

Loss of function of AMBN in cell elongation and polarization was further demonstrated using recombinant mutant AMBN protein lacking the exon 5 encoded region (AMBN Δ5). This mutant lacked the ability to induce cell clustering or elongation in HAT-7 cells. This observation can be the result of loss of AMBN -cell binding, (Su et al., 2020), or AMBN self-assembly (Wald., et al., 2017). AMBN exon 5 encoded region contains the amphipathic helix (AH) cell binding domain that recently was found to be highly conserved among mammals and had a strong evolutionary relationship with enamel prismatic structure (Su et al., 2022). The same region contains the Y/F-x-x-Y/L/F-x-Y/F self-assembly motif, and the disruption of this motif resulted in a perturbed enamel prismatic architecture (Wald et al., 2017). The Y/F-x-x-Y/L/F-x-Y/F motif within exon 5 encoded region also is the site of co-assembly with AMEL (Bapat et al., 2020).

The model can also be used to examine and characterize the polarization status of cells in 3D culture as demonstrated using immunofluorescent labeling of Par-3, claudin-1, and actin proteins. We originally developed this 3D on top culture model to generate non-uniform contact surfaces for cells to mimic the enamel extracellular matrix during development (Visakan et al., 2022a). The developing ameloblasts are in

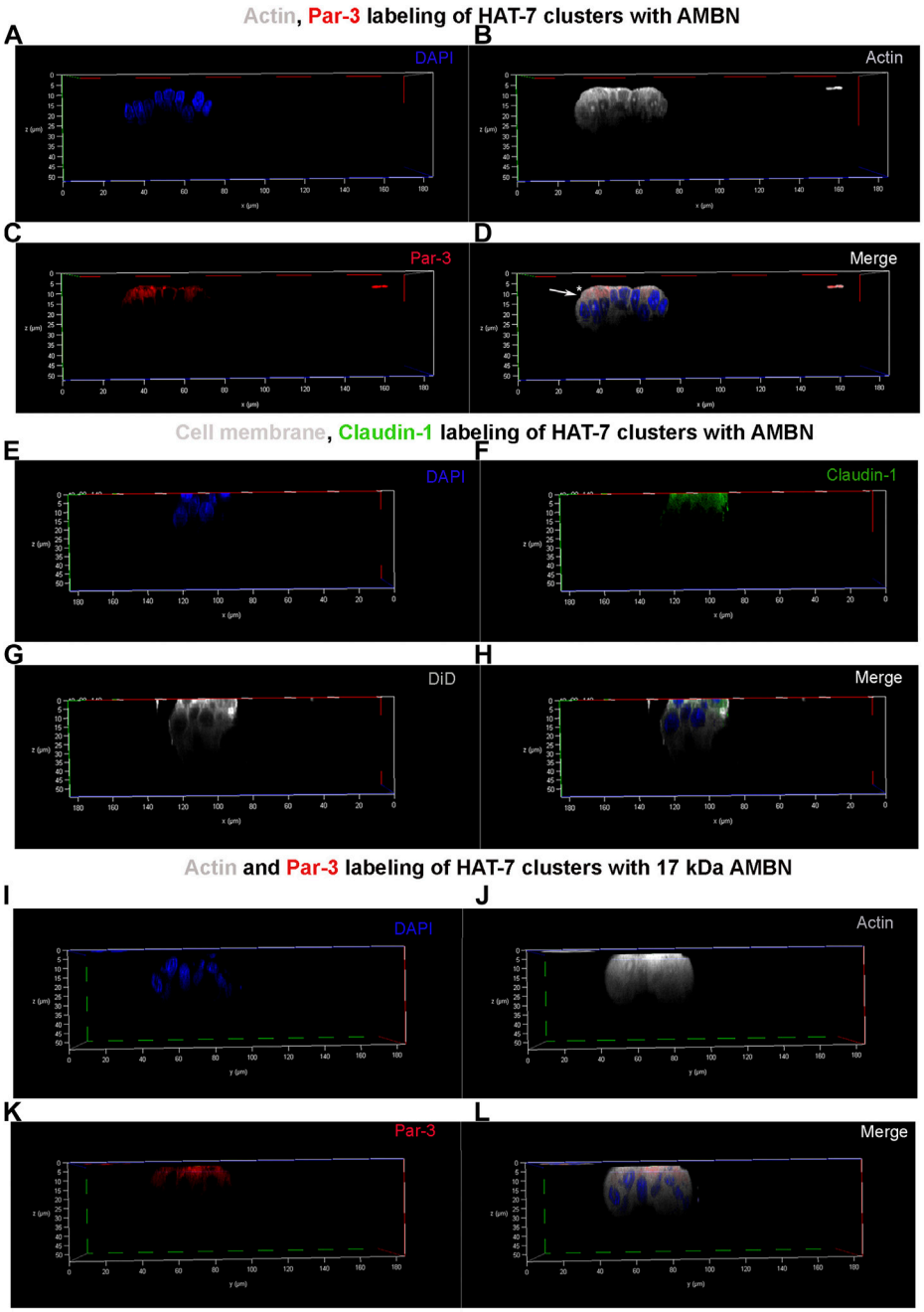

FIGURE 4
Par-3 and Claudin-1 polarization in HAT-7 clusters in a 3D axial view. **(A–C)** Individual channels for nucleus (DAPI), actin (grey pseudo color) and Par-3 (red) distribution respectively in HAT-7 cells cultured with AMBN. **(D)** Merged image of all three channels revealing a uniform symmetrical labeling of actin with an asymmetrical and polarized distribution of Par-3 (white arrow). **(E–G)** Individual channels for nucleus (blue), claudin-1 (green) and DiD (grey pseudo color) respectively in HAT-7 cells cultured with ameloblastin. **(H)** Merged images of all three channels revealing selective claudin-1 labeling within the pole of the cells basal to nucleus. DiD labeling is uniform throughout the entire outline of the cells. **(I–K)** Individual channels for nucleus (DAPI), actin (grey pseudo color) and Par-3 (red) distribution in HAT-7 cells cultured with AMBN 17 kDa cleavage fragment respectively. **(L)** Merged image of all three channels revealing a uniform symmetrical labeling of actin with an asymmetrical and polarized distribution of Par-3 like the observations in **(D)**.

contact with the ECM only along their functional apical membranes, and this is what was modeled in the modified 3D culture system. Culturing HAT-7 cells in 3D-on-top-type cultures reveal a differential cell behavior in the presence of AMEL and AMBN with the HAT-7 cells adopting distinctly different morphologies. Like previous observations with other ameloblast cell lines - ALC and LS-8 cells (Visakan et al., 2022a; Visakan et al., 2022b). HAT-7 cells exhibit preferential elongation along their *Z* axes with aspect ratios 5-times greater than control when amelogenin and ameloblastin were added to the 3D cell culture. In repeated experiments, AMBN was observed to exert a greater influence on HAT-7 elongation than amelogenin did. These morphological changes were specific to the presence of functional enamel matrix proteins, as this behavior could be reversed using heat denatured AMBN.

HAT-7 cells derived from rat molars are functional ameloblast-like cells expressing amelogenin and ameloblastin proteins (Kawano et al., 2002). They are often the cell line of choice for examining functional cell polarization (Bori et al., 2016), the epithelial-mesenchymal interactions during odontogenesis (Matsumoto et al., 2011), and for modeling disease (Földes et al., 2021). When cultured on permeable transwell filters, HAT-7 cells formed polarized epithelial layers as characterized by apical membrane permeability to CO_2 and basolateral membrane uptake of bicarbonate (Bori et al., 2016). These functional polarized layers also express the tight junctional proteins claudins-1, 4 and 8. In the 3D-on-top culture, we observed that the HAT-7 cells cultured in the presence of AMBN and 17 kDa AMBN exhibited features of structural cell polarization (Figure 4).

Confocal laser scanning microscopy revealed a selective accumulation of polarity protein Par-3 and tight junctional protein claudin-1 along the HAT-7 membrane basal to nucleus position in 3D (Figure 4). Claudin-1 was chosen as a marker for polarization as it has been shown to be highly upregulated in the elongated secretory ameloblasts (Zhang et al., 2019). Furthermore, in fully polarized mouse ameloblasts, it has been observed that Par-3 localized along the functional base and claudin-1 along the functional apical membrane (Inai et al., 2008). 3D reconstruction of Z stacks permits the precise localization of claudin-1 and Par-3 within the overall outline of the cell visualized with actin. Par-3 and claudin-1 labeling patterns in 3D culture of ALC (Visakan et al., 2022a) and HAT-7 cells (Figure 4) contrasts with what is observed *in vivo*. In 3D cultures, both proteins were observed to be localizing along the same pole of the cell. This discrepancy could be due to the differences in the height of the secretory stage ameloblasts in fully developed enamel organs compared to the individual cells in 3D culture. We have recently reported that the addition of functional AMBN to LS-8 cells in culture resulted in an upregulation of planar cell polarity protein Vangl2 (2.8 times) and cell polarity protein Par-3 (3.8 times) when compared to controls (heat denatured AMBN and AMBN Δ5) (Su et al., 2022). Vangl2 planar cell polarity protein is highly expressed particularly in the Tomes' processes of secretory stage ameloblasts (Nishikawa and Kawamoto, 2012).

Upon their secretion into the enamel matrix, amelogenin and ameloblastin are rapidly processed into N- and C-terminal cleavage fragments by MMP-20 (Bartlett and Simmer, 1999). An evolutionarily conserved novel amphipathic helix (AH) forming cell binding domain within the exon-5 encoded region of ameloblastin was recently identified (Su et al., 2019b). Using the immunofluorescent localization of peptides, it was observed that the AH domain could be specifically localized to ALC cell processes (Su et al., 2020). Furthermore, in ameloblast cell lines, the gene expression levels of cell polarity and planar cell polarity proteins were upregulated in the presence of ameloblastin (Su et al., 2022). In the present study, given the rapid *in vivo* processing of ameloblastin, the newly expressed recombinant 17 kDa ameloblastin containing the exon 5 encoded region was tested in 3D on HAT-7 cells to examine the potential *in vivo* significance of ameloblastin-cell interactions. All the cell effects that were observed with full-length ameloblastin were observed in the presence of the 17 kDa ameloblastin cleavage fragment as well. HAT-7 cells form clusters of elongated cells with polarized distributions of Par-3 (Figures 3, 4).

In conclusion, 3D cell culture models are increasingly replacing conventional 2D monolayer culture techniques, as they result in physiologically comparable cell responses (Kozlowski et al., 2009; Baker and Chen, 2012; Duval et al., 2017). However, the validity of the model lies in large part in being replicable across cell lines and substrate types. The 3D-on-top model presented here is adaptable across gel substrates (GFR Geltrex, type I collagen and gelatin) and can be used with multiple ameloblast-like cell lines (ALC, LS-8 and HAT-7) (Visakan et al., 2022a; Visakan et al., 2022b). Although the 3D system presented here permits visualization of the cells and the structures they adopt in 3D, they are limited in their localization of the EMPs within the entirety of the gel. Examination of the diffusion gradients within the gel and the effect of the gel's rheological properties remain outside the scope of this study. The interactions of the ameloblast-like cells with enamel extracellular matrix proteins can be modeled using the *in vitro* 3D cell culture system. Such 3D culture models can be expanded to observe the concerted effects of the various bioactive molecules in the extracellular milieu on the cells, and the knowledge thus gained may be translated into future biomimetic attempts at enamel repair.

Data availability statement

The original contributions presented in the study are included in the article/Supplementary Materials, further inquiries can be directed to the corresponding author.

Author contributions

GV designed and performed the experiments, analyzed the data, and wrote the manuscript. RB and JS helped with the recombinant protein design and synthesis. JM-O designed the experiments, analyzed the data, and both wrote and critically revised the manuscript. All authors contributed to the article and approved the submitted version.

Funding

This project was funded by the National Institutes of Health–National Institute of Dental and Craniofacial Research grants R01DE013414, DE-027529, and R01DE027632 to JM-O.

Acknowledgments

We would like to thank Hidemitsu Harada for providing HAT-7 cells; Salony Jassar for technical assistance with cell culture; and Emma Burris-Janssen for proofreading the manuscript.

Conflict of interest

The authors declare that the research was conducted in the absence of any commercial or financial relationships that could be construed as a potential conflict of interest.

Publisher's note

All claims expressed in this article are solely those of the authors and do not necessarily represent those of their affiliated organizations, or those of the publisher, the editors and the reviewers. Any product that may be evaluated in this article, or claim that may be made by its manufacturer, is not guaranteed or endorsed by the publisher.

Supplementary material

The Supplementary Material for this article can be found online at: https://www.frontiersin.org/articles/10.3389/fphys.2022.1069519/full#supplementary-material

References

Baker, B. M., and Chen, C. S. (2012). Deconstructing the third dimension–how 3D culture microenvironments alter cellular cues. *J. Cell Sci.* 125 (13), 3015–3024. doi:10.1242/jcs.079509

Bapat, R. A., Su, J., and Moradian-Oldak, J. (2020). Co-immunoprecipitation reveals interactions between amelogenin and ameloblastin via their self-assembly domains. *Front. Physiol.* 11, 622086. doi:10.3389/fphys.2020.622086

Bartlett, J. D., Yamakoshi, Y., Simmer, J. P., Nanci, A., and Smith, C. E. (2011). MMP20 cleaves E-cadherin and influences ameloblast development. *Cells Tissues Organs* 194 (2-4), 222–226. doi:10.1159/000324205

Bartlett, J., and Simmer, J. (1999). Proteinases in developing dental enamel. *Crit. Rev. Oral Biol. Med.* 10 (4), 425–441. doi:10.1177/10454411990100040101

Bori, E., Guo, J., Rácz, R., Burghardt, B., Földes, A., Kerémi, B., et al. (2016). Evidence for bicarbonate secretion by ameloblasts in a novel cellular model. *J. Dent. Res.* 95 (5), 588–596. doi:10.1177/0022034515625939

Boyde, A. (1997). "Microstructure of enamel," in *Ciba foundation symposium* (Wiley Online Library), 18–31.

Boyde, A. (1964). The structure and development of mammalian enamel. Doctoral dissertation. Queen Mary University of London.

Chai, H., Lee, J. J.-W., Constantino, P. J., Lucas, P. W., and Lawn, B. R. (2009). Remarkable resilience of teeth. *Proc. Natl. Acad. Sci. U. S. A.* 106 (18), 7289–7293. doi:10.1073/pnas.0902466106

Chen, L., Couwenhoven, R., Hsu, D., Luo, W., and Snead, M. (1992). Maintenance of amelogenin gene expression by transformed epithelial cells of mouse enamel organ. *Arch. Oral Biol.* 37 (10), 771–778. doi:10.1016/0003-9969(92)90110-t

Chun, Y.-H., Yamakoshi, Y., Yamakoshi, F., Fukae, M., Hu, J.-C., Bartlett, J. D., et al. (2010). Cleavage site specificity of MMP-20 for secretory-stage ameloblastin. *J. Dent. Res.* 89 (8), 785–790. doi:10.1177/0022034510366903

Duval, K., Grover, H., Han, L.-H., Mou, Y., Pegoraro, A. F., Fredberg, J., et al. (2017). Modeling physiological events in 2D vs. 3D cell culture. *Physiology* 32 (4), 266–277. doi:10.1152/physiol.00036.2016

Földes, A., Sang-Ngoen, T., Kádár, K., Rácz, R., Zsembery, Á., DenBesten, P., et al. (2021). Three-dimensional culture of ameloblast-originated HAT-7 cells for functional modeling of defective tooth enamel formation. *Front. Pharmacol.* 12, 682654. doi:10.3389/fphar.2021.682654

Fukae, M., Kanazashi, M., Nagano, T., Tanabe, T., Oida, S., and Gomi, K. (2006). Porcine sheath proteins show periodontal ligament regeneration activity. *Eur. J. Oral Sci.* 114, 212–218. doi:10.1111/j.1600-0722.2006.00309.x

Fukumoto, S., Kiba, T., Hall, B., Iehara, N., Nakamura, T., Longenecker, G., et al. (2004). Ameloblastin is a cell adhesion molecule required for maintaining the differentiation state of ameloblasts. *J. Cell Biol.* 167 (5), 973–983. doi:10.1083/jcb.200409077

Fukumoto, S., Yamada, A., Nonaka, K., and Yamada, Y. (2005). Essential roles of ameloblastin in maintaining ameloblast differentiation and enamel formation. *Cells Tissues Organs* 181 (3-4), 189–195. doi:10.1159/000091380

Guan, X., and Bartlett, J. (2013). MMP20 modulates cadherin expression in ameloblasts as enamel develops. *J. Dent. Res.* 92 (12), 1123–1128. doi:10.1177/0022034513506581

Guan, X., Xu, M., Millar, S. E., and Bartlett, J. D. (2016). Beta-catenin is essential for ameloblast movement during enamel development. *Eur. J. Oral Sci.* 124 (3), 221–227. doi:10.1111/eos.12261

Hatakeyama, J., Fukumoto, S., Nakamura, T., Haruyama, N., Suzuki, S., Hatakeyama, Y., et al. (2009). Synergistic roles of amelogenin and ameloblastin. *J. Dent. Res.* 88 (4), 318–322. doi:10.1177/0022034509334749

He, P., Zhang, Y., Kim, S. O., Radlanski, R. J., Butcher, K., Schneider, R. A., et al. (2010). Ameloblast differentiation in the human developing tooth: Effects of extracellular matrices. *Matrix Biol.* 29 (5), 411–419. doi:10.1016/j.matbio.2010.03.001

Hu, J. C.-C., Hu, Y., Lu, Y., Smith, C. E., Lertlam, R., Wright, J. T., et al. (2014). Enamelin is critical for ameloblast integrity and enamel ultrastructure formation. *PloS one* 9 (3), e89303. doi:10.1371/journal.pone.0089303

Inai, T., Sengoku, A., Hirose, E., Iida, H., and Shibata, Y. (2008). Differential expression of the tight junction proteins, claudin-1, claudin-4, occludin, ZO-1, and PAR3, in the ameloblasts of rat upper incisors. *Anat. Rec.* 291 (5), 577–585. doi:10.1002/ar.20683

Iwata, T., Yamakoshi, Y., Hu, J.-C., Ishikawa, I., Bartlett, J., Krebsbach, P., et al. (2007). Processing of ameloblastin by MMP-20. *J. Dent. Res.* 86 (2), 153–157. doi:10.1177/154405910708600209

Jiang, N., Chen, L., Ma, Q., and Ruan, J. (2018). Nanostructured Ti surfaces and retinoic acid/dexamethasone present a spatial framework for the maturation and amelogenesis of LS-8 cells. *Int. J. Nanomedicine* 13, 3949–3964. doi:10.2147/IJN.S167629

Kawano, S., Morotomi, T., Toyono, T., Nakamura, N., Uchida, T., Ohishi, M., et al. (2002). Establishment of dental epithelial cell line (HAT-7) and the cell differentiation dependent on Notch signaling pathway. *Connect. Tissue Res.* 43 (2-3), 409–412. doi:10.1080/03008200290000637

Kozlowski, M., Gajewska, M., Majewska, A., Jank, M., and Motyl, T. (2009). Differences in growth and transcriptomic profile of bovine mammary epithelial monolayer and three-dimensional cell cultures. *J. Physiol. Pharmacol.* 60 (1), 5–14.

Lacruz, R. S., Habelitz, S., Wright, J. T., and Paine, M. L. (2017). Dental enamel formation and implications for oral health and disease. *Physiol. Rev.* 97 (3), 939–993. doi:10.1152/physrev.00030.2016

Lee, G. Y., Kenny, P. A., Lee, E. H., and Bissell, M. J. (2007). Three-dimensional culture models of normal and malignant breast epithelial cells. *Nat. Methods* 4 (4), 359–365. doi:10.1038/nmeth1015

Li, W., Machule, D., Gao, C., and DenBesten, P. K. (2006). Growth of ameloblast-lineage cells in a three-dimensional Matrigel environment. *Eur. J. Oral Sci.* 114, 159–163. doi:10.1111/j.1600-0722.2006.00308.x

Matsumoto, A., Harada, H., Saito, M., and Taniguchi, A. (2011). Induction of enamel matrix protein expression in an ameloblast cell line co-cultured with a mesenchymal cell line *in vitro*. *Vitro Cell. Dev. Biol. Anim.* 47 (1), 39–44. doi:10.1007/s11626-010-9362-7

Mazumder, P., Prajapati, S., Bapat, R., and Moradian-Oldak, J. (2016). Amelogenin-ameloblastin spatial interaction around maturing enamel rods. *J. Dent. Res.* 95 (9), 1042–1048. doi:10.1177/0022034516645389

Moradian-Oldak, J., and George, A. (2021). Biomineralization of enamel and dentin mediated by matrix proteins. *J. Dent. Res.* 100 (10), 1020–1029. doi:10.1177/00220345211018405

Moradian-Oldak, J. (2012). Protein-mediated enamel mineralization. *Front. Biosci.* 17, 1996–2023. doi:10.2741/4034

Nakata, A., Kameda, T., Nagai, H., Ikegami, K., Duan, Y., Terada, K., et al. (2003). Establishment and characterization of a spontaneously immortalized mouse ameloblast-lineage cell line. *Biochem. Biophys. Res. Commun.* 308 (4), 834–839. doi:10.1016/s0006-291x(03)01467-0

Nanci, A. (2017). *Ten cate's oral histology-e-book: Development, structure, and function*. St.Louis, MO: Elsevier Health Sciences.

Nishikawa, S., and Kawamoto, T. (2012). Planar cell polarity protein localization in the secretory ameloblasts of rat incisors. *J. Histochem. Cytochem.* 60 (5), 376–385. doi:10.1369/0022155412438887

Pandya, M., Lyu, H., Luan, X., and Diekwisch, T. G. (2021). Polarized, amelogenin expressing ameloblast-like cells from cervical loop/dental pulp co-cultures in bioreactors. *Stem Cells Dev.* 30 (16), 797–805. doi:10.1089/scd.2021.0115

Sarkar, J., Simanian, E. J., Tuggy, S. Y., Bartlett, J. D., Snead, M. L., Sugiyama, T., et al. (2014). Comparison of two mouse ameloblast-like cell lines for enamel-specific gene expression. *Front. Physiol.* 5, 277. doi:10.3389/fphys.2014.00277

Shin, M., Chavez, M., Ikeda, A., Foster, B., and Bartlett, J. (2018). MMP20 overexpression disrupts molar ameloblast polarity and migration. *J. Dent. Res.* 97 (7), 820–827. doi:10.1177/0022034518758657

Su, J., Arun Bapat, R., Visakan, G., and Moradian-Oldak, J. (2022). Co-emergence of the amphipathic helix on ameloblastin with mammalian prismatic enamel. *Mol. Biol. Evol.* 39, msac205. doi:10.1093/molbev/msac205

Su, J., Bapat, R. A., and Moradian-Oldak, J. (2019a). The expression and purification of recombinant mouse ameloblastin in E. coli. *Methods Mol. Biol.* 1922, 229–236. doi:10.1007/978-1-4939-9012-2_23

Su, J., Bapat, R., Visakan, G., and Moradian-Oldak, J. (2020). An evolutionarily conserved helix mediates ameloblastin-cell interaction. *J. Dent. Res.* 99 (9), 1072–1081. doi:10.1177/0022034520918521

Su, J., Kegulian, N. C., Bapat, R. A., and Moradian-Oldak, J. (2019b). Ameloblastin binds to phospholipid bilayers via a helix-forming motif within the sequence encoded by exon 5. *ACS omega* 4 (2), 4405–4416. doi:10.1021/acsomega.8b03582

Uchida, T., Tanabe, T., Fukae, M., Shimizu, M., Yamada, M., Miake, K., et al. (1991). Immunochemical and immunohistochemical studies, using antisera against porcine 25 kDa amelogenin, 89 kDa enamelin and the 13–17 kDa nonamelogenins, on immature enamel of the pig and rat. *Histochemistry* 96 (2), 129–138. doi:10.1007/BF00315983

Visakan, G., Su, J., and Moradian-Oldak, J. (2022a). Ameloblastin promotes polarization of ameloblast cell lines in a 3-D cell culture system. *Matrix Biol.* 105, 72–86. doi:10.1016/j.matbio.2021.11.002

Visakan, G., Su, J., and Moradian-Oldak, J. (2022b). Data from ameloblast cell lines cultured in 3D using various gel substrates in the presence of ameloblastin. *Data Brief.* 42, 108233. doi:10.1016/j.dib.2022.108233

Wald, T., Spoutil, F., Osickova, A., Prochazkova, M., Benada, O., Kasparek, P., et al. (2017). Intrinsically disordered proteins drive enamel formation via an evolutionarily conserved self-assembly motif. *Proc. Natl. Acad. Sci.* 114 (9), E1641–E1650. doi:10.1073/pnas.1615334114

Zhang, Y., Zheng, L., Le, M., Nakano, Y., Chan, B., Huang, Y., et al. (2019). SATB1 establishes ameloblast cell polarity and regulates directional amelogenin secretion for enamel formation. *BMC Biol.* 17 (1), 104–116. doi:10.1186/s12915-019-0722-9

frontiers | Frontiers in Physiology

TYPE Review
PUBLISHED 05 December 2022
DOI 10.3389/fphys.2022.1071265

OPEN ACCESS

EDITED BY
Agnes Bloch-Zupan,
Université de Strasbourg, France

REVIEWED BY
Pamela Den Besten,
University of California, San Francisco, United States
Rodrigo S. Lacruz,
New York University, United States
Janet Moradian-Oldak,
University of Southern California, United States

*CORRESPONDENCE
Thomas G. H. Diekwisch,
Thomas_Diekwisch@URMC.Rochester.edu

SPECIALTY SECTION
This article was submitted to Craniofacial Biology and Dental Research, a section of the journal Frontiers in Physiology

RECEIVED 16 October 2022
ACCEPTED 21 November 2022
PUBLISHED 05 December 2022

CITATION
Diekwisch TGH (2022), Alan Fincham and the era of enamel protein Biochemistry. *Front. Physiol.* 13:1071265. doi: 10.3389/fphys.2022.1071265

Alan Fincham and the era of enamel protein Biochemistry

Thomas G. H. Diekwisch*

Department of Oral and Craniofacial Sciences Margaret and Cy Welcher Professor of Dentistry, Eastman Institute of Oral Health, University of Rochester School of Medicine and Dentistry, Rochester, NY, United States

Enamel research experienced an unprecedented period of growth during the latter part of the 20th century until today. This growth is in part due to the contributions of a number of iconic scientists such as Alan G. Fincham, the focus of the present review. Alan was involved in many of the seminal discoveries of this time, including the identification of the critical amelogenin peptides TRAP and LRAP, the determination of the amelogenin amino acid sequence, the identification of the sole serin-16 phosphorylation site, and the amelogenin nanosphere theory. Alan was also a superb mentor to graduate students and others. His experience and leadership related to problem-based learning greatly affected predoctoral dental education at the University of Southern California and in the United States.

KEYWORDS

amelogenin, TRAP, LRAP, nanospheres, problem-based learning

Introduction

During its early decades, enamel research has been an unusual discipline, with individual researchers scattered across the globe and international meetings only held every five to 10 years. These "enamel meetings" have been numbered so far from Enamel I to Enamel X, and scientific findings have been printed in proceedings, with the paper discussions recorded and transcribed in painstaking detail. Many scientists in the early years of enamel research thought that those transcribed discussions exceeded the value of the printed scientific papers.

During the mid-20th century, enamel research focused on the impact of caries on tooth enamel loss and on the unusually symmetric morphology of enamel crystals. Common techniques used to study enamel morphology included scanning electron microscopy (Boyde and Stewart 1963), polarization microscopy (Carlström, 1964) and transmission electron microscopy (Nylen 1964). In some countries such as Japan, the close collaboration between dental schools and the JEOL and Hitachi electron microscope companies allowed many dental schools to own an electron microscope and with it employ an expert in enamel ultrastructure on their faculty, resulting in a separate cosmos of enamel research in Japan and unappreciated by the remainder of the scientific world due to language differences.

While there had been several earlier studies related to enamel protein amino acid composition (Block et al., 1949; Stack 1954), more sophisticated analysis techniques during the early 1960ies resulted in detailed and comparable amino acid composition data

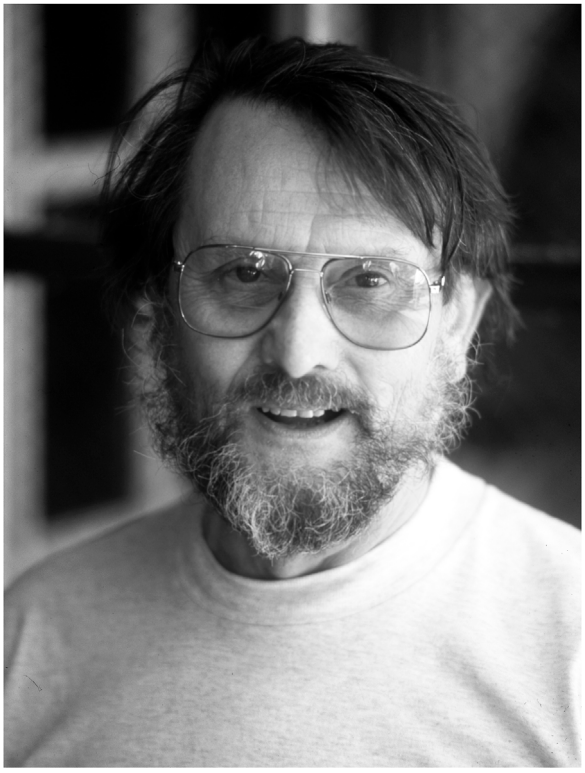

FIGURE 1
Alan Fincham (1931–2017) at the Center for Craniofacial Molecular Biology in Los Angeles. Photograph taken by the author in 1997.

for enamel from human fetuses (Eastoe 1960, 1963), fetal pigs (Piez 1961), and fetal ox (Glimcher et al., 1961). These analyses identified enamel proteins as proteins with a high content in proline, glutamic acid, histidine, tyrosine, and methionine, while cysteine, hydroxylysine, and hydroxyproline were either absent or only present in very small amounts (Eastoe 1963). Specifically, the low content of cysteine distinguished enamel proteins from keratins, and the low content in hydroxyproline and hydroxylysine together with a high content in prolines suggested that enamel proteins were unique and different from keratins and collagens (Eastoe 1963). These studies used the pliable and soluble enamel matrix as a tool to study the biochemistry of the developing enamel protein phase.

These classic studies set the stage for further biochemical studies of the developing enamel matrix and the subsequent exploration of its function. In 1979, John Eastoe coined the term "amelogenin" for the major protein in the developing enamel matrix (Eastoe 1979). However, while the physical prevalence of amelogenins in the enamel matrix was suggestive of a functional role, the essential role of amelogenins for enamel crystal formation was only confirmed after a deletion in the amelogenin gene was linked to amelogenesis imperfecta, a congenital enamel defect (Lagerström et al., 1991). Loss of amelogenin also resulted in the loss of enamel in a mouse model (Gibson et al., 2001), and antisense inhibition of amelogenins not only affected enamel crystal growth but also changed enamel matrix organization, suggesting that amelogenin function and enamel crystal growth were intimately linked (Diekwisch et al., 1993). Together, these studies provided the backdrop for the scientific work and intellectual pursuit for one of the most iconic enamel scientists, Alan G. Fincham (Figure 1).

Enamel research, the British wool industry, and the colonies

Alan Fincham was born in East Preston, West Sussex, the son of a Vicar, on the south coast of the UK in 1931. He was an avid outdoorsman, an active nature lover from an early age. After the war he was involved in the Friends Ambulance National Service, participating in flood rescue relief in Holland and earthquake relief in Crete. After this he spent 2 years at Brighton College of Art, before going on to study at the University of Leeds, graduating with a B.S in Biochemistry and Bacteriology (1959), a M. Sc. in Textile Chemistry 1961) and a Ph.D. in Biophysics (1966). Alan occasionally shared his recollections about the intimate relationship between the University of Leeds and the British wool industry, as it resulted in the sponsorship of several faculty positions that promoted mineralized tissue research in Leeds and the greater Yorkshire region. The wool industry hoped that the new recruits would work on the mineral content of wool, an important parameter for its mechanical properties. Instead, those scientists took a liking to enamel research, among them John Weatherall, Colin Robinson, Alan Fincham and several others. After graduating with a Ph.D., Alan accepted a position as a scientific research officer in the Mineral Metabolism Research Unit at the Medical Research Council in Leeds 1966) and then became a lecturer in the Department of Biochemistry at the Royal Dental Hospital School of the University of London (1967–1969).

After 2 years in London, Alan followed the path of many junior British Scientists of his days and accepted a position through the Commonwealth office as a Lecturer in Biochemistry. In Alan's case, this position was at the Mona campus of the University of the West Indies, Kingston, Jamaica. Alan had previously visited Jamaica twice before on caving expeditions and as such was familiar with the country and accepted a 3-year contract. Alan moved to Jamaica with his wife Celia and his three children in 1969. He ended up spending 18 years at UWI, first as a Lecturer (1969–1973), then as a Senior Lecturer (1973–1981), and eventually as a Reader (1981–1986). At that time, the University of the West Indies in Mona supported a sprawling Medical School enterprise, and faculty were expected to engage in teaching and research. Alan's talent as an educator soon became recognized and he was asked to oversee

the undergraduate medical curriculum, where he instituted fundamental changes focusing on the student's learning experiences rather than lectures taught by faculty. Building on his belief in independent learning and his interest in technology he was instrumental in establishing an audiovisual learning library for medical students where students could access recorded lecture lessons, the first of its kind in the West Indies. Continuing his research focus on enamel biochemistry, Alan managed to purchase and operate a high-pressure liquid chromatography apparatus in Kingston, reportedly the only one in the West Indies.

The intricate surface geology of Jamaica became the focus of a third area of Alan's scholarship. Having explored caves in his native England in Mendip (Wessex) and Yorkshire where he had become involved with cave exploration and rescue—the result of his own rescue after being trapped for 2 hours in a pit he had been exploring with a fellow student while at Leeds. His passion for cave exploration grew throughout his life and he became a leading member and President of the Jamaica Caving Club and spent countless hours tracking and mapping the caves of the island eventually publishing the first comprehensive guide to Jamaican caves "Jamaica Underground" (Fincham, 1977). Even during his Los Angeles years, Alan occasionally traveled back to Jamaica and lead caving expeditions. Ever the outdoors man, he developed an interest in fishing while in Jamaica and took up shark fishing harvesting the teeth of his catch for use in his research. As such it wasn't uncommon for him to return home on a Sunday evening with the carcass of a Black Tip or Tiger shark strapped to the roof of his old beat-up Volvo station wagon.

Amelogenin peptide biochemistry at INSERM and at NIDR

With the increasingly violent political situation in Jamaica and three now college-aged children, Alan was looking for opportunities outside of the West Indies. For 2 years (1979–1981), he moved to the National Institute of Dental Research (NIDR; now National Institute for Dental and Craniofacial Research, NIDCR) in Bethesda Washington DC as a Visiting Scientist with John Termine's group and in 1984 spent a year at the INSERM in Strasbourg, France, with Alain Belcourt. Both stays provided Alan with new scientific opportunities and the interactions necessary for his next move. During this time, Alan published a seminal paper on two functionally significant short amelogenin polypeptides, the tyrosine rich amelogenin peptide (TRAP) and the leucine rich amelogenin peptide (LRAP) (Fincham et al., 1981). At that time, Alan was also successful in isolating individual amelogenin peptides and resolving portions of the complete amelogenin amino acid sequence by N-terminal peptide sequencing (Fincham 1979; Fincham et al., 1983b). Another accomplishment was the amino acid composition determination of human enamel (Fincham et al., 1983a).

Alan's stay at NIDCR also allowed him to interact with two enamel scientists from the University of Southern California (USC), Drs. Maggie Zeichner-David and Harold C. Slavkin. These interactions eventually resulted in Alan's recruitment as a Research Associate Professor to the University of Southern California in 1985. The time at USC gave Alan exposure to many likeminded individuals interested in craniofacial and enamel research. Due to its unique faculty retention policies, USC allowed Alan's three children to study tuition-free on campus, a substantial financial incentive for Alan's family. As a result, Alan stayed at USC for 16 years, until his sudden departure in 2001.

The Center for Craniofacial Molecular Biology at USC: Hotbed for scientific discovery

USC provided Alan with multiple opportunities for intellectual and professional growth. When Alan joined, the USC's Center for Craniofacial Molecular Biology (CCMB) was still located in the Andrus Gerontology Center on USC's main campus in South Central Los Angeles. Just a few years later, CCMB moved to entirely new facilities as part of USC's new medical complex in East LA's Boyle Heights on Alcazar/Soto Street. These facilities represented the state of the art of laboratory architecture at its time, with open lab benches and faculty offices embedded into the lab environment. The Center was the scientific home to approximately 50 lab members, the majority of them postdoctoral fellows from all over the world. There were about a dozen faculty members, such as CCMB director Harold C. Slavkin and several senior scientists, including Alan Fincham, Maggie Zeichner-David, Charles Shuler, Malcolm Snead, and David Warburton from USC Childrens Hospital. Junior faculty members included Ed Lau, Mary MacDougall, Carol Wuenschell and others. At that time, the majority of scientists worked on questions related to tooth enamel, with others focusing on craniofacial biology and lung development. This environment was enriched by weekly lab meetings and presentations by invited speakers from all over the world. These scientific dynamics were an ideal environment for Alan's scientific and intellectual growth, and he was well respected by students and others alike.

Much of Alan's initial work was based on enamel protein gel electrophoresis and high-pressure liquid chromatography (HPLC). Alan started very early in the morning, usually on site at 7 am, loaded his samples onto the gel or his HPLC columns and then moved to his office to work on grants or papers. Samples were collected at 2 pm or 3 pm, allowing Alan to reach the freeway prior to afternoon traffic. When working on his HPLC, Alan showed an almost personal relationship with his columns whom he used to address as "guys". His favorite HPLC column was a unique reversed phase C4 column ideally suited to

separate amelogenins from other proteins in the developing enamel. The HPLC apparatus was frequently plagued with service issues, and more often than not, Alan was able to repair the problem without having to rely on the service technician due to his familiarity with the technology. During his Jamaica years, Alan owned the only HPLC apparatus in the West Indies and there were no service technicians available, forcing Alan to address all service issues on his own.

During the early 1990s, USC's CCMB was a sought-after home for students and postdoctoral fellows seeking to enrich their pre-faculty experience with expert knowledge in craniofacial and enamel biology. Several of these postdoctoral fellows introduced new technologies and tools for amelogenesis research to Alan, who augmented the experience of these junior scientists by providing a wealth of foundational knowledge, intellectual and technical advice. Among these were Jim Simmer, who worked with Alan on the generation of the first recombinant amelogenin, which then became an important tool for enamel studies (Simmer et al., 1994). Another CCMB recruit was Janet Moradian-Oldak, a postdoctoral fellow from Steve Weiner's lab in Israel, who offered unique insights to the study of biological mineralization.

Janet joined Alan in a quest to resolve the issue of amelogenin phosphorylation, specifically which and how many amelogenin amino acids were phophorylated. At that time, the role of phosphoproteins in enamel mineralization was of great interest as enamel was known to lack collagen, one of the known macromolecules involved in biological mineralization (Curley-Joseph and Veis 1979). Earlier research had identified four "enamel proteins", among which the 65 and 22 kDa proteins were phosphorylated while the 58 and 20 kDa proteins were not (Guenther et al., 1977). Others had suggested a total of three phosphoserins among phosphopeptides of the enamel matrix (Glimcher 1979). Using a combined approach including reversed phase HPLC, partial acid hydrolysis and mass spectroscopy Alan and Janet determined that there was only a singular phosphorylated amino acid in the bovine amelogenin, the serine in position 16 (Fincham and Moradian-Oldak 1993). This finding provided the basis for later studies related to the role of amelogenin phosphorylation in enamel crystal formation (Kwak et al., 2009; Le Norcy et al., 2018; Shin et al., 2020).

The "nanosphere theory" and new educational models

At that time, Alan was examining electron micrographs of the developing enamel matrix (Diekwisch et al., 1993, 1995) and interpreted these micrographs to indicate that the formative enamel matrix was organized into spherical subunits, which Alan called nanospheres (Fincham et al., 1995). Alan was so excited by these spherical structures that he managed to persuade lab director Harold Slavkin to purchase a dynamic light scattering detector and an atomic force microscope (Fincham et al., 1994; Fincham et al., 1995). When all three technologies revealed data consistent with the presence of 20 nm diameter spherical particles, Alan felt sufficiently comfortable to advance the nanosphere theory, a novel theory explaining amelogenesis as a process mediated by the presence of 20 nm diameter spherical amelogenin protein particles (Fincham and Moradian-Oldak 1995). This nanosphere theory greatly influenced our understanding of amelogenesis over the next 2 decades (Figure 2). An excellent history about the emergence of the nanosphere theory has been published in the Journal of Dental Research (Moradian-Oldak 2007).

Alan's long-standing work in the enamel research field, the prominent progress of his students and his recent scientific leadership established him as the ideal candidate to host one of those legendary enamel meetings. When one of the early doyens of enamel research, Ron Fearnhead moved to Japan, two successive enamel meetings were held in the Far East, Enamel IV in Odawara 1984) and Enamel V in Tsurumi (1989). Following these two very successful meetings there was a general consensus among leaders in the enamel field to convene the next enamel meeting outside of Japan, and it was upon Alan to hold the first enamel meeting on Western soil after almost 20 years. As a conference location, CCMB director Harold Slavkin suggested the UCLA conference center at Lake Arrowhead, 90 miles Northeast of Los Angeles in the San Bernardino Mountains. The conference was held from May 11–15, 1997 and included more than 100 participants from all over the world (Figure 3). Enamel VI became a highlight in Alan's career as it benefited from Alan's experience with new educational enterprises and his insight into the current state of enamel research. To facilitate maximum time for scientific exchange, Alan decided to limit presentations to 3 minutes per presenter and five slides maximum. Every presenter was also encouraged to prepare a scientific poster along with the oral presentation. All presentations were followed by approximately ten to 15 minutes discussion, and there were lively discussions every evening in front of the posterboards that lasted late into the night. Enamel research has rarely seen better times.

The faculty at USC's Center for Craniofacial Molecular Biology (CCMB) were a group of extraordinarily creative individuals who were acutely aware of the limitations of traditional top-down dental education. Partially based on Alan's experience as head of the undergraduate medical curriculum in Jamaica, CCMB's faculty decided to embark on a novel approach to dental education focused on student centered learning around clinical problems. In response to their initiative, USC's Dean Howard Landesman decided to entrust them with a pilot program under the leadership of Alan and Harold's successor as CCMB director, Chuck Shuler. Creating a new educational program from scratch involved dealing with staffing issues, instructing faculty, designing exam questions, assessing students and guiding students in constructive ways to become competent future dentists. As only

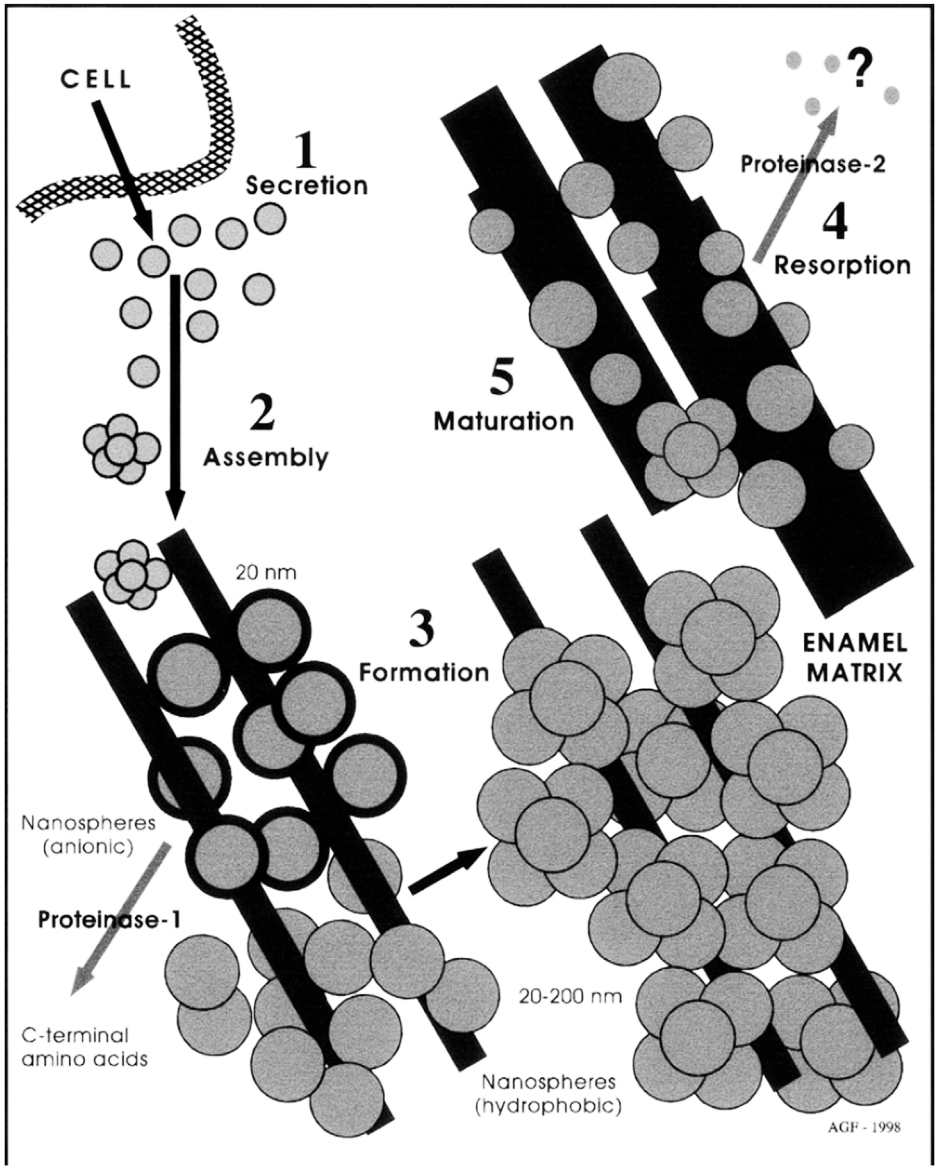

FIGURE 2
Alan Fincham's original sketch explaining the "Nanosphere Theory" (from Fincham et al., 1999, Journal of Structural Biology, Elsevier, Figure 8) with permission.

the third problem-based dental educational program in North America, PBL initially faced ample criticism and skepticism, especially among USC's conservative clinical faculty. To address their concerns, PBL student performance and educational outcomes were frequently assessed, and the results of these studies were published in the Journal of Dental Education (Fincham et al., 1997; Shuler and Fincham 1998; Fincham and Shuler 2001). Overall, these studies demonstrated that students in the PBL program performed as well or better than students in USC's world-renowned traditional program (Shuler and Fincham 1998). Beyond those numerical outcomes, students appeared readily prepared to comprehend complex clinical problems and constructively address issues that were often not accessible to traditional students. There was a real sense of occasion in the early days of CCMB PBL, and students and faculty were proudly aware that they were writing the next chapter in dental education (Fincham and Shuler 2001). Today, the majority of U.S. dental schools have adopted aspects of problem-based or integrated learning to address the need of clinical competencies and the challenge of revised National Board Examinations.

FIGURE 3
Enamel VI, group picture. Alan is in the second row from the bottom wearing an "Enamel" T-shirt. Photograph taken by the author in 1997.

The final chapter: Sudden departure and new beginnings in Cyprus

By the end of the 1990s, Alan had become one of the foremost enamel scientists and dental educators of his time. Yet, his academic rank had not been advanced beyond that of a research professor. After leaving the West Indies as a Reader, Alan was hired onto USC's research track, which includes promotions to the rank of Research Professor, but not to full academic ranks such as Associate or Full Professor. After his extensive service as an educational innovator and his dedication toward instituting PBL at CCMB, Alan justifiably expected and requested promotion to the rank of Full Professor. Enamel scientists from all over the world supported Alan's request and wrote letters of endorsement. Even USC's conservative faculty were in support of Alan's promotion. However, once Alan's promotion was to be implemented Alan received word that his case had been denied. Alan stood in disbelief and complete disapproval of what he considered profound misjudgment. In utter disappointment he packed his belongings into a couple of suitcases and took off to the island of Cyprus in the Mediterranean one week later. His official day of departure from USC was 15 August 2001.

In his retirement, Alan developed a new interest in the wildflowers of Cyprus and began the creation of an online database. He also re-engaged with his childhood passion of stamp collecting amassing a collection of thousands of stamps with a primary focus on the stamps of Jamaica and the Caribbean. During the later years of his retirement his arthritic knees damaged through years of walking and hiking in the Yorkshire Dales advanced, making travel and even daily

FIGURE 4
Alan Fincham († 16 May 2017, Cyprus) wearing a T-shirt from the Jamaican Caves Organization. Photograph dated approximately 2015, sent electronically by Dr. Fincham to the author.

activities increasingly difficult. He no longer was in the spirit of participating in enamel conferences as he loathed to attend as a "has been". Yet, his interest in enamel research was unbroken: "Please send a copy of the Proceedings when published" he requested. Enamel IX was held in November 2016 and Alan passed away on 16 May 2017, at age 83. A separate copy of the proceedings was never published. Yet Alan's spirit lives on in the minds of his students and in the greater field of enamel research (Figure 4). Many remember Alan's enthusiastic mentorship and his encyclopedic knowledge of the enamel field. Most notably, the nanosphere theory of enamel biomineralization will forever be associated with Alan's name and spirit.

Discussion

Enamel research has experienced an enormous scientific and technological growth over the past 70 years. Following earlier polarization and electron microscopy studies, emerging biochemical and molecular techniques have allowed for unprecedented insights into how enamel crystals and prisms grow. These insights have been advanced through the pioneering efforts of a number of highly reputed scientists, including the British American biochemist Alan G. Fincham. In the present review we have revisited the scientific context in which Alan performed his protein sequencing studies, identifying LRAP and TRAP polypeptides as major short polypeptides of the developing enamel matrix. We have then described the environment at the University of Southern California that helped Alan promote his nanosphere theory based on converging results from transmission electron micrographs, atomic force microscopy images and dynamic light scattering data. In addition to enamel biochemistry, Alan's other accomplishments include the establishment of a successful problem-based learning curriculum at the University of Southern California and the publication of the first book on Jamaican caves. These broad-ranging interests and their successful implementation portrait Alan Fincham as a true polymath and as a leading figure who made exceptional and seminal contributions to enamel research. The contributions and Alan's legacy as a scientist are remembered in the current volume as we once again publish papers related to an enamel meeting.

Author contributions

The author confirms being the sole contributor of this work and has approved it for publication.

Acknowledgments

The author wishes to acknowledge Katherine Fincham's information and insights into Alan's youth and their time in Jamaica. Constructive feedback by three reviewers is much appreciated. Generous funding to the author's enamel research program by the NIDCR (UH3-DE028869) is gratefully acknowledged.

Conflict of interest

The author declares that the research was conducted in the absence of any commercial or financial relationships that could be construed as a potential conflict of interest.

Publisher's note

References

Block, R. J., Horwitt, M. K., and Bolling, D. (1949). Comparative protein chemistry. The composition of the proteins of human teeth and fish scales. *J. Dent. Res.* 28, 518–524. doi:10.1177/00220345490280051501

Boyde, A., and Stewart, A. D. (1963). Scanning electron microscopy of the surface of developing mammalian dental enamel. *Nature* 198, 1102–1103. doi:10.1038/1981102a0

Carlström, D. (1964). Polarization microscopy of dental enamel with Reference to incipient carious lesions. *Adv. Oral Biol.* 1, 255–296.

Curley-Joseph, J., and Veis, A. (1979). The nature of covalent complexes of phosphoproteins with collagen in the bovine dentin matrix. *J. Dent. Res.* 58, 1625–1633. doi:10.1177/00220345790580061201

Diekwisch, T., David, S., Bringas, P., Santos, V., and Slavkin, H. C. (1993). Antisense inhibition of AMEL translation demonstrates supramolecular controls for enamel HAP crystal growth during embryonic mouse molar development. *Development* 117, 471–482. doi:10.1242/dev.117.2.471

Diekwisch, T. G. H., Berman, B. J., Gentner, S., and Slavkin, H. C. (1995). Initial enamel crystals are not spatially associated with mineralized dentine. *Cell. Tissue Res.* 279, 149–167. doi:10.1007/BF00300701

Eastoe, J. E. (1979). Enamel protein chemistry-past, present and future. *J. Dent. Res.* 58, 753–764. doi:10.1177/00220345790580022701

Eastoe, J. E. (1960). Organic matrix of tooth enamel. *Nature* 187, 411–412. doi:10.1038/187411b0

Eastoe, J. E. (1963). The amino acid composition of proteins from the oral tissues – II. The matrix proteins in dentine and enamel from developing human deciduous teeth. *Arch. Oral Biol.* 8, 633–652. doi:10.1016/0003-9969(63)90078-5

Fincham, A. G., Bahner, R., Chair, Y., Crowe, D. L., Fincham, C., Iskander, M., et al. (1997). Problem-based learning at the university of southern California school of dentistry. *J. Dent. Educ.* 61, 417–425. doi:10.1002/j.0022-0337.1997.61.5.tb03133.x

Fincham, A. G., Belcourt, A. B., Termine, J. D., Butler, W. T., and Cothran, W. C. (1983b). Amelogenins. Sequence homologies in enamel-matrix proteins from three mammalian species. *Biochem. J.* 211, 149–154. doi:10.1042/bj2110149

Fincham, A. G., Belcourt, A. B., Termine, J. D., Butler, W. T., and Cothran, W. C. (1981). Dental enamel matrix: Sequences of two amelogenin polypeptides. *Biosci. Rep.* 1, 771–778. doi:10.1007/BF01114799

Fincham, A. G., Belcourt, A. B., and Termine, J. D. (1983a). Molecular composition of the protein matrix of developing human dental enamel. *J. Dent. Res.* 62, 11–15. doi:10.1177/00220345830620010101

Fincham, A. G. (1979). Dental enamel matrix – isolation and partial sequence of a peptide component. *J. Dent. Res.* 58, 997–999. doi:10.1177/00220345790580025901

Fincham, A. G. (1977). *Jamaica Underground: The caves, sinkholes and Underground rivers of the island*. Kingston, Jamaica: University Press of the West Indies, 464.

Fincham, A. G., and Moradian-Oldak, J. (1993). Amelogenin post-translational modifications: Carboxy-terminal processing and the phosphorylation of bovine and porcine "TRAP" and "LRAP" amelogenins. *Biochem. Biophys. Res. Commun.* 197, 248–255. doi:10.1006/bbrc.1993.2468

Fincham, A. G., Moradian-Oldak, J., Diekwisch, T. G., Lyaruu, D. M., Wright, J. T., Bringas, P., et al. (1995). Evidence for amelogenin "nanospheres" as functional components of secretory-stage enamel matrix. *J. Struct. Biol.* 115, 50–59. doi:10.1006/jsbi.1995.1029

Fincham, A. G., and Moradian-Oldak, J. (1995). Recent advances in amelogenin biochemistry. *Connect. Tissue Res.* 32, 119–124. doi:10.3109/03008209509013713

Fincham, A. G., Moradian-Oldak, J., Simmer, J. P., Sarte, P., Lau, E. C., Diekwisch, T., et al. (1994). Self-assembly of a recombinant amelogenin protein generates supramolecular structures. *J. Struct. Biol.* 112, 103–109. doi:10.1006/jsbi.1994.1011

Fincham, A. G., Moradian-Oldak, J., and Simmer, J. P. (1999). The structural biology of the developing dental enamel matrix. *J. Struct. Biol.* 126, 270–299. doi:10.1006/jsbi.1999.4130

Fincham, A. G., and Shuler, C. F. (2001). The changing face of dental education: The impact of PBL. *J. Dent. Educ.* 65, 406–421. doi:10.1002/j.0022-0337.2001.65.5.tb03410.x

Gibson, C. W., Yuan, Z. A., Hall, B., Longenecker, G., Chen, E., Thyagarajan, T., et al. (2001). Amelogenin-deficient mice display an amelogenesis imperfecta phenotype. *J. Biol. Chem.* 276 (34), 31871–31875. doi:10.1074/jbc.M104624200

Glimcher, M. J., Mechanic, G., Bonar, L. C., and Daniel, E. J. (1961). The amino acid composition of the organic matrix of decalcified fetal bovine dental enamel. *J. Biol. Chem.* 236, 3210–3213. doi:10.1016/s0021-9258(18)93997-9

Glimcher, M. J. (1979). Phosphopeptides of enamel matrix. *J. Dent. Res.* 58, 790–809. doi:10.1177/00220345790580023101

Guenther, H. L., Croissant, R. D., Schonfeld, S. E., and Slavkin, H. C. (1977). Identification of four extracellular-matrix enamel proteins during embryonic-rabbit tooth-organ development. *Biochem. J.* 163, 591–603. doi:10.1042/bj1630591

Kwak, S-Y., Wiedemann-Bidlack, F. B., Beniash, E., Yamakoshi, Y., Simmer, J. P., Litman, A., et al. (2009). Role of 20-kDa amelogenin (P148) phosphorylation in calcium phosphate formation *in vitro*. *J. Biol. Chem.* 284, 18972–18979. doi:10.1074/jbc.M109.020370

Lagerström, M., Dahl, N., Nakahori, Y., Nakagome, Y., Bäckman, B., Landegren, U., et al. (1991). A deletion in the amelogenin gene (AMG) causes X-linked amelogenesis imperfecta (AIH1). *Genomics* 10 (4), 971–975. doi:10.1016/0888-7543(91)90187-j

Le Norcy, E., Lesieur, J., Sadoine, J., Rochefort, G. Y., Chaussain, C., and Poliard, A. (2018). Phosphorylated and non-phosphorylated leucine rich amelogenin peptide differentially affect ameloblast mineralization. *Front. Physiol.* 9, 55. doi:10.3389/fphys.2018.00055

Moradian-Oldak, J. (2007). The emergence of "nanospheres" as basic structural components adopted by amelogenin. *J. Dent. Res.* 86, 487–490. doi:10.1177/154405910708600603

Nylen, M. U. (1964). Electron microscope and allied biophysical approaches to the study of enamel mineralization. *J. R. Microsc. Soc.* 83, 135–141. doi:10.1111/j.1365-2818.1964.tb00522.x

Piez, K. A. (1961). Amino acid composition of some calcified proteins. *Science* 134, 841–842. doi:10.1126/science.134.3482.841

Shin, N-Y., Yamazaki, H., Beniash, E., Yang, X., Margolis, S. S., Pugach, M. K., et al. (2020). Amelogenin phosphorylation regulates tooth enamel formation by stabilizing a transient amorphous mineral precursor. *J. Biol. Chem.* 295, 1943–1959. doi:10.1074/jbc.RA119.010506

Shuler, C. F., and Fincham, A. G. (1998). Comparative achievement on National Dental Board Examination Part I between dental students in problem-based learning and traditional educational tracks. *J. Dent. Educ.* 62, 666–670. doi:10.1002/j.0022-0337.1998.62.9.tb03230.x

Simmer, J. P., Lau, E. C., Hu, C. C., Aoba, T., Lacey, M., Nelson, D., et al. (1994). Isolation and characterization of a mouse amelogenin expressed in *Escherichia coli*. *Calcif. Tissue Int.* 54, 312–319. doi:10.1007/BF00295956

Stack, M. V. (1954). Organic constituents of enamel. *J. Am. Dent. Assoc.* 48, 297–306. doi:10.14219/jada.archive.1954.0053

frontiers | Frontiers in Physiology

TYPE Original Research
PUBLISHED 08 December 2022
DOI 10.3389/fphys.2022.1019364

OPEN ACCESS

EDITED BY
Henry Margolis,
School of Dental Medicine, University of Pittsburgh, United States

REVIEWED BY
Catherine Chaussain,
Université Paris Cité, France
Pamela Den Besten,
University of California, San Francisco, United States
Elia Beniash,
University of Pittsburgh, United States

*CORRESPONDENCE
Timothy Keiderling,
tak@uic.edu
Xiubei Liao,
xiubei@uic.edu
Thomas G. H. Diekwisch,
Thomas_Diekwisch@URMC.Rochester.edu

SPECIALTY SECTION
This article was submitted to Craniofacial Biology and Dental Research, a section of the journal Frontiers in Physiology

RECEIVED 15 August 2022
ACCEPTED 22 November 2022
PUBLISHED 08 December 2022

CITATION
Zhang Y, Jin T, Zhu W, Pandya M, Gopinathan G, Allen M, Reed D, Keiderling T, Liao X and Diekwisch TGH (2022), Highly acidic pH facilitates enamel protein self-assembly, apatite crystal growth and enamel protein interactions in the early enamel matrix. *Front. Physiol.* 13:1019364. doi: 10.3389/fphys.2022.1019364

Highly acidic pH facilitates enamel protein self-assembly, apatite crystal growth and enamel protein interactions in the early enamel matrix

Youbin Zhang[1], Tianquan Jin[1], Weiying Zhu[2], Mirali Pandya[3], Gokul Gopinathan[3], Michael Allen[4], David Reed[1], Timothy Keiderling[2]*, Xiubei Liao[5]* and Thomas G. H. Diekwisch[1,3]*

[1]Department of Oral Biology, University of Illinois at Chicago, Dallas, Illinois, United States, [2]Department of Chemistry, University of Illinois at Chicago, Chicago, Illinois, United States, [3]Center for Craniofacial Research and Diagnosis, Texas A and M College of Dentistry, Dallas, Texas, United States, [4]Department of Medicine, University of Chicago, Chicago, Illinois, United States, [5]Department of Biochemistry, University of Illinois at Chicago, Chicago, Illinois, United States

Tooth enamel develops within a pH sensitive amelogenin-rich protein matrix. The purpose of the present study is to shed light on the intimate relationship between enamel matrix pH, enamel protein self-assembly, and enamel crystal growth during early amelogenesis. Universal indicator dye staining revealed highly acidic pH values (pH 3–4) at the exocytosis site of secretory ameloblasts. When increasing the pH of an amelogenin solution from pH 5 to pH 7, there was a gradual increase in subunit compartment size from 2 nm diameter subunits at pH 5 to a stretched configuration at pH6 and to 20 nm subunits at pH 7. HSQC NMR spectra revealed that the formation of the insoluble amelogenin self-assembly structure at pH6 was critically mediated by at least seven of the 11 histidine residues of the amelogenin coil domain (AA 46–117). Comparing calcium crystal growth on polystyrene plates, crystal length was more than 20-fold elevated at pH 4 when compared to crystals grown at pH 6 or pH 7. To illustrate the effect of pH on enamel protein self-assembly at the site of initial enamel formation, molar teeth were immersed in phosphate buffer at pH4 and pH7, resulting in the formation of intricate berry tree-like assemblies surrounding initial enamel crystal assemblies at pH4 that were not evident at pH7 nor in citrate buffer. Amelogenin and ameloblastin enamel proteins interacted at the secretory ameloblast pole and in the initial enamel layer, and co-immunoprecipitation studies revealed that this amelogenin/ameloblastin interaction preferentially takes place at pH 4—pH 4.5. Together, these studies highlight the highly acidic pH of the very early enamel matrix as an essential contributing factor for enamel protein structure and self-assembly, apatite crystal growth, and enamel protein interactions.

KEYWORDS

enamel, amelogenin, acidic, apatite crystals, electron microscopy

Introduction

Geological minerals require extreme temperatures, pressures, or pH for their formation, as well as long time periods for their transformation from individual ions to organized minerals (Veis and Dorvee 2013; Pandya and Diekwisch 2019). In contrast, biological minerals form at ambient temperatures and pressures, leaving control over crystal growth to conditions of the surrounding environment, including pH and the organic matrix (Veis and Dorvee 2013; Pandya and Diekwisch 2019). The organic protein matrix exerts far-reaching control over growth and habit of biological minerals such as tooth enamel (Lowenstam 1981; Diekwisch et al., 1993; Rao and Cölfen 2016). In addition, acidic pH increases hydroxyapatite formation and solubility and facilitates apatite synthesis *in vitro*, while pH elevation promotes apatite crystal growth and maturation (Larsen and Nyvad 1999; Chen et al., 2006). It has also been suggested that at acidic pH, specific protein binding sites may exist on crystal surfaces that may be released by protonation, which would lower cationic charge on both crystal surface and ionic charge on the protein (Robinson et al., 2005). Together, these studies indicate that both the organic matrix and the microenvironmental pH play a significant role in the nucleation and maturation of biological apatite crystals.

To protect ameloblast cellular compartments, individual ions and proteins are separated throughout their transport through the ameloblast layer, only to result in a dramatic convergence of minerals and proteins in the secretory enamel matrix immediately adjacent to the secretory ameloblast pole (Diekwisch et al., 1995; Pandya et al., 2017). At the secretory ameloblast pole, calcium ions, phosphate ions and enamel proteins converse and interact for the first time to form the initial enamel crystals (Pandya and Diekwisch 2021). Most notably, the concurring deposition of calcium and phosphate ions into the matrix leads to an almost instantaneous formation of apatite crystals (Jokisaari et al., 2019; Pandya and Diekwisch 2021) prompting excess proton production (Smith 1998; Smith et al., 2005; Lacruz et al., 2017). It has been speculated that acidic conditions resulting from the excess presence of free protons would then be buffered either through the presence of amelogenins or *via* bicarbonates and through other buffer systems in the extracellular matrix (Ryu et al., 1998; Smith 1998; Lacruz et al., 2010; Bori et al., 2016; Lacruz et al., 2017). In recent years, several groups have identified numerous ameloblast expressed transmembrane proteins involved in the production and transport of biocarbonates, including CFTR, AE2a,b, NBCEI, Na-hydrogen exchanger-1, carbonic anhydrase 2, as well as solute carrier family members Slc26a3, Slc26a4, and Slc26a6 (Bronckers et al., 2016). These findings underscore the high number of protons surrounding forming enamel apatite crystals and the sophistication of buffering mechanisms present in the developing enamel matrix.

While highly acidic pH has not been considered to occur during physiological amelogenesis, the first reported synthetic generation of apatite nanorods was based on an aqueous hydroxyapatite solution titrated to pH 2.8, resulting in the precipitation of 200–400 nm long apatite crystals (Chen et al., 2006). Low pH has also been popular for biochemical studies of enamel proteins since the earliest days of enamel research. Burgess and MacLaren. (1965) and Fincham. (1968) performed electrophoretic studies in starch-urea and polyacrylamide gels at extremely acidic pH values such as 3.7 and 3.0 respectively, lauding the high electrophoretic resolution attainable under these conditions. Amelogenin structure studies (pH 4) also have been conducted at acidic pH (Delak et al., 2009; Jin et al., 2009; Zhang et al., 2011; Shaw et al., 2020) to facilitate structure determination under high solubility conditions, avoiding the aggregate effects that occur near physiological pH. Several authors have reported monomeric, disordered, or small-sized (3–7 nm diameter) amelogenin assemblies at pH values between 3.0 and 5.8, compared to the 15–20 nm supramolecular assemblies detected at physiological pH (Moradian-Oldak et al., 1998; Bromley et al., 2011; Fang et al., 2011; Beniash et al., 2012). Supporting the concept of an acidic pH promoting apatite crystals growth, it has been reported that growth rates and numbers of apatite ribbons were significantly higher at pH4.5 when compared to pH7.0 (He et al., 2011). In contrast to the dearth of knowledge about the role of pH during early amelogenesis, pH changes in maturation stage enamel have been well established ever since the visually striking experiments by Takano et al. (1988), Sasaki et al. (1991). These studies have established a correlation between alternate acidic (pH 5.8–6.0) and neutral (7.0–7.2) ameloblasts at the zones of ruffle-ended and smooth-ended maturation stage ameloblasts of unerupted calf incisors (Sasaki et al., 1991). Several others have pointed to the importance of pH regulation and buffering for ameloblast differentiation and amelogenesis during the maturation stage (Wiedemann-Bidlack et al., 2007; Tye et al., 2010; Wang et al., 2010; Lacruz et al., 2012).

The present studies were prompted by the detection of an acidic pH at the exosytosis site of secretory ameloblasts. Based on this initial finding we conducted studies to uncover how such highly acidic pH might affect enamel protein assembly, crystal growth, and enamel protein interactions. To verify our hypothesis, the pH of the early enamel matrix was tested by staining freshly prepared matrix. To determine the effect of pH on amelogenin self-assembly we have conducted a series of biochemical and physicochemical studies of individual components of the enamel protein matrix. These studies

suggest that a highly acidic pH occurs at the exocytosis site of secretory ameloblasts and provide insights into the effects of pH on amelogenin self-assembly, calcium phosphate crystal growth on a nano- and macroscale, and amelogenin/ameloblastin interactions.

Materials and methods

pH detection on tissues using indicator solutions

Unerupted molar teeth from 4 months old cattle were chosen as a model to expose a fresh cut of sufficient size through the developing epithelial mesenchymal interface to perform macroscopic imaging of fresh tissue for pH analysis. For this study, jaws from 4 months old steers were obtained from Brown Packing, South Holland, IL, and impacted molar teeth were dissected using surgical tools. Molar teeth were then cut in half using a surgical blade and half molars immersed in Universal pH Indicator solution (Sigma, St. Louis, MO) for 10 min and gently rinsed with distilled water. Tissue surfaces were then covered with a coverslip, and the distribution of the pH indicator on the tissue section was imaged using light microscopy.

Circular dichroism measurements

The recombinant mouse amelogenin protein solutions were prepared at a 0.1 mg/ml concentration in PBS, and a HCl solution was used to adjust the pH for each sample solution. Each sample solution was transferred into a 1 mm pathlength quartz cuvette (Starna, Inc.), and CD spectra were measured from 180 nm to 250 nm with a 50 nm/min scanning rate, 2 s response time, 1 nm bandwidth as the average of eight scans on a JASCO 810 spectrometer (Jasco, Inc.) at room temperature. All sample spectra were corrected by subtraction of the corresponding buffer spectrum.

Attenuated total reflectance fourier transform infrared (ATR-FTIR) spectroscopy

This study used the same amelogenin protein solutions as employed for the CD studies. For measurements, the FTIR spectrometer (Bruker Vertex 80) was equipped with an ATR accessory fitted with a diamond crystal (PIKE MIRacle single reflection ATR). A volume of 40 µl of sample solution was loaded onto the crystal and dried with a mild flow of nitrogen gas to form a uniform thin film on the crystal surface. Sample absorbance spectra over the range 4500 cm^{-1} to 600 cm^{-1} were collected as an average of 1024 scans (10 kHz scan speed with a DTGS detector) and processed with 3-term Blackman-Harris apodization and zero filling of 2. Experiments were repeated 3 times. Background transmission spectra were collected on the empty ATR crystal surface under the same conditions and were used to compute the absorbance spectra.

Atomic force microscopy

Atomic force microscope (AFM) studies were carried out using an extended MultiMode AFM (MMAFM) integrated with a NanoScope IIIa controller (Veeco Instruments, Santa Barbara, CA) and a Q-Control Module (nanoAnalytics, Muenster, Germany) as previously described (Jin et al., 2009). The MMAFM was equipped with a calibrated E-type piezoelectric scanner and a glass cell for fluid TappingMode AFM (both from Veeco). The silicon AFM cantilever/probe used in this study was rectangular in shape, 130 µm in length and 35 µm in width (NSC36, MikroMasch). The advertised typical force constant and resonant frequency of this cantilever/probe is 0.6 N/m and 75 kHz respectively. Nominal sharpness of the probe-tip end radius is ≤ 10 nm. The cantilever/probes were oscillated near 30 kHz at low amplitude for fluid tapping mode AFM. Fluid damping reduces the resonant frequency of rectangular AFM cantilevers in air by approximately 50%. The AFM substrate used for protein adsorption was Grade V5, Pelco mica (10 × 40 mm) purchased from Ted Pella (Redding, CA). The mica was freshly cleaved using adhesive tape prior to use. Stock solutions of 10–20 mg/ml amelogenin M179 in 40 mM Tris were mixed and stored at 4°C and analyzed by AFM. Stock solutions were diluted typically at 1:100 into the blank AFM imaging buffer (40 mM Tris) during scanning and adsorption to mica was monitored. The pH of the imaging solution was adjusted to pH 5.0, 6.0, or 7.0 using concentrated HCl and verified using a pH electrode. Typical AFM scan rates were 1.0–1.25 Hz for 512 data points x 256 lines. The AFM images were plane-fit to correct for background sloping errors.

Transmission electron microscopy of amelogenin assembly at various pH values

To assess the dimensions and patterns of self-assembled amelogenins under changing pH, solutions of 10–20 mg/ml amelogenin M179 in DDW were adjusted to pH 5.0, pH 6.0 and pH 7.0, and allowed to air dry on 200 mesh carbon coated electron microcopy grids (Ted Pella, Redding, CA). TEM grids obtained from each individual group were quickly rinsed with DDW, blotted against filter paper, and air dried. Transmission electron microscopy was performed using a JEOL 1220 TEM as previously described (Pandya and Diekwisch, 2019).

In vitro crystal growth studies on polystyrene plates

To mimic the dehydrating conditions in the developing enamel matrix in an *in vitro* model, approximately 2 ml of 2.5 mM $CaHPO_4$ at varying pH (pH 3.0 to pH 7.0) in a 35 mm non-coated polystyrene plate was placed in a 37°C incubator and allowed to evaporate to enable crystal formation.

Crystal growth studies on TEM grids

Hydroxyapatite crystal growth studies were performed as previously described (Jin et al., 2009). Briefly, carbon-coated gold TEM grids were immersed into either a pH 4 or pH 7 crystal growth solution. The pH of the crystal growth solution was adjusted by adding either 20 mM NH_4OH or 2.5 mM $CaHPO_4$ buffer to DDW. For crystal growth studies, 2.5 mM $CaCl_2$ and 1.5 mM $(NH_4)_2HPO_4$ were added to the solution (Jin et al., 2009), which was then incubated in a moisturized container at 37°C for 2.5 h. Subsequently, TEM grids obtained from each individual reaction step were quickly rinsed with DDW, blotted against filter paper, and air dried. Transmission electron microscopy was performed using a JEOL 1220 TEM as previously described (Pandya and Diekwisch, 2019).

Nano-hydroxyapatite (HA) binding to N92 amelogenin protein

10 μg of N92 amelogenin protein were incubated in 200 μl of nano-hydroxyapatite solution (HA) (0.1 μg/μl) of varying pH (pH 3.0 to pH 8.0) at 37°C for 1 h. The pH of the HA solution was adjusted over the range of pH 3.0 to pH 8.0 using glacial acetic acid or ammonium hydroxide. After 1 h incubation on a shaker, protein-HA complexes were washed with excessive amounts of 1xPBS, three x times at 10.000 x g to remove non-specific binding. Adsorbed protein from HA was released using 100 μL of RIPA lysis buffer. 20 μL of each sample protein over the range of pH 3.0 to 8.0 were run on a 10% SDS-PAGE gel, transferred onto a PVDF membrane in a semi-dry blotting apparatus containing transfer buffer (25 mM tris-HCl, 40 mM glycine, 10% methanol) for 45 min at 75 mA. The PVDF membrane was blocked with 5% bovine serum albumin for 1 h at room temperature, incubated with a chicken amelogenin antibody at a concentration of 1:5,000 for 1 h. Thereafter, the membrane was washed with TBST three times for 10 min each and probed with a HRP-conjugated anti-chicken secondary antibody at a concentration of 1:2,000. HRP was detected using chemiluminescent substrate (Supersignal West Pico Chemiluminescent Substrate, Pierce). For densitometric analysis, band intensities of three replicate films were determined using Adobe Photoshop. Protein expression was quantified as band intensity corrected for protein loading based on pH 7.0 intensity for each corresponding band.

NMR studies

Expression vectors pASK-43 (+) were purchased from The TAG company (Göttingen, Germany). The ^{15}N labeled amide chloride and D_2O (99.5%) was purchased from Cambridge Isotope Laboratories (Andover, MA). 400 MHz PCR tubes were obtained from Kontes (Vineland, NJ). The following peptides used in this study were synthesized at the UIC core facility: TRAP (mouse amelogenin amino acids 1–45) and NLRAP (the N-terminal portion of the mouse amelogenin amino acids 1–33). Other common regents were from Sigma Aldrich (St Louis, MO). The expression of and purification of the amelogenin N-terminus (N33) were described previously (Zhang et al., 2011). The final concentration of ^{15}N enriched amelogenin for our NMR study was 1 mM. The peptides were dissolved into phosphate buffer (5 mM phosphate, 50 mM NaCl) at either pH 4.5 or pH 6.0. The beginning concentration for HSQC data acquisition using the labeled peptide (TRAP) was 0.1 mM and with the unlabeled peptide (N33) was 0.5 mM. 10% D_2O was added to all the samples for the NMR study. NMR data collection was performed on a 900 MHz Bruker NMR at the UIC Core Facility at room temperature and at either pH4.5 or pH6.0. Standard 2D HSQC spectra were acquired and processed using NMRPipe (Delaglio et al., 1995).

Transmission electron microscopy of developing mouse molar tooth organs subjected to various buffers and pH conditions

Three-day postnatal mouse molar tooth organs were prepared from postnatal mice after euthanization by CO_2 inhalation according to the guidelines of the University of Illinois, Chicago Animal Care Committee. Following sacrifice, the mouse molars were immediately dissected and either immersed in phosphate buffer at pH 7 or in phosphate buffer at pH 4 or in citrate butter at pH 4 for 2 h. Following immersion in each buffer system for 2 h, tooth organs were fixed according to Karnovsky's protocol as previously described (Diekwisch, 1998).

Citrate buffer was generated by mixing 0.5 g of citric acid monohydrate and 0.4 g of dibasic sodium phosphate in 1 L H_2O, and the pH was adjusted to either 4.0 or 7.0 by varying the amount of citric acid. Phosphate buffer was generated by mixing 5.04 g (pH 4) or 0.5 g (pH 7) of anhydrous disodium hydrogen phosphate and 0.301 g of potassium dihydrogen phosphate in 1 L H_2O. Freshly dissected 3 days postnatal mouse molar samples were then directly immersed into the buffer for 2 h and fixed thereafter in Karnovsky's.

Co-immunolocalization studies for amelogenin and ameloblastin in developing mouse molars

Molar teeth harvested from 3-day postnatal wild-type and amelogenin null mice were sacrificed according to the guidelines of the University of Illinois, Chicago Animal Care Committee, dissected, fixed in 10% buffered formalin, and prepared for paraffin histology. Paraffin sections were then subjected using immunohistochemistry as previously described (Luan et al. 2007; Walker et al. 2008). Following pre-treatment, sections were then incubated with affinity-purified polyclonal anti-amelogenin (Satchell et al., 2002) or anti-AMBN (Lu et al., 2013) antibodies at a dilution of 1:100 at 4°C overnight. Dual labeling of protein expression was performed with a Double Staining AEC/DAB kit (Abcam, Waltham, MA).

Validation of amelogenin and ameloblastin interaction *via* co-immunoprecipitation

To probe whether amelogenin and ameloblastin interact on a protein level, amelogenin (N-terminal 92 amino acids, N92) and ameloblastin (full-length) constructs were generated. Briefly, amelogenin N92 cDNA was inserted into the pNTAP vector to generate the CBP-SBP-amelogenin fusion protein, and full length ameloblastin cDNA with a c-terminal FLAG tag was inserted in the pCDNA3 vector to generate the ameloblastin-FLAG fusion protein. *In vitro* translation fusion proteins were generated from each vector (N92 amelogenin and ameloblastin-FLAG) using the TNT® Coupled Reticulocyte Lysate Systems (Promega, Madison, WI). Following *in vitro* translation, co-immunoprecipitation assays were performed to analyze the interaction between ameloblastin and amelogenin.

To pull down co-precipitated amelogenin, anti-FLAG agarose (Sigma, St. Louis, MO) beads were incubated overnight with both proteins or amelogenin only (as non-specific binding control) in modified PBS buffer (with 2 mM CaCl2, 1 mM MgCl2 at either pH4.0, pH4.5, or 5.0). After overnight incubation, beads were washed with PBS buffer 3 times, mixed with loading buffer to boil, and subjected to SDS-PAGE gel electrophoresis for Western blot using anti-CBP antibody (Abcam, Cambridge, MA) to detect amelogenin co-precipitation.

To pull down co-precipitated ameloblastin, streptavidin sepharose (GE Healthcare, Pittsburgh, PA) beads were incubated overnight with both proteins or ameloblastin only (as non-specific binding control) in modified PBS buffer (with 2 mM CaCl2, 1 mM MgCl2 at either pH4.0, pH4.5, or 5.0). After overnight incubation, beads were washed with PBS buffer 3 times, mixed with loading buffer to boil, and subjected to SDS-PAGE gel electrophoresis for Western blot using anti-FLAG antibody (Sigma, St. Louis, MO) to detect ameloblastin co-precipitation.

Results

pH indicator dyes revealed pH values between pH 3 to 4 at the exocytosis site of secretory ameloblasts

Universal pH indicator dye (Sigma, St. Louis, MO) was used to determine the pH at the ameloblast/early matrix interface freshly cut bovine developing molar slices. Universal indicator staining of freshly cut bovine molar slices revealed a dark red stained band indicative of pH 3 right between the ameloblast layer and the enamel layer at the earliest secretory stage and during the maturation stage (Figure 1). These data suggest the presence of a highly acidic localized pH in the range between pH 3 and pH 4 at the exocytosis site of secretory ameloblasts (Figure 1).

Increased amelogenin self-assembly and subunit diameter, as well as structural transformation between pH 5 to pH 8

CD spectra of amelogenins with increasing pH revealed a gradual loss of intensity for the 200 nm negative peak, suggestive of an increase in aggregation (Figure 2A). ATR spectra were typical of a disordered protein and displayed multiple changes with increasing pH, including a substantially elevated peak in the 1570 cm^{-1} region at pH 7.0 and pH 8.0, overlaying the amide II band and indicative of growth of a carboxyl bond, which may indicate an increasingly self-assembled and aggregated protein structure (Figure 2B).

Full length amelogenins were imaged between pH 5.0 and 7.0 on freshly cleaved mica and on coated electron microcopy grids using atomic force microscopy and transmission electron microscopy. At pH 5.0, atomic force microscopy revealed 2–3 nm subunits dispersed throughout the amelogenin solution while at pH 7.0, the mica surface was covered with typical 20 nm diameter spherical subunits. Remarkably, at pH 6.0 subunits consisted of 3 nm × 10 nm elongated stretches (Figures 2C–E). In contrast, subunit dimensions of amelogenin assemblies on carbon coated electron microscopy grids simply increased from 10 nm subunit sizes at pH 5.0–20 nm subunit sizes at pH 7.0 (Figures 2F–H). Together, these data suggest that during aggregation and self-assembly with increasing pH, amelogenin subunit dimensions increase in size, feature increased chemical bonds, and undergo unique intermediary configurations that may aid crystal growth.

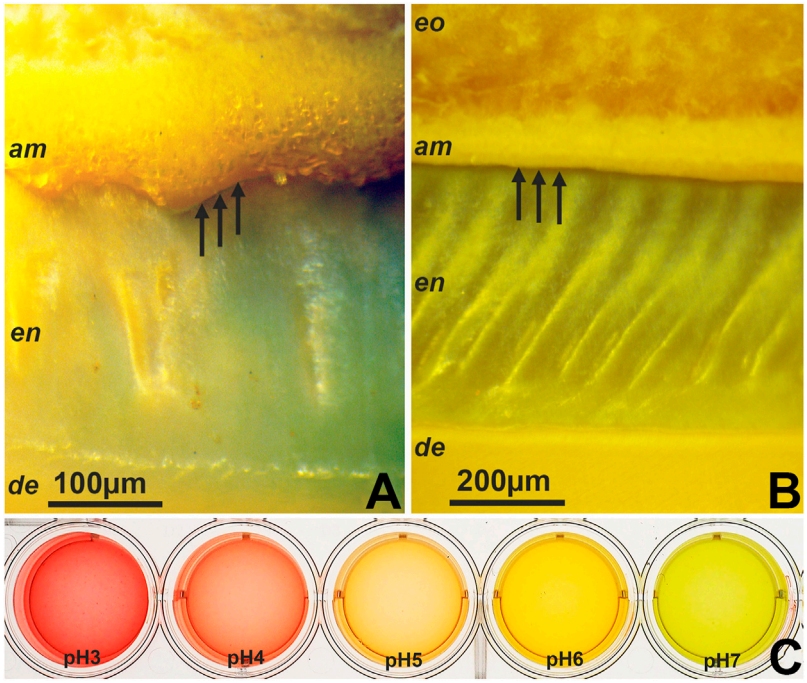

FIGURE 1
Areas of intense pH indicator staining in developing tooth enamel as revealed by pH indicator dyes. **(A,B)** pH distribution at the exostosis site of secretory ameloblasts and at the ameloblast/enamel interface during secretory stage enamel formation of freshly cut bovine molars. **(C)** Reference solutions prepared from pH3 to pH7 and stained with indicator dye. CL = cervical loop, am = ameloblasts, en = enamel, de = dentin, od = odontoblasts, eo = enamel organ.

Changes in pH greatly affected the histidine rich region of the amelogenin coil domain (H47-H69) while the non-LRAP portion of the TRAP motif (AA34-45) was the key sequence motif for amelogenin self-assembly at pH 6

Previous studies from our laboratory identified the amelogenin N-terminus as the major site for amelogenin self-assembly interactions (Zhang et al., 2011). To further query amelogenin NMR spectra for the effect of pH changes on N-terminal amelogenin interactions at low and high pH we acquired HSQCs of Amel-N (AA1 to 92) at pH 4.5 and pH 6 (Figure 3A). Prepared in solution, Amel-N was a monomer at pH 4.5 while there was a visible precipitate at pH 6.0, which did not interfere with the acquisition of HSQC spectra. When compared to the spectrum obtained at pH 4.5, a number of resonances mainly between E18 to H69 were either weakened or no longer detectable at pH 6.0, including E18, T21, L20, L23, Q27, M29, I30, Y34, H47, H48, H58, H62, H67, H68, and H69. This list includes seven of the nine histidines in the amelogenin N-terminal N92 fragment (H47, H48, H58, H62, H67, H68, H69), which comprises approximately half of all amelogenin histidines. The histidines in position 91 and 92 were little affected as residues at the amelogenin N92 N-and C-termini were not perturbed by changes in pH. Amelogenin contains four more histidines that were outside of the N92 fragment studied here. In summary, these HSQC spectra identified two possible interaction domains, 1) the histidine-rich region between amino acids 47—69 and 2) portions of the TRAP domain.

To further narrow down possible interaction sites within the TRAP domain, two peptides were synthesized, a TRAP peptide which contained the N-terminal 45 amelogenin residues and an Amel-N33 peptide containing the N-terminal 33 amelogenin residues. While the Leucine and Glycine of the TRAP peptide residues were ^{15}N enriched, the N33 peptide (N-terminus of LRAP) did not contain isotopically enriched residues. Unlabeled TRAP peptide was retained for interaction studies with N-LRAP (Figures 3E,F). HSQC spectra for interactions between TRAP peptides (Figures 3C,D) and the unlabeled N33 with the labeled TRAP peptides (Fig. E, F) were acquired at pH 4.5 (Figures 3C,E) and pH 6 (Figures 3D,F), respectively. Both peptides were entirely soluble at pH 4.5. At pH 6 the TRAP peptide formed self-assembly precipitates similar to the ones observed with the N92 peptide, while the LRAP peptide did not. The soluble fraction of the TRAP peptide demonstrated a similar but slightly weakened resonance spectrum at pH 6 compared to the spectrum at pH 4.5 (Figure 3D vs.Figure 3C). In the N-LRAP

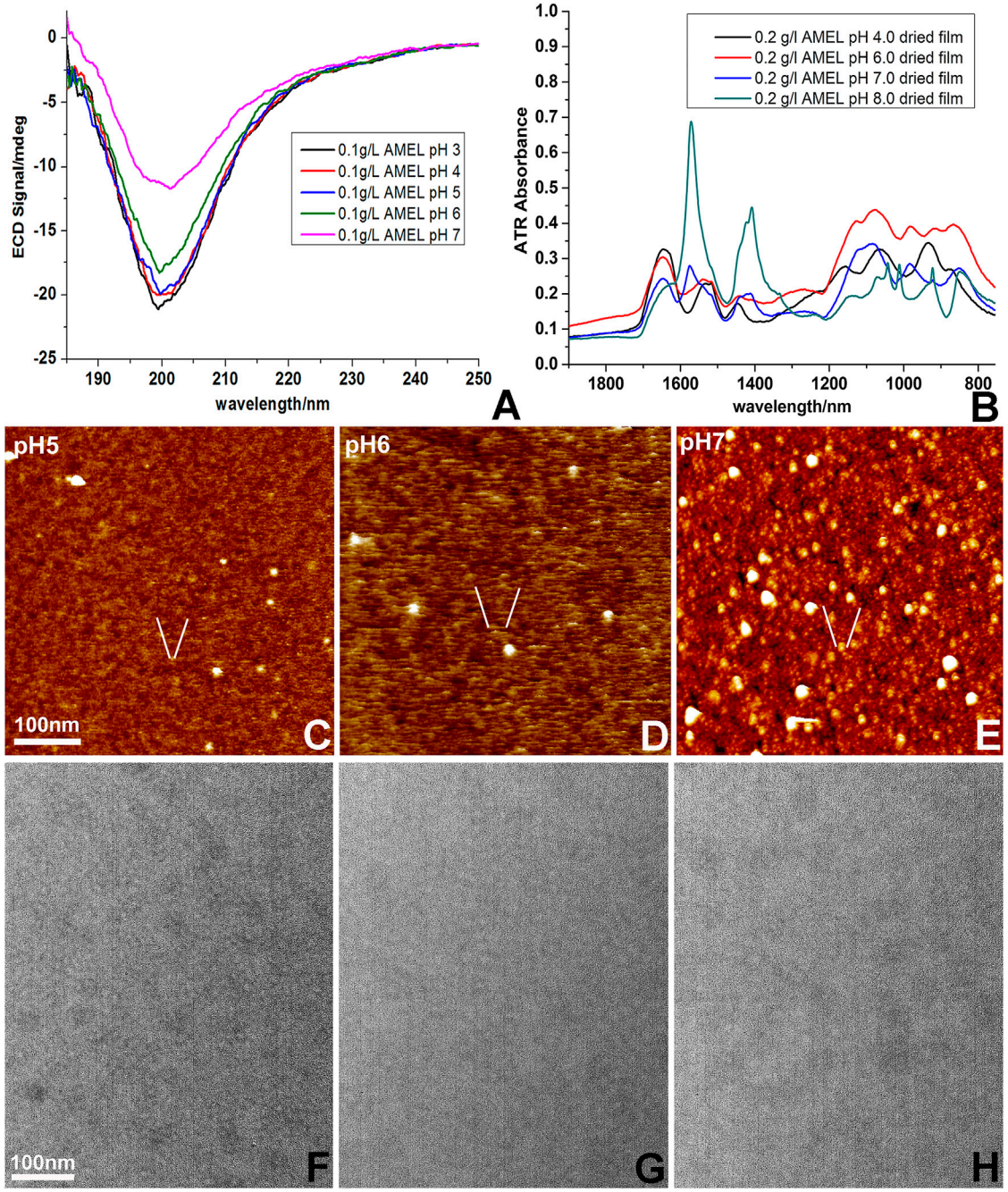

FIGURE 2
Changes in amelogenin self-assembly as a result of increasing pH. **(A)** Differences in electronic circular dichroism (ECD) spectra of amelogenin solutions as a result of increasing pH values from pH 3 to pH 7. **(B)** Dramatic changes in attenuated total reflection microscopy (ATR) spectra in amelogenin solutions ranging from pH 3 to pH 8. **(C–E)** Changes in amelogenin assemblies on freshly cut mica at pH 5, pH 6, and pH 7. **(F–H)** Increased diameter of amelogenin assemblies on carbon coated TEM grids prepared at pH 5, pH 6 **(E)**, and pH 7. A scale bar is provided for size comparisons.

peptide/TRAP interaction experiment, HSQC spectra of the selectively labeled TRAP peptide were further reduced, especially at L23 (Figure 3F vs. Figure 3E). At pH 6.0, the two leucine amino acids in positions L20 and L23 were no longer detected in the N92 spectrum while they were recognized in the TRAP spectrum (Figure 3B vs. Figure 3D), suggesting that interactions only occured in the full-length amelogenin and not in between individual amelogenin peptides.

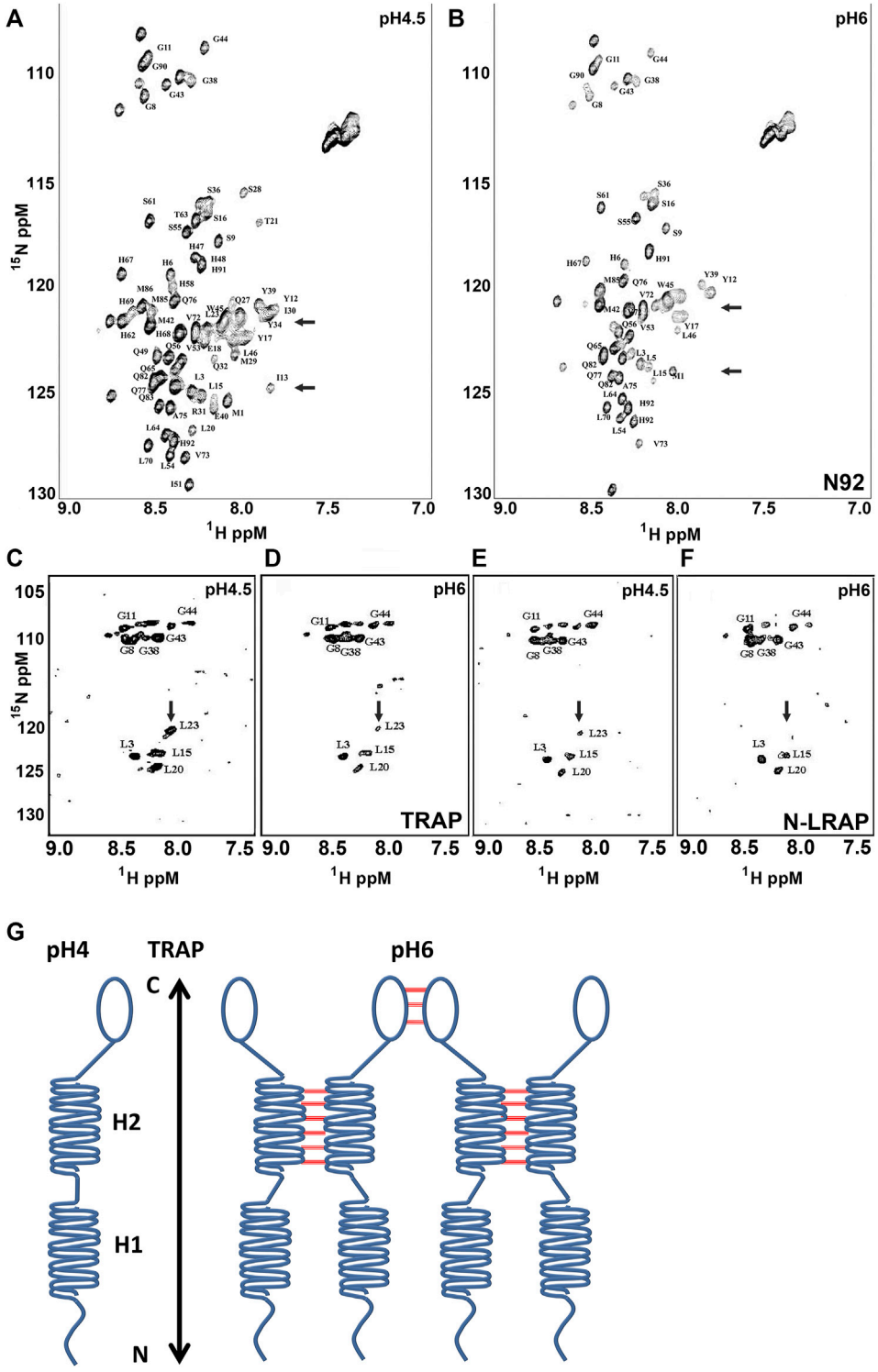

FIGURE 3
N-terminal amelogenin interactions at pH 4.5 and pH6. Figures A and B are HSQC spectra of N15 enriched Amelogenin (N92) at pH 4.5 **(A)** and pH6.0 **(B)** respectively. **(C,D)** are HSQC spectra of chemically synthesized amelogenin TRAP peptide (N1-45) with ^{15}N-enriched Gly (G8, G11, G38, G43 and G44) and Leu (L3, L15, L20 and L23) at pH 4.5 **(C)** and pH 6.0 **(D)** respectively. **(E,F)** are HSQC spectra of the selected labeled TRAP peptide in the presence of a short peptide containing the first terminal 33 amino acid residues (N33, the N-terminal portion of LRAP) at pH 4.5 **(E)** and pH6.0 **(F)**. **(G)** is a model representing proposed intermolecular interactions between amelogenin molecules, with tight intermolecular bonds between the H2 helices in the non-LRAP TRAP region (AA34-45) and weak interactions at the amelogenin C-terminus. The H1 helices in the LRAP region did not feature any notable interactions.

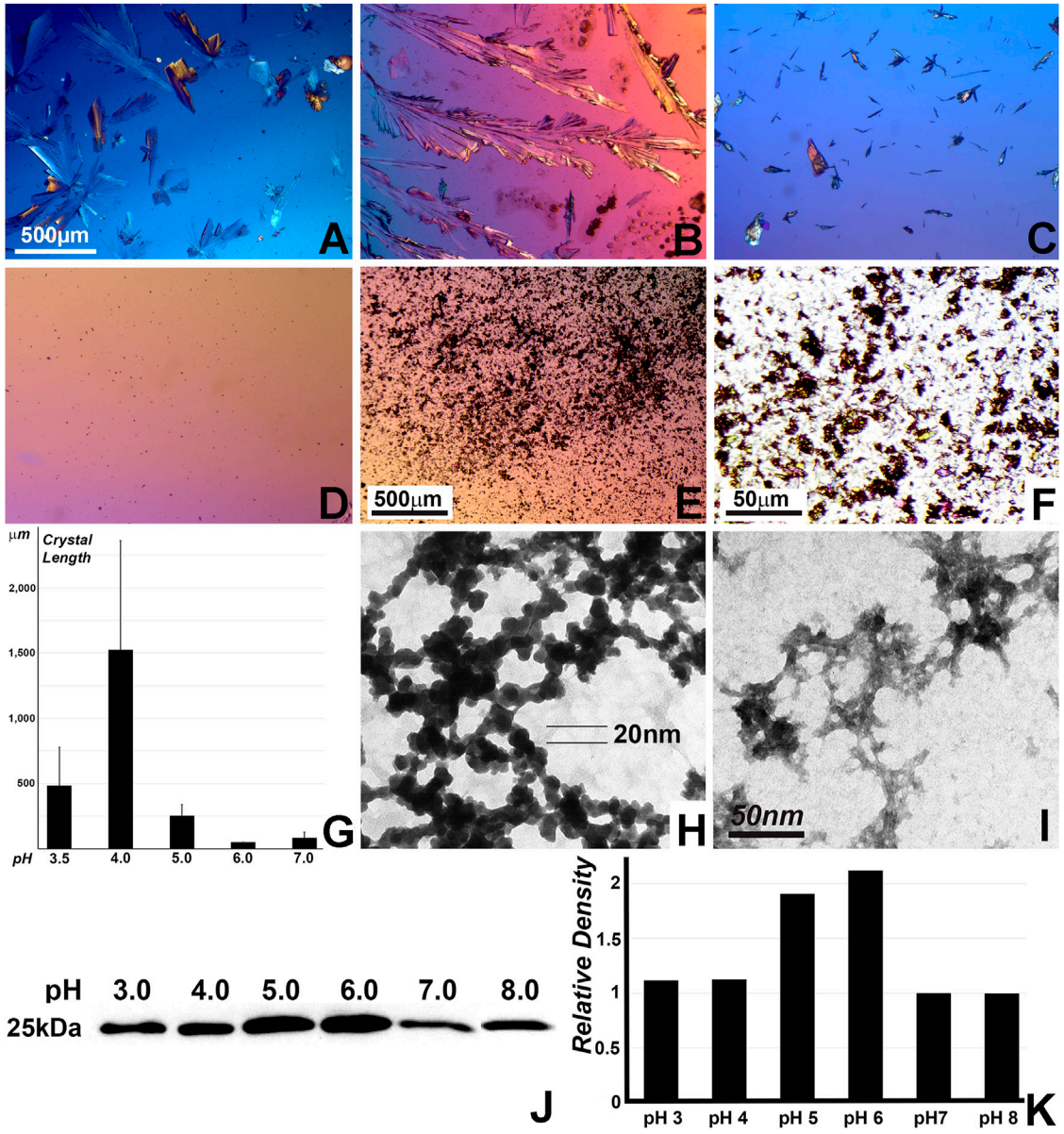

FIGURE 4
Effect of pH on calcium phosphate crystal growth and on the binding of the N-terminal amelogenin N92 to nano-hydroxyapatite. **(A–F)** Micrographs of calcium phosphate crystals grown on non-coated polystyrene plates at pH values from pH3 to pH7. **(F)** is a ten-fold enlarged view of **(E)** illustrating individual crystal shapes. **(G)** Average crystal length comparison based on the calcium phosphate growth study on polystyrene plates at pH values from pH3 to pH7 as performed in **(A–F)**. **(H,I)** Calcium phosphate crystal growth studies on carbon-coated TEM grids without the presence of protein. **(H)** calcium phosphate crystal growth at pH four and **(I)** calcium phosphate crystal growth at pH 7. The 50 nm scale bar in **(I)** is provided as a reference for both electron micrographs. **(J)** Nano-hydroxyapatite binding to N92 N-terminal amelogenin. For this study, N92 N-terminal amelogenin proteins were incubated at incremental pH values ranging from pH3 to pH8, adsorbed to hydroxyapatite, washed in lysis buffer, transferred on a PVDF membrane, and then immunoblotted for amelogenin Western blot analysis. **(K)** Densitometry of the Western blot in **(J)**.

1D homonuclear experiments were conducted to verify the effect of intermolecular interaction between N33 (N-terminus of LRAP) peptides. At pH 6.0 the 1D spectrum displayed a substantially increased line width when compared to pH4.5, typical for an aggregated peptide (data not shown). Together, these data indicate that the first 33 amino acid residues at the amelogenin N-terminus (N33) interacted with each other without forming large, precipitated nanostructures, while the C-terminus of the TRAP sequence (AA34-45) played a critical role in the formation of insoluble nanostructures at pH 6 (Figure 3G).

Preferred nucleation and elongation of apatite crystals at acidic pH and preferred apatite binding of the N-terminal amelogenin between pH 3 and 6 vs. pH 7 and pH 8

To interrogate the effect of acidic pH on apatite nucleation and crystal growth, crystal growth studies with varying pH were conducted on polystyrene dishes and on carbon coated electron microscopy grids. On plastic dishes, apatite crystal growth at pH 4.0 vastly outperformed crystal growth at other pH values, reaching crystal dimensions of 1.5 mm length in average and exceeding those grown at pH 6.0 and 7.0 approximately 100-fold (Figures 4A–G). On electron microscopy grids, mineral assemblies formed at pH 4.0 were doubled in size and number when compared to those grown at pH 7.0 (Figures 4H,I). To determine whether there was a pH-dependent change in apatite binding, N92 N-terminal amelogenin proteins were adsorbed to apatite at varying pH values, and lysed proteins were compared *via* Western blot (Figures 4J,K). Densitometry demonstrated that amelogenin adsorption to apatite was greatest at pH 5 and pH 6 (Figure 4K), suggesting that amelogenin-apatite interactions changed with pH but did not appear to directly affect the dramatic changes in self-assembly and crystal growth detected in the other experiments conducted in this study. However, changes in amelogenin binding may also have other explanations.

Enrichment of self-assembled enamel protein clusters with mineral ions in phosphate buffer at pH4 revealed grape cluster-shaped enamel protein assemblies as ion-laden reservoirs for initial enamel crystal growth

To ask how highly acidic conditions affect initial enamel matrix and crystal growth environment, 3 days old postnatal mouse molars were immersed in two different buffers at pH 4.0 for 2 h and then subjected to fixation to preserve resulting ultrastructure. The ultrastructure of samples kept in phosphate buffer at pH 7.0 has been well characterized (Diekwisch et al., 1995) and featured secretory vesicles, secretory enamel matrix and nucleating enamel crystals (Figures 5A,B). However, at pH 4.0, crystals were surrounded by intensely stained clusters of berry-shaped assemblies, resembling overgrown drapes of nanospheres (Figure 5C). In contrast, samples treated with citrate buffer at pH 4.0 displayed bundles of initial enamel apatite nanoribbons (Figures 5D,E), and only few amelogenin supramolecular assemblies (nanospheres) aligned with the crystal bundles (Figure 5F). Studies presented here suggest that acid pH clusters are reflective of intermediate stages of nanosphere assemblies during crystal formation.

AMEL and AMBN co-localized and interacted at pH 4 and pH 4.5

We then asked how acid conditions affect interactions between the two major enamel matrix proteins, amelogenin and ameloblastin. In developing 1-day old postnatal mouse molars, amelogenin was localized in the ameloblast layer and in the enamel, while ameloblastin was tightly concentrated at the ameloblast/enamel interface (Figure 6A). This tight concentration of ameloblastin at the ameloblast/enamel interface was retained in same stage molar organs of amelogenin null mice (Figure 6B). Co-immunoprecipitation studies were performed to determine how acidity and isoelectric point affected interactions between amelogenin N92 and ameloblastin (Figures 6C,D). Co-precipitates were either probed with anti-CBP to recognize SBP-CBP-Amelogenin fusion proteins or with anti-FLAG to recognize AMBN-FLAG fusion proteins generated in a separated experiment, and Western blots revealed strong amelogenin-ameloblastin interactions at pH 4.0 and 4.5, and only very weak interactions at pH 5.0 (Figs. C,D).

Discussion

The present study was prompted by the detection of an extremely acidic pH 4 environment in the earliest secretory enamel matrix and examines its implications on enamel protein self-assembly, calcium phosphate and enamel crystal growth, and enamel protein interactions. Effects of acidic pH on amelogenin self-assembly were studied using circular dichroism (CD), attenuated total reflectance Fourier transform infrared (ATR-FTIR), and atomic force microscopy (AFM). Interactions between the amelogenin TRAP domain (AA1-45) and the N-terminal portion of LRAP (AA1-33) at pH 4.5 and pH 6 were tested using NMR and HSQC spectra. Calcium phosphate and apatite crystal growth studies at pH values between pH 3.0 and 8.0 were conducted either on polystyrene plates or on TEM grids, and binding of apatite to N92 amelogenin at pH values between pH 3.0 and 8.0 was analyzed on Western blots. Freshly dissected developing molar tooth organs were immersed in either phosphate or citrate buffer at pH 4 and 7, and the effect of these two buffers at pH 4 and 7 was compared. To examine the effect of acidic pH on interactions between two major enamel proteins, amelogenin and ameloblastin were co-localized at the ameloblast/initial enamel matrix interface, and amelogenin/ameloblastin binding at pH4, pH4.5, and pH5 was compared using co-immunoprecipitation. Finally, the C-terminal amelogenin/

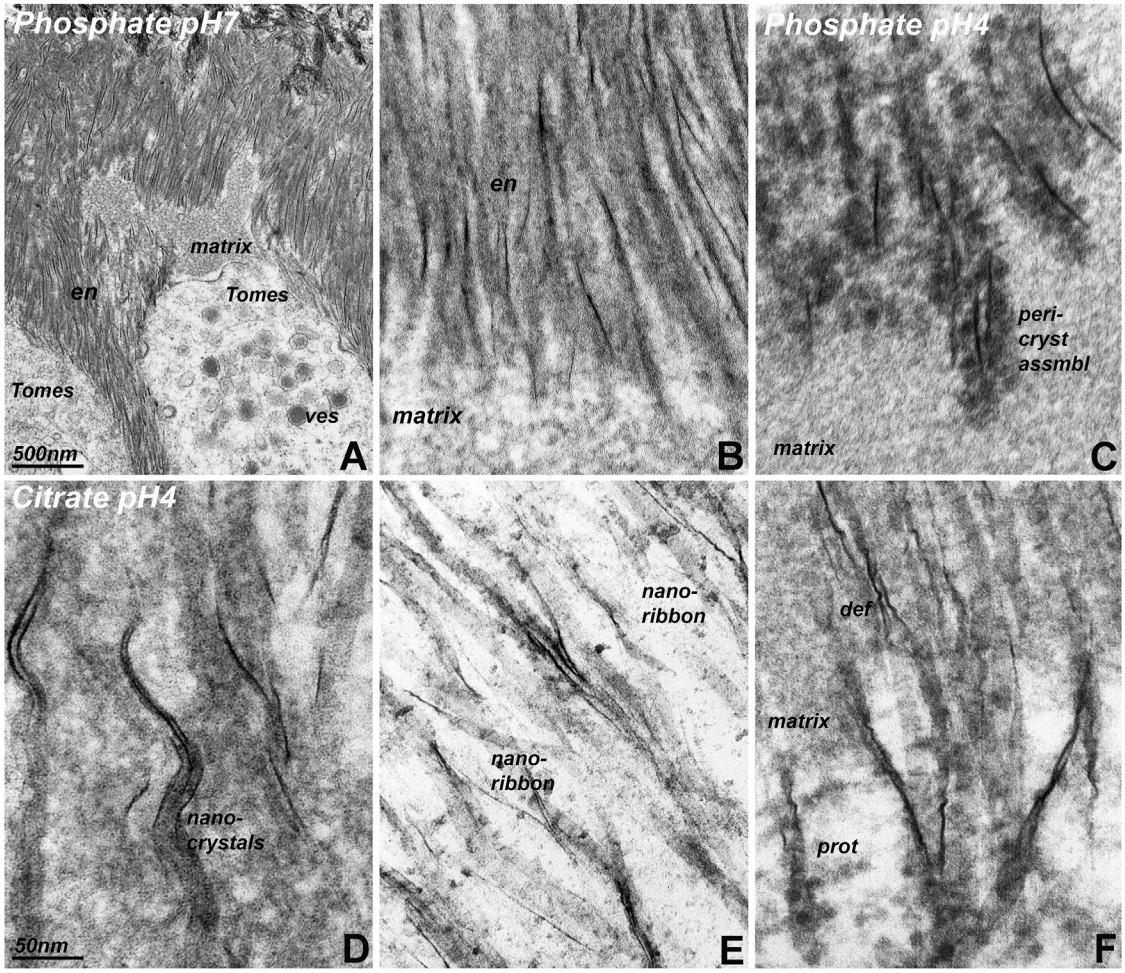

FIGURE 5
Transmission electron micrographs of initial enamel crystals embedded in enamel matrix after immersion in phosphate and citrate buffers at pH 4 and pH 7. **(A)** Overview electron micrograph illustrating the position of Tomes' process (Tomes) loaded with secretory vesicles (ves) adjacent to enamel matrix deposits (matrix) and newly formed enamel crystals (en). **(B)** is a high magnification image of the initial enamel crystal (en)/matrix (matrix) interface of the same specimen. **(A,B)** were subjected to phosphate buffer at pH 7. **(C)** Initial enamel crystal/matrix interface in a specimen subjected to phosphate buffer at pH 4. Note the intensely contrasted peri-crystalline protein matrix (peri-cryst assembl) adjacent to the newly forming enamel crystals. **(D–F)**. Initial enamel crystal/matrix interface in a specimen subjected to citrate buffer at pH 4. The use of citrate buffer illustrates components of the initial enamel mineral phase, including nanocrystals (nanocrystals), ribbons (nanoribbon), and elongated enamel crystals). Protein assemblies (prot, **(F)** were less exposed than after immersion of the specimen in phosphate buffer. Note the presence of corkscrew-like crystal deformations (def). The scale bar in **(A)** only applies to **(A)**, while the scale bar in **(D)** applies to **(B–F)**.

ameloblastin interaction domain was identified using NMR. Together, these studies provide evidence for a highly acidic microenvironment in the earliest secreted enamel matrix at the ameloblast secretory pole and characterize the effects of such an environment on amelogenin self-assembly, calcium phosphate crystal growth, and amelogenin/ameloblastin interactions.

pH indicator dyes revealed pH values between pH 3 to 4 at the exocytosis site of secretory ameloblasts. This was a remarkable finding as living organisms rarely endure extreme pH values. Exceptions are a few cyanobacteria which live in a pH 2.8–4.5 environment (Steinberg et al., 1998), the mucosal lining of the stomach which tolerates pH 1.5–2.0 gastric acid (Fujimori, 2020), and some of the acidic proteins involved in crystal nucleation such as dentin phosphoprotein (pH 2.67) (Marin and Luquet 2007; Alvares 2014). In our study, the acidic pH zone measured approximately 100 μm in thickness while the thinnest pH microelectrodes available to us were 1 mm in thickness (ThermoFisher Scientific, Carlsbad, CA), rendering pH detection with electrodes beyond detection capabilities (data not shown). Additional studies using quantifiable pH indicators (Damkier et al., 2014) might provide additional means to measure the precise pH of the enamel matrix at this stage. Previous studies have been based on extracted incisors devoid

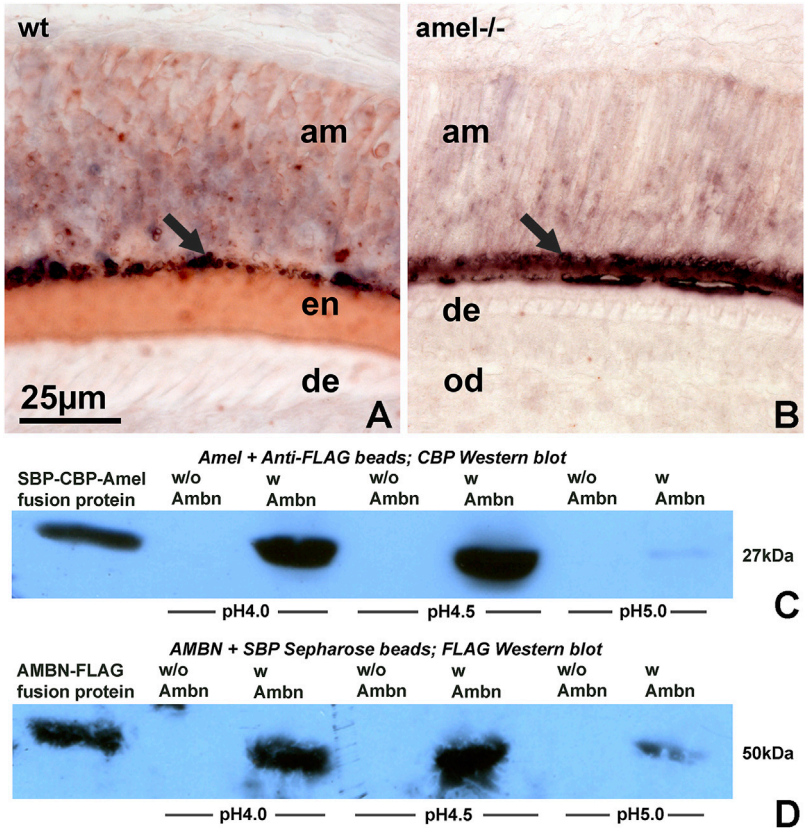

FIGURE 6
Amelogenin and ameloblastin enamel matrix molecules interact at acidic pH. **(A,B)** Double staining for amelogenin (HRP labeling, red color) and ameloblastin (AP labeling, blue/black color) on tissue sections of wild-type **(A)** and amelogenin null **(B)** molars. **(C,D)** Co-precipitation to detect possible interactions between amelogenin and ameloblastin at pH 4, pH 4.5, and pH5. Co-precipitates were either probed with anti-CBP (C, for amelogenin) or with anti-FLAG antibody (D, for ameloblastin). wt = wild-type, amel−/− = amelogenin mutant, am = ameloblasts, en = enamel, de = dentin, od = odontoblasts.

of cells and attached matrix. Studies here have allowed us to visualize the pH at the very narrow 20 um interface between ameloblasts and enamel. According to our micrographs, the zone of highly acidic pH was not only limited to the ameloblast/matrix interface but also included the secretory ameloblast vesicles, likely due to their content of inorganic monophosphate. The narrow confines of the low pH zone may be explained by the high buffering capacity of amelogenin proteins and the abundance of other buffer systems such as carbonate buffers in the early enamel matrix (Lacruz et al., 2010; Bronckers et al., 2012; Varga et al., 2018).

The presence of a thin layer of extremely acidic pH between the pH neutral ameloblasts and the otherwise fairly balanced enamel matrix begs the question whether there would be any functional advantages for such an unusually acidic interface during amelogenesis. Decades of amelogenin protein biochemistry have attested to the high degree of amelogenin solubility at pH 3 and pH 4 (Burgess and MacLaren 1965; Fincham 1968). The present study also has provided evidence for advantageous growth conditions for calcium phosphate and apatite crystals at pH 4. Furthermore, an acidic pH of 2.8 has proven advantageous for the synthesis of apatite crystals (Chen et al., 2006). Finally, electron micrographs presented in this study provide evidence for an enhanced capacity of the enamel crystal-associated enamel protein matrix to adsorb and store phosphate ions for enamel crystal growth. The extreme pH may also play a role in triggering the catalytic activity of MMP20 since metalloproteinases are known to be activated in a pH dependent fashion (Johnson et al., 2000). Amelogenin cleavage at acid pH would remove amelogenin's highly soluble C-terminus, resulting in the formation of insoluble amelogenin assemblies, which then would guide enamel apatite crystal growth through particle attachment (Jokisaari et al., 2019; Pandya and Diekwisch 2021).

Previous studies have demonstrated that the developing enamel matrix is a highly dynamic microenvironment greatly influenced by physico-chemical conditions such as temperature and pH (Diekwisch et al., 1993). In some of these studies, samples were to be prepared at 4°C to avoid the self-assembly and nanosphere formation at 37°C, which were thought to be artifacts at that time (Lyaruu et al., 1982; Lyaruu et al., 1984). In terms of pH, many protein biochemistry and 3D NMR structure studies have been conducted at pH 3 or pH 4 to avoid amelogenin aggregation or self-assembly at neutral pH such as pH 7. As much as these studies have yielded meaningful amelogenin structural data, it has not been clear whether such data were relevant *in vivo* (Delak et al., 2009; Zhang et al., 2011). In the present study we are suggesting that the enamel matrix is secreted at a highly acidic pH during the transitional stage immediately after the exit of enamel proteins from the ameloblast secretory vesicles and prior to the broadening of the enamel matrix for crystal growth. Such acidic conditions would facilitate rapid crystal growth as demonstrated in our study and as described in earlier apatite synthesis studies (Chen et al., 2006) followed by another period of enamel protein matrix self-assembly. Once equilibrated through amelogenin and other buffers, the reconfigured enamel protein matrix would then further define enamel apatite crystal growth and assembly in c-axis direction (Jokisaari et al., 2019; Pandya and Diekwisch 2021).

Changes in pH greatly affected the histidine rich region of the amelogenin coil domain (H47-H69) while the non-LRAP portion of the TRAP domain (AA34-45) emerged as the key sequence motif for amelogenin self-assembly at pH 6. Already the earliest studies in enamel protein chemistry characterized amelogenins as proteins rich in proline and histidine (Eastoe 1979). While much attention has been paid to the abundance of prolines in the amelogenin sequence (Jin et al., 2009), the relatively high number of histidines in the amelogenin molecule has remained enigmatic. Histidine is an essential amino acid uniquely characterized by a side chain pKa close to physiological pH, rendering histidine-rich proteins highly susceptible to changes in environmental pH, which then result in tautomerization or ring flips to interconvert protonated and unprotonated nitrogens (Li and Hong 2011). As a result, histidines often act as molecular switches that introduce conformational changes from simple molecular bonds to large-scale β-sheet-based conformations (Valéry et al., 2015). In terms of amelogenin, changes in pH are bound to affect the protonation of the 13 histidines of the mouse amelogenin and especially of the histidine-rich amelogenin coil region. In a highly acidic environment such as the initial enamel matrix at pH 4, histidine sidechains would be positively charged, resulting in weak intermolecular interactions. When continuous buffering causes the pH to increase to pH 6, about half of the His sidechains become neutral and hydrophobic, resulting in enhanced inter-molecular interactions, which would explain the strong amelogenin self-assembly in the developing enamel matrix as its pH turns to pH6 and above. According to previous studies (Zhang et al., 2011), this self-assembly is mostly facilitated by the α-helix rich amelogenin N-terminus. Data presented here suggest that the non-LRAP portion of the TRAP domain (AA34-45) is the key region involved in the pH associated changes in amelogenin self-assembly. According to our study, increasing pH increased the diameter of self-assembled amelogenin subunits from 2 to 3 nm at pH 5 to approximately 20 nm at pH 7, with a unique elongation phase at pH 6. The small self-assembly subunits at pH 5 might facilitate the assembly of small mineral particles and promote apatite growth through small particle attachment (Jokisaari et al., 2019; Pandya and Diekwisch 2021), while the elongated amelogenin structures at pH 6 are ideally suited to promote crystal elongation.

Our circular dichroism data match the results of earlier studies, illustrating the shallowing of the trough from a globally disordered monomer at low pH to complex amelogenin assembles at physiological pH due to protein assembly (Goto et al., 1993; Lakshminarayanan et al., 2010). ATR-FTIR spectra demonstrated substantial changes from low pH to physiological pH. However, individual spectra differed from previously published spectra (Renugopalakrishnan et al., 1986; Beniash et al., 2012), likely due to differences in sample preparation and experimental setup.

Our data demonstrated that amelogenin and ameloblastin co-localized at the secretory ameloblast cell membrane/enamel matrix interface and strongly interacted at pH 4 and pH 4.5, but no longer at pH 5. Previous studies have demonstrated distinct enamel protein presence at the ameloblast cell membrane (Satchell et al., 2002) and documented that an ameloblastin-rich enamel matrix devoid of amelogenin favors short and randomly oriented apatite crystals (Lu et al., 2011). Ameloblastin has also been shown to interact with lipid membranes and large unilamellar vesicles similar to those found in Tomes' process (Su et al., 2019). Together, these studies in conjunction with our data suggest that ameloblast ameloblastin plays a role in the adhesion of the functional enamel matrix to the ameloblast cell membrane and in the establishment of a proper environment for initial enamel crystal growth and habit.

Data availability statement

The original contributions presented in the study are included in the article/supplementary material, further inquiries can be directed to the corresponding authors.

Ethics statement

The animal study was reviewed and approved by the University of Illinois at Chicago Animal use and care committee.

Author contributions

YZ performed the ameloblastin binding studies, TJ and XL performed the NMR structural studies, MA generated the atomic force microscopy studies, DR participated in the electron microscopy study, WZ and TK performed and interpreted the ATR and CD studies, MP and GG worked on study design and critically revised the manuscript, and TD wrote and conceived the study.

Funding

Generous funding by NIDCR grants DE018900 and UG3/UH3-DE028869 to TGHD is gratefully acknowledged. Invaluable technical contributions from Xu Zhang and Smit Dangaria are greatly appreciated.

Conflict of interest

The authors declare that the research was conducted in the absence of any commercial or financial relationships that could be construed as a potential conflict of interest.

Publisher's note

All claims expressed in this article are solely those of the authors and do not necessarily represent those of their affiliated organizations, or those of the publisher, the editors and the reviewers. Any product that may be evaluated in this article, or claim that may be made by its manufacturer, is not guaranteed or endorsed by the publisher.

References

Alvares, K. (2014). The role of acidic phosphoproteins in biomineralization. *Connect. Tissue Res.* 55, 34–40. doi:10.3109/03008207.2013.867336

Beniash, E., Simmer, J. P., and Margolis, H. C. (2012). Structural changes in amelogenin upon self-assembly and mineral interactions. *J. Dent. Res.* 91, 967–972. doi:10.1177/0022034512457371

Bori, E., Guo, J., Rácz, R., Burghardt, B., Földes, A., Kerémi, B., et al. (2016). Evidence for bicarbonate secretion by ameloblasts in a novel cellular model. *J. Dent. Res.* 95, 588–596. doi:10.1177/0022034515625939

Bromley, K. M., Lakshminarayanan, R., Lei, Y.-P., Snead, M. L., and Moradian-Oldak, J. (2011). Folding, assembly, and aggregation of recombinant murine amelogenins with T21I and P41T point mutations. *Cells Tissues Organs* 194, 284–290. doi:10.1159/000324342

Bronckers, A. L. J. J., Lyaruu, D. M., Bervoets, T. J., Medina, J. F., DenBesten, P., Richter, J., et al. (2012). Murine ameloblasts are immunonegative for Tcirg1, the v-H-ATPase subunit essential for the osteoclast plasma proton pump. *Bone* 50, 901–908. doi:10.1016/j.bone.2011.12.019

Bronckers, A. L. J. J., Lyaruu, D. M., Jalali, R., and DenBesten, P. K. (2016). Buffering of protons released by mineral formation during amelogenesis in mice. *Eur. J. Oral Sci.* 124, 415–425. doi:10.1111/eos.12287

Burgess, R. C., and Maclaren, C. M. (1965). Proteins in developing bovine enamel. *Biochem. J.* 131, 471–484. doi:10.1042/bj1310471

Chen, H., Sun, K., Tang, Z., Law, R. V., Mansfield, J. F., and Clarkson, B. H. (2006). Synthesis of fluorapatite nanorods and nanowires by direct precipitation from solution. *Cryst. Growth Des.* 6, 1504–1508. doi:10.1021/cg0600086

Damkier, H. H., Josephsen, K., Takano, Y., Zahn, D., Fejerskov, O., and Frische, S. (2014). Fluctuations in surface pH of maturing rat incisor enamel are a result of cycles of H^+-secretion by ameloblasts and variations in enamel buffer characteristics. *Bone* 60, 227–234. doi:10.1016/j.bone.2013.12.018

Delaglio, F., Grzesiek, S., Vuister, G. W., Zhu, G., Pfeifer, J., and Bax, A. (1995). NMRPipe: A multidimensional spectral processing system based on UNIX pipes. *J. Biomol. NMR* 6, 277–293. doi:10.1007/BF00197809

Delak, K., Harcup, C., Lakshminarayanan, R., Sun, Z., Fan, Y., Moradian-Oldak, J., et al. (2009). The tooth enamel protein, porcine amelogenin, is an intrinsically disordered protein with an extended molecular configuration in the monomeric form. *Biochemistry* 48, 2272–2281. doi:10.1021/bi802175a

Diekwisch, T., David, S., Bringas, P., Santos, V., and Slavkin, H. C. (1993). Antisense inhibition of AMEL translation demonstrates supramolecular controls for enamel HAP crystal growth during embryonic mouse molar development. *Development* 117, 471–482. doi:10.1242/dev.117.2.471

Diekwisch, T. G., Berman, B. J., Gentner, S., and Slavkin, H. C. (1995). Initial enamel crystals are not spatially associated with mineralized dentine. *Cell. Tissue Res.* 279, 149–167. doi:10.1007/BF00300701

Diekwisch, T. G. (1998). Subunit compartments of secretory stage enamel matrix. *Connect. Tissue Res.* 38, 101–111. doi:10.3109/03008209809017026

Eastoe, J. E. (1979). Enamel protein chemistry--past, present and future. *J. Dent. Res.* 58, 753–764. doi:10.1177/00220345790580022701

Fang, P.-A., Margolis, H. C., Conway, J. F., Simmer, J. P., Dickinson, G. H., and Beniash, E. (2011). Cryogenic transmission electron microscopy study of amelogenin self-assembly at different pH. *Cells Tissues Organs* 194, 166–170. doi:10.1159/000324250

Fincham, A. G. (1968). Electrophoretic and Sephadex gel filtration studies of bovine foetal enamel matrix at acid pH. *Calcif. Tissue Res.* 2, 353–360. doi:10.1007/BF02279223

Fujimori, S. (2020). Gastric acid level of humans must decrease in the future. *World J. Gastroenterol.* 26, 6706–6709. doi:10.3748/wjg.v26.i43.6706

Goto, Y., Kogure, E., Takagi, T., Simoto, S., and Aoba, T. (1993). Molecular conformation of porcine amelogenin in solution: Three folding units at the N-terminal, central, and C-terminal regions. *J. Biochem.* 113, 55–60. doi:10.1093/oxfordjournals.jbchem.a124003

He, X., Wu, S., Martinez-Avila, O., Cheng, Y., and Habelitz, S. (2011). Self-aligning amelogenin nanoribbons in oil-water system. *J. Struct. Biol.* 174, 203–212. doi:10.1016/j.jsb.2010.11.027

Jin, T., Ito, Y., Luan, X., Dangaria, S., Walker, C., Allen, M., et al. (2009). Elongated polyproline motifs facilitate enamel evolution through matrix subunit compaction. *PLoS Biol.* 7, e1000262. doi:10.1371/journal.pbio.1000262

Johnson, L. L., Pavlovsky, A. G., Johnson, A. R., Janowicz, J. A., Man, C. F., Ortwine, D. F., et al. (2000). A rationalization of the acidic pH dependence for stromelysin-1 (Matrix metalloproteinase-3) catalysis and inhibition. *J. Biol. Chem.* 275, 11026–11033. doi:10.1074/jbc.275.15.11026

Jokisaari, J. R., Wang, C., Qiao, Q., Hu, X., Reed, D. A., Bleher, R., et al. (2019). Particle-attachment-mediated and matrix/lattice-guided enamel apatite crystal growth. *ACS Nano* 13, 3151–3161. doi:10.1021/acsnano.8b08668

Lacruz, R. S., Habelitz, S., Wright, J. T., and Paine, M. L. (2017). Dental enamel formation and implications for oral health and disease. *Physiol. Rev.* 97, 939–993. doi:10.1152/physrev.00030.2016

Lacruz, R. S., Nanci, A., Kurtz, I., Wright, J. T., and Paine, M. L. (2010). Regulation of pH during amelogenesis. *Calcif. Tissue Int.* 86, 91–103. doi:10.1007/s00223-009-9326-7

Lacruz, R. S., Smith, C. E., Moffatt, P., Chang, E. H., Bromage, T. G., Bringas, P., et al. (2012). Requirements for ion and solute transport, and pH regulation during enamel maturation. *J. Cell. Physiol.* 227, 1776–1785. doi:10.1002/jcp.22911

Lakshminarayanan, R., Bromley, K. M., Lei, Y-P., Snead, M. L., and Moradian-Oldak, J. (2010). Perturbed amelogenin secondary structure leads to uncontrolled aggregation in amelogenesis imperfecta mutant proteins. *J. Biol. Chem.* 285, 40593–40603. doi:10.1074/jbc.M110.131136

Larsen, M. J., and Nyvad, B. (1999). Enamel erosion by some soft drinks and orange juices relative to their pH, buffering effect and contents of calcium phosphate. *Caries Res.* 33, 81–87. doi:10.1159/000016499

Li, S., and Hong, M. (2011). Protonation, tautomerization, and rotameric structure of histidine: A comprehensive study by magic-angle-spinning solid-state NMR. *J. Am. Chem. Soc.* 133, 1534–1544. doi:10.1021/ja108943n

Lowenstam, H. A. (1981). Minerals formed by organisms. *Science* 211, 1126–1131. doi:10.1126/science.7008198

Lu, J. X., Xu, Y. S., Buchko, G. W., and Shaw, W. J. (2013). Mineral association changes the secondary structure and dynamics of murine amelogenin. *J. Dent. Res.* 92, 1000–1004. doi:10.1177/0022034513504929

Lu, X., Ito, Y., Kulkarni, A., Gibson, C., Luan, X., and Diekwisch, T. G. H. (2011). Ameloblastin-rich enamel matrix favors short and randomly oriented apatite crystals. *Eur. J. Oral Sci.* 119 (1), 254–260. doi:10.1111/j.1600-0722.2011.00905.x

Luan, X., Ito, Y., Holliday, S., Walker, C., Daniel, J., Galang, T. M., et al. (2007). Extracellular matrix-mediated tissue remodeling following axial movement of teeth. *J. Histochem. Cytochem.* 55, 127–140. doi:10.1369/jhc.6A7018.2006

Lyaruu, D. M., Belcourt, A., Fincham, A. G., and Termine, J. D. (1982). Neonatal hamster molar tooth development: Extraction and characterization of amelogenins, enamelins, and soluble dentin proteins. *Calcif. Tissue Int.* 34, 86–96. doi:10.1007/BF02411214

Lyaruu, D. M., Wöltgens, J. H., and Bervoets, T. J. (1984). Effect of 1-p-bromotetramisole on mineralization of hamster tooth germs *in vitro*: A light and electron microscopic study. *J. Biol. Buccale* 12, 287–296.

Marin, F., and Luquet, G. (2007). *Unusually acidic proteins in biomineralization*. Weinheim, Germany: Wiley.

Moradian-Oldak, J., Leung, W., and Fincham, A. G. (1998). Temperature and pH-dependent supramolecular self-assembly of amelogenin molecules: A dynamic light-scattering analysis. *J. Struct. Biol.* 122, 320–327. doi:10.1006/jsbi.1998.4008

Pandya, M., and Diekwisch, T. G. H. (2021). Amelogenesis: Transformation of a protein-mineral matrix into tooth enamel. *J. Struct. Biol.* 213, 107809. doi:10.1016/j.jsb.2021.107809

Pandya, M., and Diekwisch, T. G. H. (2019). Enamel biomimetics-fiction or future of dentistry. *Int. J. Oral Sci.* 11, 8. doi:10.1038/s41368-018-0038-6

Pandya, M., Liu, H., Dangaria, S. J., Zhu, W., Li, L. L., Pan, S., et al. (2017). Integrative temporo-spatial, mineralogic, spectroscopic, and proteomic analysis of postnatal enamel development in teeth with limited growth. *Front. Physiol.* 8, 793. doi:10.3389/fphys.2017.00793

Rao, A., and Cölfen, H. (2016). On the biophysical regulation of mineral growth: Standing out from the crowd. *J. Struct. Biol.* 196, 232–243. doi:10.1016/j.jsb.2016.03.021

Renugopalakrishnan, V., Strawich, E. S., Horowitz, P. M., and Glimcher, M. J. (1986). Studies of the secondary structures of amelogenin from bovine tooth enamel. *Biochemistry* 25, 4879–4887. doi:10.1021/bi00365a023

Robinson, C., Connell, S., Brookes, S. J., Kirkham, J., Shore, R. C., and Smith, D. A. M. (2005). Surface chemistry of enamel apatite during maturation in relation to pH: Implications for protein removal and crystal growth. *Arch. Oral Biol.* 50, 267–270. doi:10.1016/j.archoralbio.2004.11.017

Ryu, O. H., Hu, C. C., Zhang, C., Qian, Q., Moradian-Oldak, J., Fincham, A. G., et al. (1998). Proteolytic activity of opossum tooth extracts. *Eur. J. Oral Sci.* 106 (1), 337–344. doi:10.1111/j.1600-0722.1998.tb02195.x

Sasaki, S., Takagi, T., and Suzuki, M. (1991). Cyclical changes in pH in bovine developing enamel as sequential bands. *Arch. Oral Biol.* 36, 227–231. doi:10.1016/0003-9969(91)90090-h

Satchell, P. G., Anderton, X., Ryu, O. H., Luan, X., Ortega, A. J., Opamen, R., et al. (2002). Conservation and variation in enamel protein distribution during vertebrate tooth development. *J. Exp. Zool.* 294, 91–106. doi:10.1002/jez.10148

Shaw, W. J., Tarasevich, B. J., Buchko, G. W., Arachchige, R. M. J., and Burton, S. D. (2020). Controls of nature: Secondary, tertiary, and quaternary structure of the enamel protein amelogenin in solution and on hydroxyapatite. *J. Struct. Biol.* 212, 107630. doi:10.1016/j.jsb.2020.107630

Smith, C. E. (1998). Cellular and chemical events during enamel maturation. *Crit. Rev. Oral Biol. Med.* 9, 128–161. doi:10.1177/10454411980090020101

Smith, C. E., Chong, D. L., Bartlett, J. D., and Margolis, H. C. (2005). Mineral acquisition rates in developing enamel on maxillary and mandibular incisors of rats and mice: Implications to extracellular acid loading as apatite crystals mature. *J. Bone Min. Res.* 20, 240–249. doi:10.1359/JBMR.041002

Steinberg, C. E. W., Schäfer, H., and Beisker, W. (1998). Do acid-tolerant cyanobacteria exist? *Acta hydrochim. hydrobiol.* 26, 13–19. doi:10.1002/(SICI)1521-401X(199801)26:1<13:AID-AHEH13>3.0.CO;2-V

Su, J., Kegulian, N. C., Arun Bapat, R., and Moradian-Oldak, J. (2019). Ameloblastin binds to phospholipid bilayers via aHelix-forming motif within the sequence encoded by exon 5. *ACS Omega* 4, 4405–4416. doi:10.1021/acsomega.8b03582

Takano, Y., Matsuo, S., Wakisaka, S., Ichikawa, H., Nishikawa, S., and Akai, M. (1988). Cyclic changes in the properties of maturing enamel in the bovine permanent incisor as revealed by glyoxal bis (2-hydroxyanil) staining. *Arch. Oral Biol.* 33, 231–236.

Tye, C. E., Sharma, R., Smith, C. E., and Bartlett, J. D. (2010). Altered ion-responsive gene expression in Mmp20 null mice. *J. Dent. Res.* 89, 1421–1426. doi:10.1177/0022034510384625

Valéry, C., Deville-Foillard, S., Lefebvre, C., Taberner, N., Legrand, P., Meneau, F., et al. (2015). Atomic view of the histidine environment stabilizing higher-pH conformations of pH-dependent proteins. *Nat. Commun.* 6, 7771. doi:10.1038/ncomms8771

Varga, G., DenBesten, P., Rácz, R., and Zsembery, Á. (2018). Importance of bicarbonate transport in pH control during amelogenesis – need for functional studies. *Oral Dis.* 24, 879–890. doi:10.1111/odi.12738

Veis, A., and Dorvee, J. R. (2013). Biomineralization mechanisms: A new paradigm for crystal nucleation in organic matrices. *Calcif. Tissue Int.* 93, 307–315. doi:10.1007/s00223-012-9678-2

Walker, C. G., Ito, Y., Dangaria, S., Luan, X., and Diekwisch, T. G. H. (2008). RANKL, osteopontin, and osteoclast homeostasis in a hyperocclusion mouse model. *Eur. J. Oral Sci.* 116, 312–318. doi:10.1111/j.1600-0722.2008.00545.x

Wang, X., Suzawa, T., Ohtsuka, H., Zhao, B., Miyamoto, Y., Miyauchi, T., et al. (2010). Carbonic anhydrase II regulates differentiation of ameloblasts via intracellular pH-dependent JNK signaling pathway. *J. Cell. Physiol.* 225, 709–719. doi:10.1002/jcp.22267

Wiedemann-Bidlack, F. B., Beniash, E., Yamakoshi, Y., Simmer, J. P., and Margolis, H. C. (2007). pH triggered self-assembly of native and recombinant amelogenins under physiological pH and temperature *in vitro*. *J. Struct. Biol.* 160, 57–69. doi:10.1016/j.jsb.2007.06.007

Zhang, X., Ramirez, B. E., Liao, X., and Diekwisch, T. G. H. (2011). Amelogenin supramolecular assembly in nanospheres defined by a complex helix-coil-PPII helix 3D-structure. *PLoS One* 6, e24952. doi:10.1371/journal.pone.0024952

frontiers | Frontiers in Physiology

TYPE Original Research
PUBLISHED 14 December 2022
DOI 10.3389/fphys.2022.1063970

OPEN ACCESS

EDITED BY
Janet Moradian-Oldak,
University of Southern California,
United States

REVIEWED BY
Garry W. Buchko,
Pacific Northwest National Laboratory
(DOE), United States
Changyu Shao,
Zhejiang University, China

*CORRESPONDENCE
Jun-xia Lu,
lujx@shanghaitech.edu.cn
Stefan Habelitz,
stefan.habelitz@ucsf.edu

SPECIALTY SECTION
This article was submitted to
Craniofacial Biology and
Dental Research,
a section of the journal
Frontiers in Physiology

RECEIVED 07 October 2022
ACCEPTED 02 December 2022
PUBLISHED 14 December 2022

CITATION
Zhang J, Bai Y, Wang J, Li B, Habelitz S
and Lu J-x (2022), Calcium interactions
in amelogenin-derived
peptide assembly.
Front. Physiol. 13:1063970.
doi: 10.3389/fphys.2022.1063970

Calcium interactions in amelogenin-derived peptide assembly

Jing Zhang[1,2,3], Yushi Bai [4], Jian Wang[1], Bing Li[1], Stefan Habelitz[4]* and Jun-xia Lu[1]*

[1]School of Life Science and Technology, ShanghaiTech University, Shanghai, China, [2]University of Chinese Academy of Sciences, Beijing, China, [3]State Key Laboratory of Molecular Biology, CAS Center for Excellence in Molecular Cell Science, Shanghai Institute of Biochemistry and Cell Biology, Chinese Academy of Sciences, Shanghai, China, [4]Department of Preventative and Restorative Dental Sciences, School of Dentistry, University of California, San Francisco, San Francisco, CA, United States

Phosphorylation of serine residues has been recognized as a pivotal event in the evolution of mineralized tissues in many biological systems. During enamel development, the extracellular matrix protein amelogenin is most abundant and appears to be critical to the extreme high aspect ratios (length:width) of apatite mineral fibers reaching several millimeters in larger mammalian teeth. A 14-residue peptide (14P2, residues Gly8 to Thr21) was previously identified as a key sequence mediating amelogenin assembly formation, the domain also contains the native single phosphoserine residue (Ser16) of the full-length amelogenin. In this research, 14P2 and its phosphorylated form (p14P2) were investigated at pH 6.0 with various calcium and phosphate ion concentrations, indicating that both peptides could self-assemble into amyloid-like conformation but with differences in structural details. With calcium, the distance between ^{31}P within the p14P2 self-assemblies is averaged to be 4.4 $\pm$ 0.2Å, determined by solid-state NMR ^{31}P PITHIRDS-CT experiments. Combining with other experimental results, solid-state Nuclear Magnetic Resonance (SSNMR) suggests that the p14P2 self-assemblies are in parallel in-register β-sheet conformation and divalent calcium ions most likely connect two adjacent peptide chains by binding to the phosphate group of Ser16 and the carboxylate of Glu18 side-chain. This study on the interactions between calcium ions and amelogenin-derived peptides provides insights on how amelogenin may self-assemble in the presence of calcium ions in early enamel development.

KEYWORDS

amelogenin, assembly, mineral ions, phosphorylation, SSNMR

1 Introduction

In natural proteins, phosphorylated serine often plays a role in binding mineral ions (Addison et al., 2013). For example, Dentin Phosphoprotein (DPP) and Dentin Matrix Protein-1 (DMP-1) contain a large number of aspartic acids and phosphoserines (Alvares, 2014) and the interaction with calcium serves as the first step to recruit the mineral ions for subsequent mineralization of collagen fibrils (Prasad et al., 2010). Another example is

the silk spun by caddisfly underwater which contains phosphorylated serine-rich motifs that enable the silk to adhere to rocks (Addison et al., 2013). Amelogenin is the most abundant protein in the developing enamel matrix. It is believed that the protein matrix guides the mineral crystal deposits and results in the highly organized structure of apatite nanofibers which provide tooth enamel with extraordinary mechanical properties (Lacruz et al., 2017). However, how the protein matrix is organized in enamel mineral nucleation is still a debate. It has been shown that amelogenin could assemble into aggregates with β-amyloid properties in the presence of calcium and phosphate ions (Martinez Avila et al., 2012; Carneiro et al., 2016; Engelberth et al., 2018; Ma et al., 2019; Zhang et al., 2020). A short sequence at amelogenin N-terminal domain from residue Gly8 to Thr21 (GHPGYINFSYEVLT, 14P2, Figure 1A) has been recognized for having a strong propensity to self-associate into amyloids (Carneiro et al., 2016). The residue numbering is based on the 175-residue full-length human amelogenin (H175). NMR studies on protein aggregates formed by recombinant full-length human amelogenin also identified a region with β-strand secondary structure that overlap with 14P2 (Zhang et al., 2020). Interestingly, the same segment contains the single phosphorylated site (Ser16) in the native full-length human amelogenin (Takagi et al., 1984; Fincham et al., 1999). Different from the high calcium-binding ability provided by the dense population of phosphorylated serine in local regions in silk protein of caddisfly and in phosphoproteins of bone and dentin with dozens of phosphorylation site, the single phosphorylated residue in amelogenin is expected to play less of a role in directing enamel mineralization (Wiedemann Bidlack et al., 2011; Carneiro et al., 2016; Shin et al., 2020; Stifler et al., 2022), but may be critical in regulating protein structures and protein-protein interactions (Le Norcy et al., 2011; Wiedemann Bidlack et al., 2011; Carneiro et al., 2016). It was reported that the ratio of phosphorylated to all (phosphorylated + non-phosphorylated) amelogenin and its fragments was highest in superficial secretory and early maturation stage enamel and dephosphorylation of amelogenin was important for enamel maturation when the amorphous calcium phosphate gradually transits to crystalline apatite (Green et al., 2019).

Although amyloid is usually associated with cell toxicity and neurodegeneration, many functional amyloids have also been discovered these years playing key roles in regulating biosynthetic pathways (Fowler et al., 2007; Wu et al., 2021). The amyloid-like assemblies formed by the full-length amelogenin have proved to be able to template apatite crystal mineralization *in vitro* (Bai et al., 2020; Akkineni et al., 2022). In this work, the self-assembly of 14P2 and phosphorylated 14P2 at Ser16 (p14P2) were investigated in different solution conditions with variations in calcium and phosphate ion concentrations, since both ions are essential to enamel formation (Aoba and Moreno, 1987) and the concentrations of ions may have an effect on the status of protein assembly (Martinez Avila et al., 2012; Carneiro et al., 2016; Engelberth et al., 2018). Solid-state Nuclear Magnetic Resonance (SSNMR) is a powerful technique that is capable of studying proteins in non-crystalline solid or gel state, which is not possible with traditional protein structural characterization methods, such as x-ray crystallization and solution-NMR. NMR chemical shifts are sensitive to the nuclei's coordination states and the local structure. SSNMR homonuclear dipolar recoupling technique (PITHIRDS-CT (Tycko, 2007)) can be used to obtain the distance information between the same type of nuclei, such as the distance between two neighboring ^{13}C nuclei. SSNMR heteronuclear dipolar recoupling technique (REDOR (Gullion and Schaefer, 1989) can be used to obtain the distance information between two different types of nuclei, such as the distance between one ^{13}C nucleus and one ^{15}N nucleus. Here, SSNMR was utilized to study the assembled structures of 14P2 and p14P2 in combination with x-ray diffraction (XRD) and transmission electron microscopy (TEM) to gain a better understanding of calcium interations in amelogenin-derived peptide assembly.

2 Experimental section

2.1 Peptides self-assembly sample preparation

Peptide 14P2 (GHPGYINFSYEVLT) containing the sequence of the N-terminal domain (residues 8–21) of the human full-length amelogenin were synthesized. One site-specific isotopically labeled 14P2 peptide was synthesized, with labeling at Ile13 ^{13}CO and Val19 ^{15}NH. 14P2 peptide was purchased at ELIM Biopharmaceuticals, Inc. (CA, United States) and GL Biochem (Shanghai) Ltd. The peptide was dissolved in 0.01 M HCl first and diluted to a final concentration of 1 mg/ml using an aqueous solution containing different concentration of $CaCl_2$ and KH_2PO_4. The experiments were performed on three conditions with the final calcium and phosphate ion concentration: 1) 33.4 mM calcium and 20.9 mM phosphate ions (high concentration condition); 2) 3.3 mM calcium and 2.1 mM phosphate ions (low concentration condition); 3) 33.4 mM calcium ions. Finally, the solution pH was slowly adjusted to 6.0 by adding 0.1 M KOH and the solution was incubated at 37°C for more than a week for peptide self-assembly for the first two samples. The last sample was incubated for only 2 days. Before the experiment, all the solution was purged using N_2 gas about 2 h. During the experiment N_2 gas was purged directly to the surface of the solution.

Meanwhile, the peptide with a phosphorylated Ser 16 (p14P2) was also synthesized and purchased from Elim Biopharmaceuticals, Inc. (CA, United States) and

ChinaPeptides (Shanghai) Ltd. Five samples of peptide self-assembly were prepared with different solution conditions: 1) high concentration of calcium ions (33.4 mM) at pH 6.0; 2) low concentration of calcium ions (3.3 mM) at pH 6.0; 3) low concentration of calcium (3.3 mM) and phosphate ions (2.1 mM) at pH 6.0; 4) in absence of calcium and phosphate ions at pH 6.0; 5) 3.3 mM calcium ions at pH 7.5. The salt concentrations and the assembly conditions were according to the literature (Martinez Avila et al., 2012; Carneiro et al., 2016) and modified slightly.

2.2 X-ray diffraction (XRD)

All samples were harvested using centrifugation at 259,000 g for 1 h at room temperature (Optima Max-TL, BECKMAN COULTER, Bera, CA, United States). The precipitation contained the peptide self-assemblies aggregates in nanometer size with or without the mineral crystals. The sample was mounted on the XRD sample loop. The experiment was measured using a single crystal X-ray diffraction instrument (Bruker D8 VENTURE, Bruker, Karlsruhe, Germany) with Cu Kα radiation at 0.154184 nm wavelength operating at an acceleration voltage of 50 kV and a current of 1 mA at 298 K. The exposure time was varied from 30 to 60 s with 50 mm distance from sample to the detector. The acquired images were processed with the adxv.x86_64RHEL6 program (Scripps Research Institute, La Jolla, CA, United States). And the data were further processed and integrated to be transformed into the powder pattern with X'Pert HighScore Plus software (PANalytical B.V., Almelo, Netherlands). The structural data of crystals hydroxyapatite (HAP) and brushite were taken from the ICSD database (The Inorganic Crystal Structure Database HAP-169498-ICSD, brushite-16132-ICSD).

2.3 Transmission electron microscopy (TEM)

The samples incubated for more than 7 days were taken out periodically and observed using TEM. 5 μL drop of sample solution was pipetted onto a carbon-coated copper grid (300 meshes, Beijing Zhongjingkeyi Technology Co., Ltd., Beijing, China) for 1 min and dried with filter paper. Then the grid was quickly washed off with three drops of Milli-Q water. Subsequently, the grid was stained with 5 μL of 2% uranyl acetate in water (w/v) for 10 s and the stain solution was blotted away quickly with filter paper. To get a better staining effect, another drop of 5 μL 2% uranium acetate was loaded to the grid for 1 min and washed off with one drop of water again. Finally, the grid was dried in the air. The grids were imaged with Talos L120C Transmission Electron Microscope (FEI company, Brno, Czech Republic) at 120 kV.

2.4 Solid-state NMR experiments

All NMR experiments were carried out on a 16.4T (700 MHz, ^{1}H frequency) Bruker AVANCE NEO spectrometer. ^{13}C–^{13}C and ^{13}C-^{15}N correlation spectra were collected with a 3.2 mm triple channel HCN Bruker probe, while a 3.2 mm HCP MAS probe was utilized to perform experiments involving ^{31}P. Chemical shifts were externally referenced to DSS (40.48 ppm, using the ^{13}C downfield peak of adamantane) for ^{13}C. ^{31}P chemical shifts were indirectly referenced relative to 85% H_3PO_4 (0 ppm), calculated with the ^{31}P/^{1}H chemical shift ratio of 0.404807420. All the experiments were collected with a 2 s recycle delay.

^{1}H-^{13}C cross-polarization (CP/MAS) experiments were performed on the peptide samples with natural abundance ^{13}C under 15 kHz Magic Angle Spinning (MAS). The experiments were conducted at 273K or 288K. The CP contact time was 1.6 m with ^{1}H fields of 86.56 kHz, and the ^{1}H 90° pulse was 3.1 μs. During the acquisition, SPINAL-64 (Fung et al., 2000) ^{1}H decoupling was also applied with a ^{1}H field strength of 80.65 kHz.

1D ^{1}H-^{31}P CP and 2D ^{1}H-^{31}P HETCOR (Shi et al., 2013) experiments were acquired for all the samples at 273K with MAS speed of 20 kHz except for the condition in the absence of either ions. For that sample, the spectra were obtained with 15 kHz. The CP contact time was 1.7 ms with ^{1}H fields of 89.07 kHz, and the ^{1}H 90° pulse was 3.1 μs. Decoupling of ^{1}H was applied at a field of 80.65 kHz during acquisition. For extracting the ^{31}P chemical shift anisotropy (CSA) parameters of p14P2 samples, the 1D ^{1}H-^{31}P CP spectra were obtained at multiple MAS speeds of 0, 5, and 15 kHz. 1D ^{31}P spectra were analyzed using the program DMFIT (Massiot et al., 2002) with the Herzfeld-Berger convention (Herzfeld and Berger, 1980). The principle elements of the chemical shift tensor are the isotropic value (δ_{iso}), the asymmetry (dCS) and anisotropic (etaCS) parameters defined by $\delta_{iso} = 1/3\ (\delta_{33}+\delta_{22}+\delta_{11})$, dCS $=(\delta_{33}-\delta_{iso})$ and etaCS$=(\delta_{22}-\delta_{11})/(\delta_{33}-\delta_{iso})$, respectively.

The intermolecular ^{13}C-^{15}N distance was measured with REDOR (Gullion and Schaefer, 1989) experiment at MAS speed of 10 kHz at 268K. The experiments were tested with the lengths of 90° pulse for ^{1}H, ^{13}C and ^{15}N 3 μs, 3.5μs and 4.6μs, respectively. During the recoupling, XY-8 phase cycling was applied. ^{1}H decoupling field strength was 83 kHz with SPINAL-64 decoupling. The data points were acquired at the dephasing time of 1, 5, and 100 ms. The corresponding dephased (S) signal and the reference (S0) signal were then calculated to get the ratio S/S0 for obtaining the ^{13}C-^{15}N distance.

The intermolecular ^{13}C-^{13}C and ^{31}P-^{31}P distances were obtained using PITHIRDS-CT (Tycko, 2007) experiments with 20 kHz MAS at 273 K. The length of π pulse for dipole-dipole recoupling was one-third of the rotor period, 16.67 μs. ^{1}H decoupling fields was 80.65 kHz both during the recoupling period and the signal detection period. PITHIRDS recoupling was applied for a total of 19.2 ms in the ^{13}C homonuclear dipolar experiments with ^{13}C rf fields of 30 kHz. And PITHIRDS

TABLE 1 Protein self-assemblies, conditions and their structural properties.

Conditions	14P2	p14P2
33.4 mM [Ca^{2+}] and 20.9 mM [P], pH = 6.0	Big bundles, parallel in-register amyloid	
33.4 mM [Ca^{2+}], pH = 6.0	Twisted and flat fibrils, bundled, off-register amyloid	Twisted fibrils, bundled, in-register amyloid
3.3 mM [Ca^{2+}] and 2.1 mM [P], pH = 6.0	Flat, shorter, ribbon-like, off-register amyloid	Twisted fibrils, bundled amyloid
3.3 mM [Ca^{2+}], pH = 6.0		Twisted fibrils, bundled, in-register amyloid
3.3 mM [Ca^{2+}], pH = 7.5		Twisted fibrils, bundled
0 mM [Ca^{2+}] and 0 mM [P], pH = 6.0		Sphere

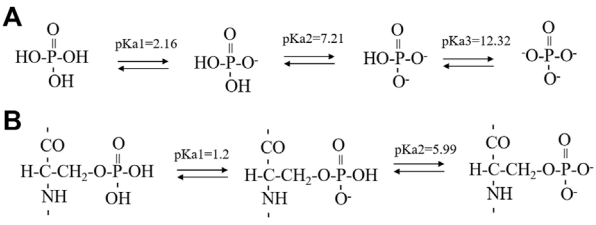

SCHEME 1
The successive steps of deprotonation of phosphoric acid **(A)** and phosphoserine **(B)**. The pKa1 value of phosphoserine was predicated by the Calculators Predictors from Chemaxon (https://chemaxon.com/products/calculators-and-predictorspka) while the pKa2 value of phosphoserine was obtained from literature using a five-residue peptide in a random conformation.

recoupling was applied for a total of 9.6 ms in the ^{31}P homonuclear dipolar experiments with ^{31}P rf fields of 30 kHz. The initial peak intensity was acquired at the effective homonuclear dipolar recoupling time of 0 ms. The peak intensity would decay as a function of the effective recoupling time. The acquired data were further processed to fit the numerical simulations using the software SIMPSON (Bak et al., 2011) to get the homonuclear distance.

3 Results

3.1 14P2 peptide formed an amyloid with varied conformations influenced by the solution conditions

Synthetic 14P2 peptide, GHPGYINFSYEVLT, was first studied at two different solution conditions at pH 6.0. High-ion concentration condition contained 33.4 mM calcium and 20.9 mM phosphate ions, while the low-ion concentration was 3.3 mM calcium and 2.1 mM phosphate ions (Table 1). The high-ion concentration is used in order to determine a clear effect of ions on protein interactions and self-assembly structures, while the low-ion cencentraion is only slightly saturated towards brushite and close to the saturation level reported for the enamel fluid in the early secretory stage of porcine amelogenesis (Aoba and Moreno, 1987). 14P2 solution remained clear at low pH and turned cloudy at pH 6.0 (Supplementary Figure S1A). As previously shown, a pH of 6.0 or lower enhances ribbon formation and prevents spontaneous mineral precipitation. The Ka2 of phosphoric acid is $10^{-7.21}$. At pH 6.0, the more acidic form [$H_2(PO_4)^-$] is prevelant but still solutions with high-ion concentration are saturated for brushite ($CaHPO_4{\cdot}2H_2O$, Ksp = $10^{-6.60}$) (Scheme 1A, Supplementary Table S1 showed a Table of degree of saturation for two minerals). The cloudiness of both solution increased after several days of incubation at 37°C, but no mineral salt precipitations were visible by eye. More than 90% peptide would be in the pellets after centrifugation for both conditions, judged by the UV reading from the supernatant. The TEM images of both sample suspensions are displayed in Figures 1B, D. For the high salt condition, the image showed thick and big bundles of assemblies. For the low salt condition, it showed flat ribbon-like structures formed by the laterally associated thin filaments. No apparent twist could be observed in the assemblies for either sample. The XRD images of the total aggregates obtained by centrifugation were displayed in Figures 1C, E, showing two diffraction rings corresponding to 4.7 and 10.1 Å, the typical protein amyloid diffraction pattern. Therefore, 14P2 peptide assembled into amyloid structures at both the high-ion concentration and low-ion concentration conditions. However, the XRD image for the high-ion concentration condition was dominated by strong crystalline mineral diffractions, obscuring a clear observation of the protein amyloid diffraction. The mineral diffraction pattern of the high-ion concentration sample was consistent with the formation of brushite ($CaHPO_4{\cdot}2H_2O$) (Figure 1F), consistent with the theoretical predication described above. However, no separate mineral particles could be observed by eye or TEM, suggesting the peptide binds tightly with the minerals forming organic-inorganic complexes. The XRD image for the low-salt condition was dominated by the peptide assembly diffraction, only showing very weak mineral diffraction peaks (Figure 1F, dark arrow), whereas the 1D ^{1}H-^{31}P cross polarization (CP)

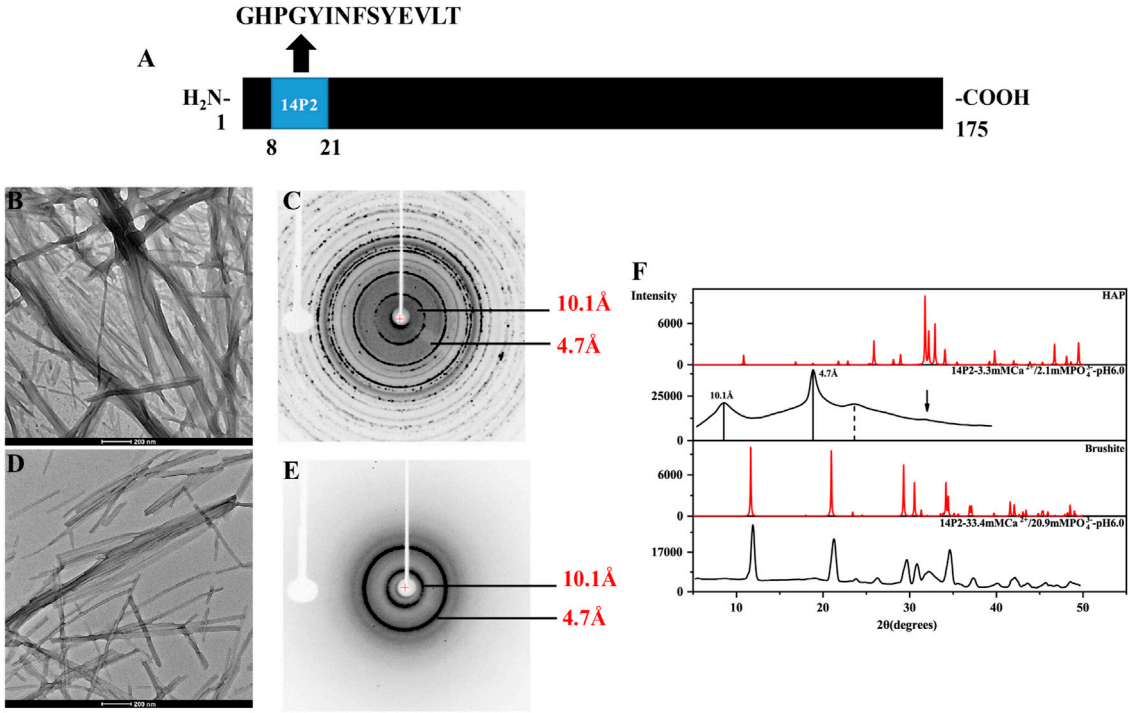

FIGURE 1
TEM images and the X-ray diffraction of the 14P2 self-assembly formed at pH 6.0 with different concentration of calcium and phosphate ions. **(A)** The location of 14P2 sequence in H175; **(B,C)** were obtained for the sample prepared in the presence of high concentration of calcium (33.4 mM) and phosphate ions (20.9 mM), **(D,E)** were obtained for the sample prepared in the presence of low concentration of calcium (3.3 mM) and phosphate ions (2.1 mM). For **(B)**, aliquots of sample suspension were taken for TEM after the peptide was incubated in the solution for 12 days; For **(D)**, the peptide was incubated for 9 days before aliquots of solution was taken for TEM; **(C,E)** were the X-ray diffraction images of 14P2 assembly, all aggregates were collected by centrifugation. The marked rings indicate the equatorial and meridional diffractions at 10.1 and 4.7 Å, respectively. **(C)** Also displayed many other Debye rings, indicating mineral salt formation; **(F)** comparison of the powder diffractogram of the peptide 14P2 assembly with the crystal hydroxyapatite (HAP) and brushite. The arrow indicated a small mineral diffraction peak for the sample prepared at low concentration of ions.

NMR spectrum of the sample pellet showed ^{31}P mineral signals at 0.6 ppm and 2.9 ppm, indicating also the mineral formation (Supplementary Figure S2A). A 3.8 Å diffraction peak in Figures 1E, F was also observed, which was not identified. The presence of bisphosphonates was attributed to this diffraction peak in a previous publication (Sanii et al., 2014). Without phosphate ions, 14P2 can assemble at pH 6.0 in the presence of 33.4 mM calcium ions. The TEM images were obtained only after 2 days' incubation, displaying both twisted and not twisted fibrils (Supplementary Figure S3).

In order to obtain more detailed structural information on the amyloid fibrils, the site-selective isotopically labeled peptides were synthesized for distance measurement using solid-state NMR. Since it was unknown whether the peptide adopted a parallel or antiparallel β-sheet conformation, two labels were utilized, one at Ile13 carbonyl carbon and the other at Val19 nitrogen, respectively (GHPGY(I^{13}CO)NFSYE (V^{15}N) LT). We hypothesized that if the peptide formed a parallel conformation, ^{13}C-^{13}C distance could be determined using solid-state NMR PITHIRDS-CT measurement (the detection limit is less than 8Å). On the other hand, if the peptide adopted an antiparallel conformation, the intermolecular ^{13}C-^{15}N distance may be within the range to be determined by solid-state NMR REDOR measurement (the detection limit is less than 7Å). Our results indicated that ^{13}C-^{15}N distance was too far to be determined for the conditions with both calcium and phosphate ions, however, ^{13}C–^{13}C distances were able to be determined for the two samples (Figure 2A). For condition 33.4 mM calcium ions without phosphate, only PITHIDRS-CT experiment was carried out. Our results showed the intermolecular I^{13}CO distance was 4.4 ± 0.4Å for 14P2 peptide assemblies obtained at 33.4 mM calcium and 20.9 mM phosphate, 6.0 ± 0.6Å for assemblies prepared at 33.4 mM calcium without phosphate while the distance was 6.6 ± 0.4Å for the peptide assemblies obtained at 3.3 mM calcium and 2.1 mM phosphate. The distance was obtained by fitting the experimental data to the simulation values assuming ^{13}C atoms were in a linear arrangement in the peptide assemblies with only a single distance. The 4.4 ± 0.4Å distance was close to the 4.7 Å obtained from XRD diffraction, consistent with an in-register

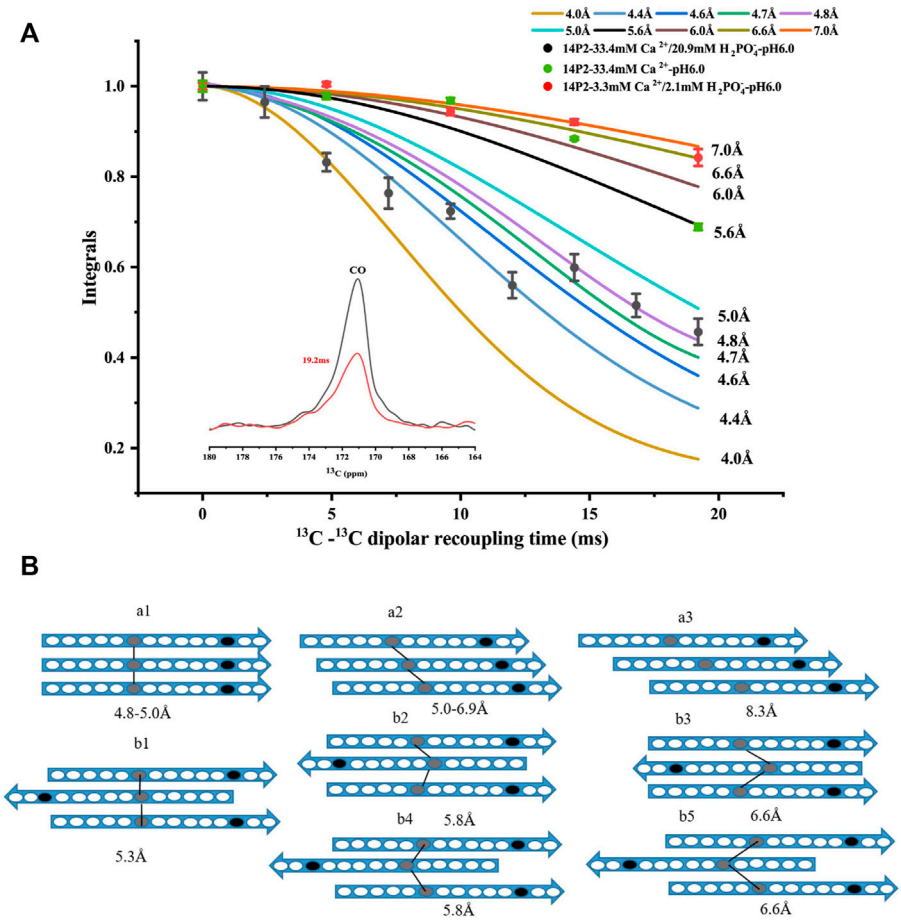

FIGURE 2
(A) ^{13}C PITHIRDS-CT experiments measuring the intermolecular ^{13}C-^{13}C distances of the 14P2 assemblies. The 14P2 Ile13 ^{13}CO and Val19 ^{15}N were labeled for the samples with both calcium and phosphate ions. Only Ile13 ^{13}CO was labeled for the sample with calcium ions but no phosphate. Comparison with the numerical simulations confirmed the 14P2 assemblies formed in the presence of 33.4 mM calcium and 20.9 mM phosphate adopted in-register parallel β-sheet structure with the intermolecular distance of 4.4 ± 0.4 Å, while the peptide assemblies formed in the low ion concentration displayed an intermolecular 13C-13C distance of 6.6 ± 0.4 Å. For 33.4 mM calcium without phosphate, the distance is 6.0 ± 0.6 Å. Each data point was taken by averaging of 2048 scans (1 h 9 min) for samples with both calcium and phosphate ions while 4000 scans (2 h 11 min) for 14P2 assembly formed with only calcium ions. **(B)** Structural models of the peptide assembly in parallel β-sheet conformation (a models) or antiparallel β-sheet conformation (b models), where gray oval represents Ile13 and black oval represents Val19. The lines were only shown for the distances within the SSNMR detection limits. The distances on the model were obtained from abeta fibrils in supplement Figure 4. Model a1 fit the distance of 4.4 ± 0.4 Å for the high-ion concentration condition (33.4 mM calcium and 20.9 mM phosphate) and model a2, b1–b5 fit the experimental constraints for 6.0 ± 0.6 Å or 6.6 ± 0.4 Å ambiguously.

parallel *β*-sheet conformation for the high salt concentration. Using the published A*β* fibril structure as a model (Supplementary Figure S4A), the parallel in-register structure (pdb:2LMN) displays a distance of 4.8–5.0 Å for two corresponding carbonyl carbon atoms at the adjacent peptides. For one-residue off-register parallel structure, there are two possibilities on the distance (5.07 Å and 6.84 Å between residue i and i+1 in this example). The schematic models were shown in Figure 2B, where model (a1) represented the in-register parallel *β*-sheet structure that fit the data best. However, the 6.0 ± 0.6Å or 6.6 ± 0.4Å distance was different from the XRD result. It indicated that although the peptide assemblies formed amyloid-like conformation, the backbone ^{13}CO-^{13}CO distance for Ile13 was different from the distance between two adjacent *β*-strands. It fit the (a2) model in Figure 2B assuming a parallel *β*-sheet structure. But it was also possible to construct from these data an antiparallel structure. An antiparallel A*β* fibril structure is shown in Supplementary Figure S4B (pdb:2LNQ), which is a structure aligned at residue i. It showed similar ^{13}CO-^{13}CO distances (5.3Å–6.6Å) between residue i and i-2, residue i and i-1 and residue i and i. But the difference in the distances was not significant for us to support a confident structural model. Therefore, the registry was ambigious for the antiparallel case. We listed all the possible

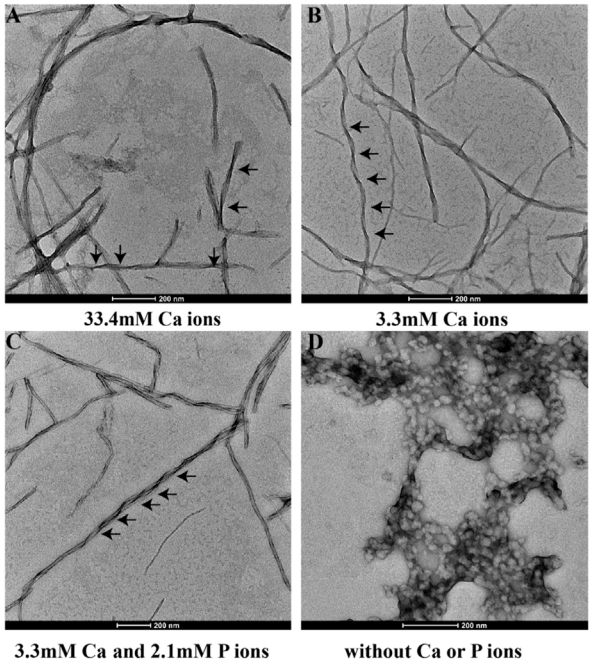

FIGURE 3
TEM images of p14P2 self-assemblies formed at pH 6.0 with or without calcium or phosphate ions. Aliquots of sample suspension were taken out after the sample was incubated for 14 days. The solution condition varied, **(A)** 33.4 mM calcium ions; **(B)** 3.3 mM calcium ions; **(C)** 3.3 mM calcium and 2.1 mM phosphate ions. **(D)** No calcium or phosphate ions.

antiparallel models (b1-b5) at Figures 2B. Our results indicated 14P2 assembled into a parallel in-register conformation only at high ion concentration (33.4 mM calcium and 20.9 mM phosphate).

3.2 The morphology of p14P2 self-assemblies was different from 14P2 self-assemblies

The effect of serine phosphorylation on the 14P2 peptide self-assemble was also investigated. Five conditions (Table 1) were tested including two conditions without inorganic phosphate ions, but with different calcium concentrations (33.4 mM or 3.3 mM); one condition with both calcium and inorganic phosphate ions (3.3 mM calcium and 2.1 mM phosphate ions); and one condition without either ion. All the conditions above were at pH 6.0. Another condition at pH 7.5, 3.3 mM calcium was also tested to check the pH effect on p14P2 assembly. Interestingly, at 33.4 mM calcium condition, the p14P2 peptide solution turned cloudy when calcium ions were added at the acidic condition (Supplementary Figure S1B). When the pH reached 6.0, the solution stayed turbid (Supplementary Figures S1C, D). Therefore, the calcium ions had interactions with the organic phosphoryl group in the peptide at acid pH condition and some peptide assemblies may already have been formed at the acid condition. For other conditions, the p14P2 solution turned cloudy in the presence of calcium ions only at pH 6.0. Judged by the pKa values reported for the phosphoryl serine in a five-residue peptide with a random structure in solution (Scheme 1B) (Bienkiewicz and Lumb, 1999), the organic phosphoryl group could be dominant by the monoanionic ($-OPO_3H^-$) at pH 2–3. At pH 6, around pKa2, the organic phosphoryl group could have monoanionic and dianionic ($-OPO_3^{2-}$) forms equally populated. Both negatively charged forms of the phosphoryl group could interact with positively charged calcium ions.

Figure 3 shows the TEM images of p14P2 self-assemblies. The samples were obtained from the solution suspension prepared using these four conditionsat pH6.0. The TEM image of the sample prepared at pH 7.5 was displayed at Supplementary Figure S5A. Different from 14P2, p14P2 assemblies in the presence of mineral ions at pH 6.0 all displayed twists with varied crossover lengths and width. The twisted fibril also tended to form super twists. When neither of the ions presented, the peptide formed less aggregates with mostly sphere structures (30–50 nm in diameter) (Figure 3D). At pH 7.5 condition, the assemblies showed less contrast in the TEM images. The XRD were also obtained for the p14P2 assemblies. The samples were collected using high-speed centrifugation, including all the aggregates formed in the preparation. All samples obtained at pH 6.0 displayed two dominant diffraction rings at 4.7 and 10.1 Å (Figure 4), supporting β-amyloid formation of the peptide. The sample prepared at pH 7.5 displayed the diffraction rings at 4.7 and 11.4 Å among all the distances shown in Supplementary Figure S5B. The result indicated that the β-amyloid conformation was maintained at pH 7.5 although the structures were not exactly the same for the two pH conditions. Additionally, in the presence of both calcium ions and inorganic phosphates (Figure 4C), no mineral diffraction was observed while p14P2 assemblies were formed.

3.3 The different organic phosphate states in the p14P2 amyloid by ^{31}P-NMR analysis

The 1D ^{1}H-^{31}P CP spectra of the samples at the four conditions at pH 6.0 were also compared (Figure 5). All the spectra displayed broad lines composed of many peaks, suggesting multiple organic phosphate states. In order to understand each phosphate species, the spectra were deconvoluted using DMFIT(Massiot et al., 2002). Figure 5D shows the spectrum from the control sample without any calcium and inorganic phosphate ions. One peak around -12 ppm was close to the chemical shift of a pyrophosphate group (Yu et al., 2019), suggesting the peptides assembled into an in-register conformation that two neighboring phosphate groups on the serine were close enough to form the phosphoanhydride

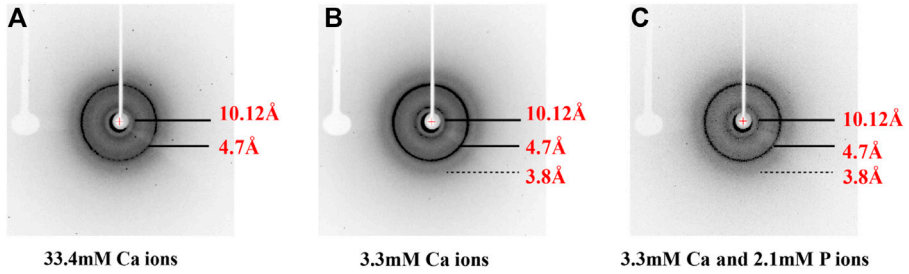

FIGURE 4
X-ray diffraction of peptide assemblies formed by incubating of p14P2 at pH 6.0 with various solution conditions. All the diffraction images illustrated the formation of the cross-β structure of p14P2 with the equatorial and meridional diffractions at 10.1 and 4.7 Å. The solution condition varied, **(A)** 33.4 mM calcium ions; **(B)** 3.3 mM calcium ions; **(C)** 3.3 mM calcium and 2.1 mM phosphate ions.

bond. However, the peak around -12 ppm represented only one of the components. The spectrum displayed one major peak at 0.6 ppm and a shoulder at 1.87 ppm. The major peak should represent free organic phosphate without binding to mineral ions and without interacting with other organic phosphate. Consistently, adding calcium ions (3.3 mM) decreased the peak intensities at 0.6 ppm, two additional peaks at 1.6 ppm and −1.38 ppm appeared (Figures 5B, C). At the high calcium ion concentration of 33.4 mM, the peak around −12 ppm disappeared while peaks at 1.6 ppm, −1.38 ppm dominated (Figure 5A). For all the spectra with calcium ions (Figures 5A–C), the peak at 0.6 ppm remained, but with much lower intensity compared to Figure 5D without calcium and inorganic phosphate ions. Together, these observations suggest that the peaks at 1.6 ppm and −1.38 ppm represent two major species of calcium-organic phosphate complexes. The 2D ^{1}H-^{31}P hetero-nuclear correlation (HETCOR) were displayed parallel to the 1D^{31}P spectra. The 1D slices of the 2D spectra are displayed above each 2D spectrum and on the right side of the 2D spectrum. The 2D spectra for samples with calcium ions (right side of Figures 5A–C) all showed the water ^{1}H correlation to the broad ^{31}P peak at (5.5 ppm/~1.6 ppm), indicating water molecules having a close interaction with the organic phosphate groups. For p14P2 assemblies without calcium ions, the correlation between water and the organic phosphate group at the serine residue was also observed as a broad peak at (5.5 ppm/~1.0 ppm). At the same time, we can observe another weak correlation peak at around ^{1}H/^{31}P (9.5 ppm/1.6 ppm) for both 33.4 mM calcium and 3.3 mM calcium conditions. The low field (higher frequency) ^{1}H peak was consistent with a protonated phosphate group (Leroy et al., 2017). The 1D slice at ^{1}H 9.5 ppm position exhibited a narrower peak centered at ^{31}P 1.6 ppm compared to the 1D slice at ^{1}H 5.5 ppm showing above each 2D spectrum, suggesting that only the peak at ^{31}P 1.6 ppm has a proton associated with it, but not the peak at −1.38 ppm.

The chemical shift anisotropy (CSA) of ^{31}P nuclei is very sensitive to its environment. It has been used as a probe to predict the organic phosphate ionization state and how they bind to calcium ions (Wu et al., 2003; Gardiennet Doucet et al., 2006; Addison et al., 2013). The CSA pattern of L-O-phosphoserine was reported in the literature (Addison et al., 2013), indicating a change of skew value [3 (δ_{22}–δ_{iso})/(δ_{11}–δ_{33})] of phosphoserine from positive to negative upon phosphoserine interactions with calcium or sodium cations. This is caused by the change of asymmetric CSA introduced to the phosphoserine environment in the interaction with mineral ions. In order to obtain the CSA parameters for p14P2 assemblies, 1D ^{1}H-^{31}P CP spectra at multiple magic-angle-spinning (MAS) speeds (15, 5 kHz and the static condition) were obtained and deconvoluted using DMFIT for 33.4 mM calcium and 3.3 mM calcium conditions (Figure 6 and Supplementary Figure S6). The results were summarized in Supplementary Table S2. The deconvolution on the 1D ^{1}H-^{31}P spectra of p14P2 amyloid at both calcium concentrations indicated that ^{31}P peaks at 1.6 ppm and −1.38 ppm showed negative skew values, supporting that these two peaks were from calcium-organic phosphate complex. The peak at −1.38 ppm had a bigger CSA span compared to the peak at 1.6 ppm, indicating a less symmetric ^{31}P nucleus environment. The peak at 0.6 ppm showed positive skew value, indicating this peak represents the organic phosphate component not binding to calcium ions. For the p14P2 self-assemblies formed without calcium and inorganic phosphate, the major peak at 0.6 ppm showed positive skew value, consistent with other samples. The information obtained from spectra at different MAS speeds generally agreed with each other at the sign of the skew values, but differed in the exact values because of the different experimental conditions. Our interpretation of CSA data is consistent with our conclusions obtained from Figure 5: the peak at 0.6 ppm represents the component not binding to calcium while the peak at 1.6 ppm represents single protonated phosphate group binding to calcium, the peak at −1.38 ppm represents dianionic phosphate group binding to calcium. A

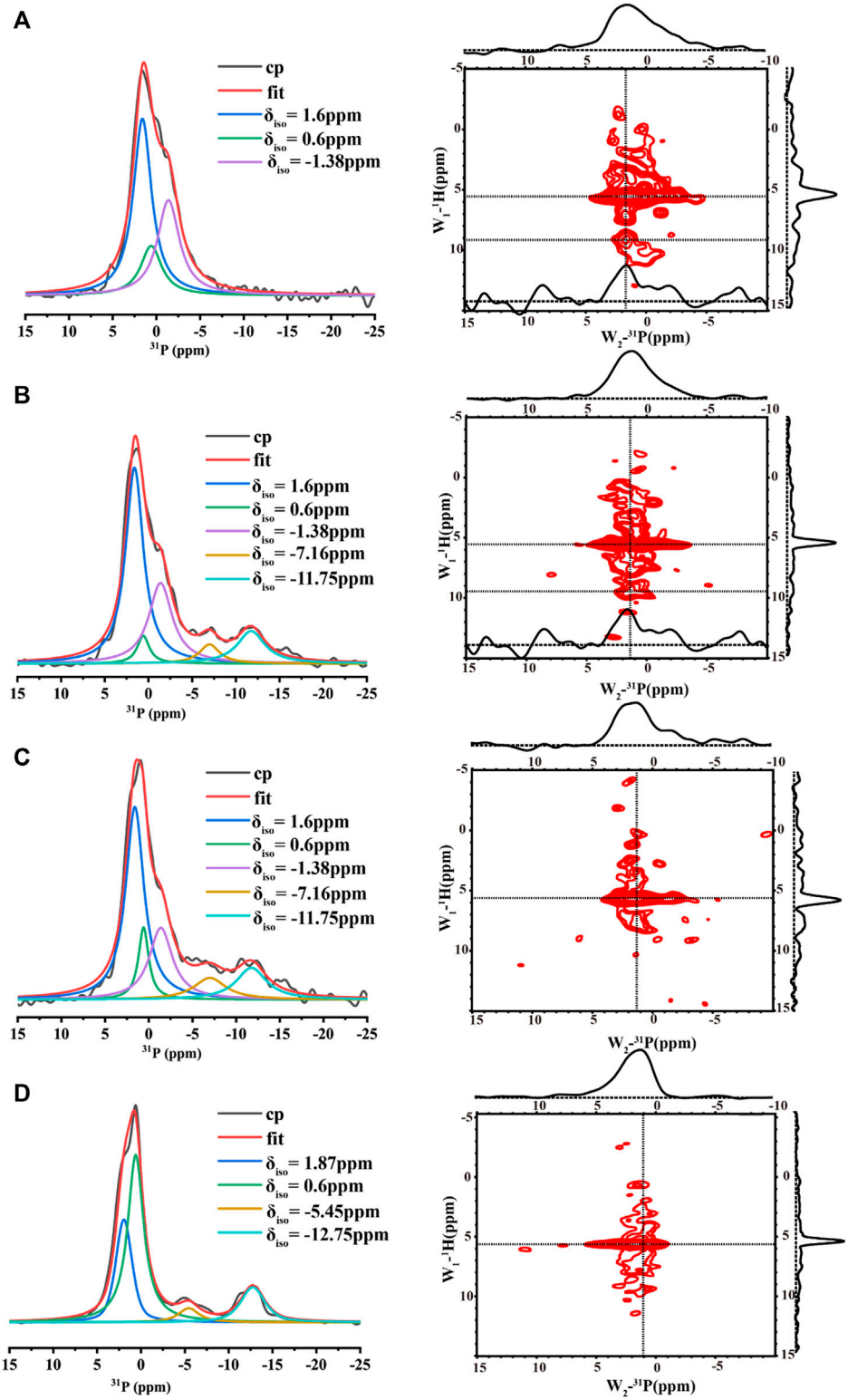

FIGURE 5
1D ^{1}H- ^{31}P CP MAS NMR spectra (left, each spectrum took about 2 h) and 2D ^{1}H- ^{31}P HETCOR spectra (right, each spectrum took about 6 h) acquired for p14P2 peptide assemblies formed at pH6.0 with different solution conditions. All the 1D spectra were deconvoluted to several components using DMFIT program with Gaus/Lor model. The raw data were shown in black, and the sum of all components from fitting were shown in red. Each component was labeled by its resonance position δ_{iso}. The solution condition was varied, **(A)** 33.4 mM calcium ions; **(B)** 3.3 mM calcium ions; **(C)** 3.3 mM calcium and 2.1 mM phosphate ions. **(D)** No calcium or phosphate ions. All the spectra were taken at 20 kHz MAS except **(D)**. The spectra in **(D)** were taken at 15 kHz MAS.

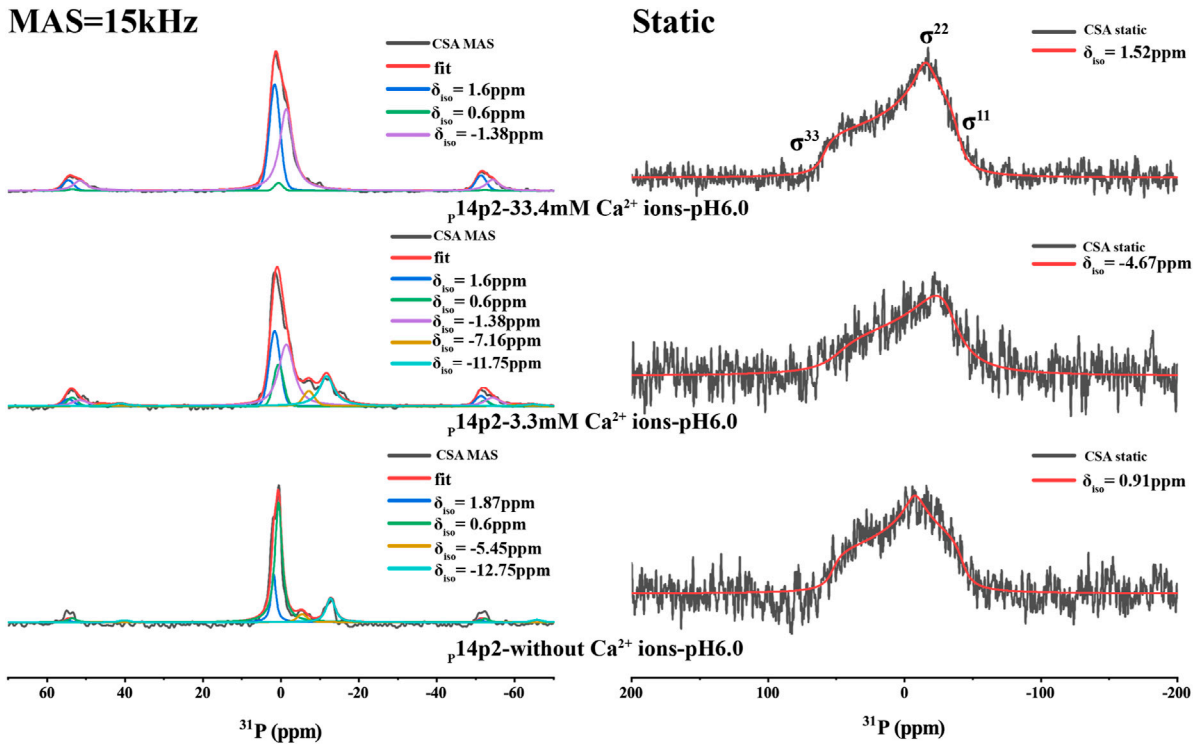

FIGURE 6
^{1}H-^{31}P CP spectra of p14P2 self-assembly formed at different solution conditions. The MAS spectra took about 6 h while the static spectra took about 15 h. The CSA parameters were obtained by fitting the spectra using DMFIT. And the fitting parameters are shown in Supplementary Table S2. The raw data are shown in black. The full DMFIT fitting spectra are shown in red. The spectra showed different resolved phosphorus resonances (δ_{iso}) that can be ascribed to the different calcium binding status or different conformation of the single phosphorus site.

negative skew value was observed for the pyrophosphate peak at around −12 ppm, suggesting the chemical environment of the pyrophosphate bonding would also increase the asymmetry of ^{31}P CSA. Other minor peaks were not discussed here. Interestingly, the organic phosphate groups was not saturated in binding to the calcium ions at 3.3 or 33.3 mM calcium ion concentration when the concentration of calcium ion was 5x or 50x of protein concentration. The existence of multiple organic phosphate peaks with different calcium coordination indicated the multiple modes of calcium binding to the phosphate group in p14P2.

The p14P2 sample prepared in the presence of both 3.3 mM calcium ions and 2.1 mM phosphate ions were different from others in that the sample contained both inorganic and organic phosphate groups (Table 1). The mineral ion concentrations in solution were the same for 14P2 self-assembly preparation at low ion concentrations. However, the morphology of the peptide self-assemblies was different from 14P2 assemblies (Figure 1C). The 1D ^{1}H-^{31}P CP spectra were also compared for the two types of peptide assemblies (Supplementary Figures S2A, B) with the same solution condition. The two 1D ^{31}P spectra were very different, while the 1D ^{1}H-^{31}P CP spectra of p14P2 self-assemblies formed in 3.3 mM calcium with or without 2.1 mM phosphate ions were almost identical (Supplementary Figures S2B, C). Therefore, p14P2 assemblies prepared in the presence of both calcium and inorganic phosphate (Supplementary Figure S2B), appear to be free of calcium phosphate minerals. This indicates that the organic phosphate competed with the inorganic phosphate in the interaction with calcium ions for p14P2, reducing the calcium concentration in solution. Therefore, the organic phosphate group had a function of inhibiting calcium phosphate precipitation by reducing the free calcium concentration in solution. This observation is consistent with the full-length amelogenin or LRAP (Le et al., 2006), which binds about 4 to 6 calcium ions per protein molecule.

3.4 The amyloid formed by p14P2 adopted in-register conformations

Solid-state NMR PITHIRDS-CT experiments were applied to study the conformation of the amyloid formed by p14P2. Since the peptide contained an organic ^{31}P group, no other isotopic

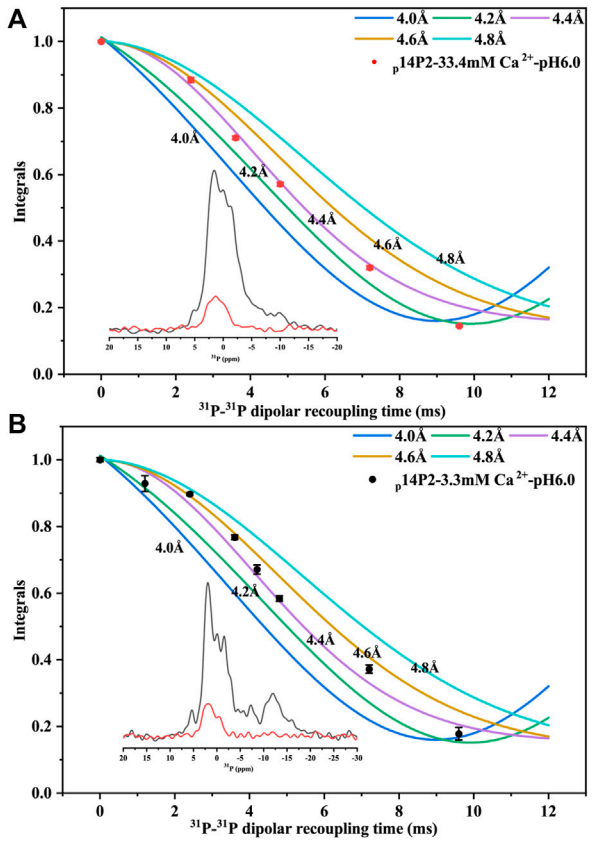

FIGURE 7
^{31}P PITHIRDS-CT experiment for intermolecular ^{31}P-^{31}P distance measurement of p14P2 self-assemblies. The intermolecular ^{31}P–^{31}P magnetic dipole–dipole couplings were measured for p14P2 self-assemblies at pSer16. Comparison with numerical simulations confirmed the intermolecular distances of 4.4 ± 0.2 Å for both p14P2 assemblies formed in the high calcium concentration **(A)** and the low calcium concentration **(B)**, supporting an in-register parallel β-sheet structure of the assemblies. The peak area was integrated from −7.6 to 5.1 ppm for 33.4 mM Ca^{2+} condition **(A)** and from −4.2 to 4.7 ppm for 3.3 mM Ca^{2+} condition **(B)**. Each data point was from a NMR spectrum collected for 5 h and 35 min.

labeling was added. The intermolecular ^{31}P-^{31}P distance was measured using PITHIRDS-CT, shown in Figure 7 for samples with 33.4 or 3.3 mM calcium. The total peak area containing multiple components centered at 1.6 ppm was used, since it was difficult to deconvolute the peaks when the peak intensity became too small with the longer ^{31}P-^{31}P recoupling time. The PITHIRDS-CT data indicated a 4.4 ± 0.2 Å distance between two neighboring phosphate groups on the serine residues, generally consistent with an in-registry conformation of the peptide assembly. The distance was measured on the side-chain of the residues, which might explain the small deviation from the 4.7 Å distance for the peptide backbone determined using XRD. The twisted morphology of the fibril may make the side-chain phosphates closer. However, it is also possible that multiple ^{31}P-^{31}P distances exist, since the peak was broad with multiple components corresponding to different phosphoserine coordination states (corresponding to peaks at 1.6, −1.38, and 0.6 ppm).

The ^{1}H-^{13}C CP spectra of p14P2 assembly at 33.4 and 3.3 mM calcium concentration or without calcium were obtained in Figure 8 indicating smaller differences when comparing samples in the presence of calcium ions and bigger differences when comparing samples with or without calcium ions. The results confirmed that the major structure of the p14P2 assemblies was the same for the two conditions with different calcium ion concentrations. The spectra showed strong signals at the aromatic region; the C_α, C_β regions of the phosphoserine and the methyl group positions for valine and isoleucine, consistent with a rigid structure of the assemblies. Interestingly, the side-chain carboxyl group signal for glutamic acid (Glu18) was also clearly observed around 184 ppm, indicating an ordered carboxyl group in the deprotonated state (Tollinger et al., 2002), suggesting this negatively charged side-chain may be involved in stabilizing the peptide assembly and calcium binding. Without calcium ions, the peak disappeared or shifted to a lower value (less than 180 ppm), supporting the influence of calcium binding on the chemical shift position of Glu18 side-chain carboxyl group. Furthermore, without calcium ions, the ^{1}H-^{13}C CP spectrum of p14P2 assembly also showed noticeable differences in other regions, such as Ile methyl group, Thr C_β, Glu C_γ and His C_β regions. Together with the results described above, this observation indicated the central role of calcium ions in determining p14P2 assembly structures. The ^{1}H-^{13}C CP spectrum of 14P2 assemblies formed at 33.4 mM calcium concentration without any phosphate was also obtained to compare to p14P2 assembly spectra, which showed a bigger difference. For example, the highest resonance at Cα region was at around 60 ppm for 14P2 assemblies, where the p14P2 assemblies only showed weak peaks. The results supported our conclusion that phosphate group significantly influenced the peptide binding with the calcium ions and affected the peptide assembly structures.

4 Discussion

In this study, we observed the direct calcium interactions with the serine phosphorous group, manifested by a gradual change of ^{31}P peaks of pSer16 in the NMR spectra upon adding calcium ions in the protein solution for the assembly (Figure 5). Furthermore, our ^{13}C NMR results suggested the nearby Glu18 was involved in calcium binding. In the absence of calcium, the peptide agglomerates showed very different spectra, especially at the Glu side-chain carboxylate region, which has a very unique position and can be identified easily. This is consistent with a previous model of p14P2 proposed by

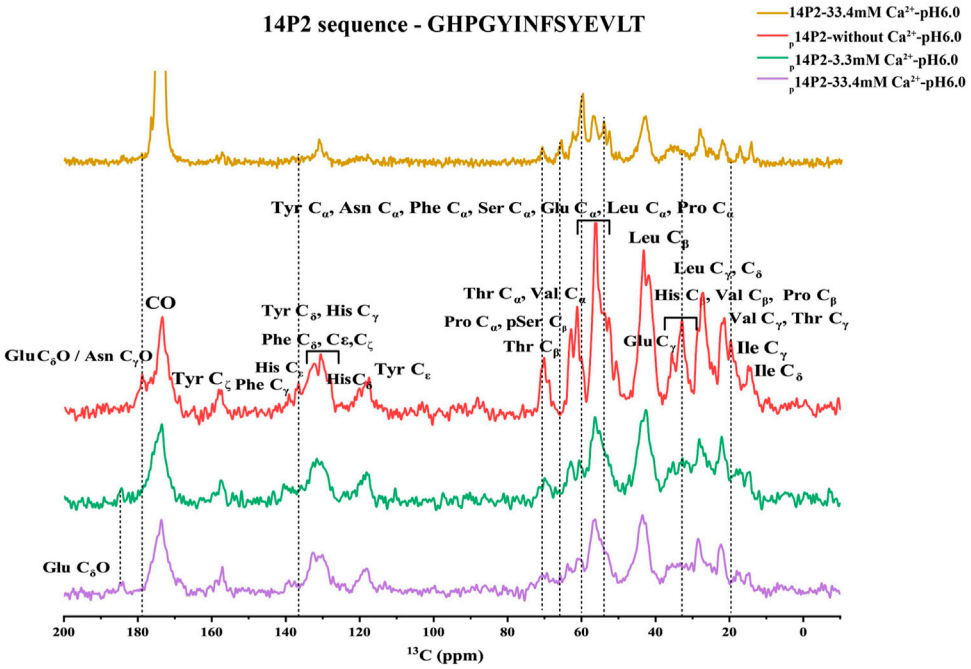

FIGURE 8
^{1}H-^{13}C CP-MAS NMR spectra of p14P2 and 14P2 assemblies. Spectra of p14P2 self-assemblies formed in 33.4 mM Ca^{2+} at pH 6.0 (purple, experimental time: 1 h 9 min), 3.3 mM Ca^{2+} at pH 6.0 (green, experimental time: 2 h 16 min), and no additional calcium or phosphate ions at pH 6.0 (red, experimental time: 1 h 9 min) and 14P2 assemblies formed at 33.4 mM calcium (gold, experimental time 5 h 40 min). The tentative assignment based on empirical values were labeled. The vertical lines (dashed line) were used to highlight some big differences for different samples.

Carneiro et al., which displayed intermolecular Ca^{2+} ions bridging from glutamate to phosphoserine (Carneiro et al., 2016).

The calcium content added was as high as 33.4 mM, 50x of the peptide or the organic phosphate concentration for p14P2, and thus much higher than observed under natural conditions. The purpose is to clearly demonstrate how the calcium ions affect the protein interactions and the structure of the protein assemblies. The twisted morphology was mostly observed for p14P2 peptide assemblies, however, a 14P2 assembly sample prepared without phosphate at 33.4 mM calcium displayed some twisted fibrils. Without phosphate, the high concentration of calcium ions can only interact with the peptide. The result suggested the calcium interaction with the peptide would promote the development of a twisted morphology for the fibrils.

For PITHIRDS-CT experiments, the experimental results were fit to the simulation curves, assuming a homogeneous structure model with a single distance. However, our sample may not be so homogeneous considering the linewidth for the carbonyl group was about 2 ppm. A distance of 4.4 ± 0.4 Å was obtained for a 14P2 peptide assembly at high mineral ion concentration, it suggested an in-register parallel conformation for 14P2. The distance is shorter than 4.7 Å expected for a parallel β-sheet structure, such as Aβ fibrils. The average intermolecular ^{31}P-^{31}P distance 4.4 Å also suggested an in-register parallel conformation for p14P2. It would need more distance information from other residues to get a confident answer. The twisted morphology of the fibril could be used to explain the short distance. The curve on the β-sheet surface might cause those phosphate groups to be closer. Also there may be multiple ^{31}P-^{31}P distances. For SSNMR dipolar-interation based distance measurement, the experimental results would mainly be determined by the shortest distances if multiple distances exist. Therefore, even if there are multiple distances, the distances that matter in the measurement should be very close to 4.4 Å. On the other hand, possibly, multiple ^{31}P-^{31}P distances within 5 Å co-exist but are located at separated structural units. In each unit, the phosphorylated serine side chain structure is unique and only a single ^{31}P-^{31}P distance exists. For example, one structure unit of the peptide assembly has a ^{31}P-^{31}P distance of 4.1 Å and the other structure unit has a ^{31}P-^{31}P distance of 4.7 Å. A combination of both could give a good fit for p14P2 assemblies prepared at 33.4 and 3.3 mM Ca^{2+} (Supplementary Figure S7). In this simulation, the contribution ratio of each structure unit was chosen to be close to the peak area ratio revealed by the deconvolution shown in Figure 5 (two peaks at 1.6 and −1.38 ppm). For p14P2 assemblies prepared at

3.3 mM Ca^{2+}, a combination of 3.8 and 4.6 Å were also tested since 3.8 Å was a distance observed by XRD.

The peptide assemblies were obtained mainly at pH 6.0 condition, and the assemblies were harvested after 1 week incubation in this research. However, we also tested p14P2 at pH 7.5. And amyloid-like strucures were observed at 2 days. Therefore, the slightly acidic pH and the long incubation time were not necessary for the amyloid assembly formation. NMR is a low sensitive technique, requiring milligrams of isotopically labeled protein samples. A slightly acidic pH and a long incubation time were chosen in this research to promote the kinetics and give a higher yield of assemblies for NMR studies. On the other hand, slightly acidic pH may be of biological significance as pH values below 6 have been observed in the vicinity of the Tomes processes of ameloblasts and exocytosing vesicles are known to have pH around 5.5 (Sasaki et al., 1991; Lacruz et al., 2010).

We surveyed the ^{31}P-^{31}P distance in brushite and HAP crystal (Supplementary Figure S8), showing that the shortest ^{31}P-^{31}P distance for brushite is 3.8 Å while ^{31}P-^{31}P distances along the c axis for HAP are between 4.0 and 4.2 Å, very close to the experimental results, although here the experimental results were on the organic phosphate. These distances indicate that the organic phosphate-calcium interaction network would be a good starting point for the inorganic ions to interact with and to promote a phase transformation from amorphous calcium phosphate to crystalline mineral oriented with the organic supramolecular template (Akkineni et al., 2022). The organic phosphate interaction network could coordinate with the calcium ions, reduce the calcium ion concentrations in solution, and bring water molecules into proper positions, all of which are necessary for a controlled calcium mineralization process. Without calcium, the peptide assembly structure was very different. Table 1 lists all the peptide samples and their different structural properties. These results emphasized the importance of calcium and phosphoserine interactions in determining the modes of protein-protein interactions. Understanding these interactions may pave the way for us to understand the driving force for the self-assembly of full-length amelogenin and its ability to guide biomineralization in enamel.

Data availability statement

The original contributions presented in the study are included in the article/Supplementary Material, further inquiries can be directed to the corresponding authors.

Author contributions

JZ investigation, writing original draft, methodology, and formal analysis. YB and SH methodology and writing-review editing. JW methodology. BL project administration. J-xL writing original draft, methodology, writing-review editing, funding acquisition, and supervision.

Funding

The work is supported by grants from the Natural Science Foundation of China (Nos 31770790 and 32171185 to J-XL) and the NIH/NIDCR (RO1DE025709, RO1DE031946 to SH).

Acknowledgments

We would like to thank the Biomolecular NMR Facility at the School of Life Science and Technology, ShanghaiTech University for SSNMR studies. TEM images were taken at the Bio-Electron Microscopy Facility of ShanghaiTech University. The authors would also like to thank the support from the Analytical Instrumentation Center (Contract No.. SPST-AIC 10112914), the School of Physical Science and Technology at ShanghaiTech University. We thank Na Yu for single-crystal crystallography.

Conflict of interest

The authors declare that the research was conducted in the absence of any commercial or financial relationships that could be construed as a potential conflict of interest.

Publisher's note

Supplementary material

The Supplementary Material for this article can be found online at: https://www.frontiersin.org/articles/10.3389/fphys.2022.1063970/full#supplementary-material

References

Addison, J. B., Ashton, N. N., Weber, W. S., Stewart, R. J., Holland, G. P., and Yarger, J. L. (2013). β-Sheet nanocrystalline domains formed from phosphorylated serine-rich motifs in caddisfly larval silk: A solid state nmr and xrd study. *Biomacromolecules* 14, 1140–1148. doi:10.1021/bm400019d

Akkineni, S., Zhu, C., Chen, J., Song, M., Hoff, S. E., Bonde, J., et al. (2022). Amyloid-like amelogenin nanoribbons template mineralization via a low-energy interface of ion binding sites. *Proc. Natl. Acad. Sci. U. S. A.* 119, e2106965119. doi:10.1073/pnas.2106965119

Alvares, K. (2014). The role of acidic phosphoproteins in biomineralization. *Connect. Tissue Res.* 55, 34–40. doi:10.3109/03008207.2013.867336

Aoba, T., and Moreno, E. C. (1987). The enamel fluid in the early secretory stage of porcine amelogenesis: Chemical composition and saturation with respect to enamel mineral. *Calcif. Tissue Int.* 41, 86–94. doi:10.1007/BF02555250

Bai, Y., Yu, Z., Ackerman, L., Zhang, Y., Bonde, J., Li, W., et al. (2020). Protein nanoribbons template enamel mineralization. *Proc. Natl. Acad. Sci. U. S. A.* 117, 19201–19208. doi:10.1073/pnas.2007838117

Bak, M., Rasmussen, J. T., and Nielsen, N. C. (2011). Simpson: A general simulation program for solid-state nmr spectroscopy. *J. Magn. Reson.* 213, 366–400. doi:10.1016/j.jmr.2011.09.008

Bienkiewicz, E. A., and Lumb, K. J. (1999). Random-coil chemical shifts of phosphorylated amino acids. *J. Biomol. NMR* 15, 203–206. doi:10.1023/a:1008375029746

Carneiro, K. M., Zhai, H., Zhu, L., Horst, J. A., Sitlin, M., Nguyen, M., et al. (2016). Amyloid-like ribbons of amelogenins in enamel mineralization. *Sci. Rep.* 6, 23105–23111. doi:10.1038/srep23105

Engelberth, S. A., Bacino, M. S., Sandhu, S., Li, W., Bonde, J., and Habelitz, S. (2018). Progression of self-assembly of amelogenin protein supramolecular structures in simulated enamel fluid. *Biomacromolecules* 19, 3917–3924. doi:10.1021/acs.biomac.8b00808

Fincham, A., Moradian Oldak, J., and Simmer, J. (1999). The structural biology of the developing dental enamel matrix. *J. Struct. Biol.* 126, 270–299. doi:10.1006/jsbi.1999.4130

Fowler, D. M., Koulov, A. V., Balch, W. E., and Kelly, J. W. (2007). Functional amyloid–from bacteria to humans. *Trends biochem. Sci.* 32, 217–224. doi:10.1016/j.tibs.2007.03.003

Fung, B., Khitrin, A., and Ermolaev, K. (2000). An improved broadband decoupling sequence for liquid crystals and solids. *J. Magn. Reson.* 142, 97–101. doi:10.1006/jmre.1999.1896

Gardiennet Doucet, C., Assfeld, X., Henry, B., and Tekely, P. (2006). Revealing successive steps of deprotonation of l-phosphoserine through ^{13}C and ^{31}P chemical shielding tensor finger prints. *J. Phys. Chem. A* 110, 9137–9144. doi:10.1021/jp062184v

Green, D. R., Schulte, F., Lee, K. H., Pugach, M. K., Hardt, M., and Bidlack, F. B. (2019). Mapping the tooth enamel proteome and amelogenin phosphorylation onto mineralizing porcine tooth crowns. *Front. Physiol.* 10, 925. doi:10.3389/fphys.2019.00925

Gullion, T., and Schaefer, J. (1989). Rotational-echo double-resonance nmr. *J. Magnetic Reson.* 81, 196–200. doi:10.1016/0022-2364(89)90280-1

Herzfeld, J., and Berger, A. E. (1980). Sideband intensities in nmr spectra of samples spinning at the magic angle. *J. Chem. Phys.* 73, 6021–6030. doi:10.1063/1.440136

Lacruz, R. S., Habelitz, S., Wright, J. T., and Paine, M. L. (2017). Dental enamel formation and implications for oral health and disease. *Physiol. Rev.* 97, 939–993. doi:10.1152/physrev.00030.2016

Lacruz, R. S., Nanci, A., Kurtz, I., Wright, J. T., and Paine, M. L. (2010). Regulation of ph during amelogenesis. *Calcif. Tissue Int.* 86, 91–103. doi:10.1007/s00223-009-9326-7

Le Norcy, E., Kwak, S.-Y., Allaire, M., Fratzl, P., Yamakoshi, Y., Simmer, J. P., et al. (2011). Effect of phosphorylation on the interaction of calcium with leucine-rich amelogenin peptide. *Eur. J. Oral Sci.* 119, 97–102. doi:10.1111/j.1600-0722.2011.00900.x

Le, T. Q., Gochin, M., Featherstone, J. D., Li, W., and DenBesten, P. K. (2006). Comparative calcium binding of leucine-rich amelogenin peptide and full-length amelogenin. *Eur. J. Oral Sci.* 114, 320–326. doi:10.1111/j.1600-0722.2006.00313.x

Lench, N. J., and Winter, G. B. (1995). Characterisation of molecular defects in x-linked amelogenesis imperfecta (aih1). *Hum. Mutat.* 5, 251–259. doi:10.1002/humu.1380050310

Leroy, C., Aussenac, F., Bonhomme Coury, L., Osaka, A., Hayakawa, S., Babonneau, F., et al. (2017). Hydroxyapatites: Key structural questions and answers from dynamic nuclear polarization. *Anal. Chem.* 89, 10201–10207. doi:10.1021/acs.analchem.7b01332

Ma, C. W., Zhang, J., Dong, X. Q., and Lu, J. X. (2019). Amyloid structure of high-order assembly of leucine-rich amelogenin revealed by solid-state nmr. *J. Struct. Biol.* 206, 29–35. doi:10.1016/j.jsb.2018.03.009

Martinez Avila, O., Wu, S., Kim, S. J., Cheng, Y., Khan, F., Samudrala, R., et al. (2012). Self-assembly of filamentous amelogenin requires calcium and phosphate: From dimers via nanoribbons to fibrils. *Biomacromolecules* 13, 3494–3502. doi:10.1021/bm300942c

Massiot, D., Fayon, F., Capron, M., King, I., Le Calvé, S., Alonso, B., et al. (2002). Modelling one-and two-dimensional solid-state nmr spectra. *Magn. Reson. Chem.* 40, 70–76. doi:10.1002/MRC.984

Prasad, M., Butler, W. T., and Qin, C. (2010). Dentin sialophosphoprotein in biomineralization. *Connect. Tissue Res.* 51, 404–417. doi:10.3109/03008200903329789

Sanii, B., Martinez Avila, O., Simpliciano, C., Zuckermann, R., and Habelitz, S. (2014). Matching 4.7-å xrd spacing in amelogenin nanoribbons and enamel matrix. *J. Dent. Res.* 93, 918–922. doi:10.1177/0022034514544216

Sasaki, S., Takagi, T., and Suzuki, M. (1991). Cyclical changes in pH in bovine developing enamel as sequential bands. *Arch. Oral Biol.* 36, 227–231. doi:10.1016/0003-9969(91)90090-h

Schwieters, C. D., Kuszewski, J. J., Tjandra, N., and Clore, G. M. (2003). The xplor-nih nmr molecular structure determination package. *J. Magn. Reson.* 160, 65–73. doi:10.1016/s1090-7807(02)00014-9

Shi, X., Yarger, J. L., and Holland, G. P. (2013). ^{2}H-^{13}C hetcor mas nmr for indirect detection of ^{2}H quadrupole patterns and spin-lattice relaxation rates. *J. Magn. Reson.* 226, 1–12. doi:10.1016/j.jmr.2012.10.013

Shin, N. Y., Yamazaki, H., Beniash, E., Yang, X., Margolis, S. S., Pugach, M. K., et al. (2020). Amelogenin phosphorylation regulates tooth enamel formation by stabilizing a transient amorphous mineral precursor. *J. Biol. Chem.* 295, 1943–1959. doi:10.1074/jbc.RA119.010506

Simmer, J., and Fincham, A. (1995). Molecular mechanisms of dental enamel formation. *Crit. Rev. Oral Biol. Med.* 6, 84–108. doi:10.1177/10454411950060020701

Stifler, C. A., Yamazaki, H., Gilbert, P. U., Margolis, H. C., and Beniash, E. (2022). Loss of biological control of enamel mineralization in amelogenin-phosphorylation-deficient mice. *J. Struct. Biol.* 214, 107844. doi:10.1016/j.jsb.2022.107844

Takagi, T., Suzuki, M., Baba, T., Minegishi, K., and Sasaki, S. (1984). Complete amino acid sequence of amelogenin in developing bovine enamel. *Biochem. Biophys. Res. Commun.* 121, 592–597. doi:10.1016/0006-291X(84)90223-7

Tollinger, M., Forman Kay, J. D., and Kay, L. E. (2002). Measurement of side-chain carboxyl p k a values of glutamate and aspartate residues in an unfolded protein by multinuclear nmr spectroscopy. *J. Am. Chem. Soc.* 124, 5714–5717. doi:10.1021/ja020066p

Tycko, R. (2007). Symmetry-based constant-time homonuclear dipolar recoupling in solid state nmr. *J. Chem. Phys.* 126, 064506. doi:10.1063/1.2437194

Wiedemann Bidlack, F. B., Kwak, S. Y., Beniash, E., Yamakoshi, Y., Simmer, J. P., and Margolis, H. C. (2011). Effects of phosphorylation on the self-assembly of native full-length porcine amelogenin and its regulation of calcium phosphate formation *in vitro*. *J. Struct. Biol.* 173, 250–260. doi:10.1016/j.jsb.2010.11.006

Wu, X. l., Hu, H., Dong, X. q., Zhang, J., Wang, J., Schwieters, C. D., et al. (2021). The amyloid structure of mouse ripk3 (receptor interacting protein kinase 3) in cell necroptosis. *Nat. Commun.* 12, 1627. doi:10.1038/s41467-021-21881-2

Wu, Y., Ackerman, J., Strawich, E., Rey, C., Kim, H.-M., and Glimcher, M. (2003). Phosphate ions in bone: Identification of a calcium-organic phosphate complex by ^{31}P solid-state nmr spectroscopy at early stages of mineralization. *Calcif. Tissue Int.* 72, 610–626. doi:10.1007/s00223-002-1068-8

Yu, Y., Guo, H., Pujari Palmer, M., Stevensson, B., Grins, J., Engqvist, H., et al. (2019). Advanced solid-state ^{1}H-^{31}P nmr characterization of pyrophosphate-doped calcium phosphate cements for biomedical applications: The structural role of pyrophosphate. *Ceram. Int.* 45, 20642–20655. doi:10.1016/j.ceramint.2019.07.047

Zhang, J., Wang, J., Ma, C., and Lu, J. (2020). Hydroxyapatite formation coexists with amyloid-like self-assembly of human amelogenin. *Int. J. Mol. Sci.* 21, 2946. doi:10.3390/ijms21082946

frontiers | Frontiers in Physiology

TYPE Correction
PUBLISHED 04 April 2023
DOI 10.3389/fphys.2023.1178589

OPEN ACCESS

APPROVED BY
Frontiers Editorial Office,
Frontiers Media SA, Switzerland

*CORRESPONDENCE
Jun-Xia Lu,
lujx@shanghaitech.edu.cn
Stefan Habelitz,
Stefan.habelitz@ucsf.edu

SPECIALTY SECTION
This article was submitted to Craniofacial Biology and Dental Research, a section of the journal Frontiers in Physiology

RECEIVED 03 March 2023
ACCEPTED 24 March 2023
PUBLISHED 04 April 2023

CITATION
Zhang J, Bai Y, Wang J, Li B, Habelitz S and Lu J-X (2023), Corrigendum: Calcium interactions in amelogenin-derived peptide assembly.
Front. Physiol. 14:1178589.
doi: 10.3389/fphys.2023.1178589

Corrigendum: Calcium interactions in amelogenin-derived peptide assembly

Jing Zhang[1,2,3], Yushi Bai [4], Jian Wang[1], Bing Li[1], Stefan Habelitz[4]* and Jun-Xia Lu[1]*

[1]School of Life Science and Technology, ShanghaiTech University, Shanghai, China, [2]University of Chinese Academy of Sciences, Beijing, China, [3]State Key Laboratory of Molecular Biology, CAS Center for Excellence in Molecular Cell Science, Shanghai Institute of Biochemistry and Cell Biology, Chinese Academy of Sciences, Shanghai, China, [4]Department of Preventative and Restorative Dental Sciences, School of Dentistry, University of California, San Francisco, San Francisco, CA, United States

KEYWORDS

amelogenin, assembly, mineral ions, phosphorylation, SSNMR

A Corrigendum on:
Calcium interactions in amelogenin-derived peptide assembly

by Zhang J, Bai Y, Wang J, Li B, Habelitz S, Lu JX. Front Physiol. 13:1063970. doi: 10.3389/fphys.2022.1063970

In the published article, there was an error in the Funding statement. We did not include funding received from an RO1 grant from the NIH/NIDCR.

The corrected Funding statement appears below.

"The work is supported by grants from the Natural Science Foundation of China (Nos 31770790 and 32171185 to J-XL) and the NIH/NIDCR (RO1DE025709, RO1DE031946 to SH)."

The authors apologize for this error and state that this does not change the scientific conclusions of the article in any way. The original article has been updated.

Publisher's note

All claims expressed in this article are solely those of the authors and do not necessarily represent those of their affiliated organizations, or those of the publisher, the editors and the reviewers. Any product that may be evaluated in this article, or claim that may be made by its manufacturer, is not guaranteed or endorsed by the publisher.

frontiers | Frontiers in Physiology

TYPE Brief Research Report
PUBLISHED 23 December 2022
DOI 10.3389/fphys.2022.1102553

OPEN ACCESS

EDITED BY
Pamela Den Besten,
University of California, San Francisco, United States

REVIEWED BY
Rodrigo S. Lacruz,
New York University, United States
Thomas G. H. Diekwisch,
University of Rochester Medical Center, United States

*CORRESPONDENCE
Elia Beniash,
ebeniash@pitt.edu

†PRESENT ADDRESS
Dept. Pathology, UCSF, San Francisco, CA, United States

SPECIALTY SECTION
This article was submitted to Craniofacial Biology and Dental Research, a section of the journal Frontiers in Physiology

RECEIVED 19 November 2022
ACCEPTED 07 December 2022
PUBLISHED 23 December 2022

CITATION
Deshmukh R, Vasquez B, Bhogadi L, Gabe CM, Lukashova L, Verdelis K, Morasso MI and Beniash E (2022), Elucidating the role of keratin 75 in enamel using Krt75^{tm1Der} knock-in mouse model.
Front. Physiol. 13:1102553.
doi: 10.3389/fphys.2022.1102553

Elucidating the role of keratin 75 in enamel using Krt75^{tm1Der} knock-in mouse model

Rutuja Deshmukh[1†], Brent Vasquez[1,2], Lasya Bhogadi[1,2], Claire M. Gabe[1,2], Lyudmila Lukashova[1], Kostas Verdelis[1,3], Maria I. Morasso[4] and Elia Beniash[1,2]*

[1]Center for Craniofacial Regeneration, Pittsburgh, PA, United States, [2]Department of Oral and Craniofacial Sciences, University of Pittsburgh School of Dental Medicine (UPSDM), Pittsburgh, PA, United States, [3]Department of Endodontics, University of Pittsburgh School of Dental Medicine (UPSDM), Pittsburgh, PA, United States, [4]Laboratory of Skin Biology, National Institute of Arthritis and Musculoskeletal and Skin Diseases, Bethesda, MD, United States

Keratin 75 (K75) was recently discovered in ameloblasts and enamel organic matrix. Carriers of A161T substitution in K75 present with the skin condition *Pseudofollicullitis barbae*. This mutation is also associated with high prevalence of caries and compromised structural and mechanical properties of enamel. Krt75^{tm1Der} knock-in mouse (KI) with deletion of Asn159, located two amino acids away from KRT75^{A161T}, can be a potential model for studying the role of K75 in enamel and the causes of the higher caries susceptibility associated with KRT75^{A161T} mutation. To test the hypotheses that KI enamel is more susceptible to a simulated acid attack (SAA), and has altered structural and mechanical properties, we conducted *in vitro* SAA experiments, microCT, and microhardness analyses on 1st molars of one-month-old WT and KI mice. KI and WT hemimandibles were subjected to SAA and contralateral hemimandibles were used as controls. Changes in enamel porosity were assessed by immersion of the hemimandibles in rhodamine, followed by fluorescent microscopy analysis. Fluorescence intensity of KI enamel after SAA was significantly higher than in WT, indicating that KI enamel is more susceptible to acid attack. MicroCT analysis of 1st molars revealed that while enamel volumes were not significantly different, enamel mineral density was significantly lower in KI, suggesting a potential defect of enamel maturation. Microhardness tests revealed that in KI enamel is softer than in WT, and potentially less resilient to damages. These results suggest that the KI enamel can be used as a model to study the role of K75 in enamel.

KEYWORDS

keratin, ameloblast, enamel matrix, dental caries, biomineralization

Introduction

Dental enamel, the hardest and most highly mineralized tissue, comprises the outer layer of tooth crowns. Enamel is the only mineralized tissue of epithelial origin and the only acellular mineralized tissue which is incapable of remodeling or repair. Despite of this limitation it can withstand millions of cycles of mastication over the lifetime without catastrophic damage due to its unique combination of high hardness and fracture toughness. These mechanical properties of enamel are determined by its unique hierarchical structure and composition (Cuy et al., 2002; Chai et al., 2009; He and Swain, 2009; Yilmaz et al., 2015; Beniash et al., 2019; DeRocher et al., 2020; Wilmers and Bargmann, 2020). The major component of enamel is mineral, carbonated hydroxyapatite, comprising ~95% of this tissue by weight. Extracellular organic matrix (ECM) of the mature enamel accounts for roughly 1% by weight with the rest being water. Despite the fact that in mature enamel ECM is a minor component, it plays an important toughening role (Baldassarri et al., 2008; Yahyazadehfar and Arola, 2015). The basic building block of enamel is the enamel rod—a bundle of high aspect ratio crystallites. Individual enamel rods run from the dentin-enamel junction (DEJ) to the enamel surface. The tracks of enamel rods are form a complex decussating pattern (Wilmers and Bargmann, 2020). The rods are embedded in an interrod matrix consisting of crystals oriented at an angle to the rod crystals (Beniash et al., 2019).

Enamel mineral is susceptible to dissolution under acidic conditions. Bacteria in enamel plaque, the biofilm on the enamel surface, produce lactic acid, which dissolves enamel mineral, leading to formation of caries lesions (Featherstone, 2000). These lesions, if left untreated, can lead to weakening of the tooth, inflammation of the pulp tissues and tooth loss. Caries is the most prevalent chronic infectious disease of the oral cavity affecting 60%–90% of children and the vast majority of adults (Petersen et al., 2005) and it is well established that genetic factors affect susceptibility to caries (Shuler, 2001; Shaffer et al., 2011; Vieira et al., 2014). At the same time, due to the multifactorial etiology, the relationships between individual polymorphisms and caries susceptibility are often weak, although a number of genes related to odontogenesis and antibacterial defense show significant associations (Vieira et al., 2014).

Although mature enamel is the most highly mineralized tissue it starts as a self-assembled protein gel (Margolis et al., 2006) in which the nascent mineral crystalline ribbons are suspended. The secretion of enamel is carried out by ameloblasts, highly specialized secretory cells of the epithelial origin (Lacruz et al., 2017). Secretory ameloblasts form a highly specialized secretory apparatus—Tomes' process, responsible for secretion of one rod and a portion of the interrod matrix. During the secretory stage ameloblasts move away from the DEJ depositing enamel rods. The secreted enamel matrix consists of three major enamel matrix proteins (EMPs)–amelogenin, comprising ~90% of the ECM, ameloblastin and enamelin (Margolis et al., 2006). EMPs undergo a series of proteolytic cleavages, which are essential for the proper enamel formation (Simmer and Hu, 2002). During the maturation phase, the mineral crystals grow in thickness and EMPs are degraded and removed (Pham et al., 2017). At the end of the maturation only a small organic fraction containing small peptides and insoluble proteinaceous matrix remains. This small fraction of heavily crosslinked proteins in mature enamel exists in a form of enamel tufts and rod sheaths (Amizuka et al., 1992). The composition of this insoluble proteinaceous matrix remains poorly understood (Duverger et al., 2016). It was established that a small fraction of enamel matrix deposited during secretory stage of amelogenesis remains, while the majority of transient proteins, collectively called amelogenins at this time, is degraded (Robinson et al., 1971; Robinson et al., 1975, 1977). It has been proposed that this insoluble fraction contains keratins (Robinson et al., 1989) and is heavily cross-linked *via* isopeptide bonds (Robinson and Hudson, 2011). However, until recently the evidence of keratins in enamel was sparse and inconclusive.

Recently a number of epithelial keratins were identified in the enamel organ using RNA-Seq (Duverger et al., 2014). One of these keratins–keratin 75 (K75, formerly K6hf) has a highly specific expression pattern. It is expressed in the inner sheath of the hair follicle, nail bed and lingual papillae (Winter et al., 1998; Wang et al., 2003). More recently, KRT75 was identified in ameloblasts and enamel ECM by immunochemistry, western blot and mass spectrometry (Duverger et al., 2014; Chiba et al., 2019; Yang et al., 2019). A single amino acid substitution KRT75^{A161T}, caused by A to G missense mutation in KRT75 gene is associated with *Pseudofolliculitis barbae* (PB) colloquially known as barber rash (Duverger et al., 2014). This gene mutation leads to Ala161 to Thr substitution at the beginning of the highly conserved A1 α-helical region of the protein. Interestingly, the same polymorphism is also associated with the higher prevalence of caries and altered structural and mechanical properties of dental enamel. Importantly, western blot analysis of forming porcine enamel revealed that, unlike other EMPs, K75 is not degraded during the maturation stage. Several other mutations in conserved regions epithelial keratins expressed in ameloblasts have also been found to be associated with higher caries susceptibility and enamel anomalies (Duverger et al., 2018; Duverger et al., 2019; Raza et al., 2022).

There are currently no animal models of PB, however Krt75^{tm1Der} knock-in (KI) mouse with deletion of Asn159, a highly conserved amino acid in the α-helix initiation motif is available (Chen et al., 2008). Asn159 is only 2 amino acids away from Ala161, which when substituted by Thr is associated with higher caries susceptibility (Duverger et al., 2014). We hypothesize that the conserved region around Ala161 is critical for K75 function and that mice with Asn159 deletion will have altered enamel properties and higher caries susceptibility. To test this hypothesis, we conducted a comparative study of molar enamel in WT and Krt75^{tm1Der} mice using Microcomputed Tomography (μCT), Light Microscopy, simulated acid attack, and microhardness (MH) analysis.

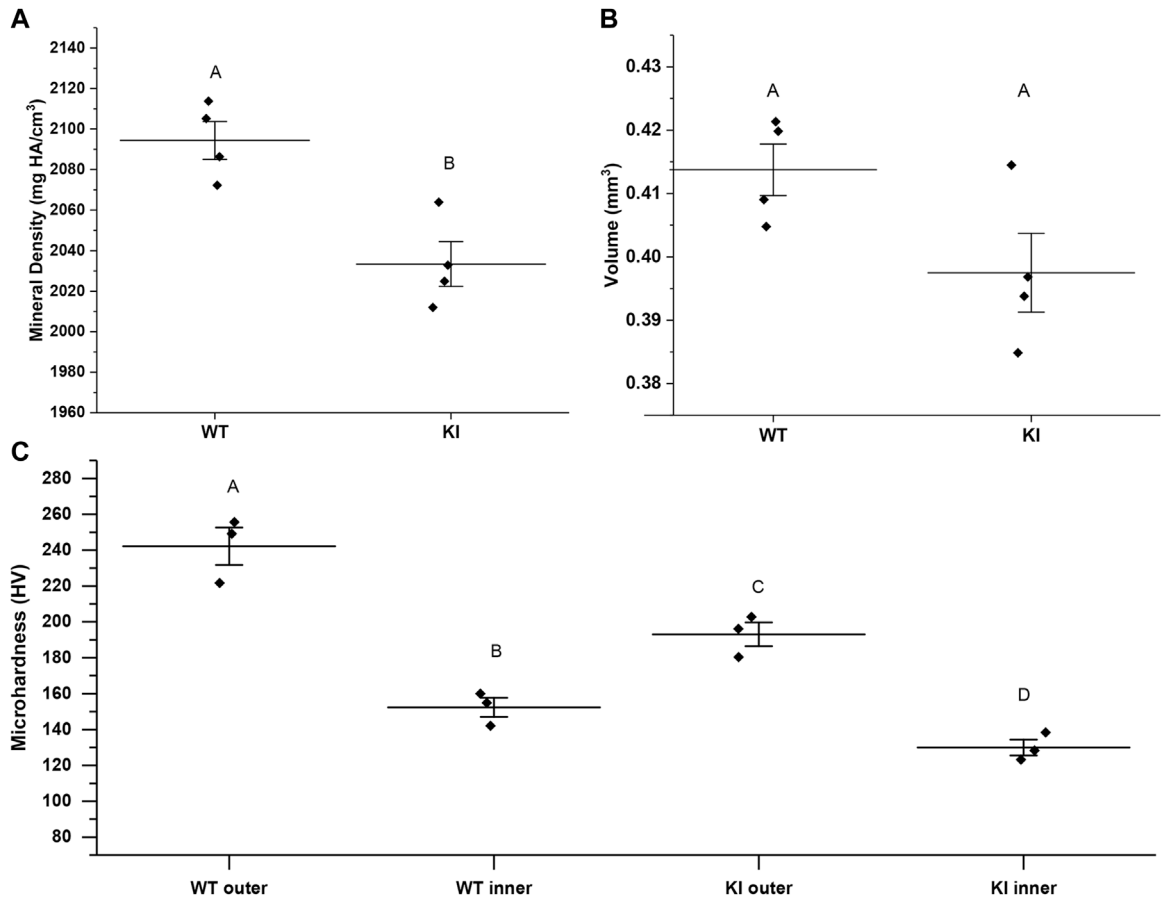

FIGURE 1
MicroCT analysis of mineral density **(A)** and volume **(B)** of enamel from 1 month-old WI and KI mice. **(C)** Microhardness values for 1-month-old WT and KI 1st molar enamel. Diamonds represent values of individual specimens. Horizontal lines indicate means and whiskers show standard errors. Similar letters indicate populations which are not significantly different from each other.

TABLE 1 Microhardness values (HV) of 1-month-old 1st molars.

	N	Mean	St. Dev	Min	Median	Max
WT outer	3	246.5	27.15	215.4	259.0	265.2
WT inner	3	153.5	19.14	137.7	148.1	174.8
KI outer	3	185.9	13.20	170.7	193.2	193.9
KI inner	3	127.6	4.526	122.5	128.8	131.3

Materials and methods

Animal model

Krt75^{tm1Der} KI mouse on the C57BL/6 background with deletion of 159Asn, two amino acids away from A161T substitution site were used for this study. The mice are housed at the University of Pittsburgh DLAR facility and all the studies were approved by the University of Pittsburgh IACUC. Mice were euthanized using carbon dioxide and secondary euthanasia was performed. Prior to analysis, hemimandibles from 1-month old WT and KI mice were dissected and stored immediately in 70% ethanol.

µCT analysis

For µCT analysis right hemi-mandibles of 1-month-old mice of WT and homozygous Krt75^{tm1Der} genotype were used. Four animals per group were used in the study. The mandibles were dissected, cleaned from soft tissues and kept in 70% ethanol. Microcomputed tomography (µCT) analysis was performed on Scanco µCT 50 (Scanco Medical, Brüttisellen, Switzerland) system. The hemimandibles were scanned at 6 µm voxel size, 55 KVp, 0.36 rotation step (180°angular range) and a 1500 m exposure per view. The scans were performed in 70% EtOH. The Scanco µCT software (HP, DEC windows Motif 1.6) was used for 3D

10.3389/fphys.2022.1102553

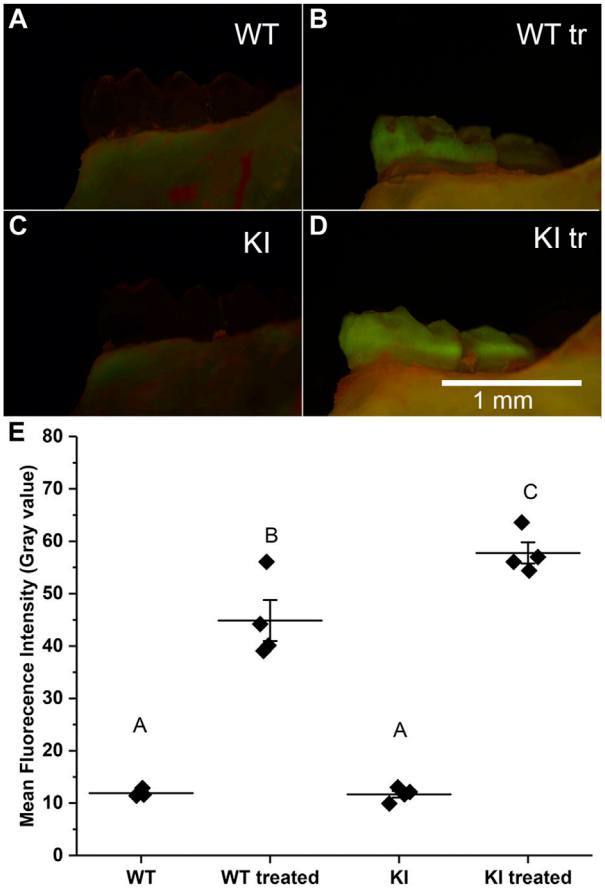

FIGURE 2
Micrographs of hemimandibles in buccal view of **(A)** untreated WT, **(B)** treated WT, **(C)** untreated KI, **(D)** treated KI. **(E)** A plot of mean fluorescence intensity (grey values) obtained for buccal surfaces of 1st molars. Diamonds represent mean fluorescence intensity for each specimen. Horizontal lines represent mean values for each group and whiskers indicate standard errors. Similar letters indicate populations which are not significantly different from each other.

reconstruction and viewing of the images. Quantitative analysis was performed on an operator-defined region of interest around the crowns of 1st molars of right hemimandibles. Volumes within the region of interest were segmented using a global threshold of 0.84 g HA/cc and total enamel volume and mineral density of enamel of the first molars were calculated.

Microhardness tests

Microhardness tests were performed on left hemimandibles from the animals used for μCT analysis. The hemimandibles were air dried and mounted in Epoxy resin (EMS, Hatfield, PA). The samples were ground using Minimet 1000 semi-automatic grinder-polisher (Buehler, Lake Bliff, IL) on the mesio-distal plane until the enamel from the first molars was exposed using 400 grit paper. The samples then were polished using 600 and 800 grit papers, followed by final polishing with 12, 6, 1, and 0.5 μm MetaDi diamond suspensions (Buehler, Lake Bluff, Il). The micro indentation test was then performed using IdentaMet 1105 microhardness tester (Buehler, Lake Bluff, Il) equipped with a CCD camera, connected to a computer equipped with OmniMet software (Buehler, Lake Bluff, Il). The tests were conducted using a Vickers hardness diamond tip with a load of 25 gf and dwell time of 5 s. Six measurements in the outer and 6 measurements in the inner enamel were taken from the mesial enamel of the first molar of each specimen and the averages of those 6 measurements were used the Vickers hardness numbers (HV) for the outer and inner enamel.

Simulated acid attack experiments

Intact right hemimandibles from 4 1-month-old mice of each genotype were used in the simulated acid attack

10.3389/fphys.2022.1102553

TABLE 2 Rhodamine Fluorescence Intensity (gray values) of 1-month-old 1st molars.

	N	Mean	St. Dev	Min	Max
WT	4	11.9	0.66	11.4	12.9
WT treated	4	44.9	7.79	39.1	56.1
KI	4	11.7	1.30	9.9	13.0
KI treated	4	57.8	4.03	54.4	63.6

experiments. The experiments were designed based on the published procedure (Vieira et al., 2015). Each mandible was mounted in a Petri dish using double sided tape and were submerged in 40 ml of the demineralization solution containing 1.3 mmol/L Ca, 0.78 mmol/L P, 0.05 mol/L acetate buffer, and 0.03 ugF/ml, pH 5.0 to induce artificial caries (Vieira et al., 2015). The teeth were exposed to the demineralizing solution for 10 h, rinsed in distilled deionized water (DDW) for 5 min followed by incubation in 2 changes of Ca^{2+}-free PBS for 5 min each. Left non-treated hemimandibles from the same animals were used as controls.

Rhodamine staining

Hemimandibles exposed to demineralizing solutions and the contralateral controls were incubated in 0.02% Rhodamine-6G in PBS for 30 min. The mandibles were rinsed in PBS on a rocking table for 5 min. The mandibles then were microphotographed using a fluorescent dissecting microscope Leica DFC 450 under the same light conditions and exposure. Micrographs of buccal, lingual and occlusal surfaces of molars were taken per each specimen. The micrographs were analyzed using Fiji (ImageJ) image processing software package. The areas of 1st molars were selected from the buccal views of all specimens and the average fluorescence intensities were calculated. The statistical analysis of the data was performed using OriginPro 2017 graphing and data analysis software package.

Statistical analysis

Statistical analyses of the data were performed using OriginPro 2017 graphing and data analysis software package. The data was analyzed using one-way ANOVA and t-tests in which equal variance was not assumed (Welch correction). Statistically significant differences were determined at p-value ≤ 0.05.

Results

µCT analysis of molar enamel

Mineral density (MD) and enamel volume (EV) data from the 1st molar enamel from 1-month-old WT ($n = 4$) and KI mice ($n = 4$) were collected and analyzed. MD of enamel from KI mice was significantly lower than that of WT (2033.42, SD = 22.07 vs. 2094.37 ± 18.69; $p = 0.006$) (Figure 1A). There were no significant differences in EV between two genotypes (Figure 1B).

Microhardness studies

Two-way ANOVA revealed that the population means were significantly different between genotypes and between outer and inner enamel ($p < 0.01$ for both). Microhardness of inner enamel was significantly lower than that of outer enamel in both genotypes ($p = 0.001$ for WT and $p = 0.02$ for KI) (Figure 1C; Table 1). Microhardness of outer enamel was significantly lower in KI than in WT ($p = 0.02$). Similarly, microhardness of inner enamel was significantly lower in KI ($p = 0.03$) (Figure 1C; Table 1).

Simulated acid attack experiments

The acid attack experiments were conducted as described in Materials and methods. The extent of demineralization was determined by changes in the fluorescence intensity of the samples after exposure to Rhodamine-6G. We hypothesized that enamel of teeth with more extensive demineralization will retain more rhodamine-6G due to the higher porosity and will therefore have higher fluorescence intensity, as has been shown previously in other systems (Lee et al., 2003; Ebacher and Wang, 2009). Our observations revealed that untreated samples had much lower fluorescence intensity than the treated samples in both groups (Figures 2A–D). Furthermore, our visual examination has strongly suggested that KI treated molars had higher levels of fluorescence than WT treated molars (Figures 2B, D).

To assess quantitative differences in average intensities (grey level) among four groups we conducted a two-way ANOVA test which showed that population means of treatment and genotype are significantly different ($p < 0.01$). The *post hoc* Bonferroni test revealed that the intensity in control specimens was substantially and significantly lower than in the treatment groups ($p < 0.0001$ in both cases) and the mean intensity values of control specimens were not significantly different (Figure 2E; Table 2). The mean intensity of KI 1st molars exposed to the simulated acid attack was significantly higher than of WT 1st molars ($p < 0.04$) suggesting that the $Krt75^{tm1Der}$ KI mice are significantly more susceptible to acid attack.

Discussion

Our studies revealed significant differences in several physical and chemical characteristics of enamel of 1st molars from 1-month old WT and Krt75^{tm1Der} KI mice. Our μCT data showed a small but highly significant decrease in enamel density. The fact that enamel in 1-month-old KI animals is less dense than that in WT of the same age potentially points out to enamel maturation problems in KI, since at this age the crowns are exposed to the environment for less than 2 weeks and it is unlikely that the lower density is due to leaching of mineral ions. At the same time, there were no differences in the volume of enamel in both genotypes and in its overall appearance. This parallels the situation in human carriers of KRT75^{A161T} polymorphism, in which the clinical appearance of the teeth is normal, however the quality of enamel is altered (Duverger et al., 2014).

Our microhardness studies of 1st molars in 1-month-old WT and KI mice demonstrate the reduced hardness of enamel in KI. These results also parallel the results of the microhardness studies of enamel in humans, which show a reduced enamel hardness in carriers of A161T substitution in K75. However in humans the reduction in hardness was only observed in the inner enamel (Duverger et al., 2014). These differences can be attributed to the differences in decussating pattern between human and rodent molar enamel. The reduction in enamel hardness can potentially lead to higher enamel wear, and increased susceptibility to accumulating microdamages.

The results of the simulated acid attack revealed a greater increase in porosity of KI enamel after the treatment, which indicates KI enamel is more soluble. Again, these results parallel the observations that KRT75^{A161T} polymorphism in humans which is associated to higher susceptibility to acid attack (Duverger et al., 2014).

Overall, these results indicate that enamel properties on Krt75^{tm1Der} KI to a large degree recapitulate the altered properties of enamel in human carriers of KRT75^{A161T} polymorphism, and that this KI can be used as a model to study the effects of point mutations in conserved regions of epithelial keratins expressed by ameloblasts on enamel properties and the susceptibility to caries. Such future studies can provide insights into roles of keratins in enamel formation and its function and will lead to a better understanding of genetic basis of caries susceptibility.

Data availability statement

The original contributions presented in the study are included in the article/Supplementary Materials, further inquiries can be directed to the corresponding author.

Ethics statement

The animal study was reviewed and approved by IACUC of University of Pittsburgh.

Author contributions

EB developed the concept of the study, secured funding, contributed to the data analysis, edited the manuscript and the figures. RD participated in mice colony maintenance, tissue disections, conducted microCT data collection and analysis, conducted the simulated acid attack studies, wrote the first draft of the manuscript and edited following versions. BV participated in mouse colony maintenance, conducted quantitative image analysis for simulated acid attack experiments, participated in manuscript writing and editing. LB participated in mouse colony maintenance, conducted microCT data collection and analysis and edited the final version of the manuscript. CMG participated in development of the experimental approaches, mouse colony maintenance, edited the final version of the manuscript. KV and LL developed the methods of data collection and analysis for microCT studies, trained others and oversaw all steps of the microCT data collection and analysis. MIM edited the final version of the manuscript, played a major role at the early stages of concept development of the project, provided KI mice and edited the final version of the manuscript.

Funding

The study was supported by R21DE029604 and R21DE029604-01S1 to EB and by S10OD021533 to KV.

Conflict of interest

The authors declare that the research was conducted in the absence of any commercial or financial relationships that could be construed as a potential conflict of interest.

Publisher's note

References

Amizuka, N., Uchida, T., Fukae, M., Yamada, M., and Ozawa, H. (1992). Ultrastructural and immunocytochemical studies of enamel tufts in human permanent teeth. *Arch. Histol. Cytol.* 55 (2), 179–190. doi:10.1679/aohc.55.179

Baldassarri, M., Margolis, H. C., and Beniash, E. (2008). Compositional determinants of mechanical properties of enamel. *J. Dent. Res.* 87 (7), 645–649. doi:10.1177/154405910808700711

Beniash, E., Stifler, C. A., Sun, C.-Y., Jung, G. S., Qin, Z., Buehler, M. J., et al. (2019). The hidden structure of human enamel. *Nat. Commun.* 10 (1), 4383. doi:10.1038/s41467-019-12185-7

Chai, H., Lee, J. J. W., Constantino, P. J., Lucas, P. W., and Lawn, B. R. (2009). Remarkable resilience of teeth. *Proc. Natl. Acad. Sci. U. S. A.* 106 (18), 7289–7293. doi:10.1073/pnas.0902466106

Chen, J., Jaeger, K., Den, Z., Koch, P. J., Sundberg, J. P., and Roop, D. R. (2008). Mice expressing a mutant Krt75 (K6hf) allele develop hair and nail defects resembling pachyonychia congenita. *J. Invest. Dermatol.* 128 (2), 270–279. doi:10.1038/sj.jid.5701038

Chiba, R., Okubo, M., Yamamoto, R., Saito, M. M., Kobayashi, S., Beniash, E., et al. (2019). Porcine keratin 75 in developing enamel. *J. Oral Biosci.* 61 (3), 163–172. doi:10.1016/j.job.2019.06.002

Cuy, J. L., Mann, A. B., Livi, K. J., Teaford, M. F., and Weihs, T. P. (2002). Nanoindentation mapping of the mechanical properties of human molar tooth enamel. *Arch. Oral Biol.* 47 (4), 281–291. doi:10.1016/s0003-9969(02)00006-7

DeRocher, K. A., Smeets, P. J., Goodge, B. H., Zachman, M. J., Balachandran, P. V., Stegbauer, L., et al. (2020). Chemical gradients in human enamel crystallites. *Nature* 583 (7814), 66–71. doi:10.1038/s41586-020-2433-3

Duverger, O., Beniash, E., and Morasso, M. I. (2016). Keratins as components of the enamel organic matrix. *Matrix Biol.* 52-54, 260–265. doi:10.1016/j.matbio.2015.12.007

Duverger, O., Carlson, J. C., Karacz, C. M., Schwartz, M. E., Cross, M. A., Marazita, M. L., et al. (2018). Genetic variants in pachyonychia congenita-associated keratins increase susceptibility to tooth decay. *PLoS Genet.* 14 (1), e1007168. doi:10.1371/journal.pgen.1007168

Duverger, O., Cross, M. A., Smith, F. J. D., and Morasso, M. I. (2019). Enamel anomalies in a pachyonychia congenita patient with a mutation in KRT16. *J. Invest. Dermatol.* 139 (1), 238–241. doi:10.1016/j.jid.2018.07.005

Duverger, O., Ohara, T., Shaffer, J. R., Donahue, D., Zerfas, P., Dullnig, A., et al. (2014). Hair keratin mutations in tooth enamel increase dental decay risk. *J. Clin. Invest.* 124 (12), 5219–5224. doi:10.1172/jci78272

Ebacher, V., and Wang, R. (2009). A unique microcracking process associated with the inelastic deformation of haversian bone. *Adv. Funct. Mat.* 19 (1), 57–66. doi:10.1002/adfm.200801234

Featherstone, J. D. B. (2000). The science and practice of caries prevention. *J. Am. Dent. Assoc.* 131 (7), 887–899. doi:10.14219/jada.archive.2000.0307

He, L. H., and Swain, M. V. (2009). Enamel-A functionally graded natural coating. *J. Dent.* 37 (8), 596–603. doi:10.1016/j.jdent.2009.03.019

Lacruz, R. S., Habelitz, S., Wright, J. T., and Paine, M. L. (2017). Dental enamel formation and implications for oral health and disease. *Physiol. Rev.* 97 (3), 939–993. doi:10.1152/physrev.00030.2016

Lee, T. C., Mohsin, S., Taylor, D., Parkesh, R., Gunnlaugsson, T., O'Brien, F. J., et al. (2003). Detecting microdamage in bone. *J. Anat.* 203 (2), 161–172. doi:10.1046/j.1469-7580.2003.00211.x

Margolis, H. C., Beniash, E., and Fowler, C. E. (2006). Role of macromolecular assembly of enamel matrix proteins in enamel formation. *J. Dent. Res.* 85 (9), 775–793. doi:10.1177/154405910608500902

Petersen, P. E., Bourgeois, D., Ogawa, H., Estupinan-Day, S., and Ndiaye, C. (2005). The global burden of oral diseases and risks to oral health. *Bull. World Health Organ.* 83 (9), 661–669. S0042-96862005000900011.

Pham, C.-D., Smith, C. E., Hu, Y., Hu, J. C. C., Simmer, J. P., and Chun, Y.-H. P. (2017). Endocytosis and enamel formation. *Front. Physiol.* 8, 529. doi:10.3389/fphys.2017.00529

Raza, R., Chhabra, G., Bilal, M., Ndiaye, M. A., Liaqat, K., Nawaz, S., et al. (2022). A homozygous missense variant in K25 underlying overlapping phenotype with woolly hair and dental anomalies. *J. Invest. Dermatol.* doi:10.1016/j.jid.2022.07.010

Robinson, C., and Hudson, J. (2011). Tuft protein: Protein cross-linking in enamel development. *Eur. J. Oral Sci.* 119, 50–54. doi:10.1111/j.1600-0722.2011.00906.x

Robinson, C., Lowe, N. R., and Weatherell, J. A. (1975). Amino-acid composition, distribution and origin of tuft protein in human and bovine dental enamel. *Arch. Oral Biol.* 20 (1), 29–42. doi:10.1016/0003-9969(75)90149-1

Robinson, C., Lowe, N. R., and Weatherell, J. A. (1977). Changes in amino acid composition of developing rat incisor enamel. *Calcif. Tissue Res.* 23 (1), 19–31. doi:10.1007/bf02012762

Robinson, C., Shore, R. C., and Kirkham, J. (1989). Tuft protein - its relationship with the keratins and the developing enamel matrix. *Calcif. Tissue Int.* 44 (6), 393–398. doi:10.1007/bf02555967

Robinson, C., Weatherell, J. A., and Hallsworth, A. S. (1971). Variatoon in composition of dental enamel within thin ground tooth sections. *Caries Res.* 5 (1), 44–57. doi:10.1159/000259731

Shaffer, J. R., Wang, X., Feingold, E., Lee, M., Begum, F., Weeks, D. E., et al. (2011). Genome-wide association scan for childhood caries implicates novel genes. *J. Dent. Res.* 90 (12), 1457–1462. doi:10.1177/0022034511422910

Shuler, C. (2001). Inherited risks for susceptibility to dental caries. *J. Dent. Educ.* 65 (10), 1038–1045. doi:10.1002/j.0022-0337.2001.65.10.tb03447.x

Simmer, J. P., and Hu, J. C. (2002). Expression, structure, and function of enamel proteinases. *Connect Tissue Res.* 43 (2–3), 441–449. doi:10.1080/03008200290001159

Vieira, A. R., Gibson, C. W., Deeley, K., Xue, H., and Li, Y. (2015). Weaker dental enamel explains dental decay. *PLoS One* 10 (4), e0124236. doi:10.1371/journal.pone.0124236

Vieira, A. R., Modesto, A., and Marazita, M. L. (2014). Caries: Review of human genetics research. *Caries Res.* 48 (5), 491–506. doi:10.1159/000358333

Wang, Z. L., Wong, P., Langbein, L., Schweizer, J., and Coulombe, P. A. (2003). Type II epithelial keratin 6hf (K6hf) is expressed in the companion layer, matrix, and medulla in anagen-stage hair follicles. *J. Invest. Dermatol.* 121 (6), 1276–1282. doi:10.1111/j.1523-1747.2003.12644.x

Wilmers, J., and Bargmann, S. (2020). Nature's design solutions in dental enamel: Uniting high strength and extreme damage resistance. *Acta Biomater.* 107, 1–24. doi:10.1016/j.actbio.2020.02.019

Winter, H., Langbein, L., Praetzel, S., Jacobs, M., Rogers, M. A., Leigh, I. M., et al. (1998). A novel human type II cytokeratin, K6hf, specifically expressed in the companion layer of the hair follicle. *J. Invest. Dermatol.* 111 (6), 955–962. doi:10.1046/j.1523-1747.1998.00456.x

Yahyazadehfar, M., and Arola, D. (2015). The role of organic proteins on the crack growth resistance of human enamel. *Acta Biomater.* 19, 33–45. doi:10.1016/j.actbio.2015.03.011

Yang, X., Yamazaki, H., Yamakoshi, Y., Duverger, O., Morasso, M. I., and Beniash, E. (2019). Trafficking and secretion of Keratin 75 by ameloblasts *in vivo*. *J. Biol. Chem.* 294, 18475–18487. doi:10.1074/jbc.RA119.010037

Yilmaz, E. D., Schneider, G. A., and Swain, M. V. (2015). Influence of structural hierarchy on the fracture behaviour of tooth enamel. *Philos. Trans. A Math. Phys. Eng. Sci.* 373 (2038), 20140130. doi:10.1098/rsta.2014.0130

frontiers | Frontiers in Physiology

TYPE Original Research
PUBLISHED 06 February 2023
DOI 10.3389/fphys.2023.1116091

OPEN ACCESS

EDITED BY
Kazuhiko Kawasaki,
The Pennsylvania State University,
United States

REVIEWED BY
Ira Kurtz,
University of California, Los Angeles,
United States
Yong-Hee Patricia Chun,
The University of Texas Health Science
Center at San Antonio, United States

*CORRESPONDENCE
Yan Zhang,
yan.zhang2@ucsf.edu

†These authors have contributed equally to this work

SPECIALTY SECTION
This article was submitted to Craniofacial Biology and Dental Research, a section of the journal Frontiers in Physiology

RECEIVED 06 December 2022
ACCEPTED 16 January 2023
PUBLISHED 06 February 2023

CITATION
Chan B, Cheng IC, Rozita J, Gorshteyn I, Huang Y, Shaffer I, Chang C, Li W, Lytton J, Den Besten P and Zhang Y (2023), Sodium/(calcium + potassium) exchanger NCKX4 optimizes KLK4 activity in the enamel matrix microenvironment to regulate ECM modeling.
Front. Physiol. 14:1116091.
doi: 10.3389/fphys.2023.1116091

Sodium/(calcium + potassium) exchanger NCKX4 optimizes KLK4 activity in the enamel matrix microenvironment to regulate ECM modeling

Barry Chan[1†], Ieong Cheng Cheng[1†], Jalali Rozita[1], Ida Gorshteyn[1], Yulei Huang[2], Ida Shaffer[1], Chih Chang[1], Wu Li[1], Jonathan Lytton[3], Pamela Den Besten[1] and Yan Zhang[1*]

[1]Department of Orofacial Sciences, University of California, San Francisco, CA, San Francisco, United States, [2]Guangdong Provincial Key Laboratory of Stomatology, Guanghua School of Stomatology, Sun-Yat-sen University, Guangzhou, China, [3]Department of Biochemistry and Molecular Biology, University of Calgary, Calgary, AB, Canada

Enamel development is a process in which extracellular matrix models from a soft proteinaceous matrix to the most mineralized tissue in vertebrates. Patients with mutant *NCKX4*, a gene encoding a K^+-dependent Na^+/Ca^{2+}—exchanger, develop a hypomineralized and hypomature enamel. How NCKX4 regulates enamel protein removal to achieve an almost protein-free enamel is unknown. We characterized the upregulation pattern of *Nckx4* in the progressively differentiating enamel-forming ameloblasts by qPCR, and as well as confirmed NCKX4 protein to primarily localize at the apical surface of wild-type ruffle-ended maturation ameloblasts by immunostaining of the continuously growing mouse incisors, posing the entire developmental trajectory of enamel. In contrast to the normal mature enamel, where ECM proteins are hydrolyzed and removed, we found significant protein retention in the maturation stage of *Nckx4*$^{-/-}$ mouse enamel. The *Nckx4*$^{-/-}$ enamel held less Ca^{2+} and K^+ but more Na^+ than the *Nckx4*$^{+/+}$ enamel did, as measured by EDX. The alternating acidic and neutral pH zones at the surface of mineralizing *Nckx4*$^{+/+}$ enamel were replaced by a largely neutral pH matrix in the *Nckx4*$^{-/-}$ enamel. *In situ* zymography revealed a reduced kallikrein-related peptidase 4 (KLK4) activity in the *Nckx4*$^{-/-}$ enamel. We showed that KLK4 took on 90% of proteinase activity in the maturation stage of normal enamel, and that recombinant KLK4 as well as native mouse enamel KLK4 both performed less effectively in a buffer with increased [Na^+] and pH, conditions found in the *Nckx4*$^{-/-}$ developing enamel. This study, for the first time to our knowledge, provides evidence demonstrating the impaired *in situ* KLK4 activity in *Nckx4*$^{-/-}$ enamel and suggests a novel function of NCKX4 in facilitating KLK4-mediated hydrolysis and removal of ECM proteins, warranting the completion of enamel matrix modeling.

KEYWORDS

enamel biomineralization, ameloblast differentiation, K^+-dependent Na^+/Ca^{2+}-exchanger, kallikrein-related peptidase 4, extracellular matrix remodeling, proteinase activity

Introduction

Extracellular matrix (ECM) remodeling is a fundamental development process that contributes to the tissue-specific mechanical and structural properties (Yue, 2014). Dental enamel, a mineralized ECM orchestrated by epithelial-derived ameloblasts, is a tissue designed to protect teeth throughout a lifetime. Enamel undergoes a series of steps to revamp the tissue architecture and ECM

composition to produce the hardest substance in our bodies. Once teeth erupt, ameloblasts commit apoptosis, leaving enamel as a non-regenerative tissue (Moradian-Oldak, 2012). Understanding how the enamel matrix is modeled and biomineralized will lay the foundation for the future regeneration of functional ameloblasts and enamel.

Enamel matrix formation goes through two major phases, a proteinaceous matrix phase and a mineralizing phase (Bartlett, 2013). During the first phase, ECM proteins are synthesized and laid out by the polarized secretory ameloblasts (SABs) until the enamel matrix grows to its full thickness between the dentin matrix and a tightly conjunct ameloblast layer. After secretion, enamel matrix proteins are immediately selectively hydrolyzed by MMP20, the predominant matrix metalloproteinase present during the proteinaceous phase of enamel formation (Llano et al., 1997; Begue-Kirn et al., 1998; Caterina et al., 2002; Bartlett et al., 2004; Kim et al., 2005; Bartlett et al., 2011; Yamakoshi et al., 2011).

The major mineralizing phase begins with a brief period of transition ameloblasts. These cells generate a number of proteinases, primarily kallikrein-related peptidase 4 (KLK4), to degrade enamel matrix proteins processed by MMP20 previously (Simmer et al., 2009; Simmer et al., 2011; Yamakoshi et al., 2013; Bartlett and Simmer, 2014). Transition ameloblasts are promptly followed by maturation ameloblasts (MABs), which endocytose and remove KLK4- processed small molecular weight peptides from the ECM, thus making space for mineral deposition and the expansion of crystallized enamel (Nagano et al., 2009). MABs cyclically modulate between cells with a ruffle-ended (with membrane infoldings) and smooth-ended appearance (no membrane infoldings) at their apical border (Warshawsky and Smith, 1974; Josephsen and Fejerskov, 1977). Ruffle-ended and smooth-ended ameloblasts overlay enamel matrix in which pH cycles between 6.2 and 7.2, respectively, correspondingly (Takagi et al., 1998). Ameloblast modulation and underlying enamel matrix pH cycling are prerequisite events ensuring normal enamel formation (Lacruz et al., 2017), but how they are connected remains unclear.

The strength of enamel owes largely to its extraordinary degree of mineralization state. While bone and dentin are composed of about 70% minerals, enamel comprises approximately 96% minerals by weight (Follet et al., 2004). Studies tracing radiolabeled calcium have shown that about 14% of the enamel calcium is fetched by SABs using a trans-ameloblastic route, while MABs are responsible for delivering the remaining 86% of calcium to the enamel (Smith, 1998). Approximately 70% of this calcium is transported by ruffle-ended MABs through a transcellular route, and the rest is delivered through a paracellular route between smooth-ended MABs (Smith, 1998). Clinical genetic analyses have shown that mutations in human genes involved in trans-ameloblastic calcium transport, including *STIM1*, *ORAI1*, and *SLC24A4*, can cause amelogenesis imperfecta (AI), an inherited defect that significantly affects enamel structure and functions (Parry et al., 2013; Seymen et al., 2014; Wang et al., 2014; Herzog et al., 2015; Lacruz and Feske, 2015; Jalloul et al., 2016; Prasad et al., 2016). STIM1 and ORAI1 are primarily responsible for calcium entry into ameloblasts from the serosal compartment at their basal end (Furukawa et al., 2017; Nurbaeva et al., 2017; Smith et al., 2017). *SLC24A4* (solute carrier family 24, member 4) is a gene symbol approved by HUGO. Six mutations in the human *SLC24A4* gene have been linked with AI, accounting for about 1% of total AI cases (Jalloul et al., 2016).

SLC24A4 is also known as NCKX4, a member of the potassium-dependent sodium/calcium exchanger family. Members of this protein family possess eleven transmembrane helices, including two pairs referred to as alpha-1 and alpha-2 repeats, which form the ion-binding and transport pockets (Altimimi and Schnetkamp, 2007; Lytton, 2007; Parry et al., 2013). NCKX proteins function to exchange $4Na^+$ inward against $1Ca^{2+}$ plus $1K^+$ outward (Schnetkamp, 1989). NCKX4 is expressed in various tissues, including the brain, lung, thymus, and the olfactory and visual sensory neurons (Li et al., 2002). Therefore, in each of these tissues, NCKX4 may play specific roles related to microenvironment Ca^{2+} homeostasis (Altimimi and Schnetkamp, 2007). For instance, NCKX4-mediated extrusion of Ca^{2+} from the cilia of olfactory receptor cells shapes the olfactory response and mediates sensory adaptation (Stephan et al., 2011). As NCKX4 is significantly upregulated in mouse maturation ameloblasts (Hu et al., 2012; Wang et al., 2014; Bronckers et al., 2015), it is a good candidate for regulating the massive calcium extrusion required for the mineralization of the enamel ECM (Hu et al., 2012; Bronckers et al., 2015; Lacruz, 2017). However, the molecular mechanisms underlying the formation of hypomaturation type of amelogenesis imperfecta in the patients carrying *SLC24A4 (NCKX4)* mutation are unclear.

We hypothesize that, in addition to functioning as a calcium/sodium exchanger, NCKX4 also participates in ECM protein hydrolysis and removal during enamel development to achieve the highest degree of biomineralization. In this study, we utilized the continuously growing mouse incisors that allow us to investigate the complete trajectory of enamel ECM protein hydrolysis and removal in adult animals. An NCKX4 null mouse model (*Nckx4*$^{-/-}$) with deletion *Nckx4*$^{-/-}$ of *Nckx4* exon 6 and 7 (Li and Lytton, 2014) provided us the opportunity to investigate the specific functions of NCKX4 in enamel matrix modeling during amelogenesis. We found that the activity of KLK4 was optimized in the slightly acidic and low sodium microenvironment, which can be found in the developing enamel matrix overlaid by wild-type ruffle-ended maturation ameloblasts. In the *Nckx4*$^{-/-}$ mouse enamel matrix, which had an increased amount of Na^+ and disrupted pH cycling, KLK4 activity was significantly compromised compared to that in *Nckx4*$^{-/-}$enamel. *In vitro* analyses validated that the activity of recombinant and mouse enamel native KLK4 was suppressed by the elevated [Na^+] and pH. Our analyses demonstrate a novel function of NCKX4 in creating an optimized microenvironment for KLK4 to effectively hydrolyze proteins of the enamel matrix and promote its subsequent biomineralization and describe a previously uncharted molecular mechanism responsible for the hypomaturation type of enamel defect in *SLC24A4* (*NCKX4*) gene mutants.

Results

NCKX4, significantly upregulated in the early maturation ameloblasts, cyclically redistributes between the ruffle-ended and smooth-ended maturation ameloblasts

To correlate the expression pattern of *Nckx4* with ameloblast functions, ameloblasts of enamel organs at the various developmental stages were collected for semi-quantitative PCR. We found that as compared to secretory ameloblasts (P5), *Nckx4* expression started to increase in the post-secretory ameloblasts (P7) and reached a peak at the early maturation stage (P8), followed by a reduction at the late maturation stage (see Figure 1A). Overall, the expression levels of

10.3389/fphys.2023.1116091

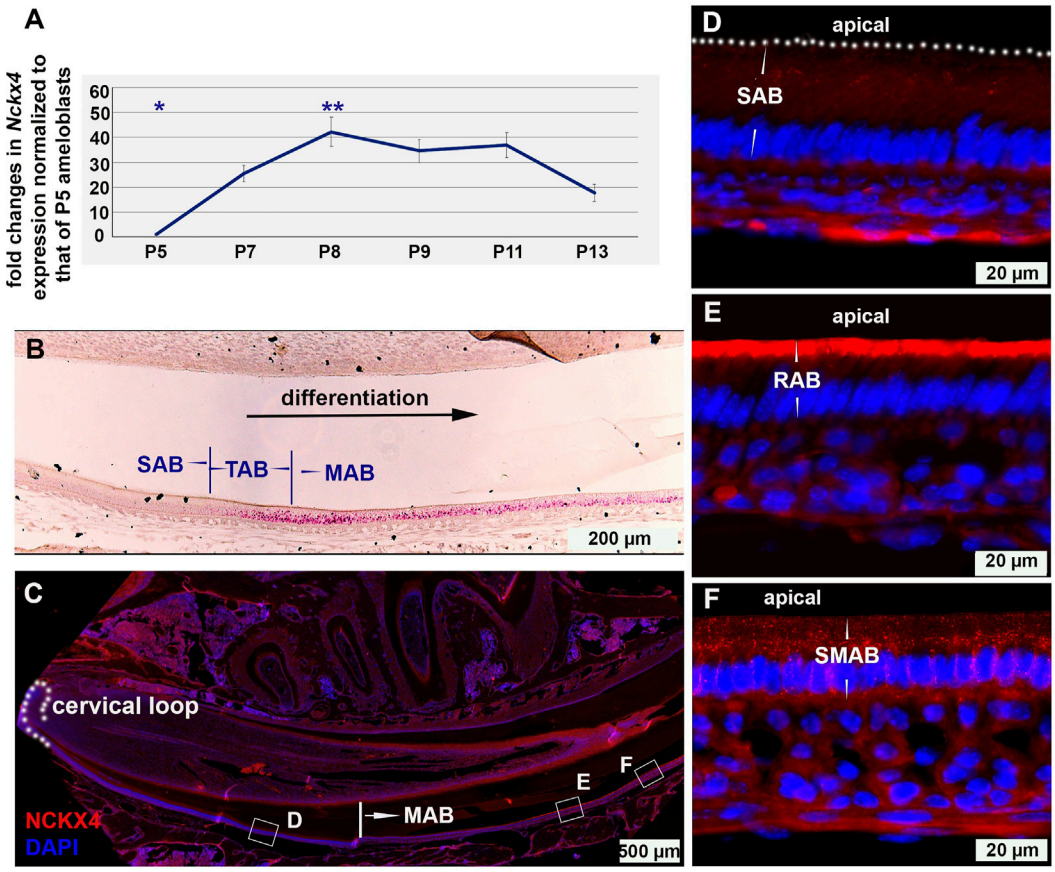

FIGURE 1
The temporal and spatial expression of NCKX4 in ameloblast lineage. **(A)** Semi-quantitative PCR analysis on the expression of *Nckx4* in the dissected ameloblasts at secretory (P5), transition (P7), early maturation (P8), mid-maturation (P9-P11), and late maturation (P13) stage of development. The average qPCR cycle threshold (Ct) of endogenous control *Gapdh* of P5 SAB is 20.4, and that of *Nckx4* of P5 SAB is 28.5. The fold changes in the expression levels of *Nckx4* in those more differentiated ameloblasts were normalized to the levels of secretory ameloblasts (P5), $n = 4$ per time point. Each n included the cells from 5 mice. The significance of differences was determined by one-way ANOVA analysis using SPSS Statistics package 19 followed by Tukey Post Hoc Tests. *$p < 0.05$ compared to P7, P8, P9, P11, and P13. **$p < 0.05$ compared to P5, P7, and P13. **(B)** *In situ* hybridization was used to assess the expression and distribution of *Nckx4* mRNA in secretory ameloblasts (SAB), transition ameloblasts (TAB), and maturation ameloblasts (MAB) on the sagittal sections of wild-type mouse incisors ($n = 3$). **(C)** Immunostaining of NCKX4 along the trajectory of ameloblast differentiation, from dental epithelial stem cells residing in the cervical loop, secretory, transition, to ruffle-ended and smooth-ended maturation ameloblasts, fully coexisting in the continuously growing mouse incisors ($n = 3$). **(D–F)** Magnified images taken from the regions boxed in panel C. The NCKX4 signal was relatively weak in secretory ameloblasts (SAB; panel D), primarily concentrated at the apical surface of ruffle-ended maturation ameloblasts (RAB; panel E), and sparsely distributed in the central cytosolic region of the smooth-ended maturation ameloblasts (SMAB; panel F).

Nckx4 in maturation ameloblasts were significantly greater than that in secretory ameloblasts. The pattern of *Nckx4* expression in the maturation stage ameloblasts, in particular in the early maturation ameloblasts, was confirmed by *in situ* RNA hybridization (RNAscope) (see Figure 1B).

Immunostaining on the full spectrum of ameloblast lineage on incisal sagittal sections showed that the NCKX4 signal apparently increased in the transition ameloblasts compared to secretory ameloblasts (Figure 1D), peaked in the early maturation ameloblast (MAB), and slightly reduced at the end of maturation stage (Figure 1C). In maturation stage ameloblasts, NCKX4 was primarily concentrated along the apical end of ruffle-ended ameloblasts (RAB) (see Figure 1E), but scattered in the cytosol of smooth-ended ameloblasts (SMAB) with reduced intensity (see Figure 1F). A recapture of the temporal and spatial expression pattern of NCKX4 aids us to understand its stage- and phase-specific functions in the enamel maturation.

NCKX4 is required for enamel biomineralization and enamel rod formation

As compared to the smooth and translucent enamel of *Nckx4*$^{+/+}$ incisor (see Figure 2A) and molars (see Figure 2B), the enamel layers on both *Nckx4*$^{-/-}$ incisor (see Figure 2C) and molars (see Figure 2D) were worn, chipped away and heavily discolored. These appearances are also found on the teeth of patients diagnosed with amelogenesis imperfecta.

MicroCT scanning showed that the enamel layer in both sagittal (see Figure 2E) and cross sections (see Figures 2E1, E2) of *Nckx4*$^{+/+}$ hemimandibles was radiopaque (indicated by red triangles in Figures 2E1, E2 for incisal enamel, orange triangles for molar enamel), and was well contrasted to the dentin and surrounding alveolar bone. Both enamel on incisors (indicated by red triangles in Figures 2F1, F2) and on molar (indicated by orange triangles in Figure 2F1) of *Nckx4*$^{-/-}$ mice had a significantly

10.3389/fphys.2023.1116091

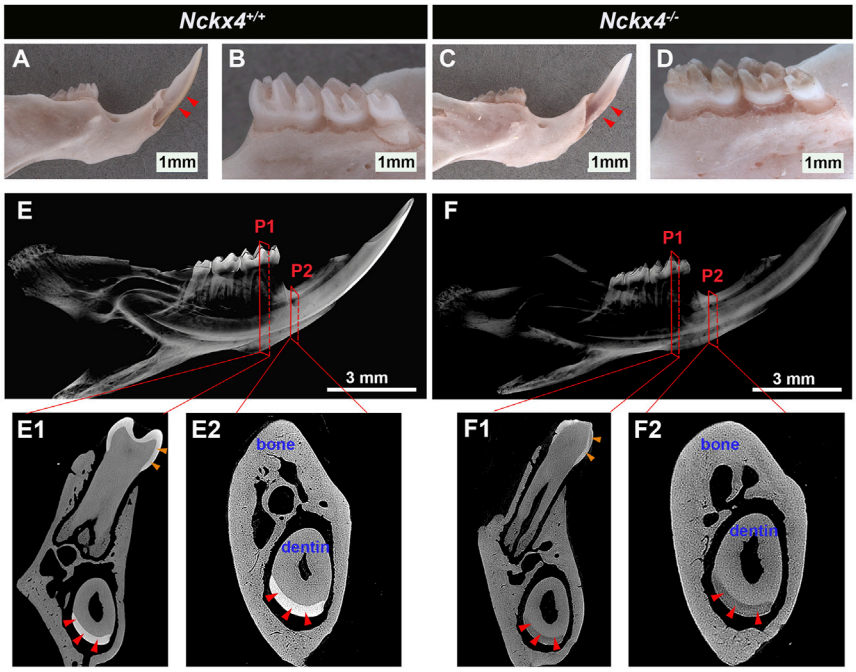

G

mineral density analysis on mineralized tissue at the panel (P1) indicated in Fig.2E and 2F			Mineral density analysis on mineralized tissue at the panel (P2) indicated in Fig.2E and 2F		
tissue	*Nckx4*$^{+/+}$	*Nckx4*$^{-/-}$	tissue	*Nckx4*$^{+/+}$	*Nckx4*$^{-/-}$
enamel	2219.4±48.37	1028.9±28.13 *	enamel	2557.7±37.24	1096.8±16.38 *
dentin	1552.2±27.07	1486.3±29.78	dentin	1466.3±27.41	1526.1±29.21
alveolar bone	1459.6±22.01	1506.1±61.34	alveolar bone	1537.5±27.26	1568.5±27.60

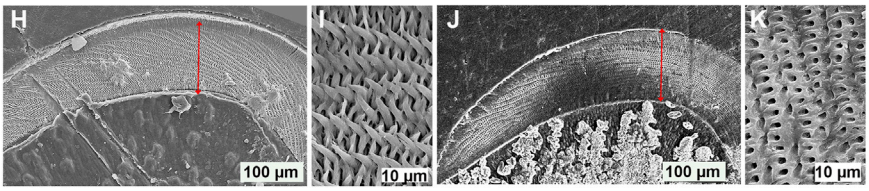

FIGURE 2
Characterization of enamel appearance, mineral density, and microstructure. **(A)** A representative image of the P7W *Nckx4*$^{+/+}$ mouse hemimandibular incisor with a sharp tip and pigmented outer enamel (indicated by red triangles). **(B)** A representative image of the *Nckx4*$^{+/+}$ mouse hemimandibular molars covered with well-formed cusps and translucent outermost enamel. **(C)** A representative image of P7W *Nckx4*$^{-/-}$ hemimandibular incisor on which white enamel was chipped off, only a small portion of enamel retained adjacent to the gingival margin region (indicated by red triangles). **(D)** A representative image of *Nckx4*$^{-/-}$ mouse hemimandibular molars on which the cusps were worn out and the outer enamel was heavily stained in brown. **(E)** A representative reconstituted 3D microCT image of the P7W *Nckx4*$^{+/+}$ mouse hemimandibles showed the radiopaque enamel layer on both molars and incisor. **(F)** A representative reconstituted 3D microCT image of the P7W *Nckx4*$^{-/-}$ mouse hemimandibles showed no well-contrasted radiopaque layer on both molars and incisor. **(E1)** A cross-section of the second buccal cusps of the *Nckx4*$^{+/+}$ first molar, designated as P1 in panel E, showed radiopaque enamel layers on the first molar (indicated by orange triangles) and on the incisor (indicated by red triangles). **(E2)** A cross-section of the onset of the mesial angle of the first molar, designated as P2 in panel E, showed the enamel layer on the incisor (indicated by red triangles). **(F1)** A cross-section at P1 in panel F shows less radiopaque enamel layers on the first molar (indicated by orange triangles) and on the incisor (indicated by red triangles). **(F2)** A cross-section at P2 in panel F shows the enamel layer on the incisor (indicated by red triangles). **(G)** The mineral density measured by EDX in the P7W *Nckx4*$^{-/-}$ mouse enamel was reduced to 53% of that in the P7W *Nckx4*$^{+/+}$ enamel in P1, and 57% in P2, $*p < 0.05$, $n = 4$, determined by unpaired two-tailed Student's *t*-test. **(H)** Scanning electron microscopy (SEM) analysis of the P7W *Nckx4*$^{+/+}$ developing enamel on which the full thickness enamel layer is marked by a red line. **(I)** A representative magnified SEM image of the P7W *Nckx4*$^{+/+}$ enamel showed that the well-aligned enamel crystals were bundled together as individual enamel rods, arranged in a decussating pattern. **(J)** The thickness of the *Nckx4*$^{-/-}$ developing enamel (marked by a red line) was comparable to that of the *Nckx4*$^{+/+}$ enamel. **(K)** A representative magnified SEM image of the *Nckx4*$^{-/-}$ enamel showed the decussating arrangement of microstructures and increased enamel space between the empty holes. These holes represent the etched and removed minerals along the rod axis.

reduced radiopacity. The mineral density in the *Nckx4*$^{-/-}$ mouse enamel was reduced to 53% of that in the *Nckx4*$^{+/+}$ enamel in P1, and 57% in P2, $n = 4$, $*p < 0.05$, determined by unpaired two-tailed Student's *t*-test (see Figure 2G).

Cross sections of mouse hemimandibles at the planes indicated by P2 in Figures 2E, F showed that there was no significant alteration in the thickness of *Nckx4*$^{-/-}$ late maturation stage enamel as compared to that in *Nckx4*$^{+/+}$ matrix (see Figures 2H, J). SEM analysis revealed a normal decussating pattern of enamel prisms in both *Nckx4*$^{+/+}$ and *Nckx4*$^{-/-}$ developing enamel. However, compared to the well-developed independent enamel rod in *Nckx4*$^{+/+}$ matrix (see Figure 2I), no individualized enamel rod was formed in *Nckx4*$^{-/-}$

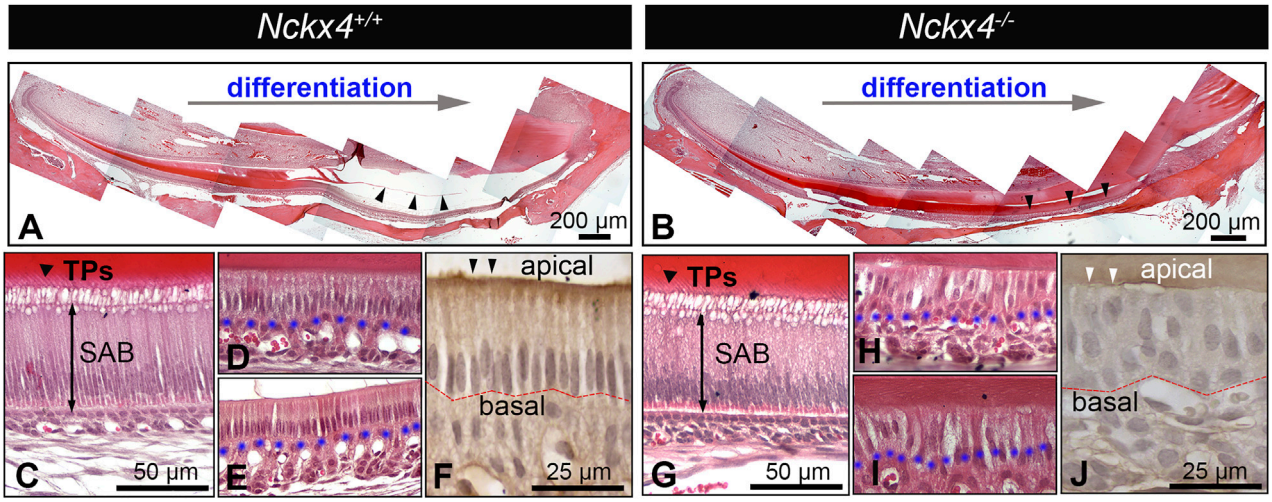

FIGURE 3
Histological analysis on ameloblasts and enamel extracellular matrix (ECM). **(A)** A representative H&E-stained sagittal section of the P7W *Nckx4*$^{+/+}$ mouse incisors showed that throughout the differentiation process, the enamel organic matrix gradually increased, reached its full thickness, then progressively diminished as indicated by the black triangles. **(B)** A representative sagittal section of the P7W *Nckx4*$^{-/-}$ mouse incisors showed that the enamel organic matrix gradually increased, reached its full thickness, then remained throughout the maturation stage, as indicated by the black triangles. **(C)** A magnified image showed the elongated secretory ameloblasts (SAB) and "picket-fence" shaped Tomes' processes (TPs) at the apical end of *Nckx4*$^{+/+}$ SAB. **(D)** A magnified image showed the reduced *Nckx4*$^{+/+}$ ruffled-ended ameloblasts and the foaming vacuolization in the apical cytoplasm. **(E)** A magnified image of the reduced *Nckx4*$^{+/+}$ smooth-ended ameloblasts. **(F)** Immunostaining showed the epithelial cell polarity biomarker PKC alpha (indicated by black triangles) present at the apical of *Nckx4*$^{+/+}$ maturation ameloblasts, which remained in a single-cell layer and maintained a well-defined boundary with papillary layer cells at their basal surface (outlined by red dotted line). **(G)** A magnified image of *Nckx4*$^{-/-}$ secretory ameloblasts (SAB) showed that their morphology resembled what is seen in panel C. **(H)** When advancing to the maturation stage, *Nckx4*$^{-/-}$ ameloblasts lost their single-cell layer arrangement, and the boundary with papillary layer cells was unclear. **(I)** In the late maturation stage, the enamel organic matrix was layer still retained, which are supposed to diminish in the normal development seen in panel E. **(J)** PKC alpha was not immunolocalized at the apical of *Nckx4*$^{-/-}$ maturation ameloblasts (indicated by white triangles). These ameloblasts were rearranged into a multiple-cell layer. The blue dotted lines in panel D,E,H, and I outline the boundary between maturation ameloblasts and the papillary layer.

enamel matrix (See Figure 2K). Therefore, NCKX4 is critical for the formation of enamel ECM with normal composition and microstructure.

Loss-of-function of NCKX4 results in alteration of enamel matrix protein removal and ameloblast morphology

H&E stained sagittal sections of *Nckx4*$^{+/+}$ hemimandibles showed a pink colored enamel matrix that gradually grew to its full thickness, then disappeared at the late development stage. The remaining EDTA demineralized enamel space is indicated by black triangles (see Figure 3A). H&E stained *Nckx4*$^{-/-}$ sections showed a similar secretory stage enamel matrix, but when advancing to its late maturation stage, the enamel matrix in *Nckx4*$^{-/-}$ mice remained present (indicated by the black triangles in Figure 3B).

Nckx4$^{+/+}$ secretory ameloblasts (SAB) were elongated and polarized with the characteristic Tomes' processes (TPs) developed at their apical surface (see Figure 3C), which are responsible for the EMP secretion and decussating pattern of enamel prisms (Zhang et al., 2019). There were no obvious morphological differences between *Nckx4*$^{+/+}$ and *Nckx4*$^{-/-}$ secretory ameloblasts (SAB) (see Figure 3G). When *Nckx4*$^{+/+}$ ameloblasts differentiated to maturation stage, as expected, their height reduced to the half of SAB, and there was a well-defined boundary from papillary layer cells at their basal surface (see Figures 3D, E). Ruffle-ended ameloblasts were identifiable as a classic appearance of a foamy vacuolization was present in their apical cytoplasm (Josephsen and Fejerskov, 1977) (see Figure 3D), while smooth-ended ameloblasts had increased intercellular spaces (see Figure 3E). However, no distinguishable ruffle-ended and smooth-ended ameloblasts were found in the *Nckx4*$^{-/-}$ maturation stage development. In addition, MAB lost their single-cell layer arrangement, and boundary from papillary layer cells was unclear.

The enamel matrix layer was retained throughout *Nckx4*$^{-/-}$ maturation stage (see Figures 3H, I). Epithelial cell polarity biomarker protein kinase C (PKC) alpha was immunolocalized at the apical of *Nckx4*$^{+/+}$ MAB (see Figure 3F), but not in the *Nckx4*$^{-/-}$ MAB (see Figure 3J).

Amelogenin proteins are retained in the *Nckx4*$^{-/-}$ mouse enamel matrix

Immunostaining on *Nckx4*$^{+/+}$ enamel matrix showed a reduced amelogenin immunoreactivity that finally disappeared as protein was removed and replaced by mineral in the mature enamel matrix (see white triangles in Figure 4A). In contrast, in *Nckx4*$^{-/-}$ mouse enamel, amelogenin immunostaining signal continued through the secretory stage, and remained even at the end of maturation stage (see Figure 4B).

SDS-PAGE showed no difference in the secretory stage enamel matrix proteins of *Nckx4*$^{+/+}$ mice as compared to *Nckx4*$^{-/-}$ mice (see Figure 4C), presenting mostly full-length amelogenin with a mass of 25 kDa, and amelogenin without the C-terminus (removed by MMP20) with a mass of 20 kDa (so called amelogenin 20). However, a considerable amount of matrix proteins remained in the maturation stage of the *Nckx4*$^{-/-}$ enamel

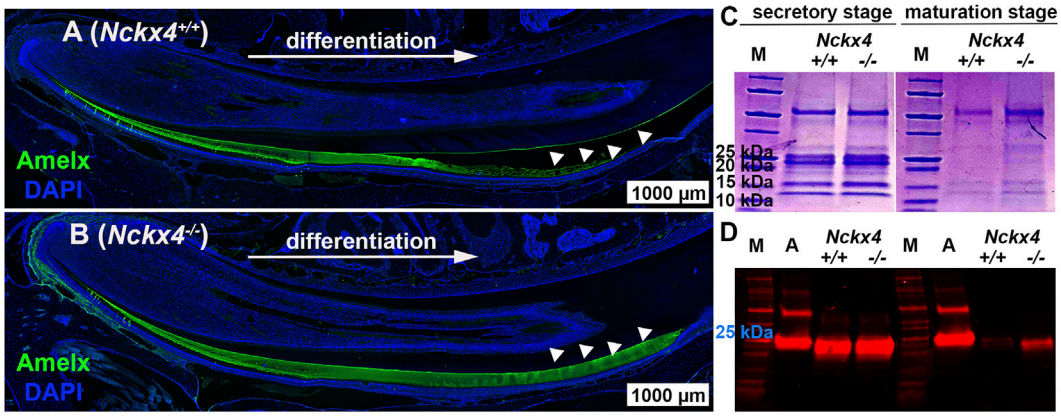

FIGURE 4
Characterization of ECM organic components in the mouse incisor enamel. **(A)** Immunostaining analysis of sagittal sections of the P7W *Nckx4*$^{+/+}$ mouse incisors showed that the amelogenin immunoreactive signal (green) gradually increased as ameloblasts continuously differentiated, reached maximal thickness, grew thinner, and at last disappeared (indicated by the white triangles). This pattern resembled the dynamic development of enamel ECM presented in Fig.3A since most of ECM proteins there were amelogenins. **(B)** In the P7W *Nckx4*$^{-/-}$ mouse incisor, amelogenin-containing matrix gradually thickened as development proceeded but remained the same thickness all the way through (indicated by white triangles). **(C)** SDS-PAGE analysis of ECM proteins collected from the P7W *Nckx4*$^{+/+}$ and *Nckx4*$^{-/-}$ mouse incisor enamel showed no detectable difference in either protein bands or band density at the secretory stage of development. However, at the maturation stage of development of the *Nckx4*$^{-/-}$ enamel, apparently more proteins with molecular weight less than 25 kDa were detected than that in *Nckx4*$^{+/+}$ controls. **(D)** Western blot analysis showed that amelogenin with a mass of 25 kDa was similarly present in the secretory stage of *Nckx4*$^{+/+}$ and *Nckx4*$^{-/-}$ enamel matrix, but a greater amount of amelogenin 20 kDa was retained in the *Nckx4*$^{-/-}$ maturation phase of enamel compared to *Nckx4*$^{+/+}$. Recombinant full-length amelogenin protein (amelogenin 25 kDa) was used as a positive control.

matrix. Western blot analysis further showed that amelogenin variants in the secretory stage of *Nckx4*$^{-/-}$ enamel were similar to those in the *Nckx4*$^{+/+}$ enamel, but more amelogenin 20 was detected in the maturation stage of *Nckx4*$^{-/-}$ enamel as compared to controls (see Figure 4D). The density analyses of the SDS-PAGE and WB data confirmed significantly more enamel matrix proteins, particularly amelogenins, retained in the *Nckx4*$^{-/-}$ maturation stage of enamel matrix compared to *Nckx4*$^{+/+}$ enamel (see Supplementary Figure S1). These results suggest that NCKX4 is necessary for processing and removing protein components as the enamel ECM models from a protein matrix to a mineralized matrix, a novel function of NCKX4 that has not been previously described.

Loss-of-function of NCKX4 increases KLK4 expression while decreasing the activity of KLK4 in enamel matrix.

During the maturation phase, KLK4 is the primary enzyme to hydrolyze amelogenin and other EMPs, allowing proteins to be removed and replaced by mineral (Smith, 1998; Ryu et al., 2002). The retention of enamel matrix proteins, in particular amelogenins in *Nckx4*$^{-/-}$ maturation enamel, led us to investigate the effect of NCKX4 deletion on the KLK4 expression and activity.

Semi-quantitative PCR analyses on mRNA extracted from enamel organ at the transition (P9), early maturation (P11) and middle maturation stage (P13) showed that an increase in *Nckx4*$^{-/-}$ expression compared to *Nckx4*$^{+/+}$ ameloblasts at all three development stages. There was an average of 2.3-fold increase in P9 cells, 1.7-fold in P11 cells, and 1.28-fold in P13 cells (see Figure 5A). The increase of *Klk4* mRNA in *Nckx4*$^{-/-}$ maturation ameloblasts was confirmed by *in situ* hybridization (see Figures 5B, C).

Western blot showed no effects of *Nckx4* deletion on the protein abundance of MMP20 in the secretory stage enamel matrix (see Figure 5D). However, consistent with increased *Klk4* mRNA expression levels, there was relatively more KLK4 present in the maturation stage of *Nckx4*$^{-/-}$ enamel matrix as compared to that in the *Nckx4*$^{+/+}$ enamel (see Figure 5E). A quantitative analysis on the density of WB immunoreactive bands confirmed that NCKX4 deletion did not affect MMP20 abundance in the secretory stage of enamel matrix, but resulted in a greater amount of KLK4 presence compared to the *Nckx4*$^{+/+}$ enamel matrix (see Figure 5F).

Through agar, fluorogenic quench peptide immobilized on the freshly microdissected maturation stage incisor segments was employed to visualize relative *in situ* KLK4 activity in the enamel matrix. The blue fluorescence signals from the hydrolyzed substrates (outlined by pink dotted line under the dentin-enamel junctions in Figure 5G), proportionally correspond to the KLK4 activity in the enamel matrix. The results demonstrated that KLK4 activity was decreased in *Nckx4*$^{-/-}$ enamel matrix, thus unable to completely process matrix proteins for enamel ECM modeling (see Figure 5H).

KLK4 activity is independent of calcium concentration but is suppressed by increased sodium concentration

As NCKX4 is a known ion transport, we first evaluated to what degree that *Nckx4* deletion affected the ion composition in enamel matrix. EDX analysis, used to measure the elemental composition in incisor centrolabial enamel underlying the mesial angle of the first molars, showed reduced relative amounts of calcium and potassium by about 50%, while sodium increased about 50% in the *Nckx4*$^{-/-}$ enamel matrix as compared to that in the *Nckx4*$^{+/+}$ enamel (see Figure 6A).

The EDX data led us to measure the KLK4 peptidase activity in the presence of various concentrations of calcium and sodium. Its results

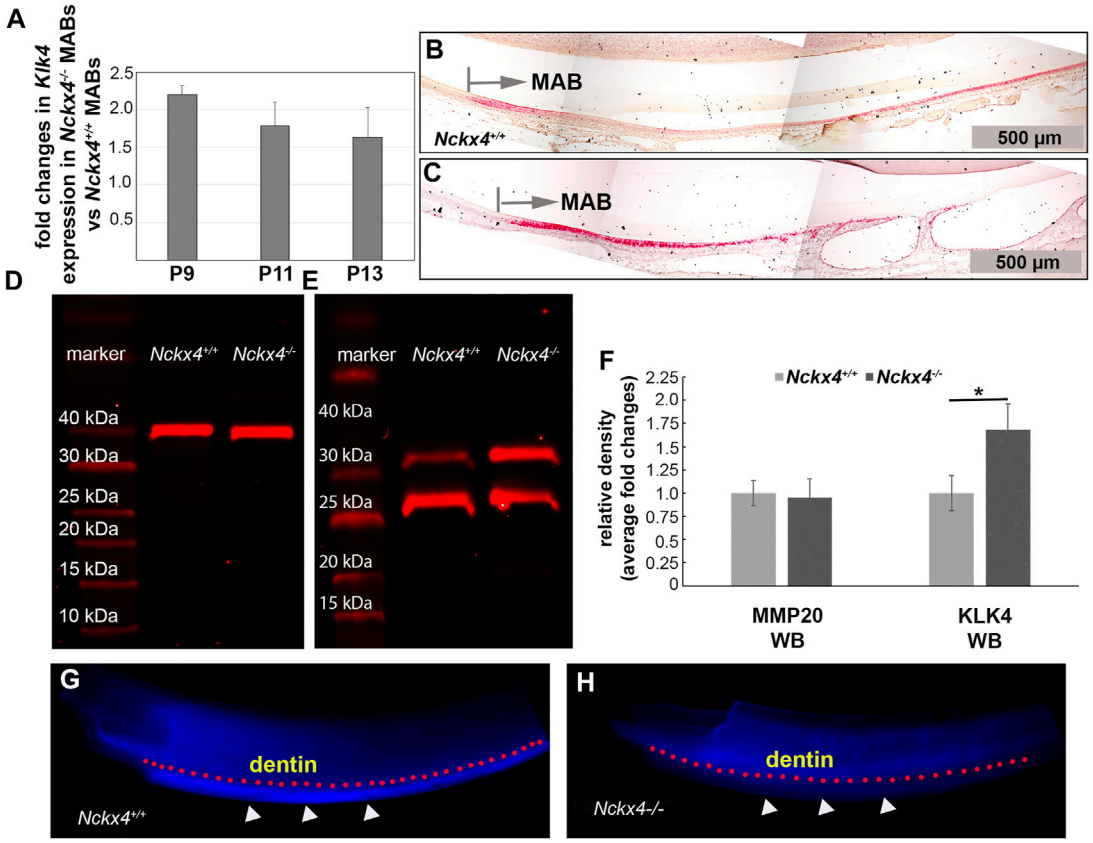

FIGURE 5
Characterization of *Klk4* mRNA expression in ameloblasts and KLK4 enzyme activity in the enamel matrix. **(A)** Semi-quantitative PCR analysis showed fold increase of *Klk4* mRNA in the *Nckx4*$^{-/-}$ ameloblasts compared to corresponding *Nckx4*$^{+/+}$ ameloblasts at P9, P11, and P13 days of development (n = 4, each n containing cells pooled from 5 mice). **(B)** *In situ* hybridization analysis of the P7W *Nckx4*$^{+/+}$ mouse incisors showed increased *Klk4* mRNA signals (in red) in the maturation ameloblasts (MAB), but the magnitude of increase progressively reduced. **(C)** Positive *Klk4* mRNA signals were enhanced in the P7W *Nckx4*$^{-/-}$ mouse MABs as compared to the same developmental stage of *Nckx4*$^{+/+}$ MABs in panel **(B) (D)** Western blot analysis showed that the abundance of MMP20 in the *Nckx4*$^{-/-}$ secretory stage enamel matrix was comparable to that in the *Nckx4*$^{+/+}$ enamel matrix. **(E)** Western blot analysis showed more KLK4 proteins (intact KLK4 and its partially hydrolyzed KLK4 fragment) present in the maturation stage of *Nckx4*$^{-/-}$ enamel compared to that in the *Nckx4*$^{+/+}$ enamel matrix. **(F)** The protein band density analyses of the western blot results in panels D and E quantified that NCKX4 deletion resulted in a greater amount of KLK4 in the *Nckx4*$^{-/-}$ enamel than in the *Nckx4*$^{+/+}$ enamel (n = 3, each n containing the enamel matrix from three mice, *$p < 0.05$, determined by unpaired two-tailed Student's t-test). **(G)** *In situ* KLK4 enzymatic analysis demonstrated that the *Nckx4*$^{+/+}$ maturation stage of enamel matrix was able to hydrolyze Arg-AMC bond in the quenched peptide BOC-Val-Pro-Arg-AMC to release fluorogenic AMC, indicated by the white triangles. A pink dotted line was drawn to outline the boundary between dentin and enamel. **(H)** *In situ* KLK4 analysis showed that much less fluorescence signal was released after the *Nckx4*$^{-/-}$ maturation stage of enamel matrix was incubated with BOC-Val-Pro-Arg-AMC peptide.

showed that while KLK4 activity was independent of calcium concentration (see Figure 6B) but it was significantly decreased in the presence of high (200 and 400 mM) NaCl, both *in vitro* (see Figure 6C) and *in situ*, where shows the suppressed KLK4 activity in the maturation stage of *Nckx4*$^{+/+}$ enamel matrix (see Figure 6D). KLK4 activity was maximized when NaCl concentration was between 100 and 150 mM. This data implies that the transitorily increased sodium concentration in confined enamel matrix caused by defective NCKX4 could adversely affect KLK4 activity.

KLK4 activity is suppressed by increased pH

We next asked if *Nckx4* deletion would affect enamel matrix acidification as a consequence of the reduced calcium phosphate formation? A pH indicator stain of freshly microdissected mandibular incisors showed that on the surface of *Nckx4*$^{+/+}$ enamel, acidic pH bands (red) and neutral pH bands cyclically alternated throughout enamel development (see Figure 7A, top panel). However, in the *Nckx4*$^{-/-}$ incisor enamel, the pH modulations failed to recur and the ECM remained neutral (see Figure 7A, lower panel).

To determine if this change in pH fluctuations affected KLK4 activity, we used an *in vitro* assay, in which the effect of pH on the ability of KLK4 to hydrolyze recombinant amelogenin 20 was measured. We used amelogenin 20 as the substrate since it is the major amelogenin species present in the early maturation stage of enamel matrix (Ryu et al., 1999). When the hydrolysis was performed in pH 5.25 or pH 6.0, there was less unhydrolyzed amelogenin 20 present on SDS-PAGE gel as compared to that in pH 6.75 or pH7.5 (see Figure 7B). The density analyses on the ratio of unhydrolyzed amelogenin20 vs the input protein confirmed that more amelogenin 20 was hydrolyzed in the acidic pH (see Figure 7C).

Furthermore, the ability of maturation stage *Nckx4*$^{+/+}$ incisor enamel matrix to hydrolyze fluorogenic peptide BOC-Val-Pro-Arg-

A

element	mass norm (%)	
	Nckx4$^{+/+}$	*Nckx4*$^{-/-}$
calcium	31.01+ 2.681*	18.62 + 2.370*
potassium	0.09 + 0.018*	0.04+ 0.0073 *
sodium	0.42 + 0.092*	0.81 + 0.169 *
phosphorous	10.2 + 1.283	10.02 + 2.197
magnesium	0.13 + 0.038	0.2 + 0.009
chlorine	0.48 + 0.102	0.3 + 0.008

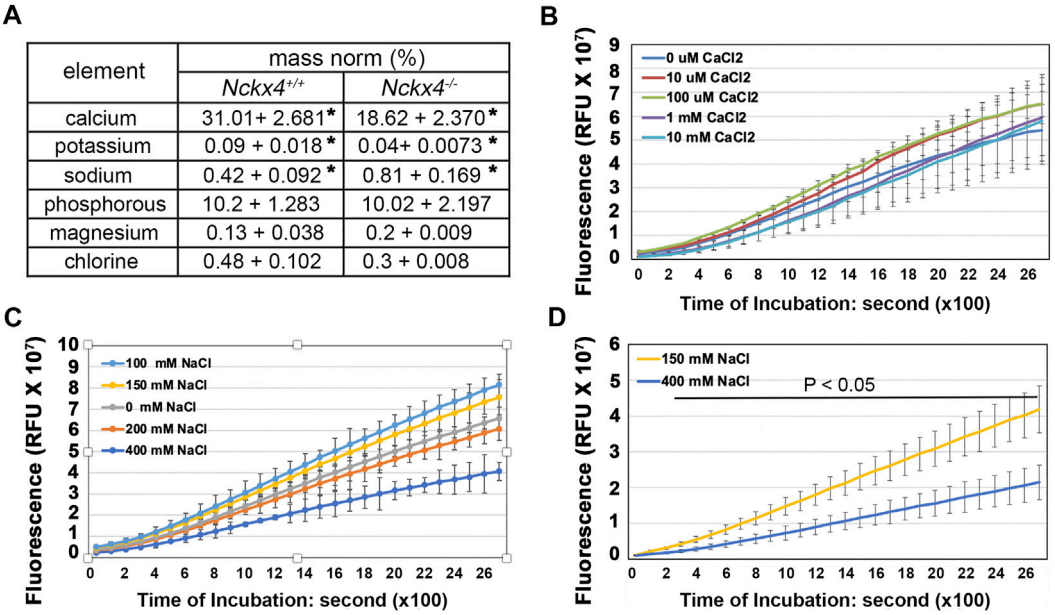

FIGURE 6
Determination of the effect of [Ca^{2+}] and [Na^{+}] on KLK4 activity. **(A)** An EDX analysis of the elements in the incisor centrolabial enamel underlying the mesial angle of the first molar showed reduced calcium and increased sodium in the *Nckx4*$^{-/-}$ matrix compared to that in the *Nckx4*$^{+/+}$ matrix. $n = 5$, $^{*}p < 0.05$, determined by two-tailed unpaired Student's *t*-test. **(B)** Recombinant KLK4's ability to hydrolyze BOC-Val-Pro-Arg-AMC peptide was not affected by various [Ca^{2+}]. **(C)** KLK4's ability to hydrolyze BOC-Val-Pro-Arg-AMC peptide was maximal in 100 and 150 mM NaCl and reduced in 200 mM NaCl. The reduction of KLK4 activity in 400 mM NaCl was significant compared to the rest of the conditions after 800s incubation ($p < 0.05$). There was no significant difference in KLK4 activity in 100 mM NaCl compared to 150 mM NaCl. $n = 4$. **(D)** The maturation stage of *Nckx4*$^{+/+}$ incisor segments was more effective in hydrolyzing BOC-Val-Pro-Arg-AMC peptide in 150 mM NaCl than in 400 mM NaCl. The difference in KLK4 activity at any time point after 200-s incubation was significant ($p < 0.05$), $n = 4$. The significance in these enzymatic analyses was determined by two-way ANOVA analysis followed by Tukey Post Hoc Tests using SPSS Statistics package 19.

AMC was also more effective in pH 6.2 than in pH 7.2 (see Figure 7D). These are the average pH found in enamel matrix under ruffle-ended ameloblasts and smooth-ended ameloblasts respectively. When there was no KLK4 present, the overall enzymatic activity of *Klk4*$^{-/-}$ mouse enamel matrix to hydrolyze BOC-Val-Pro-Arg-AMC peptide reduced to 11% of that in wild-type controls (see Figures 7D, E), indicating that KLK4 is responsible for about 89% of enzymatic activity of wild-type maturation stage of enamel matrix. There was no difference in the enzymatic activity of *Klk4*$^{-/-}$ enamel matrix in pH 6.2 and pH7.2 in term of hydrolyzing BOC-Val-Pro-Arg-AMC peptide, suggesting that other peptidases in *Klk4*$^{-/-}$ maturation stage of enamel were independent of pH.

Discussion

Enamel is an extracellular matrix (ECM) that undergoes dynamic modeling in its matrix composition and microstructure, progressing from a protein-rich matrix to a highly mineralized matrix. Clinical genetics studies have shown that mutations in the human NCKX4 gene can cause amelogenesis imperfecta, a disorder resulting from enamel malformation (Parry et al., 2013; Seymen et al., 2014; Herzog et al., 2015; Jalloul et al., 2016). Through analyzing the enamel matrix ion composition and matrix pH on mouse incisors, where the trajectory of enamel matrix modeling is fully present, and *in situ* and *in vitro* proteinase KLK4 activity, we identified an additional function of NCKX4 in regulating enamel matrix protein hydrolysis and enamel composition modeling. Our results showed that the activities of both recombinant and mouse enamel matrix native KLK4 were [Na^{+}]- and pH-dependent. By optimizing sodium concentration and pH in the encompassed enamel matrix compartment, NCKX4 promotes KLK4-mediated enamel matrix protein hydrolysis. Breaking down the enamel matrix proteins is necessary for ECM protein removal to give rise to a complete biomineralized enamel tissue.

In agreement with previous studies (Hu et al., 2012; Wang et al., 2015; Bronckers et al., 2017), we confirmed that NCKX4 was primarily present in maturation ameloblasts (MAB) during normal enamel development. In addition, we illustrated the dynamic expression pattern of *Nckx4* transcript from the transition stage of ameloblasts, to early maturation stage of ameloblasts, then to middle and maturation ameloblasts. Our immunostaining analyses on mouse incisor sagittal sections also localized NCKX4 predominately at the apical surface of ruffle-ended maturation ameloblasts (REMAs). This data further supports the significance of REMAs in transporting abundant minerals into the enamel matrix, facilitating the transformation of enamel from protein matrix to highly mineralized tissue (Smith, 1998; Katsura et al., 2014; Wang et al., 2015).

Our finding of a reduction of calcium (by approximately 50%) in the *Nckx4*$^{-/-}$ mouse enamel compared to wild-type controls supports the role of NCKX4 as a major player in transporting calcium into the enamel matrix. We found that the expression levels of *Pmca* and *Ncxs*, molecules at the apical surface of ameloblasts that are also known to

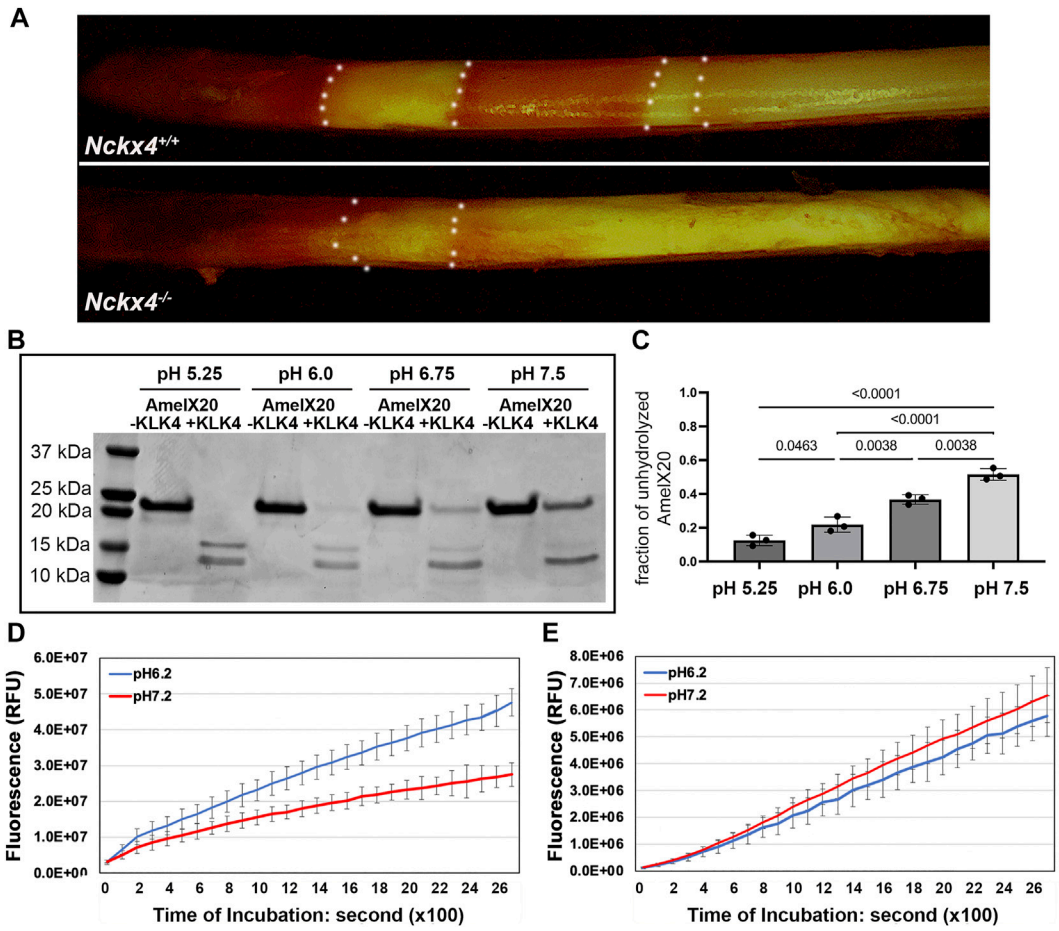

FIGURE 7
Determination of the effect of pH on KLK4 activity. **(A)** Methyl red staining revealed the cyclically alternating acidic pH bands (red) and neutral pH bands (yellow) presented on the P7W *Nckx4*$^{+/+}$ mouse incisor enamel but largely absent from the P7W *Nckx4*$^{-/-}$ mouse enamel. The boundary between acidic pH band and neutral pH band is outlined by the white dotted lines. **(B)** SDS-PAGE analysis of recombinant amelogenin 20 protein incubated overnight with or without recombinant KLK4 in buffer with various pH. **(C)** The protein band density analysis showed that the fraction of unhydrolyzed amelogenin 20 was significantly greater at pH 6.75 and pH 7.5, as compared to that in pH 5.25 and pH 6.0. Condition with pH 5.25 resulted in the least unhydrolyzed amelogenin 20, achieving the most effective digestion. Vice versa, condition with pH 7.5 gave rise to the lowest hydrolysis efficiency. The significance (p-value in the chart) was determined by one-way ANOVA analysis followed by Tukey Post Hoc Tests using SPSS Statistics package 19. **(D)** The maturation stage of *Nckx4*$^{+/+}$ incisor enamel hydrolyzed more peptides, releasing more fluorescence at pH 6.2 than at pH 7.2 at any time point after 200s incubation, $p < 0.05$, $n = 4$. The difference was determined by a two-tailed Student's t-test. **(E)** There was no difference in the hydrolysis of BOC-Val-Pro-Arg-AMC peptides between pH 6.2 and pH 7.2 by the maturation stage of incisor enamel matrix when KLK4 was deleted.

extrude calcium to enamel matrix (Nurbaeva et al., 2017; Robertson et al., 2017), were unchanged in *Nckx4*$^{-/-}$ maturation ameloblasts compared to *Nckx4*$^{+/+}$ ameloblasts by semi-quantitative PCR (data not shown). The data implies that these molecules were able to transport some amount of calcium but could not fully compensate for the loss of NCKX4.

In contrast to the wild-type mouse enamel, where ECM proteins are progressively processed and diminished, matrix proteins failed to be removed from the maturation stage of *Nckx4*$^{-/-}$ mouse enamel. Our SDS-PAGE and western blot analyses showed a retention of amelogenin 20 (the amelogenin with C-terminus removed by MMP20) in the *Nckx4*$^{-/-}$ enamel matrix. This result suggests that in addition to providing calcium, NCKX4 contributes to the hydrolysis of enamel matrix proteins at the maturation stage of amelogenesis. In principle, enamel matrix proteins of the secretory stage are primarily hydrolyzed by MMP20 (Bartlett et al., 2011); in the proceeding maturation stage, KLK4 is the primary enzyme to hydrolyze the remaining amelogenin and other EMPs (Ryu et al., 2002; Lu et al., 2008; Yamakoshi et al., 2011; Yamakoshi et al., 2013). Our quantitative enzyme activity analysis showed that KLK4 takes up about 90% of proteinase responsibility in the maturation stage of the enamel matrix. Consistent with our observation in which ameloblast morphology and underlying matrix proteins were unaffected in the secretory stage, we did not detect any significant difference in the expression of ECMs and MMP20 between *Nckx4*$^{+/+}$ and *Nckx4*$^{-/-}$ secretory ameloblasts either (data not shown). Therefore, NCKX4 ablation does not affect the production and hydrolysis of enamel matrix proteins in the protein phase of enamel matrix modeling. Surprisingly, we found increased *Klk4* mRNA in the *Nckx4*$^{-/-}$ maturation ameloblasts and KLK4 protein in the *Nckx4*$^{-/-}$ matrix. However, *in situ* KLK4 activity of the *Nckx4*$^{-/-}$ enamel matrix was reduced.

Intuitively, we first focused on investigating whether the reduced calcium in the *Nckx4*$^{-/-}$ enamel is responsible for the reduced KLK4 activity. Using fluorescence released from a quenched

peptide (a FRET peptide) as a readout of KLK4 activity, we demonstrated that KLK4 activity was calcium-independent. Considering calcium is such an abundant element in the enamel compartment encompassed by the dentin matrix and epithelial barrier, we believe that calcium-independent propensity would be advantageous to the KLK4's enamel tissue-specific function. It would be very challenging to elaborately control KLK4's activity if its activity is sensitive to calcium concentration in the confined enamel microenvironment. Overpowered KLK4 could impair the anatomy of the dentin and ameloblast layer. Thus, KLK4's calcium-independent property is critical for dentin and enamel formation.

Although KLK4 activity is calcium-independent, calcium may still indirectly affect KLK4 activity in the *Nckx4*$^{-/-}$ enamel matrix through MMP20. MMP20 is a well-known calcium-dependent metalloproteinase, which can activate KLK4 *in vitro* (Wang et al., 2006; Hadler-Olsen et al., 2011; Yamakoshi et al., 2013). Thus, the efficiency of MMP20 remaining in the early maturation stage of the enamel matrix may be adversely affected by the reduced calcium, subsequently decreasing the activity of KLK4 in the maturation stage of *Nckx4*$^{-/-}$ enamel matrix. Reduced MMP20 activity in the early maturation stage of the enamel matrix may also drive the compensatory upregulation of *Klk4* mRNA in the *Nckx4*$^{-/-}$ maturation ameloblasts.

We next assessed the effect of sodium on KLK4 activity since we also found about a 50% increase in sodium in the maturation stage of the *Nckx4*$^{-/-}$ enamel matrix. Our analysis demonstrated that KLK4 activity was greater when sodium concentration ranged from 100 mM to 150 mM than sodium at 200 mM and 400 mM. The activity of KLK4 started to decline in 200 mM NaCl and dropped more significantly in 400 mM NaCl. The sodium concentration in the secretory stage porcine enamel fluid is 140 mM (Aoba and Moreno, 1987). Given that the enamel matrix is a microenvironment confined by the dentin matrix and tightly junctional epithelial barrier, sodium concentration may likely go beyond the normal range transitorily when the major transport NCKX4 failed to remove sodium from the enamel matrix. The significance of sodium concentration in the enamel matrix protein hydrolysis is also evidenced by the previous NMR studies, which demonstrate that a high salt concentration salt promotes amelogenin nanosphere self-assembly (Buchko et al., 2008; Shaw et al., 2020), forming a complex that is less accessible to proteinases.

Removing as much sodium as possible during normal development is necessary to make adequate space for calcium and phosphate (Bronckers et al., 2015) and balance the microenvironment's osmotic pressure. Subameloblastic cysts were often found in the maturation phase of the *Nckx4*$^{-/-}$ enamel development (see Figure 5C), which is the additional evidence indicating the increased osmotic pressure possibly resulting from above physiological levels of sodium concentration. This increased sodium concentration may partially impair KLK4 activity. The high osmotic pressure could also subsequently affect ameloblast morphology and functions.

Metal ions play important roles in many enzyme-catalyzed reactions, such as magnesium to CCA-adding enzymes (Hou et al., 2005), zinc and calcium to matrix metalloproteinases (Tezvergil-Mutluay et al., 2010), and sodium to NADH dehydrogenase (Tuz et al., 2015). Metal ions can regulate an enzyme's kinetics by influencing the enzyme's conformation, redox states, and enzyme-substrate binding ability (Badarau and Page, 2006; Page and Di Cera, 2006; Page et al., 2006; Tuz et al., 2015). Monovalent cations Na^+ and K^+ can also act as non-specific buffering agents, solute exchange mediators, and enzyme stabilization agents. Levinsky *et al.* have shown that the maximum activity of urinary kallikrein is achieved in 100 mM sodium (Lieberthal et al., 1982), a similar condition that optimizes KLK4 activity in the enamel. The regulatory mechanism underlying how sodium affects the kinetic property of KLK4 remains to be determined by future studies.

During the maturation stage, calcium combines with phosphate to form hydroxyapatite crystals and produce protons, resulting in multiple acidified zones separated by the neutral pH zone on the enamel surface, a unique phenomenon called as pH cycling (Takano et al., 1988; Takano et al., 1989; Smith, 1998). As expected, with the deletion of NCKX4 and reduced ruffle-ended ameloblast-mediated calcium extrusion activity, the maturation stage enamel matrix was less acidified and largely remained neutral. Previous studies have reported that overall, enamel matrix proteins are processed more rapidly in the zones with lower pH than in the zones with neutral pH (Smith et al., 1996; Lu et al., 2008). Our *in vitro* studies demonstrated that recombinant KLK4 enzyme hydrolyzed the recombinant amelogenin 20 more effective at the lower pH up to 5.25 than at pH 7.0. Amelogenin 20, as a MMP20 hydrolyzed amelogenin product, is the primary amelogenin species present in the maturation stage enamel. These data help us further appreciate the significance of enamel matrix pH cycling in ECM modeling. We plan to investigate how pH affects KLK4 hydrolysis activity in future studies. Full-length amelogenin's structure is sensitive to pH, with increasing self-assembling propensity as the microenvironment pH increases (Delak et al., 2009; Zhang et al., 2011; Shaw et al., 2020). We hypothesize that acidic pH promotes amelogenins to form less complicated assemblies, which may be more accessible to KLK4 docking.

Our analyses also conclude that KLK4 accounts for about 89% of protein hydrolysis activity presented by the normal maturation stage enamel matrix. Other peptidases in the enamel matrix are responsible for the rest of 11% of hydrolysis activity. Furthermore, the remaining non-KLK4-associated proteinase activity is not pH-dependent. Being more effective in acidic pH may contribute to KLK4's proteinase specificity in the enamel matrix. KLK4 is a soluble and vigorous proteinase, therefore, suppressing its activity by neutral pH may be a mechanism for preventing dentin matrix proteins and ameloblast cell surface proteins from undesired hydrolysis by KLK4.

Taken together, by delivering calcium into the enamel, which facilitates hydroxyapatite formation, and moving off alkali ion sodium from enamel matrix, NCKX4 coordinately shifts pH and $[Na^+]$ in the enamel matrix, which accelerates KLK4 to hydrolyze and remove ECM proteins. This function of NCKX4 permits the progressive enamel matrix modeling and mineralization (see Figure 8).

KLK4-hydrolyzed enamel matrix proteins can be removed from enamel matrix by ameloblasts through endocytosis to make space for minerals. Therefore, KLK4 activity reduction caused by NCKX4 deletion may secondarily affect the ameloblast's endocytosis function. Thus, impaired endocytosis could also be partially responsible for the defective matrix protein retention in the *Nckx4*$^{-/-}$ enamel. In addition, we found that the deletion of NCKX4 disrupted ameloblast polarity, as indicated by the disperse distribution of PKC alpha (Figure 3), an epithelial polarization marker (Smith et al., 2007). The disrupted polarity may affect the formation of membrane infoldings, required by endosome formation at the interface between ECM and ameloblasts (Salama et al., 1987).

Identifying the factors that regulate KLK4 activity is important for enamel biology and enamel tissue regeneration and may also shed light on cancer biology. KLK4 has been identified as an indicator for breast, prostate, and ovarian cancer progression (Obiezu et al., 2001; Papachristopoulou et al., 2009; Lose et al., 2012; Wang et al., 2018).

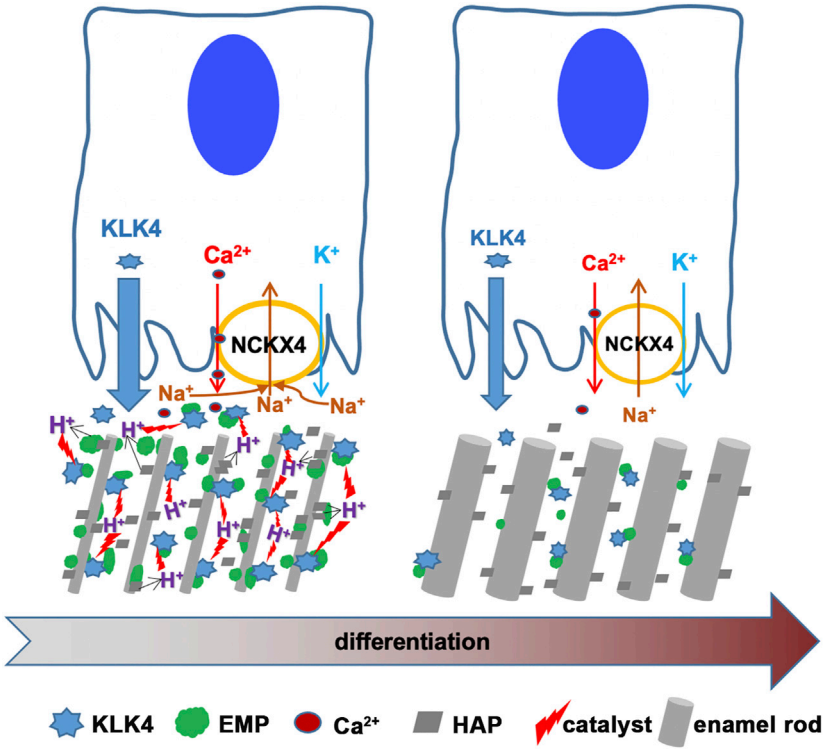

FIGURE 8
This scheme is to depict the functions of NCKX4 in calcium transport and matrix protein removal during enamel ECM modeling. KLK4 and NCKX4 are significantly upregulated in the early and mid-maturation stages of ameloblast maturation. However, the expression of both proteins declines as maturation continues. Immunostaining analysis of the full course of progressively differentiating ameloblasts localizes NCKX4 primarily at the apical surface of ruffle-ended maturation ameloblast (RAB). The molecular mechanisms of how NCKX4 interacts with KLK4 to regulate the enamel matrix modeling are illustrated here. NCKX4 transports calcium, which interacts with phosphate to produce $Ca_{10}(PO4)_6(OH)_2$ hydroxyapatite (HAP). HAP incorporates preexisting slender enamel rods constructed by secretory ameloblasts to grow enamel rods in width. Formation of each unit of HAP releases ($10Ca^{2+} + 6HPO4^{2-} + 2H_2O \rightarrow Ca_{10}(PO4)_6(OH)_2 + 8H^+$) eight protons into enamel ECM. These protons acidify ECM, which accelerates KLK4 to hydrolyze matrix proteins, facilitating them to be removed by ameloblasts to make space for progressive mineral incorporation. While transporting calcium into ECM, NCKX4 removes sodium from the enamel matrix. By coordinating the pH and sodium concentration in enamel ECM, a novel function of NCKX4 is to regulate the activity of KLK4 to model the enamel from a proteinaceous matrix into the most mineralized tissue in our body.

Regional hypoxia can induce tumor microenvironment acidification during tumor progression, which promotes the cancer cells to traverse the ECM barrier and invade local circulation for metastasis (Webb et al., 2011; Doe et al., 2012; Huang et al., 2016; Asgharzadeh et al., 2017). Shall elevated sodium concentration or/and microenvironment pH be able to inhibit KLK4 ability to clean the ECM barrier and constrain tumor cell migration? Understanding the regulation of KLK4 catalytic mechanisms may inspire us to devise potential clinical strategies to intervene in the progression of cancer as well.

Experimental procedures

Animals

NCKX4 loss-of-function mouse colony (*Nckx4*$^{-/-}$) with deletion of exon 6 and 7 (Li and Lytton, 2014) is a gift from Dr. Jonathan Lytton. KLK4 loss-of-function mouse colony (*Klk4*$^{-/-}$) was purchased from The Jackson Laboratory. All animals were maintained in the UCSF animal care facility, which is a barrier facility, accredited by Association for Assessment and Accreditation of Laboratory Animal Care (AAALAC). All experimental procedures associated with these mouse models were approved by the Institutional Animal Care and Use Committee (IACUC) under the protocol AN183449-01.

Histology and immunostaining assessment

Mice at postnatal seven-week-old (P7W) were collected by following standard IACUC protocols. Briefly, mice were anesthetized with 240 mg/kg tribromoethanol (Sigma-Aldrich), and perfuse-fixed with PBS and 4% paraformaldehyde (PFA). Hemimandibles were dissected and post-fixed with 4% PFA for 24 h at 4°C, then followed by decalcification in 8% EDTA at 4°C for 3 weeks with EDTA change every other day. The hemimandibles were then processed, embedded with wax and sectioned along their sagittal planes. Sections were stained with Hematoxylin & Eosin (H&E) for morphology assessment.

For immunostaining, the sagittal sections were boiled in 10 mM citrate buffer (pH 6.0) for 20 min to retrieve antigens. Next, the sections were incubated with GeneTex Universal Protein Blocking reagent for 1 h, followed by incubation with mouse anti-NCKX4 antibody (UC Davis/NIH NeuroMab Facility) or rabbit anti-amelogenin antibody for overnight at 4°C. Sections were then incubated with Alexa 594 fluorescein-conjugated anti-mouse IgG or FITC-conjugated anti-

rabbit IgG (Life Technologies) for 1 h at RT, followed by counterstaining with 1 μg/mL Hoechst for 5 min (Life Technologies). The slides were imaged using a high-speed Leica TCS SP5 spectrum confocal microscope. To evaluate ameloblast polarity, after blocking with Universal Protein Blocking reagent, the sections were incubated with rabbit anti-PKC (protein kinase C) alpha antibody (Abcam) for overnight at 4°C. After washing, the sections were then incubated with HRP-conjugated goat anti-rabbit antibody for 1 h at RT, at last incubated with HRP substrate (Vector®) to reveal the positive immunoreactive signals.

In situ RNA hybridization

RNAscope *in situ* hybridization 2.5 HD Red Detection Kit and mouse *Nckx4* and *Klk4* probes (Advanced Cell Diagnostics, ACDbio.) were used by following the manufacturer's instructions. Briefly, sagittal sections of mouse hemimandibles at 5 μm of thickness were boiled in the target retrieval buffer for 15 min and then pre-treated with protease plus solution at 40°C for 15 min. The sections were next incubated with probes for 2 h. After incubating with a serial of amplification reagents, the sections were incubated with Fast Red complex to develop the red precipitates in which the intensity is proportional to the mRNA expression levels of target genes. The nuclei were lightly counterstained by hematoxylin.

Macro-morphology photography and X-ray micro-tomography

P7W mouse hemimandibles were air-dried prior to imaging with a Leica M165C digital stereo microscope and a LAS V4.2 software. Hemimandibles were then subjected to X-ray micro-tomography scanning using a Micro XCT-200 system (Xradia). All scans were done at an operating voltage of 90 KVp and 66 μA of current, at an optical magnification ×2. A binning of 2 was used for 3D image reconstruction. Virtual sections were converted to bmp images using the Xradia TXM3DViewer 1.1.6. software. Mineral densities were determined following a detailed calibration protocol of the micro-XCT described previously (Djomehri et al., 2015). Ten orthogonal sections from each mouse ($n = 3$) to the long-axis of hemimandible at the plane perpendicularly across either the second buccal cusps of the first molar (P1 in Figures 2E, F) or the onset of mesial angle of the first molar (P2 in Figures 2E, F) were collected for mineral density analysis. The mineral density of calcified tissues from $Nckx4^{+/+}$ and $Nckx4^{-/-}$ mice was compared using unpaired two-tailed Student's *t*-test.

Assessment of expression levels of genes of interest by semi-quantitative PCR

Pups at postnatal day 5, 7, 8, 9, 11, and 13 (P5, P7,P8, P9, P11, and P13) were euthanized with carbon dioxide asphyxiation followed by cervical dislocation, mandibles were dissected and first molars from five mandibles were extracted and pooled as one sample. Enamel epithelium overlying these first molars is at the secretory, transition and maturation stage of development respectively (Ryu et al., 2002). The total RNA of these cells was purified using Qiagen RNeasy Micro Kit and mRNAs were reverse-transcribed into cDNA libraries using SuperScriptTM III First-Strand Synthesis System (Life Technologies). Semi-quantitative PCR was performed to quantify the relative expression levels of target genes. The sequences of primers used to amplify mouse endogenous *Gapdh* and target genes were listed as follows: *Gapdh* sense- 5′-TGGCCTTCCGTGTTCCTAC-3′, antisense- 5′-GAGTTGCTGTTGAAGTCGCA-3′; *Nckx4* sense- 5′-CACGGAGATGTCGGTGTAGGA-3′, antisense- 5′- CACCACCTG TCCAGCAAAGAG-3′; amelogenin sense- 5′-GGGACCTGGATT TTGTTTGCC-3′, antisense- 5′-TTCAAAGGGGTAAGCACCTCA;-3′; enamelin sense- 5′-GCTTTGGCTCCAATTCAAA-3′, antisense-5′-AGGACTTTCAGTGGGTGT-3′, ameloblastin sense- 5′-CTGTTA CCAAAGGCCCTGAA-3′, antisense- 5′-GCCATTTGTGAAAGG AGAGC-3′; *Mmp20* sense- 5′-TCCAAGCATTATACGGACCCC-3′, antisense- 5′-GTCACTGCATCAAAGGACGAG-3′; *Klk4* sense-5′-CGGGAGTCTTGGTGCATCC -3′, antisense- 5′- CTTGGGAGC CTTTCAGGTTATG -3′. To determine the relative expression levels of these target genes, the comparative threshold cycle method was used as previously published (Ryu et al., 1999).

Scanning electron microscopy (SEM)

Three sets of hemimandibles from either P7W $Nckx4^{+/+}$ or $Nckx4^{-/-}$ mice were embedded in epoxy, and polished in an orientation crossing to the long-axis of incisor using a series of SiC paper and diamond polishing suspension. Subsequently specimens were etched with 10% HCl for 30 s. Specimens were sputter-coated with Au-Pd, and the thickness of incisal enamel matrix and enamel rods were imaged at 20 kV using a Scanning Electron Microscope, Quanta 3D FEG (FEI) as described previously (Habelitz, 2015).

SDS-PAGE protein analysis

Hemimandibles were dissected, alveolar bone at the lingual site of hemimandibles was carefully removed to expose incisors. Incisors were fragmented using molars as reference line as previous published (Hu et al., 2007). The incisor segments under the second and third molars were used to extract secretory stage enamel matrix. The incisor segments from the bottom of the first molar to the gingival margin were used to extract the maturation stage matrix. The stage-specific enamel matrix proteins were extracted as previously described (Yamakoshi et al., 2011). The incisor segments from 6 mice were pooled and incubated in 1 mL of 0.17 N HCl/0.95% formic acid for 2 h at 4°C with constant rotation. After the undissolved material was removed by centrifugation at 3500g in 4°C, the protein supernatant was subjected to buffer exchange with 0.01% formic acid using a centrifugal 3K-filter unit (EMD Millipore). The proteins retained by the filter were eluted with 250 μL of 0.01% formic acid and used for subsequent sodium dodecyl sulfate polyacrylamide gel electrophoresis (SDS-PAGE), Coomassie Brilliant Blue staining, and western blot immunoblotting.

Western blot analyses

Equal volumes of total enamel matrix proteins from six mice at either secretory stage or maturation stage were loaded to be separated on a 15% SDS-PAGE gel. Proteins on the SDS-PAGE were transferred to a PVDF membrane. After blocking, membrane was then incubated with rabbit anti-amelogenin IgG, rabbit anti-MMP20 IgG (Millipore-

Sigma), or rabbit anti-KLK4 IgG (Abcam) for overnight at 4°C. Following washing, PVDF was secondly incubated with IRDye 680RD conjugated anti-rabbit IgG (Li-Cor) for 1 h at room temperature. The membranes were thoroughly washed and then scanned using an Odyssey Imaging System.

KLK4 activity assessment

The activity of KLK4 to hydrolyze a peptide substrate or recombinant protein amelogenin 20 (amelogenin without C-terminus) was analyzed in various buffer. Briefly, recombinant KLK4 (R&D Systems) was activated by thermolysin (R&D Systems) by following the manufacturer's instruction and previous publications (Yoon et al., 2007; Tye et al., 2011). Active KLK4 was then incubated with a fluorogenic quench peptide substrate BOC-Val-Pro-Arg-AMC (R&D Systems) in the 50 mM Tris-HCl supplemented with various concentrations of $CaCl_2$ or NaCl. To test the effect of pH, we used buffer supplemented with 50 mM Tris-HCl, 150 mM NaCl and 10 mM $CaCl_2$. Once the Arg-AMC amide bond in the peptide is hydrolyzed by KLK4, highly fluorescent AMC is released. The intensity of fluorescence proportionally indicates the activity of KLK4. One hundred microliter reaction was loaded to each well of a 96-well black plate. Each condition was quadruplicate. The plate was read at excitation and emission wavelengths of 380 nm and 460 nm respectively. A kinetic mode was set to read each well every 100 s for a total of 2,700 s interval.

To synthesize amelogenin 20, also named as rH146 in previous publication (Bai et al., 2020), a site-directed mutagenesis kit (Takara Bio.) was employed to delete C-terminus 28bp DNA from human wild-type amelogenin cDNA (rH174). After the site-specific deletion was confirmed by DNA sequencing, amelogenin 20 was expressed in T7 Express Competent *Escherichia coli* (New England Biolabs) and purified using an acid/heat treatment method described previously (Svensson Bonde and Bulow, 2012). Amelogenin 20 recombinant protein was incubated with or without active KLK4 (at a concentration ratio of 100:1) in 50 mM Tris-HCl, 150 mM NaCl and 10 mM $CaCl_2$ at various pH for overnight at 37°C with rotation. Then protein was loaded to a 15% SDS-PAGE. The gel was scanned and protein band density was measured using NIH ImageJ version 2.0.0. The percentage of undigested protein normalized to the input amelogenin 20 was calculated. An average of percentage from triplicate analyses was calculated and the significant difference among the different conditions was determined by one-way ANOVA analysis using SPSS Statistics package 19 followed by Tukey Post Hoc Tests.

To analyze the activity of native KLK4 possessed in the maturation phase of enamel matrix, the incisor segments overlying the bottom of the first molar to the gingival margin (maturations stage) were microdissected and incubated with fluorogenic peptide BOC-Val-Pro-Arg-AMC. The fluorescence was recorded every 100 s for a total of 2,700 s interval by a plate reader. To assess KLK4 enamel *in vivo* activity, the freshly microdissected incisor segments at the maturation stage as described above were quickly dipped into 1% agar in 50 mM Tris-HCl (pH 7.5), 150 mM NaCl and 10 mM $CaCl_2$ supplemented with fluorogenic peptide BOC-Val-Pro-Arg-AMC. One microliter peptide was supplemented to each 100-μL of 1% agar. Next, the incisor segments embedded by agar were incubated in a black Eppendorf tube for 30 min at 37°C. After incubation was complete, the incisal segments were photographed immediately using a Leica fluorescence microdissection microscope.

Enamel matrix element measurement

Hemimandibles from three 7-week old mice were embedded in epoxy, and polished in a cross orientation using a series of SiC paper and diamond polishing suspension starting from incisor tip and stopping when mesial angle of the first molar was exposed. For each hemimandible, six randomly areas (as illustrated in Supplementary Figure S1) were subjected to an energy dispersive X-ray spectroscopy (Quantax EDS, Bruker Nano Inc.) to collect elemental composition of Ca, P, Na *et al* at 15 keV using a variable pressure chamber. Back scattered electron (BSE) images were also collected using a field emission scanning electron microscope (Sigma VP500 field emission SEM, Carl Zeiss Microscopy). The elemental composition collected from three *Nckx4*$^{+/+}$ or *Nckx4*$^{-/-}$ mice was compared and the significance difference between two mouse models was determined by unpaired two-tailed Student's t-test.

Mouse incisor enamel matrix pH staining

To prepare the staining solution, 100 mg Methyl Red (Sigma-Aldrich) was diluted in 45 mL of 95% methanol. Four *Nckx4*$^{+/+}$ or *Nckx4*$^{-/-}$ mice at postnatal 7 weeks old (P7W) were anesthetized with 240 mg/kg tribromoethanol (Sigma-Aldrich). Hemimandibles were dissected and the surrounding alveolar bone was removed to completely expose the mandibular incisors. The enamel organ epithelium overlying the labial enamel surface was gently wiped off with ice-cold Kimwipe. The incisors were immediately soaked in 0.2% Methyl Red/95% methanol for 45 s at room temperature, then air-dried for 5 min prior to documenting the stained incisors under a Leica dissecting microscope.

Data availability statement

The original contributions presented in the study are included in the article/Supplementary Material, further inquiries can be directed to the corresponding author.

Ethics statement

The animal study was reviewed and approved by the University of California at San Francisco the Institutional Animal Care and Use Committee (IACUC).

Author contributions

YZ was responsible for the experimental design, data collection and interpretation, result verification, funding, and manuscript writing. BC and LC equally contributed to the most of data collection, data analysis, and result verification described in this manuscript. JR contributed to the experimental design and mouse hemimandible MicroCT analysis. IG collected the semi-quantitative PCR data. YH microdissected the enamel matrix proteins and ran the western blot analysis to characterize the stage-specific enamel matrix proteins. IS performed the NCKX4 immunostaining analysis. CC was

in charge of animal maintenance, genotyping, and hemimandible collection and processing. WL participated in the *in vitro* KLK4 enzyme activity analyses. JL and PD were involved in the experimental design, data discussion, and manuscript editing.

Funding

This research was funded by NIDCR grants R01 DE027076 to YZ and R01 DE27971 to PD.

Conflict of interest

The authors declare that the research was conducted in the absence of any commercial or financial relationships that could be construed as a potential conflict of interest.

Publisher's note

Supplementary material

The Supplementary Material for this article can be found online at: https://www.frontiersin.org/articles/10.3389/fphys.2023.1116091/full#supplementary-material

SUPPLEMENTARY FIGURE S1
For each hemimandible from the *Nckx4*$^{+/+}$ or *Nckx4*$^{-/-}$ mouse, six randomly areas (as illustrated in those yellow boxes) were subjected to an energy dispersive X-ray spectroscopy to collect elemental composition.

References

Altimimi, H. F., and Schnetkamp, P. P. (2007). Na+/Ca2+-K+ exchangers (NCKX): Functional properties and physiological roles. *Channels (Austin)* 1 (2), 62–69. doi:10.4161/chan.4366

Aoba, T., and Moreno, E. C. (1987). The enamel fluid in the early secretory stage of porcine amelogenesis: Chemical composition and saturation with respect to enamel mineral. *Calcif. Tissue Int.* 41 (2), 86–94. doi:10.1007/BF02555250

Asgharzadeh, M. R., Barar, J., Pourseif, M. M., Eskandani, M., Jafari Niya, M., Mashayekhi, M. R., et al. (2017). Molecular machineries of pH dysregulation in tumor microenvironment: Potential targets for cancer therapy. *Bioimpacts* 7 (2), 115–133. doi:10.15171/bi.2017.15

Badarau, A., and Page, M. I. (2006). Enzyme deactivation due to metal-ion dissociation during turnover of the cobalt-beta-lactamase catalyzed hydrolysis of beta-lactams. *Biochemistry* 45 (36), 11012–11020. doi:10.1021/bi0610146

Bai, Y., Yu, Z., Ackerman, L., Zhang, Y., Bonde, J., Li, W., et al. (2020). Protein nanoribbons template enamel mineralization. *Proc. Natl. Acad. Sci. U. S. A.* 117 (32), 19201–19208. doi:10.1073/pnas.2007838117

Bartlett, J. D., Beniash, E., Lee, D. H., and Smith, C. E. (2004). Decreased mineral content in MMP-20 null mouse enamel is prominent during the maturation stage. *J. Dent. Res.* 83 (12), 909–913. doi:10.1177/154405910408301204

Bartlett, J. D. (2013). Dental enamel development: Proteinases and their enamel matrix substrates. *ISRN Dent.* 2013, 684607. doi:10.1155/2013/684607

Bartlett, J. D., and Simmer, J. P. (2014). Kallikrein-related peptidase-4 (KLK4): Role in enamel formation and revelations from ablated mice. *Front. Physiol.* 5, 240. doi:10.3389/fphys.2014.00240

Bartlett, J. D., Yamakoshi, Y., Simmer, J. P., Nanci, A., and Smith, C. E. (2011). MMP20 cleaves E-cadherin and influences ameloblast development. *Cells Tissues Organs* 194 (2-4), 222–226. doi:10.1159/000324205

Begue-Kirn, C., Krebsbach, P. H., Bartlett, J. D., and Butler, W. T. (1998). Dentin sialoprotein, dentin phosphoprotein, enamelysin and ameloblastin: Tooth-specific molecules that are distinctively expressed during murine dental differentiation. *Eur. J. Oral Sci.* 106 (5), 963–970. doi:10.1046/j.0909-8836.1998.eos106510.x

Bronckers, A. L., Jalali, R., and Lytton, J. (2017). Reduced protein expression of the Na(+)/Ca(2+)+K(+)-Exchanger (SLC24A4) in apical plasma membranes of maturation ameloblasts of fluorotic mice. *Calcif. Tissue Int.* 100 (1), 80–86. doi:10.1007/s00223-016-0197-4

Bronckers, A. L., Lyaruu, D., Jalali, R., Medina, J. F., Zandieh-DoulaBi, B., and DenBesten, P. K. (2015). Ameloblast modulation and transport of Cl^-, Na^+, and K^+ during amelogenesis. *J. Dent. Res.* 94 (12), 1740–1747. doi:10.1177/0022034515606900

Buchko, G. W., Tarasevich, B. J., Bekhazi, J., Snead, M. L., and Shaw, W. J. (2008). A solution NMR investigation into the early events of amelogenin nanosphere self-assembly initiated with sodium chloride or calcium chloride. *Biochemistry* 47 (50), 13215–13222. doi:10.1021/bi8018288

Caterina, J. J., Skobe, Z., Shi, J., Ding, Y., Simmer, J. P., Birkedal-Hansen, H., et al. (2002). Enamelysin (matrix metalloproteinase 20)-deficient mice display an amelogenesis imperfecta phenotype. *J. Biol. Chem.* 277 (51), 49598–49604. doi:10.1074/jbc.M209100200

Delak, K., Harcup, C., Lakshminarayanan, R., Sun, Z., Fan, Y., Moradian-Oldak, J., et al. (2009). The tooth enamel protein, porcine amelogenin, is an intrinsically disordered protein with an extended molecular configuration in the monomeric form. *Biochemistry* 48 (10), 2272–2281. doi:10.1021/bi802175a

Djomehri, S. I., Candell, S., Case, T., Browning, A., Marshall, G. W., Yun, W., et al. (2015). Mineral density volume gradients in normal and diseased human tissues. *PLoS One* 10 (4), e0121611. doi:10.1371/journal.pone.0121611

Doe, M. R., Ascano, J. M., Kaur, M., and Cole, M. D. (2012). Myc posttranscriptionally induces HIF1 protein and target gene expression in normal and cancer cells. *Cancer Res.* 72 (4), 949–957. doi:10.1158/0008-5472.CAN-11-2371

Follet, H., Boivin, G., Rumelhart, C., and Meunier, P. J. (2004). The degree of mineralization is a determinant of bone strength: A study on human calcanei. *Bone* 34 (5), 783–789. doi:10.1016/j.bone.2003.12.012

Furukawa, Y., Haruyama, N., Nikaido, M., Nakanishi, M., Ryu, N., Oh-Hora, M., et al. (2017). Stim1 regulates enamel mineralization and ameloblast modulation. *J. Dent. Res.* 96 (12), 1422–1429. doi:10.1177/0022034517719872

Habelitz, S. (2015). Materials engineering by ameloblasts. *J. Dent. Res.* 94 (6), 759–767. doi:10.1177/0022034515577963

Hadler-Olsen, E., Fadnes, B., Sylte, I., Uhlin-Hansen, L., and Winberg, J. O. (2011). Regulation of matrix metalloproteinase activity in health and disease. *FEBS J.* 278 (1), 28–45. doi:10.1111/j.1742-4658.2010.07920.x

Herzog, C. R., Reid, B. M., Seymen, F., Koruyucu, M., Tuna, E. B., Simmer, J. P., et al. (2015). Hypomaturation amelogenesis imperfecta caused by a novel SLC24A4 mutation. *Oral Surg. Oral Med. Oral Pathol. Oral Radiol.* 119 (2), e77–e81. doi:10.1016/j.oooo.2014.09.003

Hou, Y. M., Gu, S. Q., Zhou, H., and Ingerman, L. (2005). Metal-ion-dependent catalysis and specificity of CCA-adding enzymes: A comparison of two classes. *Biochemistry* 44 (38), 12849–12859. doi:10.1021/bi0509402

Hu, J. C., Chun, Y. H. P., Al Hazzazzi, T., and Simmer, J. P. (2007). Enamel formation and amelogenesis imperfecta. *Cells Tissues Organs* 186 (1), 78–85. doi:10.1159/000102683

Hu, P., Lacruz, R. S., Smith, C. E., Smith, S. M., Kurtz, I., and Paine, M. L. (2012). Expression of the sodium/calcium/potassium exchanger, NCKX4, in ameloblasts. *Cells Tissues Organs* 196 (6), 501–509. doi:10.1159/000337493

Huang, S., Tang, Y., Peng, X., Cai, X., Wa, Q., Ren, D., et al. (2016). Acidic extracellular pH promotes prostate cancer bone metastasis by enhancing PC-3 stem cell characteristics, cell invasiveness and VEGF-induced vasculogenesis of BM-EPCs. *Oncol. Rep.* 36 (4), 2025–2032. doi:10.3892/or.2016.4997

Jalloul, A. H., Rogasevskaia, T. P., Szerencsei, R. T., and Schnetkamp, P. P. M. (2016). A functional study of mutations in K+-dependent Na+-Ca2+ exchangers associated with amelogenesis imperfecta and non-syndromic oculocutaneous albinism. *J. Biol. Chem.* 291 (25), 13113–13123. doi:10.1074/jbc.M116.728824

Josephsen, K., and Fejerskov, O. (1977). Ameloblast modulation in the maturation zone of the rat incisor enamel organ. A light and electron microscopic study. *J. Anat.* 124 (1), 45–70.

Katsura, K. A., Horst, J. A., ChanDra, D., Le, T. Q., Nakano, Y., Zhang, Y., et al. (2014). WDR72 models of structure and function: A stage-specific regulator of enamel mineralization. *Matrix Biol.* 38, 48–58. doi:10.1016/j.matbio.2014.06.005

Kim, J. W., Simmer, J. P., Hart, T. C., Hart, P. S., Ramaswami, M. D., Bartlett, J. D., et al. (2005). MMP-20 mutation in autosomal recessive pigmented hypomaturation amelogenesis imperfecta. *J. Med. Genet.* 42 (3), 271–275. doi:10.1136/jmg.2004.024505

Lacruz, R. S. (2017). Enamel: Molecular identity of its transepithelial ion transport system. *Cell Calcium* 65, 1–7. doi:10.1016/j.ceca.2017.03.006

Lacruz, R. S., and Feske, S. (2015). Diseases caused by mutations in ORAI1 and STIM1. *Ann. N. Y. Acad. Sci.* 1356, 45–79. doi:10.1111/nyas.12938

Lacruz, R. S., Habelitz, S., Wright, J. T., and Paine, M. L. (2017). Dental enamel formation and implications for oral health and disease. *Physiol. Rev.* 97 (3), 939–993. doi:10.1152/physrev.00030.2016

Li, X. F., Kraev, A. S., and Lytton, J. (2002). Molecular cloning of a fourth member of the potassium-dependent sodium-calcium exchanger gene family, NCKX4. *J. Biol. Chem.* 277 (50), 48410–48417. doi:10.1074/jbc.M210011200

Li, X. F., and Lytton, J. (2014). An essential role for the K+-dependent Na+/Ca2+-exchanger, NCKX4, in melanocortin-4-receptor-dependent satiety. *J. Biol. Chem.* 289 (37), 25445–25459. doi:10.1074/jbc.M114.564450

Lieberthal, W., Oza, N. B., Bernard, D. B., and Levinsky, N. G. (1982). The effect of cations on the activity of human urinary kallikrein. *J. Biol. Chem.* 257 (18), 10827–10830. doi:10.1016/s0021-9258(18)33899-7

Llano, E., Pendas, A. M., Knauper, V., Sorsa, T., Salo, T., Salido, E., et al. (1997). Identification and structural and functional characterization of human enamelysin (MMP-20). *Biochemistry* 36 (49), 15101–15108. doi:10.1021/bi972120y

Lose, F., Srinivasan, S., O'Mara, T., Marquart, L., Chambers, S., Gardiner, R. A., et al. (2012). Genetic association of the KLK4 locus with risk of prostate cancer. *PLoS One* 7 (9), e44520. doi:10.1371/journal.pone.0044520

Lu, Y., Papagerakis, P., Yamakoshi, Y., Hu, J. C. C., Bartlett, J. D., and Simmer, J. P. (2008). Functions of KLK4 and MMP-20 in dental enamel formation. *Biol. Chem.* 389 (6), 695–700. doi:10.1515/BC.2008.080

Lytton, J. (2007). Na+/Ca2+ exchangers: Three mammalian gene families control Ca2+ transport. *Biochem. J.* 406 (3), 365–382. doi:10.1042/BJ20070619

Moradian-Oldak, J. (2012). Protein-mediated enamel mineralization. *Front. Biosci. (Landmark Ed.* 17, 1996–2023. doi:10.2741/4034

Nagano, T., KakegAwA, A., Yamakoshi, Y., Tsuchiya, S., Hu, J. C. C., Gomi, K., et al. (2009). Mmp-20 and Klk4 cleavage site preferences for amelogenin sequences. *J. Dent. Res.* 88 (9), 823–828. doi:10.1177/0022034509342694

Nurbaeva, M. K., Eckstein, M., Feske, S., and Lacruz, R. S. (2017). Ca(2+) transport and signalling in enamel cells. *J. Physiol.* 595 (10), 3015–3039. doi:10.1113/JP272775

Obiezu, C. V., ScorilAs, A., Katsaros, D., Massobrio, M., Yousef, G. M., Fracchioli, S., et al. (2001). Higher human kallikrein gene 4 (KLK4) expression indicates poor prognosis of ovarian cancer patients. *Clin. Cancer Res.* 7 (8), 2380–2386.

Page, M. J., Bleackley, M. R., Wong, S., MacGillivray, R. T. A., and Di Cera, E. (2006). Conversion of trypsin into a Na(+)-activated enzyme. *Biochemistry* 45 (9), 2987–2993. doi:10.1021/bi052481a

Page, M. J., and Di Cera, E. (2006). Role of Na+ and K+ in enzyme function. *Physiol. Rev.* 86 (4), 1049–1092. doi:10.1152/physrev.00008.2006

Papachristopoulou, G., Avgeris, M., and Scorilas, A. (2009). Expression analysis and study of KLK4 in benign and malignant breast tumours. *Thromb. Haemost.* 101 (2), 381–387. doi:10.1160/th08-01-0037

Parry, D. A., Poulter, J. A., Logan, C. V., Brookes, S. J., Jafri, H., Ferguson, C. H., et al. (2013). Identification of mutations in SLC24A4, encoding a potassium-dependent sodium/calcium exchanger, as a cause of amelogenesis imperfecta. *Am. J. Hum. Genet.* 92 (2), 307–312. doi:10.1016/j.ajhg.2013.01.003

Prasad, M. K., Laouina, S., El Alloussi, M., Dollfus, H., and Bloch-ZupAn, A. (2016). Amelogenesis imperfecta: 1 family, 2 phenotypes, and 2 mutated genes. *J. Dent. Res.* 95 (13), 1457–1463. doi:10.1177/0022034516663200

Robertson, S. Y. T., Wen, X., Yin, K., Chen, J., Smith, C. E., and Paine, M. L. (2017). Multiple calcium export exchangers and pumps are a prominent feature of enamel organ cells. *Front. Physiol.* 8, 336. doi:10.3389/fphys.2017.00336

Ryu, O. H., Fincham, A. G., Hu, C. C., Zhang, C., Qian, Q., Bartlett, J. D., et al. (1999). Characterization of recombinant pig enamelysin activity and cleavage of recombinant pig and mouse amelogenins. *J. Dent. Res.* 78 (3), 743–750. doi:10.1177/00220345990780030601

Ryu, O., Hu, J. C. C., Yamakoshi, Y., Villemain, J. L., Cao, X., Zhang, C., et al. (2002). Porcine kallikrein-4 activation, glycosylation, activity, and expression in prokaryotic and eukaryotic hosts. *Eur. J. Oral Sci.* 110 (5), 358–365. doi:10.1034/j.1600-0722.2002.21349.x

Salama, A. H., Zaki, A. E., and Eisenmann, D. R. (1987). Cytochemical localization of Ca2+-Mg2+ adenosine triphosphatase in rat incisor ameloblasts during enamel secretion and maturation. *J. Histochem Cytochem* 35 (4), 471–482. doi:10.1177/35.4.2950164

Schnetkamp, P. P. (1989). Na-Ca or Na-Ca-K exchange in rod photoreceptors. *Prog. Biophys. Mol. Biol.* 54 (1), 1–29. doi:10.1016/0079-6107(89)90007-2

Seymen, F., Lee, K. E., Tran Le, C. G., YildiriM, M., Gencay, K., Lee, Z. H., et al. (2014). Exonal deletion of SLC24A4 causes hypomaturation amelogenesis imperfecta. *J. Dent. Res.* 93 (4), 366–370. doi:10.1177/0022034514523786

Shaw, W. J., Tarasevich, B. J., Buchko, G. W., Arachchige, R. M. J., and Burton, S. D. (2020). Controls of nature: Secondary, tertiary, and quaternary structure of the enamel protein amelogenin in solution and on hydroxyapatite. *J. Struct. Biol.* 212 (3), 107630. doi:10.1016/j.jsb.2020.107630

Simmer, J., Hu, Y., Lertlam, R., Yamakoshi, Y., and Hu, J. C. C. (2009). Hypomaturation enamel defects in Klk4 knockout/LacZ knockin mice. *J. Biol. Chem.* 284, 19110–19121. doi:10.1074/jbc.M109.013623

Simmer, J. P., Hu, Y., Richardson, A. S., Bartlett, J. D., and Hu, J. C. C. (2011). Why does enamel in Klk4-null mice break above the dentino-enamel junction? *Cells Tissues Organs* 194 (2-4), 211–215. doi:10.1159/000324260

Smith, C. A., Lau, K. M., Rahmani, Z., Dho, S. E., Brothers, G., She, Y. M., et al. (2007). aPKC-mediated phosphorylation regulates asymmetric membrane localization of the cell fate determinant Numb. *EMBO J.* 26 (2), 468–480. doi:10.1038/sj.emboj.7601495

Smith, C. E. (1998). Cellular and chemical events during enamel maturation. *Crit. Rev. Oral Biol. Med.* 9 (2), 128–161. doi:10.1177/10454411980090020101

Smith, C. E., Issid, M., Margolis, H. C., and Moreno, E. C. (1996). Developmental changes in the pH of enamel fluid and its effects on matrix-resident proteinases. *Adv. Dent. Res.* 10 (2), 159–169. doi:10.1177/08959374960100020701

Smith, C. E. L., Poulter, J. A., Antanaviciute, A., Kirkham, J., Brookes, S. J., Inglehearn, C. F., et al. (2017). Amelogenesis imperfecta; genes, proteins, and pathways. *Front. Physiol.* 8, 435. doi:10.3389/fphys.2017.00435

Stephan, A. B., Tobochnik, S., Dibattista, M., Wall, C. M., Reisert, J., and Zhao, H. (2011). The Na(+)/Ca(2+) exchanger NCKX4 governs termination and adaptation of the mammalian olfactory response. *Nat. Neurosci.* 15 (1), 131–137. doi:10.1038/nn.2943

Svensson Bonde, J., and Bulow, L. (2012). One-step purification of recombinant human amelogenin and use of amelogenin as a fusion partner. *PLoS One* 7 (3), e33269. doi:10.1371/journal.pone.0033269

Takagi, T., Ogasawara, T., Tagami, J., Akao, M., Kuboki, Y., Nagai, N., et al. (1998). pH and carbonate levels in developing enamel. *Connect. Tissue Res.* 38 (1-4), 181–187. doi:10.3109/03008209809017035

Takano, Y., MatSuo, S., WakiSaka, S., IcHikawa, H., NiShikawa, S., and Akai, M. (1988). A histochemical demonstration of calcium in the maturation stage enamel organ of rat incisors. *Arch. Histol. Cytol.* 51 (3), 241–248. doi:10.1679/aohc.51.241

Takano, Y., MatSuo, S., WakiSaka, S., IcHikawa, H., NiShikawa, S., and Akai, M. (1989). Histochemical localization of calcium in the enamel organ of rat incisors in early-stage amelogenesis. *Acta Anat. (Basel)* 134 (4), 305–311. doi:10.1159/000146707

Tezvergil-Mutluay, A., Agee, K. A., Hoshika, T., Carrilho, M., Breschi, L., Tjaderhane, L., et al. (2010). The requirement of zinc and calcium ions for functional MMP activity in demineralized dentin matrices. *Dent. Mater* 26 (11), 1059–1067. doi:10.1016/j.dental.2010.07.006

Tuz, K., Mezic, K. G., Xu, T., Barquera, B., and Juarez, O. (2015). The kinetic reaction mechanism of the *Vibrio cholerae* sodium-dependent NADH dehydrogenase. *J. Biol. Chem.* 290 (33), 20009–20021. doi:10.1074/jbc.M115.658773

Tye, C. E., Antone, J. V., and Bartlett, J. D. (2011). Fluoride does not inhibit enamel protease activity. *J. Dent. Res.* 90 (4), 489–494. doi:10.1177/0022034510390043

Wang, P., Magdolen, V., Seidl, C., Dorn, J., Drecoll, E., Kotzsch, M., et al. (2018). Kallikrein-related peptidases 4, 5, 6 and 7 regulate tumour-associated factors in serous ovarian cancer. *Br. J. Cancer* 119 (7), 1–9. doi:10.1038/s41416-018-0260-1

Wang, S., Choi, M., Richardson, A. S., Reid, B. M., Seymen, F., YildiriM, M., et al. (2014). STIM1 and SLC24A4 are critical for enamel maturation. *J. Dent. Res.* 93 (7), 94S–100S. doi:10.1177/0022034514527971

Wang, S. K., Hu, Y., Yang, J., Smith, C. E., Nunez, S. M., Richardson, A. S., et al. (2015). Critical roles for WDR72 in calcium transport and matrix protein removal during enamel maturation. *Mol. Genet. Genomic Med.* 3 (4), 302–319. doi:10.1002/mgg3.143

Wang, S., Zhu, J., Zhang, Y., Li, L., DenBesten, P., and Li, W. (2006). On-column activation of bovine recombinant metalloproteinase 20. *Anal. Biochem.* 356 (2), 291–293. doi:10.1016/j.ab.2005.11.045

Warshawsky, H., and Smith, C. E. (1974). Morphological classification of rat incisor ameloblasts. *Anat. Rec.* 179 (4), 423–446. doi:10.1002/ar.1091790403

Webb, B. A., Chimenti, M., Jacobson, M. P., and Barber, D. L. (2011). Dysregulated pH: A perfect storm for cancer progression. *Nat. Rev. Cancer* 11 (9), 671–677. doi:10.1038/nrc3110

Yamakoshi, Y., Richardson, A. S., Nunez, S. M., Yamakoshi, F., Milkovich, R. N., Hu, J. C. C., et al. (2011). Enamel proteins and proteases in Mmp20 and Klk4 null and double-null mice. *Eur. J. Oral Sci.* 119 (1), 206–216. doi:10.1111/j.1600-0722.2011.00866.x

Yamakoshi, Y., Simmer, J. P., Bartlett, J. D., Karakida, T., and Oida, S. (2013). MMP20 and KLK4 activation and inactivation interactions *in vitro*. *Arch. Oral Biol.* 58 (11), 1569–1577. doi:10.1016/j.archoralbio.2013.08.005

Yoon, H., Laxmikanthan, G., Lee, J., Blaber, S. I., Rodriguez, A., Kogot, J. M., et al. (2007). Activation profiles and regulatory cascades of the human kallikrein-related peptidases. *J. Biol. Chem.* 282 (44), 31852–31864. doi:10.1074/jbc.M705190200

Yue, B. (2014). Biology of the extracellular matrix: An overview. *J. Glaucoma* 23 (1), S20–S23. doi:10.1097/IJG.0000000000000108

Zhang, X., Ramirez, B. E., Liao, X., and Diekwisch, T. G. H. (2011). Amelogenin supramolecular assembly in nanospheres defined by a complex helix-coil-PPII helix 3D-structure. *PLoS One* 6 (10), e24952. doi:10.1371/journal.pone.0024952

Zhang, Y., Zheng, L., Le, M., Nakano, Y., Chan, B., Huang, Y., et al. (2019). SATB1 establishes ameloblast cell polarity and regulates directional amelogenin secretion for enamel formation. *BMC Biol.* 17 (1), 104. doi:10.1186/s12915-019-0722-9

frontiers | Frontiers in Physiology

TYPE Original Research
PUBLISHED 06 February 2023
DOI 10.3389/fphys.2023.1124444

OPEN ACCESS

EDITED BY
Janet Moradian-Oldak,
University of Southern California,
United States

REVIEWED BY
Tim Wright,
University of North Carolina at Chapel Hill,
United States
Jan Hu,
University of Michigan, United States

*CORRESPONDENCE
Pamela K. Den Besten,
pamela.denbesten@ucsf.edu
Yan Zhang,
yan.zhang2@ucsf.edu

SPECIALTY SECTION
This article was submitted
to Craniofacial Biology and Dental
Research, a section of
the journal Frontiers in Physiology

RECEIVED 15 December 2022
ACCEPTED 13 January 2023
PUBLISHED 06 February 2023

CITATION
Ngu J, Bronckers ALJJ, Katsura K, Zhang Y
and Den Besten PK (2023), Na^+ and K^+
transport and maturation stage
ameloblast modulation.
Front. Physiol. 14:1124444.
doi: 10.3389/fphys.2023.1124444

Na^+ and K^+ transport and maturation stage ameloblast modulation

Jake Ngu[1], Antonius L. J. J. Bronckers[2], Kaitlin Katsura[1], Yan Zhang[1]* and Pamela K. Den Besten[1]*

[1]Department of Orofacial Sciences, University of California, San Francisco, San Francisco, CA, United States, [2]Department of Oral Cell Biology, Academic Centre for Dentistry Amsterdam (ACTA), MOVE Research Institute, University of Amsterdam and VU University, Amsterdam, Netherlands

Introduction: Enamel mineralization requires calcium transport into the extracellular matrix for the synthesis of hydroxyapatite (HA) crystals. Formation of HA releases protons into the matrix, which are then neutralized when ameloblasts modulate from cells with apical invaginations, the so-called ruffle-ended ameloblasts (RE), to smooth-ended ameloblasts (SE). Ameloblast modulation is associated with the translocation of the calcium exchanger Nckx4 to the apical border of RE, to remove Na^+ from the enamel matrix in exchange for Ca^{2+} and K^+. As enamel matures, Na^+ and K^+ in the matrix progressively decrease. However, the transporter to remove K^+ from mineralizing enamel has not been identified.

Methods: Expression of K^+ exchangers and channels in secretory and maturation stage of enamel organs were compared following an RNA-seq analysis. Kcnj15, which encodes the Kir4.2 inwardly rectifying K^+ channel, was found to be the most upregulated internalizing K^+ transporter in maturation stage of enamel organs. Kir4.2 was immunolocalized in wt, Nckx4$^{-/-}$, Wdr72$^{-/-}$, and fluorosed ameloblasts. Regulation of Wdr72 expression by pH was characterized *in vitro* and *in vivo*.

Results: Kir4.2 immunolocalized to the apical border of wild type (wt) mouse RE and cytosol of SE, a spatial distribution pattern shared by NCKX4. In Nckx4$^{-/-}$ ameloblasts, Kir4.2 also localized to the apical surface of RE and cytosol of SE. However, in fluorosed and Wdr72$^{-/-}$ ameloblasts, in which vesicle trafficking is disrupted, Kir4.2 remained in the cytosol. *In vitro*, Wdr72 was upregulated in LS8 cells cultured in medium with a pH 6.2, which is the pH of the enamel matrix underlying RE, as compared to pH 7.2 under SE.

Conclusion: Taken together these results suggest that Kir4.2 participates in K^+ uptake by maturation ameloblasts, and that K^+ and Na^+ uptake by Kir4.2 and Nckx4, respectively, may be regulated by pH through WDR72-mediated endocytosis and membrane trafficking.

KEYWORDS

ameloblasts, KCNJ15, NCKX4, enamel, maturation, Kir4.2, Wdr72, fluorosis

Introduction

Enamel formation and mineralization is directed by epithelial derived ameloblasts and is unique among mineralizing tissues. Ameloblasts use ion-transporting transmembrane channels and transporters to deliver calcium and phosphate (Ca^{2+} and HPO_4^{2}) into the extracellular matrix to form hydroxyapatite (HA) crystals. These transporters include K^+-dependent Na^+/Ca^{2+} Exchanger-4 (Nckx4) which co-transports Ca^{2+} and K^+ into the

enamel matrix in exchange for Na^+ (Hu et al., 2012; Parry et al., 2013; Bronckers et al., 2017). Both Na^+ and K^+ pools in the enamel matrix are labile, and the decrease in both Na^+ and K^+ as enamel matures (Aoba and Moreno, 1987; Aoba et al., 1992; Lacruz, 2017), suggests that K^+ transport into the matrix by Nckx4 is removed by an additional K^+ transporter or channel.

Na^+ and K^+ in the maturing enamel of fluorotic mice (Lyaruu et al., 2014; Bronckers et al., 2015), is increased as compared to *wt* mice. Increased Na^+ in fluorotic enamel is consistent with the finding that Nckx4 trafficking is disrupted in fluorosed ameloblasts (Bronckers et al., 2017). K^+ accumulation in the enamel matrix of fluorosed mice suggests the possibility that intracellular transport of K^+ is also affected by fluorosis.

Maturation-stage ameloblasts have been compared with parallel functions to the proximal renal tubule cells of the kidney (Lacruz et al., 2013), and K^+ homeostasis is among the most important ions for maintaining cell function, particularly in regulating the electrochemical gradient across the plasma membrane (Palmer, 2015). To identify candidate K^+ transporters and channels for the removal of extracellular K^+ from the maturation enamel matrix, we compared transporters known to be important in kidney function, including Nkcc2, and Kcnj2 (ROMK), and genes coding for K^+ channels in secretory as compared to maturation stage of enamel organs. We identified Kcnj15, encoding for Kir4.2 protein, as the most highly upregulated inwardly rectifying K^+ channel. Kir4.2 (Kcnj15) immunolocalized to the apical border of wild type (*wt*) ruffle-ended ameloblasts (RE). In fluorosed and *Wdr72*$^{-/-}$ ameloblasts, where Nckx4 translocation to apical membrane is reduced (Wang et al., 2015; Bronckers et al., 2017), Kir4.2 remains primarily localized in the cytoplasm.

Expression of Wdr72, which is required for microtubule assembly and vesicle trafficking in maturation ameloblasts (Katsura et al., 2022), was upregulated in LS8 cells at acidic (pH 6.2), which is the pH of enamel matrix underlying RE. Together these results suggest that Kir4.2 (Kcnj15) removes K^+ from the extracellular enamel matrix, associated with WDR72-mediated vesicle trafficking and extracellular matrix pH.

Materials and methods

Animals and tissue collection

C57BL/6 *wt*, *Nckx4*$^{-/-}$, *Wdr72*$^{-/-}$ mouse lines, and C57BL/6 female mice given 0 or 50 ppm fluoride drinking water for 5 weeks were housed and maintained in the UCSF animal care facility, which is an Associated for Assessment and Accreditation of Laboratory Animal Care (AAALAC) accredited barrier facility. All experimental procedures associated with these animal models were approved by the Institutional Animal Care and Use Committee (IACUC) under the protocol AN183449-03.

Postnatal 40-day (P40) mice were collected following standard IACUC protocols. Mice were anesthetized with 240 mg/kg tribromoethanol (Sigma-Aldrich), and following cervical dislocation hemimandibles were removed and fixed in 4% paraformaldehyde (PFA) for 24 h at 4°C. The hemimandibles were decalcified in 8% EDTA at 4°C for 3 weeks, with EDTA solution changes every other day, and then paraffin embedded and sectioned along their sagittal planes. Kidneys were collected from *wt* mice as a control tissue and either fixed for immunohistochemistry or frozen down for Western blot analysis.

Enamel matrix element analysis

Hemimandibles from four 7-week old mice were dissected, embedded in epoxy, and polished in a cross orientation using a series of SiC papers and diamond polishing suspension starting from the incisor tip and stopping at the point of incisor eruption, near the plane of gingival sulcus. Six spots on the incisal enamel section at a plane perpendicular to incisal border of the lingual alveolar bone of each hemimandible were subjected to energy dispersive X-ray spectroscopy to collect elemental composition of K^+ and Na^+.

RNA seq analyses

First molars from 20 pups at postnatal day 5 (P5, secretory stag) and 20 pups at day 12 (P12, maturation stage) were microdissected from mouse hemimandibles. Soft tissues were removed from the pulp chambers and enamel organs from five mice were pooled as a group, resulting in four groups for each time point. Total RNA was purified using Zymo Research RNA Miniprep Kit and then sent to Novogene Co for quality control assessment, cDNA library construction, labelling and sequencing. Differential expression analysis of two conditions was performed using the DESeq2 R package, and the resulting *p*-values were adjusted using the Benjamini and Hochberg's approach for controlling the false discovery rate.

Western blotting

First molars were microdissected from hemimandibles of eight P13 mice, and soft tissues were removed from pulp chambers. The molars were rinse with PBS, combined, and protein was extracted in Pierce™ RIPA buffer (Thermo Scientific, UC280926) with a proteinase inhibitor cocktail for mammalian cells (Millipore Sigma, P8340). These samples were frozen at −80°C for 30 min, and then centrifuged for 10 min at 4°C. The concentration of protein in supernatant was measured with Pierce™ BCA protein Assay kit (Thermo Scientific, 23225). Kidney tissues were similarly collected as a positive reference. Twenty micrograms of total proteins from each sample were mixed with equal amounts of 2X SDS reducing loading buffer. Samples were loaded onto 4%–20% Mini-PROTEAN TGX SDS-PAGE gels (Bio-Rad, 4561094) and were subjected to electrophoresis with Tris/glycine/SDS running buffer at 100 V for 90 min. Proteins on SDS-PAGE gels were transferred to nitrocellulose membranes using an Invitrogen iBlot™ Gel Transfer Device. Membranes were blocked with Intercept Protein Free Blocking Buffer (LI-COR, 927-90001) and then incubated overnight with rabbit anti-KCNJ15 antibody (Novus Biologicals, NBP1-83091) at 4°C. Following wash, blots were incubated with IRDye 680RD conjugated anti-rabbit IgG (LI-COR 926-68073) for 1 h at room temperature. The membranes were thoroughly washed with PBST and Kir4.2 protein with molecular mass of 42,577 Da was visualized by using an Odyssey XF Imaging System.

Immunohistochemistry

Mouse hemimandible sagittal sections from *wt* mice were deparaffinized, rehydrated, and subjected to 10 mM sodium citrate

buffer (pH 6.0) antigen retrieval for 3 h at 60°C. The sections were then treated with 1% acetic acid in PBS to inactivate endogenous activity and then blocked with GeneTex Universal Protein Blocking reagent for 1 h, followed by overnight incubation at 4°C with rabbit anti-SLC12A1 antibody (Sigma-Aldrich® AV41388), rabbit anti-KCNJ1 antibody (Abcam ab224749), rabbit anti-KCNJ2 antibody (Abcam ab109750), or rabbit anti-KCNJ15 antibody (Novus Biologicals, NBP1-83091). After washing, sections were incubated with biotinylated swine anti-rabbit antibody (Dako E0431), followed by streptavidin, ALP (Vector® SA-5100-1) for 1 h. Vector® Red alkaline phosphatase substrate kit (Vector® SK5100) used to visualize alkaline phosphatase labeled sections, followed by counterstaining with methyl green.

Mouse hemimandibles from *wt*, *Nckx4*$^{-/-}$, *Wdr72*$^{-/-}$, and mice treated with 0 or 50 ppm fluoride for 5 weeks were similarly sectioned, treated with sodium citrate for antigen retrieval. Endogenous horseradish peroxidase activity was inactivated with 3% hydrogen peroxide in PBS, and then blocked with GeneTex Universal Protein Blocking reagent for 1 h, followed by overnight incubation at 4°C with either rabbit anti-KCNJ15 antibody (Novus Biologicals, NBP1-83091), or mouse anti-NCKX4 antibody (NeuroMab N414/25) (He et al., 2011). After washing, sections were incubated with anti-rabbit IgG HRP Conjugate (Promega W401). ImmPACT® DAB Substrate Kit, Peroxidase (Vector® SK-4105) was used to visualize HRP labeled sections and HRP, and stained sections were counterstained with hematoxylin, followed by dehydration and mounting. Slides were viewed under a Nikon Eclipse E800 microscope and images were taken with an Olympus DP74-CU camera.

Cell culture and RT-qPCR

LS-8 cells were grown in 5% FBS/1% PS/DMEM to 80% confluence, washed with PBS one time, and then cultured overnight in MEM Eagle's Media with 2% FBS/1% PS adjusted to pH 7.2 or pH 6.2. The cells were washed with PBS twice, then lysed with TRIzol™ Reagent (Ambion®, 15596018), and total RNA was purified using a Direct-zol™ RNA MiniPrep (Zymo Research, R2052) kit. The RNA concentration was quantified using a Thermo Scientific™ NanoDrop™ One Spectrophotometer, and then reverse transcribed into cDNA libraries using SuperScript™ III Reverse Transcriptase (Invitrogen™, 18080093) with 1500 ng of total RNA for each sample. qPCR was then performed using an Applied Biosystems 7500 Real-Time PCR System to quantitate the changes in the expression levels of *Wdr72* in cells grown at pH6.2 compared to that at pH 7.2 by delta delta Ct (ΔΔCt) method (Schmittgen et al., 2000; Bustin, 2002; Rao et al., 2013). The average Ct of *Wdr72* was obtained after normalizing to reference gene from a control experiment in which LS-8 cells were cultured in MEM Eagle's Media with 2% FBS/1% PS at pH 7.2, was used as a baseline. Delta Ct of *Wdr72* expression levels of 5 separate experiments at pH 7.2 ($\Delta Ct_{pH7.2}$) was obtained by normalizing the average Ct to this baseline. Then ΔΔCt was calculated by normalizing the average Ct of *Wdr72* expressed by cells grown at pH 6.2 in this same set of experiment ($\Delta Ct_{pH6.2}$) to $\Delta Ct_{pH7.2}$. The fold change was next calculated concerning $2^{-\Delta\Delta Ct}$. The significance was determined by unpaired two-tailed Student's t-test. The fold changes from five experiments were graphed by GraphPad Prism Version 9.5.0.

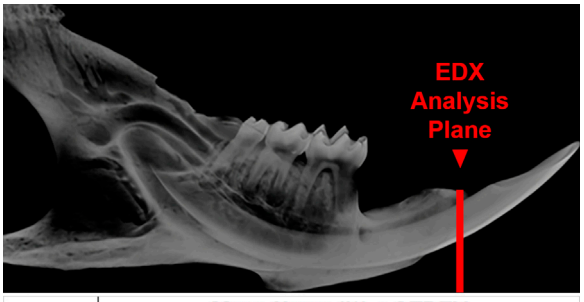

Element	Mass Norm (%) ± STDEV		
	Nckx4 $^{+/+}$ (N=4)	*Nckx4* $^{-/-}$ (N=4)	KO/WT
K^+	0.0749 ± 0.0199	0.0393 ± 0.0328	0.4924
Na^+	0.4683 ± 0.0095	0.6647 ± 0.0047	1.6502

FIGURE 1
EDX analysis of *Nckx4*$^{+/+}$ and *Nckx4*$^{-/-}$ enamel. A red line drawn on a microCT image of a mouse mandibular hemimandible shows the plane of section analyzed by EDX. The mass norm % of K^+ was decreased and Na^+ increased in the *Nckx4*$^{-/-}$ enamel matrix relative to the *Nckx4*$^{+/+}$ matrix.

Primer sequences were as follows:

Gapdh sense-5′-TGGCCTTCCGTGTTCCTAC-3′; anti-sense-5′-GAGTTGCTGTTG AAGTCGCA-3′

Wdr72 sense-5′-TCTGGGGAAGAAAAGCTCCTC-3′; anti-sense-5′-CGAAGCCGAATGACCAAAAAG-3′

Results

Increased Na^+ and decreased K^+ are found in the enamel matrix of *Nckx4*$^{-/-}$ mice compared to *Nckx4*$^{+/+}$ mice

Nckx4 exchanges 1 K^+ and 1 Ca^{2+} from the intracellular compartment, against 4 Na^+ from the (extracellular) enamel fluid. As expected, energy dispersive X-ray (EDX) analysis showed reduced relative amounts of potassium by about 50%, while sodium increased about 60% in the *Nckx4*$^{-/-}$ enamel matrix as compared to that in the *Nckx4*$^{+/+}$ enamel (Figure 1).

RNA-seq analysis identifies Kcnj15 as the most upregulated inwardly rectifying K^+ transporter in the maturation stage of enamel organs

A heatmap of well-known major K^+ transporters identified in our RNA-seq analyses confirmed that Slc24a4, the gene coding for Nckx4, was highly upregulated in maturation as compared to secretory enamel organs (Figure 2). Kcnj15, the gene encoding for the inwardly rectifying K^+ channel Kir4.2 was the most highly upregulated inwardly rectifying K^+ channel. Immunostaining showed Kir4.2 (Kcnj15), localized at the ameloblast apical border. K^+ transporters found in the kidney, including Slc12a1, which encodes for Nkcc2, and Kcnj1, which encodes for Kir1.1 (ROMK1) (Palmer, 2015), were immunonegative in ameloblasts. Interestingly, the two-pore domain K^+ channels Kcnk11 and Kcnk2, also called "leaky" and passive K^+ channel, and the outwardly

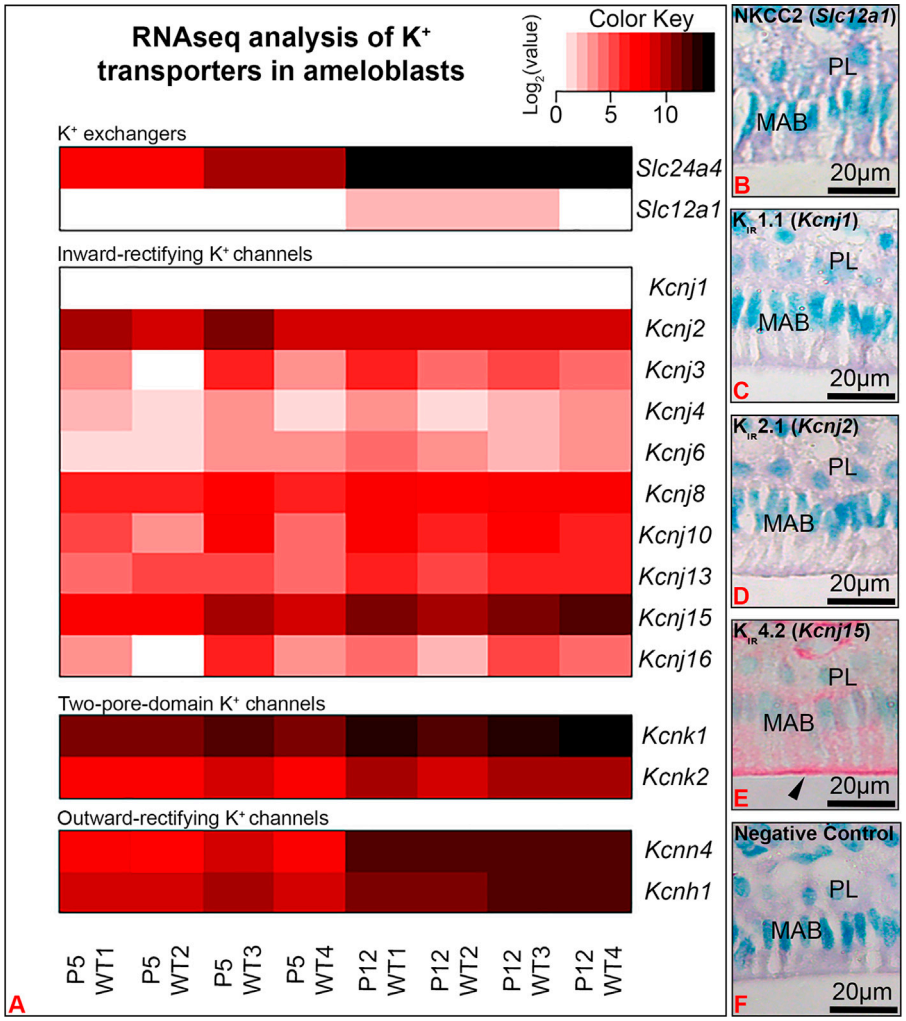

FIGURE 2
RNA-seq analysis showed Kcnj15 to be the most significantly upregulated inwardly rectifying K^+ channel in maturation (P12) as compared to secretory (P5) enamel organs. **(A)** A heat map represents the expression levels of K^+ transporters identified by RNA-seq in the P5 and P12 mouse first molar enamel organs. Immunohistochemical staining of NKCC2 (Slc12a1) **(B)**, Kir1.1 (Kcnj1) **(C)**, Kir 2.1(Kcnj2) **(D)** were immunonegative in maturation ameloblasts (MAB), while Kir4.2 (Kcnj15) was immunopositive, with increased staining at the ameloblast apical border. Negative control **(F)**. PL. papillary layer.

rectifying (transporting K^+ from the intracellular to extracellular compartment) Kcnn4 and Kcnh1 were also upregulated in maturation as compared to secretory stage of enamel organs.

Kir4.2 (Kcnj15) is synthesized by maturation stage enamel organ and spatially localizes at the ameloblast apical border

To verify protein expression of Kir4.2, we performed Western blot and immunostaining of kidney and maturation stage ameloblasts on the continuously growing mouse incisor. Western blot showed Kir4.2 to be present in the proteins extracted from mouse first molar enamel organs, with a similar size to the Kir4.2 protein labeled in the kidney control (Figure 3A). Immunostaining of kidney validated the anti-Kir4.2 antibody (Figure 3B).

In ameloblasts, Kir4.2 was enriched at the apical border of RE, whereas SE displayed a more diffuse pattern (Figures 3C, 4C). Positive immunostaining for Kir4.2 was also noted in the connective tissue cells around the dental epithelium and in cells that form walls of larger vessels near the epithelial papillary layer (Figures 2E, 3C).

Kir4.2 is localized at the apical membrane of *Nckx4*$^{-/-}$ RA, but not in fluorosed or *Wdr72*$^{-/-}$ maturation ameloblasts

The phenotype of maturation stage ameloblasts of *Nckx4*$^{-/-}$ mice appeared to be similar to SE, but Kir4.2 also localized to the ameloblast apical border, though with apparent reduced staining intensity as compare to *wt* ameloblasts (Figures 4C, G). *Wdr72*$^{-/-}$ maturation ameloblasts showed similar intensity of Kir4.2 immunostaining as compared to wt ameloblasts, but remained in the cytoplasm of ameloblasts, without localizing to the apical plasma membrane (Figures 4I–K).

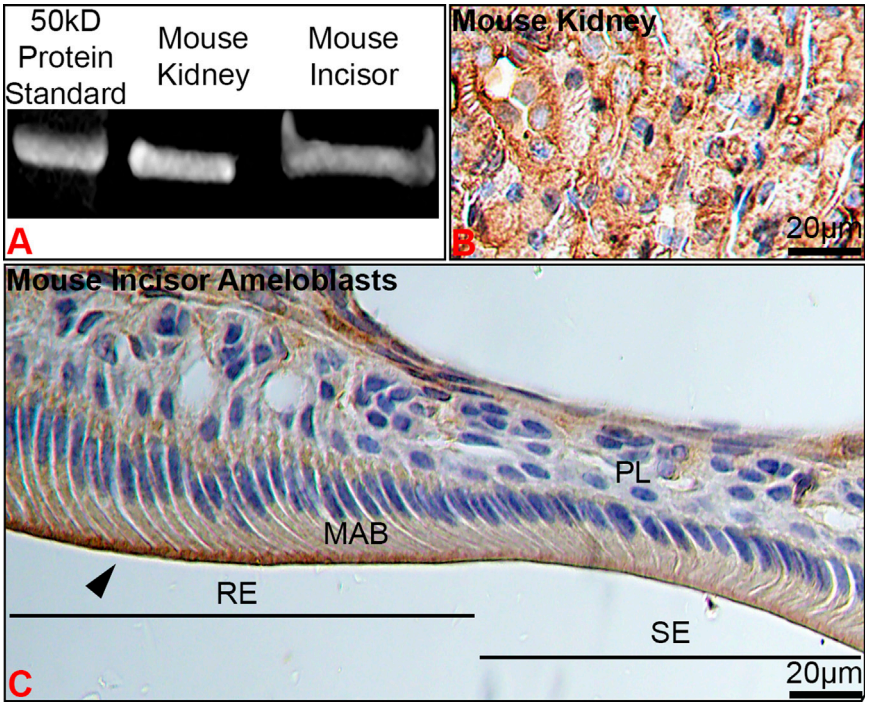

FIGURE 3
The stage- and spatial-specific presence of Kir4.2 (Kcnj15) in maturation ameloblasts. **(A)** Anti-Kir4.2 antibody identified an approximately 45 kDa protein in western blot analysis of mouse kidney and first molar enamel organs. **(B)** Kidney controls were immunopositive for Kir4.2. **(C)** Kir4.2 was immunopositive at the apical border of ruffle-ended (RE) maturation ameloblasts (MAB), and was reduced in smooth-ended (SE) ameloblasts.

In fluorosed ameloblasts, Kir4.2 immunostaining appeared reduced at the ameloblast apical border as compared to the 0 ppm fluoride control (Figures 5A, D) l, similar to similar NCKX4 (Figures 5B, E).

The expression level of *Wdr72* is increased in LS8 cells grown at acidic pH (6.2) as compared to neutral pH (7.2)

WDR72 immunostained at both the basal and apical borders, with more intense immunostaining at the apical border of RE, overlying enamel matrix with a pH of 6.2 (Figure 6A), as compared to SE which overlay an enamel matrix of pH 7.2 (Figure 6B). *In vitro*, relative expression of *Wdr72* in LS8 cells grown at pH 6.2 was significantly greater than in cells grown at pH 7.2 (Figure 6C).

Discussion

As enamel matures, HA crystals expand in width, replacing the protein matrix. This process is driven by calcium transport to the extracellular matrix as ameloblasts modulate between cells with apical ruffled-ended borders (RE) and smooth-ended borders (SE) (Josephsen and Fejerskov, 1977). To support such large quantities of Ca^{2+} in a tightly regulated series of events, several ion exchangers that maintain Na^+ and K^+ homeostasis are key to functional enamel mineralization (Bronckers et al., 2015; Lacruz, 2017; Robertson et al., 2017). One such exchanger is NCKX4, which localizes to the apical border of RE and transports 1 K^+ and 1 Ca^{2+} into the enamel matrix in exchange for 4 Na^+. Consistent with this, we found that Na^+ was relatively increased in *Nckx4*$^{-/-}$ as compared to *Nckx4*$^{+/+}$ maturation enamel, while K^+ was relatively decreased in *Nckx4*$^{-/-}$ enamel.

Among the K^+ transporter types expressed during enamel maturation, we found that Kcnj15, a gene encoding for the inwardly rectifying potassium channel, Kir4.2, to be relatively highly expressed in maturation stage ameloblasts. The Kir channels preferentially transport K^+ intracellularly (Köhling and Wolfart, 2016), and inward rectification of K^+ flux results from interactions between intracellular Mg^{2+} or polyamines, which physically block K^+ outward flux by binding to residues localized in the transmembrane and cytoplasmic regions of the channels (Hibino et al., 2010). Other K^+ channels, including the leaky two pore domain potassium channels, calcium-gated, and voltage-gated K^+ channels, mainly conduct K^+ outward. We therefore suggest that Kir4.2 (KCNJ15) at the apical surface, removes K+ from the labile pool of ions transported into the enamel matrix by NCKX4 (see Figure 7).

In *Wdr72*$^{-/-}$ and fluorosed ameloblasts, Kir4.2 remained localized in the cytoplasm. Kir proteins are transported by vesicle trafficking (Zangerl-Plessl et al., 2019), and altered vesicle trafficking, as evidenced by dislocation of Nckx4 in *Wdr72*$^{-/-}$ (Wang et al., 2015) and fluorosed (Bronckers et al., 2017) ameloblasts may have a role in translocation of Kir4.2 to the RE apical membrane. The lack and/or reduced translocation of Kir4.2 to the apical plasma membrane of fluorosed ameloblasts, may be why K+ is relatively increased in fluorosed enamel.

Wdr72 modulates endocytosis and vesicle trafficking by affecting microtubule assembly (Katsura et al., 2022). Our finding that *Wdr72*

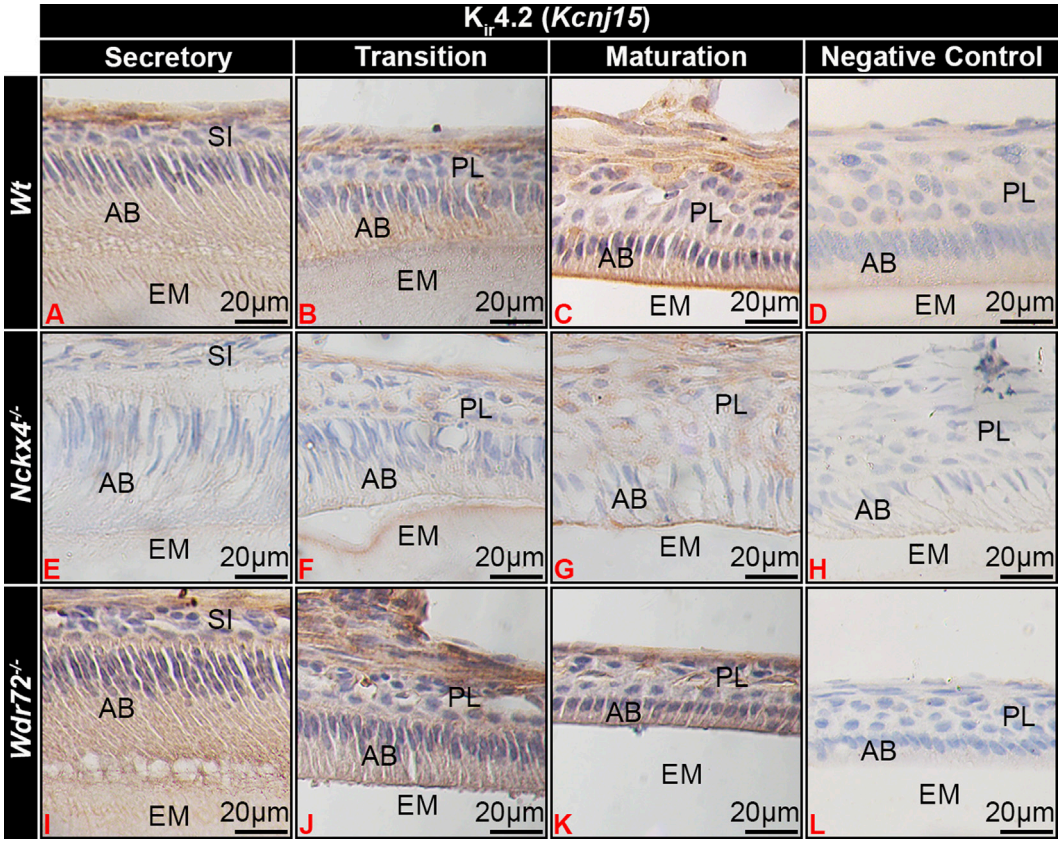

FIGURE 4
Kir4.2 immunostaining of ameloblasts. **(A)** *Wt* secretory ameloblasts (SAB) had minimal immunostaining for Kir4.2 (Kcnj15). **(B)** Transition stage ameloblasts (TAB) **(B)** had positive Kir4.2 cytoplasmic staining, which **(C)** localized to the apical border of ruffle-ended (RE) early-stage maturation ameloblasts (MAB) RE. In NCKX4 loss of function mice (*Nckx4*$^{-/-}$), Kir4.2 showed similar localization as compared to *wt* ameloblasts, with less intense immunostaining **(E–G)**. Intensity of Kir4.2 (Kcnj15) immunostaining in *Wdr72*$^{-/-}$ mice was similar to that of *wt* mice, but was not localized to the MAB apical border or *Wdr72*$^{-/-}$ mice **(I–K)**. Negative controls for MAB of each model *wt* **(D)**, *Nckx4*$^{-/-}$ **(H)**, and *Wdr72*$^{-/-}$ **(L)** were immunonegative. MAB, maturation ameloblast; EM, enamel matrix; PL, papillary layer.

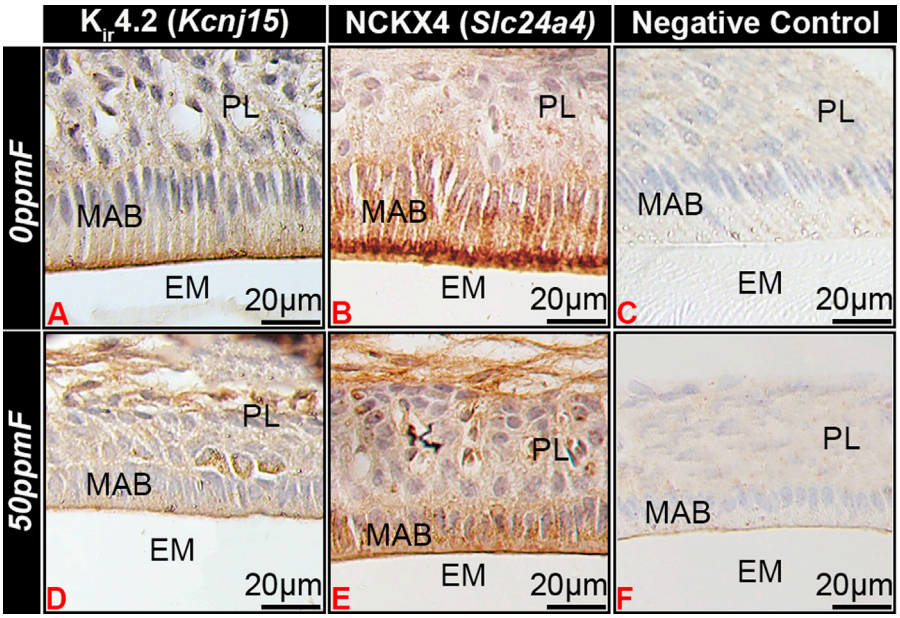

FIGURE 5
Fluorosis affects Kir4.2 (*Kcnj15*) localization in maturation ameloblasts. In mice given 0 ppm fluoride drinking water Kir4.2 (*Kcnj15* **(A)** and NCKX4 **(B)** localized to the apical border of ruffle-ended maturation stage ameloblasts. Fluorosed ameloblasts had reduced Kir4.2 (*Kcnj15*) **(D)** and NCKX4 **(E)** at the apical border as compared to 0 ppm fluoride controls. MAB, maturation ameloblast; EM, enamel matrix; PL, papillary layer.

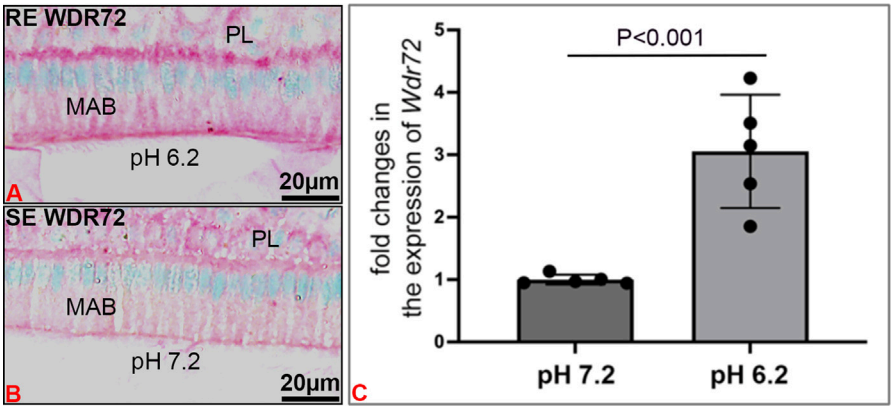

FIGURE 6
pH related effects on WDR72 expression. **(A)** Immunostaining of *wt* mouse incisor maturation stage of ameloblasts (MAB) showed increased staining of WDR72 at the basal and apical borders of ruffle-ended ameloblasts RE, associated with an acidic enamel matrix (pH 6.2), as compared to **(B)** Smooth-ended ameloblast SE which are associated with a more neutral matrix (pH 7.2) **(C)** *In vitro*, pH related changes in *Wdr72* mRNA showed increased expression at pH 6.2 as compared to pH 7.2 (unpaired Student's t-test). *N* = 5; SDs of individual samples are indicated by the dark circles on the error bar.

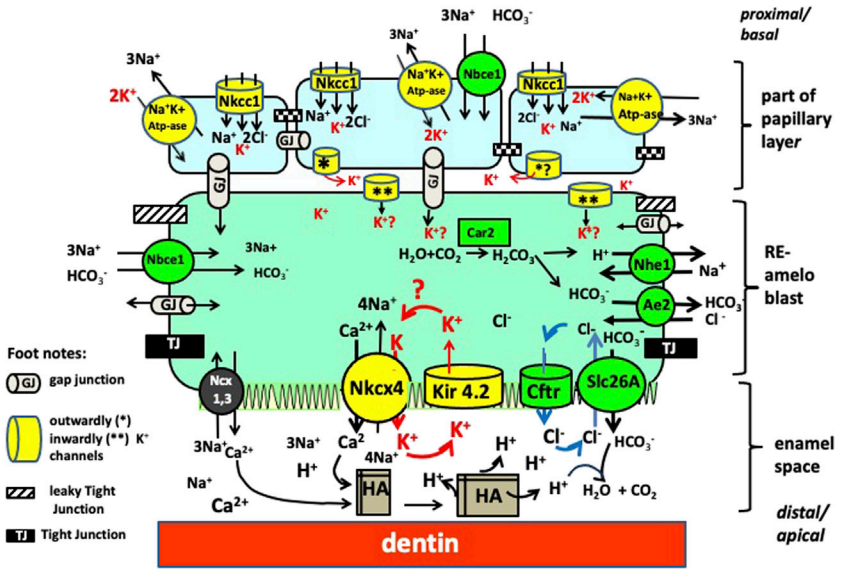

FIGURE 7
Working model for ion transport by RE ameloblasts. There are four clusters of transporters each involved in a specific function. By requiring the same ions to operate (Na^+, K^+ and Cl^-) from the pool of ions these clusters are interdependent from each other. One cluster involves mineral transport to form crystals (NaPi2 and Nckx4 mediated transport of phosphate and calcium, respectively). A second cluster is for K^+ transport (in yellow) to obtain electrochemical gradients to drive ion transport (Nckx4, Kir 4.2, Na^+K^+ ATpase, Nkcc1); Cluster 3 for pH and osmoregulation (in green, includes Cftr, Ae2, Nhe1 and members of the Slc26a family (Slc26a-a3-a4, a6, a7; Nhe1 and Car2). Cluster 4 for paracellular and intracellular transport tight junctions (black) and gap junctions (grey tubes).

expression was relatively increased at acidic pH, suggests that changes in enamel matrix pH could also affect vesicle trafficking by modulating WDR72 expression.

In fluorotic enamel there are fewer, but wider RE bands, suggesting a delayed transition from RE to SE (Smith et al., 1993). Fluorotic enamel contains less Cl^- (required for bicarbonate secretion into the enamel matrix) but more K^+ (Lyaruu et al., 2014). Enamel of Cftr-null and Ae2-null, which have even less Cl^- and more K^+ than fluorotic enamel, have no SE bands only RE bands(Bronckers et al., 2015). This suggests that local regulation of pH affects turnover of tight junctions.

Fluorotic enamel also has more Mg^{2+} than *wt* enamel, and furthermore, enamel of the more fluoride sensitive C57Bl mouse strain has more (approximately 2×) Mg^+ in the extracellular enamel matrix as compared to the more fluoride resistant FVB mouse (Bronckers and Lyaruu, 2017). The role of Mg^{2+} in the regulation of K^+ inward rectification by Kir channels may have a

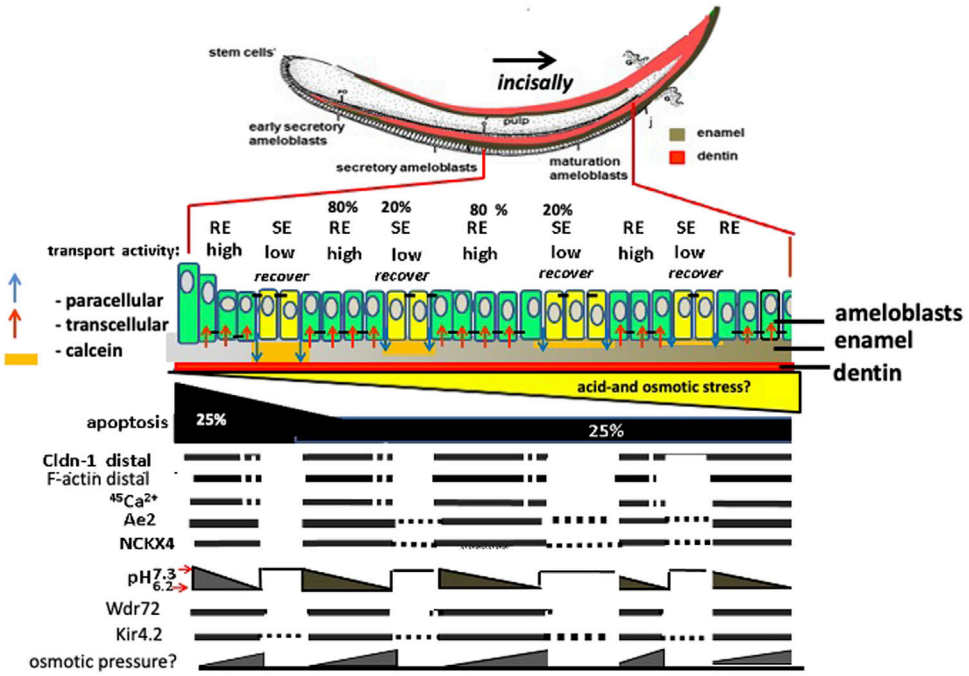

FIGURE 8
Amelogenesis in mouse incisor: major differences between expression/activity in RE compared to SE ameloblasts. Ameloblasts modulate corresponding to calcein staining of neutral pH enamel matrix orange color. Claudin 1 (Cldn1) and F-actin are increased in RE, associated TJs, and in RE, Nckx4 transports Ca^{2+} into the enamel matrix for hydroxyapatite (HA) formation. HA formation in enamel lowers the pH in enamel fluid. As matrix pH decreases, *Wdr72* increases, and NCKX4 and Kir4.2 translocate to the apical RE membrane. Paracellular transport of ions happens during transformation of RE into SE mode during which selective apical tight junctions disappear and basal tight junctions appear forming a new basal barrier. The transition of RE into SE and the flushing out of enamel fluid may result from hyperosmotic pressure of salt building up in the enamel space that causes leakage and eventually loss of the distal TJ by the inward flux of fluid.

role in the sensitivity of ameloblasts to fluoride exposure. The mechanisms by which ameloblast control Mg transport are poorly understood, but likely to involve the cation channel TRPM7 (Nakano et al., 2016; Kádár et al., 2021).

Together these results support a role or Kir4.2 (Kcnj15) mediated inward K^+ flux in maturation ameloblasts. Figure 8 illustrates the proteins and cellular changes associated with changes in RE and SE, and their relationship to TJ formation and ameloblast modulation. Future studies on the role of matrix pH, ion exchange, vesicle recycling, will further test this model and help to better understand the unique system by which maturation stage ameloblast direct enamel matrix mineralization.

Data availability statement

The data presented in the study are deposited in the GEO repository, accession number GSE222120.

Ethics statement

The animal study was reviewed and approved by the UCSF Institutional Animal Care and Use Committee (IACUC).

Author contributions

AB, YZ, and PB contributed to conception and design of the study. JN, YZ, and KK organized and analyzed data. AB and PB wrote the first draft of the manuscript. JN and YZ wrote sections of the manuscript. All authors contributed to manuscript revision, read, and approved the submitted version.

Conflict of interest

The authors declare that the research was conducted in the absence of any commercial or financial relationships that could be construed as a potential conflict of interest.

Publisher's note

All claims expressed in this article are solely those of the authors and do not necessarily represent those of their affiliated organizations, or those of the publisher, the editors and the reviewers. Any product that may be evaluated in this article, or claim that may be made by its manufacturer, is not guaranteed or endorsed by the publisher.

References

Aoba, T., and Moreno, E. C. (1987). The enamel fluid in the early secretory stage of porcine amelogenesis: Chemical composition and saturation with respect to enamel mineral. *Calcif. Tissue Int.* 41, 86–94. doi:10.1007/BF02555250

Aoba, T., Shimoda, S., and Moreno, E. C. (1992). Labile or surface pools of magnesium, sodium, and potassium in developing porcine enamel mineral. *J. Dent. Res.* 71, 1826–1831. doi:10.1177/00220345920710111201

Bronckers, A. L., Jalali, R., and Lytton, J. (2017). Reduced protein expression of the Na+/Ca2++K+-Exchanger (SLC24A4) in apical plasma membranes of maturation ameloblasts of fluorotic mice. *Calcif. Tissue Int.* 100, 80–86. doi:10.1007/s00223-016-0197-4

Bronckers, A. L., Lyaruu, D., Jalali, R., Medina, J. F., Zandieh-Doulabi, B., and Denbesten, P. K. (2015). Ameloblast modulation and transport of Cl^-, Na^+, and K^+ during amelogenesis. *J. Dent. Res.* 94, 1740–1747. doi:10.1177/0022034515606900

Bronckers, A. L., and Lyaruu, D. M. (2017). Magnesium, pH regulation and modulation by mouse ameloblasts exposed to fluoride. *Bone* 94, 56–64. doi:10.1016/j.bone.2016.10.014

Bustin, S. A. (2002). Quantification of mRNA using real-time reverse transcription PCR (RT-PCR): Trends and problems. *J. Mol. Endocrinol.* 29, 23–39. doi:10.1677/jme.0.0290023

He, W., Liu, W., Chew, C. S., Baker, S. S., Baker, R. D., Forte, J. G., et al. (2011). Acid secretion-associated translocation of KCNJ15 in gastric parietal cells. *Am. J. Physiol. Gastrointest. Liver Physiol.* 301, G591–G600. doi:10.1152/ajpgi.00460.2010

Hibino, H., Inanobe, A., Furutani, K., Murakami, S., Findlay, I., and Kurachi, Y. (2010). Inwardly rectifying potassium channels: Their structure, function, and physiological roles. *Physiol. Rev.* 90, 291–366. doi:10.1152/physrev.00021.2009

Hu, P., Lacruz, R. S., Smith, C. E., Smith, S. M., Kurtz, I., and Paine, M. L. (2012). Expression of the sodium/calcium/potassium exchanger, NCKX4, in ameloblasts. *Cells Organs* 196, 501–509. doi:10.1159/000337493

Jalali, R., Lodder, J. C., Zandieh-Doulabi, B., Micha, D., Melvin, J. E., Catalan, M. A., et al. (2017). The role of Na:K:2Cl cotransporter 1 (NKCC1/slc12a2) in dental epithelium during enamel formation in mice. *Front. Physiol.* 8, 924. doi:10.3389/fphys.2017.00924

Josephsen, K., and Fejerskov, O. (1977). Ameloblast modulation in the maturation zone of the rat incisor enamel organ. A light and electron microscopic study. *J. Anat.* 124, 45–70.

Kádár, K., Juhász, V., Földes, A., Racz, R., Zhang, Y., Löchli, H., et al. (2021). TRPM7-Mediated calcium transport in HAT-7 ameloblasts. *Int. J. Mol. Sci.* 22, 3992. doi:10.3390/ijms22083992

Katsura, K., Nakano, Y., Zhang, Y., Shemirani, R., Li, W., and Den Besten, P. (2022). WDR72 regulates vesicle trafficking in ameloblasts. *Sci. Rep.* 12, 2820. doi:10.1038/s41598-022-06751-1

Köhling, R., and Wolfart, J. (2016). Potassium channels in epilepsy. *Cold Spring Harb. Perspect. Med.* 6, a022871. doi:10.1101/cshperspect.a022871

Lacruz, R. S. (2017). Enamel: Molecular identity of its transepithelial ion transport system. *Cell. Calcium* 65, 1–7. doi:10.1016/j.ceca.2017.03.006

Lacruz, R. S., Smith, C. E., Kurtz, I., Hubbard, M. J., and Paine, M. L. (2013). New paradigms on the transport functions of maturation-stage ameloblasts. *J. Dent. Res.* 92, 122–129. doi:10.1177/0022034512470954

Lyaruu, D. M., Medina, J. F., Sarvide, S., Bervoets, T. J., Everts, V., Denbesten, P., et al. (2014). Barrier formation: Potential molecular mechanism of enamel fluorosis. *J. Dent. Res.* 93, 96–102. doi:10.1177/0022034513510944

Nakano, Y., le, M. H., Abduweli, D., Ho, S. P., Ryazanova, L. V., Hu, Z., et al. (2016). A critical role of TRPM7 as an ion channel protein in mediating the mineralization of the craniofacial hard tissues. *Front. Physiol.* 7, 258. doi:10.3389/fphys.2016.00258

Palmer, B. F. (2015). Regulation of potassium homeostasis. *Clin. J. Am. Soc. Nephrol.* 10, 1050–1060. doi:10.2215/CJN.08580813

Parry, D. A., Poulter, J. A., Logan, C. V., Brookes, S. J., Jafri, H., Ferguson, C. H., et al. (2013). Identification of mutations in SLC24A4, encoding a potassium-dependent sodium/calcium exchanger, as a cause of amelogenesis imperfecta. *Am. J. Hum. Genet.* 92, 307–312. doi:10.1016/j.ajhg.2013.01.003

Rao, X., Huang, X., Zhou, Z., and Lin, X. (2013). An improvement of the 2(-delta delta CT) method for quantitative real-time polymerase chain reaction data analysis. *Biostat. Bioinforma. Biomath.* 3, 71–85.

Robertson, S. Y. T., Wen, X., Yin, K., Chen, J., Smith, C. E., and Paine, M. L. (2017). Multiple calcium export exchangers and pumps are a prominent feature of enamel organ cells. *Front. Physiol.* 8, 336. doi:10.3389/fphys.2017.00336

Schmittgen, T. D., Zakrajsek, B. A., Mills, A. G., Gorn, V., Singer, M. J., and Reed, M. W. (2000). Quantitative reverse transcription-polymerase chain reaction to study mRNA decay: Comparison of endpoint and real-time methods. *Anal. Biochem.* 285, 194–204. doi:10.1006/abio.2000.4753

Smith, C. E., Nanci, A., and Denbesten, P. K. (1993). Effects of chronic fluoride exposure on morphometric parameters defining the stages of amelogenesis and ameloblast modulation in rat incisors. *Anat. Rec.* 237, 243–258. doi:10.1002/ar.1092370212

Wang, S. K., Hu, Y., Yang, J., Smith, C. E., Nunez, S. M., Richardson, A. S., et al. (2015). Critical roles for WDR72 in calcium transport and matrix protein removal during enamel maturation. *Mol. Genet. Med.* 3, 302–319. doi:10.1002/mgg3.143

Zangerl-Plessl, E. M., Qile, M., Bloothooft, M., Stary-Weinzinger, A., and Heyden, M. A. G. (2019). Disease associated mutations in K(IR) proteins linked to aberrant inward rectifier channel trafficking. *Biomolecules* 9, 650. doi:10.3390/biom9110650

frontiers | Frontiers in Physiology

TYPE Original Research
PUBLISHED 10 February 2023
DOI 10.3389/fphys.2023.1144712

OPEN ACCESS

EDITED BY
Janet Moradian-Oldak,
University of Southern California,
United States

REVIEWED BY
Eric Everett,
University of North Carolina at Chapel Hill,
United States
Yasuo Yamakoshi,
Tsurumi Univesity, Japan

*CORRESPONDENCE
Elia Beniash,
ebeniash@pitt.edu

SPECIALTY SECTION
This article was submitted to Craniofacial Biology and Dental Research, a section of the journal Frontiers in Physiology

RECEIVED 14 January 2023
ACCEPTED 31 January 2023
PUBLISHED 10 February 2023

CITATION
Bui AT, Lukashova L, Verdelis K, Vasquez B, Bhogadi L, Gabe CM, Margolis HC and Beniash E (2023), Identification of stages of amelogenesis in the continuously growing mandiblular incisor of C57BL/6J male mice throughout life using molar teeth as landmarks.
Front. Physiol. 14:1144712.
doi: 10.3389/fphys.2023.1144712

Identification of stages of amelogenesis in the continuously growing mandiblular incisor of C57BL/6J male mice throughout life using molar teeth as landmarks

Ai Thu Bui[1,2], Lyudmila Lukashova[2], Kostas Verdelis[2,3], Brent Vasquez[1], Lasya Bhogadi[1], Claire M. Gabe[1,2], Henry C. Margolis[1,2,4] and Elia Beniash[1,2]*

[1]Department of Oral and Craniofacial Sciences, University of Pittsburgh School of Dental Medicine (UPSDM), Pittsburgh, PA, United States, [2]Center for Craniofacial Regeneration, UPSDM, Pittsburgh, PA, United States, [3]Department of Endodontics, UPSDM, Pittsburgh, PA, United States, [4]Department of Periodontics and Preventive Dentistry, UPSDM, Pittsburgh, PA, United States

Continuously growing mouse incisors are widely used to study amelogenesis, since all stages of this process (*i.e.*, secretory, transition and maturation) are present in a spatially determined sequence at any given time. To study biological changes associated with enamel formation, it is important to develop reliable methods for collecting ameloblasts, the cells that regulate enamel formation, from different stages of amelogenesis. Micro-dissection, the key method for collecting distinct ameloblast populations from mouse incisors, relies on positions of molar teeth as landmarks for identifying critical stages of amelogenesis. However, the positions of mandibular incisors and their spatial relationships with molars change with age. Our goal was to identify with high precision these relationships throughout skeletal growth and in older, skeletally mature animals. Mandibles from 2, 4, 8, 12, 16, and 24-week-old, and 18-month-old C57BL/6J male mice, were collected and studied using micro-CT and histology to obtain incisal enamel mineralization profiles and to identify corresponding changes in ameloblast morphology during amelogenesis with respect to positions of molars. As reported here, we have found that throughout active skeletal growth (weeks 2–16) the apices of incisors and the onset of enamel mineralization move distally relative to molar teeth. The position of the transition stage also moves distally. To test the accuracy of the landmarks, we micro-dissected enamel epithelium from mandibular incisors of 12-week-old animals into five segments, including 1) secretory, 2) late secretory - transition - early maturation, 3) early maturation, 4) mid-maturation and 5) late maturation. Isolated segments were pooled and subjected to expression analyses of genes encoding key enamel matrix proteins (EMPs), *Amelx*, *Enam*, and *Odam*, using RT-qPCR. *Amelx* and *Enam* were strongly expressed during the secretory stage (segment 1), while their expression diminished during transition (segment 2) and ceased in maturation (segments 3, 4, and 5). In contrast, *Odam*'s expression was very low during secretion and increased dramatically throughout transition and maturation stages. These expression profiles are consistent with the consensus understanding of enamel matrix proteins expression. Overall, our results demonstrate the high accuracy of our landmarking method and emphasize the importance of selecting age-appropriate landmarks for studies of amelogenesis in mouse incisors.

KEYWORDS

amelogenesis, microdissection, aging, molar landmarks, transition, apical movement

1 Introduction

Determining the changes in enamel mineral formation as a function of ameloblast differentiation and changes in gene expression are key to our understanding of amelogenesis. Murine incisors are hypselodont teeth and grow continuously throughout their lifespan, unlike most other mammalian teeth, which complete their crown formation before eruption (Renvoisé and Michon, 2014). Accordingly, all stages of enamel formation (amelogenesis) are present in a single continuously growing murine incisor in a spatially determined sequence (Smith et al., 1996; Verdelis et al., 2016). Due to these unique features, murine incisors are widely used to study amelogenesis. The continuously growing murine incisor has served as a reliable model to study enamel formation from a variety of perspectives (Smith et al., 1996; Smith et al., 2005; Beniash et al., 2009; Bui et al., 2022). The development of genetic tools to specifically target and edit genes made it possible to answer mechanistic questions about the functions of EMPs and other ameloblast machinery and to better understand hereditary diseases of enamel (Gibson et al., 2001; Caterina et al., 2002; Shin et al., 2020; Liang et al., 2022). Murine models have also been used to study the effects of environmental factors on enamel formation (Jedeon et al., 2014; Jalali et al., 2017; Bui et al., 2022).

Ameloblasts are highly specialized cells, which perform specific functions, depending on the stage of amelogenesis. They undergo a complex histodifferentiation process, comprising several discrete and functional stages of amelogenesis–*i.e.,* presecretory, secretory, transition and maturation (Hu et al., 2007; Lacruz et al., 2012a; Lacruz et al., 2017; Krivanek et al., 2020). Therefore, reliable methods of collecting ameloblasts from different stages of amelogenesis are required when studying the biological roles of stage-specific ameloblasts in enamel formation, for example, through the comparison changes in patterns of gene and protein expression in association enamel mineral deposition.

The collection of distinct ameloblast populations using micro-dissection relies on the stable positions of molar teeth as landmarks for identifying the different stages of amelogenesis in mouse incisors. Micro-dissection was first developed in the rat model (Hiller et al., 1975; Smith and Nanci, 1989), which is more suitable for enamel organ tissue collection than mice because of the larger size of rat teeth. However, due to the widespread use of mice as an animal model for genetic modifications, they are commonly used to study genetic bases of dental tissue development and disease (Brookes et al., 2017; Shin et al., 2020; Liang et al., 2022). Likewise, in studies of complex environmental effects on dental development when multiple treatment conditions and/or large sample sizes are needed, mice are a preferable choice when compared to other rodents (Bui et al., 2022). While micro-dissection methods for rat enamel organs are well established (Smith and Nanci, 1989; Smith et al., 1996; Moffatt et al., 2008; Lacruz et al., 2012a; Lacruz et al., 2012b; Jedeon et al., 2014), they still require further refinement in mice. Only a handful of studies that utilize micro-dissection techniques have been conducted on mice (Smith et al., 2005; Smith et al., 2011; Houari et al., 2018; Bui et al., 2022). However, these were performed on animals of a single age and the resolution of the micro-dissection techniques used in these studies was fairly coarse. More importantly, the impact of mouse age on the positions of the incisors in mandibles and their spatial relationships with molar teeth has not been fully addressed, especially during the period of skeletal growth (Wei et al., 2017), a factor that could markedly affect findings, particularly when conducting longitudinal studies. The goal of this study was to develop a methodology to collect ameloblasts from different stages of enamel formation in mouse incisors with high precision and over the lifespan of the animal during the active skeletal growth phase, and in skeletally mature animals.

2 Materials and methods

2.1 Animals and sample collection

Male C57BL/6J mice (Jax® #000664) were bred and raised in the Division of Laboratory Animal Resources at the University of Pittsburgh, following protocols approved by the Institutional Animal Care and Use Committees, University of Pittsburgh. All mice were offered a mixture of regular hard chow (LabDiet, 5P76-Prolab Isopro RMH 3000) and gel food (Diet Gel 76AGel, ClearH_2O), under a 12-h dark-light cycle. 2-week-old (wo), 4-wo, 8-wo, 12-wo, 16-wo, 24-wo, and 18-month-old (mo) mice were used in this study. Each group contained three to five mice from different breeding pairs. A total of 51 mice were used in this study (Supplementary Table S1). Of those, 27 mice were collected for micro-CT analyses and histology, including two 12-wo and two 16-wo male mice that were obtained from Jackson Laboratory (from facilities in Ellsworth, Maine or Bar Harbor, Maine, United States), which were kept on a regular hard diet (LabDiet, 5P76-Prolab Isopro RMH 3000) only (Supplementary Table S1). Another 24 12-wo male mice from our colony were used for micro-dissection and RNA collection (Supplementary Table S1).

2.2 Micro CT analysis

Mice were euthanized with carbon dioxide, followed by decapitation. The hemimandibles were immediately cleaned of any attached soft tissues. Left hemimandibles were stored in 70% ethanol (Decon Labs 2,701) at 4°C. Left hemimandibles were scanned using a Scanco μCT 50 scanner (Scanco Medical, Brüttisellen, Switzerland) system at 6 μm voxel size, 55 KVp, 145 μA, a 0.36° rotation step (180° angular range), and a 1,500 ms exposure time per view.

Samples were orientated identically with the scan plane perpendicular to the distal root of the M2 molar to minimize the curvature of the incisor in the zone of interest (0–4 mm from the apex), using Scanco μCT software (HP, DECwindows Motif 1.6) for 3D reconstruction and viewing of images. The positions of the first, second and third molars (M1, M2, and M3, respectively) were recorded. The enamel layer was then contoured, segmented and analyzed using a threshold set at 180 mgHA/cm^3. Mineral density distribution was recorded from the cervical end toward the peak. Enamel volume (EV) profile of each enamel block of 6 μm-thickness was recorded also from the cervical end toward the peak, using the formula: EV (μm^3) = EA × 6 μm, where EA is the area of each scanned enamel slice. Illustrations of sagittal and longitudinal sections, as well as 3D reconstructions, were obtained *via* Data Viewer software (Skyscan, release 1.5.2.4, Kontich, Belgium).

2.3 Trichrome masson staining

Contralateral hemimandibles from mice used for micro-CT analysis were fixed in 10% formalin (Fisher Chemical SF100-4) for 48 h and then decalcified in 4.13% sodium EDTA (Fisher Bioreagents

BP120) for 1 month with gentle agitation at 4°C. Hemimandibles were rinsed in PBS, dehydrated using ascending ethanol concentrations (up to 100%) and embedded in paraffin using a tissue embedder (Leica ASP300S) with a 12-h cycle. The paraffin blocks were carefully oriented and sectioned with a microtome (Leica E61160) in the sagittal plane at a 7 µm thickness. The sections for histological processing were selected based on the following criteria: The section must contain 1) roots of all molar teeth, 2) an intact cervical loop and 3) an intact ameloblast layer containing all stages of amelogenesis (Figure 1A-the staining figure?). These criteria ensure that the landmarks (molars) can be accurately related to the developmental stages of incisal ameloblasts in the histological sections. The presence of molar roots in the histological sections allowed for the correlation with corresponding micro-CT reconstructions to determine the correct position of each stage of amelogenesis in relationship to the molar teeth and to the enamel densification and thickness profiles. Selected sections were stained using a Trichrome Masson's staining procedure, as previously described (Bui et al., 2022). After staining, the slides were air dried, mounted with mounting media (Thermo Scientific #4112), and observed using a light microscope (Nikon DS-Fi3) in the bright-field mode at ×4 and ×25 magnifications.

2.4 Micro-dissection procedure and landmarks

Mandible dissection, cleaning, and alveolar bone removal were carried out using previously described procedures (Molla et al., 2010; Houari et al., 2018). Briefly, freshly collected mouse mandibles were dissected on a cold plate under a dissecting microscope (Leica S8 APO) at ×2.5 magnification. A #11 blade was inserted at the mesial lingual side, between the bonny alveolar crest and the incisor tip. Keeping the scalpel parallel to the tooth's longitudinal axis, the bone covering the lingual surface of the incisor was carefully removed, and special effort was made to not disturb the enamel organ of the incisor. Importantly, for successful identification of the dissection planes, the following steps were carried out: 1) Gingiva and periosteum covering the molar roots were thoroughly removed to facilitate the visualization of these landmarks underneath the alveolar bone, 2) the bone was removed only from the lingual face of the incisor and all 3 M carefully kept intact at their original positions, 3) the lingual surface was scored using a scalpel with a #11 blade in the planes transecting the chosen molar landmarks (Figure 1B) and normal to the incisor long axis (Figure 1C), 4) the incisor was removed completely from the bone socket and a 0.3 mm piece of the apical end was cut off to eliminate contamination by pulpal mesenchymal cells and the population of undifferentiated apical papilla stem cells (SCAP) at the cervical loop (Figure 1B). Finally, strips of enamel organ containing ameloblasts were collected from five different segments, including: 1) Secretory stage (*sec*), 2) mixture of late secretory, transition and very early maturation stage (*trans*), 3) early maturation stage (*mat1*), 4) mid maturation stage (*mat2*) and 5) late maturation stage and protective ameloblasts (*mat3*) using the identified landmarks. Between collections, mandibles were rinsed twice with PBS (Gibco) to eliminate cross-contamination between fractions and to maintain cell osmolarity. Strips of the same kind were pooled from six animals for qPCR analysis.

2.5 RT-qPCR analysis

Pooled strips of enamel epithelium, acquired as described in the preceding section, were immersed in ice-cold TRIzol® Reagent lysis buffer (Ambion, Life technologies) and homogenized in a Motorized Tissue Grinder using RNAse-free pestle (Fisher). The RNA fraction was isolated with a chloroform and isoamyl alcohol (Sigma C0549) solution (24:1), mixed with 70% ethanol and then purified with a PureLink RNA Mini Kit (Invitrogen), following manufacturer's instructions. Roughly two-hundred ng of total RNA was obtained from ten to twelve hemimandibles. The RNA quantities were determined using a NanoDrop One C (Thermo Scientific) spectrophotometer. The collected samples were subjected to reverse transcriptase reaction using SuperScript IV enzyme (Thermo Fisher) for 20 min at 50°C. Real-time PCR analyses were performed with StepOne Plus Real Time PCR system (Applied Biosystems) and PowerTrack™ SYBR Green Master Mix (Thermo Fisher). Cycles comprised 30 s at 95°C and 60 s at 60°C and standard melting process at the end of 40 cycles. PCR was performed on the five pooled samples in quadruplicates and the levels of expression of three major genes coding for enamel matrix proteins (EMPs) were assessed using the following primers:

Amelx (forward primer F: AAGCATCCCTGAGCTTCAGA, reverse primer R: ACTGGCATCATTGGTTGCTG, amplicon size 371 bp),

Enamelin (F: TCCTTGTTTTCCTGGGTCTG, R: ATCCATTGG GTACTGGTGGA, 246 bp)

Odam (F: TTGACAGCTTTGTAGGCACA, R: GACCTTCTG TTCTGGAGCAA, 197 bp).

Expression levels of the EMP genes were compared with reference gene β-actin (F: GGGAAATCGTGCGTGACATC, R: GCGGCAGTGGCCATCTC, 76 bp).

2.6 Data presentation and statistical analyses

Enamel mineral density was expressed as mean values (sample numbers for each age group are indicated in Figure 2A). Distances and relationships between anatomical landmarks were calculated using Fiji package (ImageJ). Gene expression levels (mean ± SD) were obtained from four independent samples for each segment of amelogenesis. Statistical analyses were carried out using ANOVA with post-hoc testing for comparisons of the onset of amelogenesis and density profiles between different age groups (GraphPad nine software: Version 9.4.1). OriginLab software (2017) and CorelDraw (2020) were used to generate graphs and figures.

3 Results

3.1 Identifying stages of amelogenesis in 12-week-old mice using a combination of skeletal landmarks (positions of molar teeth) and the histological appearance of ameloblasts

We chose 12-wo male mice for our initial determination of skeletal landmarks of different stages of amelogenesis, since at this age mice approach skeletal maturity (Farooq et al., 2017; Wei et al., 2017). Identification of secretory, transition and maturation-stage ameloblasts in 12-wo mice in histological sections was based on the morphological

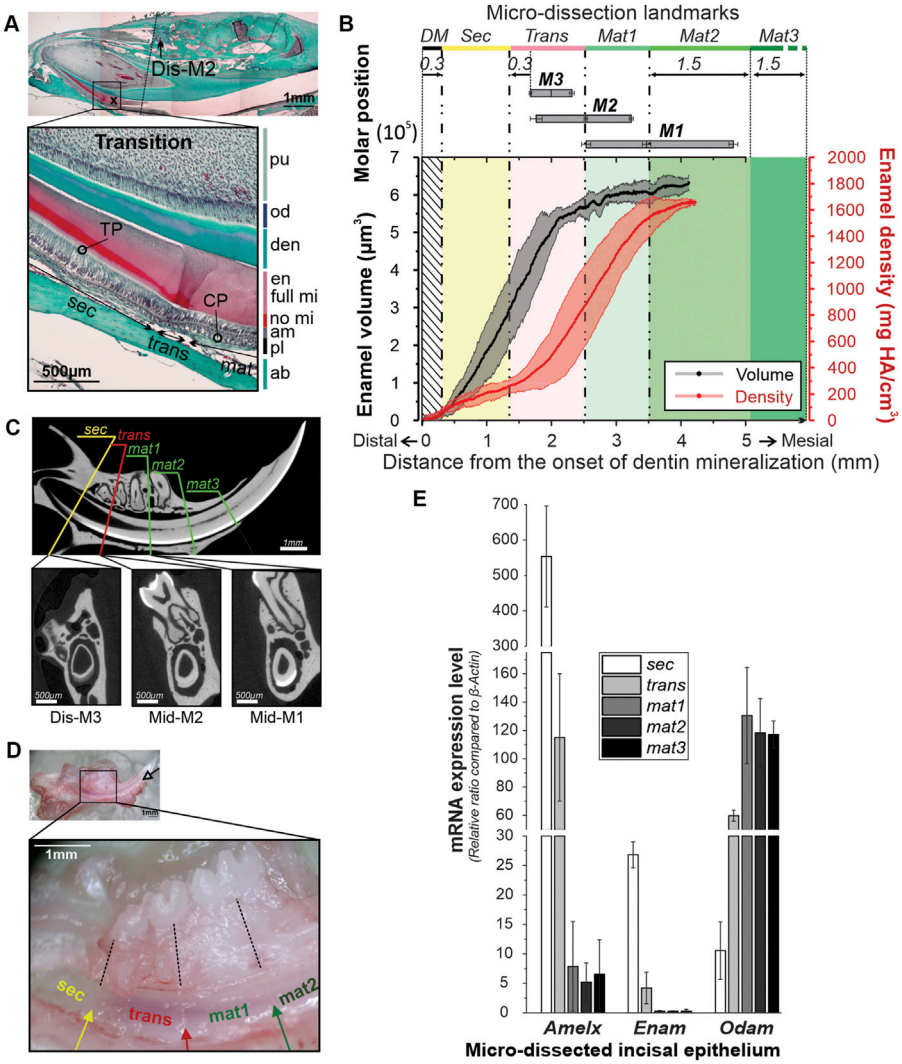

FIGURE 1
Identification of skeletal landmarks of the amelogenesis in mandibular incisors in 12-week-old mice. **(A)** Trichrome Masson staining of the mandible of a 12-wo mouse showing the correlation between transition stage ameloblasts and molar positions. ab, alveolar bone; am, ameloblasts; CP, capillaries; den, dentin; en, enamel; full mi, fully mineralized; no mi, partially mineralized; od, odontoblasts; TP, Tomes' processes; sec, secretory ameloblasts; trans, transition ameloblasts, mat, maturation ameloblasts; **(B)** average enamel volume (EV) profile (black line) and the mineral density (MD) profile (red line) from the apex toward the incisal tip. The grey and pink bands surrounding the EV and MD profiles represent ± SDs. Positions of M1, M2 and M3 represented by bars with the means and SDs of the distal, mid- and mesial planes. For definitions of Sec, Trans and Mat1-3 strips see the text. **(C)** MicroCT analysis of the skeletal landmarks. Top image shows a midsagittal section through an incisor with five lines identifying five dissection planes in respect to the positions of molar teeth. The bottom microCT transverse sections correspond to sec/trans, trans/mat1 and mat2/mat3 dissection planes. **(D)** Mandible of a male 12-wo mouse at low, X2.5, (top) and higher, ×5, magnification, showing markings on the lingual face of the incisor. Markings separating sec, trans, mat1, and mat2 segments were made in the planes intersecting distal plane of M3, mid-M2, and mid-M1, and normal to the incisor surface. Enamel organ was separated into strips based on the markings and collected for gene expression analysis. **(E)** Bar graph showing mean expression levels of *Amelx, Enam*, and *Odam*, in the five micro-dissected enamel organ strip samples. The bars are sequentially shaded on a greyscale from white -Sec, to black–Mat3. Error bars represent SDs.

characteristics of each stage, as outlined here. Specifically, secretory stage is the most proximal to the cervical loop of the incisor. Secretory ameloblasts are tall columnar cells and feature a specialized secretory apparatus–Tomes' process (TP) at the distal pole facing enamel (Figure 1A). During the secretory stage, the enamel thickness increases, while it remains constant during the maturation stage. Maturation stage ameloblasts are shorter and lack TPs. The proximal poles of secretory ameloblasts interface with stratum intermedium (SI), a thin layer of flattened or cuboidal cells, which in maturation develops into a thick papillary cell layer containing a dense capillary network (CP) (Figure 1A) (Garant and Gillespie, 1969). The organic content of secretory enamel is high and it becomes significantly lower at the maturation stage, leading to weaker histological staining (Figure 1A). The transition stage is the intermediate stage between secretion and maturation. Transitory ameloblasts are shorter than secretory ameloblasts and, although they lose their Tomes' processes, they still secrete the outer enamel layer. The transition stage length is roughly 70 μm consisting of 22.6 ± 2.8 cells (Bui et al., 2022) (Figure 1A).

Micro-CT analysis was conducted on five hemimandibles from 12-wo male mice. Using the micro-CT data, we calculated changes in enamel volume (EV) and mineral density (MD) during amelogenesis (Figure 1B; Supplementary Figure S1). The incisal EV increased sharply from the cervical loop toward the mesial root plane of the third molar (M3) for the

10.3389/fphys.2023.1144712

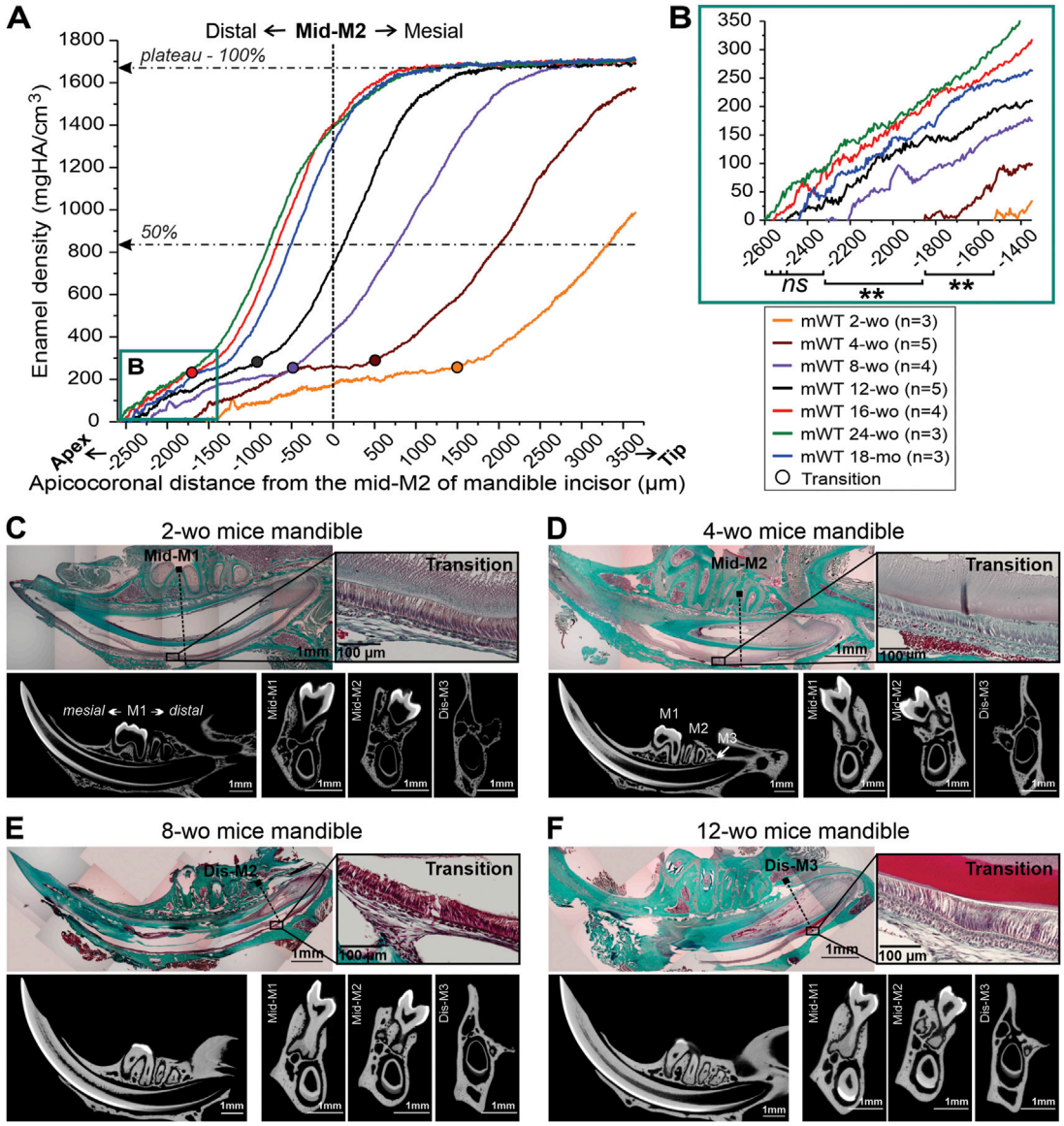

FIGURE 2
Distal movement of the transition stage and the onset of enamel mineralization in mandibular incisors of male mice of differenct ages. **(A)** Mean enamel MD profiles in incisors from mice of different ages, aligned with mid-M2 at point 0. The dotted lines intersect 50% and 100% maximum mineral density. **(B)** A close-up of the onset of incisal enamel mineralization in mice of different ages, selected in box B in Figure 2A; **: *p*-value <0.01, ns, not significant. **(C–F)** Trichrome Masson stained sections of hemimandibles, showing the relationships between transition stage ameloblasts, identified based on the morphology and molar positions in mice of different ages and the corresponding micro-CT images in midsagittal and three transverse planes intersecting the molar landmarks. **(C)** 2-week-old (2-wo), **(D)** 4-week-old (4-wo), **(E)** 8-week-old (8-wo) and **(F)** 12-week-old (12-wo); M1, M2, M3: first, second and third molar, mes-, mid-, dis-; mesial, middle, distal; wo, week-old; mo, month-old.

first 2 mm, before leveling off (Figure 1B; Supplementary Figure S1A). The mineral density in all samples followed a sigmoidal pattern, with the initial apical segment of low MD, corresponding to the phase of a steep increase in EV, followed by a segment with a high densification rate, starting at ~2 mm from the cervical loop and with a plateau at ~1,700 mg HA/cm^3 at roughly 3.5–4 mm from the cervical loop (Figure 1B; Supplementary Figure S1B). No differences were observed in EV and MD profiles between animals on a hard diet (mWT-4H and mWT-5H, see Supplementary Figure S1) and the rest of specimens, fed a mixed diet of hard pellets and gel food (mWT-H/G). Further micro-CT analysis revealed that positions of the molar teeth are highly consistent among specimens. Specifically, the distance from the onset of dentin mineralization to the distal plane of M3 is 1,646 μm, SD = ± 19 μm, to mid-M2 2,498 μm, SD = ± 24 μm and to mid-M1 3,434 μm, SD = ± 64 μm, (Figures 1B, C).

Based on our histological findings and micro-CT analysis, we have used molar teeth as landmarks to separate enamel epithelium into five segments, corresponding to different stages of amelogenesis (Figures 1A–C). The first (*sec*) segment is characterized by a steep increase in EV and low MD (Figure 1B). During secretory stage amelogenesis, the full thickness of enamel is deposited, but only a small fraction of mineral is present at this stage, which is why this segment was assigned to the secretory stage of amelogenesis (*sec*). The secretory nature of ameloblasts in this segment was also confirmed with histology (Figure 1A). This *sec* segment containing pure secretory ameloblasts was selected for strip dissection starting at

TABLE 1 Distances from the onset of dentin mineralization (Apex) to important milestones of amelogenesis in mandibular incisors of mice of different ages, outlined in Figure 3C. The last row represents maximum rates of enamel densification in mandibular incisors of mice of different ages, plotted in Figure 3D.

Distance (μm)	Age						
	2-wo	4-wo	8-wo	12-wo	16-wo	24-wo	18-month
Apex to mid-M2	1,722 ± 100[a]	2,056 ± 97	2,450 ± 190	2,494 ± 122	2,588 ± 164	2,676 ± 208	2,442 ± 305
Apex to transition	3,234 ± 97	2,486 ± 193	1,944 ± 296	1,476 ± 293	0950 ± 251	0916 ± 78	1,042 ± 231
Apex to 50% mineralization	4,918 ± 019	4,066 ± 114	3,281 ± 289	2,492 ± 329	1,965 ± 329	1,982 ± 446	2,046 ± 254
Apex to 100% mineralization	6,816 ± 252	7,135 ± 083	5,011 ± 328	4,544 ± 270	3,647 ± 737	4,558 ± 930	3,648 ± 537
Maximum rate of densification (mg HA/cm^3 per mm)	453 ± 68	550 ± 46	653 ± 80	811 ± 92	1,023 ± 132	1,010 ± 212	981 ± 122

[a]Standard deviation.

0.3 mm from the onset of dentin mineralization (DM) and ending 0.3 mm distal of the distal plane of M3 (Figures 1A–C). Using histological sections, we were able to determine the onset of the transition zone at ~0.17 mm distal to M3 (or ~1 mm distal to Mid-M2) (Figure 1D; Table 1) and is ~0.07 mm long. To avoid possible contamination with transition stage ameloblast, the last 0.13 mm of secretory stage cell layer were collected in the next strip. This strip, called *trans*, extended from 0.3 mm distal to M3 to mid-M2 and included the late secretory, whole transition and very early maturation stages (Figures 1A–C). At the distal boundary of this zone, the densification rate is low and similar to zone 1 (*sec*), containing early and mid-secretory ameloblasts. However, roughly 2 mm from the onset of DM, the densification rapidly intensifies to its highest rate of ~810 ± 92 mg HA/cm^3 per mm (Figure 1B). The increase in the rate of densification corresponds to the plateauing of the enamel volume (Figure 1B). This zone exhibits a large variation among samples in both EV and MD (Figure 1B; Supplementary Figure S1), which is likely due to the fact that the exact position of transition zone varies between the specimens (Table 1). The next strip contained the early maturation stage (*mat1*) and extended from mid-M2 to mid-M1 (Figures 1A–C). The rapid rate of densification is similar to second half of *trans*. At this stage, all samples have reached full enamel thickness and the densification rate is high. The mid-maturation segment (*mat2*) extended 1.5 mm mesial to mid-M1. Cells in this fraction are characterized by a strong yellowish-brownish hue, due to the intense iron transport during this stage (Reith, 1961; Wen and Paine, 2013). The late maturation/protective ameloblast layer (*mat3*) was collected from the end of *mat2* to the point of eruption. The cells in this layer are transparent, suggesting that iron transport is associated with *mat2* only. In summary, the landmarks associated with different stages of amelogenesis, based on the positions of molar teeth, can be easily determined (Figure 1D). Importantly, these landmarks allow for the microdissection of the incisal enamel organ into five strips of similar length (~1.5 mm), which provided sufficient amounts of material for gene and protein expression studies, when strips from five to six mice were pooled together.

3.2 Analysis of gene expression levels of micro-dissected incisal epithelium from 12-wo male mice

Figure 1D shows a 12-wo mouse mandible during the micro-dissection process. To guide this process, markings were placed at relatively equal intervals of ~1.5 mm along the ameloblast layer (Figure 1D, inset). The strips of the same kind from 12 mandibular incisors of six individual mice were pooled together to obtain at least 20 ng/μL total RNA per stage. *Mat2* and *mat3* equally contained the least RNA quantity, about 2.1 and 1.6 times less, respectively, compared to *sec* and *trans* fractions (data not shown).

To assess the accuracy of our landmarking, we have conducted analyses of EMP gene expression in different segments of the incisal enamel organ, collected as described above. Ameloblasts express different sets of genes, based on the stage of amelogenesis (Lacruz et al., 2017), which can be used as markers of specific stages of amelogenesis. For our studies we have chosen two secretory stage genes–*Enam* and *Amelx*, and one maturation stage gene - *Odam*. Expression of the three EMP coding genes was compared to the expression of reference gene *β-actin* and the expression data was normalized by calculating ratio of the gene of interest to *β-actin* and presented as the mean ratio ± SD (Figure 1E). The *Amelx* expression level was highest in *sec* samples, 553.6 ± 143 times higher than *β*-actin expression and was 85-times higher than that in the maturation segments (*mat1-3*) (6.5 ± 5.5, *Amelx*/*β-actin* ratio) and almost 5 times higher than in the *trans* segment (Figure 1E; Supplementary Table S2). *Enam* expression levels were about 5% of the *Amelx* expression level, which is consistent with the fact that Amelx constitutes 90% of secretory enamel matrix. Similarly to *Amelx*, *Enam* levels were 100-times higher in the *sec* strip than in the *mat* segments (26.8 ± 2.2 vs. 0.27 ± 0.17 *Enam*/*β-actin* ratio) and 6.4-times higher than in the *trans* strip (Figure 1E; Supplementary Table S2). In contrast, *Odam* expression was higher in the maturation stage, with no significant differential expression between the three portions of *mat1*, *mat2*, and *mat3*, with an average level of 121.8 ± 22.5 *Odam*/*β-actin* ratio. The *sec* segment expressed *Odam* at 11.5 times lower level than *mat1-3*, with a 10.5 ± 4.8 *Odam*/*β-actin* ratio (Figure 1E; Supplementary Table S2). Likewise, *Odam* levels in the *trans* segment that contains late secretory, transition and very early maturation ameloblasts was 5.6 times higher than in the *sec* strip. Overall, these results indicate that our landmarking method allows one to obtain with high accuracy segments of the incisal enamel organ, corresponding to different stages of amelogenesis.

3.3 Distal movement of incisal apices and transition stage of amelogenesis in mandibles in spatial relationship to molars over the lifespan of mice

It is a well-known fact that during craniofacial growth the apices of murine incisors undergo distal movement, however, the exact

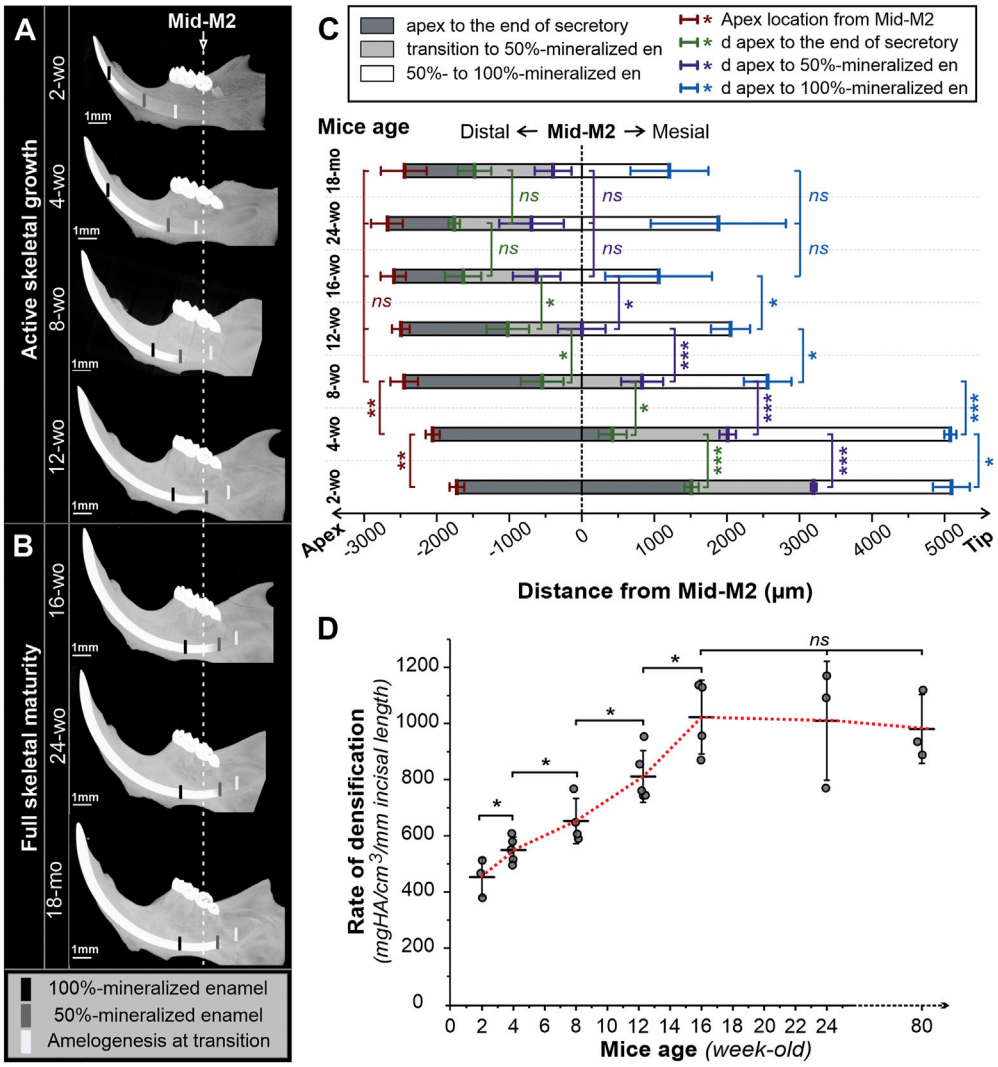

FIGURE 3
3D reconstructions of micro-CT scanned mandibles of male mice of different ages. Lingual view images of hemimandibles of mice of different ages during active skeletal growth **(A)** and at skeletal maturity **(B)**. Black, grey, and white marks indicate, respectively, the positions of fully mineralized (100%), half-mineralized (50%) enamel, and transition secretory-transition boundaries aligned to the second molar (Mid-M2) plane. **(C)** Sequences of amelogenesis in mandibular incisors in mice of different ages aligned in the mid-M2 plane. Mean distances (in μm) from the apex to the position of secretory-transition boundary (STB) (dark grey), partially mineralized enamel matrix (50% mineral density) (grey), and fully mineralized enamel (100%) (white) were presented; the positions were aligned with mid-M2. Error bars represent ± SD values; red -apex positions, green-STB, purple—50% mineralized, blue—100% mineralized **(D)** Maximum rate of enamel densification, expressed as mean ± SD (mineral density per mm incisal length). wo, week-old; mo, month-old; *, **, and *** reflect significance levels with *p*-values <0.05, 0.01, and 0.001, respectively, ns, not significantly different.

dynamics of this process are not well understood. We have conducted a systematic study of this process using a combination of histology and micro-CT. Seven groups of WT mice of different ages, from 2-wo to 18-mo, were studied. Enamel density and ameloblast morphology in mandibular incisors were analyzed to determine spatial relationships between different stages of amelogenesis with respect to molar teeth (Figure 2). Averages of mineral density of at least three animals per each age group, were aligned using the mid-M2 plane as a reference point (Figure 2A). We found this to be a valuable reference point that allows for the alignment of density profiles of different age groups, regardless of differences in incisor length and curvature. Based on the analyses of histological sections, as described in the preceding section, we have identified the onset of the transition stage for all age groups (Figures 2C–F) and marked them on the plot in Figure 2A. These studies revealed a clear trend of distal movement of the transition zone with age. In younger animals, the transition zone was located in the anterior region: 1,512 ± 97 μm mesial to mid-M2 in 2-wo mice and 424 ± 193 μm mesial to mid-M2 in 4-wo mice (Figures 2A, C, D, 3A–C; Table 1). In 8-wo mice, the position of transition was 546 ± 295 μm distal to mid-M2 (Figures 2A, E; Table 1). The position of the transition zone in 12-wo mice is located 1,020 ± 293 μm distal to mid-M2 (Figures 2A, F; Table 1) and in 16-wo and older animals it is located at 1,626 ± 218 μm distal to mid-M2 (Figure 2A; Table 1). These data indicate that the transition zone moves more than 3 mm distally from the time of eruption of first and second molars and incisors in 2-wo mice to mice at full skeletal maturity.

Moreover, not only does the transition zone move apically with age, but the apex of the incisor and the onset of enamel formation also

recede distally from the molars (Figures 2B, 3C; Table 1). The onset of enamel mineralization in 2-wo is 1,722 ± 100 μm away from the mid-M2, while it moves significantly ($p < 0.01$) further away to 2,056 ± 97 μm in 4-wo and 2,450 ± 190 μm in 8-wo mice, respectively (Figures 2B, 3A–C; Table 1). As shown, for mice older than 8-wo, this distal movement of the apices is still occurring, but these changes are not significant. However, in older mice, higher variation within each group was observed: *e.g.*, 2,588 ± 164 μm in 16-wo group ($n = 4$) versus 2,676 ± 208 and 2,442 ± 305 μm in the 24-wo ($n = 3$) and 18-mo ($n = 3$) groups, respectively.

3.4 Differences in the rate of mineralization in incisal enamel in mice of different age

In all age groups, densification of incisal enamel followed similar sigmoidal patterns, as was shown for 12-wo animals (Figure 1B; Supplementary Figure S1B), with slower densification rates in the apical portions, corresponding to the secretory stage of amelogenesis, followed by rapid densification in transition and early maturation stages, and reaching a plateau at late maturation stage (Figure 2A). Of note, although the overall shapes of the curves were similar, there were significant differences in terms of the lengths of these different stages. More specifically, the length of the secretory stage, defined as a distance from the onset of enamel mineralization to transition zone was longer in younger mice than in the older animals (Figure 2A; Table 1).

To assess the differences in dynamics of amelogenesis in mice of different ages, we have studied densification of enamel in micro-CT 3-D reconstructions of the mouse mandibles. Figure 3A comprises micro-CT images of mandibles of actively growing mice two- to 12-wo, while Figure 3B presents mandibles of older skeletally mature mice, ages 16-wo to 18-mo. All mandibles are presented in the same orientation, at the same magnification, and are aligned relative to the mid-M2 transverse plane. Average positions ($n \geq 3$) of the transition stage of amelogenesis at half (50%) and maximum (100%) enamel density are marked in the images in Figures 3A, B. Distances from the apex to the transition zone at half- and maximum density positions with respect to the mid-M2 plane were measured and plotted in Figure 3C and shown in Table 1.

Visual comparison of the micro-CT images clearly shows the distal movement of the cervical loops with respect to mid-M2 and elongation of the incisors with age (Figures 3A, B), confirming the results discussed in the preceding paragraphs. In addition to a longer secretory phase, the rate of densification in younger animals is much slower than in older animals (Figures 2A, 3A, B, D; Table 1). Hence, maturation stage ameloblasts that complete mineralization do so at a slower rate in young mice compared to that in older mice. This is readily visible when 2-wo and 4-wo mice are compared to 8-wo and older mice (Figure 3A). However, it was the 4-wo group and not the youngest 2-wo group that had the longest mineralization process (7,135 ± 83 μm and 4,066 ± 114 μm, respectively, from the apex to 100% and 50% MD) in the incisor (Figure 3C; Table 1). This might be explained by the fact that, as in 2-wo mice, the maximum enamel MD is only 1,574 ± 35 mgHA/cm^3 (data not shown), which is ~94% of maximum MD observed in mice of 4-wo and older mice, when the enamel layer reached a plateau of densification at a greater density of ~1,670 mgHA/cm^3 (Figure 2A). The maximum densification rate, represented by the linear segment of the densification curve, associated with early maturation stage (Figures 1B, 2A), increased significantly with age and reached maximum in 16-wo mice, resulting in significant shortening of incisor mineralization (Figures 2A, 3; Table 1). From this age on, the dynamics of incisal growth stabilized, as indicated by the lack of differences in positions of all three marks, and the maximum rate of densification between 16-wo, 24-wo, and 18-mo groups (Figures 3B–D; Table 1). Importantly, mice reach skeletal maturity at 14 weeks of age, while the changes in the craniofacial region occur in the first 4 weeks after birth (Wei et al., 2017). Our observations suggest that the changes in the positions of the incisors in the mandibles and the dynamics of amelogenesis correlate with postnatal craniofacial growth. Of note, standard deviations among individuals within the same group were smaller in younger mice, *e.g.*, 100% mineralization occurred at 7,135 ± 83 μm from the apex in 4-wo, while this level was reached at 5,011 ± 328 μm and 3,647 ± 737 μm in 8-wo and 16-wo, respectively (Figure 3C; Table 1). These findings suggest that the noted landmarks are more reliable in younger mice.

As a consequence of the distal movement of the apices and the transition zone, as well as changes in the rate of mineralization, when micro-dissecting mandibular incisors in different age groups, different landmarks need to be used. Specifically, in 2-wo mice, the secretory-transition boundary (STB) is located in the plane transecting the mid-M1 plane (Figure 2C). The STB is in the plane of mesial M2 root in 4-wo animals (Figure 2D). In 8-wo mice, STB moves further distally, and it starts in the distal plane of M2 (Figure 2E). As forementioned, STB micro-dissection landmarks shifted apically by ~0.3 mm from distal M3 in 12-wo. In 16-wo, the STB position varies between 0.44 and 0.97 mm distally to the distal M3 plane or 1,637 ± 251 μm from mid-M2, as shown in Figure 3C. The position of STB in older mice (24-w and 18-month) is similar to that in 16-wo mice (Figures 2A, 3B, C; Table 1), suggesting that the mice reach full skeletal maturity by 16 weeks.

4 Discussion

It is common knowledge that positions of murine mandibular incisors and their spatial relationships with molar teeth change with age. As reported here, we have found that throughout the active skeletal growth phase (weeks 2–12) the apices of the incisors and the onset of enamel mineralization move distally in relation to molar teeth. The position of the transition stage also moves distally. We also found in 16-wo and older mice that incisor length and their positions relative to molar landmarks remain unchanged, indicating that the magnitude of changes in incisors correlates with dynamic skeletal growth. The present study emphasizes the need to address the importance of age in experimental design, when studying amelogenesis and the etiology of enamel defects using mouse incisor models and when comparing results from different laboratories. The magnitude of changes in mandibular incisors is greatest at the younger ages, when overall skeletal growth rate is the highest (Farooq et al., 2017; Wei et al., 2017) in comparison to older animals. These changes include: 1) Changes in length and position of developmental stages of amelogenesis with age, 2) distal drift of incisal apices during the active skeletal growth phase, 3) the amelogenesis process shortens with age, which is quite an interesting observation, since incisors in 2-wo mice are roughly 1 mm shorter than in skeletally mature mice, and 4) changes in rates of enamel volume acquisition

and densification. Based on these facts, we believe that 12-wo mice could be considered an optimal model for fresh micro-dissection and ameloblast collection when the goal is to compare different stages of amelogenesis. The 12-wo incisor provides an ameloblast layer of sufficient length, which lends itself to easier handling and manageable micro-dissection. Moreover, at this age, the landmarks corresponding to different stages of amelogenesis are easily identifiable, which allows for better reproducibility of dissections (Figures 1, 2A, F).

To assess the accuracy and reliability of our landmarking methodology, we conducted expression analyses of genes encoding key EMPs, with distinct expression profiles in five micro-dissected segments of incisal enamel organs of 12-wo mice. The observed expression profiles are consistent with our current understanding of EMP expression in developing mouse enamel. Amelogenin (*Amelx*) the major protein in enamel matrix (>90%), is highly expressed in presecretory and secretory stages of amelogenesis (Bleicher et al., 1999; Lacruz et al., 2017). Similarly, enamelin (*Enam*) is highly expressed in the secretory stage (Gallon et al., 2013), while odontogenic ameloblast-associated protein (*Odam*), also known as Apin, is expressed by late secretory and maturation stage ameloblasts (Park et al., 2007; Moffatt et al., 2008). The expression profiles obtained in the current study are consistent with these literature reports, which demonstrate the practicality and high fidelity of our landmarking methodology. Several landmarks to assist in identification of the stages of amelogenesis in continuously growing murine incisors have been suggested for mice (Molla et al., 2010; Houari et al., 2018) and for rats (Smith and Nanci, 1989; Smith et al., 1996; Moffatt et al., 2008; Lacruz et al., 2012a). However, this is the first time that a micro-dissection approach to study mouse amelogenesis in mice of different aged was designed to achieve 1) high accuracy and confirmation by multiple approaches (i.e., micro-CT, cell morphology and gene expression profiling) and 2) maximization of collected sample yield, as the whole ameloblast cell layer is collected, which can help reduce sample size, while making multiple types of analyses possible. This approach provides means to maximize information, such as the assessment of the behavior of ameloblasts during the intermediate stage between secretory and maturation stages, which is excluded in the previously reported methods (Lacruz et al., 2010; Jedeon et al., 2014). It also allows one to compare the behavior of maturation stage ameloblasts in different parts of forming enamel, for example, between the transition stage and the very beginning of maturation, to *mat3*, which consists of protection stage ameloblasts, and to correlate these stages of histodifferentiation with profiles of EV and MD, obtained using a high-resolution micro-CT. It is important to emphasize that although this study provides an accurate guide to the positions of different stages of amelogenesis in mouse incisors with respect to molar teeth, future more in-depth studies, which similarly use a combination of histology, expression analysis and micro-CT, may be needed for mice of ages other than 12-wo if more precise information is needed for a given age group. It should also be noted that this study has been conducted on WT mice and that the key mechanistic dynamics of amelogenesis and the effects of aging illustrated here are likely to be different from those seen in genetically modified mouse models that result in altered enamel formation.

Data availability statement

The original contributions presented in the study are included in the article/Supplementary Material, further inquiries can be directed to the corresponding author.

Ethics statement

The animal study was reviewed and approved by University of Pittsburgh IACUC.

Author contributions

AB conceived the study, planned and conducted the experiments, wrote the first draft of the manuscript, prepared figures and tables, participated in revisions of the manuscript. LL and KV provided expertise and technical support for microCT studies. BV, LB, and CG participated in dissections and sample collection, participated in discussions of the data and edited the manuscript. HM participated in the planning of the experiments, discussions of the data, participated in the revisions of the manuscript and acquired financial support for the studies. EB participated in design and planning of the experiments, data analysis discussions of the data, participated in the revisions of the manuscript and acquired financial support for the studies.

Funding

This study was supported by grants R01 DE029211 and R01DE029211-S1 (to HM and EB) and by the institutional training grant R90 DE032625 R90 DE032625 from the National Institutes of Health/National Institute of Dental and Craniofacial Research.

Conflict of interest

The authors declare that the research was conducted in the absence of any commercial or financial relationships that could be construed as a potential conflict of interest.

Publisher's note

Supplementary material

The Supplementary Material for this article can be found online at: https://www.frontiersin.org/articles/10.3389/fphys.2023.1144712/full#supplementary-material

References

Beniash, E., Metzler, R. A., Lam, R. S. K., and Gilbert, P. (2009). Transient amorphous calcium phosphate in forming enamel. *J. Struct. Biol.* 166, 133–143. doi:10.1016/j.jsb.2009.02.001

Bleicher, F., Couble, M. L., Farges, J. C., Couble, P., and Magloire, H. (1999). Sequential expression of matrix protein genes in developing rat teeth. *Matrix Biol.* 18, 133–143. doi:10.1016/s0945-053x(99)00007-4

Brookes, S. J., Barron, M. J., Smith, C. E., Poulter, J. A., Mighell, A. J., Inglehearn, C. F., et al. (2017). Amelogenesis imperfecta caused by N-terminal enamelin point mutations in mice and men is driven by endoplasmic reticulum stress. *Hum. Mol. Genet.* 26, 1863–1876. doi:10.1093/hmg/ddx090

Bui, A. T., Houari, S., Loiodice, S., Bazin, D., Sadoine, J., Roubier, N., et al. (2022). Use of Dental Defects Associated with Low-Dose di(2-Ethylhexyl)Phthalate as an Early Marker of Exposure to Environmental Toxicants. *Environ. Health Perspect.* 130, 67003. doi:10.1289/EHP10208

Caterina, J. J., Skobe, Z., Shi, J., Ding, Y., Simmer, J. P., Birkedal-Hansen, H., et al. (2002). Enamelysin (matrix metalloproteinase 20)-deficient mice display an amelogenesis imperfecta phenotype. *J. Biol. Chem.* 277, 49598–49604. doi:10.1074/jbc.M209100200

Farooq, S., Leussink, S., Sparrow, L. M., Marchini, M., Britz, H. M., Manske, S. L., et al. (2017). Cortical and trabecular morphology is altered in the limb bones of mice artificially selected for faster skeletal growth. *Sci. Rep.* 7, 10527. doi:10.1038/s41598-017-10317-x

Gallon, V., Chen, L., Yang, X., and Moradian-Oldak, J. (2013). Localization and quantitative co-localization of enamelin with amelogenin. *J. Struct. Biol.* 183, 239–249. doi:10.1016/j.jsb.2013.03.014

Garant, P. R., and Gillespie, R. (1969). The presence of fenestrated capillaries in the papillary layer of the enamel organ. *Anat. Rec.* 163, 71–79. doi:10.1002/ar.1091630109

Gibson, C. W., Yuan, Z. A., Hall, B., Longenecker, G., Chen, E., Thyagarajan, T., et al. (2001). Amelogenin-deficient mice display an amelogenesis imperfecta phenotype. *J. Biol. Chem.* 276, 31871–31875. doi:10.1074/jbc.M104624200

Hiller, C. R., Robinson, C., and Weatherell, J. A. (1975). Variations in the composition of developing rat incisor enamel. *Calcif. tissue Res.* 18, 1–12. doi:10.1007/BF02546222

Houari, S., Babajko, S., Loiodice, S., Berdal, A., and Jedeon, K. (2018). Micro-dissection of enamel organ from mandibular incisor of rats exposed to environmental toxicants. *J. Vis. Exp.* 133, 1–9. 57081. doi:10.3791/57081

Hu, J. C. C., Chun, Y. H. P., Al Hazzazzi, T., and Simmer, J. P. (2007). Enamel Formation and amelogenesis imperfecta. *Cells Tissues Organs* 186, 78–85. doi:10.1159/000102683

Jalali, R., Guy, F., Ghazanfari, S., Lyaruu, D., Van Ruijven, L., Denbesten, P., et al. (2017). Mineralization-defects are comparable in fluorotic impacted human teeth and fluorotic mouse incisors. *Arch. Oral Biol.* 83, 214–221. doi:10.1016/j.archoralbio.2017.07.018

Jedeon, K., Loiodice, S., Marciano, C., Vinel, A., Canivenc Lavier, M. C., Berdal, A., et al. (2014). Estrogen and bisphenol A affect male rat enamel formation and promote ameloblast proliferation. *Endocrinology* 155, 3365–3375. doi:10.1210/en.2013-2161

Krivanek, J., Soldatov, R. A., Kastriti, M. E., Chontorotzea, T., Herdina, A. N., Petersen, J., et al. (2020). Dental cell type atlas reveals stem and differentiated cell types in mouse and human teeth. *Nat. Commun.* 11, 4816. doi:10.1038/s41467-020-18512-7

Lacruz, R. S., Hilvo, M., Kurtz, I., and Paine, M. L. (2010). A survey of carbonic anhydrase mRNA expression in enamel cells. *Biochem. Biophys. Res. Commun.* 393, 883–887. doi:10.1016/j.bbrc.2010.02.116

Lacruz, R. S., Smith, C. E., Bringas, P., Jr., Chen, Y. B., Smith, S. M., Snead, M. L., et al. (2012a). Identification of novel candidate genes involved in mineralization of dental enamel by genome-wide transcript profiling. *J. Cell. Physiol.* 227, 2264–2275. doi:10.1002/jcp.22965

Lacruz, R. S., Smith, C. E., Moffatt, P., Chang, E. H., Bromage, T. G., Bringas, P., Jr., et al. (2012b). Requirements for ion and solute transport, and pH regulation during enamel maturation. *J. Cell. Physiology* 227, 1776–1785. doi:10.1002/jcp.22911

Lacruz, R. S., Habelitz, S., Wright, J. T., and Paine, M. L. (2017). Dental enamel formation and implications for oral health and disease. *Physiol. Rev.* 97, 939–993. doi:10.1152/physrev.00030.2016

Liang, T., Wang, S.-K., Smith, C., Zhang, H., Hu, Y., Seymen, F., et al. (2022). Enamel defects in Acp4R110C/R110C mice and human ACP4 mutations. *Sci. Rep.* 12, 16477. doi:10.1038/s41598-022-20684-9

Moffatt, P., Smith, C. E., St-Arnaud, R., and Nanci, A. (2008). Characterization of Apin, a secreted protein highly expressed in tooth-associated epithelia. *J. Cell. Biochem.* 103, 941–956. doi:10.1002/jcb.21465

Molla, M., Descroix, V., Aïoub, M., Simon, S., Castañeda, B., Hotton, D., et al. (2010). Enamel protein regulation and dental and periodontal physiopathology in MSX2 mutant mice. *Am. J. Pathol.* 177, 2516–2526. doi:10.2353/ajpath.2010.091224

Park, J. C., Park, J. T., Son, H. H., Kim, H. J., Jeong, M. J., Lee, C. S., et al. (2007). The amyloid protein APin is highly expressed during enamel mineralization and maturation in rat incisors. *Eur. J. Oral Sci.* 115, 153–160. doi:10.1111/j.1600-0722.2007.00435.x

Reith, E. J. (1961). The ultrastructure of ameloblasts during matrix formation and the maturation of enamel. *J. Biophys. Biochem. Cytol.* 9, 825–839. doi:10.1083/jcb.9.4.825

Renvoisé, E., and Michon, F. (2014). An Evo-Devo perspective on ever-growing teeth in mammals and dental stem cell maintenance. *Front. Physiology* 5, 324. doi:10.3389/fphys.2014.00324

Shin, N.-Y., Yamazaki, H., Beniash, E., Yang, X., Margolis, S. S., Pugach, M. K., et al. (2020). Amelogenin phosphorylation regulates tooth enamel formation by stabilizing a transient amorphous mineral precursor. *J. Biol. Chem.* 295, 1943–1959. doi:10.1074/jbc.RA119.010506

Smith, C. E., Issid, M., Margolis, H. C., and Moreno, E. C. (1996). Developmental changes in the PH of enamel fluid and its effects on matrix-resident proteinases. *Adv. Dent. Res.* 10, 159–169. doi:10.1177/08959374960100020701

Smith, C. E., Chong, D. L., Bartlett, J. D., and Margolis, H. C. (2005). Mineral acquisition rates in developing enamel on maxillary and mandibular incisors of rats and mice: Implications to extracellular acid loading as apatite crystals mature. *J. Bone Mineral Res.* 20, 240–249. doi:10.1359/JBMR.041002

Smith, C. E., Hu, Y., Richardson, A. S., Bartlett, J. D., Hu, J. C. C., and Simmer, J. P. (2011). Relationships between protein and mineral during enamel development in normal and genetically altered mice. *Eur. J. Oral Sci.* 119, 125–135. doi:10.1111/j.1600-0722.2011.00871.x

Smith, C. E., and Nanci, A. (1989). A method for sampling the stages of amelogenesis on mandibular rat incisors using the molars as a reference for dissection. *Anatomical Rec.* 225, 257–266. doi:10.1002/ar.1092250312

Verdelis, K., Szabo-Rogers, H. L., Xu, Y., Chong, R., Kang, R., Cusack, B. J., et al. (2016). Accelerated enamel mineralization in Dspp mutant mice. *Matrix Biol.* 52-54, 246–259. doi:10.1016/j.matbio.2016.01.003

Wei, X., Thomas, N., Hatch, N. E., Hu, M., and Liu, F. (2017). Postnatal craniofacial skeletal development of female C57bl/6NCrl mice. *Front. Physiol.* 8, 697. doi:10.3389/fphys.2017.00697

Wen, X., and Paine, M. L. (2013). Iron deposition and ferritin heavy chain (Fth) localization in rodent teeth. *BMC Res. Notes* 6, 1. doi:10.1186/1756-0500-6-1

frontiers | Frontiers in Physiology

TYPE Original Research
PUBLISHED 16 February 2023
DOI 10.3389/fphys.2023.1099645

OPEN ACCESS

EDITED BY
Catherine Chaussain,
Université Paris Cité, France

REVIEWED BY
Elsa Garot,
Université de Bordeaux, France
Tian Liang,
University of Michigan, United States

*CORRESPONDENCE
Baptiste Depalle,
baptiste.depalle@outlook.com
Felicitas B. Bidlack,
fbidlack@forsyth.org

SPECIALTY SECTION
This article was submitted to Craniofacial Biology and Dental Research, a section of the journal Frontiers in Physiology

RECEIVED 16 November 2022
ACCEPTED 02 January 2023
PUBLISHED 16 February 2023

CITATION
Depalle B, Karaaslan H, Obtel N, Gil-Bona A, Teichmann M, Mascarin G, Pugach-Gordon M and Bidlack FB (2023), Rapid post-eruptive maturation of porcine enamel.
Front. Physiol. 14:1099645.
doi: 10.3389/fphys.2023.1099645

Rapid post-eruptive maturation of porcine enamel

Baptiste Depalle[1,2]*, Hakan Karaaslan[1,2], Nicolas Obtel[1,3], Ana Gil-Bona[1,2], Maren Teichmann[1,2], Gabrielle Mascarin[1], Megan Pugach-Gordon[1,2] and Felicitas B. Bidlack[1,2]*

[1]The Forsyth Institute, Cambridge, MA, United States, [2]Department of Developmental Biology, Harvard School of Dental Medicine, Boston, MA, United States, [3]École Normale Supérieure, Paris Sciences et Lettres Research University, Paris, France

The teeth of humans and pigs are similar in size, shape, and enamel thickness. While the formation of human primary incisor crowns takes about 8 months, domestic pigs form their teeth within a much shorter time. Piglets are born after 115 days of gestation with some of their teeth erupted that must after weaning meet the mechanical demands of their omnivorous diet without failure. We asked whether this short mineralization time before tooth eruption is combined with a post-eruptive mineralization process, how fast this process occurs, and how much the enamel hardens after eruption. To address this question, we investigated the properties of porcine teeth at two, four, and sixteen weeks after birth (N = 3 animals per time point) through analyses of composition, microstructure, and microhardness. We collected data at three standardized horizontal planes across the tooth crown to determine the change of properties throughout the enamel thickness and in relation to soft tissue eruption. Our findings indicate that porcine teeth erupt hypomineralized compared to healthy human enamel and reach a hardness that is similar to healthy human enamel within less than 4 weeks.

KEYWORDS

enamel, maturation, porcine (pig) model, mineralization, tooth formation, posteruptive hardening

Introduction

Porcine teeth resemble human teeth in terms of size, morphology, and enamel thickness (Robinson et al., 1987; 1988b). One major difference however is that pig teeth develop four and a half times faster than human permanent teeth (Schour L and Massler M, 1941; Tonge and McCance, 1973; Birch and Dean, 2014). As a result, pig enamel is far softer and more porous than healthy human enamel at the time of tooth eruption (Kirkham et al., 1988). However, the stunning tooth formation speed in pigs raises two questions. First, how quickly can enamel be formed using a cellular mechanism? Second, how fast and efficient is the cell-free enamel hardening after eruption? While the evolution of mineral crystals prior to tooth eruption has been characterized in depth (Kallistova et al., 2017), little is known about the development of pig enamel once it reaches the oral cavity.

There is evidence that, at the time of tooth eruption, enamel is not fully mineralized and that its maturation and hardening continue in the oral cavity (Yonan et al., 1966; Fejerskov et al., 1984; Wöltgens et al., 1990; Palti et al., 2008). However, the speed of this natural process and how deep into the enamel layer the hardening occurs has not been described. The level of enamel mineralization of permanent porcine teeth is known to reach only 85% by weight (60% by volume) at the end of cell mediated maturation, just at the time of eruption and when the tooth reaches the oral cavity (Robinson et al., 1988b; Kirkham et al., 1988). This mineral content is significantly lower than healthy human enamel where mineral content is higher than 95% by

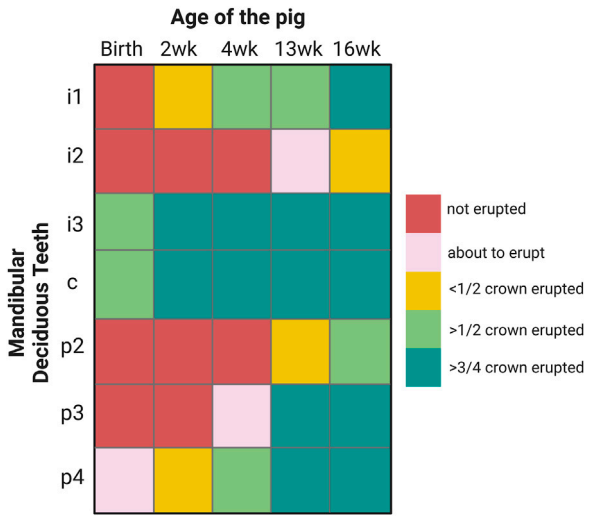

FIGURE 1
Eruption sequence of 2, 4, 13 and 16-week-old pigs that are used in this study. I: incisor, c: canine, p: premolar.

weight prior to eruption (Kirkham et al., 1988). In fact, porcine enamel is with its high protein content in erupted teeth similar to human hypomineralized enamel as described for idiopathic demarcated opacities with a reported 58.8% mineral by volume (Mahoney et al., 2004; Crombie et al., 2013; Elfrink et al., 2013).

Porcine enamel formation occurs so quickly in those teeth that are erupted at birth or shortly thereafter that the last formation stage of enamel maturation is not completed. Piglets are born with their mandibular canines and third incisors erupted. By two weeks after birth, less than half of the first lower incisor crown is erupted (Figure 1). In comparison, the first teeth to erupt in humans, incisors, also form "on the fast track" before birth (Mahoney, 2015). However, after at least 90 days prenatal and 30 days postnatal crown formation time, several months remain for enamel maturation before tooth eruption sometime after the baby's first 3 months after birth (Liversidge and Molleson, 2004; Mahoney, 2015).

The goal of this study is to advance our understanding of the speed and depth of porcine enamel hardening after tooth eruption. Our data and new insights can provide guidance for strategies of hardening hypomineralized human enamel and can inform efforts of regenerating teeth.

Materials and methods

All samples were harvested after sacrifice of Yorkshire pigs raised and weaned after 4 weeks at the animal facility of Tufts University Cummings School of Veterinary Medicine following approved IACUC regulations (protocol number G2019-72).

Choice of teeth

The selection of teeth used for this study is based on the timing and sequence of tooth eruption in pigs. The canine and third lower incisor are erupted at birth, known as needle teeth, but get clipped upon birth and were not included in this study. Here, we focused on mandibular teeth, in particular, on the first incisor which is by 2-week of age less than half erupted (Figure 1). We also used premolars. At 2 weeks of age, the fourth premolar is less than half erupted, at 4-week, the third premolar is emerging and at 13-week, less than half of the second premolar crown is erupted (Figure 1).

Sample harvesting and preparation

Pigs aged 2 weeks (n = 3), 4 weeks (n = 3) and 16 weeks (n = 2) were euthanized, mandibles dissected out and immediately transferred into dry ice for transport, then stored at −80°C until further processing (Table 1.). The first mandibular incisor was carefully extracted to minimize contamination. The erupted part of the teeth was cleaned with a toothbrush and PBS to remove pellicle and plaque. We used the second, third, and fourth premolars, and the first incisor from the lower left mandible of a 13-week-old pig for fluorescein application to the crown surface and measures of penetration as an approximation of porosity (Table. 1). Therefore, at the time of extraction, the time that a tooth spent in the oral cavity ranges from 5-week for the second premolar, 9-week for the third premolar and, to 11-week for the fourth premolar and first incisor.

Mineral density

After extraction, incisor teeth from 2, 4 and 16-week-old pigs were analyzed by microcomputed tomography microCT on a Scanco µCT40 scanner (Scanco Medical, Switzerland) with a 6 µm voxel resolution. The 3D reconstruction of the samples was reoriented to align the long axis of the tooth with the vertical axis. The enamel density varies significantly from cuspal to cervical margin and includes densities that are similar, or lower compared to dentin, resulting in an overlap in the histogram. Therefore, classic segmentation methods like intensity threshold are not applicable here. Thus, the enamel was segmented with Deep Learning in Dragonfly software (Dragonfly 4.2, The Objects). We used a UNet segmentation model with a categorical cross-entropy loss function and the Adadelta optimizer. The training was performed on a representative subset of images from the microCT tomograms and manually segmented. After segmentation, the average mineral density of

TABLE 1 Age and number of animals used for each experimental procedure.

Analysis\Age of pig	2 weeks	4 weeks	13 weeks	16 weeks
microCT, SEM Microhardness (HV)	n = 3 (1 tooth/animal)	n = 3 (1 tooth/animal)		n = 3 (1 tooth/animal)
Fluorescein penetration			n = 4 (4 teeth/animal)	

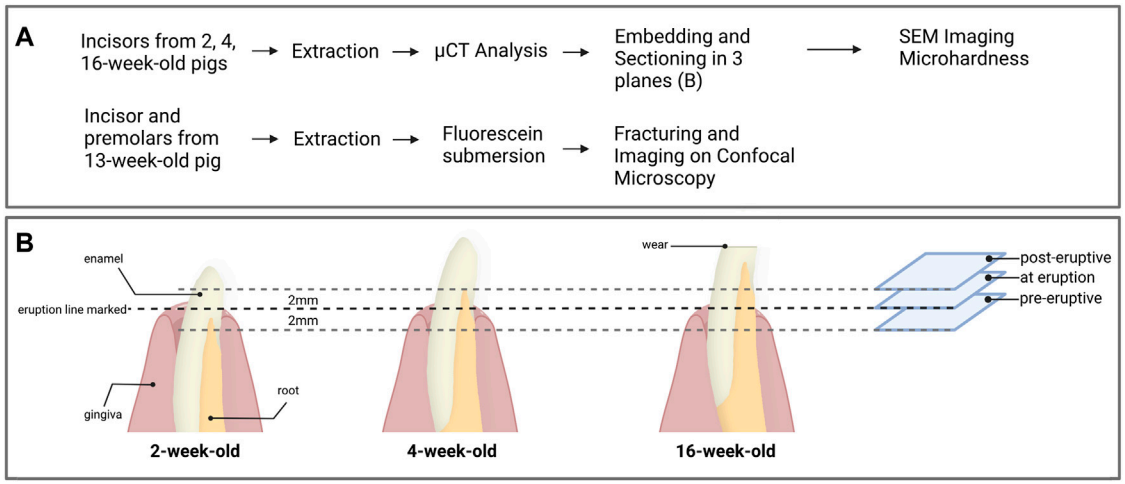

FIGURE 2
(A) Overview of the experimental workflow and **(B)** processing of the first incisors for each age groups. Prior to extraction, the eruption line was marked on the incisors from 2, 4 and 16-week-old pigs. After extraction and microCT analysis, the samples were embedded and three transverse sections were prepared 2 mm below the gingival emergence, at the level of gingival emergence, and 2 mm above the gingival eruption line. Each section was used for the acquisition of data from pre-eruptive, at eruption and post-eruptive enamel for a given tooth.

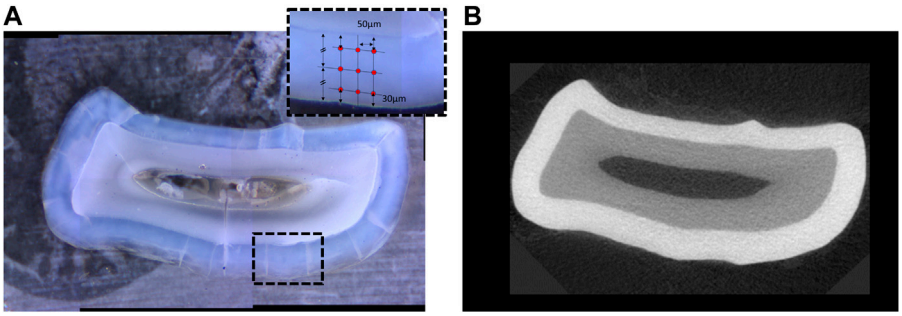

FIGURE 3
(A) Transverse section of a mandibular incisor at the level of gingival emergence, with inset in panel representing the location of the indents of the micro-indenter in one of the four quadrants of the cross-section. **(B)** Corresponding image of the same tooth in a virtual section at the level of gingival emergence from the microCT tomogram (right) showing mineral density.

enamel was computed in FIJI (version 1.53c) (Schindelin et al., 2009) from the root to the crown of the tooth. The location of the plane of gingival emergence was confirmed by matching images obtained of the cross-section of the tooth in SEM with the images from the tomogram (Figure 2). Additionally, the mineral density of enamel near the crown surface was evaluated using a mask corresponding to the outer 30 µm of enamel. For each sample, the mineral density was smoothed by computing the moving average over 5-data points. The average and standard deviation of the smoothed data from three samples is reported thereafter. As the enamel near the cervical margin is close to the microCT voxel size, the data are susceptible to artifact such as partial volume effects and segmentation errors. This can lead to noisy data and unreliable results. To minimize these effects, a minimum area of 0.02 mm^2 has been used as a threshold before computing enamel mineral density.

Sample preparation for analyses of enamel microstructure and microhardness

Following the micro-CT analysis, incisor teeth were embedded in London White resin (LR white) and sectioned transversally with a low-speed saw using a diamond blade (Isomet, Buehler). The teeth were oriented in relation to the line of gingival emergence, which was measured from the cusp of the tooth before extraction and confirmed by detection of a distinct change in enamel color. Each tooth was sectioned horizontally at the level of gingival emergence, then additional sections were placed 2 mm below and 2 mm above the eruption line (Figure 2B). At each section plane, we used the exposed face of the incisal portion of the tooth for SEM data acquisitions and the mirroring face of the cervical portion of the sample for microhardness testing. All section surfaces were polished through a series of polishing papers to 0.3 µm.

Analyses of enamel microstructure by scanning electron microscopy (SEM)

Polished sections were etched for 10 s with 0.1 M phosphoric acid, rinsed with deionized water for 1 min, air dried, and gold coated. Imaging was performed with a Zeiss Ultra 55 SEM at 3 kV and a 5 mm working distance. The imaged area was selected at the center of the buccal part of the tooth, far from any major defect at the surface of the enamel.

Microhardness testing

The polished samples were mounted with cyanoacrylate on a metallic disk and data acquired on a M400 HI Vickers testing machine (Leco, St. Joseph, MI) with a load of 25 g and a 5 s dwell time. Each tooth section was tested at two locations on the buccal and two locations on the lingual side with nine indents per site comprising three each in the inner enamel, near the dentin-enamel junction, three in the mid-enamel and three in the outer enamel, near the surface of the tooth (Figure 3).

Porosity indicated by fluorescein penetration

The second, third, and fourth premolars and the first incisor (n = 1 per tooth type) from a 13-week-old pig were ultrasonicated for 3 min to clean the enamel surface and the samples were submerged into freshly prepared 1 mM fluorescein for 45 min at 4°C. The samples were then rinsed in deionized water and fractured bucco-lingually in the midplane of the crown, glued on a glass slide with epoxy resin. A z-stack of images of the cross-section of enamel was taken by confocal microscopy on a Zeiss LSM 780 Confocal Microscope (Zeiss, Germany). A qualitative assessment of the penetration depth of fluorescein from the crown surface was assessed in maximum intensity projections.

Statistical analysis

Statistical analysis was performed using Prism 9 (Graphpad Software Inc., San Diego, CA). The microhardness values were analyzed using two-way ANOVA and multiple comparisons were performed using Tukey's test, where $\alpha = 0.05$.

Results

Mineral density increases drastically between 2 and 4 weeks after birth in the crown surface

The comparison of enamel mineral density between teeth of the same type, namely first incisors of the primary dentition, harvested from piglets at different ages shows a marked difference at the crown surface. Specifically, measures of mineral density derived from a series of virtual sections comprising 3 mm of the erupted crown height from the level of gingival emergence shows a clear progression of the mineral density as see in Figure 4. The enamel mineral density within the 30 µm surface layer of the erupted porcine incisor crown was on average 1644 ± 62 mg_{HA}/cm^3 in 2-week-old animals. These values were measured between the level of gingival eruption and 3 mm above and increased in animals 4 weeks of age, to 1977 ± 68 mg_{HA}/cm^3. No further increase was seen in the 16-week-old pigs, where the enamel mineral density at the incisor surface was 1959 ± 90 mg_{HA}/cm^3.

Between 2 and 4 weeks after birth, the crown surface porosity decreases

The enamel in the first incisor from 2-week-old pigs presents a large amount of porosity (Figures 5A,C,E). Below the gumline, large channels can be observed, running from the surface of the tooth towards the dentin-enamel junction (white arrows in

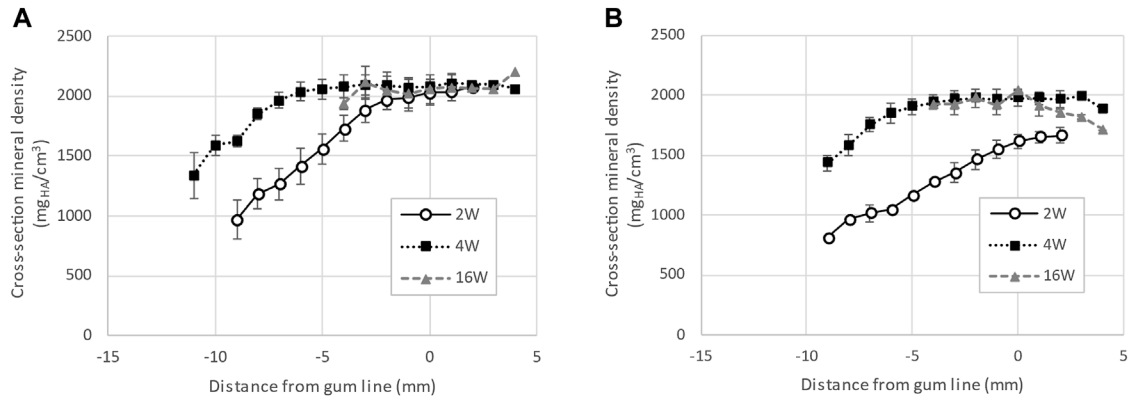

FIGURE 4
Progression of enamel mineral density for incisors, extracted from pigs aged 2, 4 and 16 weeks. Panel **(A)** shows the average density measured along the cross-section of the tooth while panel **(B)** shows the average density of the 30 µm near the surface of the tooth. The data indicates that enamel near the surface of first incisors is not fully mineralized at eruption in 2-week-old pigs.

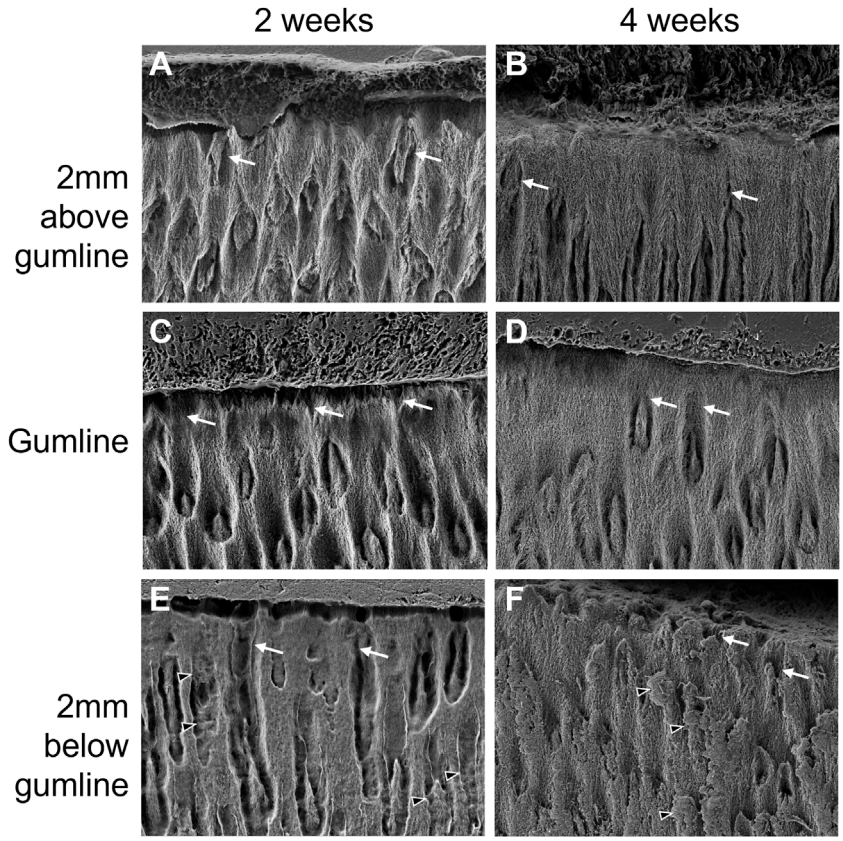

FIGURE 5
Progression of enamel surface micro-structure with eruption and with age in the first lower left incisor of pigs aged 2 weeks **(A, C, E)** and 4 weeks **(B, D, F)**. **(A, B)** show surface enamel 2 mm above the gingival eruption level, referred to as gumline, seen in **(C, D)**, with surface enamel 2 mm below the gumline in **(E, F)**. Black arrowheads: proteins; white arrows: porosity.

Figure 5). A significant amount of protein matrix can be observed along these channels as indicated by the absence of features such as sharp edges and clear shape that are characteristic for the distinct morphology of enamel crystallites (black arrowheads in Figure 5A,E,F). While the size of the channels progressively decreases in diameter when moving towards the crown of the tooth, they are still present at gumline and 2 mm above gumline. This suggests a structural porosity that would allow for exchanges with the outside environment to favor mineralization. The surface of the enamel presents some roughness which indicates that the enamel is not completely sealed, even after eruption. At 4 weeks, the incisors still present some evidence of channels running perpendicular to the surface of the tooth (Figures 5B,D,F). However, these channels appear partially sealed at the gumline and 2 mm above gumline (Figures 5D,F). The tooth surface is more mineralized, and the roughness is significantly decreased when compared to the teeth taken from younger animals.

The porosity of erupted enamel, as evaluated by the penetration of fluorescein in the tissue, significantly increases as a function of the time spent in the oral cavity (Figure 6). The second premolar, which is the last tooth to erupt, is still highly porous after 5 weeks post-eruption. At 9 weeks post-eruption, the third premolar still presents some porosity across the full cross-section of enamel. At 11 weeks post-eruption, teeth appear almost impermeable to fluorescein. Taken together, our results indicate an initially high and progressively decreasing porosity and penetration of fluorescein, suggesting that enamel permeability and exchange processes with the oral cavity change after eruption.

Fast post-eruptive hardening is the shortcut to produce functional teeth by the time of weaning

In the first incisors of 2-week-old pigs, the cross-sectional mineral density of enamel increases linearly along the length of the tooth from the cervical margin to the gum line where it reaches a plateau at a density of 2018 ± 92 mg_{HA}/cm^3. In 4-week-old pigs, the fast progress of enamel maturation occurs below the gum line. The mineral density reaches a plateau of mature enamel with a density of 2083 ± 77 mg_{HA}/cm^3 at about 5 mm below the gingival eruption line and does not further mature after. At 16 weeks after birth, the incisor crown is fully formed and has reached the occlusal plane, and the cross-sectional mineral density, including the crown surface, is mostly constant along the entire length of the tooth with a value of 2063 ± 118 mg_{HA}/cm^3.

The crown of incisors from 16-week-old animals are significantly worn which leads to a final erupted length comparable to the same tooth taken from 4-week-old pigs. Although the enamel near the

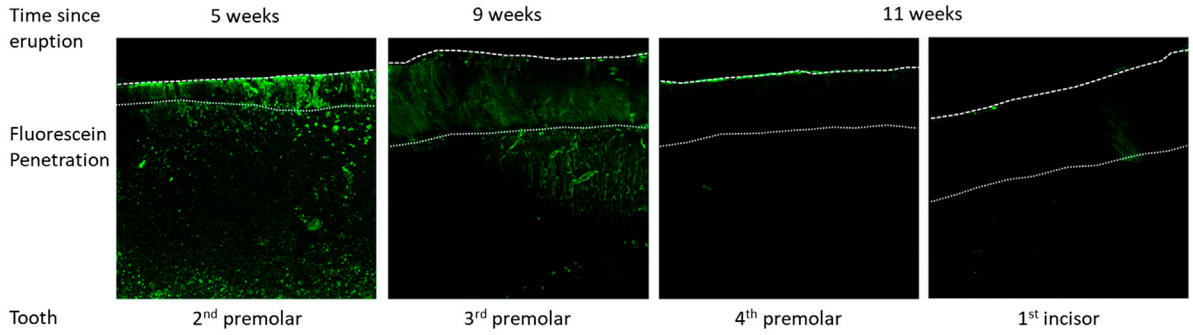

FIGURE 6
Fluorescein penetration after application on the surface of the tooth crown, followed by cleaving the tooth to expose the fracture surface that is imaged by confocal laser scanning microscopy to detect fluorescein distribution within enamel as a function of time post-eruption.

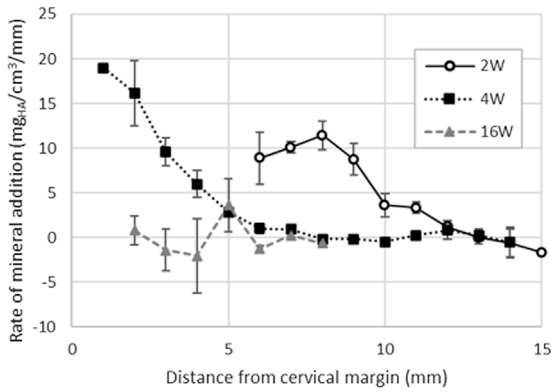

FIGURE 7
Enamel rate of mineral addition along the cervical-occlusal direction of the tooth computed for first incisors extracted from pigs aged 2, 4 and 16-week. The results indicate that the mineral addition reaches a maximum around 8 mm form the cervical margin in 2-week-old pigs. At 4-week, the tooth eruption is slowed down and enamel mineral addition is twice as fast as in 2-week-old pigs. In 16-week-old pigs, the first incisors are both fully formed and erupted as confirmed by the constantly null mineralization rate.

occlusal surface in 16-week-old pigs has a slightly decreased mineral density, there is no apparent difference in the plateau of the average cross-sectional mineral density of enamel in the erupted part of incisors form pigs aged 2-, 4- and 16 weeks. This is in contrast to the changes in mineral density at the crown surface.

Fast crown formation for the first teeth to erupt, fast pre-eruptive mineralization for later erupting teeth

We measured the progression of mineralization in incisors to evaluate differences between age groups. It is experimentally particularly challenging to measure the rate of mineralization over time. Therefore, we evaluated the mineralization rate by comparing the progression of enamel mineral density, ρ, along the length of the tooth. The rationale is that, for any given section taken at a position x along the cervical-occlusal direction of the tooth at a time t, its mineral density at time $t+1$ is equal to the mineral density of the section at a position $x+\delta x$ at time t. Therefore, instead of assessing the mineralization rate of enamel over time, we computed the progression in mineral density along the long axis of the tooth:

$$\Delta\rho = \frac{\rho(x+\delta x) - \rho(x)}{\rho(x)}$$

Where $\Delta\rho$ is the rate of mineral addition of enamel along the length of the tooth and expressed in mg_{HA}/cm^3 per mm, $\rho(x+\delta x)$ is the mineral density at the position $x+\delta x$ and $\rho(x+\delta x)$ is the mineral density at the position x. The results are calculated for $\delta x = 1$ mm and are presented in Figure 7. To account for the variation in eruption speed between teeth, we considered the rate of mineral addition during enamel formation as a function of the distance from the most newly formed enamel at the cervical margin towards the tooth cusp. Our results indicate significant differences between the age groups, though, it is important to note that the illustrated data do not reflect only the rate of mineralization over time. Rather, the measures capture a snapshot of mineral density at a single time point. The metric used here is dependent on the mineralization rate but also on the growth rate and eruption speed of the tooth.

For the full thickness of the enamel layer, the rate of mineral addition averages 9.8 ± 2.2 mg_{HA}/cm^3/mm (Figure 7) and is lower in incisors of 2-week-old pigs compared to the incisors of 4-week-old pig where it is 16.2 ± 3.6 mg_{HA}/cm^3/mm near the cervical margin. The rate of mineral addition progressively decreases along the length of the tooth.

Fast formation still produces hard enough enamel

The average microhardness values across the entire thickness of enamel ranged from 224 HV (2-week-old pre-eruptive, SD = 69) to 372 HV (4-week-old post-eruptive SD = 33) among all age groups and locations. There was a significant effect of age, $F(2, 15) = 3.73$, $p = 0.049$, indicating that the samples became harder with increasing age of individual. However, the effect of location across the entire enamel thickness was not significant, $F(2, 15) = 2.58$, $p > 0.05$, nor was the association between age and location, $F(4, 15) =$

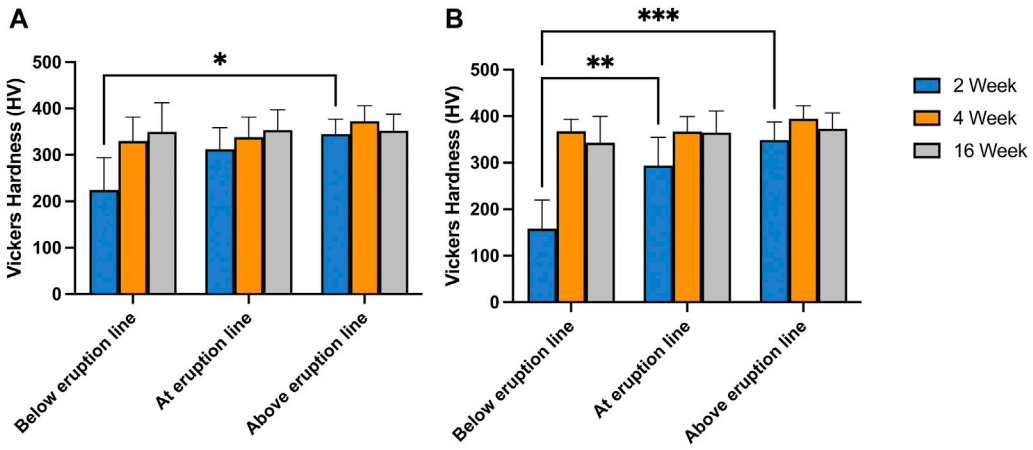

FIGURE 8
Vickers Hardness measured at various position along the length of first incisors taken from 2-, 4- and 16-week-old pigs. Panel **(A)**. presents the average hardness of enamel measured over a cross-section taken 2 mm below, at and 2 mm above gum line. In panel **(B)** only the results from tests performed 30 µm from the surface of the tooth are presented. The results indicate no significant difference between the hardness of the various locations probes for the incisors of 4- and 16-week-old pigs. In incisors from 2-week-old pigs, the hardness of enamel below gum line is significantly lower than the hardness above eruption line (p = .02) **(A)**. The surface microhardness of the same pigs below eruption line are significantly lower than the values at eruption line (p = .005) and above eruption line (p < .001) **(B)**.

1.20, $p > 0.05$ (Figure 8A). A *post hoc* Tukey multiple comparisons test showed only significant difference between the microhardness values between the pre-eruptive (224 HV, SD = 69) and post-eruptive (344 HV, SD = 31) values of the 2-week-old pigs, $p = 0.02$. These results were consistent with the mineral density data derived from microCT measures of the same teeth.

In contrast, the microhardness for surface enamel, specifically for values within 30 µm of the enamel surface, showed a significant positive association with age, $F(2, 15) = 15.38$, $p < 0.001$, indicating increasing enamel hardness with increasing age of the animal. Additionally, surface hardness was associated with the location relative from the cervical margin along the long axis of the tooth crown, $F(2, 15) = 6.86$, $p < 0.01$, indicating increasing hardness from apical to incisal. These effects were qualified by a significant interaction of age and location, $F(4, 15) = 3.53$, $p = 0.03$, reflecting the greater effect of location in the youngest animals. Post-hoc Tukey tests for the surface measurements also indicated that the pre-eruptive microhardness of the 2-week-old pigs was significantly less than the hardness at-eruption ($p = 0.005$), and the post-eruptive hardness ($p < 0.001$) (Figure 8B).

Discussion

The extremely fast growth rate and early timing of tooth eruption in pigs, especially in breeds selected for farming as used in this study, is at odds with the time required to complete enamel maturation and hardening. As a result, porcine teeth erupt with enamel that is not fully matured. Although it is known that the secretion rate of enamel matrix, that is ameloblast production, is quite variable and can increase if eruption is accelerated (Reid and Dean, 2006; Nacarino-Meneses et al., 2017; An et al., 2018), the speed of enamel maturation does not increase (Robinson et al., 1988a). Our results confirm this for porcine teeth. The enamel portion of the first incisors that is erupted at birth is hypomineralized and only 60% (by weight) mineral in 2-weeks-old pigs. The incomplete mineralization is reflected in significantly lower hardness compared to fully mature enamel of the same teeth at a later time point, as well as in comparison to human teeth.

The low mineral content is accompanied by a higher porosity of the enamel microstructure as observed by electron microscopy. The incisor enamel of 2-week-old animals presents a striking level of porosity seen as channel structures that extend form the crown surface of the tooth through the enamel layer towards the dentin enamel junction. These channels are present even after eruption, suggesting the possibility for continued exchange, facilitated by microstructural organization, for a post-eruptive mineralization process. The surface of 2-week-old enamel also presents some roughness in SEM images suggesting that the surface is not fully formed. While few channels are still present in the enamel microstructure of 4-week-old incisors, they are located in the portion of the tooth crown that is not yet erupted. The enamel crown surface of the erupted portion appears at four weeks after birth sealed and smoother. The enamel near the surface is visibly denser. This change in microstructural appearance is in agreement with the progression of mineral density measured in microCT analyses. Furthermore, the apparent change in enamel porosity over time is supported by our measures of fluorescein penetration. The penetration and attachment of fluorescein into deeper enamel layers is much higher in recently erupted teeth. In contrast, teeth that have been in the oral cavity for an extended period have a sealed crown surface and no fluorescein penetration and related fluorescence is detected in the enamel layer.

It is evident that enamel that is incompletely mineralized at the time of eruption continues to mature in the oral cavity and undergoes substantial changes that likely involve both protein removal and mineral uptake to achieve mineralization and hardening. While the erupted enamel in the incisors of 2-week-old pigs is only partially mineralized, the enamel from the same tooth is in 4-week-old pigs fully mineralized. Accordingly, for the same teeth, the enamel hardness increases within two weeks particularly at the crown surface. Organic material is abundant in enamel before eruption in the incisors at two weeks and four weeks after birth, as seen in SEM images. Fluorescein labelling clearly indicates proteins in enamel up to five weeks after eruption, although the protein is not clearly discernable in SEM images

of incisor enamel at four weeks. Interestingly, no fluorescein label is detected in enamel at 11 weeks after eruption, suggesting that mechanisms of protein removal must occur while teeth are in the oral cavity.

Our data suggests that mineralization after eruption occurs fast and leads to substantial increases of mineral density and hardness of the tooth crown within the first weeks of the animals' life. Indeed, the erupted enamel of 4-week-old pigs appears fully mature with optimal mineral density, hardness, and a microstructure similar to 16-week-old animals. While the incisal part of the incisor forms rapidly, the remaining portion of the tooth forms at a lower rate.

Although we did not directly measure the tooth crown extension rate, we computed the progression of mineral density as a function of distance from the cervical margin. The computational approach assumes that adjacent cross-sections along the long axis of a tooth follow a similar mineralization pattern. Therefore, the difference in mineral density in two adjacent cross-sections, the cervical-incisal mineral addition rate, is inversely related to the time dependent growth rate of the tooth. If the true rate of mineral maturation seen as increase of mineral content over time is constant, then it follows that the larger the difference in mineral density between two adjacent cross-sections, the more time passed for mineral to form and complete enamel maturation and the crown formation. In 4-week-old incisors, the cervical-incisal mineral addition rate measured here reaches values higher than in incisors taken from 2-week-old animals. Consequently, the incisor grows at a slower rate at 4-week when compared to 2-week, and mineral maturation is favored over early eruption of immature enamel and its posteruptive hardening. Observations that are consistent with this concept have been reported in human teeth where differences in crown formation rates are associated with the eruption sequence (Mahoney, 2015). For example, primary teeth that erupt first, such as incisors, have much faster prenatal enamel matrix deposition compared to teeth that erupt later, such as molars. When the enamel growth rate decreases, maturation of enamel prior to its eruption takes priority.

It has been suggested that human enamel is not fully mineralized at the time of eruption (Fejerskov et al., 1984) and that enamel maturation and hardening continue in the oral cavity (Yonan and Fosdick, 1964; Wöltgens et al., 1990; Palti et al., 2008; Lynch, 2013). While human teeth have been shown to be most susceptible to caries during the first years after eruption (Carlos and Gittelsohn, 1965), no data is available for the first few weeks after eruption. Post eruptive maturation has also been reported in rodents (Yonan et al., 1966). Rapid post-eruptive mineralization reported here for pigs might also be present in other species, including humans, despite the differences in enamel microstructure between porcine and human enamel. We have shown that porcine enamel appears to have a microstructure that facilitates exchange processes through channel-like structures that run from the crown surface into deeper enamel layers. The importance of surface porosity for exchange processes with the oral cavity and posteruptive mineralization have been long recognized. For example, it was shown that the permeability of human surface enamel, measured by potassium iodide uptake and back diffusion, decreases significantly with the time maxillary incisors of the permanent dentition are exposed to the oral cavity (Brudevold et al., 1982).

It is well known that enamel maturation and hardening is accompanied by the decrease in protein content. We have shown that the abundance of fluorescein, which binds to proteins, decreases in enamel with increasing time after eruption. This observation is based on two factors. One is the diminished penetration of fluorescein into enamel, determined by the decrease in porosity and surface permeability. The second factor is the amount of protein present in enamel. While we can appreciate the difference in microstructure between 2- and 4-week-old surface enamel, it is unresolved how the decrease in protein content is achieved. The molecular mechanism allowing for fast post-eruptive hardening of enamel remains to be analyzed in future studies.

Conclusion

Our study highlights that porcine enamel of mandibular incisors that are erupted at birth, can harden extremely fast, within two weeks after birth. This hardening process occurs mainly at the crown surface. The microstructure of surface enamel shows high porosity in incisors from two-week-old piglets and is decreased within 2 weeks to create a densely mineralized surface layer that seals the tooth crown in four-week-old animals. This strategy allows teeth that formed extremely fast and are hypomineralized and soft at birth to achieve the required hardness for an omnivorous diet by weaning age. The short time frame of these drastic changes in microstructure and mineral content has not previously been considered for human enamel maturation.

Data availability statement

The raw data supporting the conclusions of this article will be made available by the authors, without undue reservation.

Ethics statement

The animal study was reviewed and approved by the IACUC committee from the Tufts University Cummings School of Veterinary Medicine and The Forsyth Institute.

Author contributions

FB, BD, and MP conceived and designed the study. BD, NO, AG, MT, and GM contributed to sample preparation for the study. BD, FB, and HK interpreted the data. BD, FB, and HK drafted the manuscript. BD, FB, HK, and MP revised the manuscript. All authors approved the final version of the manuscript and took responsibility for the integrity of the data analysis.

Funding

This work was supported by NIH grants R21DE026874 (FBB) and R90DE027638 (MT, HK); R01 DE025865 (FBB).

Acknowledgments

Parts of this work were performed at the Forsyth Institute Advanced Microscopy Core (RRID:SCR_021121) and Forsyth Institute MicroCT Core (RRID:SCR_021180) facilities, and the Harvard Center for Nanoscale Systems (CNS), a member of the National Nanotechnology Coordinated Infrastructure Network (NNCI), which is supported by the National Science Foundation under NSF award no. ECCS-2025158. Figures 1, 2 were created with Biorender.com.

Conflict of interest

The authors declare that the research was conducted in the absence of any commercial or financial relationships that could be construed as a potential conflict of interest.

Publisher's note

All claims expressed in this article are solely those of the authors and do not necessarily represent those of their affiliated organizations, or those of the publisher, the editors and the reviewers. Any product that may be evaluated in this article, or claim that may be made by its manufacturer, is not guaranteed or endorsed by the publisher.

Supplementary material

The Supplementary Material for this article can be found online at: https://www.frontiersin.org/articles/10.3389/fphys.2023.1099645/full#supplementary-material

References

An, Z., Sabalic, M., Bloomquist, R. F., Fowler, T. E., Streelman, T., and Sharpe, P. T. (2018). A quiescent cell population replenishes mesenchymal stem cells to drive accelerated growth in mouse incisors. *Nat. Commun.* 9, 378. doi:10.1038/s41467-017-02785-6

Birch, W., and Dean, M. C. (2014). A method of calculating human deciduous crown formation times and of estimating the chronological ages of stressful events occurring during deciduous enamel formation. *J. Forensic Leg. Med.* 22, 127–144. doi:10.1016/j.jflm.2013.12.002

Brudevold, F., Aasenden, R., and Bakhos, Y. (1982). A preliminary study of posteruptive maturation of teeth *in situ*. *Caries Res.* 16, 243–248. doi:10.1159/000260604

Carlos, J. P., and Gittelsohn, A. M. (1965). Longitudinal studies of the natural history of caries. II. A life-table study of caries incidence in the permanent teeth. *Arch. Oral Biol.* 10, 739–751. doi:10.1016/0003-9969(65)90127-5

Crombie, F. A., Manton, D. J., Palamara, J. E. A., Zalizniak, I., Cochrane, N. J., and Reynolds, E. C. (2013). Characterisation of developmentally hypomineralised human enamel. *J. Dent.* 41, 611–618. doi:10.1016/j.jdent.2013.05.002

Elfrink, M. E. C., Ten Cate, J. M., Van Ruijven, L. J., and Veerkamp, J. S. J. (2013). Mineral content in teeth with deciduous molar hypomineralisation (DMH). *J. Dent.* 41, 974–978. doi:10.1016/j.jdent.2013.08.024

Fejerskov, O., Josephsen, K., and Nyvad, B. (1984). Surface ultrastructure of unerupted mature human enamel. *Caries Res.* 18, 302–314. doi:10.1159/000260781

Kallistova, A., Horacek, I., Slouf, M., Skala, R., and Fridrichova, M. (2017). Mammalian enamel maturation: Crystallographic changes prior to tooth eruption. *PLoS One* 12, 1–23. doi:10.1371/journal.pone.0171424

Kirkham, J., Robinson, C., Weatherell, J. A., Richards, A., Fejerskov, O., and Josephsen, K. (1988). Maturation in developing permanent porcine enamel. *J. Dent. Res.* 67, 1156–1160. doi:10.1177/00220345880670090301

Liversidge, H. M., and Molleson, T. (2004). Variation in crown and root formation and eruption of human deciduous teeth. *Am. J. Phys. Anthropol.* 123, 172–180. doi:10.1002/ajpa.10318

Lynch, R. J. M. (2013). The primary and mixed dentition, post-eruptive enamel maturation and dental caries: A review. *Int. Dent. J.* 63, 3–13. doi:10.1111/idj.12076

Mahoney, E., Ismail, F. S. M., Kilpatrick, N., and Swain, M. (2004). Mechanical properties across hypomineralized/hypoplastic enamel of first permanent molar teeth. *Eur. J. Oral Sci.* 112, 497–502. doi:10.1111/j.1600-0722.2004.00162.x

Mahoney, P. (2015). Dental fast track: Prenatal enamel growth, incisor eruption, and weaning in human infants. *Am. J. Phys. Anthropol.* 156, 407–421. doi:10.1002/ajpa.22666

Nacarino-Meneses, C., Jordana, X., Orlandi-Oliveras, G., and Köhler, M. (2017). Reconstructing molar growth from enamel histology in extant and extinct Equus. *Sci. Rep.* 7, 1–12. doi:10.1038/s41598-017-16227-2

Palti, D. G., Machado, M. A. de A. M., Silva, S. M. B. da, Abdo, R. C. C., and Lima, J. E. de O. (2008). Evaluation of superficial microhardness in dental enamel with different eruptive ages. *Braz. Oral Res.* 22, 311–315. doi:10.1590/S1806-83242008000400005

Reid, D. J., and Dean, M. C. (2006). Variation in modern human enamel formation times. *J. Hum. Evol.* 50, 329–346. doi:10.1016/j.jhevol.2005.09.003

Robinson, C., Kirkham, J., and Nutman, C. A. (1988a). Relationship between enamel formation and eruption rate in rat mandibular incisors. *Cell Tissue Res.* 254, 655–658. doi:10.1007/BF00226516

Robinson, C., Kirkham, J., Weatherell, J. A., Richards, A., Josephsen, K., and Fejerskov, O. (1987). Developmental stages in permanent porcine enamel. *Cells Tissues Organs* 128, 1–10. doi:10.1159/000146306

Robinson, C., Kirkham, J., Weatherell, J. A., Richards, A., Josephsen, K., and Fejerskov, O. (1988b). Mineral and protein concentrations in enamel of the developing permanent porcine dentition. *Caries Res.* 22, 321–326. doi:10.1159/000261131

Schindelin, J., Arganda-Carrera, I., Frise, E., Verena, K., Mark, L., Tobias, P., et al. (2009). Fiji - an Open platform for biological image analysis. *Nat. Methods* 9. doi:10.1038/nmeth.2019.Fiji

Schour, L., and Massler, M. (1941). The development of the human dentition. *J. Am. Dent. Assoc.* 28, 1153–1160.

Tonge, C. H., and McCance, R. A. (1973). Normal development of the jaws and teeth in pigs, and the delay and malocclusion produced by calorie deficiencies. *J. Anat.* 115, 1–22. Available at:http://www.ncbi.nlm.nih.gov/pubmed/4199500.

Wöltgens, J. H., Etty, E. J., and Geraets, W. G. (1990). Posteruptive age dependency of cariogenic changes in enamel of permanent teeth of children. *J. Biol. Buccale* 18, 49–53. Available at:http://www.ncbi.nlm.nih.gov/pubmed/2365676.

Yonan, T., and Fosdick, L. S. (1964). The degree of etching as a function of the age of the teeth. *J. Dent. Res.* 43, 629. doi:10.1177/00220345640430042001

Yonan, T., Nicolau, J., and Fosdick, L. S. (1966). The posteruptive maturation of teeth II. Normal posteruptive maturation of hamster teeth. *J. Dent. Res.* 45, 1701–1705. doi:10.1177/00220345660450062201

frontiers | Frontiers in Physiology

TYPE Original Research
PUBLISHED 01 March 2023
DOI 10.3389/fphys.2023.1100714

OPEN ACCESS

EDITED BY
Catherine Chaussain,
Université Paris Cité, France

REVIEWED BY
Sylvie Babajko,
INSERM U1138 Centre de Recherche des Cordeliers (CRC), France
Martin Vaeth,
University of Würzburg, Germany

*CORRESPONDENCE
Petros Papagerakis,
petros.papagerakis@usask.ca

SPECIALTY SECTION
This article was submitted to Craniofacial Biology and Dental Research, a section of the journal Frontiers in Physiology

RECEIVED 17 November 2022
ACCEPTED 17 February 2023
PUBLISHED 01 March 2023

CITATION
Said R, Mortazavi H, Cooper D, Ovens K, McQuillan I, Papagerakis S and Papagerakis P (2023), Deciphering the functions of Stromal Interaction Molecule-1 in amelogenesis using AmelX-iCre mice.
Front. Physiol. 14:1100714.
doi: 10.3389/fphys.2023.1100714

Deciphering the functions of Stromal Interaction Molecule-1 in amelogenesis using AmelX-iCre mice

Raed Said[1,2], Helyasadat Mortazavi[1,2], David Cooper[2], Katie Ovens[3], Ian McQuillan[4], Silvana Papagerakis[5,6] and Petros Papagerakis[1,2]*

[1]College of Dentistry, University of Saskatchewan, Saskatoon, SK, Canada, [2]Department of Anatomy, Physiology and Pharmacology, College of Medicine, University of Saskatchewan, Saskatoon, SK, Canada, [3]Department of Computer Science, University of Calgary, Calgary, AB, Canada, [4]Department of Computer Sciences, College of Arts and Sciences, University of Saskatchewan, Saskatoon, SK, Canada, [5]Department of Surgery, College of Medicine, University of Saskatchewan, Saskatoon, SK, Canada, [6]Department of Otolaryngology-Head and Neck Surgery, School of Medicine, University of Michigan, Ann Arbor, MI, United States

Introduction: The intracellular Ca2+ sensor stromal interaction molecule 1 (STIM1) is thought to play a critical role in enamel development, as its mutations cause Amelogenesis Imperfecta (AI). We recently established an ameloblast-specific (AmelX-iCre) Stim1 conditional deletion mouse model to investigate the role of STIM1 in controlling ameloblast function and differentiation *in vivo* (Stim1 cKO). Our pilot data (Said et al., J. Dent. Res., 2019, 98, 1002–1010) support our hypothesis for a broad role of Stim1 in amelogenesis. This paper aims to provide an in-depth characterization of the enamel phenotype observed in our Stim1 cKO model.

Methods: We crossed AmelX-iCre mice with Stim1-floxed animals to develop ameloblast-specific Stim1 cKO mice. Scanning electron microscopy, energy dispersive spectroscopy, and micro- CT were used to study the enamel phenotype. RNAseq and RT-qPCR were utilized to evaluate changes in the gene expression of several key ameloblast genes. Immunohistochemistry was used to detect the amelogenin, matrix metalloprotease 20 and kallikrein 4 proteins in ameloblasts.

Results: Stim1 cKO animals exhibited a hypomineralized AI phenotype, with reduced enamel volume, diminished mineral density, and lower calcium content. The mutant enamel phenotype was more severe in older Stim1 cKO mice compared to younger ones and changes in enamel volume and mineral content were more pronounced in incisors compared to molars. Exploratory RNAseq analysis of incisors' ameloblasts suggested that ablation of Stim1 altered the expression levels of several genes encoding enamel matrix proteins which were confirmed by subsequent RT-qPCR. On the other hand, RT-qPCR analysis of molars' ameloblasts showed non-significant differences in the expression levels of enamel matrix genes between control and *Stim1*-deficient cells. Moreover, gene expression analysis of incisors' and molars' ameloblasts showed that *Stim1* ablation caused changes in the expression levels of several genes associated with calcium transport and mitochondrial kinetics.

Conclusions: Collectively, these findings suggest that the loss of *Stim1* in ameloblasts may impact enamel mineralization and ameloblast gene expression.

KEYWORDS

enamel, calcium, ameloblast, amelogenesis, stromal interacting molecule 1 (STIM1), store operated Ca 2+ entry, mineralised tissue

Introduction

Dental enamel is the most calcified tissue in the body serving as the protective outer layer for teeth withstanding masticatory forces (Nanci, 2013a). Enamel formation, amelogenesis, is a complex process that results in the development and mineralization of dental enamel (Simmer et al., 2010; Zheng et al., 2014). Amelogenesis is carried out by ectodermally derived epithelial cells of the enamel organ, termed ameloblasts. Amelogenesis presents in two main developmental stages known as the secretory and maturation stages (Simmer et al., 2021). During the secretory stage, ameloblasts provide a proteinaceous template for enamel crystal growth, which essentially mineralizes during the maturation period (Paine et al., 2020). The functional characteristics of ameloblasts are tightly linked to their differentiation stage which confers them to a specific morphology. Indeed, during the maturation stage, ameloblasts cyclically modulate their morphology between a ruffle-ended (RA) appearance and a smooth-ended (SA) appearance which may reflect the alternation of the functional phase between resorptive and secretory (Nanci, 2013b; Paine et al., 2020).

Ca2+ is one of the most important ions in enamel, as it participates in the formation and growth of enamel crystals (Iijima et al., 2002). Indeed, enamel hydroxyapatite-like crystals form *de novo* by precipitating ions in the enamel space after passing through the semipermeable barrier created by ameloblasts (Lacruz, 2017). During crystal formation, the ameloblasts transfer large quantities of calcium from the serum into the enamel space. Approximately 60% of the minerals in the fully developed enamel are supplied during the maturation stage (Kirkham et al., 1988). It has been initially proposed that calcium transport occurs in two primary ways: paracellular and transcellular (Berdal et al., 1995; Bailleul-Forestier et al., 1996; Hubbard, 2000; Papagerakis et al., 2002). Several subsequent reports, however, showed that Ca2+ is primarily transported through high-capacity stores associated with the endoplasmic reticulum (ER), widely distributed in ameloblasts, suggesting that the store-mediated transcellular calcium transport is the dominant mode of ion transport across the ameloblast (Lacruz et al., 2012; Nurbaeva et al., 2015a). Impaired ion transport across the ameloblast may result in the hypomineralization of enamel (Lacruz and Feske, 2015; Silva-Rojas et al., 2020).

Store-operated Ca2+ entry (SOCE) has been established as a major Ca2+ influx mechanism in excitable cells and non-excitable cells (Jardín et al., 2009). Depletion of Ca2+ in the ER triggers SOCE, which entails the formation of multimers of stromal interaction molecule 1 (STIM1), an ER transmembrane protein, that is translocated to the ER-plasma membrane junction (Feske, 2009; Smyth et al., 2010). Ca2+ release-activated Ca2+ channels such as ORAI1 are opened by STIM1 once it binds to it, leading to sustained Ca2+ influx (Li et al., 2007). The STIM2 family member is also located in the ER and acts as a positive regulator of SOCE, and its functions partially overlap with STIM1 as they share >60% sequence identity (Berna-Erro et al., 2017). By allowing Ca2+ to influx into the cytoplasm by ORAI1, the cytosolic Ca2+ concentration increases and the ER Ca2+ stores are replenished *via* sarcoplasmic/ER Ca2+-ATPases (SERCAs) (Eckstein and Lacruz, 2018). Several studies showed that both *Stim1* and *Stim2* are robustly expressed in ameloblasts during their secretory and maturation stages in wild-type rodents, suggesting a crucial role for SOCE in the influx of calcium into ameloblasts (Lacruz et al., 2011; Lacruz et al., 2012; Nurbaeva et al., 2015a; Nurbaeva et al., 2015b).

Ectodermal dysplasia is characterized by defects in several ectodermal tissues, including hair, nails, sweat glands and dental enamel causing amelogenesis imperfecta (AI) (Itin and Fistarol, 2004; Furukawa et al., 2017). Based on several previous studies, patients with mutations in *STIM1* and *ORAI1* exhibit ectodermal dysplasia with amelogenesis imperfecta, which further confirms the significance of SOCE in enamel mineralization (Feske et al., 2010; Lacruz and Feske, 2015; Silva-Rojas et al., 2020). Indeed, several loss-of-function (LoF) mutations in *STIM1* and *ORAI1* have been hitherto reported in the literature that affect enamel quite severely in both primary and permanent dentition where the severely hypomineralized enamel wears extremely rapidly (Picard et al., 2009; Wang et al., 2014; Lacruz and Feske, 2015; Lian et al., 2018). Moreover, it has been demonstrated that patients with mutations in *STIM1* or *ORAI1* exhibit a severe immune impairment (Picard et al., 2009; Lian et al., 2018).

In vitro experiments with ameloblast-like cells suggest that the expression of several enamel proteins encoding genes may be regulated by SOCE (Nurbaeva et al., 2015b; Zheng et al., 2015; Eckstein et al., 2019). The mechanisms by which SOCE regulates amelogenesis *in vivo* were greatly understudied as deletion of *Orai1, Stim1*, or both *Stim1/Stim2* genes results in perinatal lethality in mice, making the effective animal models with global impaired SOCE of limited use (Said et al., 2019). To address this issue, we and others have recently established ectodermal specific (i.e., Keratin14 (K14)-Cre mediated) and ameloblast-specific (AmelX-iCre) mice models where *Stim1, Stim2,* and *Orai1* genes and some of their combinations were ablated in ameloblasts to investigate the roles of SOCE in controlling ameloblast function and differentiation *in vivo* (Eckstein et al., 2017; Furukawa et al., 2017; Eckstein et al., 2019; Said et al., 2019). All of these abovementioned mice show reduced or absent SOCE in ameloblasts and have an AI phenotype with hypomineralized enamel. The main advantage of the AmelX-Cre line used here over the K14 Cre line is its ability to target gene deletion specifically in ameloblasts from the secretory stage onwards while K14-Cre line deletes genes in all layers of the enamel organ: ameloblasts, stratum intermedium and papillary layer (Klein et al., 2017).

Pilot data from our ameloblast-specific (AmelX-iCre) *Stim1* conditional deletion mouse model (Stim1 cKO) suggest a wide role of STIM1 in amelogenesis (Said et al., 2019). This paper aimed to provide a further in-depth characterization of *Stim1* mutant incisors and molars in this Stim1 cKO model. We hypothesized that amelogenesis imperfecta due to abnormal SOCE may be caused by changes in the enamel mineralization process due to altered ion transport across the ameloblast cell

layer and changes in the expression of enamel matrix proteins and their proteases. To test these hypotheses, we ablated the *Stim1* gene from enamel-forming ameloblasts by crossing *Stim1* floxed mice with Amelogenin–iCre (AmelX-iCre) transgenic mice and analyzed their enamel phenotype and ameloblasts genetic profile. Our analysis showed that the expression of *Stim1* in the enamel cells of the knock-out mice was significantly reduced. These mice were found to have severely hypomineralized and thin enamel that wore rapidly, with lower calcium levels, all of which were similar to the human dental AI phenotypes. The mutant enamel phenotype was more severe in older Stim1 cKO mice compared to younger ones and changes in enamel volume were more pronounced in incisors compared to molars. Our gene expression analysis and suggests that ablation of *Stim1* affected the expression levels of the genes encoding enamel matrix proteins in incisors' ameloblasts more considerably than in molars' ameloblasts. Furthermore, data from our gene expression analysis of incisors' and molars' ameloblasts suggest that *Stim1* invalidation altered the expression of several genes encoding other calcium pumps and exchangers involved in calcium transport during amelogenesis in addition to genes associated with the cell mitochondrial kinetics and bioenergetics. Collectively, our results suggest that SOCE mediated by STIM1 is important for both the mineralization of dental enamel as well as the regulation of gene expression in ameloblasts, and thus the overall functioning of the cell.

Materials and methods

Generation of Stim1 cKO mice

All mice were housed in a specific pathogen-free facility and fed *ad libitum* with a normal diet and sterilized water under a periodic light/dark cycle. AmelX-iCre transgenic mice (Said et al., 2020) and Stim1$^{fl/fl}$ mice (Oh-hora et al., 2008) were mated and the progeny bred to generate the Stim1 cKO mice (AmelX-iCre^{+}; Stim1$^{fl/fl}$) mice. AmelX-iCre^{-}; Stim1$^{fl/fl}$ mice were used as a control genotype. Genotypes were determined by tail biopsy under 3% isoflurane and by conventional polymerase chain reaction (PCR) as previously reported (Said et al., 2019). Only male mice with the desired genotypes were euthanized by an overdose of carbon dioxide followed by cervical dislocation for subsequent analyses. All animal procedures and breeding programs were approved by the University of Saskatchewan Animal Care and Use Committee and the Animal Research Ethics Board (protocol # 20170014).

Dissecting microscopy

The mandibles were removed and dissected free of soft tissues then fixed by immersion in 10% neutral buffered formalin (NBF). The teeth were cleaned with non-woven gauze, displayed on the Nikon SMZ1000 (Nikon Corporation, Japan) dissection microscope and photographed using a Nikon digital camera DXM1200 (Nikon Corporation, Japan) for gross morphometric analysis.

Scanning electron microscopy and energy dispersive spectroscopy

Scanning electron microscope (SEM) evaluation was performed at the Western College of Veterinary Medicine Imaging Centre at the University of Saskatchewan (Saskatoon, Canada). Ethanol-dehydrated and air-dried samples from the control and Stim1 cKO mice were mounted on metallic stubs using conductive carbon cement and degassed in a vacuum desiccator overnight. The samples were imaged using a Hitachi SU8010 Scanning Electron Microscope (Hitachi High-Tec, Tokyo, Japan) operating at an accelerating voltage of 3.0 kV. The Hitachi SU8010 is a semi-in-lens type cold field emission that offers backscattered electron (BSE) detection and energy dispersive spectroscopy (EDS) for compositional information using the AztecLiveStandard with Ultim Max 170 Detector. For BSE incisor imaging, the bony caps and soft tissue covering the mandibular incisors were carefully removed and the labial surface of the mandibular incisors was then examined at × 150 magnification in a Hitachi SU8010 scanning electron microscope using the backscatter mode. Gray levels of the BSE images were measured using the ImageJ software. For EDS, 4 beams were generated on the cusp slopes of maxillary first molars that received no processing of the enamel surface in order not to alter its composition. Comparisons were made using a total of $n = 3$ mice per group. The mandibular incisors were sectioned using a diamond saw at their site of eruption on the level of the alveolar bone crest; this level was used to assess enamel thickness relative to dentin. Thickness was measured using the ImageJ software. Mandibular first molars were sagittally sectioned at the level of mesiobuccal cusp; this level was used to assess the prismatic structure under the SEM. The molar samples were cleaned by brushing in soapy water for at least 1 min, using a medium-to-stiff and dense artist's brush, then were put in a jar with distilled water in an ultrasonication basin for about 5 min. The samples were then polished at the following grits: 600, 800 and 1200, then they were etched with nitric acid of various concentrations (0.1%, 0.5%, 1%, 2.5%, and 5%), all prepared with distilled water (Risnes et al., 2019) and sputter coated with gold prior to imaging.

Micro–computed tomography

Hemimandibles (weeks 2, 4, 12, $n = 3$ per each genotype) were dissected, fixed for 24 h in NBF, and stored in 70% ethanol at 4°C. Hemimandibles were then scanned with a micro–computed tomography (μCT) scanner (6.7 μm isotropic voxel size, 50 kVp, 250 μA, Al 0.5 mm filter, 0.2 rotation degree step, 440 ms exposure time; Skyscan1172, Bruker microCT, Massachusetts, United States). After 2-dimensional reconstruction with NRecon the data were imported in Amira software (https://www.fei.com) for 3D evaluation. The image data were segmented employing semiautomatic tools in order to separate the enamel from the dentine and generate 3D surface models of the teeth. The threshold value for imaging was raised until enamel was the only mineral displayed in the control group and total incisor and molar enamel volumes were measured. For mineral density analysis, incisor images were obtained perpendicular to the long axis of

the incisor and parallel to the mesial root canal of the mandibular first molar as this portion of the tooth is not affected by wear yet while being fully mature and already mineralized. The mineral density (gHA/cm3) on the incisor enamel was calculated for quantitative analysis after the calibration with phantoms (SP-4002, Bruker microCT) according to the manufacturer's instructions.

Explarotary RNAseq and data processing

Whole incisor enamel organ (EO) cell populations of P28 old mice were carefully dissected, and total RNA was isolated using the RNeasy Micro Kit (Qiagen) from 3 samples (n = 1 per genotype); 1 Stim1 cKO sample (Stim1 cKO) with complete deletion of *Stim1* (AmelX-iCre^{+}; Stim1$^{fl/fl}$), 1 Stim1 heterozygous (Stim1 HT) sample with heterozygous deletion of one *Stim1* allele (AmelX-iCre^{+}; Stim1$^{fl/wt}$) and 1 control sample (Stim1 Ctrl) with no *Stim1* deletion as it was Cre negative (AmelX-iCre^{-}; Stim1$^{fl/fl}$). RNA quality was analyzed on Agilent Bioanalyzer 2100 RNA Nano chip following Agilent Technologies' recommendation. Concentration was measured by Qubit RNA HS Assay on a Qubit fluorometer (ThermoFisher). Library preparation was performed at The Centre for Applied Genomics in The Hospital for Sick Children (Toronto, Canada) following the NEB NEBNext Ultra II Directional RNA Library Preparation protocol. Briefly, 400 ng of total RNA was used as the input material and enriched for poly-A mRNA, fragmented into the 200-300-bases range for 4 min at 94°C and converted to double stranded cDNA, end-repaired and adenylated at the 3' to create an overhang A to allow for ligation of Illumina adapters with an overhang T; library fragments were amplified under the following conditions: initial denaturation at 98°C for 10 s, followed by 15 cycles of 98°C for 10 s, 60°C for 30 s and 72°C for 30 s, and finally an extension step for 5 min at 72°C; at the amplification step, each sample were amplified with a different barcoded adapters to allow for multiplex sequencing. One ul of the final RNA libraries was loaded on a Bioanalyzer 2100 DNA High Sensitivity chip (Agilent Technologies) to check for size; RNA libraries were quantified by qPCR using the Kapa Library Quantification Illumina/ABI Prism Kit protocol (KAPA Biosystems). Libraries were pooled in equimolar quantities and paired-end sequenced on 0.5 lanes of a High Throughput Run Mode flowcell with the V4 sequencing chemistry on an Illumina HiSeq 2500 platform following Illumina's recommended protocol to generate paired-end reads of 126-bases in length. Quality control of raw sequencing reads was performed using FastQC and low-quality reads were removed. PHRED score and sequence duplication levels were calculated using the Galaxy platform (Jalili et al., 2021). Trimmed paired-end reads were aligned to the mouse genome using STAR ultrafast universal RNA-seq aligner.

To calculate transcript abundances, we converted raw reads to TPM values and differential expression analysis was performed using DESeq2 package. Principal component analysis and distribution analysis were used to identify outlier samples. Differences in gene expression were considered statistically significant if the adjusted p-value was less than 0.01 with absolute fold change >2. Enrichment analysis was performed using the gene ontology (GO) found in the Galaxy platform in addition to the PANTHER tool (PANTHER 17.0) for pathway enrichment. Data visualization was done using the DESeq2 and R packages. Heatmaps and clustering of selected genes show the highest and lowest expression for each gene displayed as blue and red (min and max), respectively. Raw and processed data have been deposited in the Gene Expression Omnibus (GEO) repository with the accession number GSE218388 (https://www.ncbi.nlm.nih.gov/geo/query/acc.cgi?acc=GSE218388).

Tooth RNA extraction and quantitative PCR

Ameloblasts were carefully isolated from the molars and incisors of mice aged between P10 to P12 (n = 3 to 4 per genotype) and used for total RNA extraction (RNeasy, Qiagen). After cDNA synthesis (SuperScript III, Thermo Fisher Scientific), the gene expression levels of amelogenin (*Amelx*), ameloblastin (*Ambn*), enamelin (*Enam*), *Orai1*, *Serca1* (expressed by the *Atp2a1* gene), *Serca2* (expressed by the *Atp2a2* gene), *Serca3* (expressed by the *Atp2a3* gene), Plasma membrane Ca2+ ATPase 1 (*Pmca1*, expressed by the *Atp2b1* gene), Plasma membrane Ca2+ ATPase 4 (*Pmca4*, expressed by the *Atp2b4* gene), Na+/Ca2+-K+ exchanger (*NCKX4*, expressed by the *Slc24a4* gene), mitochondrially encoded ATP synthase membrane subunit 6 (*mt-Atp6*), Mitochondrially Encoded NADH:Ubiquinone Oxidoreductase Core Subunit 1 (*mt-Nd1*) and vimentin (*Vim*) (to exclude pulp cells contamination in molars ameloblasts) were assessed by quantitative polymerase chain reaction (RT-qPCR; Applied Biosystem PowerUp SYBR™ Green Master Mix, Thermo Fisher Scientific, Waltham, Massachusetts, United States) with the $2^{-\Delta\Delta CT}$ method. Ameloblasts were also carefully isolated from the molars (P14) and incisors (P28) to assess the expression levels of *Stim1* and *Stim2*. Quantification was calculated relative to the housekeeping B-*actin* gene. All primer sequences were obtained from previous publications or Primer Bank (http://pga.mgh.harvard.edu/primerbank/; Supplementary Table S1).

Immunohistochemistry

Mouse heads were sectioned in a coronal (P5) and sagittal plane (P14). The samples (n = 3 to 4 per genotype) were then fixed in neutral buffered formalin (NBF) and demineralized by ethylenediaminetetraacetic acid (EDTA). Paraffin sections (6 µm) were immune stained to assess STIM1, AMLEX, kallikrein 4 (KLK4) and matrix metalloprotease 20 (MMP20) protein cellular and tissue localization using a rabbit Anti-AMELX antibody (1:1000, ab153915), a rabbit Anti-STIM1 (1:200, LSC34692), a rabbit Anti-KLK4 (1:50, PA5-109888) and a rabbit Anti-MMP20 (1:100, ab198815) after antigen retrievals using proteinase K (DAKO, Santa Clara, USA). Primary antibodies were diluted with an antibody diluent containing phosphate-buffered saline (PBS), bovine serum albumin (BSA), and glycerol (DAKO, Santa Clara, United States). Following several washes by PBS + 1% BSA, the sections were incubated for 30 min with a Horseradish Peroxidase (HRP) conjugated goat anti-rabbit secondary antibody (DAKO, Santa Clara, USA). Visualization with 3-3′diaminobenzidine (DAB) was performed using the peroxidase substrate kit DAB (ab64238, Abcam

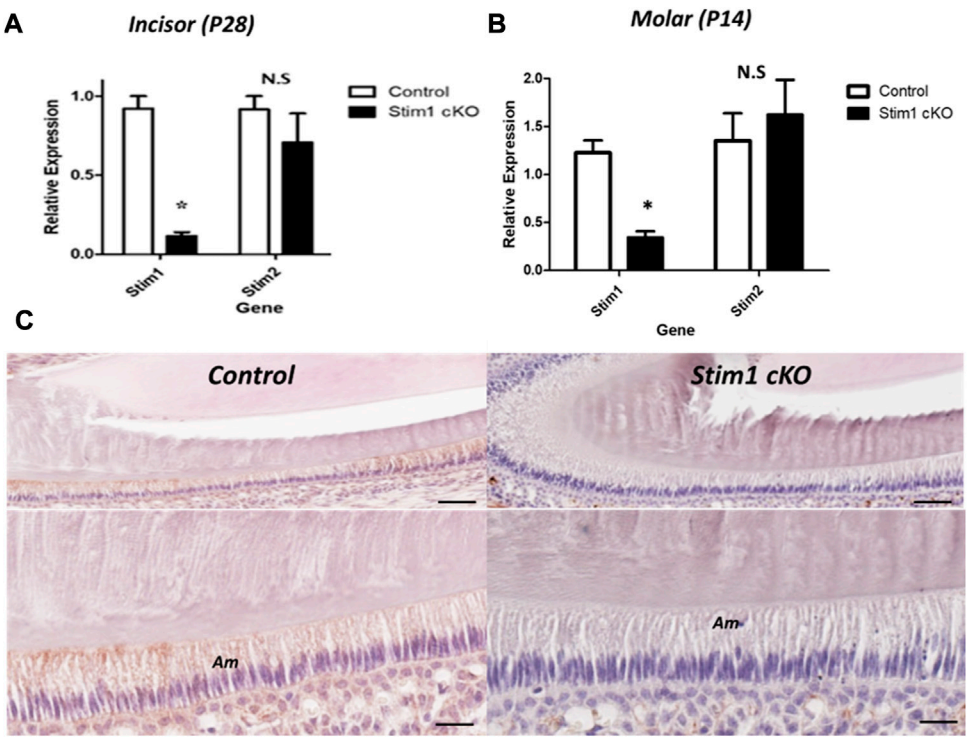

FIGURE 1
Characterization of Stim1 gene deletion. **(A,B)** RT-qPCR analysis in control and Stim1 cKO ameloblasts collected at postnatal day 28 (P28) from incisors **(A)** and at postnatal day 14 (P14) from molars **(B)** showed that the expression levels of *Stim1* were significantly reduced after *Stim1* deletion while the levels of its analog *Stim2* were not significantly reduced. **(C)** IHC of STIM1 antibody confirmed deletion of STIM1 protein in the ameloblasts of incisor teeth collected at postnatal day 14; STIM1 was robustly expressed in the ameloblasts (Am) in control mice while it was barely detected in *Stim1* conditional knock-out mice. The low mag images of the upper panel are enlarged in the lower panel for each sample. Am, ameloblasts. Scale bars; **(C)** 80 μm in low mag panels, 40 μm in high mag panels. (*$p < 0.01$), N.S; non-significant.

Laboratories, Cambridge, United Kingdom) instructions, and the reaction was stopped after 5 min of exposure. Consecutive serial sections from the same mouse models incubated with rabbit serum instead of primary antibody were used as a control. Sections were then mounted and photographed with an EVOS 5000 microscope.

Statistics

All data are presented as mean ± SEM. Student's t-test was used to compare the RT-qPCR relative gene expression, enamel thickness, BSE gray levels and mineral composition. A p-value < 0.05 was considered significant.

Results

Tissue-specific deletion of Stim1

The expression levels of *Stim1* and *Stim2* mRNA were measured to confirm the conditional deletion of *Stim1* in P14 M and P28 incisors' ameloblasts. The *Stim1* expression levels were significantly reduced in Stim1 cKO mice (Figures 1A, B). *Stim2* expression showed no significant difference between the genotypes (Figures 1A, B). Immunohistochemical analysis of two weeks old mice ameloblasts was also performed to identify the protein abundance and localization of STIM1. Control mice showed higher STIM1 signals in the maturation stage ameloblasts as compared with those in the secretory stage. Signals for STIM1 were almost undetectable in incisor ameloblasts of Stim1 cKO mice (Figure 1C). In both groups, STIM1 signals were still clearly detected in mesenchymal-derived tissues and non-ameloblast cell populations indicating that *Stim1* was successfully knocked out specifically in enamel-forming cells and the Cre recombinase effect did not leak to adjacent tissues.

Stim1 cKO mice displayed amelogenesis imperfecta (AI) phenotypes

To assess the effect of loss of STIM1 in enamel, we conducted a detailed examination of the dentition of 4 weeks old male Stim1 cKO mice and compared these to their age-matched control littermates. The teeth shape in the control and cKO mice appeared to be normal. Gross visual inspection of the incisors of Stim1 cKO mice showed an abnormal chalky-white appearance which is often associated with hypomineralization or enamel loss (Figure 2A). Stim1 cKO mice showed greatly reduced enamel at the incisor tips (Figure 2A arrows). The incisor relative enamel thickness (i.e., enamel thickness divided by enamel and dentin thickness) was

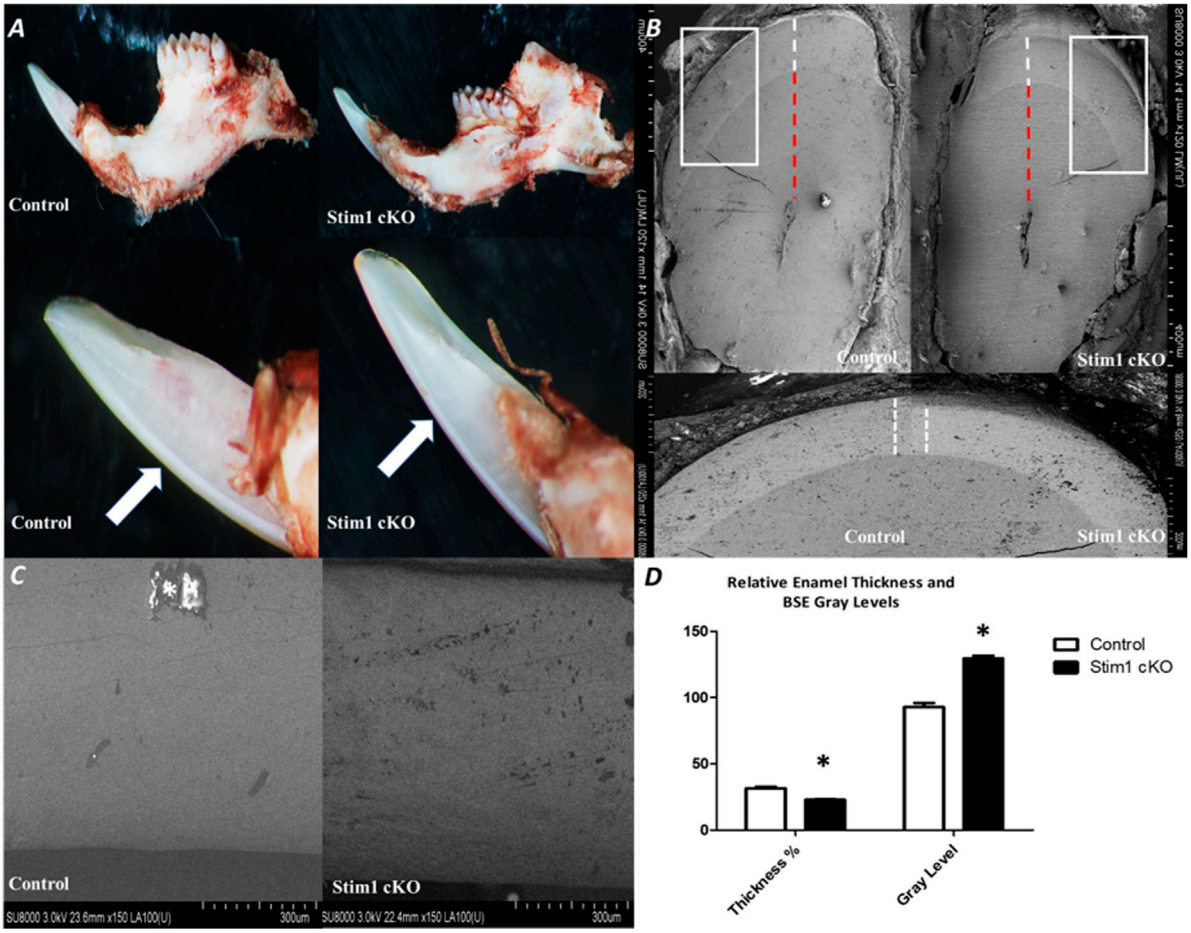

FIGURE 2
Phenotypic analysis of Stim1 cKO incisors **(A)** Gross visual inspection of the P28 incisors of Stim1 cKO mice showed an abnormal chalky-white appearance that is often associated with hypomineralization or enamel loss. Stim1cKO mice showed a greatly reduced enamel thickness closer to the incisor tips (arrows). **(B)** Stim1 cKO incisor displayed a clearly reduced enamel thickness (white dotted line) as compared with control. For quantitative analysis, we measure the enamel thickness and divided it by the total of enamel and dentin (red dotted line) to attain a more representative measure of enamel thickness relative to the crown. **(C)** Backscatter scanning electron microscopy of mid labial surface of control and Stim1 cKO incisors. The Stim1 cKO incisors showed a weaker signal with higher gray levels associated with more abraded enamel surfaces. White spots are overcharging artifacts (star). **(D)** Quantitative analysis of relative enamel thickness and BSE gray levels (*$p < 0.01$).

significantly reduced in Stim1 cKO mice compared to the control (Figure 2B). When imaged using BSE microscopy mode, Stim1 cKO incisors displayed rough enamel surfaces with a lower degree of mineralization and several gray hypomineralized spots (Figure 2C). Indeed, quantitative analysis (n = 3 per group) showed that the enamel of the incisors was thinner and less mineralized in Stim1 cKO mice compared to controls (Figure 2D). No noticeable differences were observed in the enamel phenotype of Stim1 cKO between female and male mice (data not shown).

In the molars, the number and shape of cusps were unchanged between Stim1 cKO and control mice. This indicates that no early developmental disruptions in tooth formation occurred as the number and morphology of cusps are established prenatally. However, SEM imaging revealed significant shape changes (attrition) in the cusp tips of Stim1 cKO mice relative to the control (Figure 3A, arrows). In the area of the highly resilient wavy gnarled enamel, Stim1 cKO mice showed a less compact condensation of gnarled prisms which renders the enamel significantly weaker and greatly impairs its ability to withstand occlusal forces (Figure 3B). Indeed, higher magnification of the ground sections revealed that the crystallites in the bulk enamel in Stim1 cKO mice were less impacted. Moreover, enamel rods were thin, disorganized, and more porous compared with control mice (Figure 3B, stars). This disruption of the rod-interrod pattern may be indicative of changes in the depositional pattern of the enamel matrix. The molar enamel thickness was significantly reduced in Stim1 cKO mice compared to the control.

Stim1 cKO resulted in enamel hypomineralization

To investigate the quality and quantity of enamel mineralization, control and Stim1 cKO hemimandibles were imaged by 3D microcomputed tomography (μCT) at 3 time points (2, 4 and 12 weeks). The threshold value for imaging was raised until

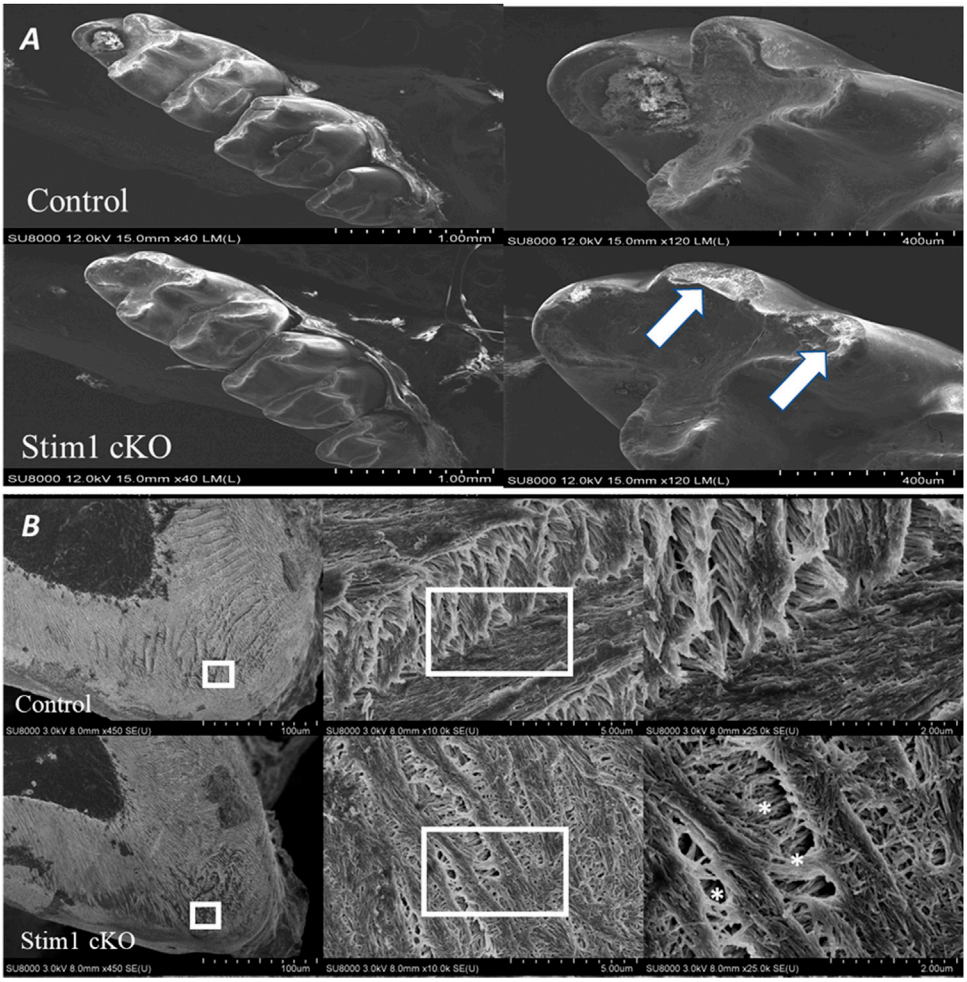

FIGURE 3
Phenotype analysis of 4-week old control and Stim1 cKO mice molars. **(A)** Representative scanning electron microscope (SEM) images of control and Stim1 cKO mice molars. The number and shape of cusps seem unchanged between Stim1 cKO and control mice. However, Stim1 cKO molars displayed significant attrition on the occlusal surfaces when compared with control. The arrows indicate the attritional defects on the occlusal surfaces of the cusps. **(B)** SEM photographs taken at a sagittal section cut through the mandibular first molar. In the area of the highly resilient wavy gnarled enamel, Stim1 cKO mice showed a less compact condensation of gnarled prisms. Higher magnification of the ground sections revealed that crystallites in the bulk enamel in Stim1 cKO mice were less impacted and enamel rods were thin, disorganized, and more porous (stars) as compared with control mice. The rectangular areas are enlarged in the right panel of each image.

enamel became the only mineral displayed in the control group (Figures 4A, B). In 4 and 12 weeks old mice, Stim1 cKO mice showed a significantly reduced volume of high-density mineral relative to the control, especially in the mastication surfaces (incisor tips and molar cusps) (Figure 4B, arrows). Quantitative measurements revealed that the enamel volume and mineral density in Stim1 cKO mice were significantly diminished when compared with the enamel of the control mice. These differences became more significantly pronounced as mice aged (Figures 4C, D). Moreover, the threshold volume of mineralized enamel was reduced in incisors more significantly compared to molars in both young (P14) and old (12 weeks) mice (Figures 4E, F).

To further assess enamel mineralization, we assessed changes in elemental composition in enamel using energy dispersive x-ray spectroscopy (EDS) (Figure 5A). Results showed that the enamel of Stim1 cKO mice is calcium deficient, with a very significant loss of the calcium amount found in controls (Figure 5B). Other key elements present in mineralized enamel, such as phosphorus, were also lower in Stim1 cKO mice than in controls albeit non-significantly. No significant difference was noted in the Ca/P ratio between the Stim1 cKO mice (1.95 ± 0.25) and control mice (2.08 ± 0.22). However, the Ca/C ratio was significantly lower in Stim1 cKO mice (1.22 ± 0.19) compared to control mice (3.60 ± 0.68). On the other hand, data extrapolated from the previous EDS analysis of the labial surface of the incisors done during our pilot study (Said et al., 2019) showed that *Stim1* deletion resulted in a more significant drop of calcium content and the both the Ca/P and Ca/C were more significantly reduced in Stim1 cKO incisors compared to control (Ca/P; 2.92 ± 0.13 in control incisors and 1.42 ± 0.18 in Stim1 cKO, Ca/C; 5.31 ± 1.48 in

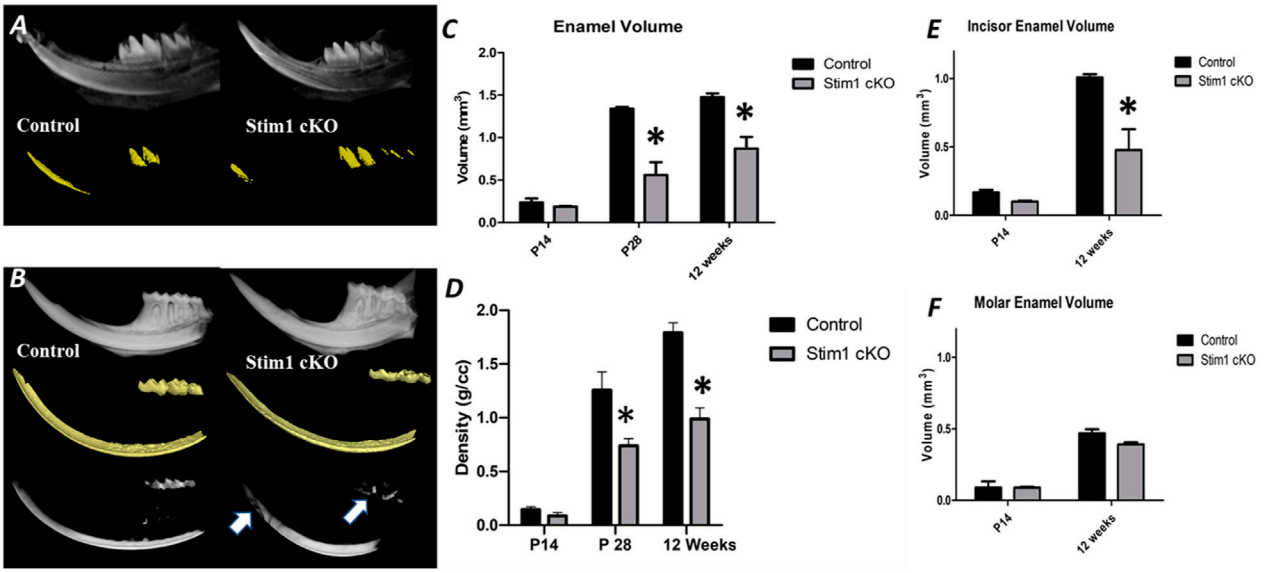

FIGURE 4
Micro-computed tomography (μCT) analysis of enamel. **(A,B)** A 3D μ CT of the control (left column) and Stim1 cKO (right column) hemimandibles collected from mice at postnatal day 14 (P14) **(A)** and 12 weeks **(B)**. The Stim1 cKO mice showed loss of enamel volume (color-coded gold) and thickness in Stim1 relative to their control littermates in incisors and molars at 12 weeks while no significant differences were noticed at P14. For 12 weeks samples the threshold value for imaging was raised until enamel was the only mineral displayed in the control group. the enamel of the teeth working surfaces (i.e., incisor tips and molar cusps) does not reach the threshold level in the Stim1 cKO mice (B, arrows). Quantitative analysis for enamel volume **(C)** and enamel mineralization **(D)** showed that Stim1 cKO enamel displayed reduced volume and mineral densities that increases with age. The threshold volume of mineralized enamel was reduced in incisors **(E)** more significantly compared to molars **(F)** in both young (P14) and old (12 weeks) mice (mean ± SEM of $n = 3$ mice per group; $^*p < 0.05$).

control incisors and 1.14 ± 0.07 in Stim1 cKO) (Supplementary Figures S1A, B).

Altered gene expression in incisors' ameloblasts of Stim1 cKO mice

To analyze the effects of SOCE deficiency in ameloblasts more comprehensively, we extracted RNA from the entire ameloblast populations isolated from the whole incisor enamel organ (EO) of P28 old mice and analyzed global gene expression by RNA sequencing (RNAseq). The ameloblasts' RNA was extracted from 3 samples ($n = 1$ per genotype); 1 Stim1 cKO sample with complete deletion of *Stim1*, 1 Stim1 HT sample with heterozygous deletion of one *Stim1* allele and 1 Stim1 Ctrl with no *Stim1* deletion as it was Cre negative. Interestingly, Stim1 heterozygous knock-out mice did not show a clear loss-of-function enamel phenotype which may indicate that the *Stim1* gene is relatively haplosufficient during amelogenesis. Moreover, hierarchical clustering of the samples showed that the Stim1 HT and Stim1 Ctrl had a relatively similar gene expression profiles (Figure 6A). The three samples showed very low read counts of vimentin when compared to the much higher read counts of *AmelX* and *Ambn* transcripts, which indicates a minimal degree of mesenchymal contamination. We identified a total of 2277 differentially expressed genes in Stim1 cKO compared to the grouped Stim1 HT and Ctrl cells, of which 1264 were significantly upregulated and 1014 genes were significantly downregulated (adjusted p-value <0.01, absolute fold change >2) (Figure 6B) (Supplementary Datasheet S1).

The exploratory RNAseq data indicate that *Stim1* deficient mice showed considerably lower average values in the expression of the enamel genes *AmelX, Enam and Ambn* and higher average values in the expression of Odontogenic ameloblast-associated protein (*Odam*) compared to both Stim1 HT and Ctrl cells (Figure 6C). Moreover, loss of *Stim1* appears to cause additional changes in the expression of several genes that encode calcium pumps and exchangers that are thought to be involved in transcellular calcium transport during amelogenesis. Indeed, Stim1 cKO ameloblasts showed higher expression levels of the SERCA3 pump (encoded by the gene *Atp2a3*) and the Plasma membrane Ca2+ ATPase 1 (PMCA1 pumps) (encoded by the *Atp2b1* gene). Furthermore, the expression levels of the Na+/Ca2+-K+ exchangers 1 & 2 (NCKX1 & 2; encoded by the genes *Slc24a1 & 2*, respectively) were also upregulated in Stim1 cKO ameloblasts (Figure 6D). NCKX4 was also upregulated in Stim1 cKO mice with an adjusted p-value that is near significance (adj. $p < 0.05$) when compared to both Stim1 HT and Stim1 Ctrl. Panther pathway analysis showed that ATP synthesis is the most enriched pathway in EO cells of Stim1 cKO mice (Supplementary Table S2). Indeed, the expression levels of several subunits of the respiratory chains' mitochondrial proteins NADH dehydrogenase and cytochrome oxidase were upregulated in Stim1 cKO ameloblasts compared to both Stim1 HT and Ctrl cells (Figure 6E).

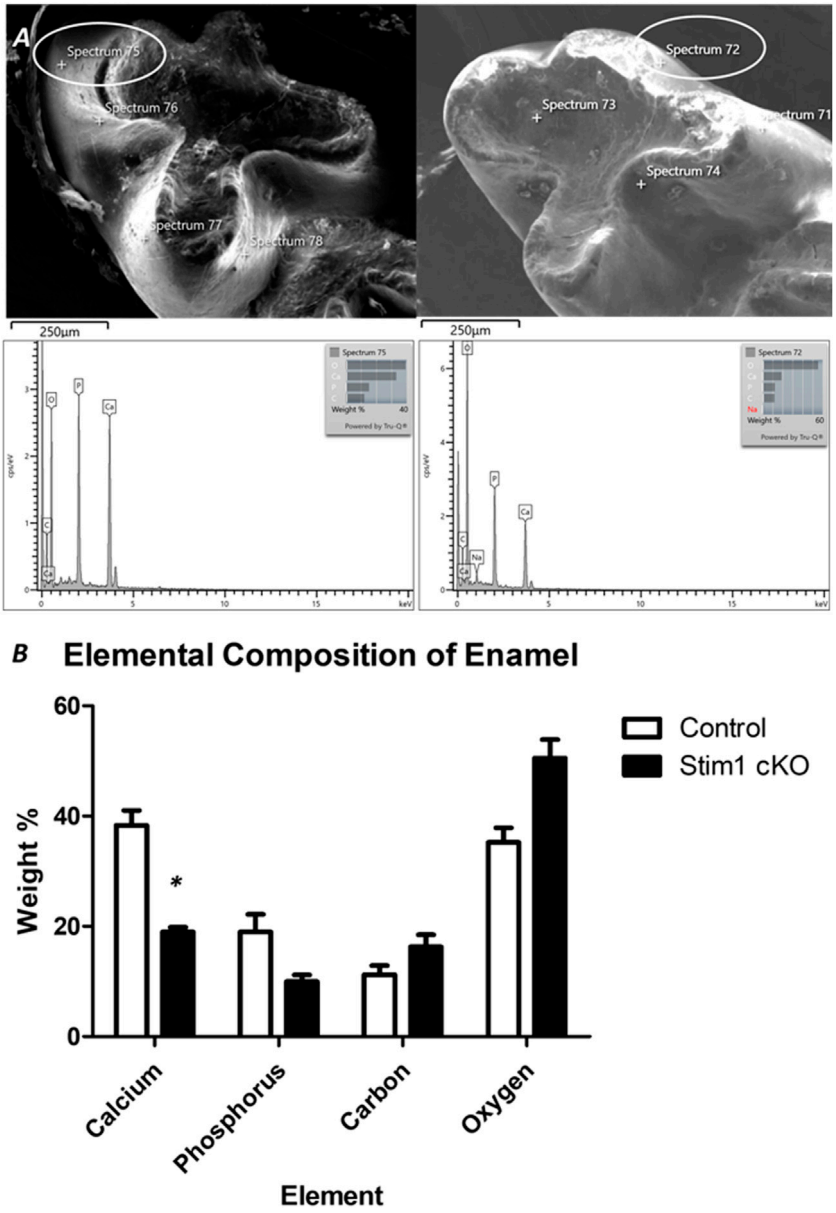

FIGURE 5
Elemental composition analysis of enamel. **(A)** To assess enamel mineralization, we analyzed changes in elemental composition in enamel using energy dispersive x-ray spectroscopy (EDS). For EDS, 4 beams were generated on the cusp slopes of maxillary first molars that received no processing of the enamel surface in order not to alter its composition. The lower row shows the peaks generated from the circled areas. **(B)** Quantitative analysis of representative average measurements taken by EDS of elemental composition of the enamel of control and Stim1 cKO enamel. Results show that the enamel of Stim1 cKO mice is Ca deficient, with a very significant loss of the Ca amount found in controls (Figure 5B). Other key elements present in mineralized enamel, such as phosphate (P), were also lower in Stim1 cKO mice compare to controls albeit non-significantly. (mean ± SEM of n = 3 mice per group; $*p < 0.05$).

To further explore these changes and attain statistical significance, we performed RT-qPCR analysis on ameloblasts isolated from the molars and incisors of mice aged between P10 to P12 (n = 3 to 4 per genotype) to asses changes in the expression levels of several genes of interest. Our analysis showed that the expression levels of the genes encoding the enamel matrix proteins *AmelX* and *Ambn* were upregulated in Stim1 cKO incisors ameloblasts compared to control (Figure 7A). However, no significant changes were observed in the molars ameloblasts albeit having lower RNA levels of *Amelx, Ambn and Enam* (Figure 7B). No clear differences were found between the Stim1 HT and Stim1 Ctrl in the expression of the main enamel genes which may explain the lack of phenotype in Stim1 HT mice. Furthermore, immunostaining for the AMELX protein was performed to supplement the qPCR results. Immunostaining showed a weaker signal AMELX in Stim1 cKO compared to their sex- and age-matched controls but the change was more pronounced in incisors' ameloblasts compared to molars

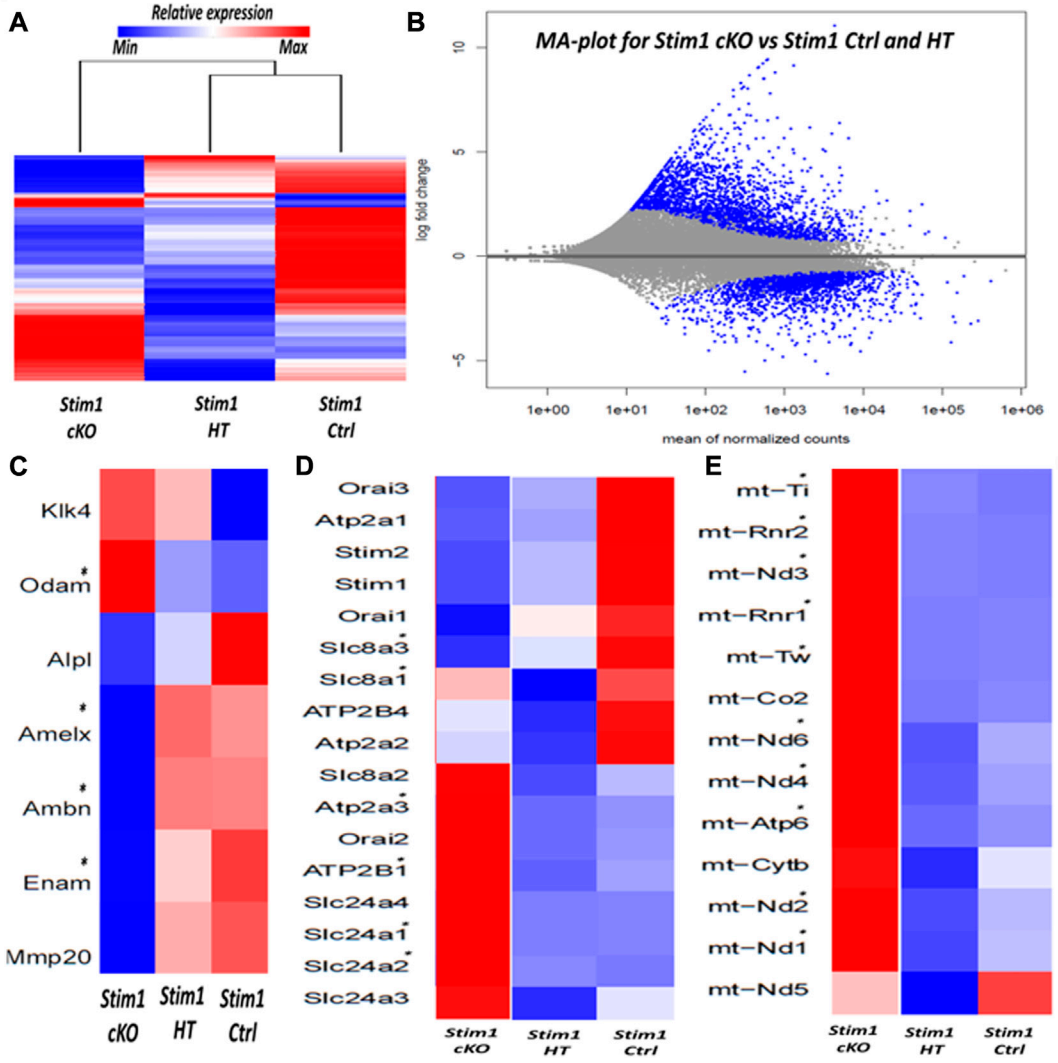

FIGURE 6
RNA sequencing of enamel organ cells in Stim1 cKO incisors mice highlights changes in enamel proteins and mitochondrial pathways **(A)** Heatmap and dendrogram showing clustering of samples with similar gene expression, the genetic profile of Stim1 HT was closely correlated to Stim1 Ctrl **(B)** MA plot of magnitude of differential gene expression in Stim1 cKO compared to both Stim1 HT and Stim1 Ctrl (shown as the log base 2 of magnitude of mean expression difference on the *y*-axis *versus* the mean of normalized counts on the *x*-axis). The differentially expressed genes (adj. $p < 0.01$, absolute fold change of more than 2) are shown in blue. **(C)** Heatmap based on the expression of enamel genes. Clear differences in expression can be observed in *AmelX, Ambn, Enam and Odam* in Stim1 cKO compared to both Stim1 HT and Stim1 Ctrl. No clear differences were found between the Stim1 HT and Stim1 Ctrl in the expression of the main enamel genes **(D)** Heatmap based on the expression of genes involved in calcium transport. Several differences in expression can be observed in genes encoding the calcium pumps SERCA3, PMCA1 in addition to the calcium exchangers NCKX1 and NCKX2 in Stim1 cKO compared to both Stim1 HT and Stim1 Ctrl. NCKX4 was also upregulated in Stim1 cKO mice with an adjusted *p*-value that is near significance (adj. $p < 0.05$) **(E)** A heatmap showing the expression levels of several mitochondrial RNA's. Of interest, expression of several NADH dehydrogenase and cytochrome oxidase subunits were upregulated in Stim1 cKO amelobalsts. No clear differences were found between the Stim1 HT and Stim1 in the expressions of most of these mitochondrial subunits (*adjusted $p < 0.01$).

(Figure 7C). We also performed immunostaing of enamel proteases MMP20 and KLK4 which also showed a weaker signal of both proteins in Stim1 cKO compared to their sex- and age-matched controls albeit the change was less clearly observed in KLK4 (Supplementary Figure S2).

As for genes involved in calcium transport, our RT-qPCR analysis showed that *Stim1* deletion has resulted in significant upregulation of several genes encoding proteins that are essential for SOCE and transcellular calcium transport during amelogenesis. However, these changes appear to be more pronounced in molars' ameloblasts. Indeed, of the 7 genes we investigated (genes encoding ORAI1, SERCA1,2,3, PMCA1,4 and NCKX 4), our results showed that Stim1 cKO incisors ameloblasts displayed a significantly higher expression of three genes involved in calcium transport (SERCA3, NCKX4 and PMCA1) compared to control while molars Stim1 cKO ameloblasts had a significantly higher expression of 6 genes (SECA2, SERCA3, NCKX4, PMCA1 and PMCA4) compared to control (Figures 8A–D). Similar to the genes encoding the enamel matrix proteins, no clear differences were found between the Stim1 HT and Stim1 Ctrl in the expression of the aforementioned genes. Finally,

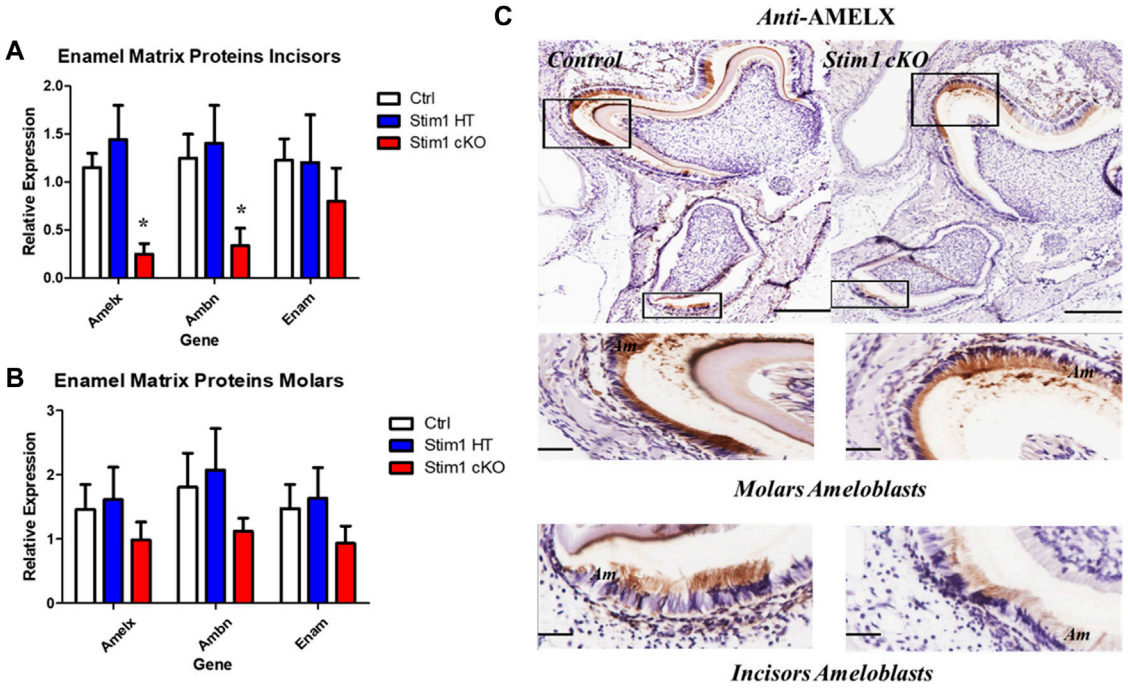

FIGURE 7
Enamel matrix genes and proteins expression analysis of Stim1 cKO mice. Gene expression analysis in incisors **(A)** and molars **(B)** ameloblasts from control and Stim1 cKO mice (mean ± SEM, n = 3~4 mice per genotype; *$p < 0.05$ compared to Ctrl). Our analysis showed that the expression levels of the genes encoding the enamel matrix proteins AmelX and Ambn were upregulated in Stim1 cKO incisors ameloblasts compared to control. However, no significant changes were observed in the molars ameloblasts albeit having lower RNA levels of AmelX, Ambn and Enam. No clear differences were found between the Stim1 HT and Stim1 Ctrl in the expression of the main enamel genes. **(C)** Immunostaining of the mandibular molar and incisor tooth buds showed reduced protein levels of Amelogenin in Stim1 cKO as compared with age-matched controls. The change was more pronounced in incisors' ameloblasts compared to molars. The rectangular areas are enlarged in the lower panels for each image. Scale bars: **(C)** 250 μm in the upper low mag panels and 50 μm in the lower high mag panels.

the expression levels of the mitochondrial RNAs *mt-ND1* and *mt-Atp6* were significantly upregulated in Stim1 cKO ameloblasts compared to controls in both incisor and molar ameloblasts (Figures 8E, F). However, the degree of upregulation was more significant in Molars' ameloblasts. No clear differences were found between the Stim1 HT and Stim1 Ctrl in the expressions of these mitochondrial genes which may further explain the lack of a clear enamel phenotype in Stim1 HT mice.

Discussion

The data presented here demonstrate that Stim1 cKO mice may serve as a valuable model for assessing the effects of Ca2+ deficiency in enamel. Abolishing SOCE resulted in the development of a clearly defective enamel phenotype and altered ameloblast function. In particular, these findings implicate SOCE channels as essential players in the mineralization process of dental enamel. In addition, our data also suggest that SOCE-mediated calcium entry influences several ameloblasts' cellular functions including enamel secretion and oxidative phosphorylation. Furthermore, our data suggest that the effects of *Stim1* deletion differs considerably between incisors and molars. Indeed, our results suggest that SOCE invalidation in incisors' ameloblasts has resulted in a higher degree of enamel hypomineralization associated with reduced enamel matrix proteins synthesis and lower mitochondrial activity and biogenesis compared to molars. Finally, our results showed that partial heterozygous deletion of *Stim1* does not appear to cause significant changes in the enamel phenotype and ameloblasts genotype.

Consistent with abnormal amelogenesis, our morphometric analysis of Stim1 cKO dentition revealed that the enamel of *Stim1* deficient mice was thinner and presented with impaired structural integrity compared to controls. The surface enamel of Stim1 cKO mice produced weaker BSE-SEM signals relative to controls, which is highly consistent with decreased mineralization. This hypomineralization was further confirmed by micro-computed topography and EDS elemental composition analysis of enamel, showing decreased mineral density and diminished calcium content, respectively. Our micro-CT analysis showed that enamel defects were more pronounced in older mutant mice compared to younger ones and the threshold volume of mineralized enamel was reduced in incisors more significantly compared to molars in both young (P14) and old (12 weeks) mice. We hypothesize that Stim1 cKO ameloblasts did form enamel during the early stages of amelogenesis, however, the enamel was mineral deficient and mechanically weaker resulting in a more rapid rate of wear and attrition with time, ensuing a stronger

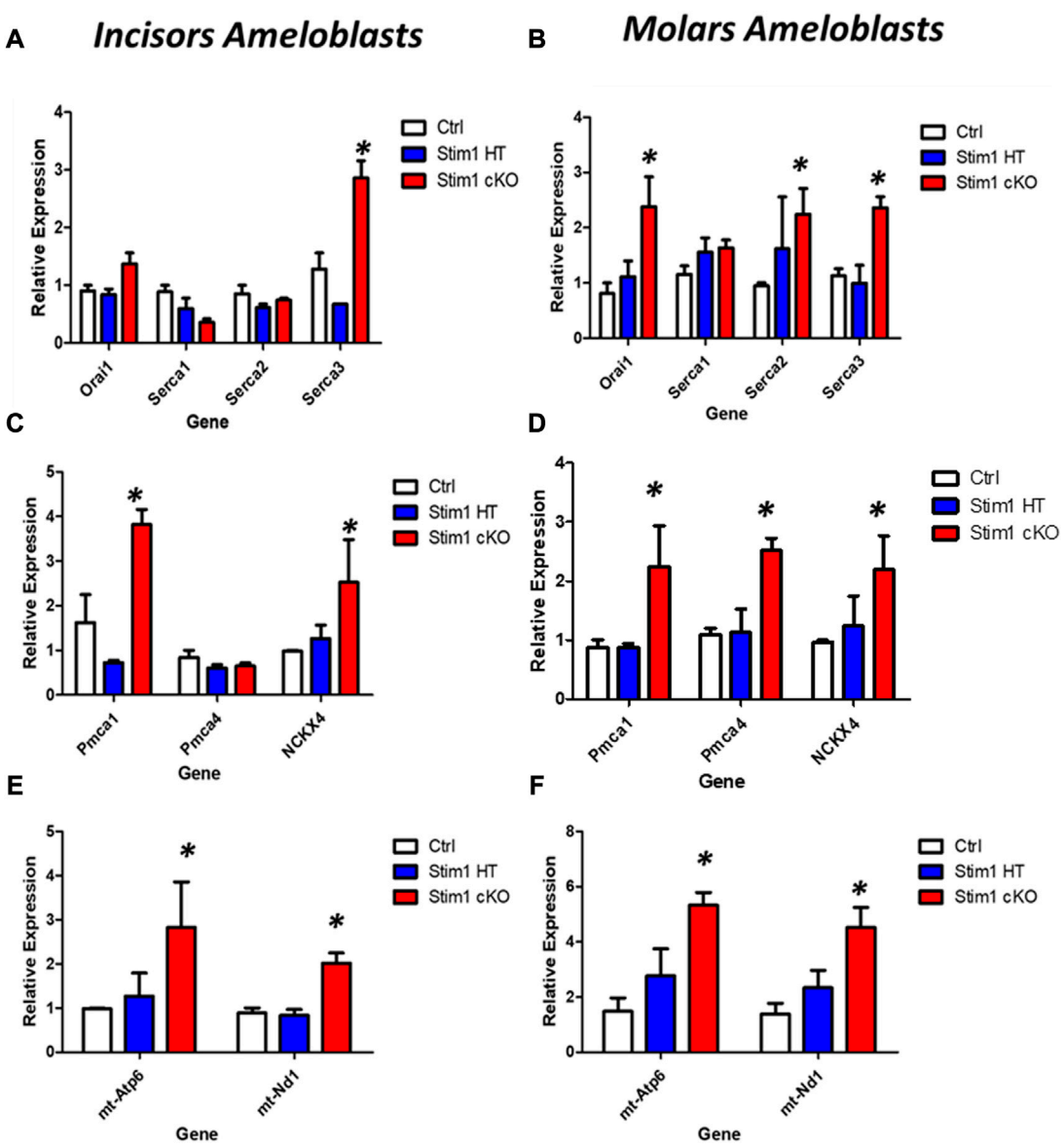

FIGURE 8
Calcium transport and mitochondrial gene expression analysis of Stim1 cKO mice. **(A–D)** Expression analysis for genes involved in calcium transport in molars and incisors ameloblasts collected from control and Stim1 cKO mice. Our RT-qPCR analysis showed that Stim1 deletion has resulted in significant upregulation of several genes encoding proteins that are essential for SOCE and transcellular calcium transport during amelogenesis. These changes appear to be more pronounced in molars' ameloblasts as the 7 genes we investigated molars Stim1 cKO ameloblasts had a significantly higher expression of 6 genes (SECA2, SERCA3, NCKX4, PMCA1 and PMCA4) compared to control (genes encoding ORAI1, SERCA1,2,3, PMCA1,4 and NCKX 4) while Stim1 cKO incisors ameloblasts displayed a significantly higher expression of three genes involved in calcium transport (SERCA3, NCKX4 and PMCA1) compared to control. Similar to the genes encoding the enamel matrix proteins, no clear differences were found between the Stim1 HT and Stim1 Ctrl in the expression of the seven genes. **(E,F)** Expression analysis for the mitochondrial genes (mt-Atp6 and mt-Nd1) in molars and incisors ameloblasts collected from control and Stim1 cKO mice. The expression levels of both mitochondrial genes were significantly upregulated in Stim1 cKO ameloblasts compared to controls in both incisor and molar ameloblasts. However, the degree of upregulation was more significant in Molars' ameloblasts. No clear differences were found between the Stim1 HT and Stim1 Ctrl in the expressions of these mitochondrial genes (mean ± SEM, n = 3~4 mice per genotype; *$p < 0.05$ compared to Ctrl).

enamel phenotype with age. The reduced mineral content observed early in the incisor enamel rendered it more susceptible to attrition compared to molars. No significant difference was noted in the Ca/P ratio between the Stim1 cKO mice and control mice molars as both elements were reduced after *Stim1* depletion. However, the Ca/C ratio was significantly lower in Stim1 cKO mice compared to control mice which may indicate that Stim1 cKO enamel matrix has a higher organic content compared to controls. On the other hand, EDS analysis of the labial surface of the incisors showed that *Stim1* deletion resulted in a more significant drop of calcium content and the both the Ca/P and Ca/C were more significantly reduced in Stim1 cKO incisors compared to control which further suggests a higher degree of enamel hypomineralization in incisors compared to molars. Finally,

Stim1 cKO enamel showed an abnormal prismatic pattern and the structural integrity of the enamel of Stim1 cKO mice appears to be significantly weaker. Generally, the enamel phenotype observed in these mice resembles the hypomineralized amelogenesis imperfecta observed in ectodermal dysplasia patients with impaired SOCE (Lacruz and Feske, 2015).

As has been described in previous reports (Lacruz et al., 2011; Lacruz et al., 2012; Nurbaeva et al., 2015a; Nurbaeva et al., 2015b; Eckstein and Lacruz, 2018), we found that expression of *Stim1* is higher in the maturation stage ameloblasts as compared to those in the secretory stage in both incisor and molars ameloblasts. Moreover, the ablation of *Stim1* did not affect the expression levels of *Stim2*. It has been previously shown that while the *Stim2* mRNA expression was as abundant as that of *Stim1* in maturation ameloblasts, the STIM1 protein levels are higher than those of STIM2 (Lacruz et al., 2012). Thus, the fact that our Stim1 cKO mice exhibited dramatically suppressed enamel mineralization despite still having a functional *Stim2* gene may be attributed to the reported difference in the production levels of STIM1 and STIM2, which indicates that STIM1 is the main ER calcium sensor in enamel. Indeed, other models with Stim2 cKO did not cause any apparent enamel phenotypes (Furukawa et al., 2017; Eckstein and Lacruz, 2018). which further suggests that STIM1 plays a more significant role in regulating Ca+ during amelogenesis.

In addition to its role in the transcellular Ca2+ transport across the ameloblasts during enamel mineralization, STIM1 and SOCE-mediated calcium entry may play an important role in regulating enamel gene expression during the secretory stage of amelogenesis. Indeed, it has been established that *Stim1* mRNA and protein are expressed in rodent teeth throughout the secretory stage of amelogenesis (Lacruz et al., 2012; Nurbaeva et al., 2015a; Chen et al., 2018). In fact, Chen et al., 2018 have shown that STIM1 protein can be clearly detected in murine ameloblasts, odontoblasts and craniofacial osteoblasts as early as postnatal day 3. SOCE-mediated signalling in ameloblasts is rendered more intriguing by the well-known role of calcium as a second messenger with a broad signalling profile. Our gene expression analysis of incisors' ameloblasts strongly suggests that SOCE-mediated signalling may affect the expression of the genes encoding main secretory enamel proteins as Stim1 cKO ameloblasts showed a considerably lower expression *AmelX, Ambn* compared to control. On the other hand, RT-qPCR analysis showed lower but non-significant differences in the average expression levels of *AmelX and Ambn* in molar ameloblasts of *Stim1* deficient mice and immunostaining showed a weaker signal AMELX in Stim1 cKO compared to their sex- and age-matched controls, but the change was more pronounced in incisors' ameloblasts compared to molars. These inconsistent and sometimes contradictory effects of SOCE ablation on enamel matrix proteins gene expression have been reflected in the literature. For example, Nurbeava et al. (2015b) showed that the expression of these enamel genes was upregulated by an increase in cytosolic [Ca2+] mediated by stimulation of SOCE with thapsigargin in both the enamel cell line LS8 and in primary EO cells. Subsequent inhibition of SOCE in LS8 cells has reversed this effect which suggest that SOCE invalidation downregulate the enamel matrix proteins expression similar to what we observed in our incisors (Nurbaeva et al., 2015b). On the other hand, RNAseq data of $Stim^{1/2K14cre}$ cKO mice showed lower but non-significant average values in the expression of *AmelX* as well as *Enam* similar to what we observed in our molars ameloblasts (Eckstein et al., 2017). Another analysis of $Stim^{1/2K14cre}$ cKO molars ameloblasts by Furukawa et al., 2017 showed no significant differences in the expression levels of *AmelX* and *Ambn* (Furukawa et al., 2017). Finally, a more recent study by Eckstein et al., 2019 showed that the expression of *AmelX* was slightly increased while *Enam* was significantly increased in EO cells of $Orai1^{K14}$ cKO mice and expression of both genes was significantly decreased in enamel cells of Orai2 null mice with no differences detected in *Ambn* in either $Orai1^{K14}$ cKO or Orai2 null mice. Based on all of the above, it appears that SOCE mediated calcium signalling may play a minor yet heterogenous role during enamel secretion in addition to its well-established role late in enamel mineralization and maturation. However, it remains unclear how the different components of SOCE affects the expression of the different main enamel matrix proteins and a more specific analysis like single cell genomics are still needed to explain this apparent heterogeneity of the results.

On the protein level, we also analyzed AMELX, MMP20 and KLK4 protein expression levels and found weaker signals in the enamel of Stim1 cKO mice thus further suggesting the overall downregulation of key ameloblast proteins in Stim1 cKO. AMELX is the most abundant enamel matrix protein (90%) and is essential for amelogenesis (Shin et al., 2020). Amelogenin-deficient mice are known to display a severe AI phenotype (Simmer et al., 2021). MMP20 and KLK4 are the most crucial proteases for the proper processing, degradation, and uptake of enamel matrix proteins by ameloblasts during enamel maturation and mineralization (Furukawa et al., 2017). In mice lacking KLK4, a defective rod-interod arrangement is observed in the first formed inner enamel near the dentino-enamel junction (Goldberg et al., 2014). Thinner and structurally abnormal incisor enamel is observed in MMP20 KO mice (Simmer et al., 2021). Generally, *AmelX, Mmp20 and Klk4* KO mice all show different degrees of enamel AI phenotype including hypoplasia, hypomineralization, and hypomaturation (Wright et al., 2008; Simmer et al., 2010). This is consistent with our findings of AI phenotype observed in our Stim1 cKO where AMELX, MMP20 and KLK4 proteins production appears to be downregulated.

Our gene expression analysis showed that *Stim1* ablation has resulted in significant upregulation of genes encoding the ATP-dependent calcium pumps SERCA3 and PMCA1 in addition to the calcium exchanger NCKX4 in incisors ameloblasts. The aforementioned 3 genes were also significantly upregulated in molars Stim1 cKO ameloblasts in addition to the 2 other isoforms of calcium pumps (SERCA2 and PMCA4) and the SOCE component ORAI1. SERCAs transport cytosolic Ca2+ into the ER lumen to replenish the intracellular stores, whereas PMCAs extrude cytosolic Ca2+ out of the cell (Bronckers, 2017). The three isoforms of SERCA pumps have been shown to be expressed in rodent ameloblast both *in vitro* and *in vivo* (Nurbaeva et al., 2015a; Nurbaeva et al., 2015b). Several reports have suggested that PMCAs may play an important role in calcium transport during amelogenesis as they were strongly expressed during both the secretory and maturation stages of amelogenesis with PMCA1 and 4 being the dominant isoforms (Borke et al., 1995; Zaki et al., 1996; Bomfim et al., 2023). NCKXs are believed to be involved in Ca2+ clearance from ameloblasts as all NCKX isoforms are expressed by rodent ameloblasts (Nurbaeva et al., 2017; Paine

et al., 2020). The NCKX4 in particular is thought to be critical for enamel maturation as it is heavily expressed in maturation-stage ameloblasts (Bronckers, 2017). This crucial role of NCKX4 in enamel mineralization has been further elucidated by studies showing that mutations in NCKX4 in humans and mice result in abnormal hypomineralized enamel similar to the enamel observed in patients with SOCE mutation (Parry et al., 2013; Khan et al., 2020). It is possible that the increased expression of SERCA and PMCA pumps observed here in Stim1 cKO enamel cells is needed to compensate for the lower cytosolic concentration and maintain some level of calcium transport during enamel maturation. The higher degree of upregulation of these pumps in addition to upregulation of ORAI1 in molars compared to incisors may explain the lower degree of hypomineralization observed in Stim1 cKO molar enamel compared to incisors. An increased expression of SERCA2 has been reported in ORAI1-deficient cells compared to control cells to enhance the ER calcium replenishing (Eckstein et al., 2019). Overexpression of STIM1 was shown to attenuates PMCA-mediated Ca2+clearance in T-lymphocytes cell lines (Ritchie et al., 2012) However, no changes in either the SERCA or PMCA pumps were reported in Stim$^{1/2K14cre}$ cKO ameloblasts. As for NCKX4, contradictory results have been reported on the effect of SOCE on this apical ion transporter. Eckstein et al. (2017) showed that NCKX4 localization was dysregulated in Stim$^{1/2K14cre}$ and attributed it to disrupted ameloblasts cytoskeletal assembly of ruffled border (Eckstein et al., 2017). On the other hand, Furukawa et al. (2017) found no obvious differences in the expression and localization NCKX4 in Stim1/2^{K14Cre} ameloblasts compared to the control. Generally, and similar to the effects on enamel matrix proteins, further studies are still needed to fully evaluate the exact state of calcium transport after SOCE dysregulation.

Among the top functions identified in the pathway analysis of the differentially expressed genes, ATP synthesis was the most prominent. Indeed, our gene expression data showed that SOCE ablation has resulted a very significant upregulation of mitochondrial gene expression which suggests an increased rate of mitochondrial biogenesis, ATP production and reactive oxygen species (ROS) production in ameloblasts. The degree of mitochondrial genes upregulation was more significant in molars ameloblasts compared to incisors. We postulate that a higher mitochondrial metabolic activity may be needed to compensate for the increased ATP demand by the upregulated ATP dependent calcium pumps (i.e., SERCAs and PMCAs) observed in Stim1 cKO ameloblasts. The higher rate of mitochondrial genes expression upregulation observed in molars may correspond to the previously noted higher rates of calcium pumps over-expression in molars ameloblasts which may further explain the lower degree of hypomineralization observed in Stim1 cKO molar enamel compared to incisors. The links between SOCE and mitochondrial homeostasis are well documented in the literature (Hawkins et al., 2010; Henke et al., 2012; Srikanth and Gwack, 2012; Deak et al., 2014). For example, Henke et al., 2012 showed that STIM1 and ORAI1 deficiency in murine fibroblasts rendered the cells more susceptible to oxidative stress, which was later rescued by STIM1 and ORAI1 overexpression (Henke et al., 2012). Moreover, they showed that Stim1 knock-out mitochondria are tubular and are metabolically more active, resulting in constitutive oxidative stress (Henke et al., 2012). The upregulation of the electron transport chain components in our Stim1 cKO EO cells suggests that *Stim1* deletion may eventually lead to a similar increased metabolic activity and increased oxidative stress and reactive oxygen species (ROS) production in ameloblasts. In the context of amelogenesis, SOCE abrogated ameloblasts of Stim1/2^{K14cre} cKO mice generated by Eckstein et al. (2017) showed abnormal mitochondrial morphology and a significant increase in ROS levels compared with control cells as the oxidative stress response and glutathione metabolism pathways were the most enriched in EO cells from Stim1/2^{K14cre} cKO mice (Eckstein et al., 2017). Furukawa et al. (2017) also suggested that SOCE mediated mitochondrial dysfunction maybe one of the main underlying mechanisms involved in the development of the AI phenotype observed in their Sitm1/2 cKO mice as well (Furukawa et al., 2017). Furthermore, ORAI1-deficient LS8 enamel cells showed a higher oxygen consumption and ATP production rate compared to ORAI2-and ORAI3-deficient or control cells (Eckstein et al., 2019). Collectively, all these data strongly suggest an abnormal mitochondrial function in *Stim1*-deficient ameloblasts and highlight the relevance of mitochondrial apparatus in enamel forming cells, an area that still needs more research.

Generally, our data suggest that SOCE dysregulation exerts a differential effect on the enamel phenotype and ameloblasts genotype between incisors and molars. Indeed, our results suggest that SOCE invalidation in incisors' ameloblasts has resulted in a higher degree of enamel hypomineralization associated with reduced enamel matrix proteins and mitochondrial biogenesis compared to molars. These differences may be attributed to the several structural and molecular differences observed between the incisor and molar enamel. Indeed, several differences of enamel phenotype were also observed between incisor and molar from other knock-out (KO) mice depleted for genes necessary for enamel secretion and maturation (Goldberg et al., 2014). For example, The Na + -independent anion exchanger 2 (Ae2) plays a role in pH modulation during the maturation phase of amelogenesis (Goldberg et al., 2014). In Ae2 KO mice, a more pronounced decrease in mineral content and the presence of a high organic matrix are observed in the incisors compared to molars(Lyaruu et al., 2008). Furthermore, αvβ 6 integrins deficient mice also show a more severely defective enamel phenotype in the incisor compared to molars (Mohazab et al., 2013). The differences in the enamel phenotype and genetic profiles between molars' and incisors' ameloblasts of Stim1 cKO mice need to be further tested in the future. A more comprehensive comparison between molars and incisors in Stim1 cKO mice is still required to fully confirm the discrepancies between the two teeth observed here. Finally, our results suggest that heterozygous partial deletion of *Stim1* does not appear to cause significant changes in the ameloblasts genetic profile and no significant changes were observed in the expression levels of the 12 genes we analyzed here between Stim1 HT and control mice.

In conclusion, this study reveals that *Stim1* plays a critical role in enamel maturation and mineralization as its abrogation has resulted in the development of a hypomineralized enamel phenotype that is more severe in incisors. In addition to its role of regulating calcium transport during enamel mineralization, gene expression analysis showed that several genes were differentially expressed in Stim1 cKO incisor ameloblasts, suggesting that SOCE-mediated signalling may play critical roles in amelogenesis. Indeed, our

data suggest that *Stim1* may regulate enamel matrix protein expression and mitochondrial function during amelogenesis. However, it must be noted that *Stim1* disruption appears to cause a diverse effects of the abovementioned pathways that considerably vary between molars and incisors ameloblasts. The main limitation of this study is the lack of a sufficient number of biological replicates in the RNAseq analysis as the global gene expression analysis presented here is only intended to serve as an exploratory pilot investigation. Additional gene and protein expression studies are still needed to comprehend the full spectrum of *Stim1* downstream targets in ameloblasts.

Data availability statement

The datasets presented in this study can be found in online repositories. The names of the repository/repositories and accession number(s) can be found in the article/Supplementary Material.

Ethics statement

The animal study was reviewed and approved by The University Animal Care Committee (UACC) at the University of Saskatchewan, Canada.

Author contributions

RS, SP, and PP conceived the study. RS performed experimental procedures, data analysis, experimental designing, and manuscript writing. HM performed data analysis and provided scientific support. DC assisted in micro-computed analysis and helped in manuscript writing. KO and IM assisted in RNA seq data analysis. SP and PP provided scientific support and helped in manuscript writing. All authors read and approved the submitted version of the manuscript.

Funding

This work was partially funded by the University of Saskatchewan College of Dentistry start-up funds to PP and by the University of Saskatchewan College of Medicine and Vice Provost Office start-up funds to SP.

Conflict of interest

The authors declare that the research was conducted in the absence of any commercial or financial relationships that could be construed as a potential conflict of interest.

Publisher's note

All claims expressed in this article are solely those of the authors and do not necessarily represent those of their affiliated organizations, or those of the publisher, the editors and the reviewers. Any product that may be evaluated in this article, or claim that may be made by its manufacturer, is not guaranteed or endorsed by the publisher.

Supplementary material

The Supplementary Material for this article can be found online at: https://www.frontiersin.org/articles/10.3389/fphys.2023.1100714/full#supplementary-material

References

Bailleul-Forestier, I., Davideau, J. L., Papagerakis, P., Noble, I., Nessmann, C., Peuchmaur, M., et al. (1996). Immunolocalization of vitamin D receptor and calbindin-D28k in human tooth germ. *Pediatr. Res.* 39, 636–642. doi:10.1203/00006450-199604000-00013

Berdal, A., Papagerakis, P., Hotton, D., Bailleul-Forestier, I., and Davideau, J. L. (1995). Ameloblasts and odontoblasts, target-cells for 1,25-dihydroxyvitamin D3: A review. *Int. J. Dev. Biol.* 39, 257–262.

Berna-Erro, A., Jardin, I., Salido, G. M., and Rosado, J. A. (2017). Role of STIM2 in cell function and physiopathology. *J. Physiol.* 595, 3111–3128. doi:10.1113/JP273889

Bomfim, G. H. S., Giacomello, M., and Lacruz, R. S. (2023). PMCA Ca(2+) clearance in dental enamel cells depends on the magnitude of cytosolic Ca(2). *FASEB J. Off. Publ. Fed. Am. Soc. Exp. Biol.* 37, e22679. doi:10.1096/fj.202201291R

Borke, J. L., Zaki, A. E.-M., Eisenmann, D. R., and Mednieks, M. I. (1995). Localization of plasma membrane Ca2+ pump mRNA and protein in human ameloblasts by *in situ* hybridization and immunohistochemistry. *Connect. Tissue Res.* 33, 139–144. doi:10.3109/03008209509016993

Bronckers, A. L. J. J. (2017). Ion transport by ameloblasts during amelogenesis. *J. Dent. Res.* 96, 243–253. doi:10.1177/0022034516681768

Chen, Y., Ramachandran, A., Zhang, Y., Koshy, R., and George, A. (2018). The ER Ca2+ sensor STIM1 can activate osteoblast and odontoblast differentiation in mineralized tissues. *Connect. Tissue Res.* 59 (Suppl. 1), 6–12. doi:10.1080/03008207.2017.1408601

Clarke, A. J. (2013). "Ectodermal dysplasias," in *Brenner's encyclopedia of genetics*. Second Edition (Wiley Online Library), 448–450. doi:10.1016/B978-0-12-374984-0.00462-9

Deak, A. T., Blass, S., Khan, M. J., Groschner, L. N., Waldeck-Weiermair, M., Hallström, S., et al. (2014). IP3-mediated STIM1 oligomerization requires intact mitochondrial Ca2+ uptake. *J. Cell Sci.* 127, 2944–2955. doi:10.1242/jcs.149807

Eckstein, M., and Lacruz, R. S. (2018). CRAC channels in dental enamel cells. *Cell Calcium* 75, 14–20. doi:10.1016/j.ceca.2018.07.012

Eckstein, M., Vaeth, M., Aulestia, F. J., Costiniti, V., Kassam, S. N., Bromage, T. G., et al. (2019). Differential regulation of Ca(2+) influx by ORAI channels mediates enamel mineralization. *Sci. Signal.* 12, eaav4663. doi:10.1126/scisignal.aav4663

Eckstein, M., Vaeth, M., Fornai, C., Vinu, M., Bromage, T. G., Nurbaeva, M. K., et al. (2017). Store-operated Ca2+ entry controls ameloblast cell function and enamel development. *JCI Insight* 2, e91166. doi:10.1172/jci.insight.91166

Feske, S. (2009). ORAI1 and STIM1 deficiency in human and mice: Roles of store-operated Ca2+ entry in the immune system and beyond. *Immunol. Rev.* 231, 189–209. doi:10.1111/j.1600-065X.2009.00818.x

Feske, S., Picard, C., and Fischer, A. (2010). Immunodeficiency due to mutations in ORAI1 and STIM1. *Clin. Immunol.* 135, 169–182. doi:10.1016/j.clim.2010.01.011

Furukawa, Y., Haruyama, N., Nikaido, M., Nakanishi, M., Ryu, N., Oh-Hora, M., et al. (2017). Stim1 regulates enamel mineralization and ameloblast modulation. *J. Dent. Res.* 96, 1422–1429. doi:10.1177/0022034517719872

Goldberg, M., Kellermann, O., Dimitrova-Nakov, S., Harichane, Y., and Baudry, A. (2014). Comparative studies between mice molars and incisors are required to draw an overview of enamel structural complexity. *Front. Physiol.* 5, 359. doi:10.3389/fphys.2014.00359

Habibah, T. U., Amlani, D. V., and Brizuela, M. (2022). *Hydroxyapatite dental material*. StatPearls. Available at: https://www.ncbi.nlm.nih.gov/books/NBK513314/%0Ahttp://www.ncbi.nlm.nih.gov/pubmed/30020686.

Hawkins, B. J., Irrinki, K. M., Mallilankaraman, K., Lien, Y. C., Wang, Y., Bhanumathy, C. D., et al. (2010). S-glutathionylation activates STIM1 and alters mitochondrial homeostasis. *J. Cell Biol.* 190, 391–405. doi:10.1083/jcb.201004152

Henke, N., Albrecht, P., Pfeiffer, A., Toutzaris, D., Zanger, K., and Methner, A. (2012). Stromal interaction molecule 1 (STIM1) is involved in the regulation of mitochondrial shape and bioenergetics and plays a role in oxidative stress. *J. Biol. Chem.* 287, 42042–42052. doi:10.1074/jbc.M112.417212

Hubbard, M. J. (2000). Calcium transport across the dental enamel epithelium. *Crit. Rev. Oral Biol. Med.* 11, 437–466. doi:10.1177/10454411000110040401

Iijima, M., Moriwaki, Y., Wen, H. B., Takagi, T., Fincham, A. G., and Moradian-Oldak, J. (2002). Effects of ionic flow and amelogenins on the lengthwise growth of octacalcium phosphate crystals in a model system of tooth enamel formation. *Mater. Res. Soc. Symp. - Proc.* 724, N6.4–109. doi:10.1557/proc-724-n6.4

Itin, P. H., and Fistarol, S. K. (2004). Ectodermal dysplasias. *Am. J. Med. Genet. C Semin. Med. Genet.* 131C (1), 45–51. doi:10.1002/ajmg.c.30033

Jalili, V., Afgan, E., Gu, Q., Clements, D., Blankenberg, D., Goecks, J., et al. (2021). The Galaxy platform for accessible, reproducible and collaborative biomedical analyses: 2020 update. *Nucleic Acids Res.* 48, W395–W402. doi:10.1093/NAR/GKAA434

Jardín, I., López, J. J., Redondo, P. C., Salido, G. M., and Rosado, J. A. (2009). Store-operated Ca2+ entry is sensitive to the extracellular Ca2+ concentration through plasma membrane STIM1. *Biochim. Biophys. Acta - Mol. Cell Res.* 1793, 1614–1622. doi:10.1016/j.bbamcr.2009.07.003

Khan, S. A., Khan, M. A., Muhammad, N., Bashir, H., Khan, N., Muhammad, N., et al. (2020). A novel nonsense variant in SLC24A4 causing a rare form of amelogenesis imperfecta in a Pakistani family. *BMC Med. Genet.* 21, 97. doi:10.1186/s12881-020-01038-6

Kirkham, J., Robinson, C., Weatherell, J. A., Richards, A., Fejerskov, O., and Josephsen, K. (1988). Maturation in developing permanent porcine enamel. *J. Dent. Res.* 67, 1156–1160. doi:10.1177/00220345880670090301

Klein, O. D., Duverger, O., Shaw, W., Lacruz, R. S., Joester, D., Moradian-Oldak, J., et al. (2017). Meeting report: A hard look at the state of enamel research. *Int. J. Oral Sci.* 9, e3. doi:10.1038/ijos.2017.40

Lacruz, R. S. (2017). Enamel: Molecular identity of its transepithelial ion transport system. *Cell Calcium* 65, 1–7. doi:10.1016/j.ceca.2017.03.006

Lacruz, R. S., and Feske, S. (2015). Diseases caused by mutations in ORAI1 and STIM1. *Ann. N. Y. Acad. Sci.* 1356, 45–79. doi:10.1111/nyas.12938

Lacruz, R. S., Smith, C. E., Bringas, P., Chen, Y. B., Smith, S. M., Snead, M. L., et al. (2012). Identification of novel candidate genes involved in mineralization of dental enamel by genome-wide transcript profiling. *J. Cell. Physiol.* 227, 2264–2275. doi:10.1002/jcp.22965

Lacruz, R. S., Smith, C. E., Chen, Y. B., Hubbard, M. J., Hacia, J. G., and Paine, M. L. (2011). Gene-expression analysis of early- and late-maturation-stage rat enamel organ. *Eur. J. Oral Sci.* 119, 149–157. doi:10.1111/j.1600-0722.2011.00881.x

Li, Z., Lu, J., Xu, P., Xie, X., Chen, L., and Xu, T. (2007). Mapping the interacting domains of STIM1 and Orai1 in Ca2+ release-activated Ca2+ channel activation. *J. Biol. Chem.* 282, 29448–29456. doi:10.1074/jbc.M703573200

Lian, J., Cuk, M., Kahlfuss, S., Kozhaya, L., Vaeth, M., Rieux-Laucat, F., et al. (2018). ORAI1 mutations abolishing store-operated Ca2+ entry cause anhidrotic ectodermal dysplasia with immunodeficiency. *J. Allergy Clin. Immunol.* 142, 1297–1310.e11. doi:10.1016/j.jaci.2017.10.031

Lyaruu, D. M., Bronckers, A. L. J. J., Mulder, L., Mardones, P., Medina, J. F., Kellokumpu, S., et al. (2008). The anion exchanger Ae2 is required for enamel maturation in mouse teeth. *Matrix Biol.* 27, 119–127. doi:10.1016/j.matbio.2007.09.006

Mohazab, L., Koivisto, L., Jiang, G., Kytömäki, L., Haapasalo, M., Owen, G. R., et al. (2013). Critical role for αvβ6 integrin in enamel biomineralization. *J. Cell Sci.* 126, 732–744. doi:10.1242/jcs.112599

Nanci, A. B. T.-T. C. O. H. (2013a). in *Chapter 1 - structure of the oral tissues*. Editor E. Eighth (St. Louis (MO): Mosby), 1–13. doi:10.1016/B978-0-323-07846-7.00001-X

Nanci, A. B. T.-T. C. O. H. (2013b). in *Chapter 7 - enamel: Composition, formation, and structure*. Editor E. Eighth (St. Louis (MO): Mosby), 122–164. doi:10.1016/B978-0-323-07846-7.00007-0

Nurbaeva, M. K., Eckstein, M., Concepcion, A. R., Smith, C. E., Srikanth, S., Paine, M. L., et al. (2015a). Dental enamel cells express functional SOCE channels. *Sci. Rep.* 5, 15803–15810. doi:10.1038/srep15803

Nurbaeva, M. K., Eckstein, M., Feske, S., and Lacruz, R. S. (2017). Ca2+ transport and signalling in enamel cells. *J. Physiol.* 595, 3015–3039. doi:10.1113/JP272775

Nurbaeva, M. K., Eckstein, M., Snead, M. L., Feske, S., and Lacruz, R. S. (2015b). Store-operated Ca2+ entry modulates the expression of enamel genes. *J. Dent. Res.* 94, 1471–1477. doi:10.1177/0022034515598144

Oh-hora, M., Yamashita, M., Hogan, P. G., Sharma, S., Lamperti, E., Chung, W., et al. (2008). Dual functions for the endoplasmic reticulum calcium sensors STIM1 and STIM2 in T cell activation and tolerance. *Nat. Immunol.* 9, 432–443. doi:10.1038/ni1574

Paine, M. L., Boyde, A., and Lacruz, R. S. (2020). *Transport functions of ectoderm epithelial cells forming dental enamel BT - ion transport across epithelial tissues and disease: Ion channels and transporters of epithelia in health and disease - Vol. 2*. Editors K. L. Hamilton and D. C. Devor (Cham: Springer International Publishing), 363–382. doi:10.1007/978-3-030-55310-4_11

Papagerakis, P., Macdougall, M., and Berdal, A. (2002). Differential epithelial and mesenchymal regulation of tooth-specific matrix proteins expression by 1,25-dihydroxyvitamin D 3 *in vivo*. *Connect. Tissue Res.* 43, 372–375. doi:10.1080/03008200290000655

Parry, D. A., Poulter, J. A., Logan, C. V., Brookes, S. J., Jafri, H., Ferguson, C. H., et al. (2013). Identification of mutations in SLC24A4, encoding a potassium-dependent sodium/calcium exchanger, as a cause of amelogenesis imperfecta. *Am. J. Hum. Genet.* 92, 307–312. doi:10.1016/j.ajhg.2013.01.003

Picard, C., McCarl, C.-A., Papolos, A., Khalil, S., Lüthy, K., Hivroz, C., et al. (2009). STIM1 mutation associated with a syndrome of immunodeficiency and autoimmunity. *N. Engl. J. Med.* 360, 1971–1980. doi:10.1056/nejmoa0900082

Rathee, M., and Jain, P. (2021). "Embryology, teeth," in *StatPearls* (StatPearls Publishing).

Risnes, S., Saeed, M., and Sehic, A. (2019). *Scanning electron microscopy (SEM) methods for dental enamel BT - odontogenesis: Methods and protocols*. Editor P. Papagerakis (New York, NY: Springer New York), 293–308. doi:10.1007/978-1-4939-9012-2_27

Ritchie, M. F., Samakai, E., and Soboloff, J. (2012). STIM1 is required for attenuation of PMCA-mediated Ca2+ clearance during T-cell activation. *EMBO J.* 31, 1123–1133. doi:10.1038/emboj.2011.495

Said, R., Lobanova, L., Papagerakis, S., and Papagerakis, P. (2020). Calcium sets the clock in ameloblasts. *Front. Physiol.* 11, 920. doi:10.3389/fphys.2020.00920

Said, R., Zheng, L., Saunders, T., Zeidler, M., Papagerakis, S., and Papagerakis, P. (2019). Generation of amelx-iCre mice supports ameloblast-specific role for Stim1. *J. Dent. Res.* 98, 1002–1010. doi:10.1177/0022034519858976

Shin, N. Y., Yamazaki, H., Beniash, E., Yang, X., Margolis, S. S., Pugach, M. K., et al. (2020). Amelogenin phosphorylation regulates tooth enamel formation by stabilizing a transient amorphous mineral precursor. *J. Biol. Chem.* 295, 1943–1959. doi:10.1074/jbc.RA119.010506

Silva-Rojas, R., Laporte, J., and Böhm, J. (2020). STIM1/ORAI1 loss-of-function and gain-of-function mutations inversely impact on SOCE and calcium homeostasis and cause multi-systemic mirror diseases. *Front. Physiol.* 11, 604941. doi:10.3389/fphys.2020.604941

Simmer, J. P., Hu, J. C. C., Hu, Y., Zhang, S., Liang, T., Wang, S. K., et al. (2021). A genetic model for the secretory stage of dental enamel formation. *J. Struct. Biol.* 213, 107805. doi:10.1016/j.jsb.2021.107805

Simmer, J. P., Papagerakis, P., Smith, C. E., Fisher, D. C., Rountrey, A. N., Zheng, L., et al. (2010). Regulation of dental enamel shape and hardness. *J. Dent. Res.* 89, 1024–1038. doi:10.1177/0022034510375829

Smyth, J. T., Hwang, S. Y., Tomita, T., DeHaven, W. I., Mercer, J. C., and Putney, J. W. (2010). Activation and regulation of store-operated calcium entry. *J. Cell. Mol. Med.* 14, 2337–2349. doi:10.1111/j.1582-4934.2010.01168.x

Srikanth, S., and Gwack, Y. (2012). Orai1, STIM1, and their associating partners. *J. Physiol.* 590, 4169–4177. doi:10.1113/jphysiol.2012.231522

Wang, S., Choi, M., Richardson, A. S., Reid, B. M., Seymen, F., Yildirim, M., et al. (2014). STIM1 and SLC24A4 are critical for enamel maturation. *J. Dent. Res.* 93, 94S–100S. doi:10.1177/0022034514527971

Wright, J. T., Hart, T. C., Hart, P. S., Simmons, D., Suggs, C., Daley, B., et al. (2008). Human and mouse enamel phenotypes resulting from mutation or altered expression of AMEL, ENAM, MMP20 and KLK4. *Cells Tissues Organs* 189, 224–229. doi:10.1159/000151378

Zaki, A. E., Hand, A. R., Mednieks, M. I., Eisenmann, D. R., and Borke, J. L. (1996). Quantitative immunocytochemistry of Ca(2+)-Mg2+ ATPase in ameloblasts associated with enamel secretion and maturation in the rat incisor. *Adv. Dent. Res.* 10, 245–251. doi:10.1177/08959374960100022101

Zheng, L., Ehardt, L., Mcalpin, B., About, I., Kim, D., Papagerakis, S., et al. (2014). The tick tock of odontogenesis. *Exp. Cell Res.* 325, 83–89. doi:10.1016/j.yexcr.2014.02.007

Zheng, L., Zinn, V., Lefkelidou, A., Taqi, N., Chatzistavrou, X., Balam, T., et al. (2015). Orai1 expression pattern in tooth and craniofacial ectodermal tissues and potential functions during ameloblast differentiation. *Dev. Dyn.* 244, 1249–1258. doi:10.1002/dvdy.24307

frontiers | Frontiers in Physiology

TYPE Original Research
PUBLISHED 15 March 2023
DOI 10.3389/fphys.2023.1088703

OPEN ACCESS

EDITED BY
Rodrigo S. Lacruz,
New York University, United States

REVIEWED BY
Thomas G. H. Diekwisch,
University of Rochester Medical Center, United States
Carmen Llena Puy,
University of Valencia, Spain

*CORRESPONDENCE
Jie Jia,
hdjiajie@foxmail.com

†These authors have contributed equally to this work and share first authorship

SPECIALTY SECTION
This article was submitted to Craniofacial Biology and Dental Research, a section of the journal Frontiers in Physiology

RECEIVED 03 November 2022
ACCEPTED 22 February 2023
PUBLISHED 15 March 2023

CITATION
Zhang Y, Wang Y, Zhang Z, Wang Y and Jia J (2023), Study on machine learning of molar incisor hypomineralization in an endemic fluorosis region in central China. *Front. Physiol.* 14:1088703. doi: 10.3389/fphys.2023.1088703

Study on machine learning of molar incisor hypomineralization in an endemic fluorosis region in central China

Yimeng Zhang[1†], Yu Wang[2†], Zhaoxin Zhang[1], Yuqi Wang[1] and Jie Jia[1,3*]

[1]Henan University School of Stomatology, Kaifeng, China, [2]The Key Laboratory of Clinical Resources Translation, Henan University, Kaifeng, China, [3]The First Affiliated Hospital of Henan University, Kaifeng, China

Objectives: The aim of the present study was to develop a machine learning model to predict the risk of molar incisor hypomineralization (MIH) and to identify factors associated with MIH in an endemic fluorosis region in central China.

Methods: A cross-sectional study was conducted with 1,568 schoolchildren from selected regions. The clinical examination included an investigation of MIH based on the European Academy of Paediatric Dentistry (EAPD) criteria. In this study, supervised machine learning (e.g., logistic regression) and correlation analysis (e.g., Spearman correlation analysis) were used for classification and prediction.

Results: The overall prevalence of MIH was 13.7%. The nomograph showed that non-dental fluorosis (DF) had a considerable influence on the early occurrence of MIH and that this influence became weaker as DF severity increased. We examined the association between MIH and DF and found that DF had a protective correlation with MIH; the protective effect became stronger as DF severity increased. Furthermore, children with defective enamel were more likely to experience caries, and dental caries were positively correlated with MIH (OR = 1.843; 95% CI: 1.260–2.694). However, gender, oral hygiene, and exposure to poor-quality shallow underground water did not increase the likelihood of developing MIH.

Conclusions: DF should be considered a protective factor within the multifactorial etiology of MIH.

KEYWORDS

molar incisor hypomineralization (MIH), prevalence, dental fluorosis (DF), dental caries, machine learning (ML)

1 Introduction

The European Academy of Paediatric Dentistry (EAPD) defines molar incisor hypomineralization (MIH) as enamel mineralization defects in one to four permanent first molars, with or without the involvement of the permanent incisors (Weerheijm et al., 2003). MIH-affected teeth clinically display demarcated opacity on the occlusal or buccal surfaces of the crowns (da Costa-Silva et al., 2010; Jeremias et al., 2013). MIH may be confused with dental fluorosis (DF), which shows diffuse opacity when the same teeth are

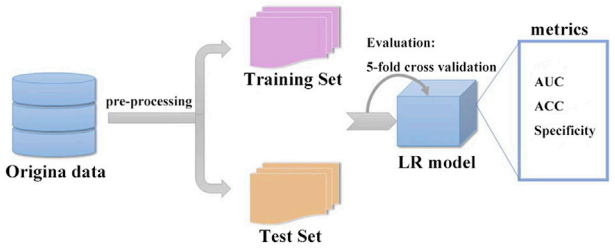

FIGURE 1
Structure of the supervised machine learning algorithm, which can describe this network working principle satisfactorily. The derivation cohort was randomly split into two datasets: a training set (70%) and an internal validation set (30%). After training and validation, we successfully constructed a logistic regression model (LR model).

affected. To date, researchers have performed many studies on the prevalence of MIH, but the study of MIH in endemic fluorosis regions is very limited.

The correlation between MIH and DF remains unclear. Studies have indicated that the presence of naturally fluoridated waters does not increase the incidence of MIH (Balmer et al., 2012; Schmalfuss et al., 2016); however, the severity of MIH is likely to be associated with DF (Fernandes et al., 2021). Significantly, the prevalence rate of MIH was lower in fluoridated areas of Northern England than in non-fluoridated areas (Balmer et al., 2012). A similar situation existed in Brazil, where a significant negative association between MIH and DF at the tooth level has been observed (Duarte et al., 2021). Therefore, it is important to study the relationship between MIH and DF, as well as the severity of MIH and DF.

Recently, machine learning methods have been used to predict a variety of diseases. Machine learning methods may be used to overcome some limitations of current analytical approaches and to find associations by applying computer algorithms to large datasets with numerous, multidimensional variables, capturing high-dimensional relationships among clinical features to obtain data-driven outcomes (Schwalbe and Wahl, 2020). Thus, we sought to develop a machine learning-based risk stratification model to explore the risk of MIH in an endemic fluorosis region in central China.

The aim of this study was to determine the prevalence of MIH and to predict its occurrence by utilizing machine learning and to explore the association between MIH and dental fluorosis in children living in an endemic fluorosis region in central China.

2 Material and methods

2.1 Ethical considerations and sample

The present study was performed with the approval of the Medical Ethics Committee of The First Affiliated Hospital of Henan University (2019LCSY-002). Signed informed consent was obtained from the caregivers and children prior to their participation in the study.

A cross-sectional study was conducted from April to June 2021 with a representative sample of schoolchildren aged 8 and 10 years in Lankao County, which is located on the eastern boundary of Henan Province. This county has endemic fluorosis, with fluoride concentrations ranging from 1.22 to 3.90 mg/L (Wang et al., 2008; Wang and Cao, 2013), which exceed the standard for drinking water quality in China (1.0 mg/L; GB5749-2006).

The formula for calculating a minimum number of randomly selected children was as follows: sample size (n) = $[Z^2 \times P(1-P)]/d^2$, where Z is the statistical level of confidence for a 95% confidence interval (CI; Z = 1.96), P is the expected prevalence, and d is the precision (Naing et al., 2006). Recent studies have revealed that the global average prevalence of MIH is 12.9% (11.7%–14.3%) (Schwendicke et al., 2018). According to the formula, this study required 169 participants. Schools were selected randomly according to the number of schools in each town, and a stratified sample of pupils was selected from each school according to the total number of pupils in the school. The inclusion criteria were as follows: residents of both sexes, aged 8–10 years, born and raised locally, with all four permanent first molars and incisors fully erupted. The exclusion criteria were as follows: having no erupted permanent first molar and incisor, undergoing fixed orthodontic treatment with brackets or bands on permanent first molars, and defects less than 1 mm in diameter.

2.2 Training and calibration of examiners

The European Academy of Paediatric Dentistry (EAPD) (Weerheijm et al., 2003) criteria for MIH were used in this study. Calibration exercises were conducted among three MIH investigators using clinical photographs of 26 patients. The tooth defects of patients covered all the degrees of MIH and other enamel defects, such as dental fluorosis, hypoplasia, and amelogenesis. The validity of using clinical photographs to study enamel defects was previously confirmed by Sabieha and Rock (1998), Wong et al. (2006), and Yi et al. (2021). After 1 month of training, three examiners were able to correctly diagnose all cases independently. Cohen's kappa coefficients for inter- and intra-rater reliability were 0.92 and 0.89 for dental fluorosis, 0.86 and 0.75 for dental caries, and 0.65 and 0.77 for MIH, respectively. Furthermore, during this month, three investigators examined 10 enamel defect patients who visited the Department of Stomatology, which guaranteed that the three investigators were familiar with the diagnosis and management of children with MIH.

2.3 Dental examination

Participants were advised to brush their teeth before the exam, and the teeth stayed slightly wet during the process of inspection. The items to be prepared included a simple dental chair with a dental light source (DYNAMIC, China), disposable oral treatment plates, disposable gloves, and cotton balls.

MIH: Clinical examinations were carried out by unified trained specialist dentists and comprised examination for developmental enamel defects and dental caries using the EAPD criteria (Weerheijm et al., 2003). To guarantee between-examiner reproducibility, the examinations were performed jointly by two dentists. A specially designed chart was used to record sex, the year of birth, the presence of MIH, the number of affected incisors and

TABLE 1 Baseline features of the included cohorts.

Characteristic	Total (n = 1,568), n (%)	MIH group (n = 215), n (%)	Normal group (n = 1,353), n (%)	χ^2	P
Sex				0.648	0.421
Male	755 (48.15)	109 (50.7)	646 (47.75)		
Female	813 (51.85)	106 (49.3)	707 (52.25)		
Water quality				2.881	0.090
Normal quality	769 (49.04)	117 (54.42)	652 (48.19)		
Lower quality	799 (50.96)	98 (45.58)	701 (51.81)		
MIH degree					
Mild		85 (39.53)			
Severe		130 (60.47)			
Dental fluorosis				58.267	<0.001
Normal	709 (45.22)	148 (68.84)	561 (41.46)		
Mild	778 (49.62)	65 (30.23)	713 (52.7)		
Severe	81 (5.16)	2 (0.93)	79 (5.84)		
Dental decay				129.371	<0.001
normal	406 (25.89)	37 (17.21)	369 (27.27)		
Only permanent teeth	88 (5.61)	32 (14.88)	56 (4.14)		
Only deciduous teeth	852 (54.34)	74 (34.42)	778 (57.5)		
Permanent teeth and deciduous teeth	222 (14.16)	72 (33.49)	150 (11.09)		
Oral hygiene				0.106	0.745
Fair	133 (8.48)	17 (7.91)	116 (8.57)		
Poor	1,435 (91.52)	198 (92.09)	1,237 (91.43)		

molars, and the maximum degree of severity. Severity was quantified according to clinical appearance (Ghanim et al., 2017) and was classed as 1) mild, including white and yellow demarcated opacities; or 2) severe, including posteruptive enamel breakdown (PEB), atypical restoration, atypical carious lesions, and missing due to MIH.

Dental fluorosis: The Thysltrup–Fejerskov (TF) criteria were used to determine the occurrence of dental fluorosis with an ordinal scale from 0 to 9 (Thylstrup and Fejerskov, 1978). Based on the loss of structure, teeth with a TF of 0 were classified as normal, those with a TF of 1-4 were classified as mild, and those with a TF greater than 5 were classified as severe.

Dental caries: Clinical dental caries (manifest caries) were recorded as decayed, missing, or filled teeth (DMF). Decay was defined as visible tooth substance loss without the characteristics of developmental defects, pits, or fissures.

Oral hygiene status: Oral hygiene was recorded using the simplified oral hygiene index (OHI-S) described by Greene and Vermillion (1964). The level of oral hygiene was evaluated according to the debris index and was classed as fair (0) or poor (1).

2.4 Databases and data preprocessing

To develop the machine learning models, we used a derivation cohort of children who met the inclusion criteria. The raw dataset contained the study subjects' demographics and the results of the comprehensive oral examination. Initially, the dataset used for preprocessing and classification was collected. The main characteristics of this dataset included MIH, MIH severity, DF, DF severity, dental decay, oral hygiene, water quality, and sex.

2.5 Machine learning methods and statistical validation strategies

The derivation cohort was randomly split into two datasets: a training cohort (70%) used to train the machine learning model and tune the parameters, and an internal validation cohort (30%) used to test the developed model on unseen data and to fine-tune the hyperparameters. For training, the original data space was balanced by oversampling using SMOTE. It worked by adding

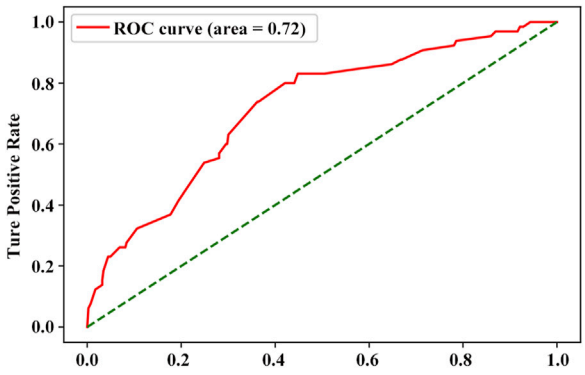

FIGURE 2
ROC curve for MIH in participants. ROC, receiver operating characteristic curve.

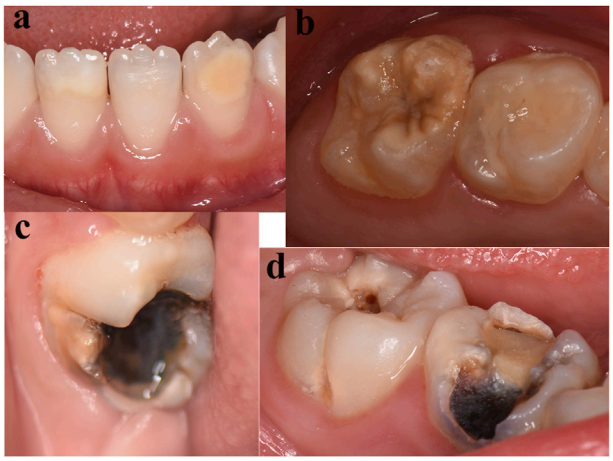

FIGURE 3
Phenotype of MIH. The majority of hypomineralized permanent teeth exhibited white **(A)** and yellow **(B)** demarcated lesions. **(C)** Atypical carious lesions associated with demarcated opacities in the first permanent molar. **(D)** Typical caries in the first permanent molars and atypical restorations in the primary molars.

small samples from the data space to diminish the biased behavior of imbalanced data, thus changing the size of the training data space. In this study, supervised machine learning (e.g., logistic regression) and correlation analysis (e.g., Spearman correlation analysis) were used for classification and prediction. Once the number of models was considered for this particular study, we used accuracy (ACC), specificity (SPEC), and the ROC curve and area under the curve (AUC) to validate the prediction performance for binary classes (Figure 1).

2.6 Statistical analysis

The completed examination records were analyzed by the SPSS Statistics 22.0 program (IBM SPSS, Chicago, IL, United States of America), Python (version 3.9.7), and R (version 4.1.3). The presence of MIH was considered a dependent variable. Dental caries and dental fluorosis were considered independent variables. Confidence intervals of 95% were calculated for prevalence. Chi-squared tests and Fisher's exact tests were used for comparisons and correlations. Logistic regression was conducted to analyze factors that could affect MIH. Significance was set at a p-value of < 0.05.

3 Results

3.1 Distribution characteristics of MIH in the population

A total of 1,586 children were invited to participate. Of these, 18 were not in accordance with the inclusion criteria. The clinical characteristics and demographics of the study population are shown in Table 1. The dataset consisted of 1,568 samples with two types: MIH (215, 13.7%) and non-MIH. This record included 755 male and 813 female. Patients with MIH consisted of a greater proportion of males—;109 (14.4%) were male and 106 (13.0%) were female, —but the difference was not statistically significant. For permanent teeth, caries activity in Lankao City was low, at 5.6% in only permanent teeth and 14.2% in permanent and deciduous teeth. As expected, the percentage of dental fluorosis was as high as 54.8% (Table 1). There was a higher percentage of children with poor oral hygiene in this region (91.5%).

A supervised machine learning algorithm (e.g., logistic regression) was used to check for the occurrence of MIH. A total of 1,568 samples were analyzed, and six variables were included. During data preprocessing, the diagnosis of non-MIH or MIH was encoded using a binary encoder as 0 and 1, respectively. The ROC curve analysis was significant for this model, displaying an area under the curve of 0.72 (Figure 2). This model showed an accuracy of 70% and a specificity of 72%.

3.2 Distribution of MIH severity

The typical clinical phenotype of MIH is shown in Figure 3, including mild and severe types. With respect to the distribution of MIH severity among affected index teeth, demarcated opacities comprised the predominant type of defects (Table 2).

3.3 Distribution of caries

The examined population presented a mixed dentition, and data from primary and permanent dentitions were presented separately (18,714 deciduous and 18,918 permanent teeth) (Table 3).

3.4 Nomogram development and validation

Based on a supervised machine learning algorithm, we constructed nomograms for predicting the occurrence of MIH, as shown in Figure 4. Non-DF had a great influence on the early occurrence of MIH. Significantly, the more severe the DF, the lower the occurrence.

TABLE 2 Severity of MIH (number of teeth).

	Mild type	Severe type			Total
	Demarcated opacity	Post-eruptive enamel breakdown	Atypical restoration	Atypical caries and missing duo to MIH	
	n %	n %	n %	n %	n %
Total	285 (59.1)	38 (7.9)	7 (1.5)	152 (31.5)	482 (100)

TABLE 3 Incidence of caries (number of teeth).

	Decay	Missing	Filling	Normal	Total
	n (%)	n (%)	n (%)	n (%)	n (%)
Permanent teeth	513 (2.71)	7 (0.04)	35 (0.19)	18,363 (97.06)	18,918 (100)
Deciduous teeth	3,773 (20.16)	21 (0.11)	52 (0.28)	14,868 (79.45)	18,714 (100)

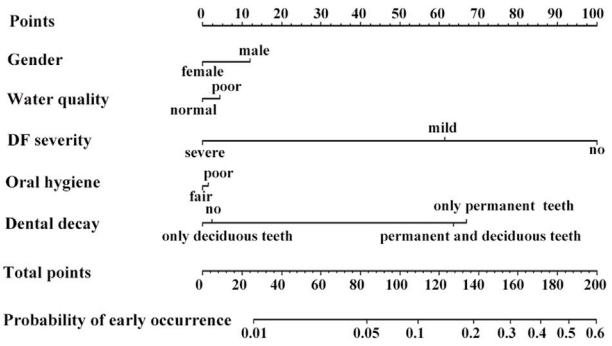

FIGURE 4
Nomograms to predict the probability of MIH occurrence. Non-DF had a significant influence on MIH occurrence, which decreased with increasing DF severity. Dental decay had a certain effect on it. However, exposure to low-quality shallow underground water did not increase the likelihood of developing MIH.

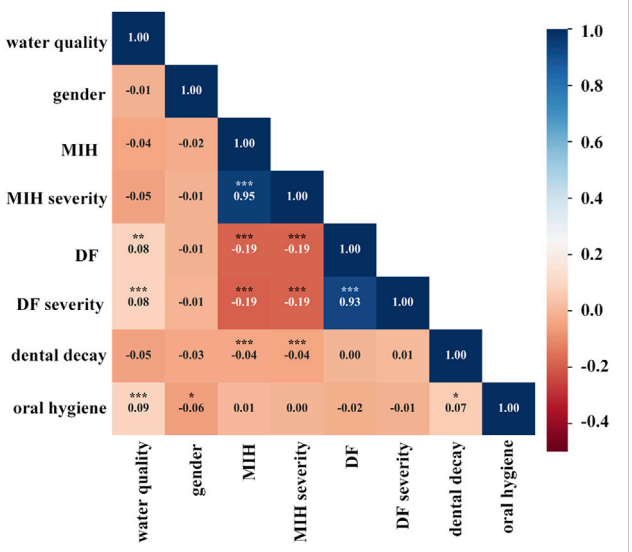

FIGURE 5
Correlation heatmap of clinical characteristics using Spearman correlations. Heatmap shows the positive (red) or negative (blue) correlations of all parameters, with color intensity reflecting the strength of the correlation (−0.4 to +1). MIH and MIH severity were negatively correlated with DF and DF severity and also had negligible associations with dental caries. *$p < 0.05$; **$p < 0.01$; ***$p < 0.001$.

Dental decay of permanent teeth was related to the occurrence of MIH. However, exposure to poor-quality shallow underground water did not increase the likelihood of developing MIH. Gender and oral hygiene had no influence on the occurrence.

3.5 Factors associated with MIH

A correlation heatmap of all parameters was generated using Spearman correlation coefficients. Figure 5 illustrates the correlation heatmaps of the core data features. MIH and MIH severity were negatively correlated with DF and DF severity. As in the logistic regression analysis, DF had a protective correlation with MIH, and the protective effect became stronger as DF severity increased. However, dental caries were positively correlated with MIH (OR = 1.843; 95% CI: 1.260–2.694) (Table 4), which was inconsistent with the heatmap. The heatmap showed a negligible correlation between MIH and dental caries.

Both the correlation heatmap and logistic regression analysis showed that the quality of underground water was not robustly

10.3389/fphys.2023.1088703

TABLE 4 Logistic regression analysis of the associations between the variable of interest and MIH.

Variable	*p*-value	OR (95%CI)
Drinking water quality		
Normal quality		1
Poor quality	0.396	0.880 (0.654–1.183)
Dental caries		
Absent		1
Present	0.002	1.843 (1.260–2.694)
Dental fluorosis degree		
Absent		1
Mild	<0.001	0.349 (0.255–0.478)
Severe	0.001	0.091 (0.022–0.375)

correlated with MIH or MIH severity. Not surprisingly, the quality of underground water was correlated with DF and DF severity. A similar correlation was found between dental decay and oral hygiene.

To find the relationship between MIH and DF, we used a pair plot. In Python, the pair plot showed that MIH (Figure 6A) was strongly negatively correlated with DF and DF severity. The severity of MIH was reduced, followed by the incidence of DF and the strength of DF severity (Figure 6B).

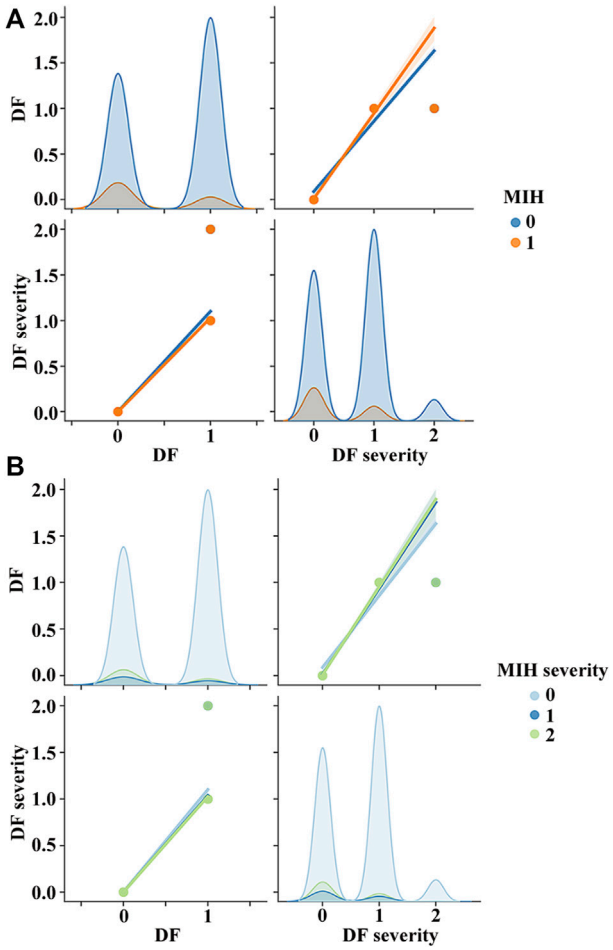

FIGURE 6
Pair plot was used to show relations among MIH, MIH severity, DF, and DF severity. During data preprocessing, the diagnoses of MIH or non-MIH, as well as DF or non-DF, were encoded using a binary encoder as 0 and 1. Thus, MIH or DF became 1, and non-MIH or non-DF became 0. Depending on the severity of MIH or DF, the level of MIH or DF was classed as normal (0), mild (1), or severe (2). **(A)** MIH was strongly negatively correlated with DF and DF severity. **(B)** Severity of MIH was reduced, followed by the incidence of DF and the strength of DF severity.

4 Discussion

In this study, we used data from 1,568 children to develop machine learning-based risk scores to predict the risk for MIH in an endemic fluorosis region in central China. Lankao is a typical quality-induced water shortage area, where there are various underground waters of poor quality, such as saltwater, brackish water, and high-hardness water. However, some regions have normal-quality groundwater that can be drunk directly. All participants were born and raised locally, and the natural groundwater source was the only drinking water before 2015. We have certitude that local shallow groundwater affected the permanent tooth mineralization of the recruited children.

MIH prevalence values reported by different studies are heterogeneous, varying from 2.4% to 44% in different areas (Dietrich et al., 2003; Calderara et al., 2005; Jasulaityte et al., 2007; Preusser et al., 2007; Ng et al., 2015) and from 2.8% to 25.5% in China (Cho et al., 2008; Sui et al., 2017; Li and Li, 2012; Zhang et al., 2020, Zhang et al.). The prevalence in this study was 13.7%, similar to the estimated world average of 12.9% (Schwendicke et al., 2018). Although there was a higher proportion of female patients with MIH, which is in agreement with a previous study (Mejare et al., 2005), the difference was not statistically significant. Spearman correlation analysis also indicated that sex does not seem to be a determining factor.

We qualified MIH as mild or severe to evaluate its severity, according to the criteria described by Mathu-Muju and Wright (2006). MIH is most often encountered in a mild form (Garcia-Margarit et al., 2014; Mittal and Sharma, 2015), which is consistent with the results of this study, in which 59.1% of the MIH cases were mild and 40.9% were severe at the tooth level (Table 2).

Recent developments in MIH research have focused on prevalence, and there are few prediction studies of early occurrence. In this study, a supervised machine learning model was constructed by incorporating a variety of factors that impact the occurrence of MIH in endemic fluorosis regions. The nomograms showed that sex had no influence on occurrence, which is consistent with previous studies (Yi et al., 2021; Sosa-Soto et al., 2022). Exposure to low-quality shallow underground water did not increase the likelihood of developing MIH. Significantly, non-DF had a substantial influence on the early occurrence of MIH, and the more severe the DF, the lower the occurrence.

A definitive conclusion has not been reached regarding the association between MIH prevalence and dental fluorosis. Thus, we explored the relationship between MIH and DF in children living in this endemic fluorosis region. As expected, the prevalence of fluorosis was as high as 54.8%. Spearman correlation analysis showed that MIH was negatively correlated with DF and DF severity; logistic regression analysis showed that DF had a protective correlation with MIH and that the effect of protection became more obvious with increasing severity. This finding accords with previous studies, showing that the prevalence of MIH was lower in the fluoridated area (10.8%) than in all non-fluoridated areas combined (17.35%) (Balmer et al., 2012). At the surface level, MIH frequency was lower in the presence of DF (Restrepo et al., 2022). Poisson regression analysis in a previous study showed that the *p*-value of the association between dental fluorosis and MIH was 0.084 and the OR ratio 0.63 (95% CI: 0.37–1.06) (Fernandes et al., 2021), which is similar to our findings. Enamel in patients diagnosed with MIH and fluorosis may not have completed maturation during amelogenesis (Malmberg et al., 2019; Fernandes et al., 2021). One possible explanation is that the affected teeth that initially erupt are hypomineralized; however, relatively long-term exposure to optimum levels of fluoride encourages remineralization. Finally, this continued remineralization could reduce or even change the defective clinical appearance.

According to the Fourth National Oral Health Survey in 2005, the caries prevalence in permanent teeth in China was 38.5% for the 12-year age group (Chen et al., 2018; Quan et al., 2018). The caries activity in Lankao City was low (14.2% of all teeth and 5.6% of only permanent teeth), which indicated that the high fluoride concentration of local water endowments truly prevented dental caries. In the nomograms, children with defective enamel were more prone to experiencing caries; logistic regression analysis showed that dental caries were positively correlated with MIH (OR = 1.843; 95% CI: 1.260–2.694). Most studies have shown a relationship between increased dental caries and children with MIH compared to those without MIH (Heitmüller et al., 2013; Petrou et al., 2015; Kosma et al., 2016). Furthermore, severe MIH cases had significantly higher caries prevalence than those with mild MIH (91.7% and 68.7%, respectively, $p < 0.01$; data not shown), suggesting that severe MIH increases the likelihood of caries in hypomineralized teeth. Teeth affected by MIH present a porous enamel surface due to poor mineral quality, which increases the likelihood of developing dental caries.

Unexpectedly, the prevalence of poor oral hygiene reached 91.5% in this region (Table 1), which increased the incidence of caries and worsened the severity of lesions. The nomogram showed that oral hygiene status did not affect the occurrence of MIH, and Spearman correlation analysis also found no relationship between oral hygiene status and MIH or MIH severity.

Altogether, the present study constructed a supervised machine learning algorithm to predict the occurrence of MIH in an endemic fluorosis region in central China, and the nomograph showed that MIH occurrence decreased with increasing DF severity. Then, we examined the association between MIH and DF and found a negative relationship, suggesting that DF should be considered a protective factor within the multifactorial etiology of MIH Zang et al., 2019.

Data availability statement

The original contributions presented in the study are included in the article/supplementary material; further inquiries can be directed to the corresponding author.

Ethics statement

The studies involving human participants were reviewed and approved by the Medical Ethics Committee of The First Affiliated Hospital of Henan University (2019LCSY-002). Written informed consent to participate in this study was provided by each participant's legal guardian or next of kin. Written informed consent was obtained from the individual(s) and minor(s) and their legal guardians or next of kin for the publication of any potentially identifiable images or data included in this article.

Author contributions

YZ, YuW, and JJ designed the research and wrote the manuscript. YZ, YuW, ZZ, and YqW conducted the epidemiological studies. All authors reviewed the results and approved the final version of the manuscript.

Funding

This study was supported by the scientific research project of the Public Health Department of Henan (SBGJ202102197) and the scientific research project of the Education Department of Henan (21A320005).

Acknowledgments

The authors thank Professor Yanfang Ren (Eastman Institute for Oral Health, University of Rochester Medical Center) for guidance in this epidemiological study.

Conflict of interest

The authors declare that the research was conducted in the absence of any commercial or financial relationships that could be construed as a potential conflict of interest.

Publisher's note

References

Balmer, R., Toumba, J., Godson, J., and Duggal, M. (2012). The prevalence of molar incisor hypomineralisation in Northern England and its relationship to socioeconomic status and water fluoridation. *Int. J. Paediatr. Dent.* 22, 250–257.

Calderara, P. C., Gerthoux, P. M., Mocarelli, P., Lukinmaa, P. L., Tramacere, P. L., and Alaluusua, S. (2005). The prevalence of Molar Incisor Hypomineralisation (MIH) in a group of Italian school children. *Eur. J. Paediatr. Dent.* 6, 79–83.

Chen, X., Ye, W., Zhan, J. Y., Wang, X., Tai, B. J., Hu, Y., et al. (2018). Periodontal status of Chinese adolescents: Findings from the 4th national oral health survey. *Chin. J. Dent. Res.* 21, 195–203.

Cho, S. Y., Ki, Y., and Chu, V. (2008). Molar incisor hypomineralization in Hong Kong Chinese children. *Int. J. Paediatr. Dent.* 18, 348–352.

Da Costa-Silva, C. M., Jeremias, F., De Souza, J. F., Cordeiro Rde, C., Santos-Pinto, L., and Zuanon, A. C. (2010). Molar incisor hypomineralization: Prevalence, severity and clinical consequences in Brazilian children. *Int. J. Paediatr. Dent.* 20, 426–434.

Dietrich, G., Sperling, S., and Hetzer, G. (2003). Molar incisor hypomineralisation in a group of children and adolescents living in Dresden (Germany). *Eur. J. Paediatr. Dent.* 4, 133–137.

Duarte, M. B. S., Carvalho, V. R., Hilgert, L. A., Ribeiro, A. P. D., Leal, S. C., and Takeshita, E. M. (2021). Is there an association between dental caries, fluorosis, and molar-incisor hypomineralization? *J. Appl. Oral Sci.* 29, e20200890.

Fernandes, I. C., Forte, F. D. S., and Sampaio, F. C. (2021). Molar-incisor hypomineralization (MIH), dental fluorosis, and caries in rural areas with different fluoride levels in the drinking water. *Int. J. Paediatr. Dent.* 31, 475–482.

Garcia-Margarit, M., Catalá-Pizarro, M., Montiel-Company, J. M., and Almerich-Silla, J. M. (2014). Epidemiologic study of molar-incisor hypomineralization in 8-year-old Spanish children. *Int. J. Paediatr. Dent.* 24, 14–22.

Ghanim, A., Silva, M. J., Elfrink, M. E. C., Lygidakis, N. A., Marino, R. J., Weerheijm, K. L., et al. (2017). Molar incisor hypomineralisation (MIH) training manual for clinical field surveys and practice. *Eur. Arch. Paediatr. Dent.* 18, 225–242.

Greene, J. C., and Vermillion, J. R. (1964). The simplified oral hygiene index. *J. Am. Dent. Assoc.* 68, 7–13.

HeitmüLLER, D., Thiering, E., Hoffmann, U., Heinrich, J., Manton, D., KüHNISCH, J., et al. (2013). Is there a positive relationship between molar incisor hypomineralisations and the presence of dental caries? *Int. J. Paediatr. Dent.* 23, 116–124.

Jasulaityte, L., Veerkamp, J. S., and Weerheijm, K. L. (2007). Molar incisor hypomineralization: Review and prevalence data from the study of primary school children in kaunas/Lithuania. *Eur. Arch. Paediatr. Dent.* 8, 87–94.

Jeremias, F., Koruyucu, M., Kuchler, E. C., Bayram, M., Tuna, E. B., Deeley, K., et al. (2013). Genes expressed in dental enamel development are associated with molar-incisor hypomineralization. *Arch. Oral Biol.* 58, 1434–1442.

Kosma, I., Kevrekidou, A., Boka, V., Arapostathis, K., and Kotsanos, N. (2016). Molar incisor hypomineralisation (MIH): Correlation with dental caries and dental fear. *Eur. Arch. Paediatr. Dent.* 17, 123–129.

Li, L., and Li, J. (2012). Investigation of molar-incisor hypomineralization among children from 6 to 11 years in Lucheng district, Wenzhou city. *Shanghai Kou Qiang Yi Xue* 21, 576–579.

Malmberg, P., NoréN, J. G., and Bernin, D. (2019). Molecular insights into hypomineralized enamel. *Eur. J. Oral Sci.* 127, 340–346.

Mathu-Muju, K., and Wright, J. T. (2006). Diagnosis and treatment of molar incisor hypomineralization. *Compend Contin. Educ. Dent.* 27, 604–610.

Mejare, I., Bergman, E., and Grindefjord, M. (2005). Hypomineralized molars and incisors of unknown origin: Treatment outcome at age 18 years. *Int. J. Paediatr. Dent.* 15, 20–28.

Mittal, N., and Sharma, B. B. (2015). Hypomineralised second primary molars: Prevalence, defect characteristics and possible association with molar incisor hypomineralisation in Indian children. *Eur. Arch. Paediatr. Dent.* 16, 441–447.

Naing, L., Winn, T., and Rusli, B. N. (2006). Practical issues in calculating the sample size for prevalence studies. *Archives Orofac. Sci.* 1.

Ng, J. J., Eu, O. C., Nair, R., and Hong, C. H. (2015). Prevalence of molar incisor hypomineralization (MIH) in Singaporean children. *Int. J. Paediatr. Dent.* 25, 73–78.

Petrou, M. A., Giraki, M., Bissar, A. R., Wempe, C., SchäFER, M., Schiffner, U., et al. (2015). Severity of MIH findings at tooth surface level among German school children. *Eur. Arch. Paediatr. Dent.* 16, 271–276.

Preusser, S. E., Ferring, V., Wleklinski, C., and Wetzel, W. E. (2007). Prevalence and severity of molar incisor hypomineralization in a region of Germany -- a brief communication. *J. Public Health Dent.* 67, 148–150.

Quan, J. K., Wang, X. Z., Sun, X. Y., Yuan, C., Liu, X. N., Wang, X., et al. (2018). Permanent teeth caries status of 12- to 15-year-olds in China: Findings from the 4th national oral health survey. *Chin. J. Dent. Res.* 21, 181–193.

Restrepo, M., Rojas-GualdróN, D. F., De Farias, A. L., Girotto-Bussaneli, D., and Santos-Pinto, L. (2022). Association between frequency and severity of dental fluorosis and molar incisor hypomineralization. *J. Clin. Pediatr. Dent.* 46, 30–34.

Sabieha, A. M., and Rock, W. P. (1998). A comparison of clinical and photographic scoring using the TF and modified DDE indices. *Community Dent. Health* 15, 82–87.

Schmalfuss, A., Stenhagen, K. R., Tveit, A. B., Crossner, C. G., and Espelid, I. (2016). Canines are affected in 16-year-olds with molar-incisor hypomineralisation (MIH): An epidemiological study based on the tromsø study: "Fit futures. *Eur. Arch. Paediatr. Dent.* 17, 107–113.

Schwalbe, N., and Wahl, B. (2020). Artificial intelligence and the future of global health. *Lancet* 395, 1579–1586.

Schwendicke, F., Elhennawy, K., Reda, S., Bekes, K., Manton, D. J., and Krois, J. (2018). Global burden of molar incisor hypomineralization. *J. Dent.* 68, 10–18.

Sosa-Soto, J., PadróN-Covarrubias, A. I., MáRQUEZ-Preciado, R., Ruiz-RodríGUEZ, S., Pozos-GuilléN, A., Pedroza-Uribe, I. M., et al. (2022). Molar incisor hypomineralization (MIH): Prevalence and degree of severity in a Mexican pediatric population living in an endemic fluorosis area. *J. Public Health Dent.* 82, 3–10.

Sui, W., Wu, H. Y., Yuan, J., L., Yao, H., and Hong, Y., L. (2017). Epidemiological study of molar incisor hypomineralization in primary school students in Soozhow China. *Chin. J. Conservative Dent.* 27, 103–107.

Thylstrup, A., and Fejerskov, O. (1978). Clinical appearance of dental fluorosis in permanent teeth in relation to histologic changes. *Community Dent. Oral Epidemiol.* 6, 315–328.

Wang, C., and Cao, P. (2013). Distribution characteristics and causes of main components exceeding standard of primary inferior groundwater in Lankao County. *Resour. Guide·Earth Sci. Technol.* 46-47, 50.

Wang, J., S., Feng, L., Huang, J., and Yang, L., and (2008). Groundwater quality analysis and protection countermeasures in Lankao county of henan province. *Ground Water* 30, 105–107.

Weerheijm, K. L., Duggal, M., MejàRE, I., Papagiannoulis, L., Koch, G., Martens, L. C., et al. (2003). Judgement criteria for molar incisor hypomineralisation (MIH) in epidemiologic studies: A summary of the European meeting on MIH held in athens, 2003. *Eur. J. Paediatr. Dent.* 4, 110–113.

Wong, H. M., Mcgrath, C., Lo, E. C., and King, N. M. (2006). Association between developmental defects of enamel and different concentrations of fluoride in the public water supply. *Caries Res.* 40, 481–486.

Yi, X., Chen, W., Liu, M., Zhang, H., Hou, W., and Wang, Y. (2021). Prevalence of MIH in children aged 12 to 15 years in Beijing, China. *Clin. Oral Investig.* 25, 355–361.

Zang, P.,N., Gao, Y., Y., Tian, J., and Huang, R., Z. (2019). Epidemiological sampling survey of MIH in children in Shanxi Province. *19th Natl. Annu. Meet. Oral Prev. Med. Prof. Comm. Chin. Stomatological Assoc.*

Zhang, Q., Xing, Y., Z., Xia, T., Liu, J., and Deng, J. (2020). Current situation and influencing factors of molar-incisor hypomineralization among children aged 6-10 years in Wuhan city. *Pract. Prev. Med.* 27, 1199–1202.

frontiers | Frontiers in Physiology

TYPE Original Research
PUBLISHED 09 May 2023
DOI 10.3389/fphys.2023.1130175

OPEN ACCESS

EDITED BY
Frédéric Lézot,
Institut National de la Santé et de la Recherche Médicale (INSERM), France

REVIEWED BY
Olivier Duverger,
National Institute of Dental and Craniofacial Research (NIH), United States
Tim Wright,
University of North Carolina at Chapel Hill, United States

*CORRESPONDENCE
Agnes Bloch-Zupan,
agnes.bloch-zupan@unistra.fr

†These authors contributed equally to this work and share first authorship

SPECIALTY SECTION
This article was submitted to Craniofacial Biology and Dental Research, a section of the journal Frontiers in Physiology

RECEIVED 22 December 2022
ACCEPTED 06 March 2023
PUBLISHED 09 May 2023

CITATION
Bloch-Zupan A, Rey T, Jimenez-Armijo A, Kawczynski M, Kharouf N, O-Rare consortium, Dure-Molla MdL, Noirrit E, Hernandez M, Joseph-Beaudin C, Lopez S, Tardieu C, Thivichon-Prince B, ERN Cranio Consortium, Dostalova T, Macek M Jr, International Consortium, Alloussi ME, Qebibo L, Morkmued S, Pungchanchaikul P, Orellana BU, Manière M-C, Gérard B, Bugueno IM and Laugel-Haushalter V (2023), *Amelogenesis imperfecta*: Next-generation sequencing sheds light on Witkop's classification.
Front. Physiol. 14:1130175.
doi: 10.3389/fphys.2023.1130175

Amelogenesis imperfecta: Next-generation sequencing sheds light on Witkop's classification

Agnes Bloch-Zupan[1,2,3,4,5*†], Tristan Rey[4,6†], Alexandra Jimenez-Armijo[4†], Marzena Kawczynski[3], Naji Kharouf[7], O-Rare consortium, Muriel de La Dure-Molla[8], Emmanuelle Noirrit[9], Magali Hernandez[10], Clara Joseph-Beaudin[11], Serena Lopez[12], Corinne Tardieu[13], Béatrice Thivichon-Prince[14], ERN Cranio Consortium, Tatjana Dostalova[15], Milan Macek Jr[15], International Consortium, Mustapha El Alloussi[16], Leila Qebibo[17], Supawich Morkmued[18], Patimaporn Pungchanchaikul[18], Blanca Urzúa Orellana[19], Marie-Cécile Manière[1,3], Bénédicte Gérard[6], Isaac Maximiliano Bugueno[1,3,4] and Virginie Laugel-Haushalter[1,4,6]

[1]Université de Strasbourg, Faculté de Chirurgie Dentaire, Strasbourg, France, [2]Université de Strasbourg, Institut d'études avancées (USIAS), Strasbourg, France, [3]Hôpitaux Universitaires de Strasbourg (HUS), Pôle de Médecine et Chirurgie Bucco-dentaires, Hôpital Civil, Centre de référence des maladies rares orales et dentaires, O-Rares, Filiére Santé Maladies rares TETE COU, European Reference Network ERN CRANIO, Strasbourg, France, [4]Université de Strasbourg, Institut de Génétique et de Biologie Moléculaire et Cellulaire (IGBMC), IN-SERM U1258, CNRS- UMR7104, Illkirch, France, [5]Eastman Dental Institute, University College London, London, United Kingdom, [6]Hôpitaux Universitaires de Strasbourg, Laboratoires de diagnostic génétique, Institut de Génétique Médicale d'Alsace, Strasbourg, France, [7]Université de Strasbourg, Laboratoire de Biomatériaux et Bioingénierie, Inserm UMR_S 1121, Strasbourg, France, [8]Rothschild Hospital, Public Assistance-Paris Hospitals (AP-HP), Reference Center for Rare Oral and Den-tal Diseases (O-Rares), Paris, France, [9]Centre Hospitalier Universitaire (CHU) Rangueil, Toulouse, Competence Center for Rare Oral and Den-tal Diseases, Toulouse, France, [10]Centre Hospitalier Régional Universitaire de Nancy, Université de Lorraine, Competence Center for Rare Oral and Dental Diseases, Nancy, France, [11]Centre Hospitalier Universitaire de Nice, Competence Center for Rare Oral and Dental Diseases, Nice, France, [12]Centre Hospitalier Universitaire de Nantes, Competence Center for Rare Oral and Dental Diseases, Nantes, France , [13]APHM, Hôpitaux Universitaires de Marseille, Hôpital Timone, Competence Center for Rare Oral and Dental Diseases, Marseille, France, [14]Centre Hospitalier Universitaire de Lyon, Competence Center for Rare Oral and Dental Diseases, Lyon, France, [15]Department of Stomatology (TD) and Department of Biology and Medical Genetics (MM) Charles University 2nd Faculty of Medicine and Motol University Hospital, Prague, Czechia, [16]Faculty of Dentistry, International University of Rabat, CReSS Centre de recherche en Sciences de la Santé, Rabat, Morocco, [17]Unité de génétique médicale et d'oncogénétique, CHU Hassan II, Fes, Morocco, [18]Faculty of Dentistry, Khon Kaen University, Khon Kaen, Thailand, [19]Instituto de Investigación en Ciencias Odontológicas, Facultad de Odontología, Universidad de Chile, Santiago, Chile

Amelogenesis imperfecta (AI) is a heterogeneous group of genetic rare diseases disrupting enamel development (Smith et al., Front Physiol, 2017a, 8, 333). The clinical enamel phenotypes can be described as hypoplastic, hypomineralized or hypomature and serve as a basis, together with the mode of inheritance, to Witkop's classification (Witkop, J Oral Pathol, 1988, 17, 547–553). AI can be described in isolation or associated with others symptoms in syndromes. Its occurrence was estimated to range from 1/700 to 1/14,000. More than 70 genes have currently been identified as causative.

Objectives: We analyzed using next-generation sequencing (NGS) a heterogeneous cohort of AI patients in order to determine the molecular etiology of AI and to improve diagnosis and disease management.

Methods: Individuals presenting with so called "isolated" or syndromic AI were enrolled and examined at the Reference Centre for Rare Oral and Dental Diseases (O-Rares) using D4/phenodent protocol (www.phenodent.org). Families gave written informed consents for both phenotyping and molecular analysis and diagnosis using a dedicated NGS panel named GenoDENT. This panel explores currently simultaneously 567 genes. The study is registered under NCT01746121 and NCT02397824 (https://clinicaltrials.gov/).

Results: GenoDENT obtained a 60% diagnostic rate. We reported genetics results for 221 persons divided between 115 AI index cases and their 106 associated relatives from a total of 111 families. From this index cohort, 73% were diagnosed with non-syndromic amelogenesis imperfecta and 27% with syndromic amelogenesis imperfecta. Each individual was classified according to the AI phenotype. Type I hypoplastic AI represented 61 individuals (53%), Type II hypomature AI affected 31 individuals (27%), Type III hypomineralized AI was diagnosed in 18 individuals (16%) and Type IV hypoplastic-hypomature AI with taurodontism concerned 5 individuals (4%). We validated the genetic diagnosis, with class 4 (likely pathogenic) or class 5 (pathogenic) variants, for 81% of the cohort, and identified candidate variants (variant of uncertain significance or VUS) for 19% of index cases. Among the 151 sequenced variants, 47 are newly reported and classified as class 4 or 5. The most frequently discovered genotypes were associated with *MMP20* and *FAM83H* for isolated AI. *FAM20A* and *LTBP3* genes were the most frequent genes identified for syndromic AI. Patients negative to the panel were resolved with exome sequencing elucidating for example the gene involved ie *ACP4* or digenic inheritance.

Conclusion: NGS GenoDENT panel is a validated and cost-efficient technique offering new perspectives to understand underlying molecular mechanisms of AI. Discovering variants in genes involved in syndromic AI (*CNNM4, WDR72, FAM20A* . . .) transformed patient overall care. Unravelling the genetic basis of AI sheds light on Witkop's AI classification.

KEYWORDS

enamel, amelogenesis imperfecta, genetics, rare diseases, NGS, next-generation sequencing

Introduction

Enamel is the only mineralized structure of the body with an ectodermal origin. It has extraordinary mechanical and chemical properties. It is strongest and hardest material in the body and acts as an efficient barrier against environmental assaults whether mechanical, chemical, or physical. Enamel is incapable of regeneration or repair as ameloblasts, the specialized post-mitotic ectoderm-derived cells that produce the enamel matrix, disappear when the teeth erupt within the oral cavity. Normally, these ameloblasts produce proteins (enamelin, amelogenin, ameloblastin . . .) in the secretory phase, mineralize this matrix and then mature it, in the maturation phase, by removing almost all the scaffold proteins *via* enzymes (KLK4, MMP20) to allow hydroxyapatite-crystal growth towards 96%–98% mineral content.

Amelogenesis imperfecta (AI) is a heterogeneous group of rare inherited diseases affecting amelogenesis, i.e. the enamel developmental process, in both primary and permanent dentitions and may be evident as an isolated trait or associated to other symptoms in syndromes. Amelogenesis imperfecta may manifest in different forms based on the phenotypic nature of the observed enamel defect, divided in three categories: hypoplastic (quantitative defect i.e. thinner enamel, pitted or striae enamel, enamel agenesis), hypomineralized (softer rough colored undermineralized enamel) or -hypomature (relatively hard but colored not translucent enamel). In 1988, Witkop (Witkop, 1988) proposed a revised classification of amelogenesis imperfecta considering the nature of the enamel defects as well the mode of inheritance (Table 1) and dividing AI into 4 classes (Type I hypoplastic, Type II hypomaturation, Type III hypocalcified, Type IV hypomaturation/hypoplastic with taurodontism). This classification was challenged by other authors cited in (Crawford et al., 2007) who proposed to add molecular data. More than 70 genes have been associated to "isolated" or "syndromic" AI. These genes encode a wide array of potential activities in amelogenesis, from enamel matrix

TABLE 1 Witkop's classification of amelogenesis imperfecta phenotypes and associated mode of inheritance (Witkop and Sauk, 1976; Witkop 1988) and current knowledge about corresponding associated genes.

TYPE	Class	Phenotype	Mode of inheritance	Phenotype OMIM number #	Genes
I -HYPOPLASTIC	**IA**	**HYPOPLASTIC, PITTED**	**AD**	**104530**	***LAMA3, LAMB3, LAMC2, COL7A1, COL17A1, ITGB6/4***
				616221	
	IB	**HYPOPLASTIC, LOCAL**	**AD**	**104500**	***ENAM***
	IC	**HYPOPLASTIC, LOCAL**	**AR**	**204650**	***ENAM***
				617297	*ACP4?*
	ID	**HYPOPLASTIC, SMOOTH**	**AD**	620104	*SP6?*
	IE	**HYPOPLASTIC, SMOOTH**	**XLD**	**301200**	***AMELX, ARHGAP6,*** *HCCS?*
	IF	**HYPOPLASTIC, ROUGH**	**AD**	**616270**	***AMBN***
	IG	**ENAMEL AGENESIS**	**AR**	**204690**	***FAM20A***
	IH		AR	**616221**	***ITGB6***
	IJ		AR	**617297**	***ACP4 = ACPT***
	IK		AD	**620104**	***SP6***
II -HYPOMATURATION	**IIA**	**HYPOMATURATION, PIGMENTED**	**AR**	**204700**	***KLK4, MMP20, WDR72, ODAPH = C4orf26, SLC24A4, GPR68***
				612529	
				613211	
				614832	
				615887	
				617217	
	IIB	**HYPOMATURATION**	**XLR**	**301200**	*AMELX?*
	IIC	**SNOW CAPPED TEETH**	**XL**	**301200**	***AMELX—ARHGAP6***
	IID	**SNOW CAPPED TEETH**	**AD**	**?**	**?**
III -HYPOCALCIFIED	**IIIA**		**AD**	**130900**	***FAM83H*** **(*AD*)**, ***AMTN*** **(*AD*)**
				617607	
	IIIB		**AR**	**618386**	***RELT*** **(*AR*)** *(IIIC?)*
IV -HYPOMATURATION-HYPOPLASTIC WITH TAURODONTISM	**IVA**	**HYPOMATURATION-HYPOPLASTIC WITH TAURODONTISM**	**AD**	**104510**	***DLX3***
	IVB	**HYPOPLASTIC-HYPOMATURATION**	**AD**	**104510**	***DLX3***
		WITH TAURODONTISM			
V -SYNDROMIC AI					*TSC1, FAM20A, DLX3, LTBP3, CNNM4, ROGDI, SLC13A5, SLC10A7, GALNS, AIRE, ORAI1, STIM1, PORCN, PEX1, PEX6, PEX26, CLDN16, CLDN19, FAM20C, SLC4A4, ATP6V1A . . .*

Bold values correspond to the original Witkop's classification.

proteins, to intracellular vesicle trafficking, to ameloblast attachment to the matrix or neighbor cells, to ion transport, to mineralization, to matrix-protein degradation. Critically, the syndromic manifestations of AI and other defects have proven to be an efficient strategy for elucidating the processes of odontogenesis providing better identification into new genes/proteins and their role in the physiopathology of enamel defects as well as the recognition of

new clinical entities. Furthermore, some of these identified genes are involved in both syndromic and non-syndromic rare diseases.

In this paper, we propose to revise Witkop's classification in the light of recent progress in genetics and genomics. The next-generation sequencing panel GenoDENT (Prasad et al., 2016a; Rey et al., 2019) and exome sequencing (WES) (Laugel-Haushalter et al., 2019) have improved understanding and recognition of AI and associated syndromes. We report in this paper individuals with pathogenic variants in known genes involved in AI but also individuals with variants in new candidate genes and individuals presenting variants of uncertain significance (VUS) in known genes. It is our hope that the clinical pictures provided with the proposed classification will assist clinicians in AI recognition. By combining clinical and genetic diagnosis we expect to reveal previously undiscovered rare diseases with a broader clinical spectrum thus improving our diagnoses and management. This strategy would emphasize the role of dentists in the new era of personalized medicine.

Material and methods

Individual's phenotypes

Individuals were enrolled and examined in the Reference Center (CRMR) for rare oral and dental diseases or in one of the 16 affiliated Competence Centers (CCMR) of the French O-Rares network, Filière TETECOU) or by their treating practitioners from France and other countries (ex. the ERN CRANIO). They were recruited between 2009 and 2021. When possible, parents and relatives were also included in the study.

Oral phenotype was documented using the D[4]/phenodent registry protocol, a Diagnosing Dental Defects Database [see www.phenodent.org, for assessment form], which is approved by CNIL (French National commission for informatics and liberty, number 908416). This clinical study is registered at https://clinicaltrials.gov: NCT01746121 and NCT02397824, and with the MESR (French Ministry of Higher Education and Research) Bioethics Commission as a biological collection "Orodental Manifestations of Rare Diseases" DC-2012-1,677 within DC-2012-1,002 and was acknowledged by the CPP (person protection committee) Est IV 11 December 2012.

The individuals presenting AI and the non-affected family members gave written informed consents in accordance with the Declaration of Helsinki, both for the D[4]/phenodent registry and for genetic analyses performed on salivary samples (Oragene® DNA OG-250, OG_650 commercial kits (DNA Genotek Inc., Ottawa, Ont, Canada). Genomic DNA was extracted according to the manufacturer's protocol included in the biological collection.

The terminology used to describe dental and enamel abnormalities has been detailed in (de La Dure-Molla et al., 2019).

Individuals' biological samples were sent to the reference center of Strasbourg, France for genetical analysis.

Individual's genotypes

Next-generation sequencing panel genodent

The GenoDENT panel has been evolving through times from its first published version (Prasad et al., 2016a). The last updated version 6.0 explores 567 genes (Supplementary Table S1).

The GenoDENT panel interrogates two categories of genes: a diagnostic panel (248 genes known as responsible for rare diseases with orodental expression in human) and a discovery panel (319 candidate genes reported as being involved in tooth development or orodental anomalies in animal models for example).

Probe design was performed on the Agilent SureDesign portal (https://erray.chem.agilent.com/suredesign, Agilent, United States) in order to capture, by complementarity, the exonic sequence as well as 25 bases of their flanking intronic sequences. Libraries were prepared with the Agilent SureSelect QXT protocol and sequenced on a NextSeq 550 (Illumina, San Diego, United States). GenoDENT is implemented in a diagnostic setting and its results are directly available for the individual medical file and genetic counselling. Variants are classified according to the American College of Medical Genetics (ACMG) classification (Richards et al., 2015; Harrison et al., 2019). Upon identification of variants of class 4 (probably pathogenic) or 5 (pathogenic), extended familial segregation is performed *via* Sanger sequencing; a detailed report is written and sent to the geneticist. A variant of uncertain significance (VUS) or class 3 should not be used in clinical decision-making. Class 2 are likely benign polymorphisms.

Whole exome sequencing

Trio whole Exome Sequencing (WES) was performed on trio for individuals 7.10, 7.11, 9.1, 9.2, 9.3, 17.1, 17.2, 17.3, 17.4, 18.3, 18.8, 18.10, and 24.2 by Integragen (Evry, France, 2014). Exons of DNA samples were captured using in-solution enrichment methodology (SureSelect Human All Exon Kits, Agilent, Massy, France) with the company's biotinylated oligonucleotide probe library (Agilent Human All Exon v5+UTR 75 Mb Kit) and sequenced with an Illumina HISEQ 2000 (Illumina, San Diego, United States) as paired-end 75 bp reads, resulting in an average coverage of 80X.

Bioinformatics analysis

STARK (Stellar Tools from raw sequencing data Analysis to variant RanKing) is a bioinformatics pipeline based on the GATK recommendations used to process the NGS data (DePristo et al., 2011). Annotation and ranking of SNV/indel were performed by VaRank (Geoffroy et al., 2015) in combination with the Alamut Batch software (Interactive Biosoftware, Rouen, France). Variant effect on the nearest splice site was predicted using MaxEntScan (Yeo and Burge, 2004), NNSplice (Reese et al., 1997) and Splice Site Finder (Shapiro and Senapathy, 1987).Very stringent criteria were applied to filter out non-pathogenic variants: 1) variants represented with an allele frequency of more than 1% in public variation databases including the 1,000 Genomes (The 1000 Genomes Project Consortium et al., 2015), the GnomAD database (Exome Aggregation Consortium et al., 2016) or our internal exome database, 2) variants in 5′ or 3′ UTR, 3) variants with intronic

TABLE 2 Variations found in individuals presenting with syndromic amelogenesis imperfecta.

Patient number	Diagnosis/AI	Gene	Variant and location	Zygosity	Mode of inheritance	Rank	Effect of the mutation	Consistent with the known disease phenotype	Family segregation	Status
17.1 (female)	Hypoplastic, short stature	***LTBP3 Chr11(GRCh37): NM_001130144.3***	c.421C>T; p.(Gln141*) Exon 2 Huckert M et al. (2015)	compound heterozygous	AR	4	non-sense	Yes	S(A,C)	exome
			c.1531 + 1G>T; p.? Intron 8 Huckert M et al. (2015)		AR	4	splice		S(A,C)	
17.2 (female)	Hypoplastic, short stature	***LTBP3 Chr11(GRCh37): NM_001130144.3***	c.2071_2084del; p.(Tyr691Leufs*95) Exon 14 Huckert M et al. (2015)	homozygous	AR	4	frameshift	Yes	S(A,C) S(U,R) MoFa(U,C)	exome
17.3 (male)	Hypoplastic, short stature	***LTBP3 Chr11(GRCh37): NM_001130144.3***	c.2216del; p.(Gly739Alafs*7) Exon 15 Huckert M et al. (2015)	homozygous	AR	4	frameshift	Yes	MoFa(U,C)	exome
17.4 (male)	Hypoplastic, short stature	***LTBP3 Chr11(GRCh37): NM_001130144.3***	c.2356del; p.(Val786Trpfs*82) Exon 17 Huckert M et al. (2015)	homozygous	AR	4	frameshift	Yes	MoFa(U,C) 3S(A,C)	exome
17.5 (female)	Hypoplastic, short stature	***LTBP3 Chr11(GRCh37): NM_001130144.3***	c.3087del; p.(Asn1030Thrfs*47) Exon 22	homozygous	AR	4	frameshift	Yes	MoFa(U,C)	panel
17.6 (female)	Hypoplastic, short stature	***LTBP3 Chr11(GRCh37): NM_001130144.3***	c.3629-2A>G; p.? Intron 26	homozygous	AR	4	splice	Yes	MoFa(U,C)	panel
Patient number	**Diagnosis/AI**	**Gene**	**Variant and location**	**Zygosity**		**Rank**	**Effect of the mutation**	**Consistent with the known disease phenotype**	**Family segregation**	**Status**
18.1 (female)	Hypoplastic AI, nephrocalcinosis	***FAM20A*** *Chr17(GRCh37): NM_017565.4*	c.34_35del; p.(Leu12Alafs*67) Exon 1 Cho et al. (2012)	compound heterozygous	AR	5	frameshift	Yes	S(A,C)	panel
			c.610del; p.(Ala204Profs*12) Exon 3		AR	4	frameshift		S(A,C)	
18.2 (male)	Hypoplastic AI, nephrocalcinosis	***FAM20A*** *Chr17(GRCh37): NM_017565.4*	c.53_54delinsAG; p.(Leu18Arg) Exon 1	putative compound heterozygous	AR	3	missense	Yes	NA	panel
			c.976_978del; p.(Glu326del) Exon 7		AR	3	deletion		NA	
18.3 (male)	Hypoplastic AI, nephrocalcinosis	***FAM20A*** *Chr17(GRCh37): NM_017565.4*	c.217C>T; p.(Arg73*) Exon 1 Jaureguiberry et al. (2012)	compound heterozygous	AR	4	non-sense	Yes	Fa(U,C) S(A,C)	exome
			c.727C>T; p.(Arg243*) Exon 5 Jaureguiberry et al. (2012)		AR	4	non-sense		Mo(U,C) S(A,C)	

(Continued on following page)

10.3389/fphys.2023.1130175

TABLE 2 (*Continued*) Variations found in individuals presenting with syndromic amelogenesis imperfecta.

Patient number	Diagnosis/AI	Gene	Variant and location	Zygosity	Mode of inheritance	Rank	Effect of the mutation	Consistent with the known disease phenotype	Family segregation	Status
18.4 (female)	Hypoplastic AI, nephrocalcinosis	***FAM20A*** *Chr17(GRCh37): NM_017565.4*	c.406C>T; p.(Arg136*) Exon 2 O'Sullivan et al. (2011)	homozygous	AR	5	non-sense	Yes	NA	panel
18.5 (male)	Hypoplastic AI, nephrocalcinosis	***FAM20A*** *Chr17(GRCh37): NM_017565.4*	c.915_918del; p.(Phe305Leufs*76) Exon 6 Jaureguiberry et al. (2012)	compound heterozygous	AR	4	frameshift	Yes	Fa(U,C)	panel
			c.928 + 2T>C; p.? Intron 6		AR	4	splice		Mo(U,C)	
18.6 (male)	Hypoplastic AI, nephrocalcinosis	***FAM20A*** *Chr17(GRCh37): NM_017565.4*	c.915_918del; p.(Phe305Leufs*76) Exon 6 Jaureguiberry et al. (2012)	compound heterozygous	AR	4	frameshift	Yes	S(A,C) Mo(U,C)	panel
		FAM20A *Chr17(GRCh37): NM_017565.4*	c.1301 + 5G>A; p.? Intron 9		AR	3	splice	Yes	S(A,C) Fa(U,C)	panel
18.7 (female)	Hypoplastic AI, nephrocalcinosis	***FAM20A*** *Chr17(GRCh37): NM_017565.4*	c.1106_1107delAG; p.(Glu369Glyfs*10) Exon 7 Prasad et al. (2016a)	homozygous	AR	4	frameshift	Yes	NA	panel
18.8 (female)	Hypoplastic AI, nephrocalcinosis	***FAM20A*** *Chr17(GRCh37): NM_017565.4*	c.1361 + 1G>A; p.? Intron 10	homozygous	AR	4	splice	Yes	NA	exome
18.9 (female)	Hypoplastic AI, nephrocalcinosis	***FAM20A*** *Chr17(GRCh37): NM_017565.4*	c.1369A>T; p.(Lys457*) Exon 11 Jaureguiberry et al. (2012)	homozygous	AR	4	non-sense	Yes	S(A,C)	panel
18.10 (female)	Hypoplastic AI, nephrocalcinosis	***FAM20A*** *Chr17(GRCh37): NM_017565.4*	c.1369A>T; p.(Lys457*) Exon 11 Jaureguiberry et al. (2012)	homozygous	AR	4	non-sense	Yes	MoFa(U,C)	exome
Patient number	**Diagnosis/AI**	**Gene**	**Variant and location**	**Zygosity**		**Rank**	**Effect of the mutation**	**Consistent with the known disease phenotype**	**Family segregation**	**Status**
19.1 (male)	Hypoplastic, pits, mucopolysaccharidosis IV	**GALNS Chr16(GRCh37): NM_000512.5**	c.121-31T>C; p.? Intron 1 Prasad et al. (2016b)	compound heterozygous	AR	3	splice	Yes	Mo(U,C)	panel
			c.953C>G; p.(Thr312Ser) Exon 9 Yamada et al. (1998)		AR	5	missense		Fa(U,C)	
19.2 (female)	Hypoplastic, pits, mucopolysaccharidosis IV	***GALNS Chr16(GRCh37): NM_000512.5***	c.1156C>T; p.(Arg386Cys) Exon 11 Ogawa et al. (1995)	heterozygous	AR	5	missense	Yes	Mo(U,R) Fa(U,R)	panel
			c.1558T>C; p.(Trp520Arg) Exon 14 Zanetti et al. (2021)	heterozygous	AR	2	missense		M(U,Chom)	

(Continued on following page)

10.3389/fphys.2023.1130175

TABLE 2 (*Continued*) Variations found in individuals presenting with syndromic amelogenesis imperfecta.

Patient number	Diagnosis/AI	Gene	Variant and location	Zygosity	Mode of inheritance	Rank	Effect of the mutation	Consistent with the known disease phenotype	Family segregation	Status
Patient number	**Diagnosis/AI**	**Gene**	**Variant and location**	**Zygosity**		**Rank**	**Effect of the mutation**	**Consistent with the known disease phenotype**	**Family segregation**	**Status**
20.1 (female)	Hypoplastic, banding pattern, Lyonisation, Microphthalmia with linear skin defects (MLS) syndrome	***AMELX-ARHGAP6 ChrX(GRCh37): g.125958-12725766del***	ChrX(GRCh37):g.125958-12725766del Many genes including AMELX	heterozygous	XL	4	deletion	Yes	NA	panel
Patient number	**Diagnosis/AI**	**Gene**	**Variant and location**	**Zygosity**		**Rank**	**Effect of the mutation**	**Consistent with the known disease phenotype**	**Family segregation**	**Status**
21.1 (male)	Hypoplastic, Smith Magenis syndrome	***RAI1***	arr[GRCh37] 17p11.2(17280004_20239827)x1 Many genes including RAI1	heterozygous	AD	4	deletion	-	NA	panel
Patient number	**Diagnosis/AI**	**Gene**	**Variant and location**	**Zygosity**		**Rank**	**Effect of the mutation**	**Consistent with the known disease phenotype**	**Family segregation**	**Status**
22.1 (male)	Hypoplastic, Loeys-Dietz syndrome	***TGFBR2* Chr4(GRCh37): NM_003242.6**	c.1561T>C; p.(Trp521Arg) Exon 7 Mátyás et al. (2006)	heterozygous	AD	5	missense	Yes	Fa(U,R) Mo(A,NA)	panel
Patient number	**Diagnosis/AI**	**Gene**	**Variant and location**	**Zygosity**		**Rank**	**Effect of the mutation**	**Consistent with the known disease phenotype**	**Family segregation**	**Status**
23.1 (female)	Hypoplastic, Kohlschutter-Tonz like syndrome	***SLC13A5* Chr17(GRCh37): NM_177550.5**	c.203C>A; p.(Pro68Gln) Exon 2 Schossig et al. (2017)	compound heterozygous	AR	4	missense	Yes	S(A,C)	panel
			c.434C>A; p.(Thr145Lys) Exon 4 Schossig et al. (2017)		AR	4	missense		S(A,C)	
Patient number	**Diagnosis/AI**	**Gene**	**Variant and location**	**Zygosity**		**Rank**	**Effect of the mutation**	**Consistent with the known disease phenotype**	**Family segregation**	**Status**
24.1 (female)	Hypomature, Kohlschutter Tonz syndrome	***ROGDI Chr16(GRCh37): NM_024589.3***	c.46 + 37_46-30del; p.? Intron 1 Tucci et al. (2013)	compound heterozygous	AR	4	deletion	Yes	Mo(U,C)	Insbruck
			c.507del; p.(Glu170Argfs*72) Exon 7 Tucci et al. (2013)		AR	4	deletion		Fa(U,C)	
24.2 (female)	Hypomature, Kohlschutter Tonz syndrome	***ROGDI Chr16(GRCh37): NM_024589.3***	c.117 + 1G>T; p.? Intron 2 Huckert et al. (2014)	homozygous	AR	4	splice	Yes	NA	panel

(Continued on following page)

10.3389/fphys.2023.1130175

TABLE 2 (*Continued*) Variations found in individuals presenting with syndromic amelogenesis imperfecta.

Patient number	Diagnosis/AI	Gene	Variant and location	Zygosity	Mode of inheritance	Rank	Effect of the mutation	Consistent with the known disease phenotype	Family segregation	Status
24.3 (female)	Hypomature, Kohlschutter Tonz syndrome	***ROGDI Chr16(GRCh37): NM_024589.2***	c.366dup; p.(Ala123Serfs*19) Exon 6 Tucci et al. (2013)	compound heterozygous	AR	4	frameshift	Yes	Mo(U,C)	panel
			c.402C>G; p.(Tyr134*) Exon 6 Aswath al. (2018)		AR	4	non-sense		Fa(U,C)	
Patient number	**Diagnosis/AI**	**Gene**	**Variant and location**	**Zygosity**		**Rank**	**Effect of the mutation**	**Consistent with the known disease phenotype**	**Family segregation**	**Status**
25.1 (male)	Hypomature/ Hypomineralized, short stature, intra-uterine growth retardation, skeletal dysplasia, submucosal cleft palate	***SLC10A7* Chr4(GRCh37): NM_001300842.3**	c.269T>G; p.(Leu90Arg) Exon 3	homozygous	AR	3	missense	Yes	MoFa(U,C)	panel
25.2 (female)	Hypomature/ Hypomineralized, short stature, intra-uterine growth retardation, skeletal dysplasia	***SLC10A7* Chr4(GRCh37): NM_001300842.3**	c.908C>T; p.(Pro303Leu) Exon 11 Laugel-Haushalter et al. (2019)	homozygous	AR	4	missense	Yes	MoFa3S(U,C)	exome
Patient number	**Diagnosis/AI**	**Gene**	**Variant and location**	**Zygosity**		**Rank**	**Effect of the mutation**	**Consistent with the known disease phenotype**	**Family segregation**	**Status**
26.1 (female)	Hypomineralized, Jalili syndrome	***CNNM4 Chr2(GRCh37): NM_020184.4***	c.586T>C; p.(Ser196Pro) Exon 1 Parry et al. (2009)	homozygous	AR	4	missense	Yes	S(A,C) Mo(U,C)	panel
26.2 (male)	Hypomineralized, Jalili syndrome	***CNNM4 Chr2(GRCh37): NM_020184.4***	c.1495G>A; p.(Val499Met) Exon 2 Prasad MK et al. (2016b)	homozygous	AR	4	missense	Yes	NA	panel
Patient number	**Diagnosis/AI**	**Gene**	**Variant and location**	**Zygosity**		**Rank**	**Effect of the mutation**	**Consistent with the known disease phenotype**	**Family segregation**	**Status**
27.1 (female)	Hypoplastic, Trichodentoosseus syndrome	***DLX3 Chr17(GRCh37): NM_005220.3***	c.561_562del; p.(Tyr188Glnfs*13) Exon 3 Dong et al. (2005)	heterozygous	AD	4	frameshift	Yes	MoS(A,C)	panel
27.2 (male)	Hypoplastic, Trichodentoosseus syndrome	***DLX3 Chr17(GRCh37): NM_005220.3***	c.561_562del; p.(Tyr188Glnfs*13) Exon 3 Dong et al. (2005)	heterozygous	AD	4	frameshift	Yes	Fa(A,C)	panel

Variations found in 11 different genes in 31 individuals presenting with syndromic amelogenesis imperfecta. Forty-two variants were found, 7 variants are of uncertain significance.

Variants known before the panel implementation are reported in grey, variants previously reported by the team are represented in salmon, variants published thanks to the panel are represented in blue or green, variants reported for the first time are highlighted in green. Familial segregation is also reported when available and reported in this format: Family member code (Phenotype code, Genotype code). Fa: father; Mo: mother; S: sibling; D: daughter; So: son; Co: cousin; A: affected; U: unaffected; NA: not available; C: carrier; R: reference genotype.

10.3389/fphys.2023.1130175

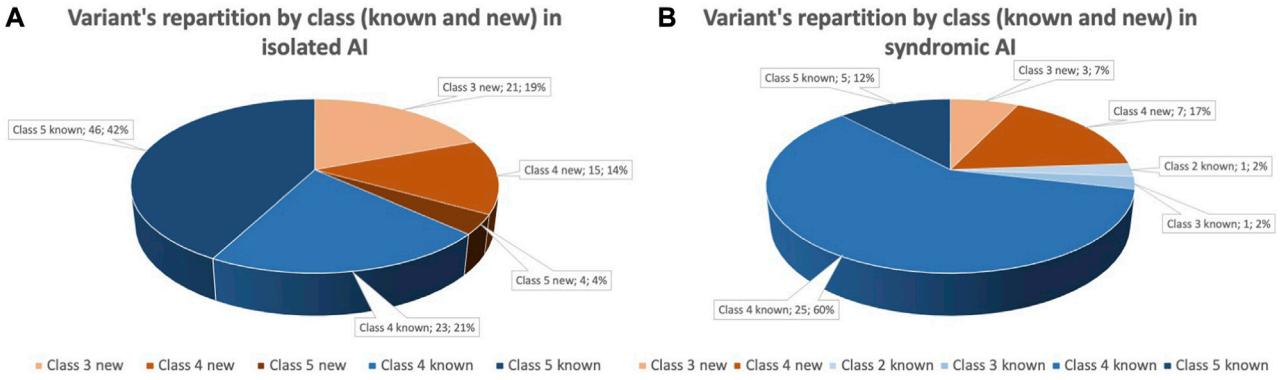

FIGURE 1
Identified variants within the cohort grouped by pathogenic class and novelty. Variant were classified following ACMG recommendations. **(A)** Variant's repartition by pathogenic class and novelty for individual affected by isolated AI. Forty variants (37%) are newly identified variants (orange gradient), 69 (63%) variants are already reported in literature (blue gradient). Among variants reported, 50 (46%) are pathogenic (class 5), 38 (35%) are likely pathogenic (class 4) and 21 (19%) are of uncertain significance. **(B)**. Variant's repartition by pathogenic class and novelty for individual affected by syndromic AI. Seven variants (24%) are newly identified variants (orange gradient), 32 variants (76%) are already reported in literature (blue gradient). Among variants reported, 5 (12%) are pathogenic (class 5), 32 (77%) are likely pathogenic (class 4), 4 (9%) are of uncertain significance (class 3) and 1 (2%) is probably begin (class 2).

locations and no prediction of local splice effect, and 4) synonymous variants without pathogenic prediction of local splice effect. Annotations of structural variations (SV) were performed by AnnotSV (Geoffroy et al., 2018).

Sanger sequencing and segregation

Primers' design was done using the Amplifix v1.5.4 software. Primers were then ordered from Eurofin MWG (Supplementary Table S2). The amplicons' sizes were checked by electrophoresis on the Caliper LabChip GX (Life science). After enzymatic purification with the Illustra™ Exoprostar™ kit (Sigma Aldrich) to remove dNTPs and salts, the PCR product was used to perform a sequence reaction with the BigDye™ Terminator v1.1 Cycle Sequencing Kit (Applied Biosystems, Thermofisher Scientific). The BigDye Xterminator™ Purification Kit (Applied Biosystems by Thermofisher Scientific) was used to purified product. This purified product was then loaded on the 3,500 Series Genetic Analyzers (Applied Biosystems, Thermofisher Scientific) sequencer. Final sequence data were analyzed with SEQUENCE Pilot (JSI medical systems).

Results

We report genetic results for 221 individuals divided between 115 amelogenesis imperfecta (AI) index cases (71 females and 44 males) and 106 relatives from 111 families. Among index cases, 73% were diagnosed with non-syndromic AI and 27% with syndromic AI. Clinical phenotype was assessed according to Witkop's classification and repartition for index's phenotype is: Type I hypoplastic AI (61 individuals, 53%), Type II hypomature AI (31 individuals, 27%), Type III hypomineralized AI (18 individuals 16%) and Type IV hypoplastic-hypomature with taurodontism AI (5 individuals, 4%).

Genetic variants were analyzed using NGS GenoDENT panel and following the ACMG recommendations (Richards et al., 2015; Harrison et al., 2019). Pathogenic variant (class 5) or likely pathogenic variant (class 4) were identified for 81% of the reported index individuals. Non-conclusive variants of uncertain significance (VUS) (class 3) represented the remaining 19%.

Among the 151 sequenced variants identified for indexes, 47 are newly reported and classified as class 4 or 5 (Table 2; Supplementary Table S3).

More specifically for isolated AI individuals, 109 variants are described with 40 newly reported (four class 5, 15 class 4 and 21 VUS) and 69 already reported (46 class 5 and 23 class 4). For syndromic AI, 42 variants are listed with ten newly reported (7 class 4, 3 VUS) and 32 already reported (5 class 5, 25 class 4, 1 class 2 and 1 VUS) (Figure 1). For some individuals two variants have been reported in the case of an autosomal recessive (AR) disorder and heterozygous compound variants (23 isolated AI individuals and 10 syndromic). VUS have been identified in different situations: nine times as solo heterozygous variant, two times as homozygous variant, four times as two heterozygous VUS and seven times as heterozygous associated with a pathogenic variant.

The most frequently discovered genotypes were associated with *MMP20*, *FAM83H* and then *AMELX* and *ENAM* variants for isolated AI (Figure 2). We didn't find any variant in *GPR68*, *STIM1*, *RELT*, *ITGB6/4*, *AMTN* and *SP6 genes*. In individuals presenting syndromic AI we reported variants in *LTBP3*, *FAM20A* and *GALNS*, *SLC13A5*, *DLX3*, *RAI1*, *TGFBR2*, *CNNM4*, *SLC10A7*, *ROGDI* (Figure 3) but didn't find any variant in *TP63*, *TSC1-2*, *AIRE*, *CLDN16*, *CLDN19*, *ORAI1*, *STIM1*, *RELT*, *PEX26*, *PEX1*, *PEX6*, *PORCN* and *MSX2*.

Familial segregation, with Sanger sequencing, of variants previously identified in index cases was performed on

10.3389/fphys.2023.1130175

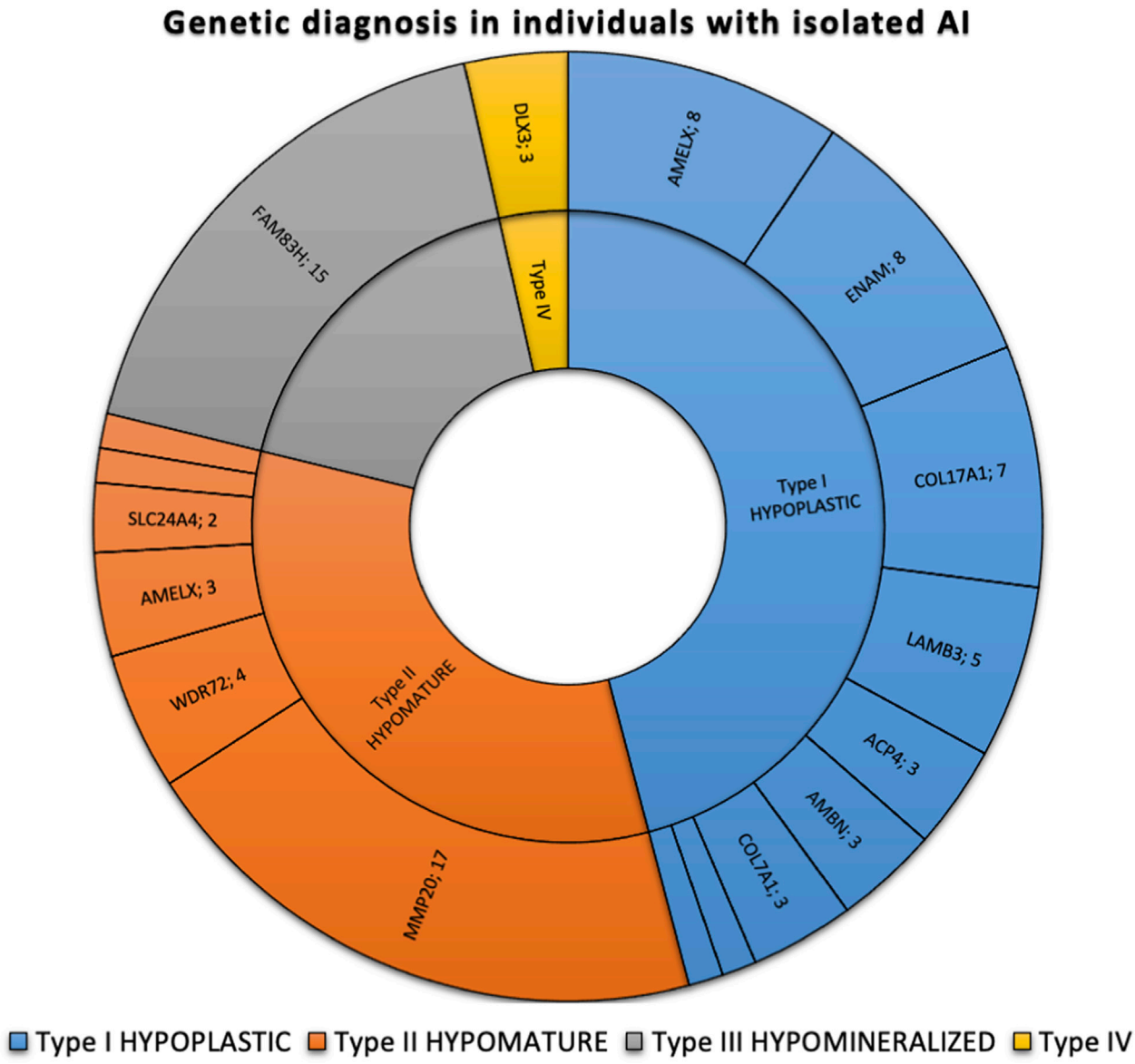

FIGURE 2
Phenotypic and genetic diagnosis in 86 individuals with isolated AI. Number of patients per main type of AI and per gene. Type I hypoplastic AI represents 39 individuals (45.3%) in blue associated with 9 different genes (*AMELX, ENAM, COL17A1, LAMB3, ACP4, AMBN, COL7A1, LAMA3, LAMC2*). Type II hypomature AI represents 28 individuals (32.6%) in orange associated with 6 different genes (*MMP20, WDR72, AMELX, SLC24A4, KLK4*). Type III hypomineralized AI represents 16 individuals (18.6%) in grey associated with 2 different genes (*FAM83H, WDR72*). Type IV hypoplastic-hypomature with taurodontism AI represents 3 individuals (3.5%) in yellow in 1 gene (*DLX3*).

106 individuals. Among them, 33 affected individuals were carrier of the familial variant, 35 non-affected individuals were carrier of one of the two familial variants in the context of a recessive pathology, 31 non-affected individuals did not carry the familial variant. Phenotype/genotype correlation was not conclusive for 7 individuals mostly because sufficient phenotypic information was not available.

Through this deliberate yet targeted strategy, we were able to identify pathogenic variants in known genes involved in AI as expected. In addition, we identified variants in candidate genes previously unreported in AI as well as individuals presenting novel VUS in known genes. As it is nearly impossible in the field of rare disease to create an exhaustive repertoire of pathological variants, we present the findings of this study following (Witkop, 1988) classification, gene by gene linking phenotypic clinical description with the associated genotype.

Additionally, working with this panel of variants, with annotated gene functions, and with the genotype/phenotype associations described in the cited literature, we aim to refine the clinical classification on the basis of Witkop's classification to integrate the current understanding of AI in the context of genetic data, with an initial segregation of phenotypes as "isolated" or "syndromic". Listed below are the proposed categories and sub-categories under this novel "GenoDENT" classification.

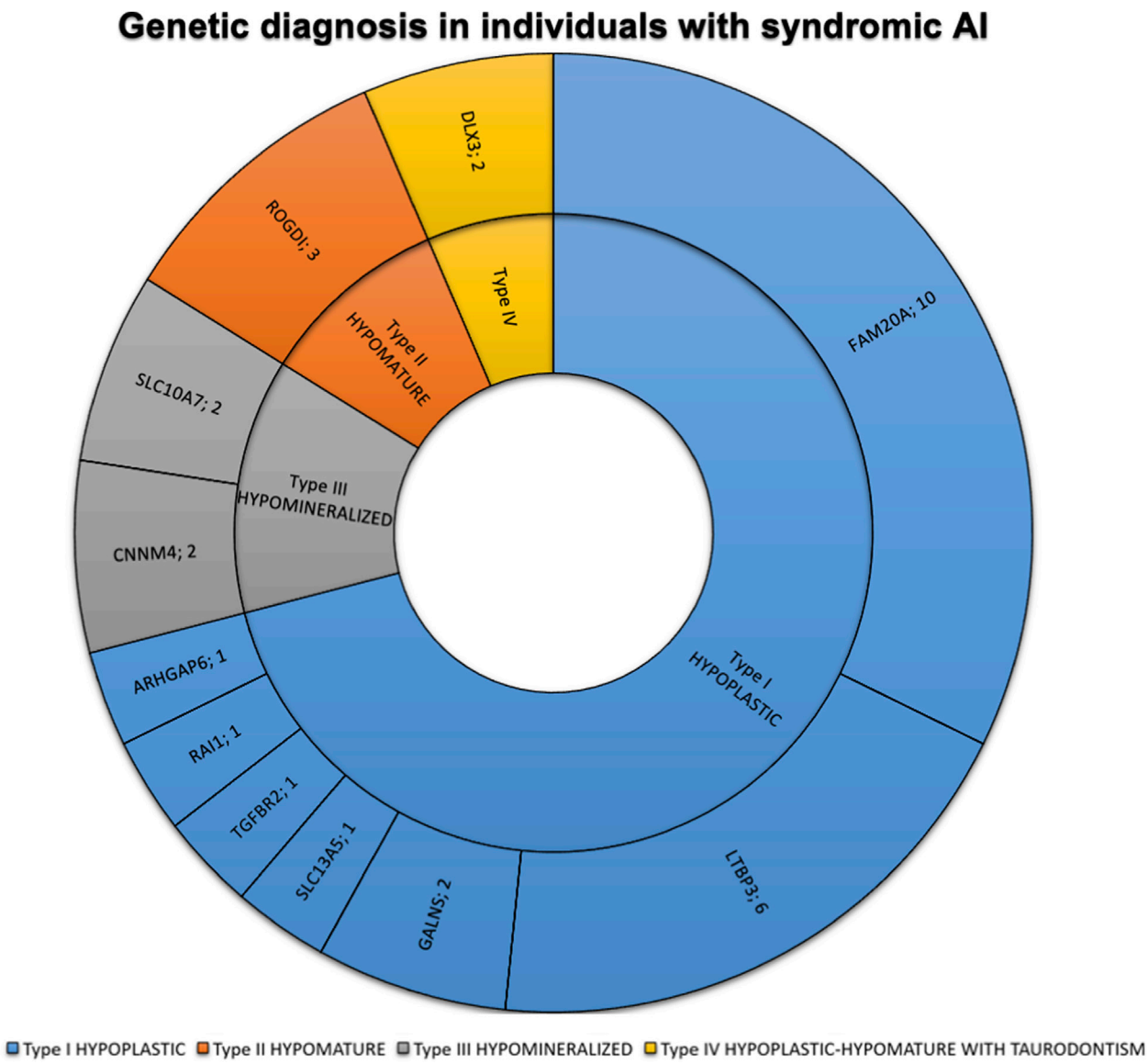

FIGURE 3
Phenotypic and genetic diagnosis in 31 individuals with syndromic AI. Number of patients per main type of AI and per gene. Type I hypoplastic AI represents 22 individuals (71%) in blue associated with 7 different genes (*FAM20A, LTBP3, GALNS, ARHGAP6, RAI1, SLC13A5, TGFBR2*). Type II hypomature AI represents 3 individuals (9.7%) in orange associated with 1 gene (*ROGDI*). Type III hypomineralized AI represents 4 individuals (12.9%) in grey associated with 2 different genes (*CNNM4, SLC10A7*). Type IV hypoplastic-hypomature with taurodontism AI represents 2 individuals (6.5%) in yellow in 1 gene (*DLX3*).

"ISOLATED" AMELOGENESIS IMPERFECTA

AI can occur with or without associated syndromic conditions. These following proposed classes of AI expand on Witkop's classification to describe non-syndromic AI diseases at a genetic level.

Type I—Hypoplastic

Hypoplastic AI describes quantitative enamel defects such as localized hypoplasia, generalized hypoplasia, enamel pits, enamel striae, groove defects, thin but mineralized enamel, or in extreme cases, the complete absence of enamel. Anomalies observed in hypoplastic AI, result from failure during the enamel matrix secretory stage (Wang et al., 2015). Four forms of hypoplastic AI—the pitted, local, smooth and rough forms - are autosomal dominant (type IA, IB, ID and IF), three are autosomal recessive (type IC, IG and IJ), and one is X-linked (type IE) (Witkop and Sauk, 1976).

Type IA—Hypoplastic, pitted, autosomal dominant *COL17A1, COL7A1, LAMA3, LAMB3* (#104530), *LAMC2, ITGB6* (#616221)

Enamel may display pits on the labial or buccal surfaces often arranged in rows and columns. Often these pits are obvious as they

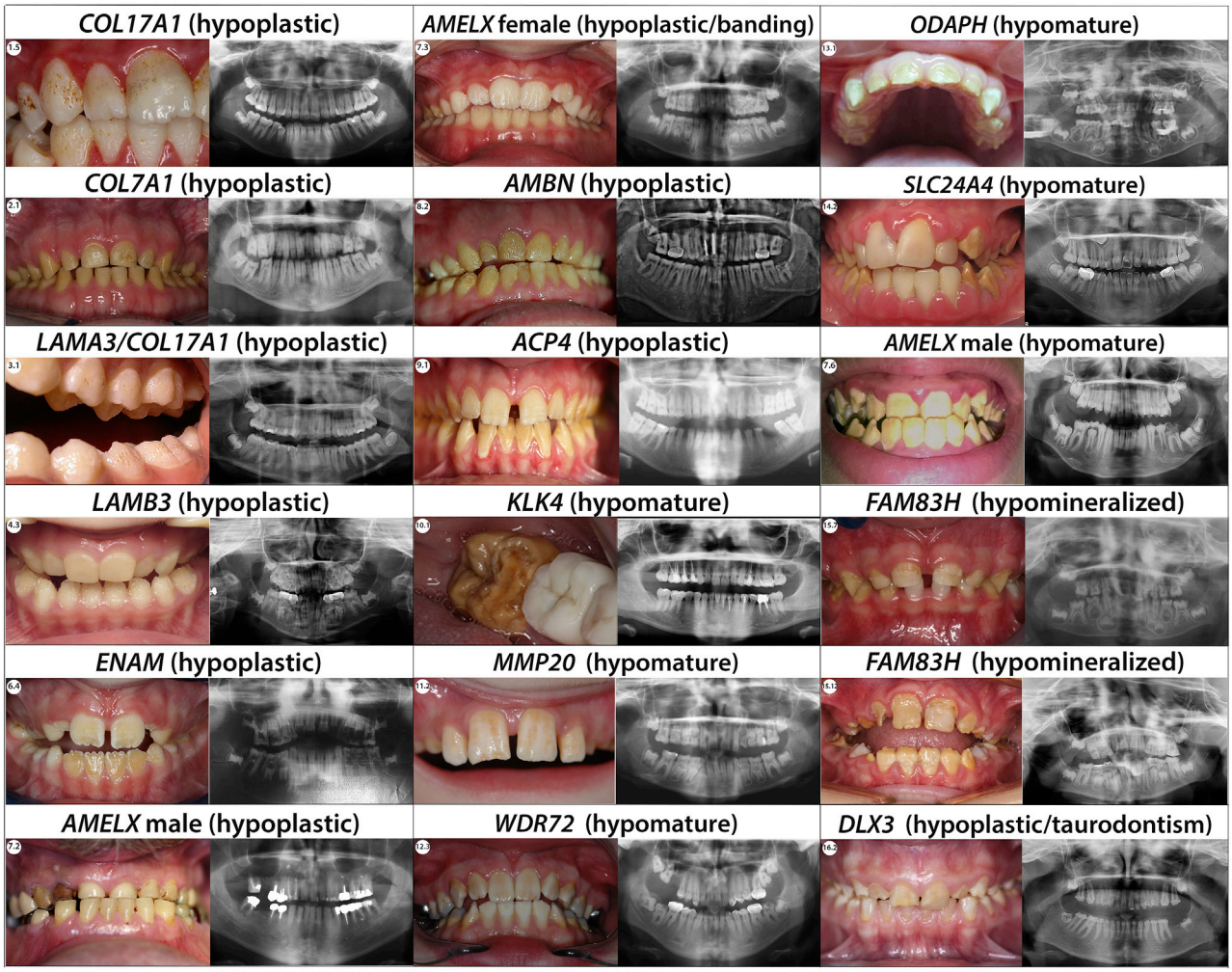

FIGURE 4
Phenotype/Genotype correlation for isolated AI. Typical phenotype/genotype correlation observed in patients presenting with isolated Amelogenesis imperfecta (intraoral pictures and radiographs). Patients who are carrier of *AMELX* mutations can present with different types of AI. Indeed, the phenotype can be either hypoplastic (severe with almost no enamel in male and with a lyonization banding pattern in female) or hypomature depending on the mutation's localisation. When the mutations occur in a MMP20 cleavage site the *AMELX* related AI observed is a X-linked hypomature AI.

are colored by extrinsic stains that can be removed by professional cleaning.

The genes implicated in this subtype of AI encode proteins of the extracellular matrix, important for the attachment of the ameloblast cells to their matrix, structural component of hemidesmosomes *COL17A1*, anchoring fibril to the basement membrane *COL7A1*, laminin constituting chains *LAMA3, LAMB3, LAMC2*, integrins adhesion receptors that function in signaling from the extracellular matrix to the cell *ITGB6* (a receptor for the laminins). *COL7A1* gene encodes the alpha-1 chain of type VII collagen (Burgeson et al., 1985). *COL17A1* encodes the homotrimer type XVII collagen (COL17). *LAMA3, LAMB3, LAMC2* genes encode laminin α3, laminin β3, and laminin γ2, respectively, forming together the heterotrimer laminin-332 (LM-332).

Both LM-332 and COL17 are crucial in ameloblast differentiation and enamel formation, mutations of which result in enamel defects consisting of hypoplasia, pitting, roughness, thinning or furrowing of enamel (Yuen et al., 2012).

These same genes, under an autosomal recessive inheritance transmission are responsible for various forms of epidermolysis bullosa (EB: Non-Herlitz junctional epidermolysis bullosa (nH-JEB) *COL17A1*; recessive dystrophic epidermolysis bullosa (RDEB) *COL7A1;* junctional EB (JEB) LAMA3, *LAMB3, LAMC2*) (Masunaga, 2006). In EB, the phenotype synopsis includes nails dystrophy, skin hyperhidrosis and hyperkeratosis, blistering of skin and mucosa, eye defects, hair anomalies with alopecia or loss of eyelashes and an abnormal dentition with extensive enamel hypoplasia, focal pitting, and discoloration.

COL17A1

In our current study, we found six individuals (1.1–1.6) presenting with, hypoplastic pitted AI. The enamel appears

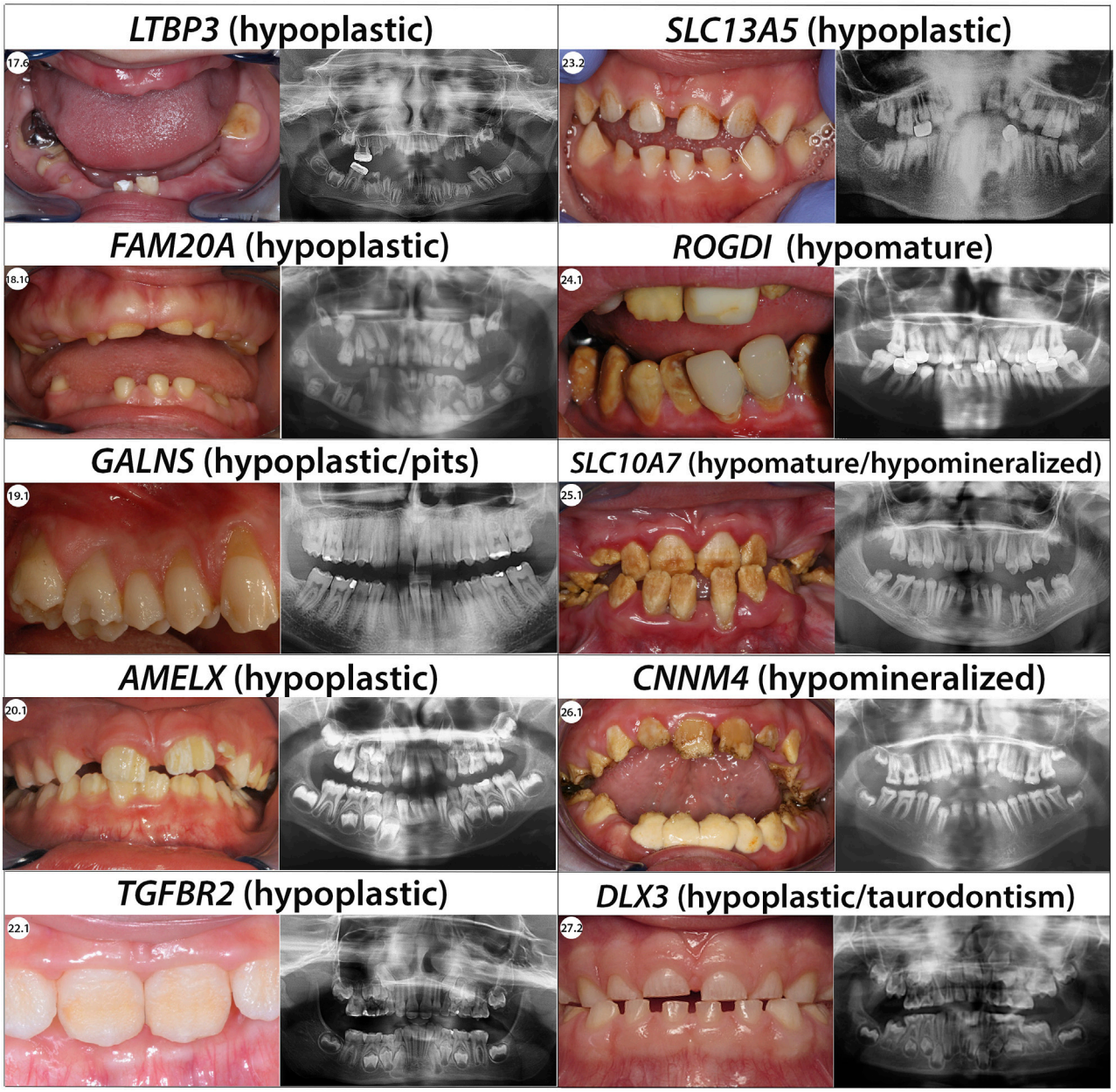

FIGURE 5
Phenotype/Genotype correlation for syndromic AI.

pitted, rough, of normal hardness and presents yellow-brown extrinsic stains. Radiographs show normal enamel opacity (Figure 4; Supplementary Figure S1A).

We identified heterozygous loss of function variants in *COL17A1* gene in each of them (Supplementary Table S3; Supplementary Figure S2A). In individuals 1.2, 1.5, and 1.6 the heterozygous variants we identified were originally described as pathogenic in EB individuals. The heterozygous variant found in individual 1.2 was also found in her affected sister and daughters (Supplementary Figure S3.1). The heterozygous variant found in individual 1.6 was also detected in his mother but the parents' phenotype was not known (Supplementary Figure S3.2). Individuals 1.1, 1.3 and 1.4 and their variants were already described in an autosomal dominant mode by our team in (Prasad et al., 2016b). Heterozygous variants in *COL17A1* gene, historically discovered in EB families, were reported in the literature as responsible for enamel defects and an AI phenotype in heterozygous carriers, including parents non-affected with EB (McGrath et al., 1996; Prasad et al., 2016a; b).

COL7A1

We report three individuals (2.1, 2.2 and 2.3) presenting with an hypoplastic pitted AI phenotype with thin enamel and yellow

discoloration (Figure 4; Supplementary Figure S1B). Panoramic X-rays show thinner enamel. We found in these 3 individuals *COL7A1* heterozygous variants not previously described (Supplementary Table S3; Supplementary Figure S1B, S2B).

Individual 2.1 has an intronic heterozygous variant (NM_000094.4:c.2440 + 3A>C) in intron 19. This variant is predicted to have an impact on the splicing site possibly leading to an, in phase, exon 18 skipping. Exon 18 codes for a Fibronectin type III domain involved in interactions with integrins. A variant implicating a similar splice site defect has been described in an individual presenting epidermolysis bullosa with enamel defects (c.2440 + 1G>T) (Vahidnezhad et al., 2017).

Individual 2.2 and 2.3 both carry a heterozygous missense variant NM_000094.4:c.3605G>A; p.(Arg1202His) and NM_000094.4:c.3785T>C; p.(Met1262Thr) located respectively in the Von Willebrand factor type A and Collagen triple helix repeat protein domains. No other missense variant was described in the Von Willebrand domain, but other missense variants have been described as pathogenic in the Collagen triple helix domain (Yenamandra et al., 2018). Individual 2.2 has an affected sibling carrying the same variant. Individual 2.3 inherited his variant from his affected mother (Supplementary Figures S3.3, S3.4).

All these variants were, so far, classified as VUS and further investigations would be needed to determine their impacts on the phenotype.

Variants in this gene were only previously reported in individuals with epidermolysis bullosa in autosomal dominant or recessive conditions.

LAMA3

We report one individual (3.1) presenting severe hypoplastic AI carrying a mutation in *LAMA3*. A digenic inheritance with variants in both in *COL17A1*, and *LAMA3* has been previously described (Prasad et al., 2016a) (Supplementary Table S3; Supplementary Figure S2C). The heterozygous variant, transmitted by her affected mother, in *COL17A1* NM_000494.4:c.1141 + 1G>A is a pathogenic variant altering the splicing site in exon 14. The individual also carries an heterozygous variant in *LAMA3* not inherited from her mother NM_000227.6:c.1650_1659del; p.(Ile550Metfs*46). We hypothesize this additional mutation could explain the phenotype severity gradient between 3.1 and her mother. Indeed, both are presenting hypoplastic AI but in 3.1 the phenotype is more severe, and the pits are numerous and clearly visible (Figure 4; Supplementary Figure S1C).

LAMB3

Each of the individuals reported in this publication (4.1, 4.2, 4.3, 4.4 and 4.5) carrying mutations in *LAMB3* present with hypoplastic AI with an irregular pitted and thinner enamel and no sign of epidermolysis bullosa (Figure 4; Supplementary Figure S1C).

Among the pathogenic variants reported in this gene, bi-allelic loss of function variants was described in patients with severe EB and AI. Dominant heterozygous frameshift variations were reported in patients with isolated AI: all those variations were located in the last two exons of *LAMB3* gene. For these published patients, a dominant negative effect was proposed by Smith (Smith et al., 2019). In our cohort, two patients have such 3′end variations: patients 4.4 and 4.5, NM_000228.3: c.2926del; p.(Val976Trpfs*54) and c.3305del; p.(Gly1102Valfs*7) (Supplementary Figure S3.5; Supplementary Figure S2D).

We also report in our cohort, three patients with isolated AI and a non-sense mutation located before the 3′end of the gene (4.1, 4.2 and 4.3) 4.1 and 4.3 were reported in (Prasad et al., 2016a) and reanalyzed in the context of this publication. Revisiting these data showed that 4.1 also presented a non-sense mutation in position 42 (c.124C>T; p.(Arg42*)); we also detected a new missense variant c.3490C>T; p.(Arg1164Cys) which is predicted to be deleterious by SIFT (v6.2.0) and Polyphen-2. Familial segregation showed that those two variations affected both alleles in this patient (Supplementary Figure S3.6).

Patient 4.2 has one premature stop codon in position 635 and on the second allele, a splice variation was detected, c.1288 + 1G>T (Supplementary Figure S3.7). This variation was previously reported by Kiritsi et al. (2015) and the authors confirmed the impact of the splice variant by mRNA study: the variation induced an in-frame skipping of exon 11 and was predicted to produce an incomplete protein p.(Ser378_Arg430delinsCys). According to (Kiritsi et al., 2015), the patient presented with AI and a mild form of EB with favorable evolution.

The clinical synopsis of *LAMB3*-related AR epidermolysis bullosa, junctional 1A intermediate includes enamel hypoplasia, enamel pitting and corneal erosion, corneal scarring besides skin, hair and nails defects. Notably, individual 4.2 has a history of recurrent corneal ulcers and might therefore present a mild form of EB.

Patient 4.3 has a stop mutation in position 635. A splice variation was also detected in this patient c.944-14C>G but mRNA analysis could not be performed and familial segregation was not possible.

The first two cases (4.1 and 4.2) could thus be compatible with a recessive form of AI: those patients combined one null allele and a possible hypomorphic second allele. An AR clinical continuum may go from severe EB/AI in patients with biallelic null variations to mild EB/AI or isolated AI in patients with one null mutation occurring with a hypomorphic allele.

LAMC2

A 4-year-old individual (5.1) displayed a hypoplastic/hypomature AI phenotype. The primary dentition showed thin white opaque enamel (Supplementary Figure S1C).

We found a heterozygous *LAMC2* variant NM_005562.3: c.493C>T; p.(Arg165Cys) with an allele frequency of 0.2% in GnomAD, predicted deleterious by SIFT (v4.0.3) and PolyPhen-2 and located in the Laminin EGF domain (Supplementary Table S3; Supplementary Figure S2E). Heterozygous variants in this gene have not previously been associated with AI in human but this gene is known to be involved in enamel formation defects in mice (Wazen et al., 2016) and the patient's phenotype is similar to the one observed in mice. The allele is inherited from her mother but her phenotype was not available (Supplementary Figure S3.8).

ITGB6

Individuals with AR variants in integrin-β6 (*ITGB6*), have been described as affected with hypoplastic pitted and hypomineralized

AI. Enamel is less dense, presents disorganized prisms, and severe pitting in the coronal side of tooth with pigmentations (Poulter et al., 2014a; Wang S.-K. et al., 2014; Seymen et al., 2015a). Though this established phenotype infers a Type 1A classification, no *ITGB6* pathogenic variants were found in our cohort.

Type IB—hypoplastic local, autosomal dominant, #104500

Whereas other genes with this mode of inheritance may yet to be discovered, our survey of the literature and our cohort currently suggest that this classification is composed only for mutations of *ENAM*.

ENAM

ENAM encodes enamelin, the largest enamel matrix protein, composed of 1,142 amino acid. It is a secretory protein with a 39 amino acid signal peptide. During amelogenesis, the protein is found among the developing crystallites in the enamel rods and interrods (Daubert et al., 2016). Its presence is necessary for correct prism morphogenesis, contributing to thicker enamel (Shore et al., 2010). Variants in ENAM cause hypoplastic AI (Mårdh et al., 2002; Kim et al., 2005a), in which defective enamel is thin or absent, with horizontal row of pits, linear depressions, or one large hypoplastic area. These defects appear most prominent on the buccal surfaces of the teeth involving the middle third of the enamel.

Non-sense variants disrupting the enamelin domain, splice variants, small deletions and insertions and one big insertion have been described to be causative of Amelogenesis imperfecta (Hu and Yamakoshi, 2003).

We identified in our cohort eight individuals with hypoplastic AI manifest as thin, rough enamel in permanent teeth, columns of pits, and linear depressions in enamel. Hypoplastic enamel is clearly identified in panoramic X-Rays especially visible on unerupted teeth (Figure 4; Supplementary Figure S1D).

We detected *ENAM* heterozygous variants in each of these individuals (Supplementary Table S3; Supplementary Figure S2F). Three new, never reported, variants are described in this paper. Individual 6.1 presented a missense heterozygous variant in exon 3 NM_031889.3:c.101T>C; p.(Leu34Pro) (Supplementary Table S3). Missense variants in the N-terminal domain have previously been described, reportedly negatively impacting ameloblast secretory pathway leading to endothelial reticulum (ER) stress and an activated unfolded protein response (Brookes et al., 2017). With this proposed mechanism, a functional analysis could improve identification of the VUS towards pathogenic.

For individual 6.3, we detected a heterozygous 1bp duplication on a splice site NM_031889.3:c.588 + 1 dup; p.(Asn197Glufs*25). This variant was also detected in her affected sister and father (Supplementary Figure S3.9). The variant occurred at the same position than the already described deletion c.588+1delG; p.(Asn197Ilefs*81) found in individuals 6.4, 6.5, 6.6 (Supplementary Figure S3.10) and 6.7 (Supplementary Figure S3.11). Interestingly in 6.3 the phenotype seemed slightly different to the one observed in the four individuals carrying the deletion with an hypoplastic but also hypomature whitish enamel. Individual 6.3 also presented agenesis of 16, 26, 36, 46 but no further variant explaining the missing teeth was identified.

Individual 6.8, his affected sister, and their mother were all heterozygous for a non-sense mutation in exon 9 NM_031889.3: c.664C>T; p.(Gln222*) (Supplementary Figure S3.12).

Truncating variants earlier and later in the protein were already described in this gene and found to be causative of hypoplastic amelogenesis imperfecta (Ozdemir et al., 2005a; Seymen et al., 2014a).

Type IC -hypoplastic local, autosomal recessive, #204650

ENAM mutations also currently comprise the entire classification of type 1C, though further genes may await discovery.

ENAM

The phenotype is more severe than in local hypoplastic autosomal dominant AI and has also been linked to *ENAM* variants but in a recessive mode of inheritance (2 alleles affected). This leads to the conclusion that *ENAM* variants associated phenotype is dosage dependent. Indeed, Ozdemir et al., 2005a, Hart et al., 2003 described families for which carriers of only one *ENAM* variant were less affected presenting only localized enamel pitting, whereas family members with compound heterozygous or homozygous *ENAM* variants presented severe hypoplastic AI. Lindemeyer et al., 2010 also described the case of a nine-year-old boy with homozygous variants in *ENAM* and severe hypoplastic AI and smooth teeth.

We did not detect any cases AR mode of inheritance associated with *ENAM* in our cohort.

Type ID - Hypoplastic, smooth, autosomal dominant

This type of AI shows crowns with a yellow to brown color. The enamel tends to be thin in some teeth and absent in others. The tooth surfaces are smooth to uneven and sensitive to temperature changes and touch. Radiographs reveal a lack of enamel.

As the texture of the crowns is smooth, the attrition is apparent on the occlusal surfaces (Burzynski et al., 1973). No gene has previously been associated to this category, but here we propose *SP6* as the first possible gene classified in this type of AI based on our literature survey.

SP6

SP6 encodes a transcription factor expressed during amelogenesis and involved in regulating proliferation and differentiation of ameloblasts (Nakamura et al., 2004; 2008; Utami et al., 2011; Muto et al., 2012; Ruspita et al., 2020). Autosomal dominant pathogenic variants have been published in two unrelated families in association with severe hypoplastic AI (Smith et al., 2020; Kim et al., 2021b). Interestingly in the two families, the same amino acid (Ala273) was modified. No variant in this gene was evident in our cohort.

Type IE—hypoplastic, smooth, x-linked dominant, #301200

The surface of the enamel can vary, showing smooth, rough, pitted, or local defects (Witkop, 1988). Due to random X chromosome inactivation in female (Lyonisation effect), differences exist in phenotypic expression between affected males and heterozygous females. Affected males (XY) have only a very thin, smooth enamel, which appears nearly homogeneous. Females (XX) present a milder phenotype with a banding pattern featuring hypoplastic enamel rough/pitted, vertically ridged and normal enamel. Radiographically, thinner enamel contrasts normally from dentin.

AMELX

AMELX, Amelogenin X-linked, has been identified as the gene involved in this AI. The gene resides in intron 1 of *ARHGAP6* in the opposite orientation (Iwase et al., 2007). Amelogenins are highly conserved proteins secreted by ameloblasts that constitute 90% of the enamel organic matrix. As the proteins are digested and removed in maturation phase, mineral crystals grow in well-organized prism patterns (Gibson et al., 2001).

Genotype-phenotype correlation revealed that variants in the N-terminal (Lagerström et al., 1991; Kim et al., 2004) and C-terminal parts (Greene et al., 2002) of AMELX cause hypoplastic AI.

In our cohort, we identified five females (7.1, 7.3, 7.4, 7.8 and 7.11) presenting the typical hypoplastic AI banding pattern (Figure 4; Supplementary Figure S1E).

We identified heterozygous variation in *AMELX* in each of these individuals (Supplementary Table S3; Supplementary Figure S2G). Female individuals 7.1 to 7.3 were carrying a non-sense *AMELX* variant NM_182680.1:c.11G>A; p.(Trp4*) firstly reported by (Hart et al., 2002b). Individual 7.4 carried a newly reported variant NM_182680.1(*AMELX*):c.47C>A; p.(Ala16Asp) predicted damaging by SIFT (v6.2.0) and Polyphen-2 and inherited by her affected father (Supplementary Figure S3.13). Individuals 7.5 to 7.7 were presenting already reported missense variant. Individuals 7.8 to 7.11 were carrying frameshift variant originally reported by (Lench and Winter, 1995).

Male individual 7.9 is the cousin of 7.8 female and carried the same variant (Supplementary Figure S3.14). He presented the characteristic female lyonisation banding pattern thus requiring further understanding and clarification. His karyotype revealed XXY aneuploidy, the most common disorder of sex chromosomes in humans, with a prevalence of one in 500 males. This finding explained the lyonisation pattern in a male and was consistent with his associated behavioral disorder.

Individual 7.11 is the mother of 7.10 male. The mother presented the typical female hypoplastic banding pattern. The boy showed a severe hypoplastic AI with almost no enamel associated with delayed dental eruption and behavioral issues. As the boy's phenotype presented as syndromic, this family was directly sequenced by whole exome sequencing. We identified a pathogenic 1bp deletion leading to a premature stop codon c.541del; p.(Leu181Cysfs*8), a mutation previously reported (Kindelan et al., 2000) in both the mother and the boy (Supplementary Figure S3.15). This variation clearly explained the AI phenotype but no other variation was discovered as possibly explaining behavioral issues presented by this boy.

Male individuals 7.5, 7.6 and 7.7 presented a different hypomature amelogenesis imperfecta phenotype with a smooth yellow opaque enamel (Supplementary Figure S1E). Individuals 7.6 and 7.7 carry a c.208C>A; p.(Pro70Thr) variant first described by Collier et al., 1997 (Supplementary Figures S3.16, S3.17). Functional analyses showed that this variant is reducing the interactions between amelogenin and the MMP20, metalloproteinase degrading amelogenin in the maturation phase (Tanimoto et al., 2008). Therefore, depending on the patho-physiological mechanism, *AMELX* might also be the gene involved in the hypomature form of AI type IIC (snow-capped teeth X-linked) or eventually IIB (hypomaturation X-linked). This would be discussed further in these mentioned categories.

Individual 7.7 also had a frequently reported heterozygous variant in *WNT10* gene (c.682T>A; p.(Phe228Ile), explaining the 12, 15, 22, 28 agenesis.

Type IF—amelogenesis imperfecta, hypoplastic, autosomal recessive #616270

Hypoplastic enamel in the primary and permanent dentitions, showing a rough and discolored appearance is the hallmark of this AI. The enamel may be absent, pitted, or thinner. We currently list only *AMBN* as the causative gene defect in this class.

AMBN

AMBN gene (4q13.3), containing 13 exons was discovered as the causative gene for non-syndromic autosomal recessive amelogenesis imperfecta (Toyosawa et al., 2000). It encodes ameloblastin (AMBN, also named "amelin" or "sheathlin"), the second most abundant enamel matrix protein, critical to amelogenesis (Lu et al., 2018).

Four cases have been reported so far in the literature with AMBN variants associated with non-syndromic AI (Poulter et al., 2014b; Lu et al., 2018; Liang et al., 2019).

In our cohort we identified three individuals with a hypoplastic amelogenesis imperfecta combined with recessive variants in *AMBN* (Supplementary Table S3; Figure 4; Supplementary Figures S1F, S2H). Individuals 8.1, and 8.2 presented compounds heterozygous variants never described before. 8.1 displayed a splice variant in intron 1 NM_016519.6:c.15 + 1G>A and a non-sense variant in exon 8 c.577G>T; p.(Gly193*) (Supplementary Figure S3.18). 8.2 was carrying a non-sense variant in exon 5 NM_016519.6:c.209C>G; p.(Ser70*) and a splice variant in intron 7 c.571-1G>C. The non-sense mutation hadn't previously been described, however Poulter et al. (2014b) described a large deletion resulting in the loss of exon 6. Individual 8.3 was already described in (Prasad et al., 2016a). We detected a homozygous splice variant in intron 6 never described before NM_016519.6:c.532-1G>C. This is the first splicing variant described in this gene.

Type IG—enamel agenesis, autosomal recessive enamel-renal syndrome (ERS), #204690

Commonly described as an isolated AI, enamel agenesis may be observed concomitantly with other orodental and/or systemic features such as nephrocalcinosis in Enamel Renal Syndrome (ERS, MIM#204690), or gingival hyperplasia in Amelogenesis Imperfecta and Gingival Fibromatosis Syndrome (AIGFS, MIM#614253 moved to MIM#204690) (O'Sullivan et al., 2011).

FAM20A

These conditions are allelic, and are now considered as a spectrum of ERS and due to recessive variants in *FAM20A* gene (17q24.2; 11 exons (Nalbant et al., 2005; Jaureguiberry et al., 2012). FAM20A is a secreted glycoprotein, Golgi Associated Secretory Pathway Pseudokinase and its intact signal sequence is required for secretion. Various human tissues reveal high transcript levels in lung and liver and intermediate levels in thymus and ovary (Nalbant et al., 2005).

The clinical phenotype is highly distinctive and when recognized leads to the clinical diagnosis and the subsequent exploration *via* ultrasound of the presence of renal calcifications.

The diagnostic criteria of ERS are based on oral findings, including clinical (severe enamel hypoplasia, delayed or absent tooth eruption, gingival hyperplasia) and radiographic signs (non-erupting teeth, pulp calcifications and hyperplastic dental follicle) (de la Dure-Molla et al., 2014). Associated focal ectopic calcification features, along with the presence of renal abnormalities are also pathognomonic of ERS (Torres et al., 2018). Dental defects are present since the primary dentition, with no declared tooth pain or sensitivity (Dourado et al., 2019). Nephrocalcinosis (NC) and other kidney disorders have been included as frequent findings, especially in the early adulthood (Dellow et al., 1998; Martelli-Júnior et al., 2011). In that sense, it is speculated that even those individuals with oral characteristics showing no renal defects, but with biallelic *FAM20A* variants, will eventually develop NC (Dourado et al., 2019) and should be tested for and followed for NC and other renal defects.

As the phenotype was initially described as isolated AI, it appears in "isolated" AI in the original classification. However, as nephrocalcinosis is observed in these patients, it should be reclassified as syndromic AI. Therefore, data concerning patients with *FAM20A* variations will be discussed in the syndromic section (Table 2, Supplementary Figures S1M, S2R, S3.39, S3.40, S3.41, S3.42).

Type IJ—amelogenesis imperfecta, autosomal recessive, #617297

In this type of AI, the enamel is thin with irregular surface and teeth appears yellow.

ACP4

This phenotype is associated with recessive homozygous or compound heterozygous variants in *ACP4* gene encoding testicular acid phosphatase (Seymen et al., 2016; Smith C. E. et al., 2017). All variants reported so far were localized in the histidine phosphatase domain. This domain contains conserved Histidine residues that are phosphorylated during the catalytic activity of the protein and other residues that are forming a phosphate pocket and interact with the phospho group of substrates before, during and after its transfer to the Histidine residue. Variants were reported mostly in exon 4 and 7 and only one was reported in exon 3 (Seymen et al., 2016; Smith C. E. et al., 2017).

We found three unrelated families (individuals 9.1, 9.2 and 9.3) with hypoplastic amelogenesis imperfecta, with thin enamel with irregular surface, and a yellowish color. X-rays showed a thinner enamel of normal density, long teeth, and slim roots (Figure 4; Supplementary Figure S1G).

These families were previously negative on the GenoDENT panel first version (Prasad et al., 2016a), and were further investigated by whole exome sequencing analysis. We found compound heterozygous variants in the *ACP4* gene (Supplementary Table S3; Supplementary Figure S2I). Indeed *ACP4,* discovered in 2016 (Seymen et al., 2016), was not on the first version of GenoDENT but was added at version 0.4. Individual 9.1 had a previously reported missense variant in exon 4 NM_033068.3:c.331C>T; p.(Arg111Cys) and a splice variant in intron 6 c.645 + 1G>A; p.? which was predicted to lead to an in frame exon 6 skipping. This is the first case reported incidence of a splice variant of *ACP4*. Individual 9.2 had an already described missense variant in exon 4 NM_033068.3:c.428C>T; p.(Thr143Met) and a second variant not yet reported in exon 7, in the histidine phosphatase domain c.736G>A, p.(Val246Met). This variant is predicted damaging by SIFT (v6.2.0) and Polyphen-2. Individual 9.3 had 2 new missense variants, the first one is in exon 6, NM_033068.3:c.626T>C; p.(Leu209Pro) is in the domain but the second one is in the exon 11, in cytoplasmic domain c.1199C>A; p.(Ala400Asp). No variants were reported in the cytoplasmic part of the protein. Our results are generally consistent with previously described variants, but also suggest that the cytoplasmic region of the protein, as well as the extracellular region could have a role in amelogenesis.

Individual 9.3 also had agenesis of teeth 18, and 28, consistent with one of the most frequent variant found in *WNT10A* gene NM_025216.3:c.682T>A; p.(Phe228Ile).

Type II—Hypomaturation

Hypomature amelogenesis imperfecta relates to a qualitative rather than a quantitative (hypoplastic) enamel defect. Enamel maturation begins when final enamel thickness has been reached and concentrates on proteolytic degradation and removal of secreted matrix proteins as well as on hydroxyapatite crystal growth (Robinson, 2014). Enamel might be less translucid, opaque (snow-capped), pigmented but rather hard and protective. Two forms of hypomature amelogenesis imperfecta - the pigmented and the snow-capped are autosomal dominant (type IIA and IIC) and two are X-linked (type IIB and IID) (Witkop and Sauk, 1976).

Type IIA—hypomaturation, pigmented, autosomal recessive, A1 #204700 *KLK4*; A2 # 612529 *MMP20*; A3 # 613211 *WDR72*; A4 # 614832 *ODAPH*; A5 # 615887 *SLC24A4*; A6 # 617217 *GPR68*

This type of AI is characterized by pigmented hypomature enamel. The overall volume of the teeth is preserved, but enamel is hypomineralized therefore not differentially contrasting from dentin on X-rays. Enamel is colored from white opaque to brown. It is prone to post-eruptive breakdown. These AI have been associated with homozygous or compound heterozygous variants in six genes: *KLK4, MMP20, WDR72, C4ORF26, SLC24A4,* and *GPR68*.

All individuals (Figure 4; Supplementary Figure S1H,I) we are reporting in this section present a hypomature AI phenotype. Radiographs showed a lack of contrast between enamel and dentin.

KLK4

*KLK4*encodes an enamel matrix protease requiring cleavage for its activation after secretion by ameloblasts. *KLK4* encodes a serine protease that, once activated during maturation stage, will degrade enamel proteins to allow the growth in width and thickness of enamel crystallites (Simmer et al., 2009).

Truncating variants in this gene have been previously described (Wang et al., 2013; Seymen et al., 2015b; Smith C. E. L. et al., 2017). In our cohort, individual 10.1 displayed pigmented hypomature, hypomineralized enamel. As a compound heterozygous, he is carrying a previously reported non-sense variant (Hart et al., 2004) associated with a new missense mutation in *KLK4* NM_004917.4: c.443G>T; p.(Cys148Phe) and c.458G>A; p.(Trp153*) (Supplementary Table S3; Supplementary Figure S2J and Supplementary Figure S3.19). The missense variant is affecting a highly conserved amino-acid and is predicted to be deleterious by SIFT and Polyphen-2. This is the first report of the putative pathogenic missense variants c.443G>T; p.(Cys148Phe) in this gene.

MMP20

MMP20 encodes a zinc-dependent endopeptidase activated during the secretion stage and continuing to be expressed by ameloblasts during the maturation stage. It supports enamel maturation by degrading the enamel protein matrix. As KLK4 and MMP20 seem to work in a collaborative manner, it is not surprising to note a similar dental phenotype in individuals with *KLK4* (Hart et al., 2004) or *MMP20* (Kim et al., 2005b) variants. We found 16 individuals (Supplementary Table S3; Supplementary Figure S2K) presenting with hypomature AI both in their primary and permanent dentitions; their phenotypes are similar to the ones described in the literature and associated with *MMP20* recessive inheritance (Kim et al., 2005b; Ozdemir et al., 2005b; Papagerakis et al., 2008; Lee et al., 2010; Gasse et al., 2013; 2017; Kim et al., 2017; 2020; Wang et al., 2020; Nikolopoulos et al., 2021).

Individuals 11.1, 11.2, 11.3 and 11.4 have compound heterozygous variants in *MMP20* gene (Supplementary Figures S3.20, 3.21, 3.22). All have in common the first variant NM_004771.4: c.103A>C; p.(Arg35 =). This pathogenic variant was firstly reported in Prasad et al., 2016a in individual V2.13. Its splicing impact was then functionally demonstrated by Kim et al., 2020. For individual 11.4 the second variant c.1362C>G; p.(Tyr454*) is novel and has been discovered thanks to GenoDENT panel. Other variants truncating the protein were already described in this gene (Papagerakis et al., 2008; Kim et al., 2017) but never so late in the protein. Indeed c.1362C>G; p.(Tyr454*) occurred in the last exon, inducing the truncation of the hemopoxin domain involved in binding inhibitors of metallopeptidases. It is also plausible that the domain may restrict cleavage site selection (Lee et al., 2010). We have tentatively classified this variant as probably damaging. We also report another new heterozygous pathogenic mutation found in individual 11.8 c.359dup; p.(Asn120Lysfs*9), along with a second variant on the other allele (Supplementary Figure S3.23) already reported c.954-2A>T (Kim et al., 2005b). This new variant was classified as probably damaging in light of later truncations being so described (Kim et al., 2017). The GenoDENT panel highlighted a compound heterozygous VUS in individual 11.11 c.530G>A; p.(Gly177Glu) associated to a known pathogenic variant (c.954-2A>T) (Kim et al., 2005b) (Supplementary Figure S3.24). This missense VUS creates an amino-acid substitution of the conserved Gly177 in the Matrixin protein domain, involved in the peptidase activity, and is likely predicted deleterious by SIFT (v4.0.3), VariantTaster (v2021) and PolyPhen-2. This VUS was not previously reported in the GnomAD database.

Individuals 11.12 and 11.13 both have a heterozygous variant NM_004771.4:c.566T>C; p.(Leu189Pro) already reported by the team (Gasse et al., 2017) along with respectively c.910G>A; p.(Ala304Thr) described in (Lee et al., 2010) and a novel variant in individual 11.3 reported c.1126C>T; p.(Gln376*). Due to the lack of parental DNA, we could not confirm the relative position of the variant in individual 11.13. It would however lead to the loss of almost all the hemopoxin domain, so, we classified this variant as probably damaging. Individuals 11.14 to 11.17 are all homozygous for the pathogenic variant c.954-2A>T (Supplementary Figure S3.25).

WDR72

WDR72 is a transporter, it encodes a protein predicted to be an intracellular vesicle coat protein that is mostly expressed during maturation stage but also at secretory stage. The stronger expression has nevertheless been detected during maturation initiation (El-Sayed et al., 2009; Katsura et al., 2014). WDR72 has recently been confirmed as regulating vesicle trafficking in ameloblasts (Katsura et al., 2022) and being involved in distal renal tubular acidosis (Khandelwal et al., 2021).

We identified four individuals with hypomature AI (Figure 4).

New variants in *WDR72* were identified by GenoDENT (Supplementary Table S3; Supplementary Figure S2L) in individuals 12.1, 12.2 and 12.4. Individual 12.1 presented a homozygous deletion including a part of intron 1 and the beginning of exon 2 NM_182758.4:c.-13 + 989_7del. In individual 12.2, we detected, a non-sense mutation in exon 2 and a 10 bp deletion at the intron 9 splice site. Truncating variation are known to be pathogenic but no splice variants were previously described in this gene. Intriguingly, the 12.2 phenotype is more complex than in other reported individuals as this patient also presented with small teeth, tooth agenesis, mild deafness and nephrocalcinosis. The recent description of the role of WDR72 in kidney-associated diseases and the syndromic nature of the diseases

presented by 12.2 would demand possible future consideration of WDR72 in a class of syndromic AI. Individual 12.3 is compound heterozygous for two known pathogenic variants reported in (Prasad et al., 2016a). In individual 12.4 we detected two novel compound heterozygous 1 bp deletion in exon 15 c.2388del; p.(Lys796Asnfs*16) and c.2146del; p.(Ala716Profs*10), resulting in a frameshift and a premature stop codon a known mechanism in this disease (Supplementary Figure S3.26).

ODAPH

C4ORF26, named also ODAPH, odontogenesis associated phosphoprotein, function is not yet well defined. *ODAPH* encodes a proline rich protein expressed during the secretory and maturation stage, suggesting a possible role in hydroxyapatite crystallization (Parry et al., 2012). ODAPH is important to maintain the integrity of the atypical basal lamina at maturation stage (Ji et al., 2021). Our cohort included individual 13.1 with hypomature AI (Figure 4). This individual was previously described in (Prasad et al., 2016b). He carries a small homozygous deletion NM_178497.5:c.39_46del; p.(Cys14Glyfs*18) identified using the GenoDENT panel (Supplementary Table S3; Supplementary Figure S2M). The phenotype was consistent with previous individuals described with truncating variants in this gene (Parry et al., 2012).

SLC24A4

SLC24A4 is a potassium-dependent sodium/calcium exchanger expressed by maturation stage ameloblasts (Hu P. et al., 2012). It likely performs a role in calcium provision to the enamel during maturation (Wang S. et al., 2014). One large deletion encompassing intron 14 to exon 17 has been described (Seymen et al., 2014b) whereas Prasad et al., 2016a described a homozygous deletion including the last three exons (15,16 and 17) and Parry et al., 2013 a non-sense homozygous variant.

Two individuals (14.1 and 14.2) with hypomature AI (Figure 4) showed novel homozygous *SLC24A4* variants using our GenoDENT panel (Supplementary Table S3; Supplementary Figures S1I, S2N). Individual 14.1 was already described in (Prasad et al., 2016a) with a homozygous deletion including the 3 last exon (15,16 and 17) of the *SLC24A4* gene NM_153646.4:c.(1,537 + 1_1538-1)_*67. Individual 14.2 and her affected sister carried a homozygous variant affecting a splice site with strong exon skipping predictions c.1716 + 5G>A (Supplementary Figure S3.27). No splice variant has previously been reported so we have classified this variant as a VUS pending functional analysis.

GPR68

GPR68 is a proton-sensing protein present during all stages of amelogenesis. It has been suggested that the protein acts as a pH sensor directing ameloblasts to switch between the ruffle ended and smooth ended conformations during the maturation stage (Parry et al., 2016b).

pH-Sensing G-protein-Coupled Receptor (GPR68) has been showed to be implied in ameloblast (Ludwig et al., 2003; 2003; Tomura et al., 2008; Frick et al., 2009) and odontoblast (Yang et al., 2006; Pereverzev et al., 2008) function. First human pathogenic variants were reported in (Parry et al., 2016b) associated with hypomaturation AI in three families (#617217). The clinical phenotype showed an enamel of apparent normal thickness but poorly mineralized, with brown discoloration. Weaker enamel tended to be prematurely lost secondary to attrition or masticatory stress, especially in the posterior teeth. Only few other cases, were additionally published, associated with the same type of AI (Seymen et al., 2021; Spedicati et al., 2021). No variants in this gene were found in our cohort.

Type IIB—hypomaturation, x-linked recessive

No gene has been clearly implicated in this category but we hypothesize that such phenotypes may be due to *AMELX* defects. Indeed, when *AMELX* mutations occur at specific MMP20 cleavage sites, the resulting phenotype is impaired matrix degradation and hypomature enamel. Thus, this category reasonably includes male individuals 7.5, 7.6 and 7.7 presenting a hypomature phenotype (Suplementary Figure 1E).

Type IIC—snow capped teeth, X-linked

In this form, both primary and permanent dentitions were affected. In males, primary teeth were opaque ground-glass white, and secondary teeth were mottled yellow-brown and white. Enamel had normal thickness, moderately soft, and did not contrast from dentin on x-ray. The teeth chipped and abraded more easily than normal teeth, but the loss of enamel was not as rapid as in the hypocalcified form (Rathi et al., 2014). Because of the appearance of the teeth in this form, referred to as snow-capped in its most marked form, confusion with fluorosis sometimes occurs (Rao and Witkop, 1971).

AMELX

Complete deletion of *AMELX* has been associated to this phenotype (Hu J. C.-C. et al., 2012).

We did not find this phenotype among our cohort.

Type IID—snow capped teeth, autosomal dominant

As with Type IIC, the phenotype is that of snow-capped appearance, except the X-linkage can be ruled out based on male: female incident rates. No gene has yet been implicated in this category. Although we identified individuals in our cohort with snow-capped teeth, we could not define a gene potentially responsible for this clinical entity.

Type III—hypomineralization

Hypocalcified amelogenesis imperfecta is characterized by an enamel of normal thickness but soft, porous and shedding easily from the dentin. The color of enamel can range from white to creamy yellow (Mendoza et al., 2007).

Enamel can be easily lost after eruption (post eruptive breakdown). These teeth are very sensitive even to physical contact with a toothbrush. Oral microbiome evolving in calculus is largely depositing on teeth resulting in severe gingivitis. Both autosomal dominant and autosomal recessive classifications are described related to three known genes in total.

Two categories are described: autosomal dominant (type IIIA associated to *FAM83H* variants and IIIB associated to *AMTN* variants) and - autosomal recessive (type IIIC associated to *RELT* variants).

We identified individuals with variants in *FAM83H* gene, we didn't detect any individual with *AMTN* or *RELT* variants in our cohort.

Type IIIA—amelogenesis imperfecta, hypomineralization type autosomal dominant #130900

To date, two genes are associated to the hypomineralized autosomal dominant inheritance subtype of AI.

FAM83H

Family with sequence similarity 83, member H (FAM83H), is an intracellular protein with ubiquitous expression (Lee et al., 2011). It reaches maximum expression in ameloblasts during the secretory stages. FAM83H regulates the organization of the keratin cytoskeleton and is involved in desmosome formation (Kuga et al., 2016). Variants identified in *FAM83H* cause autosomal dominant hypocalcified AI (Mendoza et al., 2007; Kim et al., 2008).

We report 15 individuals (15.1-15.15) presenting with hypocalcified amelogenesis imperfecta (Figure 4), affecting both primary and permanent dentitions with secondary loss of enamel, and colored teeth. Occlusal and incisal wear gave a conical form to the canines. There was no difference in radio-opacity between enamel and dentin.

The 15 individuals carried autosomal dominant variants in exon 5 (Supplementary Table S3; Supplementary Figures S1J, S2O, S3.28–3.37). This is consistent with previously reported variants as each of the variants identified to date have mapped to this largest and final exon of *FAM83H*. All of them except the one encountered in 15.13 are frameshift or non-sense variants, a mechanism already described as disease causing. Only three of those individuals had a novel variant: 15.1 NM_198488.5:c.930_939dup; p.(Val314Argfs*14), 15.6 c.1309_1311delinsTAG; p.(His437*) and 15.9 c.1375C>T; p.(Gln459*). Individual 15.4 c.1282C>T; p.(Gln428*) carries a variant previously described in (Prasad et al., 2016a). Individual 15.13 is the only one presenting a missense variant NM_198488.5:c.1498C>G; p.(Leu500Val). He also displays a variant in *WDR72* NM_182758.4:c.1283T>G; p.(Ile428Ser) (Supplementary Figure S3.36). The phenotype in this individual appears more severe possibly due to the compound effect of the two variants or to his more advanced age and accentuated tooth wear.

AMTN

Amelotin, encoded by *AMTN*, is a proline, leucine, threonine and glutamine rich protein binding to ODAM (odontogenic, ameloblast associated) and SCPPPQ1 (secretory calcium-binding phosphoproteins proline-glutamine rich 1) to form aggregates able to maintain the attachment between ameloblasts and the produced enamel during maturation stage (Holcroft and Ganss, 2011; Fouillen et al., 2017).

A large deletion in *AMTN* spanning exon 3–6 has been reported yet to cause hypomineralized AI (Smith et al., 2016). No variant in this gene was found among our cohort.

Type IIIB or IIIC-amelogenesis imperfecta, hypomineralization type autosomal recessive #618386

This type of AI is characterized by hypocalcified enamel in both primary and permanent dentitions. A normal or near-normal enamel volume can be found prior to tooth eruption. Post-eruptive changes are rapid and lead to enamel loss, enamel disintegrates from occlusal surfaces of the molars, leaving a ring of intact enamel remaining on the sides. Some people also have anterior open bite (Kim et al., 2019; Nikolopoulos et al., 2020). Homozygous frameshift, missense, and splice junction variants in *RELT* have been described in affected individuals (Kim et al., 2019).

RELT

The protein encoded by this gene is a member of the TNF-receptor superfamily able to activate the NF-kappaB pathway and selectively bind TNF receptor-associated factor 1 (TRAF1).

In mice, *Relt* is expressed in the odontoblast and ameloblast layers, specifically in secretory stage ameloblasts where there is ~20-fold higher expression than in maturation stage ameloblasts. It has been published that $Relt^{-/-}$ incisor enamel was of normal thickness but rough-surfaced and generally hypomineralized correlating with the phenotype found in humans. *RELT* was originally classified as causative of a new type of AI called type IIIC (#618386) but following Witkop's classification, as recessive hypocalcified hypoplastic AI, it could be classified in type IIIB.

We did not detect any individuals with *RELT* variants in our cohort.

Type IV—hypomaturation-hypoplastic with taurodontism #104510

Amelogenesis imperfecta, hypomaturation-hypoplastic type or hypoplastic-hypomature type, with taurodontism (AIHHT) is an autosomal dominant trait associated with enamel defects and enlarged pulp chambers (Dong et al., 2005). The difference between the two subtypes is slight and is based on the dominance of the hypomaturation *versus* the hypoplastic phenotype. So far, only one gene (*DLX3*) was associated to the hypomature-hypoplastic type IVA and no gene was described for the hypoplastic-hypomature type IVB.

Type IVA—hypomaturation-hypoplastic with taurodontism autosomal dominant #104510

For this phenotype, enamel thickness is supposed to be normal and hypomaturation is predominant over hypoplasia. Enamel appears as mottled yellow white to yellow brown with pits on the buccal surfaces. Taurodontism with large pulp chambers is observed on radiographs. Only one gene has thus far been proposed to cause this defect: *DLX3* (Wimalarathna et al., 2020).

DLX3

DLX3 is an important transcription factor involved in osteogenic differentiation (Sun et al., 2019). It is located on chromosome 17q21.3-q22, and contains 3 coding exons (Scherer et al., 1995; Price et al., 1998). *DLX3* plays a role in craniofacial development, and in the development of the ventral forebrain. DLX3 has three main domains: The N- and C-terminus transactivation domains, and a central sequence-specific DNA-binding distal-less-like homeodomain, encoded by exons 2 and 3. The homeodomain can interact directly with DNA in a sequence-specific way and regulates the expression of target genes throughout numerous developmental processes (Whitehouse et al., 2019). Only one missense variant had been described in *DLX3* gene for AI with taurodontism and attenuated tricho-dento-osseous syndrome in exon 2 by (Whitehouse et al., 2019).

Individuals 16.1 and 16.2 showed hypoplastic amelogenesis imperfecta with taurodontism (Figure 4), and enamel surface with striae (16.1), or thinner enamel (16.2). Taurodontism was really apparent on 16.2. 16.3 presented an hypomature/hypoplastic enamel and smaller 12, 22, as well as probable third molar agenesis. Dental agenesis could be linked to the additional variant discovered in *WNT10A* gene NM_025216.3:c.637G>A; p.(Gly213Ser). Dental radiographs confirmed the decreased thickness of enamel, and various degrees of molar taurodontism (Supplementary Figure S1K). In 16.1 we detected a heterozygous missense variant in exon 1 NM_005220.3:c.92C>G; p.(Thr31Ser) predicted possibly damaging by Polyphen-2 and localized in the distal-less-like homeobox protein domain. In individual 16.2 the heterozygous variant was located in exon 3 c.537C>A; p.(Asn179Lys) concerning a well conserved amino acid and predicted damaging by SIFT (v6.2.0) and Polyphen-2. Individual 16.3 carries the variant c.710A>G; p.(Tyr237Cys) (Supplementary Table S3; Supplementary Figure S2P). 16.1-16.3 did not present any bone nor hair additional phenotypes.

As this gene has also been linked to tricho-dento-osseus syndrome, we will describe further syndromic individuals linked to *DLX3*, in the coming syndromic section of this publication, illustrating therefore the tight and thin border between isolated and syndromic AI.

Type IVB—hypoplastic-hypomaturation with taurodontism, autosomal dominant

Enamel is thin with big hypoplastic areas. Hypoplasia is more pronounced than hypomaturation. Taurodontism with large pulp chambers is observed on X-Rays. No gene has ever been implicated with this phenotype (Wimalarathna et al., 2020). We suggest that types IVA and IVB might be a single subtype.

Syndromic amelogenesis imperfecta

Amelogenesis imperfecta can be found in isolation as previously described but also in association with extra-oral clinical signs (Supplementary Table S4). Recognition of AI subtype as well as associated symptoms could orientate clinical diagnosis, refine genetic diagnosis and contribute to improving patient care. After identification of the implicated gene, retro-phenotyping will also help assess and confirm overall clinical diagnosis.

In this paper we are discussing extra-oral key phenotypes for syndromes in which enamel defects are well characterized. Other genes associated to syndromes with insufficient characterization or minor enamel defects are classified by major extra oral clinical signs. To facilitate recognition of AI subtypes and further diagnosis we will describe and classify syndromic AI according to the 3 main defects categories, hypoplastic, hypomature and hypomineralized AI and their mode of inheritance (Figure 5; Table 2; Supplementary Table S4).

Syndromic hypoplastic AI

Hypoplastic AI is the hallmark of numerous syndromes. To date 22 genes have been associated to syndromes including hypoplastic AI in their clinical synopsis. Thirteen genes (*FAM20A*, *GALNS*, *TSC1*, *TSC2*, *TP63*, *MSX2*, *FAM20C*, *ARHGAP6*, *RAI1*, *PEX1*, *PEX2*, *PEX26, TGFBR2* and *ATP6V1A*) have been associated with clinical signs within the head and neck area, eleven with skin, nail and hair defects (*TSC1*, *TSC2*, *TP63*, *ARHGAP6*, *PORCN*, *TGFBR2*, *PEX1*, *PEX2*, *PEX26*, *ORAI1* and *STIM1*), three with immune deficit (*AIRE*, *ORAI1* and *STIM1*), seven with skeletal defects (*LTBP3*, *GALNS*, *TP63*, *MSX2*, *PORCN*, and *FAM20C*), five with neurological issues (*ATP6V1A*, *SLC13A5*, *PEX1*, *PEX2* and *PEX26*), two with cardiovascular defects (*LTBP3, TGFBR2*), and eight with genitourinary defects (*FAM20A* and *FAM20C*, *CLDN19*, *CLDN16*, *WDR72, TSC1, TSC2, RAI1*). It is therefore of importance to explore these potential associated phenotypes while taking medical history and examination.

Dental anomalies and short stature DASS #601216 Verloes Bourguignon syndrome, Platyspondyly with hypoplastic AI absent enamel—AR—*LTBP3*

DASS is characterized by short stature with brachyolmia as well as hypoplastic amelogenesis imperfecta with almost absent enamel (Huckert et al., 2015). Some individuals exhibit valvular and/or vascular defects, including mitral valve prolapse, aortic root dilation, and aortic as well as other arterial aneurysms and dissections (Dugan et al., 2015; Guo et al., 2018).

Associated tooth agenesis was described by (Noor et al., 2009; Dugan et al., 2015). Clinical oral examination showed also microstomia, tooth crowding, high arched palate. Teeth were small and had a yellowish color. Radiographic findings included thin enamel with reduced radiopacity, irregular alveolar bone level, and alveolar bone infectious lesions (Intarak et al., 2019).

LTBP3

DASS is an autosomal recessive disorder caused by homozygous or compound heterozygous variants in *LTBP3* gene (11q12) (Li et al., 1995; Huckert et al., 2015). *LTBP3* encodes latent transforming growth factor-beta-binding protein 3, modulating TGFbeta bioavailability in the extracellular matrix. Deleterious variants in *LTBP3* have also been associated with autosomal dominant Geleophysic dysplasia 3 (#617809). Ultrastructural enamel defects showed an absence of initial aprismatic enamel layer and an abnormal secretion of non-prismatic bulk enamel, suggesting LTBP3 plays a role in the life cycle of ameloblasts especially at the secretory stages with Tomes process formation (Huckert et al., 2015).

We identified *LTBP3* as the gene behind short stature and absent enamel (individuals 17.1–17.4) using exome sequencing (Huckert et al., 2015). GenoDENT panel was subsequently exanded with addition of this gene and we identified in 2 unrelated consanguineous families, additional individuals 17.5 and 17.6 with a similar phenotype and two new homozygous loss of function variants (Table 2; Supplementary Figures S1L, S2Q, S3.38). Teeth were small, spaced, and had a yellowish color. No enamel, impacted teeth, and irregular alveolar bone level were visible on panoramic radiographs. The first pathogenic variant (Individual 17.5) NM_001130144.3:c.3087del; p.(Asn1030Thrfs*47) was a one nucleotide deletion leading to a frameshift and a premature stop codon. The second variant (17.6) was an intronic mutation c.3629-2A>G which led to an aberrant exon 27 splice site. This would probably induce exon 27 skipping resulting in a 132 bp in phase deletion equivalent to a 44 amino acid deletion (position 1,211–1,254).

Mucopolysaccharidosis type IVA #25300—AR—*GALNS*

Mucopolysaccharidosis type IVA is characterized by intracellular accumulation of excessive glycosaminoglycans (GAGs): chondroitin-6-sulfate (C6S) and keratan sulfate (KS) mainly in bone, cartilage, and its extracellular matrix. GAG accumulation leads to unique skeletal dysplasia in MPS IVA individuals.

Most MPS IVA individuals usually look healthy at the neonatal period; however, bone abnormalities in the spine can be seen through X-rays even at birth in a severe form of individuals with MPS IVA. Skeletal symptoms are found later in childhood or adolescence. The most common symptoms include short stature, skeletal dysplasia, dental anomalies, and corneal clouding (Peracha et al., 2018; Akyol et al., 2019; Sawamoto et al., 2020). There is variable severity, but individuals with the severe phenotype usually do not survive past the second or third decade of life (Montaño et al., 2008).

Primary and permanent posterior teeth are described with concave buccal surfaces with pitting, pointed cusps, and concave occlusal surfaces. The enamel is hypoplastic with rough surface. The color varies from whitish-opaque to more yellowish-grey. Enamel surface is too weak to resist minor stress explaining the strong abrasion. The characteristic teeth color may be explained by the high porosity of enamel changing its optical properties (Rølling et al., 1999).

It is important to know that dental findings are found in MPS IVA, but not in MPS IVB. On radiographs, the enamel is thin but with normal radiodensity (Supplementary Figures S1N, S2S).

GALNS

Mucopolysaccharidosis type IVA (MPS IVA; Morquio syndrome A) is an autosomal recessive lysosomal storage disease caused by variants in the galactosamine-6-sulfate sulfatase gene (*GALNS*), located on chromosome 16q24.3. *GALNS* contains 14 exons and 13 introns (Sawamoto et al., 2020).

We report two individuals with compound heterozygous variations in the *GALNS* gene. Individual 19.1 was previously described by our team (Prasad et al., 2016a).

In individual 19.2, we found a missense variant NM_000512.5: c.1156C>T; p.(Arg386Cys) firstly described by (Ogawa et al., 1995), the second variant c.1558T>C; p.(Trp520Arg) was a class 2 variant so we cannot conclude that this variant is indeed involved in the individual phenotype as it is inherited by her homozygous unaffected mother (Table 2). Nevertheless, individual 19.2 presents the typical enzymatic deficiency and was given a confirmed MPS clinical diagnosis. So, either this class 2 variant contributes to the phenotype, or the individual is carrying another variant in this gene not detected by the panel such as a deep intronic variation. Such deep intronic variants have already been described in *GALNS* (Caciotti et al., 2018).

Autoimmune polyglandular syndrome type I #240300 autoimmune polyendocrine syndrome, type I, with or without Reversible Metaphyseal dysplasia—AD, AR—*AIRE*

Autoimmune polyglandular syndrome type I (APS-1) is a rare, autosomal recessive autoimmune disease.

The main symptom triad in APS-1 comprises chronic mucocutaneous candidiasis, adrenal insufficiency, and hypoparathyroidism. Various autoimmune diseases and ectodermal abnormalities are also commonly associated with the syndrome including enamel hypoplasia in permanent teeth (Suh et al., 2019). In addition to enamel defects in permanent teeth, hypoplastic pits and hypomature patches in deciduous teeth with underlying changes in the prismatic enamel ultrastructure are observed. The enamel looks severely hypoplastic throughout, except for the most cervical region. Deciduous teeth display opacities and yellowish cervical patches, suggestive of enamel hypomaturation. They are chalky with yellowish patches. The microstructure of the enamel prisms suggests an impaired mineralization, and prisms are clearly different. It was found that, in APS-1, auto-antibodies attack ameloblasts amongst other cells types, making it the first known disease of dental hard tissues with an auto-immune aetiology (Pavlic and Waltimo-Sirén, 2009).

AIRE

The disease has been associated to variations in the autoimmune regulator gene (*AIRE*) which consists of 14 exons (Nagamine et al., 1997) and is located on chromosome 21q22 (Aaltonen et al., 1997). AIRE protein is localized in the cell nucleus, where it forms distinct speckles (Björses et al., 1999). Analysis of its multidomain structure

reveals that human AIRE belongs to the group of proteins able to bind to chromatin and regulate the process of gene transcription (Perniola, 2018). No variant in this gene were found in our cohort.

Tuberous sclerosis # *605284*—AD—*TSC1-2*

Tuberous sclerosis complex (TSC) is characterized by frequent neuropsychiatric disorders including, in a variable way, intellectual disability, attention-deficit/hyperactivity disorders, autism spectrum disorders (ASD), psychiatric disorders and learning difficulties, seizures, the development of benign tumors, and oral manifestations. The most common oral manifestations are fibromas, gingival hyperplasia and enamel hypoplasia. Other less frequent oral findings are a high arched palate, bifid uvula, cleft lip and/or palate, delayed dental eruption and the presence of diastemas. Enamel hypoplasia is present in the permanent dentition of almost all individuals, and is associated with an increased risk of caries. This anomaly typically affects the vestibular surfaces of several teeth (Harutunian et al., 2011).

TSC1-TSC2

Individuals with TSC present variants of the *TSC1* and *TSC2* genes, which intervene in cell cycle regulation. The *TSC1* gene (9q34) encodes hamartin, a protein that interacts with tuberin (TSC2) to form a protein complex that inhibits signal transduction to the downstream effectors of the mammalian target of rapamycin (MTOR) (Inoki et al., 2002). The *TSC1* gene consists of 23 exons, of which the last 21 contain coding sequence and the second is alternatively spliced (Slegtenhorst et al., 1997).

The *TSC* gene on chromosome 16 was named *TSC2*. *TSC2* has 41 small exons spanning 45 kb of genomic DNA and encodes a 5.5-kb mRNA (van Bakel et al., 1997). No variants of *TSC1* or *TSC2* were identified in our cohort.

EEC syndrome-3 (EEC3) #604292 Rapp-Hodgkin syndrome #129400—AD—*TP63*

Ectrodactyly, ectodermal dysplasia, and cleft lip/palate syndrome 3 EEC3 (#604292 Maas et al., 1996; Celli et al., 1999; Rinne et al., 2006; Kosaki et al., 2008), ankyloblepharon-ectodermal defects, cleft lip/palate syndrome AEC (#106260), Rapp-Hodgkin (#129400), Acro dermatoungual lacrimal tooth syndrome ADULT (#103285), SHFM4 (#605289), Hay-Wells syndrome (#106260), and limb-mammary syndrome (#603543) are autosomal dominant allelic conditions due to mutations in the same gene, namely, *TP63* (15 exons, 3q28) (Yang et al., 1999) encoding tumor protein 63.

In EEC 3, ectodermal defects manifest as sparse and fine hair, dry skin, soft nails and decrease in sweet capacity (Sutton and van Bokhoven, 2010). (Sripathomsawat et al., 2011) also reported individuals with enamel hypoplasia and hypodontia.

Rapp-Hodgkin syndrome (RHS) is characterized by anhidrotic ectodermal dysplasia and cleft lip/palate. The face of the individuals is characteristic. They have narrow nose and small mouth, wiry, slow growing, and uncombable hair, sparse eyelashes and eyebrows, obstructed lacrimal puncta/epiphora, bilateral stenosis of external auditory canals, microsomia, hypodontia, cone-shaped incisors, enamel hypoplasia, and dystrophic nails (Kantaputra et al., 2003). The first individuals described in the literature were: a mother and her son and daughter (Rapp and Hodgkin, 1968) presenting with anhidrotic ectodermal dysplasia, cleft lip, and cleft palate and an unusually narrow and a small mouth.

TP63

TP63 plays an important role allowing cells to undergo apoptosis in response to DNA damage (Flores et al., 2002) and is involved in tumor and metastasis suppression (Su et al., 2010). Given its broad expression pattern, we suggest that *TP63* mutation affect the cell differentiation or fate of ameloblasts in development, though we await experimental evidence. Kantaputra et al., 2003 identified a heterozygous missense variant (S545P) in the *TP63* gene in a Thaï teenager presenting all the characteristics of the syndrome. No variant in this gene is reported in this publication.

Craniosynostosis 2 # 604757—AD—*MSX2*

Craniosynostosis is the premature fusion of calvarial sutures.

MSX2

The gene is located on chromosome 5q34-q35 (Jabs et al., 1993). (Hassan et al., 2004) showed that Msx2 regulates the expression of osteocalcin and therefore is implicated in the control of bone formation. This gene is reported for craniosynostosis in human. Two previous publications (Aïoub et al., 2007; Molla et al., 2010) reported that, in the targeted deletion mouse model *Msx2*$^{-/-}$, Msx2 was implicated in both isolated enamel dysplasia (regulating amelogenin, enamelin) and syndromic enamel dysplasia (through alterations in cell-cell junctions). To date one duplication of the entire gene *MSX2* has been reported in a syndromic (craniofacial, eye and limb anomalies) individual associated with hypoplastic AI (Plaisancié et al., 2015). No variant in this gene was identified in our cohort.

Raine syndrome # 259775—AR—*FAM20C*

Raine syndrome is an autosomal recessive disease characterized by neonatal osteosclerotic bone dysplasia with a poor prognosis and individuals who generally die within the first few weeks of life. The density of all bones is increased and it is especially evident for the skull. The face is dysmorphic with a narrow prominent forehead, proptosis, depressed nasal bridge, and midface hypoplasia. The periosteal bone formation is typical of the disease and extends along the diaphysis of long bones adjacent to areas of cellular soft tissue (Simpson et al., 2007; 2009).

The syndrome was firstly described *postmortem* by (Raine et al., 1989) on a female fetus presenting with microcephaly, exophthalmos, hypoplastic nose and midface, gum hyperplasia, cleft palate, low-set ears, osteosclerosis and hypoplastic lungs. Simpson et al., 2009 reported the first two unrelated individuals who survived during the childhood and showing typical features of the Raine syndrome. Hypoplastic amelogenesis imperfecta was observed in patients surviving childhood (Acevedo et al., 2015).

FAM20C

(Simpson et al., 2007) identified homozygous and compound heterozygous variants in *FAM20C* (7p22) in individuals with Raine syndrome. FAM20C is a Golgi associated secreted protein kinase, partnering with FAM20A, phosphorylating small integrin-binding ligand N-linked glycoproteins SIBLINGS, among other proteins, and playing a substancial role in osteogenesis and amelogenesis. No variant in this gene was identified in our cohort.

Focal dermal hypoplasia #305600—XLD—*PORCN*

Focal dermal hypoplasia (FDH) also named Golz or Golz-Gorlin syndrome is an X-linked dominant syndrome. FDH features include atrophy and linear pigmentation of the skin, herniation of fat through the dermal defects, and multiple papillomas of the mucous membranes or skin. In addition, digital anomalies consist of syndactyly, polydactyly, camptodactyly, and oligodactyly, ridged dysplastic nails, alopecia (scalp, eyebrow, and eyelashes). Ocular anomalies (coloboma of iris and choroid, strabismus, microphthalmia) have also been present in some cases. Intellectual disability occurs in some individuals. Striated trabecular bones (osteopathia striata) are a constant feature (Larrègue and Duterque, 1975; Happle and Lenz, 1977; Alsharif et al., 2018; Frisk et al., 2018). There is considerable diversity in the severity of the craniofacial and oral manifestations between individuals. The face is asymmetric, the nose displays hypoplastic alae and the philtrum looks flat in some cases. More severely affected individuals show thin lips with very little vermillion. Dental manifestations are the most commonly observed oral findings, presenting widely spaced teeth, including hypoplastic teeth, showing both hypoplasia and yellow brown hypomineralized areas of enamel. The developmental dental defects vary and include notching of the incisal edges of teeth and marked mamelons, localized hypoplastic vertical enamel groves, and hypodontia (Wright et al., 2016).

PORCN

Most of the individuals with FDH are female, with heterozygous or mosaic variants in the *PORCN* gene. Males (mosaic variants) account for 10% of affected individuals; heterozygous non-mosaic variants are lethal in males (Deidrick et al., 2016).

PORCN gene is located in chromosome Xp11.23, and contains 15 exons and spans about 12 kb. The first exon is non-coding (Caricasole et al., 2002). *PORCN* encodes and endoplasmic reticulum protein: the protein-serine O-palmitoleoyl transferase porcupine or porcupine O-acyltransferase. Although the exact function of the PORCN protein is uncertain, proteins in the porcupine (PORC) family are involved in WNT (wingless and int homologue) signaling pathway which is extremely important for embryonic development (Durmaz et al., 2018) including odontogenesis. No variant in this gene was identified in our cohort.

MLS syndrome with associated hypoplastic enamel X—ARHGAP6

Microphthalmia with linear skin defects (MLS) syndrome is an X-linked disorder that has been linked to different loci. One such condition includes associated AI in a hypoplastic form.

ARHGAP6

Because the Amelogenin gene (*AMELX*) is nested within intron 1 of *ARHGAP6,* partial deletions in *ARHGAP6* can completely remove *AMELX* giving a distinctive enamel phenotype resembling "snow-capped" teeth (Hu J. C.-C. et al., 2012). This phenotype was already described in isolated hypomature AI IIC section.

Ras homologue GTPase activation protein 6 (*ARHGAP6*), belongs to the Rho GTPase-activating protein (RhoGAP) family. *ARHGAP6* does not appear essential for normal enamel formation. Failed *ARHGAP6* expression did not appreciably alter the severity of enamel defects when *AMELX* was absent (Hu J. C.-C. et al., 2012).

We report one individual (20.1) carrying a 12 Mb deletion of the Xp22.2 region (Table 2). This region is including not only the *AMELX* gene but also the full *ARHGAP6* gene.

This female individual suffers from microphthalmia with linear skin defects (MLS) syndrome and associated hypoplastic enamel with a banding pattern characteristic of the female lyonisation effect (bands of normal enamel next to defective enamel; AI hypoplastic IE) (Supplementary Figure S1N).

Smith-Magenis syndrome # 182290—AD—*RAI1*

Smith-Magenis syndrome is an autosomal dominant disease which occurs mostly *de novo*. Clinical phenotype includes moderate intellectual deficiency with frequent behavioral issues (temper tantrums, nail yanking, insertion of foreign objects into body orifices, self-injurious behaviors), sleep disturbance, dysmorphic facial features. Affected patients can present with variable congenital anomalies (heart defects, structural renal anomalies, scoliosis) including oral anomalies like AI or dental agenesis (Vieira et al., 2012).

RAI1

The syndrome is in 90% of the cases due to a 3.7 Mb deletion in chromosome 17p11.2 encompassing the *RAI1* gene (Vieira et al., 2012).

We identified with the GenoDENT panel, in individual 21.1, a deletion in the 17p11.2 region leading to a possible diagnosis of Smith-Magenis syndrome with hypoplastic AI (Table 2). The exact size of the deletion was further characterized by array analysis. Individual 21.1 presented the classical 3.7 Mb deletion associated with the syndrome as well as classical associated phenotype including the hypoplastic enamel described by (Wright et al., 2015).

Loeys-Dietz syndrome 2 # 610168—AD—*TGFBR2*

Loeys-Dietz syndrome type 2 is characterized by micrognathia, retrognathia, hypertelorism, bifid uvula, cardiovascular anomalies, pectus deformity, joint laxity, scoliosis, hand and feet anomalies, skin texture and color anomalies and hypoplastic AI (Jani et al., 2020).

TGFBR2

Variants in *TGFBR2* have been associated with Loeys Dietz syndrome type 2. TGFBR2 codes for a transmembrane protein with a serine/threonine-kinase domain forming a heterodimeric complex with TGF-beta type I receptor, TGFBR1, binding TGF-beta, TGF-beta1, TGF-beta2 and TGF-beta3, ligands. This receptor/ligand complex phosphorylates proteins, which then enter the nucleus and regulate the transcription of genes related to cell proliferation, cell cycle arrest, wound healing, immunosuppression, and tumorigenesis.

Here we report an individual 22.1 with a heterozygous missense variant in the *TGFBR2* NM_003242.6:c.1561T>C; p.(Trp521Arg) (Table 2; Supplementary Figures S1O, S3.43) and diagnosed with

Loeys-Dietz syndrome including hypoplastic amelogenesis imperfecta. This variation was already reported by (Mátyás et al., 2006). The variant is most probably transmitted by the affected mother though we were not able to access the mother's DNA to confirm.

Developmental and epileptic encephalopathy 93 #618012—AD—*ATP6V1A*

Developmental and epileptic encephalopathy 93 is an autosomal dominant disorder with, among other features, delayed psychomotor and impaired intellectual developments, as well as early onset epilepsy. Additional clinical features like microcephaly and hypoplastic amelogenesis imperfecta were observed in epileptic encephalopathy (Guerrini et al., 2022).

ATP6V1A

This disorder has been associated with *ATP6V1A* (ATPase, H + Transporting, Lysosomal, 70-KD, V1 Subunit A). It codes for a component of vacuolar ATPase, a multimeric enzyme, an ATP-dependent protein pump function, which mediates acidification of eukaryotic intracellular organelles and is necessary to activate mTORC1 (Zoncu et al., 2011). No variant in this gene was found among our cohort.

Hypomagnesemia 3, renal # 248250—AR—*CLDN16*

Familial hypomagnesemia with hypercalciuria and nephrocalcinosis is an autosomal recessive progressive renal disorder with progressive loss of the renal function characterized by excessive urinary Ca^{2+} and Mg^{2+} excretion (Müller et al., 2006). Hypoplastic, hypomature amelogenesis imperfecta is also detected in some individuals (Bardet et al., 2016).

CLDN16

(Simon et al., 1999) identified homozygous and compound heterozygous variants in the *CLDN16* gene in ten individuals presenting renal hypomagnesemia. CLDN16 is localized on chromosome 3q28, and consists of 5 exons and encodes a protein of 305 AA with 4 transmembrane domains and intracellular N and C termini (Simon et al., 1999). *CLDN16* is required for cell division (Kittler et al., 2004), is selectively expressed at tight junctions of renal epithelial cells and plays a central role in the reabsorption of divalent cations (Kausalya et al., 2006). No variant in this gene was identified among our cohort.

Renal Hypomagnesemia-5 with ocular involvement # 248190—AR—*CLDN19*

Renal hypomagnesemia-5 with ocular involvement (HOMG5) is an autosomal recessive disorder characterized by severe renal magnesium wasting, progressive renal failure, nephrocalcinosis, and severe visual impairment (Konrad et al., 2006). Hypoplastic, hypomature amelogenesis imperfecta is also present in some individuals (Yamaguti et al., 2017).

CLD19

Konrad et al., 2006 found two different homozygous missense variants in the *CLDN19* gene in families with renal magnesium wasting, renal failure, and severe ocular involvement. Indeed, the syndrome is caused by homozygous or compound heterozygous variants in the claudin-19 gene on chromosome 3q28. Claudins, such as CLDN19, are transmembrane proteins found in tight junctions. Tight junctions form barriers that control the passage of ions and molecules across an epithelial sheet and the movement of proteins and lipids between apical and basolateral domains of epithelial cells (Lee et al., 2006). No variant in this gene was identified among our cohort.

Heimler syndrome #234580 and #616617—AR—*PEX1* and *PEX6*

Heimler syndrome-1 (HMLR1) is an autosomal recessive syndrome reported as the mildest form of the peroxisomal biogenesis disorder spectrum (PBD 1A (Zellweger)). This disease is characterized by sensorineural hearing loss, enamel hypoplasia of the permanent dentition and nail abnormalities with Beau lines (transverse ridges) of the toenails and white patches in the fingernails (leukonychia) (Heimler et al., 1991; Pollak et al., 2003), with or without retinal dystrophy (Ratbi et al., 2015; Mechaussier et al., 2020). In contrast to individuals with PBDs at the severe end of the clinical spectrum (neurologic dysfunction, craniofacial abnormalities, liver dysfunction, and biochemically absence of peroxisomes), Heimler affected individuals showed no identifiable dysmorphic or additional neurologic features.

PEX1

Ratbi et al. (2015) identified homozygous and compound heterozygous variants in the peroxisome biogenesis factor 1 gene (*PEX1*) in 4 families, including the family reported by (Heimler et al., 1991). Human PEX1 gene is located on chromosome 7q21, and is composed of 24 exons and encodes a 147-kD protein member of the AAA protein family (ATPases associated with diverse cellular activities). Those proteins participate in a broad range of cellular processes, as indicated by the designation AAA which comes from ATPases associated with diverse cellular activities and are specially required for peroxisomal matrix protein import (Portsteffen et al., 1997; Reuber et al., 1997). No variant in this gene was identified among our cohort.

PEX6

Another form of Heimler syndrome (HMLR2; #616617) is caused by a variant in the *PEX6* gene (601,498) located on chromosome 6p21, consisting of 17 exons and 16 introns, spanning about 14 kb (Zhang et al., 1999). No variant in this gene was identified among our cohort.

Peroxisome biogenesis disorder PBD 7A (Zellweger) #614872 7B #614873—AR—*PEX26*

It has been shown by (Neuhaus et al., 2017) that *PEX26* is responsible for Zellweger Syndrome. Patient carrying recessive variant present hypoplastic AI (Kim et al., 2021a). No variant in this gene is reported in this publication.

Developmental and epileptic encephalopathy 25, with AI #615905—AR—*SLC13A5*

Individuals with developmental and epileptic encephalopathy 25 present epileptic seizures since the first days of life in most of the cases, and a developmental outcome ranging from mild to severe

intellectual disability, plus variable combinations and degrees of ataxia, and in addition, teeth with hypoplastic enamel (Hardies et al., 2015). Several individuals have been reported suffering from early onset, regular and difficult to control seizures. In some cases, seizures could be controlled with conventional antiepileptic treatment but showed deterioration of gait which improved after usage of another antiepileptic medication.

Oral manifestations encompass delayed eruption of permanent teeth, small and cylindrical teeth with wide interdental spaces, and yellowish to brownish discolorations. Lower permanent incisors are described as sharp and thin; premolars and molars seem extremely worn. Clinically, the enamel of primary and permanent teeth is hypoplastic with a smooth, hard and pitted surface. Dental panoramic radiographs show a lack of enamel in both dentitions. Histologically, the enamel layer is very thin. No lines of Retzius or enamel prisms are visible and the surface presents small pits. These pits are a common sign for hypoplastic AI. The dentin presents a normal structure (Schossig et al., 2017).

SLC13A5

Developmental and epileptic encephalopathy 25 with amelogenesis imperfecta is a rare disease caused by variants in *SLC13A5* genes. *SLC13A5* is located in the chromosome 17p13-p12, and contains at least 12 exons (Inoue et al., 2002). *SLC13A5* encodes a high affinity sodium-dependent citrate transporter, which is mainly expressed in liver and brain. Neurons are considered incapable of *de novo* synthesis of tricarboxylic acid cycle intermediates; therefore, they rely on the uptake of intermediates, such as citrate, to maintain their energy status and neurotransmitter production (Hardies et al., 2015).

This epilepic encephalopathy was described as Kolschütter-Tönz like syndrome (KTS like) as the phenotype is similar to the one observed in individuals with variations in the *ROGDI* gene except for the enamel defects: AI is hypoplastic in patient with *SLC13A5* variations and hypomature in individuals with *ROGDI* mutations. Kolschütter-Tönz syndrome will be described later in the paper as individuals present a hypomature AI.

We report one individual 23.1 carrying a compound heterozygous missense variants affecting exons 2 and 4 NM_177550.5:c.203C>A; p.(Pro68Gln), c.434C>A; p.(Thr145Lys) showing a hypoplastic AI with thin opaque enamel (Table 2; Supplementary Figures S1O, S2T). The *SLC13A5* individual in our panel, is an individual described with *SLC13A5* variant discovered through GenoDENT panel after the identification of the gene by WES in another family of the Schossig et al., 2017 cohort (Schossig et al., 2017) with a phenotype described as Kohlschütter-Tonz like syndrome (KTS).

Syndromic hypomature AI

Hypomature AI is also manifest in syndromic conditions. Three genes have thus far been identified as causing syndromes with associated hypomature AI.

Immunodeficiency 9 # 612782—AR—*ORAI1*

Primary immunodeficiency-9 (IMD9) is a recessive disease characterized by early onset of recurrent infections due to defective T-cell activation. The individuals present congenital myopathy resulting in muscle weakness, and features of ectodermal dysplasia including a hypomature amelogenesis imperfecta with soft dental enamel (McCarl et al., 2009).

ORAI1

By analyzing individuals described by (Feske et al., 1996), (Feske, 2010) showed for the first time that individuals with this type of immune dysfunction were homozygous for a variant in the *ORAI1* gene. Indeed, the disease is caused by homozygous or compound heterozygous variants in *ORAI1* (610,277). This gene located on chromosome 12q24, encodes a subunit of the plasma membrane calcium channel CRAC essential for store-operated calcium entry (Vig et al., 2006) and the channel function. The gene is expressed in cells and organs involved in immunity ($CD4^+$ and $CD8^+$ T-cells, $CD19^+$ B-cells, and in a subset of cells in the thymus, spleen, and tonsils) but also in sarcolemma of muscle fibers, eccrine sweat glands, skin, vascular endothelium, hepatocytes, lung, and kidney (McCarl et al., 2009) and in ameloblast (Nurbaeva et al., 2015). No variant in this gene was identified among our cohort.

Immunodeficiency 10 # 612783—AR—*STIM1*

Immunodeficiency-10 is a primary autosomal recessive immunodeficiency, characterized by recurrent infections due to defective T- and NK-cell function. The individuals also have hypotonia, hypohidrosis and hypomature amelogenesis imperfecta. (Picard et al., 2009; Parry et al., 2016a) reported the disease for the first time in 3 siblings from central Europe who had recurrent infection due to defective T-cells, muscle hypotonia and enamel defects. They identified defects in cellular store-operated calcium entry, which is required for lymphocyte activation.

STIM1

Immunodeficiency 10 is due to a homozygous truncating variant in the *STIM1* gene (Picard et al., 2009; Parry et al., 2016a). STIM1 gene is located to chromosome 11p15.5 and contains 12 exons (Parker et al., 1996; Sabbioni et al., 1999). It encodes a 746 AA calcium sensor that conveys the calcium load of the endoplasmic reticulum to store-operated channels at the plasma membrane (Yuan et al., 2007) and mediate the gating of CRAC channels (McNally et al., 2012). ORAI1 and STIM1 are interacting as the ORAI1 membrane calcium channel is activated by the calcium sensor STIM1 when calcium reservoirs are depleted (Lacruz and Feske, 2015). AI, related to Immunodeficiency 10, is classified as hypomineralized on OMIM but due to recent publications we transfer it to hypomature AI section (Wang S. et al., 2014; Furukawa et al., 2017). No variant in this gene was identified among our cohort.

Kohlschütter-Tonz syndrome #226750—AR—*ROGDI*

This autosomal recessive syndrome was firstly described by (Kohlschütter et al., 1974) in a family of central Switzerland in which 5 brothers were affected but with no mention of the gene involved. Kohlschütter-Tonz syndrome (KTS) is characterized by severe global developmental delay, seizures, and AI affecting both primary and permanent teeth. The teeth present a yellow to brown discoloration. The most severely affected individuals have profound intellectual disability, never acquire speech, and

become bedridden early in life (Mory et al., 2012; Schossig et al., 2012).

ROGDI

(Schossig et al., 2012) reported for the first time the causative gene by identifying homozygous or compound heterozygous variants in ROGDI gene in 3 members of 3 unrelated families with KTS. ROGDI maps to chromosome 16p13.3., contains 11 exons and spans over 5.98 kb. It encodes a leucine-zipper protein with high expression in the human brain and spinal cord (Mory et al., 2012).

Both variants in *ROGDI* and *SLC13A5* cause epileptic encephalopathy and AI. Whereas *ROGDI* mutation manifests in an hypomature-hypomineralized AI with a rough colored dental surface and with seizure onset may be as late as age 3, individuals mutated for *SLC13A5* present hypoplastic AI, a smooth the dental surface sometimes with only mild discoloration and seizure onset is within the first days after birth.

Here we report three individuals with stop variants in *ROGDI* (24.1, 24.2, 24.3) (Table 2; Supplementary Figures S1P, S2U). Individuals 24.1 and 24.3 present compound heterozygous variants (Supplementary Figures S3.44) already described in the literature, while 27.2 has a homozygous variant found with our panel and previously published in (Huckert et al., 2014).

Syndromic hypomineralized AI

Two syndromic conditions associated with hypomineralized AI have been described.

Short stature, amelogenesis imperfecta, and skeletal dysplasia with scoliosis #618363—AR—*SLC10A7*

Affected individuals present with short stature, joints dislocation, advanced carpal ossification, abnormal vertebrae, hyperlordosis or kyphoscoliosis, small epiphyses and hypomineralized AI. Enamel has a yellow-brown appearance with a rough surface. Tooth crowns are short and widely spaced. Variable features include facial dysmorphism, moderate hearing impairment, and mildly impaired intellectual development. The phenotype severity is variable. Indeed, an individual with a milder phenotype was reported in (Laugel-Haushalter et al., 2019).

SLC10A7

This autosomal recessive syndrome was firstly described by (Dubail et al., 2018) in 6 unrelated individuals. It is due to variants in the *SLC10A7* gene encoding a calcium transporter.

The key phenotype to distinguish individuals with mutation in *SLC10A7*, within the wide spectrum of skeletal dysplasia, was the hypomineralized/hypomature enamel defects observed in all the individuals and the hypoplastic lower jaw.

Here we report 2 individuals with homozygous variants in *SLC10A7*. Individual 25.1 presents a novel homozygous variant in the gene. The variant identified by GenoDENT NGS panel affects exon 3 NM_001300842.3c.269T>G; p.(Leu90Arg) in which another homozygous variant was already described to be pathogenic (Ashikov et al., 2018). Individual 25.2 was already described in (Laugel-Haushalter et al., 2019, WES). She has a homozygous missense variant in the very last exon of the gene c.908C>T; p.(Pro303Leu) (Table 2; Supplementary Figure S3.45) and presents a mild phenotype of the disease but with the characteristic enamel defects (Supplementary Figures S1Q, S2V).

Jalili syndrome #217080—AR—*CNNM4*

The autosomal recessive syndrome was first described by (Jalili and Smith, 1988) in 29 individuals and is characterized by cone-rod dystrophy and AI. Nystagmus and photophobia are present from infancy or early childhood and progress with age. Enamel of primary and permanent teeth is hypomineralized (only 50% of mineralization), with a dark brown discoloration, and individuals are more susceptible to dental caries (Parry et al., 2009).

CNNM4

The disorder is caused by homozygous or compound heterozygous variants in *CNNM4* gene (607,805) sitting on chromosome 2q11.2. More than 24 different variants have been identified on individuals all around the world but the molecular mechanism of the disease remains unclear (Daneshmandpour et al., 2019). CNNM4 encodes a deduced 775 amino-acids protein. (Guo et al., 2005) hypothesized that the protein may have a role in metal ion transport and homeostasis. Indeed, (Yamazaki et al., 2013) showed in mice the role of Cnnm4 in Mg^{2}+ transport. The protein is localized in keratocytes, in the retina, and in developing teeth specifically in ameloblasts (Parry et al., 2009; Polok et al., 2009).

Here we report two individuals with homozygous missense variants in this gene. In individual 26.1 we detected a homozygous missense variant, firstly described by (Parry et al., 2009): NM_020184.4:c.1495G>A; p.(Val499Met) (Table 2; Supplementary Figure S3.46). Other missense variants, were reported as pathogenic and causative of Jalili syndrome. Individual phenotype was consistent with the literature and described clinical synopsis. The “hypoplastic” enamel appearance of both primary and permanent teeth was due to extensive post-eruptive loss of soft enamel detaching easily from dentin. The teeth displayed yellow-brownish coloration with brown spots (Supplementary Figures S1R, S2W). Individual 26.2 has already been reported in (Prasad et al., 2016a) c.1495G>A; p.(Val499Met).

Syndromic hypoplastic/hypomature with taurodontism AI

One syndromic condition with hypoplastic/hypomature AI with taurodontism has been identified.

Tricho-dento-osseus syndrome #190320—AD—*DLX3*

Tricho-dento-osseous (TDO) syndrome is a rare autosomal dominant condition characterized by various dental and non-dental findings (Jagtap et al., 2019) (Duverger et al., 2017).

TDO emcompasses abnormal development of ectoderm derived structures. Patients presents with head and neck and skeletal phenotypes. Dysplastic nails, curly hair, abnormal density of bone, taurodontism, and hypoplastic amelogenesis imperfecta are common features of this disorder. The enamel appears extremely thin, with enlarged pulp chambers, and root furcations displaced apically. Mandibular prognathism, delayed teeth eruption, teeth discoloration, periapical abscesses, apically positioned furcation, shortened roots, other non-dental abnormalities are variably

present. Dental and non-dental features are variable even among affected individuals in the same family (Jain et al., 2017). The management of TDO individuals require a multidisciplinary approach involving both dentists and physicians. Periodic radiographic follow-up is required to prevent further complications such as osteomyelitis (Jagtap et al., 2019).

DLX3

TDO is caused by variants in a transcriptional regulator, Distal-less homeobox 3 gene, *DLX3*.

Here we describe two unrelated individuals, one girl (27.1) and one boy (27.2) presenting with tricho-dento-osseous syndrome (Supplementary Figure S1S). They are both carrying the same *DLX3* heterozygous frameshift variant in exon 3 NM_005220.3: c.561_562del; p.(Tyr188Glnfs*13) (Table 2; Supplementary Figures 3.47 and 3.48). This variant firstly described by (Dong et al., 2005) is altering the two amino-acids of the DNA-binding homeodomain and truncating the protein by 88 amino-acids.

Discussion

AI classification has always been evolving since the one proposed by (Weinmann et al., 1945). These early classifications were based mostly on detailed phenotypic observations (Darling, 1956; Witkop, 1957). Later it was recognized that the mode of inheritance was important to classified AI so, (Schulze, 1970) and (Witkop, 1971) proposed a classification encompassing the phenotype observation and the mode of inheritance. This classification system has been updated and improved since 1988 by (Witkop, 1988) and is currently the mostly frequently used classification demonstrating its extraordinary accuracy grounded on expert clinical skills. A classification based not only on the phenotype and the mode of inheritance but also on the genetic molecular defects was proposed since 1995 by (Aldred and Crawford, 1995), (Hart et al., 2002a) and (Aldred et al., 2003) but this was never fully achieved due to the lack of knowledge and technologies to complete both a clinical and a molecular diagnosis. In 2007 (Crawford et al., 2007) stated that laboratory genetic diagnosis was at that time only a research tool.

It is however now commonly accepted that the mode of inheritance and underlying genomic change are important to improve genetic counselling of affected individuals and their families.

Here we propose a Witkop's classification evolution including the phenotypical observations (hypoplastic, hypomature, hypomineralized and hypoplastic-hypomature with taurodontism), the mode of inheritance and the genetic diagnosis.

This is now possible as progresses in next-generation sequencing techniques, their availability and now reduced costs have opened the door to personalized oral medicine. GenoDENT NGS panel, exploring 567 genes involved in orodental development and diseases, was set up in research (Prasad et al., 2016a) and transferred in hospital diagnostic laboratories in 2019 (Rey et al., 2019). Its 60% diagnostic rate testify of its reliability and utility in the context of diagnosis, counselling and evolution of treatment options.

It took more than 10 years to gather an informative AI cohort (221 individuals from 111 families) with detailed clinical information (D[4]/phenodent).

Since the discovery of the first gene underlying an amelogenesis imperfecta from mapping of *AMELX* in 1989 (Lau et al., 1989) to its causative role in AI in 1990 (Lagerström et al., 1990; 1991); more than 70 genes have been discovered as important for amelogenesis and its defects. The most recent ones are *CLAUDIN 10* (Sewerin et al., 2022) and *ATP6V1A* (Guerrini et al., 2022). Knowledge is evolving fast on amelogenesis (Simmer et al., 2021) and enamel disturbances in rare diseases. (de La Dure-Molla et al., 2019) listed among 408 rare diseases with orodental manifestations, 105 conditions with enamel defects either isolated (21) or syndromic (84). In our cohort, 73% were diagnosed with non-syndromic amelogenesis imperfecta and 27% with syndromic amelogenesis imperfecta.

The boundaries between isolated and syndromic forms of AI are shrinking as novel information on genes, role of the proteins and associated symptoms and diseases are evolving. This was well illustrated by *FAM20A* and the recognition of enamel-renal syndrome (ERS); enamel-renal-gingival syndrome, hypoplastic amelogenesis imperfecta with nephrocalcinosis, amelogenesis imperfecta and gingival fibromatosis syndrome as allelic conditions and the subsequent transition from an isolated AI to a syndromic disease requiring a different holistic care. *WDR72* was identified in 2009 (El-Sayed et al., 2009). It was recently associated to distal renal tubular acidosis (Khandelwal et al., 2021) and this finding rapidly confirmed in 2019 that isolated *WDR72* associated hypomature AI was in fact a possible syndromic condition (Zhang et al., 2019). AI diagnosis should always bare in mind possible associated symptoms leading to a syndrome diagnosis.

AI clinical subtype recognition can be difficult as phenotype is evolving through time and might transform from a hypomineralized form to a visible "hypoplastic" form thanks to post-eruptive enamel breakdown. The terms hypocalfication and hypomaturation were used by Witkop (1988) before knowing the genes or mechanisms involved in amelogenesis and the pathogenesis of AI. It is now known from the timing of protein expression that these terms are not accurate and both the hypocalcified and hypomaturation phenotypes have as primary feature hypomineralization. *MMP20,* for example, is expressed during the secretory stage and continues to be expressed during the maturation stage yet is classified as hypomature AI and it is hypomineralized.

Clinically "hypocalcified" refers to softer enamel with post eruptive breakdown and "hypomature" to less mineralized but strong enough enamel preserving the teeth morphology therefore corresponding to a more advanced maturation process and the state of degradation of enamel matrix proteins.

The Witkop's classification terminology could be adjusted to use only names (I HYPOPLASIA, II HYPOMATURATION, III HYPOMINERALIZATION *versus* HYPOCALCIFICATION, IV HYPOMATURATION/HYPOPLASIA with TAURODONTISM) or only adjectives (hypoplastic, hypomature, hypomineralized, hypomature/hypoplastic). May be sections II and III of the classification should be united in a single hypomineralization section.

This paper gathers in the Supplementary Figures many clinical intraoral pictures and panoramic radiographs of genotype related amelogenesis imperfecta. This resource is meant to help clinicians improving their AI diagnosis and search for associated symptoms.

Dental anomalies and enamel defects are very precise key diagnostic clues (Boch-Zupan et al., 2012; de La Dure-Molla et al., 2019) helping, when recognized, to orientate a clinical diagnosis towards a broader genetic rare disease recognition. These AI phenotypes can be precise diagnostic signatures. Among them the clinical features linked to ERS (almost no enamel, impacted teeth, intrapulpal calcifications, root anomalies . . .) would immediately suggest a possible ERS and orientate the clinical team towards kidney investigations *via* ultrasound seeking nephrocalcinosis. In Heimler syndrome, the AI is only present in the permanent dentition and its recognition linked to seusorineural hearing loss could suggest the diagnosis.

Following genetic diagnosis, retro-phenotyping can also lead to the search and recognition of additional traits and the diagnosis of broader rare diseases. For example, the diagnosis of Jalili syndrome or amelogenesis imperfecta and dystrophy of the cones and rods of the retina was subsequently made in a 4-year-old boy who attended a rare disease competence center for enamel problems management. The genetic diagnosis pointed to the presence of autosomal bi–allelic recessive variants in the *CNNM4* gene with further confirmation of the presence of a retinal dystrophy. This transformed an isolated enamel restricted diagnosis to a broader rare disease identification.

Genotype recognition can change a clinical diagnosis: two patients with 2 different diagnoses: spondyloepiphyseal dysplasia and mucopolysaccharidosis type 4A (ORPHA: 309,297) were investigated for associated hypoplastic amelogenesis imperfecta (quantitative enamel defects). The results of the GenoDENT test showed variants in the *GALNS* gene responsible for mucopolysaccharidosis type 4A. The test changed the medical diagnosis for one of the patients. A revised diagnosis facilitates access to other treatments and care.

Phenotype/genotype identification can also lead to accurate information and genetic counselling, guide therapeutic management and facilitate the discovery of new genes and diseases.

Patients with negative results on the panel were further explored with exome sequencing and through international collaborations and larger cohort gathering new genes such as *LTBP3* (Huckert et al., 2015), *SLC13A5* (Schossig et al., 2017), *SLC10A7* (Laugel-Haushalter et al., 2019) were identified. Whole genome sequencing (WGS), as the PFMG 2025 initative (https://pfmg2025.aviesan.fr/en/; rare diseases with orodental manifestations https://pfmg2025.aviesan.fr/professionnels/preindications-et-mise-en-place/formes-syndromiques-de-maladies-rares-a-expression-bucco-dentaire/) could facilitate the discovery of the underlying genetic defects causing both non-syndromic and syndromic AI.

In this cohort we identified 151 variants. Among these, 124 were classified as likely pathogenic or pathogenic (class 4 or 5) and 47 were newly reported. It is interesting to notice that the most frequent genes identified in isolated AI were *AMELX* in hypoplastic, *MMP20* in hypomature and *FAM83H* in hypomineralized AI and *LTBP3* and *FAM20A* in syndromic conditions.

Our results allowed to provide for 81% of the index individuals a definitive genetic diagnosis, and for 19%, variants of unknown significance (VUS) were identified. Twenty-one new VUS were detected in patients with isolated AI and 3 new VUS in patients with syndromic AI.

However, for those uncertain variants, like new candidate genes, or for variants in different domains of the protein or with different possible physiopathological mechanisms, it could be difficult to confirm their pathogenicity and these variants are subsequently classified as variant of unknow significance (VUS).

To reclassify those variants and provide a clear genetic diagnostic it is important to develop reliable, easy to perform *in vitro* assays and functionally validate these variants. Furthermore, functional characterization will open new potential strategies for curative treatments.

Enamel defects have also been reported in others syndromes and the question remains to qualify them as amelogenesis imperfecta. For instance, genes associated with - skin, nails and hair defects among other symptoms are *ATR* (Tanaka et al., 2012), *CLDN1* (Feldmeyer et al., 2006), *COG6* (Shaheen et al., 2013), *FGF10, FGFR3, FGFR2* (Hollister et al., 1973), *HRAS* (Goodwin et al., 2014), *KRAS, NRAS, KRT14* (Tabata et al., 1996), *MBTPS2* (Martino et al., 1992); - with eye defects *NAA10*; - with skeletal anomalies *AKT1, B3GAT3, CYP27B1, CTSK, EVC1, EVC2, ERCC4, ERCC8, GJA1, GNAS, IDUA, IRX5, NDN, PTDSS1, SNORD116, RUNX2, TBCE, VDR*; - genito-urinary anomalies *HNF1B, VPS33B, VIPAR*; - intellectual disability *PSPA, GALC*; Usher syndrome *MYO7A, USH2A, PD2D7, ADGRV1, CLRN1*.

Amelogenesis is at the crossroad of many developmental processes and careful examination of the oral cavity of syndromic patients should be mandatory to deliver appropriate preventive care and follow up targeting oral health.

It is crucial that the team of health professionals involved in diagnosing and managing a possibly syndromic patient knows the value of an expert examination of the oral cavity and the importance of an acute diagnosis of these developmental defects assisting syndrome diagnosis (Bloch-Zupan et al., 2021). On the other hand, it is important that the dentist who can recognize abnormal teeth can convey the right information towards the medical team. Expert reference rare diseases reference centres can assist patients and their treating practitioners in diseases diagnosis and management according to evidence-based information.

Undergraduate, postgraduate and continuous education is important to ensure best management options for rare diseases patients.

Gathering data from large cohorts and pooling information from registries should also lead to a better understanding of the prevalence of AI as a whole or the various AI types and rare diseases. The prevalence stated in the literature from 1:700 to 1:14,000, according to the populations studied may not reflect reality. These data are of importance to facilitate financial undertaking and reimbursement by health authorities of comprehensive lifelong treatments.

Further actions are also needed to update International Classification of Diseases (ICD), The Systematized Nomenclature in Medicine (SNOMED), Orphanet and ontologies (HPO, Orphanet . . .) and to develop guidelines (https://www.has-sante.fr/jcms/p_3284538/fr/20amelogeneses-imparfaites) to ensure precision, personalized oral medicine and its dedication to treatment of individuals suffering from amelogenesis imperfecta.

Witkop's classification was and is still remarkable. It serves as a good basis to understand the nature of enamel defects and as a guide towards its revision as knowledge on genetics and pathophysiology is increasing. JT Wright (2023) in a recent paper discussed these issues and concluded upon the opportunity, thanks to advanced genetics, to "elaborating a more accurate and informative nosology for these conditions in order to improve communication between patients, families, clinicians and researchers".

The revised classification presented here, developed thanks to GenoDENT NGS panel, will hopefully provide a useful tool for accelerating genotype/phenotype causal relations and improved patient outcomes.

Data availability statement

The variants were submitted in ClinVar (https://www.ncbi.nlm.nih.gov/clinvar/), a freely available, public archive of human genetic variants and interpretations of their significance to disease, maintained at the National Institutes of Health (Landrum et al, 2018). Their accession numbers are: SCV003843192, SCV003843249, SCV003843250, SCV003843251, SCV003843254, SCV003843255, SCV003843256, SCV003843257, SCV003843258, SCV003843259, SCV003843870, SCV003843871, SCV003843872, SCV003843873, SCV003843875, SCV003843877, SCV003843878, SCV003843879, SCV003843881, SCV003843887, SCV003843888, SCV003843252, SCV003843247, SCV003843883, SCV003843886, SCV003842949, SCV003843193, SCV003842321, SCV003842323, SCV003842272, SCV003842271, SCV003842273, SCV003842270, SCV003842952, SCV003842312, SCV003842315, SCV003842322, SCV003842325, SCV003842326, SCV003842947, SCV003842948, SCV003842953, SCV003842954, SCV003842955, SCV003842957, SCV003843190, SCV003843191.

Ethics statement

The studies involving human participants were registered at https://clinicaltrials.gov: NCT01746121 and NCT02397824, and with the MESR (French Ministry of Higher Education and Research) Bioethics Commission as a biological collection "Orodental Manifestations of Rare Diseases" DC-2012-1,677 within DC-2012-1,002 and was acknowledged by the CPP (person protection committee) Est IV 11 December 2012. Written informed consent to participate in this study was provided by the participants' legal guardian/next of kin. Written informed consent was obtained from the individual(s), and minor(s)' legal guardian/next of kin, for the publication of any potentially identifiable images or data included in this article.

Author contributions

AB-Z, MK, AJ-A, IMB, M-CM, NK and all participating clinicians (O-Rares consortium: MLD-M, EN, MH, CJ-B, SL, CT, BT-P and other members; ERN Cranio and International consortia: TD, MM, MEA, LQ, SM, PP, NR, BUO and other members) enrolled participating individuals, collected the salivary samples and detailed the individuals' phenotype. TR, VLH, and BG identified the molecular basis of the disease through NGS assays. VL-H, TR, AJA, IMB, and AB-Z analysed the data and wrote the manuscript. AB-Z, TR, AJ-A, and VL-H designed the study and were involved from conception, funding seeking to drafting and critical review of the manuscript. All authors therefore contributed to conception, design, data acquisition, analysis, and interpretation, drafted and critically revised the manuscript. All authors gave final approval and agreed to be accountable for all aspects of the work. All authors gave final approval and agreed to be accountable for all aspects of the work.

Group members of Consortia

O-Rare Consortium

O-Rares Consortium: French Reference and Competence centers, healthcare network for rare oral and dental diseases CRMR/CCMR O-Rares, French Filière "TETECOU" and associated paediatric/genetic teams (Centres de Génétique et Centres de Référence Anomalies du Développement et Syndromes Malformatifs, Filière AnDDI Rares). Edouard Euvrard, Juliette Piard (Centre Hospitalier Universitaire de Besançon; Hôpital Jean Minjoz); Marie José Boileau, Elsa Garot, Didier Lacombe (CHU de Bordeaux—Hôpital Pellegrin); Victorin Ahossi, Laurence Faivre (CHU Dijon, Hôpital François Mitterrand); Caroline Delfosse (CHU de Lille); Klauss Dieterich, Service de génétique Hôpital Couple Enfant, Grenoble; Jean-Pierre Duprez, Jean-Jacques Morrier, Béatrice Thivichon-Prince, Béatrice Richard, Nathalie Guffon-Fouilhoux, Linda Pons, Massimiliano Rossi (Hospices Civils de Lyon, Groupement Centre, Pôle d'Activités Médicales d'Odontologie, Centre de soins Dentaires; Service de génétique, Centre de Référence Anomalies du Développement); Corinne Tardieu, Isabelle Blanchet (APHM, Hôpital de la Timone Enfants, Marseille); Dominique Droz, Magali Hernandez, Bruno Leheup (CHRU de Nancy—Hôpitaux de Brabois); Serena Lopez, Bertand Isidor (CHU de Nantes—Hôtel Dieu); Michèle Muller- Bolla, Clara Joseph-Beaudin (CHU de Nice); Muriel de La Dure Molla, Benjamin Fournier, Ariane Berdal (Hôpital Rothschild, APHP, Paris); Alain Verloes (AP-HP, Hôpital Robert Debré, Paris); Sandrine Marlin (AP-HP, Hôpital Necker Enfants Malades, Paris); Tiphaine Davit-Béal (AP-HP, Paris and CHU de Rennes); Marie Paule Gelle (CHU Reims, Hôpital Maison Blanche, Pôle: Odontologie); Bérénice Doray (CHU de la Réunion Site SUD (Terre Sainte)); Jean-Louis Sixou, Alinoe Lavillaurex, Sylvie Odent (CHU Rennes); Marine Lebrun (CHU Saint-Etienne); Agnès Bloch-Zupan, Isaac Maximiliano Bugueno, François Clauss, Jean-Christophe Dahlet, Jean-Luc Davideau, Olivier Etienne, Bruno Grollemund, Mathilde Huckert, Sophie Jung, Marzena Kawczynski, Adeline Loing, Marie-Cécile Manière, Prune Sadones, Marion Strub, Delphine Wagner, Yves Alembik, Salima El Chehadeh, Hélène Dollfus, Elise Schaefer, Sylvie Soskin, Anne De-Saint-Martin (Hôpitaux Universitaires de Strasbourg); Isabelle Bailleul-Forestier, Emmanuelle Noirrit, Frédéric Vaysse, Nicolas Chassaing (CHU de Toulouse—Hôpital Rangueil); Annick Toutain (CHU de Tours).

European reference network, ERN CRANIO, Consortium

Tatjana Dostalova, Milan Macek Jr, University Hospital Motol and 2nd Faculty of Medicine, Charles University, Prague, Czeck Republic.

International Consortium

Mustapha El Alloussi, Faculty of Dentistry, International University of Rabat,CReSS Centre de recherche en Sciences de la Santé, Morocco; Leeila Qebibo, Unité de génétique médicale et d'oncogénétique, CHU Hassan II, Fez, Morocco; Supawich Morkmued, Patimaporn Pungchanchaikul, Faculty of Dentistry, Khon Kaen University, Khon Kaen, Thailand; Nicole Revencu, Centre de Génétique humaine UCL Cliniques universitaires Saint-Luc, Bruxelles, Belgium; Blanca Urzúa Orellana, Instituto de Investigación en Ciencias Odontológicas, Facultad de Odontología, Universidad de Chile, Chile; Juliane Leonhardt Amar, Switzerland; Zouari Noura, Service de Pédiatrie, Hôpital universitaire Sahloul, Sousse Tunisie.

Funding

This work was financed by and contributed to the actions of the project No. 1.7 "RARENET: a trinational network for education, research and management of complex and rare disorders in the Upper Rhine" co-financed by the European Regional Development Fund (ERDF) of the European Union in the frame-work of the INTERREG V and previously INTERREG IV Upper Rhine program as well as to the ERN (Euro-pean reference network) CRANIO initiative. ABZ is a USIAS 2015 Fellow of the Institute of Advanced Studies (Institut d'Etudes Avancées) de l'Université de Strasbourg, France. This work was also supported by grants from the French Ministry of Health (National Program for Clinical Research, PHRC 2008 N°4266 Amelogenesis imperfecta), the University Hospital of Strasbourg (HUS, API, 2009–2012, "Development of the oral cavity: from gene to clinical phenotype in Human". This work of the Interdisciplinary Thematic Institute IMCBio, as part of the ITI 2021-2028 program of the University of Strasbourg, CNRS and Inserm, was supported by IdEx Unistra (ANR-10-IDEX-0002), and by SFRI-STRAT'US project (ANR 20-SFRI-0012) and EUR IMCBio (ANR-17-EURE-0023) under the framework of the French Investments for the Future Program. This study was possible thanks to the Projet EGENODENT financed by the Fonds d'Intervention Régionale (FIR) of the Agence Régionale de Santé Grand Est (2019-2022). We are grateful to funding provided by Filiére TETECOU and "Pierre Henri et ses amis" patient support groups. This work is the baseline of the HDH data challenge D-IA-GNO-DENT (2021-2023).

Acknowledgments

We are grateful to the families and individuals for their participation and invaluable contribution as well as to the patient support group: Amélogenèse France. We thank deeply health professionals contributing to patient's care (William BACON, Guy BASSONPIERRE, Jacques BELLEHSEN, Michèle BURGET, Emilie CHARPIOT, François CHARTON, Albert COSTI, Gabriel DOMINICI, Arnaud FROEHLY, Pierre HATTENBERGER, Guillaune HENGY, Clarisse HUCHON, Florence JOUANET, Véronique LAULY-SPIELMANN, Fabienne MACHWIRTH, Phillippe NEUMANN, Caroline RAYNAUD, Laurent RIGUET, Christine SCHINI, Jean-Marc SCHWEITZER, Pierre STOCKEL, Pierre WAHL). The computing resources for this work were provided by the BICS and BISTRO bioinformatics platforms in Strasbourg. We thank Patrick REILLY for critical reading and English language improvement of the manuscript

Conflict of interest

The authors declare that the research was conducted in the absence of any commercial or financial relationships that could be construed as a potential conflict of interest.

Publisher's note

Supplementary material

The Supplementary Material for this article can be found online at: https://www.frontiersin.org/articles/10.3389/fphys.2023.1130175/full#supplementary-material

SUPPLEMENTARY FIGURE S1
Clinical intraoral photographs and panoramic radiographs detailing the phenotype of amelogenesis imperfecta patient for each associated genotype. Isolated AI: A COL17A1; B COL7A1; C LAMA3, LAMB3, LAMC2; D ENAM; E AMELX, F AMBN, G ACP4, H KLK4, MMP20; I WDR72, C4ORF26/ODAPH and SLC24A4; J FAM83H; K DLX3; Syndromic AI: L LTBP3; M FAM20A; N GALNS 2700 and ARHGAP6; O TGFBR2 and SLC13A5; P ROGDI; Q SLC10A7; R CNNM4; S DLX3. **Isolated AI**. **A *COL17A1*** Hypoplastic pitted amelogenesis imperfecta. Patients present pitted rough enamel with normal hardness. Some patients present a yellowish discoloration with brown extrinsic stains within the pits. Radiographs show normal density but sometimes thinner enamel. Patients 1.1, 1.3, and 1.4 were already described in Prasad et al., 2016 **B *COL7A1*** Hypoplastic amelogenesis imperfecta. Pitted, and thin enamel with yellow-brownish discoloration. Spaced teeth, and incisal and occlusal attrition reflect thinner enamel. **C *LAMA3, LAMB3 and LAMC2*** Hypoplastic amelogenesis imperfecta. Patient 3.1 presents a digenic mutation affecting both COL17A1 and LAMA3 genes. Enamel displays pits arranged in rows and columns. Comparing with COL17A1 mutations related phenotype, the enamel seems more pitted. Both primary and permanent dentition are affected. LAMB3 Patients 4.1 and 4.3 are 8-year-old. Enamel presents pits, and yellowish discoloration more pronounced in incisors. In the radiographs, enamel shows a normal density however unerupted teeth in 4.2, 4.3, 4.4 are clearly dysplastic. Patient 5.1 of 4-year-old, presents a mutation in LAMC2 showing a primary dentition with thin white enamel. Patient 3.1 and 4.1 were already described in Prasad et al. (2016). **D *ENAM*** Hypoplastic autosomal dominant amelogenesis imperfecta.

Thin enamel with white spots, and yellowish discoloration in some cases. In some cases, tooth size might be reduced, and teeth appear slim. Enamel pits, and linear depressions are visible. Patient 6.3 presents agenesis of 16, 26, 36, 46, and stainless-steel crowns covering primary lower molars, with an hypoplastic/hypomature AI. Hypoplastic enamel is visible also on non-erupted teeth in panoramic radiographs. **E *AMELX*** Hypoplastic amelogenesis imperfecta displaying in female individuals a banding pattern (Lyonisation effect) (patients 7.1, 7.3, 7.4, 7.8, 7.11), with vertically ridged teeth, alternating bands of normal and hypoplastic enamel mainly on incisors and spaced yellowish teeth smaller than normal. Male patients (7.2, 7.10) phenotype is more severe with almost no enamel. Patient 7.10 presents a delayed dental eruption. 7.9 is a male displaying a banding pattern AI phenotype similar to females. Further exploration established 7.9 with a XXY karyotype. Radiographs show a thinner with normal density enamel in patients 7.3, 7.6, 7.7, 7.7. In patients 7.2, 7.5, 7.10 there is no obvious contrast between enamel and dentin but enamel is very thin. Hypomature amelogenesis imperfecta (7.5, 7.6, 7.7): Patient 7.7 has agenesis of 12, 15, 22, 28 caused by an additional mutation in WNT10A gene. **F *AMBN*** Hypoplastic amelogenesis imperfecta. Affects both primary and permanent dentition. Patients present rough irregular pitted enamel. The enamel surface acquires a yellowish color with age. Patient 8.1 is 10- year-old, and presents an associated open bite. Individual 8.2 has an end-to-end bite. Patient 8.3 was already described in Prasad et al. (2016). He presents restorations on upper and lower incisors, and first molars. On radiographs, the enamel is almost absent. **G *ACP4*** Hypoplastic amelogenesis imperfecta. Thin enamel with irregular surface, and yellowish discoloration. Patient 9.2 has composite crowns on all her teeth, suggesting a generalized AI. Patient 9.3 presents agenesis of 18, 28 due to a mutation in WNT10A gene. X-rays show a thinner but normal density enamel, long teeth and slim roots. **H *KLK4 and MMP20*** Hypomature amelogenesis imperfecta. Patient 10.1 present a mutation in KLK4 gene showing molars with soft brown enamel, with a lack of radio-contrast between enamel and dentin. Opaque, smooth, and pigmented enamel with incisal and occlusal attrition in primary and permanent dentition is visible in patients with MMP20 variants. i.e., in patient 11.6 and 11.11 both dentition are affected. Thinner enamel than normal detaches easily from the dentin. Patient 11.2 was already published in Prasad et al. (2016) and presents taurodontism. Patients 11.5, 11.6, 11.9, 11.11, were published in Gasse et al. (2017). Patient 11.8 presents stainless steel crowns in molars with pronounced mammelons in permanent incisors. In X-rays, lack of contrast between enamel and dentin is clearly visible. **I *WDR72, C4ORF26/ODAPH, and SLC24A4*** Hypomature amelogenesis imperfecta. Yellow-brownish soft enamel with a mottled appearance that detaches easily from the dentin. Both primary and permanent teeth are affected. Radiographs show a lack of contrast between enamel and dentin. 12.1-4 (WDR72). 13.1 ODAPH. Individual 14.1 (SLC24A4) had primary molars with stainless steel crowns, and an agenesis of 45. Patient 14.2 presented an impacted 13, all permanent incisors were covered by composite veneers, and stainless-steel crowns protected the first lower molars, hypomature enamel is clearly present on other teeth. Radiographs show a lack of contrast between enamel and dentin. Patient 12.2, 13.1 and 14.1 were already published in Prasad et al., 2016. **J *FAM83H*** Hypomineralized amelogenesis imperfecta. Primary and permanent dentitions are affected with soft, colored enamel that detaches easily from the dentin (post eruptive breakdown). Spaced teeth with occlusal and incisal wear giving a conic form in canines are related to secondary enamel loss. Patients complain from high sensitivity. Patients 15.4, 15.6 present slight taurodontism as seen on x-ray. Patients 15.3, 15.5, 15.10 and 15.14 have stainless steel pediatric crowns on primary molars. 15.10, 15.12, 15.13, 15.14 present a clear open bite. Radiographs show no difference in radioopacity between enamel and dentin. **K *DLX3*** Hypoplastic—Hypomature amelogenesis imperfecta with taurodontism. 16.1 has a rough enamel surface, with white and brown spots. A stria as an hypoplastic defect is visible on lower incisal edges. Slight taurodontism is present. 16.2 showed very thin enamel and marked molar taurodontism. 37 is missing. Teeth colour is very "dentin" like as enamel is so thin. 16.3 presented with an hypoplastic clearly hypomature AI with taurodontism (16, 26, 36, 46 and even primary molars), white spots, and brown extrinsic stains. Dental radiographs show normal radiolucency of enamel even if thinner. **Syndromic AI L *LTBP3* (Verloes Bourguignon syndrome, Platyspondyly with AI)** Hypoplastic amelogenesis imperfecta. There is almost no enamel. Delayed teeth eruption. Large pulp chambers, Small, and spaced teeth, with a yellowish color. **M *FAM20A* (Enamel Renal Syndrome)** Hypoplastic amelogenesis imperfecta. There is almost no enamel. Eruption delay and microdontia, with spaced teeth, showing a yellow discoloration, and reduced enamel thickness affecting both dentitions. Patient 18.8 has a prosthetic rehabilitation on upper incisors. The radiographs analysis shows a delayed and impaired eruption of permanent dentition, ankylosed permanent teeth, hyperplasia of follicular sac, intrapulpal calcifications, root formation anomalies. Gingival hyperplasia is clearly visible. **N *GALNS* (Mucopolysaccharidosis type IV) and *ARHGAP6* (Linear skin defects with multiple congenital anomalies 1)** Hypoplastic amelogenesis imperfecta. Patients 19.1 and 19.2 affected with GALNS mutations have teeth with a rough thin enamel surface. On radiograph enamel is thin but with normal radioopacity. Female individual 20.1 has an AMELX deletion displaying a similar phenotype than the isolated form with a banding pattern of normal and hypoplastic enamel, she is affected by MLS syndrome. **O *TGFBR2* (Loeys-Dietz syndrome) and *SLC13A5* (Kohlschutter-Tonz like syndrome)** Hypoplastic amelogenesis imperfect. Patient 22.1 has a TGFBR2 mutation, teeth have a rough surface with pits, the enamel color is opaque yellowish. Panoramic radiograph shows normal enamel radiodensity. In patient 23.1 enamel is thin with opaque yellowish colour, and brown extrinsic stains. SLC13A5 mutation was already reported in Schossig et al. (2017). **P *ROGDI* (Kohlschutter-Tonz syndrome)** Hypomature amelogenesis imperfecta. Individuals present a yellow-brownish discoloration of enamel affecting both primary and permanent dentitions. Stainless steel crowns are covering the molars in patients 24.1 and 24.3. Patient 24.2 was published in Huckert et al., 2016. **Q *SLC10A7* (Short stature, amelogenesis imperfecta, and skeletal dysplasia with scoliosis)** Hypomature/Hypomineralized amelogenesis imperfecta affecting both the 2809 primary and permanent dentition with a yellowish enamel. Patient 25.2 presents stainless steel crowns on upper and lower molars and was already published in Laugel-Haushalter et al. (2019). The radiographs show similar density between dentin and enamel. **R *CNNM4* (Jallili Syndrome)** Hypomineralized amelogenesis imperfecta. 26.1 Extensive post eruptive breakdown and loss of enamel, yellow-brownish coloration with brown spots. High calculus accumulation on rough enamel surface clearly visible in lower incisors. 26.2 Primary dentition affected by AI, the enamel appears thin as it easily wears off from dentin. Stainless still crowns restorations in molars. **S *DLX3* (Tricho-Dento-Osseus syndrome)** Hypoplastic/hypomature? amelogenesis imperfecta with taurodontism. Patient 27.1 and 27.2 are affected by TDO syndrome. Dental radiographs show stronger radiolucency of thin enamel and taurodontism. Patient 27.2 is 6-year-old.

SUPPLEMENTARY FIGURE S2

Variants and corresponding protein domain. A gene is composed of exons represented by vertical lines and the initiation codon (ATG) and stop codon (TGA) are visualized by a black arrow. The variations detected in this study are symbolized by an arrow associated with the patient number in bold if homozygous. Green arrows correspond to variations never described before. Blue arrows correspond to variations already published by our team in Prasad et al. 2016. Orange arrows correspond to variations published by our team in collaborative studies. Gray arrows correspond to variations already known. Triangles symbolize splice variants, circle missenses variants, square nonsense variants, oval small deletion, rectangle small insertion, horizontal line bigger deletion. The shapes are coloured in blue when the individual is a male, in pink when the person is a female and purple for a male with suspected sex chromosome abnormalities. The corresponding protein domains are represented according to the PFAM database. The arrows indicate the localization of the detected variant with predictable protein impact. **A *COL17A1* variations and corresponding protein domain.** The gene transcript NM_000494.4 is made of 56 exons represented by vertical lines. **B *COL7A1* variations and corresponding protein domain.** The gene transcript NM_000094.4 is composed of 119 exons represented by vertical lines. **C *LAMA3* variations and corresponding protein domain. The** gene transcript NM_198129.4 is composed of 75 exons represented by vertical lines. **D *LAMB3* variations and corresponding protein domain.** The gene transcript NM_000228.3 is composed of 23 exons represented by vertical lines.**E *LAMC2* variations and corresponding protein domain.** The gene transcript NM_005562.3 is composed of 23 exons represented by vertical lines.**F *ENAM* variations and corresponding protein domain.** The gene transcript NM_031889.3 is composed of 9 exons represented by vertical lines. **G *AMELX* variations and corresponding protein domain.** The gene transcript NM_182680.1 is compoed of 7 exons represented by vertical lines. **H *AMBN* variations and corresponding protein domain** The gene transcript NM_016519.6 is composed of 13 exons represented by vertical lines.**I *ACP4* variations and corresponding protein domain.** The gene transcript NM_033068.3 is composed of 11 exons represented by vertical lines.**J *KLK4* variations and corresponding protein domain.** The gene transcript NM_004917.4 is composed of 5 exons represented by vertical lines. **K *MMP20* variations and corresponding protein domain.** The gene transcript NM_004771.4 is composed of 10 exons represented by vertical lines. **L *WDR72* variations and corresponding protein domain.** The gene transcript NM_182758.4 is composed of 20 exons represented by vertical lines. **M *ODAPH* variations**

and corresponding protein domain. The gene transcript NM_178497.5 is composed of 2 exons represented by vertical lines. **N *SLC24A4* variations and corresponding protein domain.** The gene transcript NM_153646.4 is composed of 17 exons represented by vertical lines.**O *FAM83H* variations and corresponding protein domain.** The gene transcript NM_198488.5 is composed of 5 exons represented by vertical lines.**P *DLX3* variations and corresponding protein domain.** The gene transcript NM_005220.3 is composed of 3 exons represented by vertical lines.**Q *LTBP3* variations and corresponding protein domain.** The gene transcript NM_001130144.3 is composedd of 28 exons represented by vertical lines.**R *FAM20A* variations and corresponding protein domain.** The gene transcript NM_017565.4 is composed of 11 exons represented by vertical lines.**S *GALNS* variations and corresponding protein domain.** The gene transcript NM_000512.5 is composed of 14 exons represented by vertical lines.**T *SLC13A5* variations and corresponding protein domain.** The gene transcript NM_177550.5 is composed of 12 exons represented by vertical lines.**U *ROGDI* variations and corresponding protein domain.** The gene transcript NM_024589.3 is composedd of 11 exons represented by vertical lines.**V *SLC10A7* variations and corresponding protein domain.** The gene transcript NM_001300842.3 is composed of 13 exons represented by vertical lines.**W *CNNM4* variations and corresponding protein domain.** The gene transcript NM_020184.4 is composed of 7 exons represented by vertical lines.

SUPPLEMENTARY FIGURE S3

Familial segregation of variants by Sanger sequencing (GRCh37). 1. Variant segregation in individual's 1.2 family. Individual 1.2 (I.1) is heterozygous for the variant NM_000494.4(*COL17A1*): c.1745-2A>C; p.?. Her affected sister and her two affected daughters are also heterozygous c.1745-2A>C. 2. Variant segregation in individual's 1.6 family. Individual 1.6 (II.1) is heterozygous for the variant NM_000494.4(*COL17A1*): c.3327del; p.(Pro1110Argfs*21). The variant is inherited from his mother. Phenotype of both parents was not available. 3. Variant segregation in individual's 2.2 family. Individual 2.2 (II.4) and her affected brothers (II.1 and II.3) are heterozygous for the variant NM_000094.4(*COL7A1*): c.3605G>A; p.(Arg1202His). Parental DNA were not available. 4. Variant segregation in individual's 2.3 family. Individual 2.3 (II.1) is heterozygous for the variant NM_000094.4(*COL7A1*): c.3785T>C; p.(Met1262Thr). The variant is inherited from his affected mother (I.2). Father (I.1) DNA and phenotype are not available. 5.Variant segregation in individual's 4.4 family. Individual 4.4 (II.1) is heterozygous for the variant NM_000228.3(*LAMB3*): c.2926del; p.(Val976Trpfs*54). The variant is inherited from his heterozygous father (I.1). 6. Variant segregation in individual's 4.1 family. Individual 4.1 (II.1) is compound heterozygous for the variant NM_000228.3(*LAMB3*): c.124C>T; p.(Arg42*) and c.3490C>T; p.(Arg1164Cys). 7. Variant segregation in individual's 4.2 family. Individual 4.2 (II.1) is compound heterozygous for the variant NM_000228.3(*LAMB3*): c.1288+1G>T; p.? and c.1903C>T; p.(Arg635*). 8. Variant segregation in individual's 5.1 family. Individual 5.1 (II.1) is heterozygous for the variant NM_005562.3(*LAMC2*): c.493C>T; p.(Arg165Cys). The variant is inherited from her mother (I.2). Parental phenotype is not available. 9. Variant segregation in individual's 6.3 family. Individual 6.3 (II.1), her affected sister (II.2) and affected father (I.1) are all heterozygous for the variant NM_031889.3(*ENAM*): c.588+1dup; p.?.10. Variant segregation in individual's 6.6 family. Individual 6.6 (II.1) is heterozygous for the variant NM_031889.3(*ENAM*): c.588+1del; p.?. Father (I.1) DNA and phenotype are unavailable (NA). 11. Variant segregation in individual's 6.7 family. Individual 6.7 (II.1), his affected sister (II.3) and mother (I.2) are heterozygous for the variant NM_031889.3(*ENAM*): c.588+1del; p.?. His second non -affected sister (II.2) and his father (I.1) do not carry the variant. 12. Variant segregation in individual's 6.8 family. Individual 6.8 (II.1), his affected sister (II.2) and mother (I.2) are heterozygous for the variant NM_031889.3(*ENAM*): c.664C>T; p.(Gln222*). His father does not carry the variant and his mother's phenotype is unavailable. 13. Variant segregation in individual's 7.4 family. Individual 7.4 (II.1) is heterozygous for the variant NM_182680.1(*AMELX*): c.47C>A; p.(Ala16Asp). The variant is inherited from her affected hemizygous father (I.1). 14. Variant segregation in individual's 7.8 family. Individual 7.8 (III.1) is heterozygous for the variant NM_182680.1(*AMELX*): c.473del; p.(Pro158Hisfs*31). The variant spread inside affected members of the family. The variant is heterozygous for females II.2 and II.3 and for male III.2 and hemizygous for 7.8's (III.1) grandfather (I.1). Individual 7.9 (III.2) is a male with a XXY karyotype explaining his heterozygous genotype. 15. Variant segregation in individual's 7.10 family. Individual 7.10 (II.1) is hemizygous for the variant NM_182680.1(*AMELX*): c.541del; p.(Leu181Cysfs*8). The variant is inherited from his affected heterozygous mother (I.2).16. Variant segregation in individual's 7.6 family. Individual 7.6 (II.1) and his brother (II.2) are hemizygous for the variant NM_182680.1(*AMELX*): c.208C>A; p.(Pro70Thr). Parental results are not available. 17. Variant segregation in individual's 7.7 family. Individual 7.7 (II.1) is hemizygous for the variant NM_182680.1(*AMELX*): c.208C>A; p.(Pro70Thr). The variant is inherited from mother (I.2) who are heterozygous as his sister (II.2). Their phenotypes are not available. 18. Variant segregation in individual's 8.1 family. Individual 8.1 (II.1) is heterozygous for the two variants NM_016519.6(*AMBN*): c.15+1G>A; p? and c.577G>T; p.(Gly193*). Her mother I.2 is heterozygous only for c.15+1G>A and her father (I.1) result are not available. 19. Reads visualization of individual 10.1 (II.1) highlighting two heterozygous compound variants NM_004917.4(*KLK4*) c.443G>T; p.(Cys148Phe) and c.458G>A; p.(Trp153*). Parental DNA was not available. 20. Variant segregation in individual's 11.1 family. Individual 11.1 (II.1) is heterozygous for the two variants NM_004771.4(*MMP20*): c.103A>C; p.(Arg35=) and c.389C>T; p.(Thr130Ile). The variant c.103A>C is inherited from his heterozygous mother (I.2) and the variant c.389C>T by his heterozygous father (I.1).21. Variant segregation in individual's 11.3 family. Individual 11.3 (II.1) and his sister (II.2) are compound heterozygous for the two variants NM_004771.4(*MMP20*): c.103A>C; p.(Arg35=) and c.954-2A>T; p.?. His mother (I.2) and brother (II.3) are heterozygous only for c.103A>C. His father (I.1) and second brother (II.1) are heterozygous only for c.954-2A>T.22. Variant segregation in individual's 11.4 family. Individual 11.4 (II.1) is compound heterozygous for the two variants NM_004771.4(*MMP20*): c.103A>C; p.(Arg35=) and c.1362C>G; p.(Tyr454*). The variant c.103A>C is inherited from his heterozygous mother (I.2) and the variant c.1362C>G from his heterozygous father (I.1).23. Variant segregation in individual's 11.8 family. Individual 11.8 (II.1) is compound heterozygous for the two variants NM_004771.4(*MMP20*): c.359dup; p.(Asn120Lysfs*9) and c.954-2A>T; p?. The variant c.359dup is inherited from his heterozygous father (I.1) and the variant c.954-2A>T from his heterozygous mother (I.2).24. Variant segregation in individual's 11.11 family. Individual 11.11 (II.1) is compound heterozygous for the two variants NM_004771.4(*MMP20*): c.530G>A; p.(Gly177Glu) and c.954-2A>T; p?. The variant c.530G>A is inherited from her heterozygous mother (I.2) and the variant c.954-2A>T from her heterozygous father (I.1).25. Variant segregation in individual's 11.15 family. Individual 11.15 (II.1) and her affected brother (II.2) are homozygous for NM_004771.4(*MMP20*): c.954-2A>T; p?. Their parents (I.1 and I.2) are heterozygous for c.954-2A>T.26. Reads visualization of individual 12.4 (II.1) with IGV using the paired-end sorting option highlighting two heterozygous compound variants NM_182758.4(*WDR72*): c.2146del; p.(Ala716Profs*10) and c.2388del ; p.(Lys796Asnfs*16). Arrow indicates informative read pairs for allelic relative position of the two variants. Parental DNA was not available.27. Variant segregation in individual's 14.2 family. Individual 14.2 (II.1) and her affected sister (II.2) are homozygous for the variant NM_153646.4(*SLC24A4*): c.1716+5G>A; p.?. Parents' DNA and phenotype are not available.28. Variant segregation in individual's 15.1 family. Individual 15.1 (II.1) is heterozygous for the variant NM_198488.5(*FAM83H*): c.930_939dup; p.(Val314Argfs*14). Her non-affected sister (II.2) do not carry the variant. Parents' DNA and phenotype are not available.29. Variant segregation in individual's 15.2 family. Individual 15.2 (II.1) is heterozygous de novo for the variant NM_198488.5(*FAM83H*): c.973C>T; p.(Arg325*). Her parents do not carry the variant and SNP filiation controls were verified.30. Variant segregation in individual's 15.6 family. Individual 15.6 (II.1) is heterozygous for the variant NM_198488.5(*FAM83H*):c.1309_1311delinsTAG; p.(His437*). This variant is inherited from her father (I.1) also heterozygous. 31Variant segregation in individual's 15.7 family. Individual 15.7 (II.1) is heterozygous de novo for the variant NM_198488.5(*FAM83H*): c.1374C>G; p.(Tyr458*). His parents do not carry the variant and SNP filiation controls were verified.32. Variant segregation in individual's 15.8 family. Individual 15.8 (II.1) is heterozygous de novo for the variant NM_198488.5(*FAM83H*): c.1374C>G; p.(Tyr458*). His parents do not carry the variant and SNP filiation controls were verified.33. Variant segregation in individual's 15.9 family. Individual 15.9 (II.1) is heterozygous for the variant NM_198488.5(*FAM83H*): c.1375C>T; p.(Gln459*). The variant is inherited from her father also heterozygous.34. Variant segregation in individual's 15.10 family. Individual 15.10 (II.1) is heterozygous de novo for the variant NM_198488.5(*FAM83H*): c.1379G>A; p.(Trp460*). Her parents do not carry the variant and SNP filiation controls were verified.35. Variant segregation in individual's 15.12 family. Individual 15.12 (II.1) and his brother (II.3) are heterozygous for the variant NM_198488.5(*FAM83H*): c.1387C>T; p.(Gln463*). Individual 16.12 (II.1) and his brother (II.3) are homozygous for the variant NM_182758.4(*WDR72*): c.1283T>G; p.(Ile428Ser). This variant is inherited from their mother (I.2) also heterozygous.36. Variant segregation in individual's 15.13 family. Individual 15.13 (II.1) and her brother (II.3) are heterozygous for the variant NM_198488.5(*FAM83H*): c.1498C>G; p.(Leu500Val). The variant *FAM83H*: c.1498C>G is not inherited from their mother and she is heterozygous for the *WDR72* c.1283T>G. Their father results are not available.37. Variant segregation in individual's 15.14 family. Individual 15.14 (II.1) is heterozygous for the variant NM_198488.5(*FAM83H*): c.1993C>T; p.(Gln665*). The variant is inherited from her

father (I.1).38. Variant segregation in individual's 17.6 family. Individual 17.6 (II.1) is homozygous for the variant NM_001130144.3(*LTBP3*): c.3629-2A>G; p?. Her parents (I.1 and I.2) are heterozygous for the variant.39. Variant segregation in individual's 18.3 family. Individual 18.3 (II.1) and his sister (II.2) are compound heterozygous for the variants NM_017565.4(*FAM20A*): c.217C>T; p.(Arg73*) and c.727C>T; p.(Arg243*). The mother (I.2) is heterozygous for the variant c.727C>T and the father (I.1) is heterozygous for the variant c.217C>T.40. Variant segregation in individual's 18.5 family. Individual 18.5 (II.1) is compound heterozygous for the variants NM_017565.4(*FAM20A*): c.915_918del; p.(Phe305Leufs*76) and c.928+2T>C; p?. Her mother (I.2) is heterozygous for c.928+2T>C and her father is heterozygous for c.915_918del.41. Variant segregation in individual's 18.6 family. Individual 18.6 (II.1) and his brother (II.2) are compound heterozygous for the variants NM_017565.4(*FAM20A*): c.915_918del; p.(Phe305Leufs*76) and c.1301+5G>A; p?. Their mother (I.2) is heterozygous for c.915_918del and their father is heterozygous for c.1301+5G>A.42. Variant segregation in individual's 18.9 family. Individual 18.9 (II.1) and his brother (II.2) are homozygous for the variant NM_017565.4(FAM20A): c.1369A>T; p.(Lys457*). Their mother (I.2) is heterozygous for c.1369A>T and their father's (I.1) result is not available.43. Variant segregation in individual's 22.1 family. Individual 22.1 (II.1) is heterozygous for the variant NM_003242.6(*TGFBR2*): c.1561T>C; p.(Trp521Arg). His father (I.1) do not carry the variant and his mother's (I.2) DNA is not available.44. Variant segregation in individual's 24.3 family. Individual 24.3 (II.1) is compound heterozygous for the variants NM_2024589.2(*ROGDI*): c.366dup; p.(Ala123Serfs*19) and c.366dup; p.(Tyr134*). The variant c.366dup is inherited from her mother (I.2) and the variant c.366dup from her father (I.1).45. Variant segregation in individual's 25.1 family. Individual 25.1 (II.1) is homozygous for the variant NM_001300842.3(*SLC10A7*): c.269T>G; p.(Leu90Arg). His mother (I.2) and father (I.1) are heterozygous for the variant.46. Variant segregation in individual's 26.1 family. Individual 26.1 (II.1) and her sister (II.2) are homozygous for the variant NM_2020184.4(*CNNM4*): c.586T>C; p.(Ser196Pro). Her mother (I.2) is heterozygous and her father's (I.1) DNA is not available.47. Variant segregation in individual's 27.1 family. Individual 27.1 (II.1), her brother (II.2) and mother (I.2) are heterozygous for the variant NM_005220.3(*DLX3*): c.561_562del; p.(Tyr188Glnfs*13). Her father's (I.1) DNA is not available.48. Variant segregation in individual's 27.2 family. Individual 27.2 (II.1) is heterozygous for the variant NM_005220.3(*DLX3*): c.561_562del; p.(Tyr188Glnfs*13). This variant is inherited from his affected heterozygous father (I.1).

SUPPLEMENTARY TABLE S1
List of gene sequenced in version 6.0 of the GenoDENT panel. Exons and 25 bp in flanking introns of these genes were sequenced using Next Generation Sequencing technics.

SUPPLEMENTARY TABLE S2
List of primer's sequences used for Sanger sequencing.

SUPPLEMENTARY TABLE S3
Variations found in individuals presenting with isolated amelogenesis imperfecta. Variations found in 17 different genes in 85 individuals presenting with isolated amelogenesis imperfecta. One hundred eleven variants were found, 19 variants are of uncertain significance. Variants known and previously published are reported in grey, variants previously reported by the team are represented in salmon, variants published thanks to GenoDENT panel are represented in blue or green, new variants reported for the first time are highlighted in green. Familial segregation is also reported when available and reported as: Family member code (Phenotype code, Genotype code): Fa: father; Mo: mother; S: sibling; D: daughter; So: son; Co: cousin; A: affected; U: unaffected; NA: not available; C: carrier; R: reference genotype.

SUPPLEMENTARY TABLE S4
Key diagnostic clinical signs associated to AI in syndromes.

References

Aaltonen, J., Horelli-Kuitunen, N., Fan, J.-B., Björses, P., Perheentupa, J., Myers, R., et al. (1997). High-resolution physical and transcriptional mapping of the autoimmune polyendocrinopathy–candidiasis–ectodermal dystrophy locus on chromosome 21q22.3 by FISH. *Genome Res.* 7, 820–829. doi:10.1101/gr.7.8.820

Acevedo, A. C., Poulter, J. A., Alves, P. G., de Lima, C. L., Castro, L. C., Yamaguti, P. M., et al. (2015). Variability of systemic and oro-dental phenotype in two families with non-lethal Raine syndrome with FAM20C mutations. *BMC Med. Genet.* 16, 8. doi:10.1186/s12881-015-0154-5

Aïoub, M., Lézot, F., Molla, M., Castaneda, B., Robert, B., Goubin, G., et al. (2007). Msx2 –/– transgenic mice develop compound amelogenesis imperfecta, dentinogenesis imperfecta and periodontal osteopetrosis. *Bone* 41, 851–859. doi:10.1016/j.bone.2007.07.023

Akyol, M. U., Alden, T. D., Amartino, H., Ashworth, J., Belani, K., Berger, K. I., et al. (2019). Recommendations for the management of MPS IVA: Systematic evidence- and consensus-based guidance. *Orphanet J. Rare Dis.* 14, 137. doi:10.1186/s13023-019-1074-9

Aldred, M. J., and Crawford, P. J. (1995). Amelogenesis imperfecta-towards a new classification. *Oral Dis.* 1, 2–5. doi:10.1111/j.1601-0825.1995.tb00148.x

Aldred, M. J., Savarirayan, R., and Crawford, P. J. M. (2003). Amelogenesis imperfecta: A classification and catalogue for the 21st century. *Oral Dis.* 9, 19–23. doi:10.1034/j.1601-0825.2003.00843.x

Alsharif, S., Hindi, S., and Khoja, F. (2018). Unilateral focal dermal hypoplasia (goltz syndrome): Case report and literature review. *Case Rep. Dermatol* 10, 101–109. doi:10.1159/000488521

Ashikov, A., Abu Bakar, N., Wen, X.-Y., Niemeijer, M., Rodrigues Pinto Osorio, G., Brand-Arzamendi, K., et al. (2018). Integrating glycomics and genomics uncovers SLC10A7 as essential factor for bone mineralization by regulating post-Golgi protein transport and glycosylation. *Hum. Mol. Genet.* 27, 3029–3045. doi:10.1093/hmg/ddy213

Aswath, N., Ramakrishnan, S. N., Teresa, N., and Ramanathan, A. (2018). A novel ROGDI gene mutation is associated with Kohlschutter-Tonz syndrome. *Oral Surg. Oral Med. Oral Pathol. Oral Radiol.* 125 (1), e8–e11. doi:10.1016/j.oooo.2017.09.016

Bardet, C., Courson, F., Wu, Y., Khaddam, M., Salmon, B., Ribes, S., et al. (2016). Claudin-16 deficiency impairs tight junction function in ameloblasts, leading to abnormal enamel formation. *J. Bone Min. Res.* 31, 498–513. doi:10.1002/jbmr.2726

Björses, P., Pelto-Huikko, M., Kaukonen, J., Aaltonen, J., Peltonen, L., and Ulmanen, I. (1999). Localization of the APECED protein in distinct nuclear structures. *Hum. Mol. Genet.* 8, 259–266. doi:10.1093/hmg/8.2.259

Bloch-Zupan, A., Bugueno, I. M., and Manière, M. C. (2021). Protocole National de Diagnostic et de Soins (PNDS): Amélogenèses imparfaites. Synthèse à destination du chirurgien-dentiste et du médecin traitant. https://www.has-sante.fr/jcms/p_3284538/fr/.

Bloch-Zupan, A., Sedano, H., and Scully, C. (2012). *Dento/oro/craniofacial anomalies and genetics*. 1st Ed. Amsterdam: Elsevier. 9780124160385.

Brookes, S. J., Barron, M. J., Smith, C. E. L., Poulter, J. A., Mighell, A. J., Inglehearn, C. F., et al. (2017). Amelogenesis imperfecta caused by N-terminal enamelin point mutations in mice and men is driven by endoplasmic reticulum stress. *Hum. Mol. Genet.* 26, 1863–1876. doi:10.1093/hmg/ddx090

Burgeson, R. E., Morris, N. P., Murray, L. W., Duncan, K. G., Keene, D. R., and Sakai, L. Y. (1985). The structure of type VII collagen. *Ann. N. Y. Acad. Sci.* 460, 47–57. doi:10.1111/j.1749-6632.1985.tb51156.x

Burzynski, N. J., Gonzalez, W. E., and Snawder, K. D. (1973). Autosomal dominant smooth hypoplastic amelogenesis imperfecta. Report of a case. *Oral Surg. Oral Med. Oral Pathol.* 36, 818–823. doi:10.1016/0030-4220(73)90333-2

Caciotti, A., Tonin, R., Mort, M., Cooper, D. N., Gasperini, S., Rigoldi, M., et al. (2018). Mis-splicing of the GALNS gene resulting from deep intronic mutations as a cause of Morquio a disease. *BMC Med. Genet.* 19, 183. doi:10.1186/s12881-018-0694-6

Caricasole, A., Ferraro, T., Rimland, J. M., and Terstappen, G. C. (2002). Molecular cloning and initial characterization of the MG61/PORC gene, the human homologue of the Drosophila segment polarity gene Porcupine. *Gene* 288, 147–157. doi:10.1016/S0378-1119(02)00467-5

Celli, J., Duijf, P., Hamel, B. C., Bamshad, M., Kramer, B., Smits, A. P., et al. (1999). Heterozygous germline mutations in the p53 homolog p63 are the cause of EEC syndrome. *Cell.* 99 (2), 143–153. doi:10.1016/s0092-8674(00)81646-3

Collier, P. M., Sauk, J. J., Rosenbloom, S. J., Yuan, Z. A., and Gibson, C. W. (1997). An amelogenin gene defect associated with human X-linked amelogenesis imperfecta. *Arch. Oral Biol.* 42 (3), 235–242. doi:10.1016/s0003-9969(96)00099-4

Crawford, P. J. M., Aldred, M., and Bloch-Zupan, A. (2007). Amelogenesis imperfecta. *Orphanet J. Rare Dis.* 2, 17. doi:10.1186/1750-1172-2-17

Daneshmandpour, Y., Darvish, H., Pashazadeh, F., and Emamalizadeh, B. (2019). Features, genetics and their correlation in Jalili syndrome: A systematic review. *J. Med. Genet.* 56, 358–369. doi:10.1136/jmedgenet-2018-105716

Darling, A. I. (1956). Some observations on amelogenesis imperfecta and calcification of the dental enamel. *Proc. R. Soc. Med.* 49, 759–765. doi:10.1177/003591575604901007

Daubert, D. M., Kelley, J. L., Udod, Y. G., Habor, C., Kleist, C. G., Furman, I. K., et al. (2016). Human enamel thickness and ENAM polymorphism. *Int. J. Oral Sci.* 8, 93–97. doi:10.1038/ijos.2016.1

de La Dure-Molla, M., Fournier, B. P., Manzanares, M. C., Acevedo, A. C., Hennekam, R. C., Friedlander, L., et al. (2019). Elements of morphology: Standard terminology for the teeth and classifying genetic dental disorders. *Am. J. Med. Genet. A* 179, 1913–1981. doi:10.1002/ajmg.a.61316

de la Dure-Molla, M., Quentric, M., Yamaguti, P. M., Acevedo, A.-C., Mighell, A. J., Vikkula, M., et al. (2014). Pathognomonic oral profile of Enamel Renal Syndrome (ERS) caused by recessive FAM20A mutations. *Orphanet J. Rare Dis.* 9, 84. doi:10.1186/1750-1172-9-84

Deidrick, K. K. M., Early, M., Constance, J., Stein, M., and Fete, T. J. (2016). Cognitive and psychological functioning in focal dermal hypoplasia. *Am. J. Med. Genet. C Semin. Med. Genet.* 172, 34–40. doi:10.1002/ajmg.c.31471

Dellow, E. L., Harley, K. E., Unwin, R. J., Wrong, O., Winter, G. B., and Parkins, B. J. (1998). Amelogenesis imperfecta, nephrocalcinosis, and hypocalciuria syndrome in two siblings from a large family with consanguineous parents. *Nephrol. Dial. Transpl.* 13 (12), 3193–3196. doi:10.1093/ndt/13.12.3193

DePristo, M. A., Banks, E., Poplin, R., Garimella, K. V., Maguire, J. R., Hartl, C., et al. (2011). A framework for variation discovery and genotyping using next-generation DNA sequencing data. *Nat. Genet.* 43, 491–498. doi:10.1038/ng.806

Dong, J., Amor, D., Aldred, M. J., Gu, T., Escamilla, M., and MacDougall, M. (2005). DLX3 mutation associated with autosomal dominant amelogenesis imperfecta with taurodontism. *Am. J. Med. Genet. A* 133A, 138–141. doi:10.1002/ajmg.a.30521

Dourado, M. R., Dos Santos, C. R. R., Dumitriu, S., Iancu, D., Albanyan, S., Kleta, R., et al. (2019). Enamel renal syndrome: A novel homozygous FAM20A founder mutation in 5 new Brazilian families. *Eur. J. Med. Genet.* 62 (11), 103561. doi:10.1016/j.ejmg.2018.10.013

Dubail, J., Huber, C., Chantepie, S., Sonntag, S., Tüysüz, B., Mihci, E., et al. (2018). SLC10A7 mutations cause a skeletal dysplasia with amelogenesis imperfecta mediated by GAG biosynthesis defects. *Nat. Commun.* 9, 3087. doi:10.1038/s41467-018-05191-8

Dugan, S. L., Temme, R. T., Olson, R. A., Mikhailov, A., Law, R., Mahmood, H., et al. (2015). New recessive truncating mutation in LTBP3 in a family with oligodontia, short stature, and mitral valve prolapse. *Am. J. Med. Genet. A* 167, 1396–1399. doi:10.1002/ajmg.a.37049

Durmaz, C. D., McGrath, J., Liu, L., and Karabulut, H. G. (2018). A novel PORCN frameshift mutation leading to focal dermal hypoplasia: A case report. *Cytogenet Genome Res.* 154, 119–121. doi:10.1159/000487580

Duverger, O., Ohara, T., Bible, P. W., Zah, A., and Morasso, M. I. (2017). DLX3-Dependent regulation of ion transporters and carbonic anhydrases is crucial for enamel mineralization. *J. Bone Min. Res.* 32, 641–653. doi:10.1002/jbmr.3022

El-Sayed, W., Parry, D. A., Shore, R. C., Ahmed, M., Jafri, H., Rashid, Y., et al. (2009). Mutations in the beta propeller WDR72 cause autosomal-recessive hypomaturation amelogenesis imperfecta. *Am. J. Hum. Genet.* 85, 699–705. doi:10.1016/j.ajhg.2009.09.014

Exome Aggregation ConsortiumLek, M., Karczewski, K. J., Minikel, E. V., Samocha, K. E., Banks, E., et al. (2016). Analysis of protein-coding genetic variation in 60,706 humans. *Nature* 536, 285–291. doi:10.1038/nature19057

Feldmeyer, L., Huber, M., Fellmann, F., Beckmann, J. S., Frenk, E., and Hohl, D. (2006). Confirmation of the origin of NISCH syndrome. *Hum. Mutat.* 27, 408–410. doi:10.1002/humu.20333

Feske, S., Müller, J. M., Graf, D., Kroczek, R. A., Dräger, R., Niemeyer, C., et al. (1996). Severe combined immunodeficiency due to defective binding of the nuclear factor of activated T cells in T lymphocytes of two male siblings. *Eur. J. Immunol.* 26 (9), 2119–2126. doi:10.1002/eji.1830260924

Feske, S. (2010). CRAC channelopathies. *Pflugers Arch.* 460, 417–435. doi:10.1007/s00424-009-0777-5

Flores, E. R., Tsai, K. Y., Crowley, D., Sengupta, S., Yang, A., McKeon, F., et al. (2002). p63 and p73 are required for p53-dependent apoptosis in response to DNA damage. *Nature* 416, 560–564. doi:10.1038/416560a

Fouillen, A., Dos Santos Neves, J., Mary, C., Castonguay, J.-D., Moffatt, P., Baron, C., et al. (2017). Interactions of AMTN, ODAM and SCPPPQ1 proteins of a specialized basal lamina that attaches epithelial cells to tooth mineral. *Sci. Rep.* 7, 46683. doi:10.1038/srep46683

Frick, K. K., Krieger, N. S., Nehrke, K., and Bushinsky, D. A. (2009). Metabolic acidosis increases intracellular calcium in bone cells through activation of the proton receptor OGR1. *J. Bone Min. Res.* 24, 305–313. doi:10.1359/jbmr.081015

Frisk, S., Grandpeix-Guyodo, C., Popovic Silwerfeldt, K., Hjartarson, H. T., Chatzianastassiou, D., Magnusson, I., et al. (2018). Goltz syndrome in males: A clinical report of a male patient carrying a novel PORCN variant and a review of the literature. *Clin. Case Rep.* 6, 2103–2110. doi:10.1002/ccr3.1783

Furukawa, Y., Haruyama, N., Nikaido, M., Nakanishi, M., Ryu, N., Oh-Hora, M., et al. (2017). Stim1 regulates enamel mineralization and ameloblast modulation. *J. Dent. Res.* 96, 1422–1429. doi:10.1177/0022034517719872

Gasse, B., Karayigit, E., Mathieu, E., Jung, S., Garret, A., Huckert, M., et al. (2013). Homozygous and compound heterozygous MMP20 mutations in amelogenesis imperfecta. *J. Dent. Res.* 92, 598–603. doi:10.1177/0022034513488393

Gasse, B., Prasad, M., Delgado, S., Huckert, M., Kawczynski, M., Garret-Bernardin, A., et al. (2017). Evolutionary analysis predicts sensitive positions of MMP20 and validates newly- and previously-identified MMP20 mutations causing amelogenesis imperfecta. *Front. Physiol.* 8, 398. doi:10.3389/fphys.2017.00398

Geoffroy, V., Herenger, Y., Kress, A., Stoetzel, C., Piton, A., Dollfus, H., et al. (2018). AnnotSV: An integrated tool for structural variations annotation. *Bioinformatics* 34, 3572–3574. doi:10.1093/bioinformatics/bty304

Geoffroy, V., Pizot, C., Redin, C., Piton, A., Vasli, N., Stoetzel, C., et al. (2015). VaRank: A simple and powerful tool for ranking genetic variants. *PeerJ* 3, e796. doi:10.7717/peerj.796

Gibson, C. W., Yuan, Z. A., Hall, B., Longenecker, G., Chen, E., Thyagarajan, T., et al. (2001). Amelogenin-deficient mice display an amelogenesis imperfecta phenotype. *J. Biol. Chem.* 276, 31871–31875. doi:10.1074/jbc.M104624200

Goodwin, A. F., Tidyman, W. E., Jheon, A. H., Sharir, A., Zheng, X., Charles, C., et al. (2014). Abnormal Ras signaling in Costello syndrome (CS) negatively regulates enamel formation. *Hum. Mol. Genet.* 23, 682–692. doi:10.1093/hmg/ddt455

Greene, S. R., Yuan, Z. A., Wright, J. T., Amjad, H., Abrams, W. R., Buchanan, J. A., et al. (2002). A new frameshift mutation encoding a truncated amelogenin leads to X-linked amelogenesis imperfecta. *Arch. Oral Biol.* 47, 211–217. doi:10.1016/s0003-9969(01)00111-x

Guerrini, R., Mei, D., Kerti-Szigeti, K., Pepe, S., Koenig, M. K., Von Allmen, G., et al. (2022). Phenotypic and genetic spectrum of ATP6V1A encephalopathy: A disorder of lysosomal homeostasis. *Brain* 145, 2687–2703. doi:10.1093/brain/awac145

Guo, D., Ling, J., Wang, M.-H., She, J.-X., Gu, J., and Wang, C.-Y. (2005). Physical interaction and functional coupling between ACDP4 and the intracellular ion chaperone COX11, an implication of the role of ACDP4 in essential metal ion transport and homeostasis. *Mol. Pain* 1, 15–8069. doi:10.1186/1744-8069-1-15

Guo, D., Regalado, E. S., Pinard, A., Chen, J., Lee, K., Rigelsky, C., et al. (2018). LTBP3 pathogenic variants predispose individuals to thoracic aortic aneurysms and dissections. *Am. J. Hum. Genet.* 102, 706–712. doi:10.1016/j.ajhg.2018.03.002

Happle, R., and Lenz, W. (1977). Striation of bones in focal dermal hypoplasia: Manifestation of functional mosaicism? *Br. J. Dermatol* 96, 133–135. doi:10.1111/j.1365-2133.1977.tb12534.x

Hardies, K., de Kovel, C. G. F., Weckhuysen, S., Asselbergh, B., Geuens, T., Deconinck, T., et al. (2015). Recessive mutations in SLC13A5 result in a loss of citrate transport and cause neonatal epilepsy, developmental delay and teeth hypoplasia. *Brain* 138, 3238–3250. doi:10.1093/brain/awv263

Harrison, S. M., Biesecker, L. G., and Rehm, H. L. (2019). Overview of specifications to the ACMG/AMP variant interpretation guidelines. *Curr. Protoc. Hum. Genet.* 103, e93. doi:10.1002/cphg.93

Hart, P. S., Aldred, M. J., Crawford, P. J. M., Wright, N. J., Hart, T. C., and Wright, J. T. (2002a). Amelogenesis imperfecta phenotype-genotype correlations with two amelogenin gene mutations. *Arch. Oral Biol.* 47, 261–265. doi:10.1016/s0003-9969(02)00003-1

Hart, P. S., Hart, T. C., Michalec, M. D., Ryu, O. H., Simmons, D., Hong, S., et al. (2004). Mutation in kallikrein 4 causes autosomal recessive hypomaturation amelogenesis imperfecta. *J. Med. Genet.* 41, 545–549. doi:10.1136/jmg.2003.017657

Hart, P. S., Hart, T. C., Simmer, J. P., and Wright, J. T. (2002b). A nomenclature for X-linked amelogenesis imperfecta. *Arch. Oral Biol.* 47, 255–260. doi:10.1016/s0003-9969(02)00005-5

Hart, T. C., Hart, P. S., Gorry, M. C., Michalec, M. D., Ryu, O. H., Uygur, C., et al. (2003). Novel ENAM mutation responsible for autosomal recessive amelogenesis imperfecta and localised enamel defects. *J. Med. Genet.* 40 (12), 900–906. doi:10.1136/jmg.40.12.900

Harutunian, K., Figueiredo, R., and Gay-Escoda, C. (2011). Tuberous sclerosis complex with oral manifestations: A case report and literature review. *Med. Oral Patol. Oral Cir. Bucal* 16, e478–e481. doi:10.4317/medoral.16.e478

Hassan, M. Q., Javed, A., Morasso, M. I., Karlin, J., Montecino, M., Wijnen, A. J. van, et al. (2004). Dlx3 transcriptional regulation of osteoblast differentiation: Temporal recruitment of Msx2, Dlx3, and Dlx5 homeodomain proteins to chromatin of the osteocalcin gene. *Mol. Cell. Biol.* 24, 9248–9261. doi:10.1128/MCB.24.20.9248-9261.2004

Heimler, A., Fox, J. E., Hershey, J. E., and Crespi, P. (1991). Sensorineural hearing loss, enamel hypoplasia, and nail abnormalities in sibs. *Am. J. Med. Genet.* 39, 192–195. doi:10.1002/ajmg.1320390214

Holcroft, J., and Ganss, B. (2011). Identification of amelotin- and ODAM-interacting enamel matrix proteins using the yeast two-hybrid system. *Eur. J. Oral Sci.* 119 (1), 301–306. doi:10.1111/j.1600-0722.2011.00870.x

Hollister, D. W., Klein, S. H., De Jager, H. J., Lachman, R. S., and Rimoin, D. L. (1973). The lacrimo-auriculo-dento-digital syndrome. *J. Pediatr.* 83, 438–444. doi:10.1016/s0022-3476(73)80268-9

Hu, J. C.-C., Chan, H.-C., Simmer, S. G., Seymen, F., Richardson, A. S., Hu, Y., et al. (2012a). Amelogenesis imperfecta in two families with defined AMELX deletions in ARHGAP6. *PLoS One* 7, e52052. doi:10.1371/journal.pone.0052052

Hu, J. C.-C., and Yamakoshi, Y. (2003). Enamelin and autosomal-dominant amelogenesis imperfecta. *Crit. Rev. Oral Biol. Med.* 14, 387–398. doi:10.1177/154411130301400602

Hu, P., Lacruz, R. S., Smith, C. E., Smith, S. M., Kurtz, I., and Paine, M. L. (2012b). Expression of the sodium/calcium/potassium exchanger, NCKX4, in ameloblasts. *Cells Tissues Organs* 196, 501–509. doi:10.1159/000337493

Huckert, M., Mecili, H., Laugel-Haushalter, V., Stoetzel, C., Muller, J., Flori, E., et al. (2014). A novel mutation in the ROGDI gene in a patient with kohlschütter-tönz syndrome. *Mol. Syndromol.* 5, 293–298. doi:10.1159/000366252

Huckert, M., Stoetzel, C., Morkmued, S., Laugel-Haushalter, V., Geoffroy, V., Muller, J., et al. (2015). Mutations in the latent TGF-beta binding protein 3 (LTBP3) gene cause brachyolmia with amelogenesis imperfecta. *Hum. Mol. Genet.* 24, 3038–3049. doi:10.1093/hmg/ddv053

Inoki, K., Li, Y., Zhu, T., Wu, J., and Guan, K.-L. (2002). TSC2 is phosphorylated and inhibited by Akt and suppresses mTOR signalling. *Nat. Cell. Biol.* 4, 648–657. doi:10.1038/ncb839

Inoue, K., Zhuang, L., and Ganapathy, V. (2002). Human Na+-coupled citrate transporter: Primary structure, genomic organization, and transport function. *Biochem. Biophys. Res. Commun.* 299, 465–471. doi:10.1016/S0006-291X(02)02669-4

Intarak, N., Theerapanon, T., Thaweesapphithak, S., Suphapeetiporn, K., Porntaveetus, T., and Shotelersuk, V. (2019). Genotype-phenotype correlation and expansion of orodental anomalies in LTBP3-related disorders. *Mol. Genet. Genomics* 294, 773–787. doi:10.1007/s00438-019-01547-x

Iwase, M., Kaneko, S., Kim, H., Satta, Y., and Takahata, N. (2007). Evolutionary history of sex-linked mammalian amelogenin genes. *Cells Tissues Organs* 186, 49–59. doi:10.1159/000102680

Jabs, E. W., Müller, U., Li, X., Ma, L., Luo, W., Haworth, I. S., et al. (1993). A mutation in the homeodomain of the human MSX2 gene in a family affected with autosomal dominant craniosynostosis. *Cell.* 75, 443–450. doi:10.1016/0092-8674(93)90379-5

Jagtap, R., Alansari, R., Ruprecht, A., and Kashtwari, D. (2019). Trichodentoosseous syndrome: A case report and review of literature. *BJR Case Rep.* 5, 20190039. doi:10.1259/bjrcr.20190039

Jain, P., Kaul, R., Saha, S., and Sarkar, S. (2017). Tricho-dento-osseous syndrome and precocious eruption. *J. Clin. Exp. Dent.* 9, e494–e497. doi:10.4317/jced.53348

Jalili, I. K., and Smith, N. J. (1988). A progressive cone-rod dystrophy and amelogenesis imperfecta: A new syndrome. *J. Med. Genet.* 25, 738–740. doi:10.1136/jmg.25.11.738

Jani, P., Nguyen, Q. C., Almpani, K., Keyvanfar, C., Mishra, R., Liberton, D., et al. (2020). Severity of oro-dental anomalies in Loeys-Dietz syndrome segregates by gene mutation. *J. Med. Genet.* 57, 699–707. doi:10.1136/jmedgenet-2019-106678

Jaureguiberry, G., De la Dure-Molla, M., Parry, D., Quentric, M., Himmerkus, N., Koike, T., et al. (2012). Nephrocalcinosis (enamel renal syndrome) caused by autosomal recessive FAM20A mutations. *Nephron Physiol.* 122, 1–6. doi:10.1159/000349989

Ji, Y., Li, C., Tian, Y., Gao, Y., Dong, Z., Xiang, L., et al. (2021). Maturation stage enamel defects in Odontogenesis-associated phosphoprotein (Odaph) deficient mice. *Dev. Dyn.* 250, 1505–1517. doi:10.1002/dvdy.336

Kantaputra, P. N., Hamada, T., Kumchai, T., and McGrath, J. A. (2003). Heterozygous mutation in the SAM domain of p63 underlies rapp-hodgkin ectodermal dysplasia. *J. Dent. Res.* 82, 433–437. doi:10.1177/154405910308200606

Katsura, K. A., Horst, J. A., Chandra, D., Le, T. Q., Nakano, Y., Zhang, Y., et al. (2014). WDR72 models of structure and function: A stage-specific regulator of enamel mineralization. *Matrix Biol.* 38, 48–58. doi:10.1016/j.matbio.2014.06.005

Katsura, K., Nakano, Y., Zhang, Y., Shemirani, R., Li, W., and Den Besten, P. (2022). WDR72 regulates vesicle trafficking in ameloblasts. *Sci. Rep.* 12, 2820. doi:10.1038/s41598-022-06751-1

Kausalya, P. J., Amasheh, S., Günzel, D., Wurps, H., Müller, D., Fromm, M., et al. (2006). Disease-associated mutations affect intracellular traffic and paracellular Mg2+ transport function of Claudin-16. *J. Clin. Investig.* 116, 878–891. doi:10.1172/JCI26323

Khandelwal, P., Maheshnull, V., Mathur, V. P., Raut, S., Geetha, T. S., Nair, S., et al. (2021). Phenotypic variability in distal acidification defects associated with WDR72 mutations. *Pediatr. Nephrol.* 36, 881–887. doi:10.1007/s00467-020-04747-5

Kim, J.-W., Lee, S.-K., Lee, Z. H., Park, J.-C., Lee, K.-E., Lee, M.-H., et al. (2008). FAM83H mutations in families with autosomal-dominant hypocalcified amelogenesis imperfecta. *Am. J. Hum. Genet.* 82, 489–494. doi:10.1016/j.ajhg.2007.09.020

Kim, J.-W., Seymen, F., Lin, B. P.-J., Kiziltan, B., Gencay, K., Simmer, J. P., et al. (2005a). ENAM mutations in autosomal-dominant amelogenesis imperfecta. *J. Dent. Res.* 84, 278–282. doi:10.1177/154405910508400314

Kim, J.-W., Simmer, J. P., Hart, T. C., Hart, P. S., Ramaswami, M. D., Bartlett, J. D., et al. (2005b). MMP-20 mutation in autosomal recessive pigmented hypomaturation amelogenesis imperfecta. *J. Med. Genet.* 42, 271–275. doi:10.1136/jmg.2004.024505

Kim, J.-W., Zhang, H., Seymen, F., Koruyucu, M., Hu, Y., Kang, J., et al. (2019). Mutations in RELT cause autosomal recessive amelogenesis imperfecta. *Clin. Genet.* 95, 375–383. doi:10.1111/cge.13487

Kim, J. W., Simmer, J. P., Hu, Y. Y., Lin, B. P., Boyd, C., Wright, J. T., et al. (2004). Amelogenin p.M1T and p.W4S mutations underlying hypoplastic X-linked amelogenesis imperfecta. *J. Dent. Res.* 83 (5), 378–383. doi:10.1177/154405910408300505

Kim, Y. J., Abe, Y., Kim, Y.-J., Fujiki, Y., and Kim, J.-W. (2021a). Identification of a homozygous PEX26 mutation in a heimler syndrome patient. *Genes. (Basel).* 12, 646. doi:10.3390/genes12050646

Kim, Y. J., Kang, J., Seymen, F., Koruyucu, M., Gencay, K., Shin, T. J., et al. (2017). Analyses of MMP20 missense mutations in two families with hypomaturation amelogenesis imperfecta. *Front. Physiol.* 8, 229. doi:10.3389/fphys.2017.00229

Kim, Y. J., Kang, J., Seymen, F., Koruyucu, M., Zhang, H., Kasimoglu, Y., et al. (2020). Alteration of exon definition causes amelogenesis imperfecta. *J. Dent. Res.* 99, 410–418. doi:10.1177/0022034520901708

Kim, Y. J., Lee, Y., Zhang, H., Song, J.-S., Hu, J. C.-C., Simmer, J. P., et al. (2021b). A novel de novo SP6 mutation causes severe hypoplastic amelogenesis imperfecta. *Genes. (Basel).* 12, 346. doi:10.3390/genes12030346

Kindelan, S. A., Brook, A. H., Gangemi, L., Lench, N., Wong, F. S., Fearne, J., et al. (2000). Detection of a novel mutation in X-linked amelogenesis imperfecta. *J. Dent. Res.* 79, 1978–1982. doi:10.1177/00220345000790120901

Kiritsi, D., Huilaja, L., Franzke, C.-W., Kokkonen, N., Pazzagli, C., Schwieger-Briel, A., et al. (2015). Junctional epidermolysis bullosa with LAMB3 splice-site mutations. *Acta Derm. Venereol.* 95, 849–851. doi:10.2340/00015555-2073

Kittler, R., Putz, G., Pelletier, L., Poser, I., Heninger, A.-K., Drechsel, D., et al. (2004). An endoribonuclease-prepared siRNA screen in human cells identifies genes essential for cell division. *Nature* 432, 1036–1040. doi:10.1038/nature03159

Kohlschütter, A., Chappuis, D., Meier, C., Tönz, O., Vassella, F., Herschkowitz, N., et al. (1974). Familial epilepsy and yellow teeth-a disease of the CNS associated with enamel hypoplasia. *Helv. Paediatr. Acta* 29, 283–294.

Konrad, M., Schaller, A., Seelow, D., Pandey, A. V., Waldegger, S., Lesslauer, A., et al. (2006). Mutations in the tight-junction gene claudin 19 (CLDN19) are associated with renal magnesium wasting, renal failure, and severe ocular involvement. *Am. J. Hum. Genet.* 79, 949–957. doi:10.1086/508617

Kosaki, R., Naito, Y., Torii, C., Takahashi, T., Nakajima, T., and Kosaki, K. (2008). Split hand foot malformation with whorl-like pigmentary pattern: Phenotypic expression of somatic mosaicism for the p63 mutation. *Am. J. Med. Genet. A* 146A, 2574–2577. doi:10.1002/ajmg.a.32415

Kuga, T., Sasaki, M., Mikami, T., Miake, Y., Adachi, J., Shimizu, M., et al. (2016). FAM83H and casein kinase I regulate the organization of the keratin cytoskeleton and formation of desmosomes. *Sci. Rep.* 6, 26557. doi:10.1038/srep26557

Lacruz, R. S., and Feske, S. (2015). Diseases caused by mutations in ORAI1 and STIM1. *Ann. N. Y. Acad. Sci.* 1356, 45–79. doi:10.1111/nyas.12938

Lagerström, M., Dahl, N., Iselius, L., Bäckman, B., and Pettersson, U. (1990). Mapping of the gene for X-linked amelogenesis imperfecta by linkage analysis. *Am. J. Hum. Genet.* 46, 120–125.

Lagerström, M., Dahl, N., Nakahori, Y., Nakagome, Y., Bäckman, B., Landegren, U., et al. (1991). A deletion in the amelogenin gene (AMG) causes X-linked amelogenesis imperfecta (AIH1). *Genomics* 10, 971–975. doi:10.1016/0888-7543(91)90187-j

Landrum, M. J., Lee, J. M., Benson, M., Brown, G. R., Chao, C., Chitipiralla, S., et al. (2018). ClinVar: Improving access to variant interpretations and supporting evidence. *Nucleic Acids Res.* 46 (D1), D1062–D1067. doi:10.1093/nar/gkx1153

Larrègue, M., and Duterque, M. (1975). Letter: Striated osteopathy in focal dermal hypoplasia. *Arch. Dermatol* 111 (10), 1365. doi:10.1001/archderm.1975.01630220129019

Lau, E. C., Mohandas, T. K., Shapiro, L. J., Slavkin, H. C., and Snead, M. L. (1989). Human and mouse amelogenin gene loci are on the sex chromosomes. *Genomics* 4, 162–168. doi:10.1016/0888-7543(89)90295-4

Laugel-Haushalter, V., Bär, S., Schaefer, E., Stoetzel, C., Geoffroy, V., Alembik, Y., et al. (2019). A new SLC10A7 homozygous missense mutation responsible for a milder phenotype of skeletal dysplasia with amelogenesis imperfecta. *Front. Genet.* 10, 504. doi:10.3389/fgene.2019.00504

Lee, K.-E., Ko, J., Le, C. G. T., Shin, T. J., Hyun, H.-K., Lee, S.-H., et al. (2015). Novel LAMB3 mutations cause non-syndromic amelogenesis imperfecta with variable expressivity. *Clin. Genet.* 87, 90–92. doi:10.1111/cge.12340

Lee, N. P. Y., Tong, M. K., Leung, P. P., Chan, V. W., Leung, S., Tam, P.-C., et al. (2006). Kidney claudin-19: Localization in distal tubules and collecting ducts and dysregulation in polycystic renal disease. *FEBS Lett.* 580, 923–931. doi:10.1016/j.febslet.2006.01.019

Lee, S.-K., Seymen, F., Kang, H.-Y., Lee, K.-E., Gencay, K., Tuna, B., et al. (2010). MMP20 hemopexin domain mutation in amelogenesis imperfecta. *J. Dent. Res.* 89, 46–50. doi:10.1177/0022034509352844

Lee, S. K., Lee, K. E., Jeong, T. S., Hwang, Y. H., Kim, S., Hu, J. C., et al. (2011). FAM83H mutations cause ADHCAI and alter intracellular protein localization. *J. Dent. Res.* 90 (3), 377–381. doi:10.1177/0022034510389177

Lench, N. J., and Winter, G. B. (1995). Characterisation of molecular defects in X-linked amelogenesis imperfecta (AIH1). *Hum. Mutat.* 5, 251–259. doi:10.1002/humu.1380050310

Li, X., Yin, W., Pérez-Jurado, L., Bonadio, J., and Francke, U. (1995). Mapping of human and murine genes for latent TGF-β binding protein-2 (LTBP2). *Mamm. Genome* 6, 42–45. doi:10.1007/BF00350892

Liang, T., Hu, Y., Smith, C. E., Richardson, A. S., Zhang, H., Yang, J., et al. (2019). AMBN mutations causing hypoplastic amelogenesis imperfecta and Ambn knockout-

NLS-lacZ knockin mice exhibiting failed amelogenesis and Ambn tissue-specificity. *Mol. Genet. Genomic Med.* 7, e929. doi:10.1002/mgg3.929

Lindemeyer, R. G., Gibson, C. W., and Wright, T. J. (2010). Amelogenesis imperfecta due to a mutation of the enamelin gene: Clinical case with genotype-phenotype correlations. *Pediatr. Dent.* 32 (1), 56–60.

Lu, T., Li, M., Xu, X., Xiong, J., Huang, C., Zhang, X., et al. (2018). Whole exome sequencing identifies an AMBN missense mutation causing severe autosomal-dominant amelogenesis imperfecta and dentin disorders. *Int. J. Oral Sci.* 10, 26. doi:10.1038/s41368-018-0027-9

Ludwig, M.-G., Vanek, M., Guerini, D., Gasser, J. A., Jones, C. E., Junker, U., et al. (2003). Proton-sensing G-protein-coupled receptors. *Nature* 425, 93–98. doi:10.1038/nature01905

Maas, S. M., Jong, T. P. V. M. de, Buss, P., and Hennekam, R. C. M. (1996). EEC syndrome and genitourinary anomalies: An update. *Am. J. Med. Genet.* 63, 472–478. doi:10.1002/(SICI)1096-8628(19960614)63:3<472::AID-AJMG11>3.0

Mårdh, C. K., Bäckman, B., Holmgren, G., Hu, J. C., Simmer, J. P., and Forsman-Semb, K. (2002). A nonsense mutation in the enamelin gene causes local hypoplastic autosomal dominant amelogenesis imperfecta (AIH2). *Hum. Mol. Genet.* 11(9), 1069–1074. doi:10.1093/hmg/11.9.1069

Martelli-Júnior, H., dos Santos Neto, P. E., de Aquino, S. N., de Oliveira Santos, C. C., Borges, S. P., Oliveira, E. A., et al. (2011). Amelogenesis imperfecta and nephrocalcinosis syndrome: A case report and review of the literature. *Nephron Physiol.* 118 (3), 62–65. doi:10.1159/000322828

Martino, F., D'Eufemia, P., Pergola, M. S., Finocchiaro, R., Celli, M., Giampà, G., et al. (1992). Child with manifestations of dermotrichic syndrome and ichthyosis follicularis-alopecia-photophobia (IFAP) syndrome. *Am. J. Med. Genet.* 44, 233–236. doi:10.1002/ajmg.1320440222

Masunaga, T. (2006). Epidermal basement membrane: Its molecular organization and blistering disorders. *Connect. Tissue Res.* 47, 55–66. doi:10.1080/03008200600584157

Mátyás, G., Arnold, E., Carrel, T., Baumgartner, D., Boileau, C., Berger, W., et al. (2006). Identification and *in silico* analyses of novel TGFBR1 and TGFBR2 mutations in Marfan syndrome-related disorders. *Hum. Mutat.* 27, 760–769. doi:10.1002/humu.20353

McCarl, C.-A., Picard, C., Khalil, S., Kawasaki, T., Röther, J., Papolos, A., et al. (2009). ORAI1 deficiency and lack of store-operated Ca2+ entry cause immunodeficiency, myopathy, and ectodermal dysplasia. *J. Allergy Clin. Immunol.* 124, 1311–1318. doi:10.1016/j.jaci.2009.10.007

McGrath, J. A., Li, K., Dunnill, M. G. S., McMillan, J. R., Christiano, A. M., Eady, R. A., et al. (1996). Compound heterozygosity for a dominant Glycine substitution and a recessive internal duplication mutation in the type XVII collagen gene results in junctional epidermolysis bullosa and abnormal dentition. Am. J. Pathol. 148 (6), 1787–1796.

McNally, B. A., Somasundaram, A., Yamashita, M., and Prakriya, M. (2012). Gated regulation of CRAC channel ion selectivity by STIM1. *Nature* 482, 241–245. doi:10.1038/nature10752

Mechaussier, S., Perrault, I., Dollfus, H., Bloch-Zupan, A., Loundon, N., Jonard, L., et al. (2020). Heimler syndrome. *Adv. Exp. Med. Biol.* 1299, 81–87. doi:10.1007/978-3-030-60204-8_7

Mendoza, G., Pemberton, T. J., Lee, K., Scarel-Caminaga, R., Mehrian-Shai, R., Gonzalez-Quevedo, C., et al. (2007). A new locus for autosomal dominant amelogenesis imperfecta on chromosome 8q24.3. *Hum. Genet.* 120, 653–662. doi:10.1007/s00439-006-0246-6

Molla, M., Descroix, V., Aïoub, M., Simon, S., Castañeda, B., Hotton, D., et al. (2010). Enamel protein regulation and dental and periodontal physiopathology in Msx2 mutant mice. *Am. J. Pathol.* 177, 2516–2526. doi:10.2353/ajpath.2010.091224

Montaño, A. M., Tomatsu, S., Brusius, A., Smith, M., and Orii, T. (2008). Growth charts for patients affected with Morquio A disease. *Am. J. Med. Genet. Part A* 146A, 1286–1295. doi:10.1002/ajmg.a.32281

Mory, A., Dagan, E., Illi, B., Duquesnoy, P., Mordechai, S., Shahor, I., et al. (2012). A nonsense mutation in the human homolog of Drosophila rogdi causes kohlschutter–tonz syndrome. *Am. J. Hum. Genet.* 90, 708–714. doi:10.1016/j.ajhg.2012.03.005

Müller, D., Kausalya, P. J., Meij, I. C., and Hunziker, W. (2006). Familial hypomagnesemia with hypercalciuria and nephrocalcinosis: Blocking endocytosis restores surface expression of a novel claudin-16 mutant that lacks the entire C-terminal cytosolic tail. *Hum. Mol. Genet.* 15, 1049–1058. doi:10.1093/hmg/ddl020

Muto, T., Miyoshi, K., Horiguchi, T., and Noma, T. (2012). Dissection of morphological and metabolic differentiation of ameloblasts via ectopic SP6 expression. *J. Med. Investig.* 59, 59–68. doi:10.2152/jmi.59.59

Nagamine, K., Peterson, P., Scott, H. S., Kudoh, J., Minoshima, S., Heino, M., et al. (1997). Positional cloning of the APECED gene. *Nat. Genet.* 17, 393–398. doi:10.1038/ng1297-393

Nakamura, T., de Vega, S., Fukumoto, S., Jimenez, L., Unda, F., and Yamada, Y. (2008). Transcription factor epiprofin is essential for tooth morphogenesis by regulating epithelial cell fate and tooth number. *J. Biol. Chem.* 283, 4825–4833. doi:10.1074/jbc.M708388200

Nakamura, T., Unda, F., de-Vega, S., Vilaxa, A., Fukumoto, S., Yamada, K. M., et al. (2004). The Krüppel-like factor epiprofin is expressed by epithelium of developing teeth, hair follicles, and limb buds and promotes cell proliferation. *J. Biol. Chem.* 279, 626–634. doi:10.1074/jbc.M307502200

Nalbant, D., Youn, H., Nalbant, S. I., Sharma, S., Cobos, E., Beale, E. G., et al. (2005). FAM20: An evolutionarily conserved family of secreted proteins expressed in hematopoietic cells. *BMC Genomics* 6, 11. doi:10.1186/1471-2164-6-11

Neuhaus, C., Eisenberger, T., Decker, C., Nagl, S., Blank, C., Pfister, M., et al. (2017). Next-generation sequencing reveals the mutational landscape of clinically diagnosed usher syndrome: Copy number variations, phenocopies, a predominant target for translational read-through, and PEX26 mutated in heimler syndrome. *Mol. Genet. Genomic Med.* 5, 531–552. doi:10.1002/mgg3.312

Nikolopoulos, G., Smith, C. E. L., Brookes, S. J., El-Asrag, M. E., Brown, C. J., Patel, A., et al. (2020). New missense variants in RELT causing hypomineralised amelogenesis imperfecta. *Clin. Genet.* 97, 688–695. doi:10.1111/cge.13721

Nikolopoulos, G., Smith, C. E. L., Poulter, J. A., Murillo, G., Silva, S., Lamb, T., et al. (2021). Spectrum of pathogenic variants and founder effects in amelogenesis imperfecta associated with MMP20. *Hum. Mutat.* 42, 567–576. doi:10.1002/humu.24187

Noor, A., Windpassinger, C., Vitcu, I., Orlic, M., Rafiq, M. A., Khalid, M., et al. (2009). Oligodontia is caused by mutation in LTBP3, the gene encoding latent TGF-beta binding protein 3. *Am. J. Hum. Genet.* 84, 519–523. doi:10.1016/j.ajhg.2009.03.007

Nurbaeva, M. K., Eckstein, M., Concepcion, A. R., Smith, C. E., Srikanth, S., Paine, M. L., et al. (2015). Dental enamel cells express functional SOCE channels. *Sci. Rep.* 5, 15803. doi:10.1038/srep15803

Ogawa, T., Tomatsu, S., Fukuda, S., Yamagishi, A., Rezvi, G. M., Sukegawa, K., et al. (1995). Mucopolysaccharidosis IVA: Screening and identification of mutations of the N-acetylgalactosamine-6-sulfate sulfatase gene. *Hum. Mol. Genet.* 4, 341–349. doi:10.1093/hmg/4.3.341

O'Sullivan, J., Bitu, C. C., Daly, S. B., Urquhart, J. E., Barron, M. J., Bhaskar, S. S., et al. (2011). Whole-Exome sequencing identifies FAM20A mutations as a cause of amelogenesis imperfecta and gingival hyperplasia syndrome. *Am. J. Hum. Genet.* 88, 616–620. doi:10.1016/j.ajhg.2011.04.005

Ozdemir, D., Hart, P. S., Firatli, E., Aren, G., Ryu, O. H., and Hart, T. C. (2005a). Phenotype of ENAM mutations is dosage-dependent. *J. Dent. Res.* 84, 1036–1041. doi:10.1177/154405910508401113

Ozdemir, D., Hart, P. S., Ryu, O. H., Choi, S. J., Ozdemir-Karatas, M., Firatli, E., et al. (2005b). MMP20 active-site mutation in hypomaturation amelogenesis imperfecta. *J. Dent. Res.* 84, 1031–1035. doi:10.1177/154405910508401112

Papagerakis, P., Lin, H.-K., Lee, K. Y., Hu, Y., Simmer, J. P., Bartlett, J. D., et al. (2008). Premature stop codon in MMP20 causing amelogenesis imperfecta. *J. Dent. Res.* 87, 56–59. doi:10.1177/154405910808700109

Parker, N. J., Begley, C. G., Smith, P. J., and Fox, R. M. (1996). Molecular cloning of a novel human gene (D11S4896E) at chromosomal region 11p15.5. *Genomics* 37, 253–256. doi:10.1006/geno.1996.0553

Parry, D. A., Brookes, S. J., Logan, C. V., Poulter, J. A., El-Sayed, W., Al-Bahlani, S., et al. (2012). Mutations in C4orf26, encoding a peptide with *in vitro* hydroxyapatite crystal nucleation and growth activity, cause amelogenesis imperfecta. *Am. J. Hum. Genet.* 91, 565–571. doi:10.1016/j.ajhg.2012.07.020

Parry, D. A., Holmes, T. D., Gamper, N., El-Sayed, W., Hettiarachchi, N. T., Ahmed, M., et al. (2016a). A homozygous STIM1 mutation impairs store-operated calcium entry and natural killer cell effector function without clinical immunodeficiency. *J. Allergy Clin. Immunol.* 137, 955–957. doi:10.1016/j.jaci.2015.08.051

Parry, D. A., Mighell, A. J., El-Sayed, W., Shore, R. C., Jalili, I. K., Dollfus, H., et al. (2009). Mutations in CNNM4 cause Jalili syndrome, consisting of autosomal-recessive cone-rod dystrophy and amelogenesis imperfecta. *Am. J. Hum. Genet.* 84, 266–273. doi:10.1016/j.ajhg.2009.01.009

Parry, D. A., Poulter, J. A., Logan, C. V., Brookes, S. J., Jafri, H., Ferguson, C. H., et al. (2013). Identification of mutations in SLC24A4, encoding a potassium-dependent sodium/calcium exchanger, as a cause of amelogenesis imperfecta. *Am. J. Hum. Genet.* 92, 307–312. doi:10.1016/j.ajhg.2013.01.003

Parry, D. A., Smith, C. E. L., El-Sayed, W., Poulter, J. A., Shore, R. C., Logan, C. V., et al. (2016b). Mutations in the pH-sensing G-protein-coupled receptor GPR68 cause amelogenesis imperfecta. *Am. J. Hum. Genet.* 99, 984–990. doi:10.1016/j.ajhg.2016.08.020

Pavlic, A., and Waltimo-Sirén, J. (2009). Clinical and microstructural aberrations of enamel of deciduous and permanent teeth in patients with autoimmune polyendocrinopathy-candidiasis-ectodermal dystrophy. *Arch. Oral Biol.* 54, 658–665. doi:10.1016/j.archoralbio.2009.03.009

Peracha, H., Sawamoto, K., Averill, L., Kecskemethy, H., Theroux, M., Thacker, M., et al. (2018). Molecular genetics and metabolism, special edition: Diagnosis, diagnosis and prognosis of Mucopolysaccharidosis IVA. *Mol. Genet. Metab.* 125, 18–37. doi:10.1016/j.ymgme.2018.05.004

Pereverzev, A., Komarova, S. V., Korcok, J., Armstrong, S., Tremblay, G. B., Dixon, S. J., et al. (2008). Extracellular acidification enhances osteoclast survival through an NFAT-independent, protein kinase C-dependent pathway. *Bone* 42, 150–161. doi:10.1016/j.bone.2007.08.044

Perniola, R. (2018). Twenty years of AIRE. *Front. Immunol.* 9, 98. doi:10.3389/fimmu.2018.00098

Picard, C., McCarl, C.-A., Papolos, A., Khalil, S., Lüthy, K., Hivroz, C., et al. (2009). STIM1 mutation associated with a syndrome of immunodeficiency and autoimmunity. *N. Engl. J. Med.* 360, 1971–1980. doi:10.1056/NEJMoa0900082

Plaisancié, J., Collet, C., Pelletier, V., Perdomo, Y., Studer, F., Fradin, M., et al. (2015). MSX2 gene duplication in a patient with eye development defects. *Ophthalmic Genet.* 36, 353–358. doi:10.3109/13816810.2014.886270

Pollak, C., Floy, M., and Say, B. (2003). Sensorineural hearing loss and enamel hypoplasia with subtle nail findings: Another family with heimler's syndrome. *Clin. Dysmorphol.* 12, 55–58. doi:10.1097/00019605-200301000-00010

Polok, B., Escher, P., Ambresin, A., Chouery, E., Bolay, S., Meunier, I., et al. (2009). Mutations in CNNM4 cause recessive cone-rod dystrophy with amelogenesis imperfecta. *Am. J. Hum. Genet.* 84, 259–265. doi:10.1016/j.ajhg.2009.01.006

Portsteffen, H., Beyer, A., Becker, E., Epplen, C., Pawlak, A., Kunau, W.-H., et al. (1997). Human PEX1 is mutated in complementation group 1 of the peroxisome biogenesis disorders. *Nat. Genet.* 17, 449–452. doi:10.1038/ng1297-449

Poulter, J. A., Brookes, S. J., Shore, R. C., Smith, C. E. L., Abi Farraj, L., Kirkham, J., et al. (2014a). A missense mutation in ITGB6 causes pitted hypomineralized amelogenesis imperfecta. *Hum. Mol. Genet.* 23, 2189–2197. doi:10.1093/hmg/ddt616

Poulter, J. A., Murillo, G., Brookes, S. J., Smith, C. E. L., Parry, D. A., Silva, S., et al. (2014b). Deletion of ameloblastin exon 6 is associated with amelogenesis imperfecta. *Hum. Mol. Genet.* 23, 5317–5324. doi:10.1093/hmg/ddu247

Prasad, M. K., Geoffroy, V., Vicaire, S., Jost, B., Dumas, M., Le Gras, S., et al. (2016a). A targeted next-generation sequencing assay for the molecular diagnosis of genetic disorders with orodental involvement. *J. Med. Genet.* 53, 98–110. doi:10.1136/jmedgenet-2015-103302

Prasad, M. K., Laouina, S., El Alloussi, M., Dollfus, H., and Bloch-Zupan, A. (2016b). Amelogenesis imperfecta: 1 family, 2 phenotypes, and 2 mutated genes. *J. Dent. Res.* 95, 1457–1463. doi:10.1177/0022034516663200

Price, J. A., Bowden, D. W., Tim Wright, J., Pettenati, M. J., and Hart, T. C. (1998). Identification of a mutation in DLX3 associated with tricho-dento-osseous (TDO) syndrome. *Hum. Mol. Genet.* 7, 563–569. doi:10.1093/hmg/7.3.563

Raine, J., Winter, R. M., Davey, A., and Tucker, S. M. (1989). Unknown syndrome: Microcephaly, hypoplastic nose, exophthalmos, gum hyperplasia, cleft palate, low set ears, and osteosclerosis. *J. Med. Genet.* 26, 786–788. doi:10.1136/jmg.26.12.786

Rao, S., and Witkop, C. J. (1971). Inherited defects in tooth structure. *Birth Defects Orig. Artic. Ser.* 7, 153–184.

Rapp, R. S., and Hodgkin, W. E. (1968). Anhidrotic ectodermal dysplasia: Autosomal dominant inheritance with palate and lip anomalies. *J. Med. Genet.* 5, 269–272. doi:10.1136/jmg.5.4.269

Ratbi, I., Falkenberg, K. D., Sommen, M., Al-Sheqaih, N., Guaoua, S., Vandeweyer, G., et al. (2015). Heimler syndrome is caused by hypomorphic mutations in the peroxisome-biogenesis genes PEX1 and PEX6. *Am. J. Hum. Genet.* 97, 535–545. doi:10.1016/j.ajhg.2015.08.011

Rathi, N., Mattoo, K., and Bhatnagar, S. (2014). Extending the use of a diagnostic occlusal splint to overcome existing lacunae of vertical dimension transfer in full mouth rehabilitation cases. *Am. J. Med. Case Rep.* 2, 291–297. doi:10.12691/ajmcr-2-12-9

Reese, M. G., Eeckman, F. H., Kulp, D., and Haussler, D. (1997). Improved splice site detection in Genie. *J. Comput. Biol.* 4, 311–323. doi:10.1089/cmb.1997.4.311

Reuber, B. E., Germain-Lee, E., Collins, C. S., Morrell, J. C., Ameritunga, R., Moser, H. W., et al. (1997). Mutations in PEX1 are the most common cause of peroxisome biogenesis disorders. *Nat. Genet.* 17, 445–448. doi:10.1038/ng1297-445

Rey, T., Tarabeux, J., Gerard, B., Delbarre, M., Le Béchec, A., Stoetzel, C., et al. (2019). Protocol GenoDENT: Implementation of a new NGS panel for molecular diagnosis of genetic disorders with orodental involvement. *Methods Mol. Biol.* 1922, 407–452. doi:10.1007/978-1-4939-9012-2_36

Richards, S., Aziz, N., Bale, S., Bick, D., Das, S., Gastier-Foster, J., et al. (2015). Standards and guidelines for the interpretation of sequence variants: A joint consensus recommendation of the American College of medical genetics and genomics and the association for molecular pathology. *Genet. Med.* 17, 405–424. doi:10.1038/gim.2015.30

Rinne, T., Hamel, B., van Bokhoven, H., and Brunner, H. G. (2006). Pattern of p63 mutations and their phenotypes-update. *Am. J. Med. Genet. A* 140, 1396–1406. doi:10.1002/ajmg.a.31271

Robinson, C. (2014). Enamel maturation: A brief background with implications for some enamel dysplasias. *Front. Physiol.* 5, 388. doi:10.3389/fphys.2014.00388

Rølling, I., Clausen, N., Nyvad, B., and Sindet-Pedersen, S. (1999). Dental findings in three siblings with Morquio's syndrome. *Int. J. Paediatr. Dent.* 9, 219–224. doi:10.1046/j.1365-263x.1999.00127.x

Ruspita, I., Das, P., Xia, Y., Kelangi, S., Miyoshi, K., Noma, T., et al. (2020). An msx2-sp6-follistatin pathway operates during late stages of tooth development to control amelogenesis. *Front. Physiol.* 11, 582610. doi:10.3389/fphys.2020.582610

Sabbioni, S., Veronese, A., Trubia, M., Taramelli, R., Barbanti-Brodano, G., Croce, C. M., et al. (1999). Exon structure and promoter identification of STIM1 (alias GOK), a human gene causing growth arrest of the human tumor cell lines G401 and RD. *Cytogenet Celll Genet.* 86, 214–218. doi:10.1159/000015341

Sawamoto, K., Álvarez González, J. V., Piechnik, M., Otero, F. J., Couce, M. L., Suzuki, Y., et al. (2020). Mucopolysaccharidosis IVA: Diagnosis, treatment, and management. *Int. J. Mol. Sci.* 21. 1517. doi:10.3390/ijms21041517

Scherer, S. W., Heng, H. H. Q., Robinson, G. W., Mahon, K. A., Evans, J. P., and Tsui, L.-C. (1995). Assignment of the human homolog of mouse Dlx3 to Chromosome 17q21.3-q22 by analysis of somatic cell hybrids and fluorescence *in situ* hybridization. *Mamm. Genome* 6, 310–311. doi:10.1007/BF00352432

Schossig, A., Bloch-Zupan, A., Lussi, A., Wolf, N. I., Raskin, S., Cohen, M., et al. (2017). SLC13A5 is the second gene associated with Kohlschütter-Tönz syndrome. *J. Med. Genet.* 54, 54–62. doi:10.1136/jmedgenet-2016-103988

Schossig, A., Wolf, N. I., Fischer, C., Fischer, M., Stocker, G., Pabinger, S., et al. (2012). Mutations in ROGDI cause kohlschütter-tönz syndrome. *Am. J. Hum. Genet.* 90, 701–707. doi:10.1016/j.ajhg.2012.02.012

Schulze, C. (1970). "Developmental abnormalities of the teeth and jaws," in *Thoma's oral pathology*. Editors R. J. Gorlin and H. M. Goldman (St Louis: C. V. Mosby), 112–122.

Sewerin, S., Piontek, J., Schönauer, R., Grunewald, S., Rauch, A., Neuber, S., et al. (2022). Defective claudin-10 causes a novel variation of HELIX syndrome through compromised tight junction strand assembly. *Genes. Dis.* 9, 1301–1314. doi:10.1016/j.gendis.2021.06.006

Seymen, F., Kim, Y. J., Lee, Y. J., Kang, J., Kim, T.-H., Choi, H., et al. (2016). Recessive mutations in ACPT, encoding testicular acid phosphatase, cause hypoplastic amelogenesis imperfecta. *Am. J. Hum. Genet.* 99, 1199–1205. doi:10.1016/j.ajhg.2016.09.018

Seymen, F., Lee, K.-E., Koruyucu, M., Gencay, K., Bayram, M., Tuna, E. B., et al. (2014a). ENAM mutations with incomplete penetrance. *J. Dent. Res.* 93, 988–992. doi:10.1177/0022034514548222

Seymen, F., Lee, K.-E., Koruyucu, M., Gencay, K., Bayram, M., Tuna, E. B., et al. (2015a). Novel ITGB6 mutation in autosomal recessive amelogenesis imperfecta. *Oral Dis.* 21, 456–461. doi:10.1111/odi.12303

Seymen, F., Lee, K.-E., Tran Le, C. G., Yildirim, M., Gencay, K., Lee, Z. H., et al. (2014b). Exonal deletion of SLC24A4 causes hypomaturation amelogenesis imperfecta. *J. Dent. Res.* 93, 366–370. doi:10.1177/0022034514523786

Seymen, F., Park, J.-C., Lee, K.-E., Lee, H.-K., Lee, D.-S., Koruyucu, M., et al. (2015b). Novel MMP20 and KLK4 mutations in amelogenesis imperfecta. *J. Dent. Res.* 94, 1063–1069. doi:10.1177/0022034515590569

Seymen, F., Zhang, H., Kasimoglu, Y., Koruyucu, M., Simmer, J. P., Hu, J. C.-C., et al. (2021). Novel mutations in GPR68 and SLC24A4 cause hypomaturation amelogenesis imperfecta. *J. Pers. Med.* 12, 13. doi:10.3390/jpm12010013

Shaheen, R., Ansari, S., Alshammari, M. J., Alkhalidi, H., Alrukban, H., Eyaid, W., et al. (2013). A novel syndrome of hypohidrosis and intellectual disability is linked to COG6 deficiency. *J. Med. Genet.* 50, 431–436. doi:10.1136/jmedgenet-2013-101527

Shapiro, M. B., and Senapathy, P. (1987). RNA splice junctions of different classes of eukaryotes: Sequence statistics and functional implications in gene expression. *Nucleic Acids Res.* 15, 7155–7174. doi:10.1093/nar/15.17.7155

Shore, R. C., Bäckman, B., Elcock, C., Brook, A. H., Brookes, S. J., and Kirkham, J. (2010). The structure and composition of deciduous enamel affected by local hypoplastic autosomal dominant amelogenesis imperfecta resulting from an ENAM mutation. *Cells Tissues Organs* 191, 301–306. doi:10.1159/000258703

Simmer, J. P., Hu, J. C.-C., Hu, Y., Zhang, S., Liang, T., Wang, S.-K., et al. (2021). A genetic model for the secretory stage of dental enamel formation. *J. Struct. Biol.* 213, 107805. doi:10.1016/j.jsb.2021.107805

Simmer, J. P., Hu, Y., Lertlam, R., Yamakoshi, Y., and Hu, J. C.-C. (2009). Hypomaturation enamel defects in Klk4 knockout/LacZ knockin mice. *J. Biol. Chem.* 284, 19110–19121. doi:10.1074/jbc.M109.013623

Simon, D. B., Lu, Y., Choate, K. A., Velazquez, H., Al-Sabban, E., Praga, M., et al. (1999). Paracellin-1, a renal tight junction protein required for paracellular Mg2+ resorption. *Science* 285, 103–106. doi:10.1126/science.285.5424.103

Simpson, M. A., Hsu, R., Keir, L. S., Hao, J., Sivapalan, G., Ernst, L. M., et al. (2007). Mutations in FAM20C are associated with lethal osteosclerotic bone dysplasia (Raine syndrome), highlighting a crucial molecule in bone development. *Am. J. Hum. Genet.* 81, 906–912. doi:10.1086/522240

Simpson, M. A., Scheuerle, A., Hurst, J., Patton, M. A., Stewart, H., and Crosby, A. H. (2009). Mutations in FAM20C also identified in non-lethal osteosclerotic bone dysplasia. *Clin. Genet.* 75, 271–276. doi:10.1111/j.1399-0004.2008.01118.x

Slegtenhorst, M. van, Hoogt, R. de, Hermans, C., Nellist, M., Janssen, B., Verhoef, S., et al. (1997). Identification of the tuberous sclerosis gene TSC1 on chromosome 9q34. *Science* 277, 805–808. doi:10.1126/science.277.5327.805

Smith, C. E. L., Kirkham, J., Day, P. F., Soldani, F., McDerra, E. J., Poulter, J. A., et al. (2017a). A fourth KLK4 mutation is associated with enamel hypomineralisation and structural abnormalities. *Front. Physiol.* 8, 333. doi:10.3389/fphys.2017.00333

Smith, C. E. L., Murillo, G., Brookes, S. J., Poulter, J. A., Silva, S., Kirkham, J., et al. (2016). Deletion of amelotin exons 3-6 is associated with amelogenesis imperfecta. *Hum. Mol. Genet.* 25, 3578–3587. doi:10.1093/hmg/ddw203

Smith, C. E. L., Poulter, J. A., Brookes, S. J., Murillo, G., Silva, S., Brown, C. J., et al. (2019). Phenotype and variant spectrum in the LAMB3 form of amelogenesis imperfecta. *J. Dent. Res.* 98, 698–704. doi:10.1177/0022034519835205

Smith, C. E. L., Whitehouse, L. L. E., Poulter, J. A., Wilkinson Hewitt, L., Nadat, F., Jackson, B. R., et al. (2020). A missense variant in specificity protein 6 (SP6) is associated with amelogenesis imperfecta. *Hum. Mol. Genet.* 29, 1417–1425. doi:10.1093/hmg/ddaa041

Smith, C. E., Whitehouse, L. L., Poulter, J. A., Brookes, S. J., Day, P. F., Soldani, F., et al. (2017b). Defects in the acid phosphatase ACPT cause recessive hypoplastic amelogenesis imperfecta. *Eur. J. Hum. Genet.* 25, 1015–1019. doi:10.1038/ejhg.2017.79

Spedicati, B., Cocca, M., Palmisano, R., Faletra, F., Barbieri, C., Francescatto, M., et al. (2021). Natural human knockouts and mendelian disorders: Deep phenotyping in Italian isolates. *Eur. J. Hum. Genet.* 29, 1272–1281. doi:10.1038/s41431-021-00850-9

Sripathomsawat, W., Tanpaiboon, P., Heering, J., Dötsch, V., Hennekam, R. C. M., and Kantaputra, P. (2011). Phenotypic analysis of Arg227 mutations of TP63 with emphasis on dental phenotype and micturition difficulties in EEC syndrome. *Am J M Genet A* 155, 228–232. doi:10.1002/ajmg.a.33768

Su, X., Chakravarti, D., Cho, M. S., Liu, L., Gi, Y. J., Lin, Y.-L., et al. (2010). TAp63 suppresses metastasis through coordinate regulation of Dicer and miRNAs. *Nature* 467, 986–990. doi:10.1038/nature09459

Suh, J., Choi, H. S., Kwon, A., Chae, H. W., Lee, J.-S., and Kim, H.-S. (2019). A novel compound heterozygous mutation of the AIRE gene in a patient with autoimmune polyendocrine syndrome type 1. *Ann. Pediatr. Endocrinol. Metab.* 24, 248–252. doi:10.6065/apem.2019.24.4.248

Sun, S., Yu, M., Fan, Z., Yeh, I.-T., Feng, H., Liu, H., et al. (2019). DLX3 regulates osteogenic differentiation of bone marrow mesenchymal stem cells via Wnt/β-catenin pathway mediated histone methylation of DKK4. *Biochem. Biophys. Res. Commun.* 516, 171–176. doi:10.1016/j.bbrc.2019.06.029

Sutton, V. R., and van Bokhoven, H. (2010). "TP63-Related disorders," in *GeneReviews® [Internet]*. Editors M. P. Adam, D. B. Everman, G. M. Mirzaa, R. A. Pagon, S. E. Wallace, L. J. H. Bean, et al. (Seattle (WA): University of Washington, Seattle), 1993–2022.

Tabata, M. J., Matsumura, T., Liu, J. G., Wakisaka, S., and Kurisu, K. (1996). Expression of cytokeratin 14 in ameloblast-lineage cells of the developing tooth of rat, both *in vivo* and *in vitro*. *Arch. Oral Biol.* 41, 1019–1027. doi:10.1016/s0003-9969(96)00087-8

Tanaka, A., Weinel, S., Nagy, N., O'Driscoll, M., Lai-Cheong, J. E., Kulp-Shorten, C. L., et al. (2012). Germline mutation in ATR in autosomal- dominant oropharyngeal cancer syndrome. *Am. J. Hum. Genet.* 90, 511–517. doi:10.1016/j.ajhg.2012.01.007

Tanimoto, K., Le, T., Zhu, L., Witkowska, H. E., Robinson, S., Hall, S., et al. (2008). Reduced amelogenin-MMP20 interactions in amelogenesis imperfecta. *J. Dent. Res.* 87, 451–455. doi:10.1177/154405910808700516

The 1000 Geno; mes Project ConsortiumGibbs, R. A., Boerwinkle, E., Doddapaneni, H., Han, Y., Korchina, V., et al. (2015). A global reference for human genetic variation. *Nature* 526, 68–74. doi:10.1038/nature15393

Tomura, H., Wang, J.-Q., Liu, J.-P., Komachi, M., Damirin, A., Mogi, C., et al. (2008). Cyclooxygenase-2 expression and prostaglandin E2 production in response to acidic pH through OGR1 in a human osteoblastic cell line. *J. Bone Min. Res.* 23, 1129–1139. doi:10.1359/jbmr.080236

Torres, L. H. S., de-Azevedo-Vaz, S. L., Barroso, D. R. C., Silva, D. N., Velloso, T. R. G., and de Barros, L. A. P. (2018). Enamel-renal-syndrome: Case report. *Spec. Care Dent.* 38 (3), 172–175. doi:10.1111/scd.12288

Toyosawa, S., Fujiwara, T., Ooshima, T., Shintani, S., Sato, A., Ogawa, Y., et al. (2000). Cloning and characterization of the human ameloblastin gene. *Gene* 256, 1–11. doi:10.1016/S0378-1119(00)00379-6

Tucci, A., Kara, E., Schossig, A., Wolf, N. I., Plagnol, V., Fawcett, K., et al. (2013). Kohlschütter-Tönz syndrome: Mutations in ROGDI and evidence of genetic heterogeneity. *Hum. Mutat.* 34 (2), 296–300. doi:10.1002/humu.22241

Utami, T. W., Miyoshi, K., Hagita, H., Yanuaryska, R. D., Horiguchi, T., and Noma, T. (2011). Possible linkage of SP6 transcriptional activity with amelogenesis by protein stabilization. *J. Biomed. Biotechnol.* 2011, 320987. doi:10.1155/2011/320987

Vahidnezhad, H., Youssefian, L., Zeinali, S., Saeidian, A. H., Sotoudeh, S., Mozafari, N., et al. (2017). Dystrophic epidermolysis bullosa: COL7A1 mutation landscape in a multi-ethnic cohort of 152 extended families with high degree of customary consanguineous marriages. *J. Investig. Dermatol* 137, 660–669. doi:10.1016/j.jid.2016.10.023

van Bakel, I., Sepp, T., Ward, S., Yates, J. R. W., and Green, A. J. (1997). Mutations in the TSC2 gene: Analysis of the complete coding sequence using the protein truncation test (PTT). *Hum. Mol. Genet.* 6, 1409–1414. doi:10.1093/hmg/6.9.1409

Vieira, G. H., Rodriguez, J. D., Carmona-Mora, P., Cao, L., Gamba, B. F., Carvalho, D. R., et al. (2012). Detection of classical 17p11.2 deletions, an atypical deletion and RAI1 alterations in patients with features suggestive of Smith-Magenis syndrome. *Eur. J. Hum. Genet.* 20, 148–154. doi:10.1038/ejhg.2011.167

Vig, M., Peinelt, C., Beck, A., Koomoa, D. L., Rabah, D., Koblan-Huberson, M., et al. (2006). CRACM1 is a plasma membrane protein essential for store-operated Ca2+ entry. *Science* 312, 1220–1223. doi:10.1126/science.1127883

Wang, S.-K., Choi, M., Richardson, A. S., Reid, B. M., Lin, B. P., Wang, S. J., et al. (2014b). ITGB6 loss-of-function mutations cause autosomal recessive amelogenesis imperfecta. *Hum. Mol. Genet.* 23, 2157–2163. doi:10.1093/hmg/ddt611

Wang, S.-K., Hu, Y., Simmer, J. P., Seymen, F., Estrella, N. M. R. P., Pal, S., et al. (2013). Novel KLK4 and MMP20 mutations discovered by whole-exome sequencing. *J. Dent. Res.* 92, 266–271. doi:10.1177/0022034513475626

Wang, S.-K., Zhang, H., Chavez, M. B., Hu, Y., Seymen, F., Koruyucu, M., et al. (2020). Dental malformations associated with biallelic MMP20 mutations. *Mol. Genet. Genomic Med.* 8, e1307. doi:10.1002/mgg3.1307

Wang, S., Choi, M., Richardson, A. S., Reid, B. M., Seymen, F., Yildirim, M., et al. (2014a). STIM1 and SLC24A4 are critical for enamel maturation. *J. Dent. Res.* 93, 94S-100S–100S. doi:10.1177/0022034514527971

Wang, X., Zhao, Y., Yang, Y., and Qin, M. (2015). Novel ENAM and LAMB3 mutations in Chinese families with hypoplastic amelogenesis imperfecta. *PLoS One* 10, e0116514. doi:10.1371/journal.pone.0116514

Wazen, R. M., Viegas-Costa, L. C., Fouillen, A., Moffatt, P., Adair-Kirk, T. L., Senior, R. M., et al. (2016). Laminin γ2 knockout mice rescued with the human protein exhibit enamel maturation defects. *Matrix Biol.* 52 (54), 207–218. doi:10.1016/j.matbio.2016.03.002

Weinmann, J. P., Svoboda, J. F., and Woods, R. W. (1945). Hereditary disturbances of enamel formation and Calcification**From the research department, loyola university, school of Dentistry, chicago College of dental surgery, and the department of health and welfare, bureau of health, division of dental health, augusta, Maine. *J. Am. Dent. Assoc.* 32, 397–418. doi:10.14219/jada.archive.1945.0063

Whitehouse, L. L. E., Smith, C. E. L., Poulter, J. A., Brown, C. J., Patel, A., Lamb, T., et al. (2019). Novel DLX3 variants in amelogenesis imperfecta with attenuated tricho-dento-osseous syndrome. *Oral Dis.* 25, 182–191. doi:10.1111/odi.12955

Wimalarathna, A., Abeyasinghe, U., Jayasooriya, P., and Herath, C. (2020). Amelogenesis imperfecta: A literature review based guide to diagnosis and management. *J. M. Dent.* 10, 94–101. doi:10.46875/jmd.v10i3.532

Witkop, C. J. (1988). Amelogenesis imperfecta, dentinogenesis imperfecta and dentin dysplasia revisited: Problems in classification. *J. Oral Pathol.* 17, 547–553. doi:10.1111/j.1600-0714.1988.tb01332.x

Witkop, C. J. (1957). Hereditary defects in enamel and dentin. *Acta Genet. Stat. Med.* 7, 236–239. doi:10.1159/000150974

Witkop, C. J. (1971). Manifestations of genetic diseases in the human pulp. *Oral Surg. Oral Med. Oral Pathol.* 32, 278–316. doi:10.1016/0030-4220(71)90232-5

Witkop, C. J., and Sauk, J. J. (1976). "Heritable defects of enamel," in *Oral facial genetics*. Editors R. Stewart and G. Prescott (St. Louis: C.V. Mosby Company), 151–226.

Wright, J. T., Carrion, I. A., and Morris, C. (2015). The molecular basis of hereditary enamel defects in humans. *J. Dent. Res.* 94, 52–61. doi:10.1177/0022034514556708

Wright, J. T. (2023). Enamel phenotypes: Genetic and environmental determinants. *Genes.* 14, 545. doi:10.3390/genes14030545

Wright, J. T., Puranik, C. P., and Farrington, F. (2016). Oral phenotype and variation in focal dermal hypoplasia. *Am. J. Med. Genet. C Semin. Med. Genet.* 172C, 52–58. doi:10.1002/ajmg.c.31478

Yamada, N., Fukuda, S., Tomatsu, S., Muller, V., Hopwood, J. J., Nelson, J., et al. (1998). Molecular heterogeneity in mucopolysaccharidosis IVA in Australia and Northern Ireland: Nine novel mutations including T312S, a common allele that confers a mild phenotype. *Hum. Mutat.* 11 (3), 202–208. doi:10.1002/(SICI)1098-1004(1998)11:3<202::AID-HUMU4>3.0.CO;2-J

Yamaguti, P. M., Neves, F. de A. R., Hotton, D., Bardet, C., Dure-Molla, M. de L., Castro, L. C., et al. (2017). Amelogenesis imperfecta in familial hypomagnesaemia and hypercalciuria with nephrocalcinosis caused by CLDN19 gene mutations. *J. Med. Genet.* 54, 26–37. doi:10.1136/jmedgenet-2016-103956

Yamazaki, D., Funato, Y., Miura, J., Sato, S., Toyosawa, S., Furutani, K., et al. (2013). Basolateral Mg2+ extrusion via CNNM4 mediates transcellular Mg2+ transport across epithelia: A mouse model. *PLoS Genet.* 9, e1003983. doi:10.1371/journal.pgen.1003983

Yang, A., Schweitzer, R., Sun, D., Kaghad, M., Walker, N., Bronson, R. T., et al. (1999). p63 is essential for regenerative proliferation in limb, craniofacial and epithelial development. *Nature* 398, 714–718. doi:10.1038/19539

Yang, M., Mailhot, G., Birnbaum, M. J., MacKay, C. A., Mason-Savas, A., and Odgren, P. R. (2006). Expression of and role for ovarian cancer G-protein-coupled receptor 1 (OGR1) during osteoclastogenesis. *J. Biol. Chem.* 281, 23598–23605. doi:10.1074/jbc.M602191200

Yenamandra, V. K., Vellarikkal, S. K., Chowdhury, M. R., Jayarajan, R., Verma, A., Scaria, V., et al. (2018). Genotype-phenotype correlations of dystrophic epidermolysis

bullosa in India: Experience from a tertiary care centre. *Acta Derm. Venereol.* 98, 873–879. doi:10.2340/00015555-2929

Yeo, G., and Burge, C. B. (2004). Maximum entropy modeling of short sequence motifs with applications to RNA splicing signals. *J. Comput. Biol.* 11, 377–394. doi:10.1089/1066527041410418

Yuan, J. P., Zeng, W., Huang, G. N., Worley, P. F., and Muallem, S. (2007). STIM1 heteromultimerizes TRPC channels to determine their function as store-operated channels. *Nat. Cell. Biol.* 9, 636–645. doi:10.1038/ncb1590

Yuen, W. Y., Pasmooij, A. M. G., Stellingsma, C., and Jonkman, M. F. (2012). Enamel defects in carriers of a novel LAMA3 mutation underlying epidermolysis bullosa. *Acta Derm. Venereol.* 92, 695–696. doi:10.2340/00015555-1341

Zanetti, A., D'Avanzo, F., AlSayed, M., Brusius-Facchin, A. C., Chien, Y. H., Giugliani, R., et al. (2021). Molecular basis of mucopolysaccharidosis IVA (Morquio A syndrome): A review and classification of GALNS gene variants and reporting of 68 novel variants. *Hum. Mutat.* 42 (11), 1384–1398. doi:10.1002/humu.24270

Zhang, H., Koruyucu, M., Seymen, F., Kasimoglu, Y., Kim, J.-W., Tinawi, S., et al. (2019). WDR72 mutations associated with amelogenesis imperfecta and acidosis. *J. Dent. Res.* 98, 541–548. doi:10.1177/0022034518824571

Zhang, Z., Suzuki, Y., Shimozawa, N., Fukuda, S., Imamura, A., Tsukamoto, T., et al. (1999). Genomic structure and identification of 11 novel mutations of the PEX6 (peroxisome assembly factor-2) gene in patients with peroxisome biogenesis disorders. *Hum. Mutat.* 13, 487–496. doi:10.1002/(SICI)1098-1004(1999)13:6<487::AID-HUMU9>3.0.CO;2-T

Zoncu, R., Bar-Peled, L., Efeyan, A., Wang, S., Sancak, Y., and Sabatini, D. M. (2011). mTORC1 senses lysosomal amino acids through an inside-out mechanism that requires the vacuolar H(+)-ATPase. *Science* 334, 678–683. doi:10.1126/science.1207056

Frontiers in Physiology

Understanding how an organism's components work together to maintain a healthy state

The second most-cited physiology journal, promoting a multidisciplinary approach to the physiology of living systems - from the subcellular and molecular domains to the intact organism and its interaction with the environment.

Discover the latest Research Topics

See more →

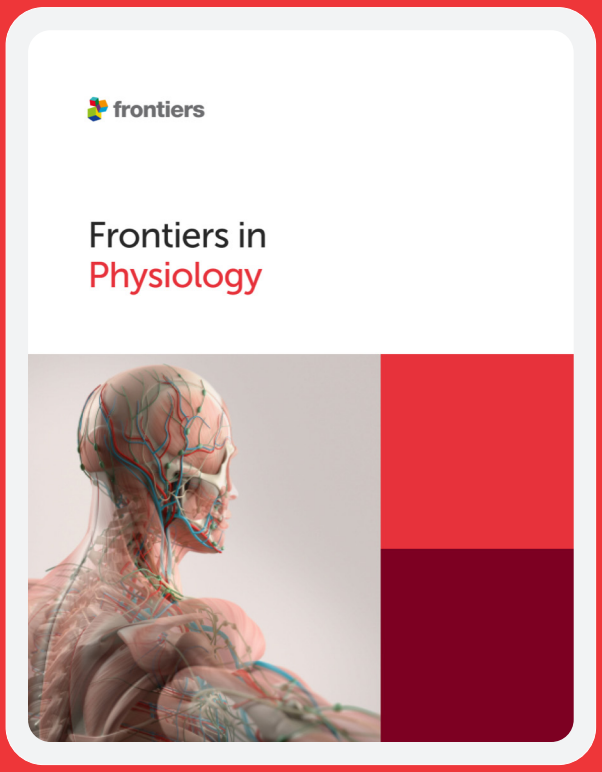

Frontiers

Avenue du Tribunal-Fédéral 34
1005 Lausanne, Switzerland
frontiersin.org

Contact us

+41 (0)21 510 17 00
frontiersin.org/about/contact